

Microstrip Lines and Slotlines

Second Edition

K.C. Gupta
Ramesh Garg
Inder Bahl
Prakash Bhartia

Artech House
Boston • London

Library of Congress Cataloging-in-Publication Data

Microstrip lines and slotlines/K.C. Gupta ... [et al.]. — 2nd ed.

p. cm.

Previous ed. catalogued under: Gupta, K.C.

Includes bibliographical references and index.

ISBN 0-89006-766-X (alk. paper)

1. Strip transmission lines. 2. Microwave transmission lines. 3. Microwave integrated circuits. I. Gupta, K.C.

TK7876.G79 1996

621.381'331—dc20

95-51852

CIP

British Library Cataloguing in Publication Data

Microstrip lines and slotlines. — 2nd ed.

1. Strip transmission lines 2. Microwave circuits I. Gupta, K.C. (Kuldip C.)

621.3'8132

ISBN 0-89006-766-X

Cover design by Dutton & Sherman Design.

© 1996 ARTECH HOUSE, INC.

685 Canton Street

Norwood, MA 02062

All rights reserved. Printed and bound in the United States of America. No part of this book may be reproduced or utilized in any form or by any means, electronic or mechanical, including photocopying, recording, or by any information storage and retrieval system, without permission in writing from the publisher.

All terms mentioned in this book that are known to be trademarks or service marks have been appropriately capitalized. Artech House cannot attest to the accuracy of this information. Use of a term in this book should not be regarded as affecting the validity of any trademark or service mark.

International Standard Book Number: 0-89006-766-X

Library of Congress Catalog Card Number: 95-51852

10 9 8 7 6 5 4 3

Contents

Preface to the Second Edition	xi
Preface to the First Edition	xv
Chapter 1 Microstrip Lines I: Quasi-Static Analyses, Dispersion Models, and Measurements	1
1.1 Introduction	1
1.1.1 Planar Transmission Structures	1
1.1.2 Microstrip Field Configuration	2
1.1.3 Methods of Microstrip Analysis	5
1.2 Quasi-Static Analyses of a Microstrip	6
1.2.1 Modified Conformal Transformation Method	6
1.2.2 Finite Difference Method	12
1.2.3 Integral Equation Method	14
1.2.4 Variational Method in the Fourier Transform Domain	15
1.2.5 Segmentation and Boundary Element Method (SBEM)	18
1.3 Microstrip Dispersion Models	23
1.3.1 Coupled TEM Mode and TM Mode Model	24
1.3.2 An Empirical Relation	24
1.3.3 Dielectric-Loaded Ridged Waveguide Model	25
1.3.4 Empirical Formulae for Broad Frequency Range	27
1.3.5 Planar Waveguide Model	29
1.3.6 Some Comments	32
1.4 Microstrip Transitions	33
1.4.1 Coaxial-to-Microstrip Transition	34
1.4.2 Waveguide-to-Microstrip Transition	37

1.5	Microstrip Measurements	43
1.5.1	Substrate Dielectric Constant	45
1.5.2	Characteristic Impedance	49
1.5.3	Phase Velocity or Effective Dielectric Constant	50
1.5.4	Attenuation Constant	54
	References	56
Chapter 2	Microstrip Lines II:	
	Fullwave Analyses, Design Considerations, and Applications	61
2.1	Methods of Fullwave Analysis	61
2.2	Analysis of an Open Microstrip	63
2.2.1	Integral Equation Method in the Space Domain	64
2.2.2	Galerkin's Method in the Spectral Domain	66
2.2.3	Discussion of Results	68
2.3	Analysis of an Enclosed Microstrip	71
2.3.1	Integral Equation Methods	71
2.3.2	Finite Difference Method	76
2.3.3	Discussion of Results	79
2.4	Design Considerations	83
2.4.1	Microstrip Losses	83
2.4.2	Power Handling Capability	87
2.4.3	Effect of Tolerances	95
2.4.4	Effect of Dielectric Anisotropy	98
2.4.5	Design Equations	102
2.4.6	Frequency Range of Operation	111
2.5	Other Types of Microstrip Lines	115
2.5.1	Suspended and Inverted Microstrip Lines	115
2.5.2	Multilayered Dielectric Microstrip	117
2.5.3	Thin Film Microstrip (TFM)	118
2.5.4	Valley Microstrip Lines	122
2.6	Microstrip Applications	122
2.6.1	Lumped Elements	126
2.6.2	Passive Components	135
2.6.3	Active Components	138
2.6.4	Packages and Assemblies	143
2.6.5	Superconducting Microstrip Circuits	145
	References	152
Chapter 3	Microstrip Discontinuities I:	
	Quasi-Static Analysis and Characterization	159
3.1	Introduction	159
3.2	Discontinuity Capacitance Evaluation	161
3.2.1	Matrix Inversion Method	161
3.2.2	Variational Method	167

3.2.3	Galerkin's Method in the Fourier Transform Domain	171
3.2.4	Use of Line Sources With Charge Reversal	173
3.3	Discontinuity Inductance Evaluation	175
3.4	Characterization of Various Discontinuities	179
3.4.1	Open Ends	180
3.4.2	Gaps in a Microstrip	183
3.4.3	Steps in Width	189
3.4.4	Bends	194
3.4.5	T-Junctions	196
3.4.6	Cross Junctions	200
3.4.7	Notch	204
3.5	Compensated Microstrip Discontinuities	204
3.5.1	Step in Width	205
3.5.2	Bends	205
3.5.3	T-Junction	208
	References	210
Chapter 4	Microstrip Discontinuities II:	
	Fullwave Analysis and Measurements	213
4.1	Planar Waveguide Analysis	213
4.1.1	Discontinuity Characterization	213
4.1.2	Compensation of Discontinuity Reactances	234
4.1.3	Radiation and Parasitic Coupling	234
4.2	Fullwave Analysis of Discontinuities	245
4.2.1	Galerkin's Method in the Spectral Domain	246
4.2.2	Integral Equation Solution in the Space Domain	249
4.2.3	Time Domain Methods for Microstrip Discontinuity Characterization	250
4.3	Discontinuity Measurements	255
4.3.1	Linear Resonator Method	256
4.3.2	Ring Resonator Method	260
4.3.3	Scattering Parameters Measurement Method	263
	References	266
Chapter 5	Slotlines	269
5.1	Introduction	269
5.2	Slotline Analysis	271
5.2.1	Approximate Analysis	271
5.2.2	Transverse Resonance Method	274
5.2.3	Galerkin's Method in the Spectral Domain	277
5.3	Design Considerations	282
5.3.1	Closed-Form Expressions	282
5.3.2	Effect of Metal Thickness	286

5.3.3	Effect of Tolerances	287
5.3.4	Losses in Slotline	287
5.4	Slotline Discontinuities	292
5.4.1	Short End	292
5.4.2	Open End	294
5.5	Other Slotline Configurations	295
5.5.1	Coupled Microstrip-Slotline	295
5.5.2	Conductor-Backed Slotline	297
5.5.3	Conductor-Backed Slotline with a Superstrate	300
5.6	Slotline Transitions	302
5.6.1	Coaxial-to-Slotline Transition	302
5.6.2	Microstrip-to-Slotline Cross-Junction Transition	305
5.7	Slotline Applications	313
5.7.1	Circuits Using T-Junctions	313
5.7.2	Circuits Using Wideband 180° Phase Shift	324
5.7.3	Hybrid/de Ronde's Branchline Couplers	327
5.7.4	Other Types of Slotline Circuits	334
References		334
Appendix 5.A:	Susceptance Calculation for the Transverse Resonance Method	337
Appendix 5.B:	Sensitivity Expressions for Slotline Impedance and Wavelength	338
Chapter 6 Finlines		341
6.1	Introduction	341
6.2	Analysis of Finlines	344
6.2.1	Transverse Resonance Method	344
6.2.2	Galerkin's Method in the Spectral Domain	346
6.3	Design Considerations	349
6.3.1	Closed-Form Solutions	349
6.3.2	LSE-Mode Dispersion Model	356
6.3.3	Synthesis Equations	358
6.3.4	Conductor Loss in Finlines	360
6.4	Transitions	360
6.4.1	Finline-to-Waveguide Taper Transitions	360
6.4.2	Finline-to-Microstrip Taper Transitions	364
References		369
Appendix 6.A:	Susceptance Expression for the Unilateral Finline	371
Chapter 7 Coplanar Lines: Coplanar Waveguide and Coplanar Strips		375
7.1	Introduction	375
7.2	Analysis	379
7.2.1	Quasi-Static CPW Analysis Based on the Conformal Mapping Method	379

7.2.2	Quasi-Static Analysis of Coplanar Strips (CPS)	400
7.2.3	Fullwave Analysis	405
7.3	Design Considerations	411
7.3.1	Design Equations	411
7.3.2	Dispersion	412
7.3.3	Effect of Metallization Thickness	414
7.4	Losses	415
7.4.1	Dielectric Loss	415
7.4.2	Conductor Loss	417
7.4.3	Radiation and Surface Wave Losses	422
7.5	Effect of Tolerances	426
7.6	Comparison With Microstrip Line and Slotline	430
7.7	Transitions	432
7.7.1	Coax-to-CPW Transitions	433
7.7.2	Microstrip-to-CPW Transitions	434
7.7.3	Slotline-to-CPW Transitions	436
7.7.4	CPW-to-CPS Transition	439
7.7.5	CPS-to-Slotline Transitions	440
7.8	Discontinuities in Coplanar Waveguide	441
7.9	Coplanar Line Circuits	443
7.9.1	Circuits With Series and Shunt Reactances in CPW	443
7.9.2	Circuits Using Slotline-CPW Junctions	446
	References	451
Chapter 8	Coupled Microstrip Lines	457
8.1	Introduction	457
8.2	General Analysis of Coupled Lines	458
8.2.1	Methods of Analysis	458
8.2.2	Coupled Mode Approach	460
8.2.3	Even- and Odd-Mode Approach	464
8.3	Characteristics of Coupled Microstrip Lines	467
8.3.1	Quasi-Static Analysis	467
8.3.2	Fullwave Analysis	475
8.3.3	Dispersion Models	483
8.4	Measurements on Coupled Microstrip Lines	487
8.4.1	Impedance Measurements	487
8.4.2	Phase Constant Measurements	488
8.5	Design Considerations for Coupled Microstrip Lines	490
8.5.1	Design Equations	490
8.5.2	Losses	498
8.5.3	Effect of Fabrication Tolerances	502

8.5.4	Coupled Microstrip Lines With Dielectric Overlays	504
8.5.5	Effect of Dielectric Anisotropy	507
8.6	Coupled Multiconductor Microstrip Lines	508
8.7	Discontinuities in Coupled Microstrip Lines	512
8.7.1	Network Model	513
8.7.2	Open-End Discontinuity	516
	References	517
	About the Authors	521
	Index	525

Preface to the Second Edition

Since the first edition of this book was published in 1979, the technology of microwave integrated circuits has matured. Today monolithic microwave integrated circuits (MMICs) with designs based on microwave transistors (including MESFETs, HEMTs, and HBTs) and microstrip line (and some coplanar waveguide) technologies find applications in several telecommunications systems, radars, electronic warfare, microwave instruments, and satellite communications. Extensive references to the first edition of this book in the research and technical development papers published in professional journals around the world have led us to believe that *Microstrip Lines and Slotlines* has contributed toward these technological developments over the last decade and a half. During the last couple of years, since the previous edition of the book went out of print, there have been a number of inquiries for a sequel and an update to the original well received first edition.

As with the first edition, this book is primarily intended for design engineers and research and development specialists who need to use planar transmission structures such as microstrips and coplanar waveguides in RF, microwave and millimeter-wave circuits, and antenna systems. The book is also likely to be helpful to professors and students in advanced undergraduate and graduate electronics and telecommunications engineering courses.

The extensive revisions incorporated in this edition are based on the authors' own work and the extensive results that have been reported by others in journals and at conferences around the world over the last sixteen years. To augment the expertise of the three previous authors, we expanded the contributing authors to include Dr. Bhartia from the Defence Research Establishment Atlantic, Canada. Chapter 6 on finlines is largely his contribution.

Revisions in Chapter One include updated formulas, the segmentation and boundary element method for microstrip analysis, and a new section on microstrip transitions. The increase in the number of references (for this chapter) from 35

to 88 is an indication of the extensive developments reported in this area. Chapter Two has been revised to include two new sections entitled "Other Types of Microstrip Lines" and "Microstrip Applications." Additionally, it offers an extensive update of the information useful for design. In Chapter Two, the number of references has increased from 60 to 140.

As before, Chapters Three and Four deal with the characterization of microstrip discontinuities. The significance of these discontinuities in circuit design is now well established, and most of the available microwave circuit simulators incorporate discontinuities' models. However, a need for improvements and extensions persists. The major revision in Chapter Three is the updating of the expressions for characterizations of various discontinuities reported in Section 3.4. A new section on "Compensated Microstrip Discontinuities" has been added. The number of references has increased from 25 to 42. Chapter Four has been restructured with a complete section on "Planar Analysis of Microstrip Discontinuities," which includes subsections entitled "Compensation of Discontinuities Reactances" and "Radiation and Parasitic Coupling". In addition, the topic of "Time-Domain Methods for Discontinuity Characterization" has been added to the section on "Fullwave Analysis," and "Scattering Parameters Measurement Method" has been added to the section on "Discontinuity Measurements." The number of references has increased from 13 to 48.

The two chapters on Slotlines contained in the first edition of this book are now combined in Chapter Five. This is indicative of the fact that slotline circuits have not emerged to be as popular as was anticipated sixteen years ago. Revisions include closed-form expressions for design on low dielectric constant substrates and expanded discussions on losses, discontinuities, microstrip-slot junctions, and T-junction circuits. A new section on "Other Slotline Configurations" has been added. Fifty-five references are listed (compared to 27 in the two chapters of the first edition).

Chapter Six, a new chapter on finlines, discusses analysis methods, design considerations, and transitions to waveguides and microstrips. For readers desiring more detailed information, 49 references are included.

Chapter Seven on coplanar lines emphasizes the increasingly popular coplanar waveguide (CPW) structure. This chapter has gone through the most extensive revision. Sections on "Quasi-Static Analyses" are expanded to include several additional configurations; efficient basis functions are included in the "Fullwave Analysis" section; and an expression for dispersion is included in the section on "Design Considerations." The section on losses has an expanded discussion on conductor loss and a new subsection on "Radiation and Surface Wave Losses." Throughout the chapter additional graphs and data are provided for GaAs because of its importance in MMICs. Two new sections on transitions and discontinuities have been added. The number of references has increased from 21 to 122.

The last chapter on Coupled Microstrip Lines has expanded discussions on fullwave analysis, dispersion models, design equations, and losses. Two new sections

on “Multiconductor Transmission Lines” and “Discontinuities in Coupled Micro-strip Lines” have been added. Again, the number of references has increased from 45 to 81.

We believe that this thoroughly revised second edition contains the most up-to-date body of knowledge on this topic. We hope that *Microstrip Lines and Slotlines* will be helpful to design and research engineers in continued development and applications of planar transmission line techniques.

The authors express their appreciation to colleagues in several organizations and a number of publishing houses for copyright permissions for figures and other material from their works. These items are duly acknowledged in the text. Thanks are also due to our colleagues in the authors’ organizations. In particular, the assistance of Helen Frey at University of Colorado, Linda Blankenship at ITT GaAs Technology Center, and Bob Sibley at Defence Research Establishment Atlantic, Canada, is thankfully acknowledged. Finally, we would like to record the support and cooperation of the staff at Artech House, including Mark Walsh, Kimberly Collignon, and Kate Feininger.

K.C. Gupta
Ramesh Garg
Inder Bahl
Prakash Bhartia

Preface to the First Edition

Microwave integrated circuits use planar transmission structures like microstrip lines as the basic building block. In addition, slotlines and coplanar lines are also used. When used along with microstrip, these lines add to the flexibility of circuit design and improve the performance for some circuit functions. All these transmission lines have planar configuration, and their characteristics are controlled by dimensions in a single plane. Theory and design of these lines have been reported in numerous articles widely scattered in technical literature, but there is no comprehensive description of these lines available at one place. In particular the design information is not readily available. *Microstrip Lines and Slotlines* intends to present a detailed account of these lines.

This book describes analyses and design of microstrip lines and slotlines, coplanar waveguides, coplanar strips and various coupled lines. The features discussed include quasi-static and fullwave analyses, design considerations and measurement procedures.

The present book is intended for graduate students, research workers and design engineers in the microwave circuits area. The book can be used as a supplementary text for a course on mathematical/numerical methods in electromagnetics. Sections on design considerations (2.4, 3.4, 5.3, 7.3 and 8.5) could be used directly for the design of various lines without going into details of analysis.

The preparation of *Microstrip Lines and Slotlines* started with a set of lecture notes prepared for a graduate course on 'Microwave Integrated Circuits Design' taught at the University of Waterloo (Canada) in Fall 1975. These notes were revised for a series of seminars on 'Lignes Microruban' delivered at l'Ecole Polytechnique Federale de Lausanne (Switzerland) in the summer of 1976. A revised version of the notes was used for a similar series of seminars at Technical University of Denmark, Lyngby (Denmark) in Fall 1976. This material has also been used for a graduate course on this topic at the Indian Institute of Technology Kanpur

(I.I.T./K.) in Fall 1977. Work on the design of microwave integrated circuits at the Advanced Centre for Electronic Systems (I.I.T./K.) has contributed considerably to the material in the book, especially the sections on design considerations.

The text is divided into eight chapters. The first two chapters describe analysis and design of microstrip lines. There are two chapters on microstrip discontinuities. These are followed by two chapters on slotlines and a chapter on coplanar lines. The eighth chapter deals with various types of coupled lines.

For all these transmission structures and for microstrip discontinuities as well, quasi-static and fullwave analyses are discussed. There are sections on measurement of the characteristics of microstrip lines, microstrip discontinuities and coupled lines. Detailed design considerations for various lines are presented. These include design equations, effects of tolerances and enclosures, losses, etc. Special circuit functions that can be achieved by using slotlines and coplanar waveguides are discussed. A comparison of the characteristics of various lines is given in Chapter 7.

Several discussions with colleagues at the University of Waterloo, l'Ecole Polytechnique Federale de Lausanne and the Technical University of Denmark during the early stages of the book are gratefully acknowledged. Discussions with several colleagues at I.I.T. Kanpur are thankfully appreciated. Facilities extended by the Department of Electrical Engineering and the Advanced Centre for Electronic Systems at I.I.T./K. are acknowledged. The typing of manuscript has been handled efficiently by Mr. C.M. Abraham, and the artwork has been done by Mr. R.K. Bajpai.

K.C. Gupta
Ramesh Garg
I.J. Bahl

CHAPTER 1

Microstrip Lines I: Quasi-Static Analyses, Dispersion Models, and Measurements

1.1 INTRODUCTION

1.1.1 Planar Transmission Structures

One of the principal requirements for a transmission structure to be suitable as a circuit element in *microwave integrated circuits* (MICs) is that the structure should be “planar” in configuration. A planar configuration implies that the characteristics of the element can be determined by the dimensions in a single plane. For example, the width of a microstrip line on a dielectric substrate can be adjusted to control its impedance. When the impedance can be controlled by dimensions in a single plane, the circuit fabrication can be conveniently carried out by techniques of photolithography and photoetching of thin films. Use of these techniques at microwave and millimeter wave frequencies has led to the development of hybrid and monolithic MICs. Microwave integrated circuits have been widely discussed in the literature [1–6].

There are several transmission structures that satisfy the requirement of being planar. The most common of these are: (i) microstrip, (ii) coplanar waveguide, (iii) slotline, and (iv) coplanar strips. Cross-sectional views of these lines are shown in Figure 1.1. A microstrip line is the most popular of these transmission structures, mainly due to the fact that the mode of propagation in a microstrip is almost transverse electro magnetic (TEM). This allows an easy approximate analysis and yields wide band circuits. Also simple transitions to coaxial circuits are feasible. Chapters 1 and 2 present various aspects of microstrip analysis and design. Slotline,

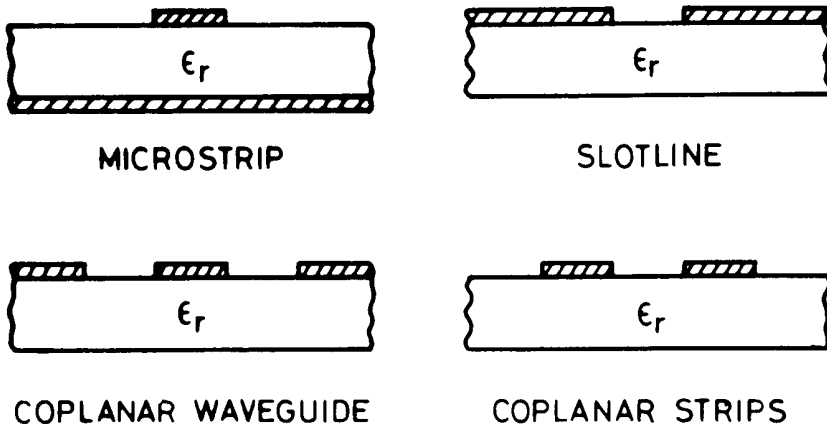


Figure 1.1 Planar transmission lines used in microwave integrated circuits.

coplanar strips, and coplanar waveguide are discussed in later chapters. A comparison of the characteristics of these lines is given in Section 7.6.

There are several variations of the microstrip configuration that have also been suggested for use in MICs. These include the inverted microstrip, suspended microstrip, microstrip with overlay, strip dielectric waveguide, and inverted strip dielectric waveguide. Cross-sectional views of these structures are given in Figure 1.2, and their analysis is available in references [7–10].

Another very commonly used transmission line that resembles a microstrip line is the stripline [11,12], shown in Figure 1.3. This is also called a triplate line. Most of the basic circuit design ideas implemented in a stripline are also applicable to microstrip line circuits.

1.1.2 Microstrip Field Configuration

A microstrip is a two-conductor transmission line that can be considered to have evolved conceptually from a two-wire line as shown in Figure 1.4. Transformation from (a) to (b) is essentially a change in the shape of the conductors, whereas that from (b) to (c) involves placing a conducting sheet at the plane of symmetry. The final configuration (d) is obtained by inserting a thin dielectric slab between the two conductors. As a consequence of the last step, the dielectric medium of the transmission line becomes inhomogeneous.

Microstrip lines differ considerably from other transmission lines. For example, comparing it with a stripline, one observes that the microstrip structure is open at the top. This open configuration makes a microstrip very convenient for use in MICs where discrete lumped devices (active or passive) must be mounted in the

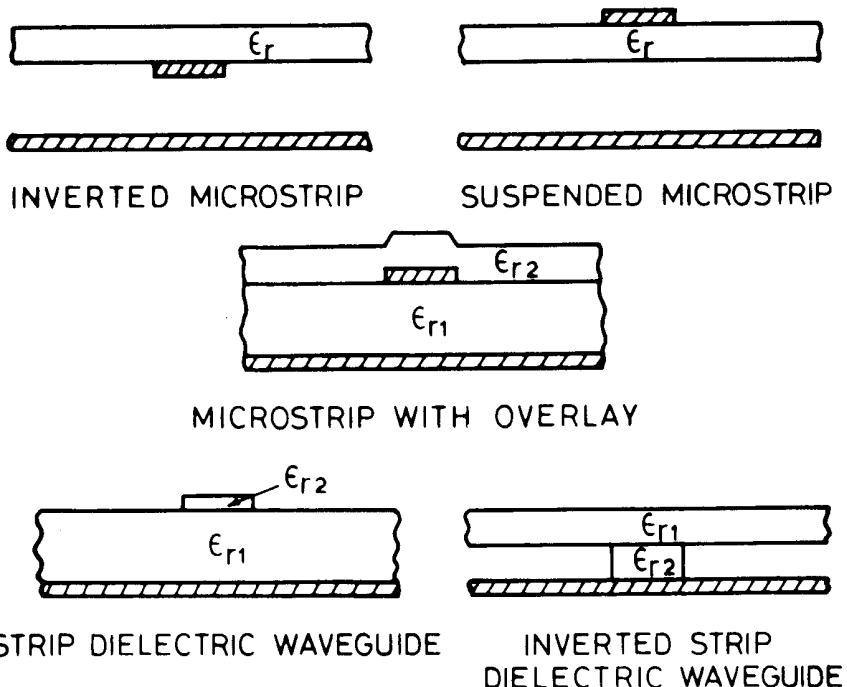


Figure 1.2 Various transmission lines derived from a microstrip.

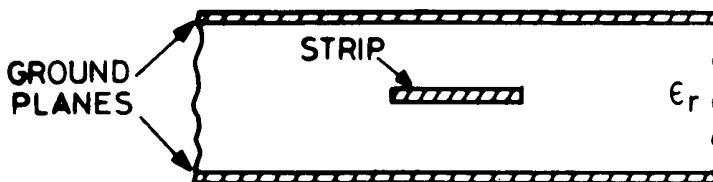


Figure 1.3 Stripline configuration.

circuit. Also, small adjustments or tuning can possibly be incorporated after the circuit has been fabricated. However, along with these advantages, the open structure of a microstrip causes some complications in microstrip analysis and design. This is due to the fact that the presence of the dielectric-air interface modifies the mode of propagation in a microstrip to a non-TEM hybrid mode (as compared to a pure TEM-mode in a stripline).

Simple arguments based on the known quasi-static field distribution of the microstrip and Maxwell's equations can be presented to show that a microstrip

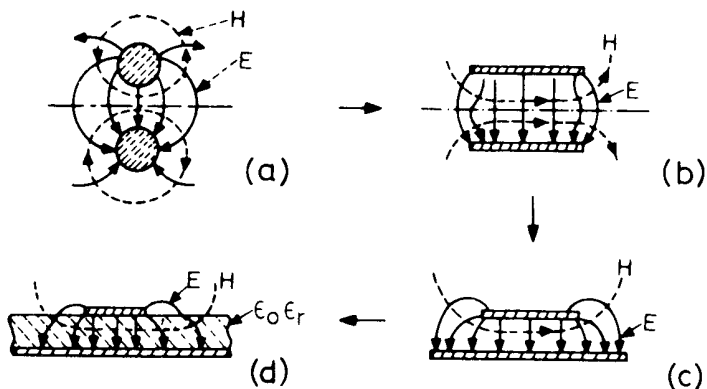


Figure 1.4 Conceptual evolution of a microstrip from a two-wire line.

structure cannot support a pure TEM wave. Continuity of the tangential component of the electric field along a dielectric-air interface (see Figure 1.5) yields

$$E_x|_d = E_x|_a \quad (1.1)$$

where subscripts d and a refer to the dielectric and the air side of the interface, respectively. Using Maxwell's equations, one may thus write

$$(\nabla \times \mathbf{H})_x|_d = \epsilon_r (\nabla \times \mathbf{H})_x|_a \quad (1.2)$$

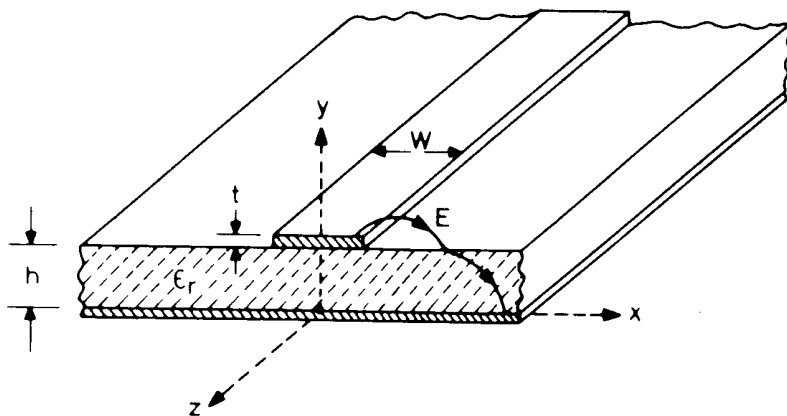


Figure 1.5 Microstrip configuration.

Expanding (1.2) and using the continuity of the normal component of the magnetic flux, we obtain (for the case when $\mu_r = 1$)

$$\epsilon_r \frac{\partial H_z}{\partial y}|_a - \frac{\partial H_z}{\partial y}|_d = (\epsilon_r - 1) \frac{\partial H_y}{\partial z} \quad (1.3)$$

As ϵ_r is not equal to unity and $H_y \neq 0$, (1.3) implies that the expression on the left-hand side should be a nonzero quantity, which can only be true if H_z is nonzero. Thus we note that for Maxwell's equations to hold good for the configuration of Figure 1.5, the longitudinal component of \mathbf{H} must exist.

Similar arguments can be advanced to show that E_z , the longitudinal component of the electric field, is also a nonzero quantity. It may be pointed out that it is only the fringing components E_x and H_x at the dielectric-air interface that lead to the non-TEM nature of the microstrip mode. Since these fringing field components are much smaller than the main field (within the substrate below the strip), the departure from the TEM behavior should be small. This conjecture is supported by the results based on a rigorous fullwave analysis of the microstrip, which will be discussed later in the book.

1.1.3 Methods of Microstrip Analysis

As with any other transmission line structure, the analysis methods for a microstrip line are aimed at determining the characteristic impedance and propagation constant (phase velocity and attenuation constant). The various methods of microstrip analysis may be divided into two main groups as shown in Figure 1.6. In the first group, which comprises quasi-static methods, the nature of the mode of propagation is considered to be pure TEM and the microstrip characteristics are calculated

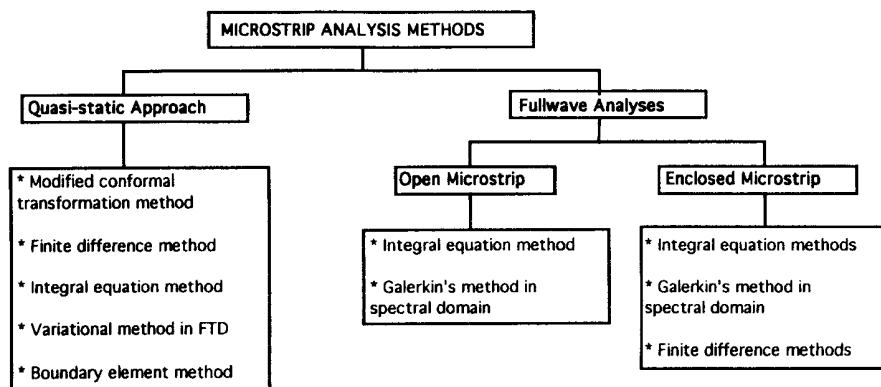


Figure 1.6 Various methods of microstrip analysis.

from the electrostatic capacitance of the structure. It is found that this analysis is adequate for designing circuits at lower frequencies (below X-band) where the strip width and the substrate thickness are much smaller than the wavelength in the dielectric material. The methods in the second group take into account the hybrid nature of the mode of propagation. The techniques followed for fullwave analysis are more rigorous and analytically complex. An important outcome of the fullwave analysis is information about the dispersive nature of the microstrip line. This includes variation of characteristic impedance, Z_0 , and phase velocity (or effective dielectric constant, ϵ_{re}) with frequency. As a fullwave analysis becomes fairly complicated, several quasi-empirical methods known as “dispersion models” have been developed for finding variations of Z_0 and ϵ_{re} with frequency.

The methods of quasi-static analysis are discussed in this chapter. Microstrip dispersion models, transitions, and measurement techniques are also included. Techniques of fullwave analysis are described in the next chapter.

1.2 QUASI-STATIC ANALYSES OF A MICROSTRIP

In quasi-static analyses, the mode of wave propagation in a microstrip is assumed to be pure TEM. Transmission characteristics are then calculated from the values of two capacitances, one (C_a) for a unit length of the microstrip configuration with the dielectric substrate replaced by air, and the other (C) for a unit length of the microstrip with the dielectric substrate present. Values of characteristic impedance Z_{0m} and the phase constant β can be written in terms of these capacitances as

$$Z_{0m} = Z_{0m}^a (C_a/C)^{1/2} \quad (1.4)$$

and

$$\beta = \beta_0 (C/C_a)^{1/2} \quad (1.5)$$

where $Z_{0m}^a = 1/(cC_a)$ and $\beta_0 = \omega/c$, where c is the velocity of electromagnetic waves in free space. There are various methods available for calculating the electrostatic capacitances C_a and C . Five of these are listed in Figure 1.6 and will be discussed in the following subsections.

1.2.1 Modified Conformal Transformation Method

An exact conformal transformation for the impedance of a zero-thickness, homogeneous dielectric microstrip has been given by Schneider [9]. The transformation from the microstrip (z -plane) to a parallel plate capacitor (z' -plane) is expressed in terms of the logarithmic derivative of the theta function θ_4 and a parameter $\kappa = K'/K$ as

$$z = -\frac{2hK}{\pi} \frac{\partial}{\partial z'} \ell_n [\theta_4(z', \kappa)] \quad (1.6)$$

where $K = K(m)$ and $K' = K'(m)$ are complete elliptic integrals of the first kind with modulus m . The characteristic impedance Z_{0m} of the microstrip of width W and height h (and $t = 0$) is obtained by solving the equations

$$\frac{W}{h} = \frac{2}{\pi} \frac{\partial}{\partial \zeta} \ell_n [\theta_4(\zeta, \kappa)] \quad (1.7)$$

$$dn^2(2K\zeta) = E/K \quad (1.8)$$

$$Z_{0m}^a = \frac{1}{2} (\mu_0 / \epsilon_0)^{1/2} K'/K \quad (1.9)$$

where μ_0 and ϵ_0 are the free-space permeability and permittivity constants, respectively, and Z_{0m}^a is the characteristic impedance of the microstrip with the dielectric substrate replaced by air. The function $E = E(m)$ is the complete elliptic integral of the second kind and dn is the Jacobian elliptic function. The logarithmic derivative of the theta function is given by the (rapidly converging) series expansion

$$\frac{\partial}{\partial \zeta} \ell_n [\theta_4(\zeta, \kappa)] = 4\pi \sum_{n=1}^{\infty} \frac{\sin(2n\pi\zeta)}{\exp(n\pi\kappa) - \exp(-n\pi\kappa)} \quad (1.10)$$

Equations (1.7) to (1.9) can be used for the design of microstrip lines as follows. For a given characteristic impedance Z_{0m}^a , K'/K is calculated from (1.9). The modulus m for the elliptic functions is found by looking up tables for K'/K . Also E and K are determined using this value of m . The solution of (1.8) now gives the value of ζ . For known ζ and $\kappa (= K'/K)$, W/h for the microstrip is calculated from (1.7) and (1.10). A practical solution to this set of equations is obtained with the help of a computer or with numerical tables. The conformal transformation given by Schneider yields Z_{0m}^a , the characteristic impedance for a homogeneously filled microstrip line. It is perhaps because of this limitation that the above method is not used very frequently.

The most widely used technique for microstrip analysis was introduced by Wheeler [13,14] in 1964–65. The method uses a conformal transformation for the evaluation of C_s and introduces a concept of effective dielectric constant for the evaluation of C . The conformal transformation selected is such that the resulting expressions are explicit and can be written in terms of simple functions. The transformation used for the wide strip ($W/h > 2$) is

$$z = j\pi + d \tanh(z'/2) - z' \quad (1.11)$$

The variable z refers to the microstrip plane (see Figure 1.7) and z' is the plane in which the microstrip configuration transforms into a parallel plate capacitor configuration. The parameter d is approximately equal to g' of Figure 1.7(b). The dielectric-air boundary of the microstrip substrate is transformed into an elliptical-looking curve ba' as shown in Figure 1.7(b). To evaluate the capacitance C , it is necessary to introduce approximations in order to modify the dielectric-air boundary. The curved dielectric-air boundary of Figure 1.7(b) is approximated by a rectangular boundary as shown in Figure 1.7(c). The area ($\pi s'$) over the curve is written in terms of a “parallel area” $\pi s''$ and a “series area” $\pi(s' - s'')$. These series and parallel areas can be expressed in terms of an equivalent parallel area s given by (Figure 1.7(d))

$$s = s'' + (s' - s'')/\epsilon_r \quad (1.12)$$

The effective filling fraction can then be written as

$$q = (g' - a' + s)/g' \quad (1.13)$$

The effective dielectric constant is related to the effective filling fraction as

$$\epsilon_{re} = (1 - q) + q \epsilon_r \quad (1.14)$$

Different expressions for ϵ_{re} are derived for a wide microstrip ($W/h > 2$) and for a narrow microstrip ($W/h < 2$) because of the different approximations used in the two cases. For wide strips [15]

$$q = 1 - \frac{1}{d} \ell_n \frac{d+c}{d-c} + \frac{0.732}{d\epsilon_r} \left[\ell_n \frac{d+c}{d-c} - \cosh^{-1}(0.358d + 0.595) \right] \\ + \frac{\epsilon_r - 1}{d\epsilon_r} \left[0.386 - \frac{1}{2(d-1)} \right] \quad (1.15)$$

where $d = 1 + \sqrt{1 + c^2}$ and c is found implicitly from

$$\frac{\pi}{2} \frac{W}{h} = c - \sinh^{-1} c \quad (1.16)$$

and for narrow strips

$$\epsilon_{re} = \frac{\epsilon_r + 1}{2} + \frac{\epsilon_r - 1}{2} \frac{\ell_n(\pi/2) + (1/\epsilon_r) \ell_n(4/\pi)}{\ell_n(8h/W)} \quad (1.17)$$

Formulas for the impedance of microstrip lines can be derived from these results. It is an advantage of the transformation selected by Wheeler that the impedance

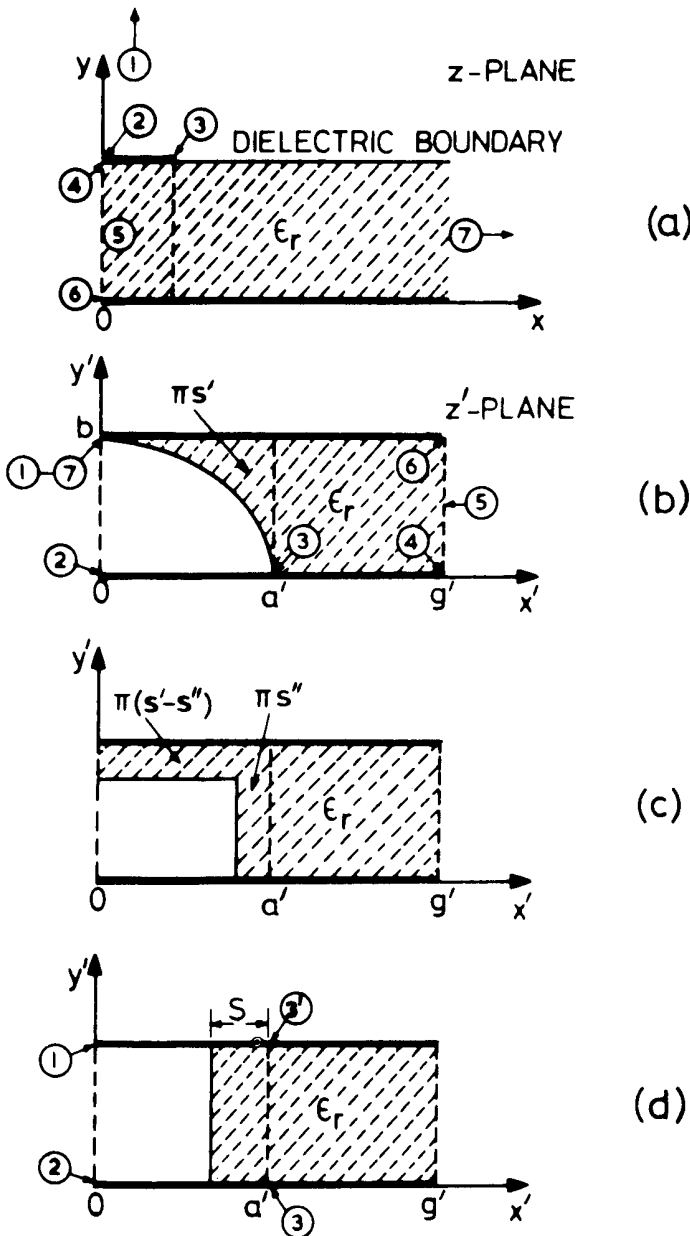


Figure 1.7 Conformal transformation and evaluation of the effective dielectric constant (from [14], © 1965 IEEE. Reprinted with permission.).

formulas can be written explicitly both for analysis (Z_{0m} in terms of W/h and ϵ_r) and for synthesis (W/h in terms of Z_{0m} and ϵ_r). These relations are listed below. For wide strips ($W/h > 2$)

$$Z_{0m} = \frac{377}{(\epsilon_r)^{1/2}} \left[\frac{W}{h} + 0.883 + \frac{\epsilon_r + 1}{\pi \epsilon_r} \left\{ \ell_n \left(\frac{W}{2h} + 0.94 \right) + 1.451 \right\} + 0.165 \frac{\epsilon_r - 1}{\epsilon_r^2} \right]^{-1} \quad (1.18)$$

and for narrow strips ($W/h < 2$)

$$Z_{0m} = \frac{377}{2\pi\{(\epsilon_r + 1)/2\}^{1/2}} \left[\ell_n \left(\frac{8h}{W} \right) + \frac{1}{8} \left(\frac{W}{2h} \right)^2 - \frac{1}{2} \frac{\epsilon_r - 1}{\epsilon_r + 1} \left\{ \ell_n \frac{\pi}{2} + \frac{1}{\epsilon_r} \ell_n \frac{4}{\pi} \right\} \right] \quad (1.19)$$

where W is the strip width and h is the thickness of the substrate. Expressions giving the strip width for a desired impedance may be written [2] for wide strips ($W/h > 2$) as

$$\begin{aligned} \frac{W}{2h} \pi &= \frac{377\pi}{2(\epsilon_r)^{1/2} Z_{0m}} - 1 - \ell_n \left\{ \frac{377\pi}{(\epsilon_r)^{1/2} Z_{0m}} - 1 \right\} \\ &\quad + \frac{\epsilon_r - 1}{2\epsilon_r} \left[\ell_n \left\{ \frac{377\pi}{2(\epsilon_r)^{1/2} Z_{0m}} - 1 \right\} + 0.293 - \frac{0.517}{\epsilon_r} \right] \end{aligned} \quad (1.20)$$

and for narrow strips ($W/h < 2$) as

$$2h/W = \frac{1}{4} e^{h'} - \frac{1}{2} e^{-h'}$$

where

$$h' = \left(\frac{\epsilon_r + 1}{2} \right)^{1/2} \frac{Z_{0m}}{60} + \frac{\epsilon_r - 1}{\epsilon_r + 1} \left(0.226 + \frac{0.120}{\epsilon_r} \right) \quad (1.21)$$

However, Wheeler's analysis does not lead to closed form expressions for the effective dielectric constant when $W/h \geq 2$. Such expressions have been derived empirically by curve fitting the numerical data and will be discussed in Section 2.4.

Values of the characteristic impedance and effective dielectric constant of a microstrip, based on the method discussed above, may be obtained from Figure 1.8. In this figure, the value of $\sqrt{\epsilon_r}$ is plotted as a function of W/h for various values of the substrate dielectric constant ϵ_r . The variation of the characteristic impedance

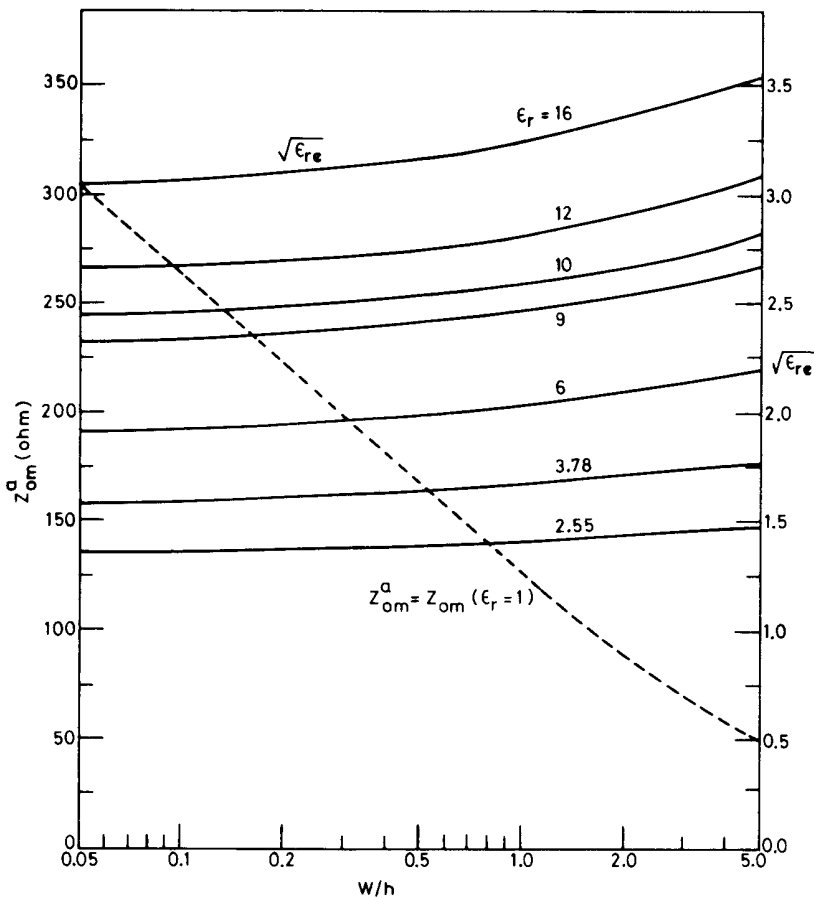


Figure 1.8 Characteristic impedance and effective dielectric constant of microstrip lines calculated using Wheeler's method.

for air microstrip (Z_{0m}^a for $\epsilon_r = 1$) is also shown by a dotted curve. The impedance for any value of ϵ_r can be obtained by dividing Z_{0m}^a by the corresponding value of $\sqrt{\epsilon_{re}}$. It may be seen from Figure 1.8 that the impedance value decreases when the strip width-to-height ratio (W/h) of the substrate is increased because an increase in W (or decrease in h) increases the line capacitance.

Since the wavelength in microstrip λ_m is related to ϵ_{re} by the expression

$$\lambda_m = \frac{\lambda_0}{\sqrt{\epsilon_{re}}} \quad (1.22)$$

we notice from Figure 1.8 that λ_m is a function of W/h and hence of Z_{0m} . This implies that, for example, the length for a quarter wave section of $25\text{-}\Omega$ impedance would be different from that of a section of $100\text{-}\Omega$ impedance (at the same frequency!). This factor must be kept in mind while designing microstrip circuits.

It may be pointed out that in the modified conformal transformation method discussed above, the thickness of the microstrip conductor is ignored and the analysis is restricted to an open microstrip without any enclosure.

The conformal mapping approach for calculating the capacitance has also been extended to the analysis of multilayer microstrip lines [16]. Two types of three-layered structures have been considered: a substrate consisting of two layers of different dielectric constants and a single-layered substrate microstrip structure with a dielectric cover layer. Expressions for filling factors and for effective permittivity for these two cases are available in [16].

1.2.2 Finite Difference Method

Another method for quasi-static analysis of microstrip lines is based on the numerical solution of Laplace's equation in the finite difference form [17]. This method is more suitable for enclosed microstrip lines, and the finite thickness of the microstrip conductor can easily be incorporated into the analysis. Laplace's equation may be written in finite difference form by considering the configuration shown in Figure 1.9. Potentials at the points A, B, C, D in the immediate vicinity of a point P may be written as

$$\phi_A = \phi_P - \frac{\Delta \partial \phi}{\partial x} + \frac{\Delta^2}{2!} \frac{\partial^2 \phi}{\partial x^2} - \frac{\Delta^3}{3!} \frac{\partial^3 \phi}{\partial x^3} + \dots \quad (1.23)$$

$$\phi_B = \phi_P + \frac{\Delta \partial \phi}{\partial x} + \frac{\Delta^2}{2!} \frac{\partial^2 \phi}{\partial x^2} + \frac{\Delta^3}{3!} \frac{\partial^3 \phi}{\partial x^3} + \dots \quad (1.24)$$

$$\phi_C = \phi_P - \frac{\Delta \partial \phi}{\partial y} + \frac{\Delta^2}{2!} \frac{\partial^2 \phi}{\partial y^2} - \frac{\Delta^3}{3!} \frac{\partial^3 \phi}{\partial y^3} + \dots \quad (1.25)$$

$$\phi_D = \phi_P + \frac{\Delta \partial \phi}{\partial y} + \frac{\Delta^2}{2!} \frac{\partial^2 \phi}{\partial y^2} + \frac{\Delta^3}{3!} \frac{\partial^3 \phi}{\partial y^3} + \dots \quad (1.26)$$

When we ignore the fourth- and higher order terms and use $(\partial^2 \phi / \partial x^2 + \partial^2 \phi / \partial y^2) = 0$, the above relations yield

$$\phi_A + \phi_B + \phi_C + \phi_D \approx 4 \phi_P \quad (1.27)$$

The most common method of solving finite difference equation (1.27) is the "relaxation method." In this method one starts with assumed values of ϕ at all the grid points. These values are modified successively as follows:

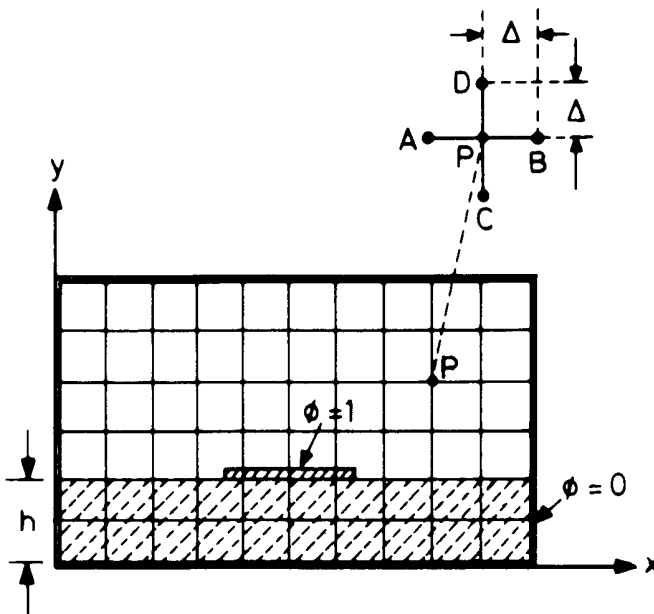


Figure 1.9 Enclosed microstrip configuration for analysis by the finite difference method.

$$\text{New } \phi_p = \text{old } \phi_p - \alpha R_p \quad (1.28)$$

where the “residuals” R_p are given by

$$R_p = \phi_p - (\phi_A + \phi_B + \phi_C + \phi_D)/4 \quad (1.29)$$

This successive “relaxation” is carried out until the differences between the old and new values become less than the allowed error. The speed of convergence of the “relaxation” process is determined by the constant α . Relation (1.29) needs to be modified for points near the dielectric-air boundary and corners. A detailed discussion of the method is given by Green [18]. The solution of Laplace’s equation by the method discussed above yields information about the potential distribution in the microstrip cross-section, from which the field distributions and the charge on the strip can be calculated. We have

$$Q = \epsilon_0 \epsilon_r \oint \mathbf{E}_n \cdot d\mathbf{s} \quad (1.30)$$

where the integral is taken over a surface that encloses the strip conductor. The capacitance is obtained as the ratio of charge to voltage. Again two capacitances C

and C_a are evaluated and the microstrip parameters Z_{0m} and β calculated using (1.4) and (1.5), respectively.

1.2.3 Integral Equation Method

The quasi-static analysis of a microstrip may also be formulated in the form of an integral equation rather than a differential equation. We consider the Poisson equation in terms of a line charge distribution and define a Green's function G as

$$\nabla_t^2 G(x, y; x_0, y_0) = -\frac{1}{\epsilon_0 \epsilon_r} \delta(y - y_0) \delta(x - x_0) \quad (1.31)$$

where subscript t refers to transverse coordinates (x and y) and coordinates x_0, y_0 refer to the source location and x, y to the field point. Thus $G(x, y; x_0, y_0)$ is the potential at (x, y) produced by a line charge of unit magnitude located at (x_0, y_0) . The function G satisfies the boundary and the interface conditions of the microstrip configuration but not the source condition. Using Green's function, an integral equation of the following form can be formulated and solved to determine the charge distribution:

$$\phi(x, y) = \int G(x, y; x_0, y_0) \rho(x_0, y_0) dx_0 \quad (1.32)$$

where ϕ and ρ are the potential and the charge distributions, respectively, and the integration is carried out over the surface of the microstrip conductor at $y_0 = h$. The analysis can be divided into two parts: first, the formulation of a suitable Green's function G , and second, the solution of the integral equation (1.32) by writing it in the form of a matrix equation and carrying out the matrix inversion numerically. The matrix equation corresponding to (1.32) may be written as

$$[\mathbf{v}] = [\mathbf{p}] \cdot [\mathbf{q}] \quad (1.33)$$

where $[\mathbf{v}]$ and $[\mathbf{q}]$ are column matrices representing the potential ϕ and the charge q , respectively, and the matrix $[\mathbf{p}]$ can be recognized as the matrix of Maxwell's potential coefficients. Since the conductors may be presumed to be at known potentials, the matrix $[\mathbf{v}]$ is known and (1.33) may be solved for $[\mathbf{q}]$ by inversion of the matrix $[\mathbf{p}]$. Total charge Q and capacitance C for the microstrip can then be calculated as

$$C = Q/v = \sum_j \sum_k (\mathbf{p}^{-1})_{jk} \quad (1.34)$$

where $(\mathbf{p}^{-1})_{jk}$ is the j th term of the inverse of the $[\mathbf{p}]$ matrix. Green's function G for the microstrip configuration is obtained from the theory of images for a charge

placed in front of a dielectric-air interface and has been described by Sylvester [19]. The method of images is illustrated in Figure 1.10. In this figure, the partial image coefficient K is given by

$$K = (1 - \epsilon_r) / (1 + \epsilon_r) \quad (1.35)$$

The Green's function G for the configuration as shown in Figure 1.10 may be written as [19]

$$\begin{aligned} G(h, x) &= \frac{1}{2\pi(\epsilon_r + 1)\epsilon_0} \\ &\cdot \left\{ \sum_{n=1}^{\infty} K^{n-1} \right. \\ &\cdot \ell_n \left[\left\{ \left(4n^2 + \left(\frac{x - x_0}{h} \right)^2 \right) \left(4n^2 + \left(\frac{x + x_0}{h} \right)^2 \right) \right\} \right] / \\ &\left. \cdot \left\{ \left(4(n-1)^2 + \left(\frac{x - x_0}{h} \right)^2 \right) \left(4(n-1)^2 + \left(\frac{x + x_0}{h} \right)^2 \right) \right\} \right] \end{aligned} \quad (1.36)$$

Since K is negative, (1.36) becomes an alternating series that is convergent and lends itself to the simple estimation of the truncation error. It has been found that for value of ϵ_r between 2 and 20, the number of terms of (1.36) sufficient to ensure convergence to seven significant figures lies between 15 to 150. Green's function for thick conductor microstrip lines has also been reported [19].

1.2.4 Variational Method in the Fourier Transform Domain

The search for microstrip analysis techniques that are computationally more efficient has led to the variational method in the *Fourier transform domain* (FTD). There are two significant features of this method [20]. First, a variational method for calculating the capacitance C from the charge density ρ is used. This avoids the need for an accurate knowledge of the charge density distribution. Second, a major portion of analysis is carried out in FTD with the result that the integral equation for the potential gets replaced by an algebraic product of an approximate $\tilde{\rho}$ and a factor \tilde{g} derived in FTD (see (1.41)).

The variational expression for the capacitance (upper bound) may be written as [20]

$$\frac{1}{C} = \frac{1}{Q^2} \int_s \rho(x) \phi(x, h) dx \quad (1.37)$$

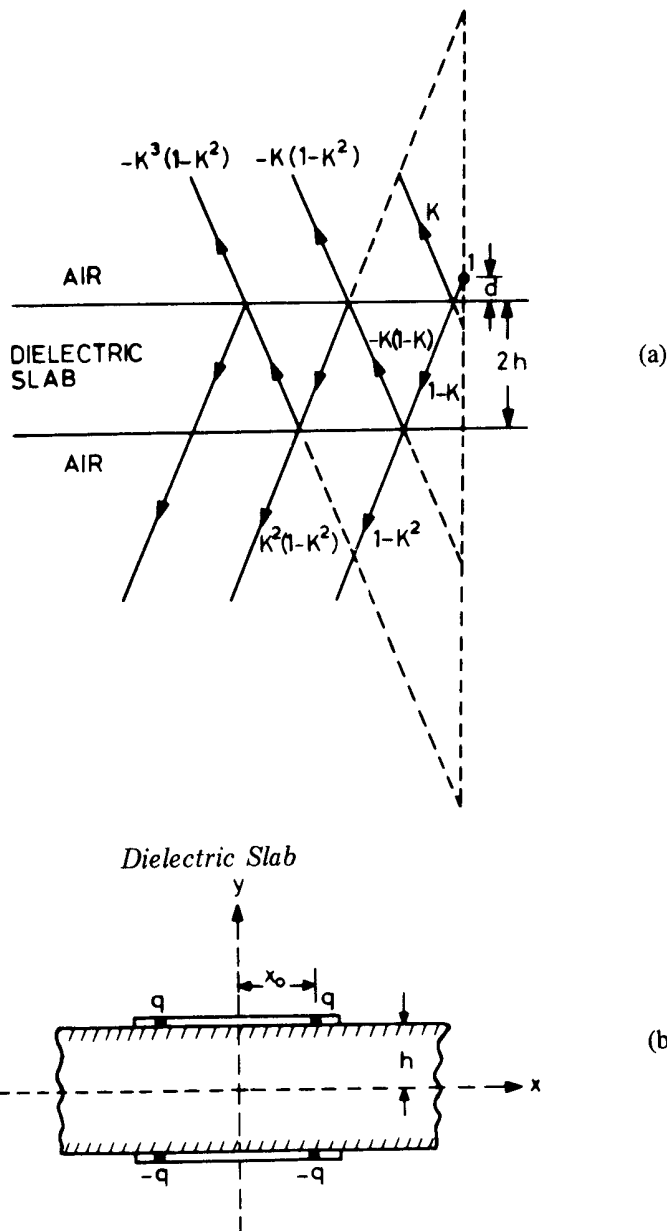


Figure 1.10 (a) Multiple images of a line charge in front of a dielectric slab and (b) microstrip configuration used in the integral equation method.

where

$$Q = \int_s \rho(x) dx \quad (1.38)$$

Here s indicates that the integral is over the strip conductor. Taking the Fourier transform of (1.37) along the x -axis and using Parseval's formula one gets

$$\frac{1}{C} = \frac{1}{2\pi Q^2} \int_{-\infty}^{\infty} \tilde{\rho}(\alpha) \tilde{\phi}(\alpha, h) d\alpha \quad (1.39)$$

where the superscript \sim indicates a transformed function obtained from the transformation:

$$\tilde{f}(\alpha) = \int_{-\infty}^{\infty} f(x) e^{j\alpha x} dx \quad (1.40)$$

It may be pointed out that it is simpler to evaluate $\tilde{\phi}(\alpha, h)$ than to evaluate $\phi(x, h)$ since

$$\tilde{\phi}(\alpha, h) = \frac{1}{\epsilon_0} \tilde{\rho}(\alpha) \tilde{g}(\alpha) \quad (1.41)$$

whereas $\phi(x, h)$ is an integral given by

$$\phi(x, h) = \frac{1}{\epsilon_0} \int_{-W/2}^{W/2} \rho(x') g(x, h; x', h) dx' \quad (1.42)$$

The potential function in the transform domain, $\tilde{\phi}(\alpha)$ is evaluated as follows. Except for $y = h$, the transform of potential $\tilde{\phi}(\alpha, y)$ satisfies the Laplace equation in the (α, y) -plane, namely;

$$\left(-\alpha^2 + \frac{d^2}{dy^2} \right) \tilde{\phi}(\alpha, y) = 0 \quad (1.43)$$

Boundary conditions to be satisfied by $\tilde{\phi}(\alpha, y)$ may be listed as:

$$\text{at } y = 0 \quad \tilde{\phi}(\alpha, 0) = 0 \quad (1.44a)$$

$$\text{across } y = h \quad \tilde{\phi}(\alpha, h + 0) = \tilde{\phi}(\alpha, h - 0) \quad (1.44b)$$

$$\text{at } y = \infty \quad \tilde{\phi}(\alpha, \infty) = 0 \quad (1.44c)$$

and for $\frac{d}{dy} \tilde{\phi}$ at $y = h$, we have

$$\frac{d}{dy} \tilde{\phi}(\alpha, h + 0) = \epsilon_r \frac{d}{dy} \tilde{\phi}(\alpha, h - 0) - \frac{1}{\epsilon_0} \tilde{\rho}(\alpha) \quad (1.44d)$$

In the region $0 \leq y \leq h$, the general solution satisfying (1.44) is a linear combination of $\exp(-\alpha y)$ and $\exp(\alpha y)$; whereas for $y \geq h$, the solution is of the form $\exp(-|\alpha|y)$ alone. Using the boundary conditions given in (1.44), the solution for $\tilde{\phi}(\alpha, y)$ at $y = h$ is given by

$$\tilde{\phi}(\alpha, h) = \frac{1}{\epsilon_0} \tilde{\rho}(\alpha) \tilde{g}(\alpha) = \frac{\tilde{\rho}(\alpha)}{\epsilon_0 |\alpha| [1 + \epsilon_r \coth(|\alpha|h)]} \quad (1.45)$$

$\tilde{\phi}(\alpha, h)$ given by (1.45) is used in (1.39) to evaluate the capacitance C .

We still must find $\tilde{\rho}(\alpha)$ before C can be computed. However, since (1.37) is variational, one may use an approximate trial function for $\rho(x)$ and incur only a second-order error in the value of capacitance. A trial function that maximizes the value of C gives the closest value to the exact result for the capacitance. Variation of the charge proportional to $|x|$ yields the following expression for $\tilde{\rho}(\alpha)$ [20]:

$$\frac{\tilde{\rho}(\alpha)}{Q} = \frac{2 \sin(\alpha W/2)}{\alpha W/2} - \left\{ \frac{\sin(\alpha W/4)}{\alpha W/4} \right\}^2 \quad (1.46)$$

Results obtained by this method agree well with those of the modified conformal transformation method discussed earlier. This method can also be used to take into account the effect of finite strip thickness and enclosure. It can easily be extended for a microstrip on composite substrates or where a dielectric overlay exists over the microstrip [21]. In these situations one simply has to find an appropriate expression for $\tilde{g}(\alpha)$ and use the above procedure. For a microstrip with a composite substrate (the lower layer with dielectric constant ϵ_{r1} and height h and the upper layer with dielectric constant ϵ_{r2} and height s) and shielded by a top metallic wall at a distance d from the strip, the value of $\tilde{g}(\alpha)$ is given as

$$\begin{aligned} \tilde{g}(\alpha) = & \frac{\epsilon_{r1} \coth(|\alpha|h) + \epsilon_{r2} \coth(|\alpha|s)}{|\alpha| [\epsilon_{r1} \coth(|\alpha|h) [\epsilon_{r3} \coth(|\alpha|d) + \epsilon_{r2} \coth(|\alpha|s)]]} \\ & + \epsilon_{r2} [\epsilon_{r2} + \epsilon_{r3} \coth(|\alpha|d) \coth(|\alpha|s)]} \end{aligned} \quad (1.47)$$

1.2.5 Segmentation and Boundary Element Method (SBEM)

A recently developed analysis method [22] is based on a combination of the segmentation method [23, 24] and the boundary element method [24, 25]. This method

is well suited for multiconductor microstrip-like transmission structures with multi-layered dielectric substrates. The cross-section of the microstrip configuration is first separated into several homogeneous regions and analyzed separately by the boundary element method. The results are then combined to yield the final result by using the segmentation method. This strategy makes it possible to take into account local modifications of the transmission line configuration by conducting new analyses only at those regions nearby the modification.

The boundary element method is widely used in structural analysis and acoustics [25, 26] and has drawn more attention in the last few years. Some applications in electromagnetics have also been reported [27, 28]. For the quasi-TEM mode microstrip line analysis, we solve the Laplace equation in the cross-sectional plane of the transmission structure. Instead of dealing with the differential equation directly, we use the integral equation form of the Poisson equation (which is derived using Green's third identity [29, 30]):

$$\frac{1}{2}\Phi(r) = \oint_S \left(\Phi(r') \frac{\partial G(r, r')}{\partial n(r')} - G(r, r') \frac{\partial \Phi(r')}{\partial n(r')} \right) dr' + \int_D \rho(r') G(r, r') dv(r') \quad (1.48)$$

where $\Phi(r)$ is the potential at any point on the contour S , $G(r, r')$ is the Green's function that satisfies Poisson's equation for a point charge at r' in the homogeneous domain D bounded by the contour S , $n(r')$ is the normal vector at r' on the contour S pointing toward the domain, and $\rho(r')$ is the charge density function (see Figure 1.11).

The method described in [22] is based on the solution for the "basic capacitance matrix" (the relation between the boundary voltages and boundary electric flux) for each homogeneous region first (see Figure 1.12). Then the segmentation method [31] is used to connect all of these basic capacitance matrices into one matrix, which is the relation between potential and charges on all the conductor surfaces. By using the segmentation method, those fields (Φ and $\partial\Phi/\partial n$) on the dielectric interfaces are treated as dummy variables and need not be really evaluated. This saves time in comparison to the traditional boundary element method. As a

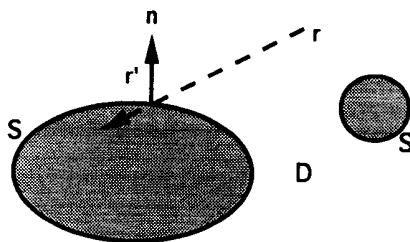


Figure 1.11 Definitions of the notation used in (1.48).

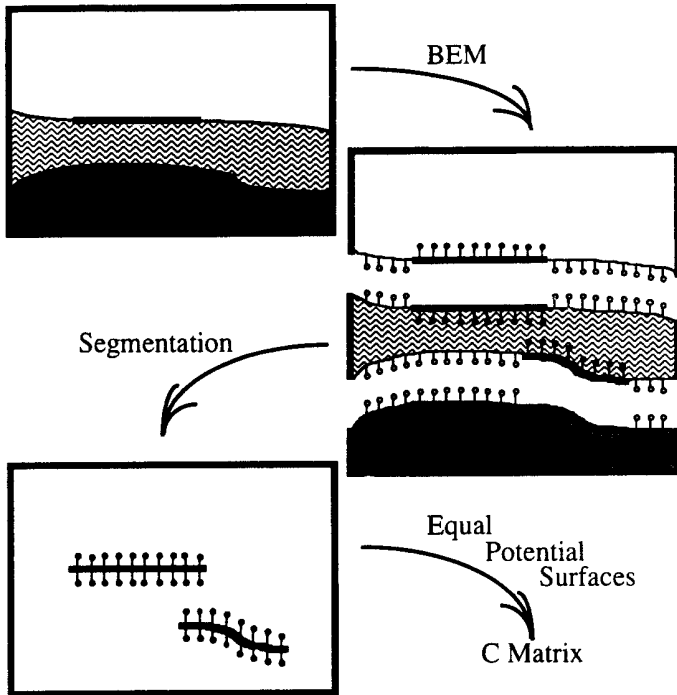


Figure 1.12 Calculation of capacitance matrices by using segmentation and the boundary element method.

last step, the condition of equal potential on each conductor surface is applied to this matrix, and this yields the final capacitance matrix \mathbf{C} or, in the case of a single microstrip line, capacitance per unit length.

For each of these homogeneous regions, the equation

$$\frac{1}{2}\Phi(r) = \oint_s \left(\Phi(r') \frac{\partial G(r, r')}{\partial n(r')} - G(r, r') \frac{\partial \Phi(r')}{\partial n(r')} \right) dr' \quad (1.49)$$

is solved by using the weighted residual method [25]. Here the pulse function is used as the basis function and the delta function is used as the testing function. The free space Green's function for a line charge is used as $G(r, r')$, that is,

$$G(r, r') = -\frac{\ell_n|r - r'|}{2\pi\epsilon} \quad (1.50)$$

where ϵ is the permittivity for that homogeneous region. This results in a system of linear equations or in the matrix form

$$\overline{\overline{\mathbf{H}}}\overline{\Phi} = \overline{\overline{\mathbf{U}}}\overline{\mathbf{Q}} \quad (1.51)$$

where

$$\overline{\Phi} = [\Phi_1 \Phi_2 \dots \Phi_N]^T \quad (1.52)$$

$$\overline{\mathbf{Q}} = [(-\epsilon)\partial\Phi/\partial n_1 \ (-\epsilon)\partial\Phi/\partial n_2 \ \dots \ (-\epsilon)\partial\Phi/\partial n_N]^T \quad (1.53)$$

$$H_{ij} = 1/2 \quad \text{for } i = j \quad (1.54)$$

$$= \frac{-1}{2\pi} \int_{l_j} \vec{n}_j \cdot \vec{r}_{ij} / |\vec{r}_{ij}|^2 \ dl' \quad \text{for } i \neq j \quad (1.55)$$

$$U_{ij} = \frac{W_i}{2\pi\epsilon} \left[\ell_n \frac{2}{W_i} + 1 \right] \quad \text{for } i = j \quad (1.56)$$

$$= -\frac{1}{2\pi\epsilon} \int_{l_j} \ell_n |\vec{r}_{ij}| \ dl' \quad \text{for } i \neq j \quad (1.57)$$

The integrals in (1.55) and (1.57) are carried out numerically by the Gaussian quadrature formula [24]. It also should be noted that the $\overline{\overline{\mathbf{U}}}$ matrix is not symmetrical because of (1.55). The basic capacitance matrix $\overline{\overline{\mathbf{C}}}_B$ for this region is then defined as

$$\overline{\overline{\mathbf{C}}}_B = [\overline{\overline{\mathbf{U}}}]^{-1} \overline{\overline{\mathbf{H}}} \quad (1.58)$$

where $\overline{\overline{\mathbf{C}}}_B$ has units of Farads/meter. However, because the definition of $\overline{\mathbf{Q}}$ in (1.53), $\overline{\overline{\mathbf{C}}}_B$ is not a real capacitance matrix unless all this region's boundary is conductor. It also should be noted that each element of $\overline{\overline{\mathbf{C}}}_B$ is proportional to ϵ , the permittivity for that homogeneous region. If the geometry of this region is kept unchanged and the permittivity is changed to a new value, the basic capacitance matrix does not need to be calculated using (1.58) again; instead, each element of the original \mathbf{C}_B needs only to be scaled to the new permittivity value. (This makes the calculation of inductance matrix \mathbf{L} for this transmission-line system much easier when the capacitance matrix \mathbf{C} has been calculated using SBEM.) Once the basic capacitance matrices have been calculated for all the homogeneous regions, they are connected

to each other using the boundary condition on dielectric interfaces. This is done by the segmentation method.

Suppose we have two basic capacitance matrices $\bar{\mathbf{C}}_{B1}$ and $\bar{\mathbf{C}}_{B2}$ (Figure 1.13), for homogeneous region 1 and region 2, respectively, given by

$$\begin{bmatrix} Q_{p1} \\ Q_q \end{bmatrix} = \bar{\mathbf{C}}_{B1} \begin{bmatrix} \Phi_{p1} \\ \Phi_q \end{bmatrix} = \begin{bmatrix} C_{p1p1} & C_{p1q} \\ C_{qp1} & C_{qq} \end{bmatrix} \begin{bmatrix} \Phi_{p1} \\ \Phi_q \end{bmatrix} \quad (1.59)$$

and

$$\begin{bmatrix} Q_{p2} \\ Q_r \end{bmatrix} = \bar{\mathbf{C}}_{B2} \begin{bmatrix} \Phi_{p2} \\ \Phi_r \end{bmatrix} = \begin{bmatrix} C_{p2p2} & C_{p2r} \\ C_{rp2} & C_{rr} \end{bmatrix} \begin{bmatrix} \Phi_{p2} \\ \Phi_r \end{bmatrix} \quad (1.60)$$

The ports q in region 1 need to be connected to the ports r in region 2 using the boundary condition on dielectric interfaces; that is, the electric flux should be continuous ($Q_q = -Q_r$) and the voltage should be continuous ($\Phi_q = \Phi_r$). Equations (1.59) and (1.60) are combined to form the new equation

$$\begin{bmatrix} Q_p \\ Q_q \\ Q_r \end{bmatrix} \equiv \begin{bmatrix} Q_{p1} \\ Q_{p2} \\ Q_q \\ Q_r \end{bmatrix} = \begin{bmatrix} C_{p1p1} & 0 & | & C_{p1q} & | & 0 \\ 0 & C_{p2p2} & | & 0 & | & C_{p2r} \\ \hline \cdots & \cdots & | & \cdots & | & \cdots \\ C_{qp1} & 0 & | & C_{qq} & | & 0 \\ \hline \cdots & \cdots & | & \cdots & | & \cdots \\ 0 & C_{rp2} & | & 0 & | & C_{rr} \end{bmatrix} \begin{bmatrix} \Phi_{p1} \\ \Phi_{p2} \\ \Phi_q \\ \Phi_r \end{bmatrix} \equiv \begin{bmatrix} C_{pp} & C_{pq} & C_{pr} \\ C_{qp} & C_{qq} & 0 \\ C_{rp} & 0 & C_{rr} \end{bmatrix} \begin{bmatrix} \Phi_p \\ \Phi_q \\ \Phi_r \end{bmatrix} \quad (1.61)$$

This equation contains all the information about these two regions. Using the boundary conditions and the second and third rows of equation (1.61), it can be shown that

$$\Phi_q = -[C_{qq} + C_{rr}]^{-1}[C_{qp} + C_{rp}]\Phi_p \quad (1.62)$$

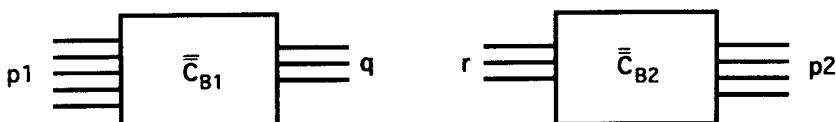


Figure 1.13 Definition of the notation used in the segmentation method.

which relates the voltages at the interconnected $\bar{\bar}{\mathbf{C}}_B$ ports to the voltages at the unconnected ports. So, the basic capacitance matrix $\bar{\bar}{\mathbf{C}}_B$ for the combination of these two regions is given from the first row of (1.61) as

$$\bar{\bar}{\mathbf{C}}_B = C_{pp} - [C_{pq} + C_{pr}][C_{qq} + C_{rr}]^{-1}[C_{qp} + C_{rp}] \quad (1.63)$$

which gives the relation between the voltage and electric flux at unconnected ports only.

The segmentation method is applied to connect all the basic capacitance matrices and to eliminate all the ports on the dielectric interfaces. This results in a matrix that relates the potential and charges on all conductor surfaces. The last condition that needs to be applied is that all the ports on the same conductor should have the same potential. This condition can easily be applied by simply summing the related elements in the matrix. All the elements that relate the charges on conductor i due to the voltage on conductor j should be added to become the element C_{ij} of the final capacitance matrix \mathbf{C} . It should be noted that, in the whole process of this capacitance matrix calculation, we try to avoid calculating the fields we do not need so that the process can be as efficient as possible. The boundary element method helps us to concentrate only on the boundary fields, and the segmentation method helps us to eliminate the unknown fields at the dielectric interfaces. In cases where the fields on the dielectric interfaces or the fields in the domain are needed, (1.62) can be used to recover all the details.

In addition to the five methods for quasi-static analysis of microstrip lines discussed in this chapter, several other numerical electromagnetic analysis techniques are applicable to microstrip line. An overview of these methods is available in [32]. The finite element method [33] has been used for quasi-static analysis of microstrip lines, and a computer program based on this method is available in [33].

1.3 MICROSTRIP DISPERSION MODELS

The quasi-static methods of microstrip analysis do not take into account the non-TEM nature of the microstrip mode. The non-TEM behavior causes the effective dielectric constant (ϵ_{re}) and impedance Z_{0m} of the microstrip to be functions of frequency. Of these two, the variation of the effective dielectric constant is more significant. An exact evaluation of these variations involves a fullwave analysis of the microstrip configuration, which will be discussed in Chapter 2. However, there are several semi-empirical techniques [34–50] available that lead to a closed-form solution for the dependence of ϵ_{re} and Z_{0m} on frequency. These dispersion models may be listed as follows:

- Model based on coupling between TEM and TM_0 surface wave modes [34];
- An empirical relation for frequency-dependent phase velocity [35];

- Model based on LSE mode using a dielectric loaded ridged waveguide and its modifications [36, 39, 43];
- Model based on coupling between a TEM mode and a TE mode transmission line [37];
- Model based on coupling between the LSE mode and surface-wave mode [47];
- Empirical formulae based on fullwave numerical data [41, 44, 49];
- Planar waveguide model [38].

Some of these dispersion models are discussed briefly in this section.

1.3.1 Coupled TEM Mode and TM Mode Model

In this model [34] the deviation from the TEM behavior or the dispersion is considered to be caused by the coupling between the fundamental TEM mode and the lowest order surface wave TM_0 mode. Using the theory of coupled modes, the frequency-dependent effective dielectric constant may be written as

$$\epsilon_{\text{re}}(f) = \left[0.5(\sqrt{\epsilon_{\text{re}}(0)} + \sqrt{\epsilon_{\text{cTM}}}) + \left\{ \epsilon_{12}^2 + 0.25(\sqrt{\epsilon_{\text{re}}(0)} - \sqrt{\epsilon_{\text{cTM}}})^2 \right\}^{1/2} \right]^2 \quad (1.64)$$

where $\epsilon_{\text{re}}(0)$ is the quasi-static value of the effective dielectric constant and ϵ_{cTM} is the effective dielectric constant for the TM_0 mode. An expression for the coupling parameter ϵ_{12} , obtained by a series of qualitative arguments, may be written as

$$\epsilon_{12}^2 = k(\sqrt{\epsilon_r} - 1)^2 (W/h)^{n_3} (f/f_e)^{n_2} \quad (1.65)$$

where f_e is the frequency at which the phase velocity of the TEM mode equals the phase velocity of the TM_0 mode and k , n_2 , n_3 are three constants found empirically for the best fit between the behavior of the coupled line model and the experimental results. The values of n_2 , n_3 , and k are $4/3$, $3/4$, and 0.22 , respectively; and the range of validity for the model is stated as $2 \leq \epsilon_r \leq 104$, $0.025 \text{ in} \leq h \leq 0.125 \text{ in}$, $0.9 \leq W/h \leq 6$, and $f < 0.5 f_e$.

1.3.2 An Empirical Relation [35]

Based on the results of various theoretical and experimental studies of dispersion, it may be noted that:

1. The normalized phase velocity v_p is a monotonically decreasing function of frequency f .
2. v_p and its first-order derivative at $f = 0$ are given by

$$v_p|_{f=0} = 1/\sqrt{\epsilon_{re}(0)} \quad \text{and} \quad \left. \frac{\partial v_p}{\partial f} \right|_{f=0} = 0 \quad (1.66)$$

3. v_p and its derivative at $f \rightarrow \infty$ are given by

$$v_p|_{f \rightarrow \infty} = 1/\sqrt{\epsilon_r} \quad \text{and} \quad \left. \frac{\partial v_p}{\partial f} \right|_{f \rightarrow \infty} = 0 \quad (1.67)$$

4. The second derivative of v_p is zero in the vicinity of the cutoff frequency (f_c) of the lowest order transverse electric surface wave mode; that is,

$$\left. \frac{\partial^2 v_p}{\partial f^2} \right|_{f=f_c} = 0 \quad (1.68)$$

The above conditions are fulfilled by the relation [35]

$$v_p = \frac{1}{\sqrt{\epsilon_r \epsilon_{re}(0)}} \frac{\sqrt{\epsilon_{re}(0)} f_n^2 + \sqrt{\epsilon_r}}{f_n^2 + 1} \quad (1.69)$$

where $\epsilon_{re}(0)$ is the quasi-static value of ϵ_{re} and f_n is defined by

$$f_n = \frac{f}{f_c} = \frac{4h \sqrt{\epsilon_r - 1}}{\lambda_0} \quad (1.70)$$

where h is the substrate thickness.

Comparison with experimental results shows that the error in (1.69) is less than 3 percent.

1.3.3 Dielectric-Loaded Ridged Waveguide Model [36]

This model for the microstrip dispersion is based on the study of another structure that resembles a microstrip as far as inhomogeneity of the dielectric medium is concerned but has a shape that can be analyzed mathematically. This structure is shown in Figure 1.14. The configuration shown in Figure 1.14(b) corresponds to the microstrip cross section shown in Figure 1.14(a). The dimensions of the structure are chosen such that it has the same electrical characteristics at zero frequency as the microstrip. The structure is analyzed for dispersion, and the results are compared with measured microstrip dispersion values to determine the unknown parameter H'/h . The comparison shows that H'/h and related parameters are nearly constant or vary linearly with characteristic impedance. This feature is used to

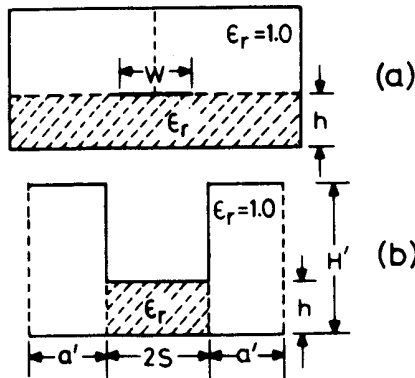


Figure 1.14 Ridged waveguide model for a microstrip line (from [36], © 1973 IEEE. Reprinted with permission.).

derive a simple formula that can be used to predict the dispersion of a microstrip transmission line. The resulting dispersion formula may be written as

$$\epsilon_{re}(f) = \epsilon_r - \frac{\epsilon_r - \epsilon_{re}(0)}{1 + (f^2/f_p^2)G} \quad (1.71)$$

where

$$f_p = Z_{0m}/(2\mu_0 h) \quad (1.72)$$

or

$$f_p(\text{GHz}) = 0.398 Z_{0m}/h \text{ (mm)}$$

and

$$G = 0.6 + 0.009 Z_{0m} \quad (Z_{0m} \text{ in ohms}) \quad (1.73)$$

In (1.71), $\epsilon_{re}(f)$ is the frequency-dependent effective dielectric constant and $\epsilon_{re}(0)$ is the zero-frequency (quasi-static) value of ϵ_{re} .

Modification of Getsinger's Formula

Edwards and Owens [39] have reported extensive measurement results of dispersion in microstrip lines of characteristic impedance ranging from 10Ω to 100Ω over

the frequency range of 2 GHz to 18 GHz. They have pointed out that measured results show better agreement with Getsinger's formula when G of (1.73) is modified as

$$G = \left\{ \frac{Z_{0m} - 5}{60} \right\}^{1/2} + 0.004 Z_{0m} \quad (1.74)$$

The experiments of Edwards and Owens [39] were carried out on sapphire substrates ($\epsilon_r = 10.73$ to 11.50), and their results were found to be in good agreement with the fullwave analysis using Galerkin's method in the spectral domain (discussed later in Section 2.2.2). Modification of (1.71), which results in a more accurate formula, has also been suggested. This may be written as

$$\epsilon_{re}(f) = \epsilon_r - \frac{\epsilon_r - \epsilon_{re}(0)}{1 + P} \quad (1.75)$$

where

$$P = (h/Z_{0m})^{1.33}[0.43 f^2 - 0.009 f^3] \quad (1.76)$$

with h in millimeters and f in gigahertz.

1.3.4 Empirical Formulae for Broad Frequency Range

The aforementioned dispersion models have been tested by comparison with experimental results up to 18 GHz and, in general, found to be in good agreement. However, they have limited range in terms of frequency, dielectric constant values, and W/h ratios. Several dispersion formulae have been developed by fitting fullwave numerical data in order to extend the validity range of the above-described dispersion model expressions.

Yamashita et al. [41] published a dispersion model that is valid up to 100 GHz. The following expressions describe the dispersion in ϵ_{re} :

$$\epsilon_{re}(f) = \left(\frac{\sqrt{\epsilon_r} - \sqrt{\epsilon_{re}(0)}}{1 + 4F^{-1.5}} + \sqrt{\epsilon_{re}(0)} \right)^2 \quad (1.77)$$

where

$$F = \frac{4h\sqrt{\epsilon_r - 1}}{\lambda_0} \left\{ 0.5 + \left[1 + 2 \log_{10} \left(1 + \frac{W}{h} \right) \right]^2 \right\} \quad (1.78)$$

and $\epsilon_{re}(0)$ is the quasi-static value obtained earlier. The model is applicable in the range $2 \leq \epsilon_r \leq 16$, $0.06 \leq W/h \leq 16$, and $f \leq 100$ GHz.

In 1982, Kirschning and Jansen improved the accuracy of dispersion characteristics and claimed accuracy better than 0.6 percent up to 60 GHz. The following expressions are valid over the range $1 \leq \epsilon_r \leq 20$, $0.1 \leq W/h \leq 100$, and $0 \leq h/\lambda_0 \leq 0.13$ [44]:

$$\epsilon_{re}(f) = \epsilon_r - \frac{\epsilon_r - \epsilon_{re}(0)}{1 + P(f)} \quad (1.79)$$

where

$$P(f) = P_1 P_2 \{(0.1844 + P_3 P_4) 10 f h\}^{1.5763} \quad (1.80)$$

and

$$\begin{aligned} P_1 &= 0.27488 + \{0.6315 + 0.525/(1 + 0.157 f h)^{20}\} (W/h) \\ &\quad - 0.065683 \exp(-8.7513 W/h) \\ P_2 &= 0.33622 \{1 - \exp(-0.03442 \epsilon_r)\} \\ P_3 &= 0.0363 \exp(-4.6 W/h) [1 - \exp(-(f h/3.87)^{4.97})] \\ P_4 &= 1 + 2.751 [1 - \exp(-(\epsilon_r/15.916)^8)] \end{aligned}$$

The frequency f is in gigahertz and the thickness h is in centimeters.

Kobayashi [49] further improved the accuracy of the dispersion model in terms of dielectric constant and frequency range. Since his formula has no restriction on the h/λ_0 ratio, it will predict more accurately the distortion in pulse propagation along a microstrip line. The proposed model uses normalizing frequency f_{50} at which the dispersion is 50 percent and the expressions for f_{50} is derived using extensive fullwave numerical data. The Kobayashi's dispersion formula for the effective relative dielectric constant is given by

$$\epsilon_{re}(f) = \epsilon_r - \frac{\epsilon_r - \epsilon_{re}(0)}{1 + (f/f_{50})^m} \quad (1.81)$$

where

$$\begin{aligned}
 f_{50} &= \frac{f_{k,\text{TM}_0}}{0.75 + \{0.75 - (0.332/\epsilon_r^{1.73})\}W/h} \\
 f_{k,\text{TM}_0} &= \frac{c \tan^{-1}\left(\epsilon_r \sqrt{(\epsilon_{re}(0) - 1)/(\epsilon_r - \epsilon_{re}(0))}\right)}{2\pi h \sqrt{\epsilon_r - \epsilon_{re}(0)}} \\
 m &= m_0 m_e \\
 m_0 &= 1 + \frac{1}{1 + \sqrt{W/h}} + 0.32 \left(\frac{1}{1 + \sqrt{W/h}} \right)^3 \\
 m_e &= \begin{cases} 1 + \frac{1.4}{1 + W/h} \left\{ 0.15 - 0.235 \exp\left(-\frac{0.45f}{f_{50}}\right) \right\} & \text{where } W/h \leq 0.7 \\ 1 & \text{where } W/h > 0.7 \end{cases}
 \end{aligned} \tag{1.82}$$

and c is the velocity of light. The above equations are claimed to predict dispersion better than 0.6 percent in the range $1 \leq \epsilon_r \leq 128$ and $0.1 \leq W/h \leq 10$.

The closed-form expression describing the effect of frequency on Z_{0m} has also been reported and is given below [42]

$$Z_{0m}(f) = Z_{0m} \frac{\epsilon_{re}(f) - 1}{\epsilon_{re}(0) - 1} \sqrt{\frac{\epsilon_{re}(0)}{\epsilon_{re}(f)}} \tag{1.83}$$

where Z_{0m} is the quasi-static value.

1.3.5 Planar Waveguide Model

It has been shown [38] that the dynamic properties of a microstrip (including higher order modes) can be approximated by a planar waveguide model. In this model, the microstrip is represented by a parallel plate waveguide of width W_{eff} and height h is shown in Figure 1.15a. The top and bottom plates are of infinite conductivity, and there are magnetic walls at the sides. It is filled with a medium of dielectric constant ϵ_{re} . The value of ϵ_{re} at zero frequency is determined from a quasi-static analysis. The effective width W_{eff} and the effective dielectric constant ϵ_{re} are frequency dependent. The frequency dependence of the effective dielectric constant describes the influence of the dispersion on the phase velocity, whereas the frequency dependence of the effective width describes the influence of the dispersion on the characteristic impedance. It is found, from the results of the fullwave analysis discussed later in Chapter 2, that the phase velocity of the waves in a microstrip decreases with increasing frequency. Thus the value of ϵ_{re} increases with frequency. Also, the characteristic impedance of a microstrip increases with frequency (Section 2.4). This increase in impedance can be explained only by a

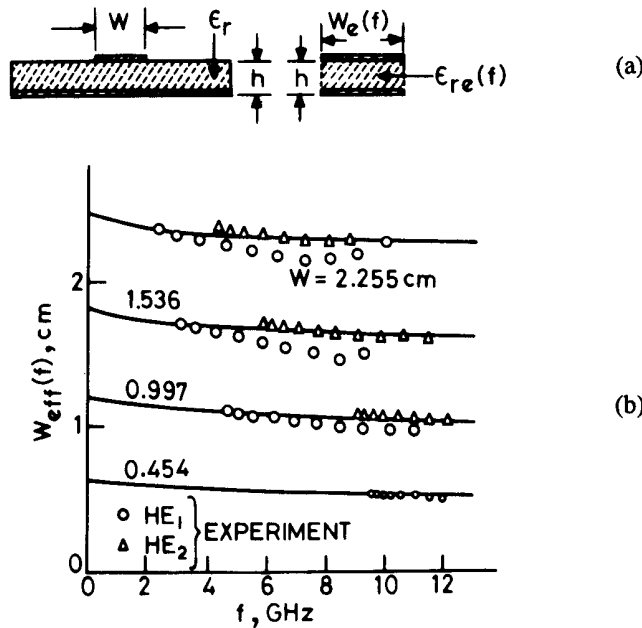


Figure 1.15 (a) Planar waveguide model for a microstrip line and (b) variation of the effective width with frequency $\epsilon_r = 9.7$, $h = 0.0635$ cm (from [38], © 1975 IEE (U.K.). Reprinted with permission.).

hypothetical decrease in the effective strip width caused by the concentration of electric field lines below the strip at higher frequency. The decrease of the effective strip width with frequency is described by the empirical relation [38]

$$W_{eff}(f) = W + \frac{W_{eff}(0) - W}{1 + f/f_b} \quad (1.84a)$$

where

$$f_b = c / (2W\sqrt{\epsilon_r})$$

$$\begin{aligned} W_{eff}(0) &= \text{effective width calculated from quasi-static analysis} \\ &= 120\pi h / (Z_{0m}\sqrt{\epsilon_{re}(0)}) \end{aligned}$$

Frequency-dependent impedance is given by

$$Z_{0m}(f) = 120 \pi h / (W_{eff}(f)\sqrt{\epsilon_{re}(f)}) \quad (1.84b)$$

A comparison of the experimental results with the values calculated using (1.84) is shown in Figure 1.15(b). Further, knowing $W_{\text{eff}}(f)$ one can calculate the cut-off frequencies for higher order modes from the relation [38]

$$f_c(m, 0) = \frac{mc}{2\sqrt{\epsilon_{\text{re}}(f)} W_{\text{eff}}(f)} \quad (1.85)$$

The guide wavelength for hybrid modes in terms of $f_c(m, 0)$ is given by

$$\lambda_{\text{HE}_m} = \frac{\lambda_0}{\sqrt{\epsilon_{\text{re}}(f)} \sqrt{1 - [f_c(m, 0)/f]^2}} \quad (1.86)$$

Measured and calculated cut-off frequencies of the first two higher order modes are shown in Figure 1.16 [38]. The two modes indicated as $m = 1$ and $m = 2$ in this figure are the HE_1 and HE_2 modes, respectively. There is a fairly good agreement between the measured results and theoretical values.

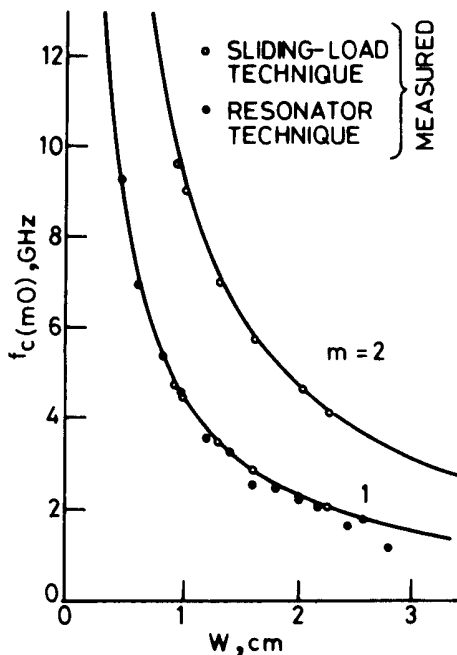


Figure 1.16 Cut-off frequencies for higher order modes in a microstrip computed from the planar waveguide model: $\epsilon_r = 9.7$, $h = 0.0635$ cm (from [38], © 1975 IEE (U.K.). Reprinted with permission.).

1.3.6 Some Comments

The aforementioned models assume an open microstrip line on a nonmagnetic substrate ($\mu_r = 1$) and that the thickness effect is included in the quasi-static value $\epsilon_{re}(0)$. Atwater [48] and Edwards [6] reported dispersion data comparison for several microstrip lines using many dispersion models. York and Compton [51] provided a comparison between the measured data and the several above-described dispersion models up to 18 GHz for several substrate thicknesses. Microstrip lines used for comparison were fabricated on alumina and plastic substrates having an impedance range from 35Ω to 70Ω . A summary of their comparison is given in Table 1.1, which shows that the models of Edwards and Owens [39], Kirschning and Jansen [44] and Kobayashi [49] gave the most consistent results when compared with measured data. Figure 1.17 compares measured and simulated [52] $\sqrt{\epsilon_{re}(f)}$ as a function of frequency for a microstrip on 0.97-mm alumina substrate ($\epsilon_r = 9$) with $W/h = 0.867$.

The frequency dependence of the effective dielectric constant describes the influence of dispersion on the phase velocity, whereas the frequency dependence

Table 1.1
Average Percent Deviation Between the Measured Dispersion and the Models
Listed in [51] (© 1990 IEEE. Reprinted with permission.)

ϵ_r	Thickness (mm)	Z_{0m} (Ω)	[44]	[49]	[41]	[42]	[47]	[36]	[39]	[37]	[35]
9.80	0.655	50	0.51	0.37	1.56	3.14	1.27	0.70	0.34	1.41	1.91
9.80	0.655	50	0.47	0.55	1.38	2.95	1.69	0.76	0.62	1.83	2.32
9.80	0.648	35	0.38	0.28	1.46	3.07	0.94	1.06	0.69	1.85	3.80
9.80	0.648	50	0.39	0.32	1.39	2.92	1.50	0.77	0.43	1.69	2.23
9.80	0.648	70	0.56	0.55	1.35	3.00	1.89	0.95	0.65	1.44	0.84
9.80	0.668	50	0.58	0.84	1.13	2.71	1.99	0.69	0.95	2.16	2.69
9.80	0.668	50	0.54	0.67	1.04	2.54	1.84	0.51	0.74	1.95	2.45
9.80	0.635	50	0.31	0.32	1.31	2.95	1.60	0.78	0.47	1.80	2.24
9.80	0.635	70	0.32	0.32	1.17	2.80	1.81	0.69	0.41	1.50	1.10
2.20	1.605	50	0.56	0.51	0.65	1.18	1.99	2.57	0.78	1.87	2.67
2.20	1.605	70	0.52	0.54	0.41	0.88	1.24	2.49	0.45	1.61	2.50
2.20	0.780	50	0.56	0.58	0.54	0.48	0.68	1.01	0.53	0.39	1.67
2.20	0.780	70	0.53	0.53	0.56	0.50	0.56	1.01	0.76	0.51	0.98
2.33	1.524	50	0.48	0.46	0.50	0.45	0.81	1.28	0.61	0.99	1.51
2.33	1.524	35	0.46	0.43	0.59	0.51	0.77	1.12	0.86	1.17	1.21
2.17	0.686	50	0.41	0.42	0.52	0.41	0.80	1.02	0.75	0.50	1.14
2.33	0.787	50	0.53	0.55	0.57	0.45	0.78	1.10	0.71	0.44	1.59
2.50	0.762	50	0.23	0.27	0.47	0.41	0.71	1.14	0.63	0.37	1.50

Note: The results for 18 different resonators are given, and the smallest deviation for each case is shown in bold print.

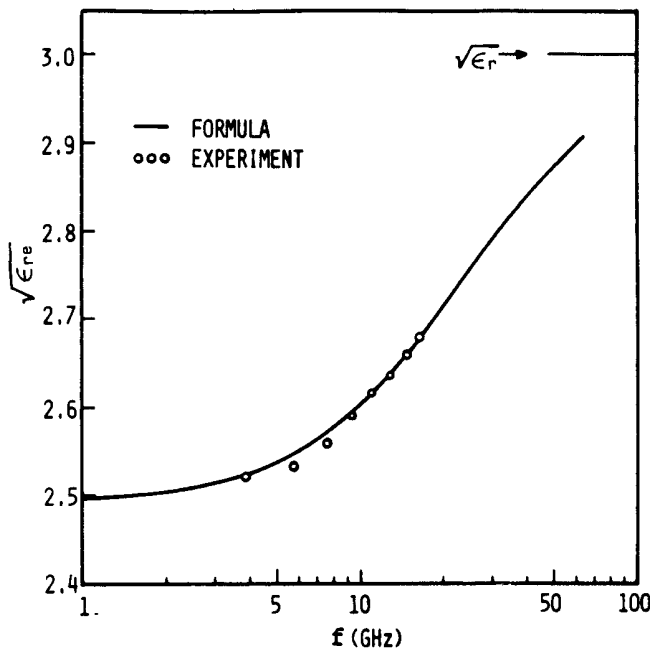


Figure 1.17 The measured dispersion of a microstrip line on an Alumina substrate: $\epsilon_r = 9.0$, $W/h = 0.867$, $h = 0.97$ mm (from [52], © 1981 IEEE. Reprinted with permission.).

of the effective width describes the influence of the dispersion on the characteristic impedance. Fortunately for high-impedance lines and thin substrates, the changes in ϵ_{re} and Z_{0m} with frequency are very small. The frequency below which dispersion effects may be neglected is given by the relation

$$f_d = 0.3 \sqrt{\frac{Z_{0m}}{h\sqrt{\epsilon_r} - 1}} \quad (1.87)$$

where f_d is in gigahertz and h is in centimeters. Equation (1.87) shows that f_d is higher for high-impedance lines on thin substrates. For example, a 50Ω line on a $100\text{-}\mu\text{m}$ -thick GaAs substrate has negligible dispersion below 11 GHz.

1.4 MICROSTRIP TRANSITIONS

A microwave transition is an interface used to launch microwave power from one transmission line to another with the minimum possible reflective and dissipative losses. This structure is also called a *launcher*. The desirable features of a microstrip transition are:

1. Low transmission and reflection losses over the operating bandwidth;
2. Easily connectable and disconnectable to a microstrip with reproducible results;
3. In-line design and simple fabrication;
4. Adaptability to different substrate thicknesses.

The design of these transitions consists of two parts: mechanical design to match physically both electrical and magnetic field distributions between the two media as close as possible in order to keep the discontinuity reactances small, and the electrical design to match the impedances and any other interface discontinuity reactances over the operating frequency range to minimize losses. Generally, fields are matched by shaping the structure, and the impedance matching and discontinuity reactance compensation are realized by using $\lambda/4$ transformers or tapered sections. Various microstrip transitions used in practice are, for example, coaxial-to-microstrip, waveguide-to-microstrip, microstrip-to-coplanar waveguide, and microstrip-to-slotline. Microstrip-to-slotline and microstrip-to-coplanar waveguide transitions will be treated in Chapters 5 and 7, respectively. Coaxial-to-microstrip and waveguide-to-microstrip transitions are briefly described in this section.

1.4.1 Coaxial-to-Microstrip Transition

A coaxial-to-microstrip transition is the simplest and in general is broadband because both media support TEM mode. This transition is generally realized by shaping the coaxial connector's structure and has been well treated in the literature [4, 6, 53–56].

Figure 1.18 shows typical in-plane and right-angle coaxial-to-microstrip transitions. The center conductor pin in these connectors is generally soldered to the microstrip for high reliability. In an in-plane transition, there should be no gap between the microstrip ground plane and the fixture's top surface and between the connector's flange and the fixture front side. Any such gap, as shown in Figure 1.19, will result in an additional discontinuity reactance due to long ground plane current flow.

In general, the coaxial-to-microstrip transition can be represented by a simple equivalent circuit as shown in Figure 1.20, where L_s and C_s are the series inductance and shunt capacitance, respectively. The design of such a transition consists of either minimizing these reactances or compensating for them by making $\sqrt{L_s/C_s} = 50 \Omega$ or any other characteristic impedance value used.

An accurate characterization of packaged microwave circuits such as broadband MMIC power amplifiers require coaxial-to-microstrip transitions with VSWR lower than 1.2. In such cases, minimizing the interface discontinuity reactances is desired rather than compensating for the discontinuities, which limits the frequency range. This is accomplished by matching both the electric and magnetic field

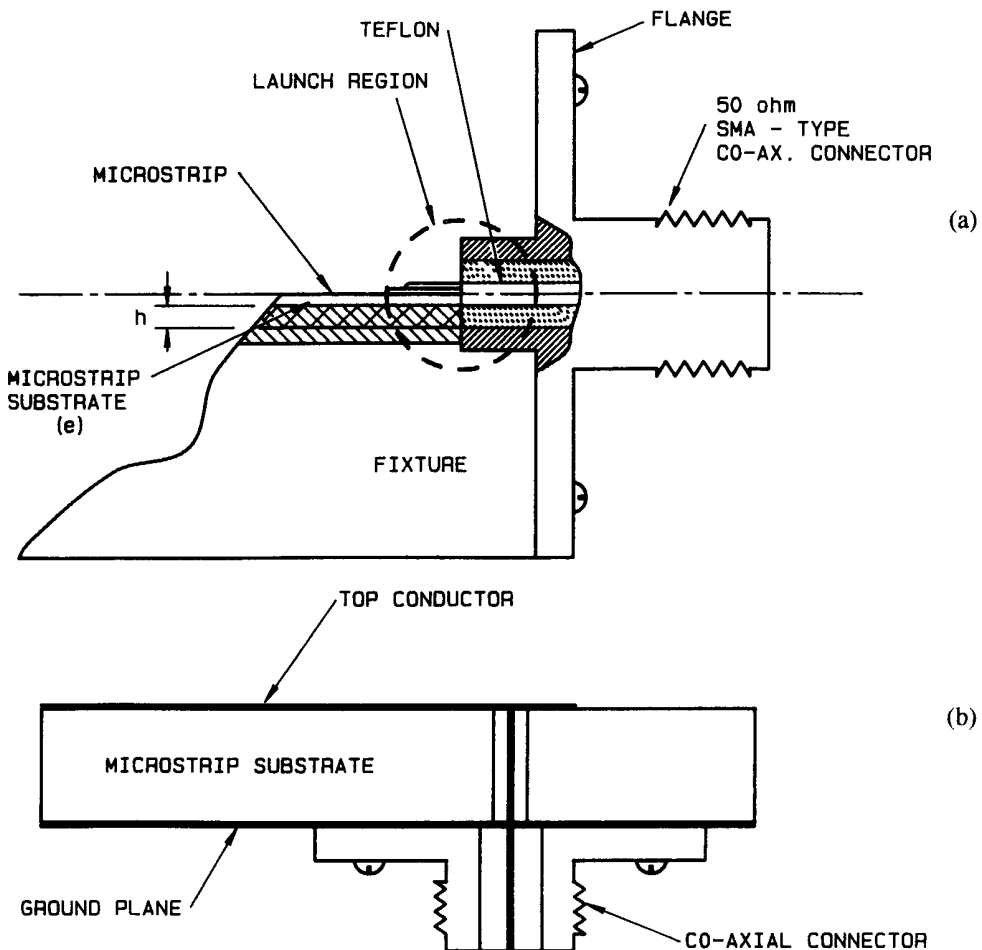


Figure 1.18 Typical coaxial-to-microstrip transitions: (a) in-plane and (b) right-angle.

patterns of the two media at the interface using an off-centered inner conductor as shown in Figure 1.21 [54]. In this case the center conductor of the coaxial connector is gradually shifted down so that its end touches the microstrip conductor. Throughout the connector length, the characteristic impedance of 50Ω is maintained.

Figure 1.22(a) shows the Eisenhart transition with APC 7 connector that uses 7-mm of outer diameter coaxial line. The transition was tested by connecting back-to-back using a 5.1-cm-long 50Ω microstrip line on 25-mil alumina substrate. The measured VSWR shown in Figure 1.22(b) was less than 1.12 up to 18 GHz, implying

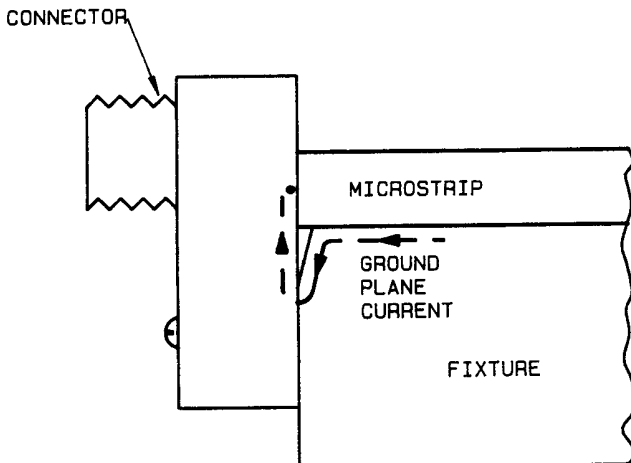


Figure 1.19 Effect of the gap, between the connector flange and the front-side wall of the fixture, on the ground plane current.

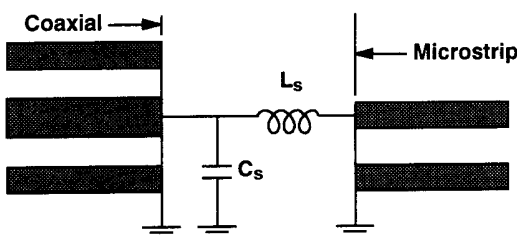


Figure 1.20 Equivalent circuit representation of a coaxial-to-microstrip transition.

that each transition's VSWR is less than 1.06. A similar transition is also available with SMA connectors. These transitions are called Eisenhart connectors. The Eisenhart connectors were characterized using $50\text{-}\Omega$ microstrip lines printed on 10-, 15-, 20-, and 25-mil-thick alumina substrates ($\epsilon_r = 9.9$). Figure 1.23(a) shows the test structure used to characterize these connectors. For Eisenhart connector evaluation and consequently coaxial-to-microstrip transition model development, microstrip lines were 243-mil long. Figure 1.23(b) shows measured and modeled responses for a 15-mil-thick microstrip line. Two different line lengths were used (printed in 15-mil-thick substrate) to extract connector losses from total measured losses. Figure 1.24 shows the transition model values as a function of substrate thickness. In general, Eisenhart connectors work very well up to 18 GHz.

Several other coaxial-to-microstrip interface discontinuity minimization techniques have also been used in practice. One of them, shown in Figure 1.25, uses

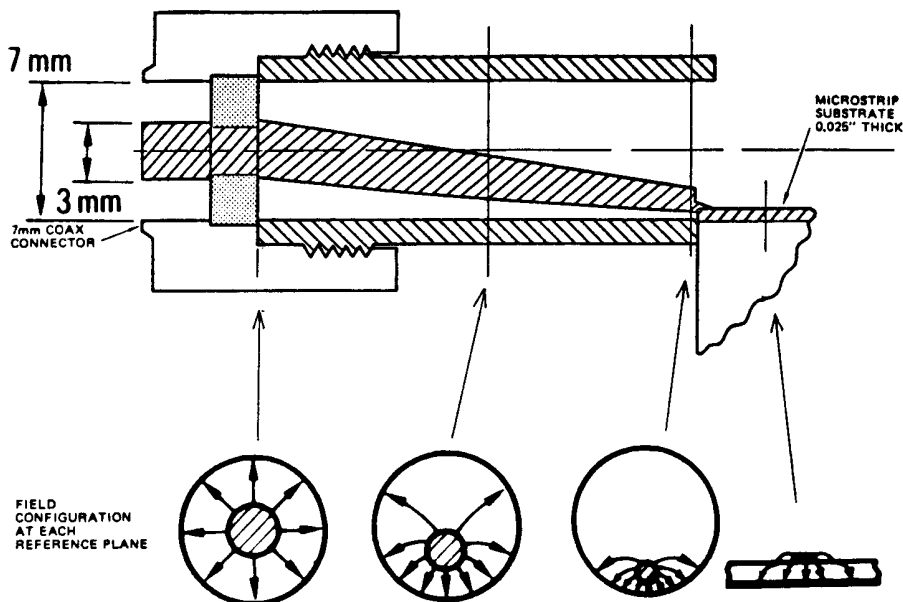


Figure 1.21 High-performance coaxial-to-microstrip transition.

a metal screw in order to reduce the transition capacitance [53]. This transition uses a hole in the fixture for the screw and a circular hole in the ground plane of the microstrip near the transition. The coaxial connector is of the SMA type, and the microstrip shown uses 0.5-mm-thick sapphire substrate. Measured VSWR was less than 1.01 over the 1-GHz to 18-GHz frequency range [6].

1.4.2 Waveguide-to-Microstrip Transition

The use of microstrip in millimeter-wave ICs up to 110 GHz has generated a requirement for broadband waveguide-to-microstrip transitions, as nearly all laboratory equipment is fitted with rectangular waveguide RF connectors. Since the maximum operating bandwidth of a millimeter-wave waveguide is about 50%, the waveguide-to-microstrip transition bandwidth is limited to the waveguide operating bandwidth. Several different techniques [57–66] have been used to design a waveguide-to-microstrip transition; however, the commonly used method employs a ridged waveguide as an intermediate step because of broad bandwidth, better field match, and wider range of available impedances. Electric field matching from a rectangular waveguide to a microstrip through a ridged waveguide is shown in Figure 1.26. The waveguide wave impedance is transformed to a microstrip characteristic impedance by using a broadband stepped ridged waveguide transformer [57]. It

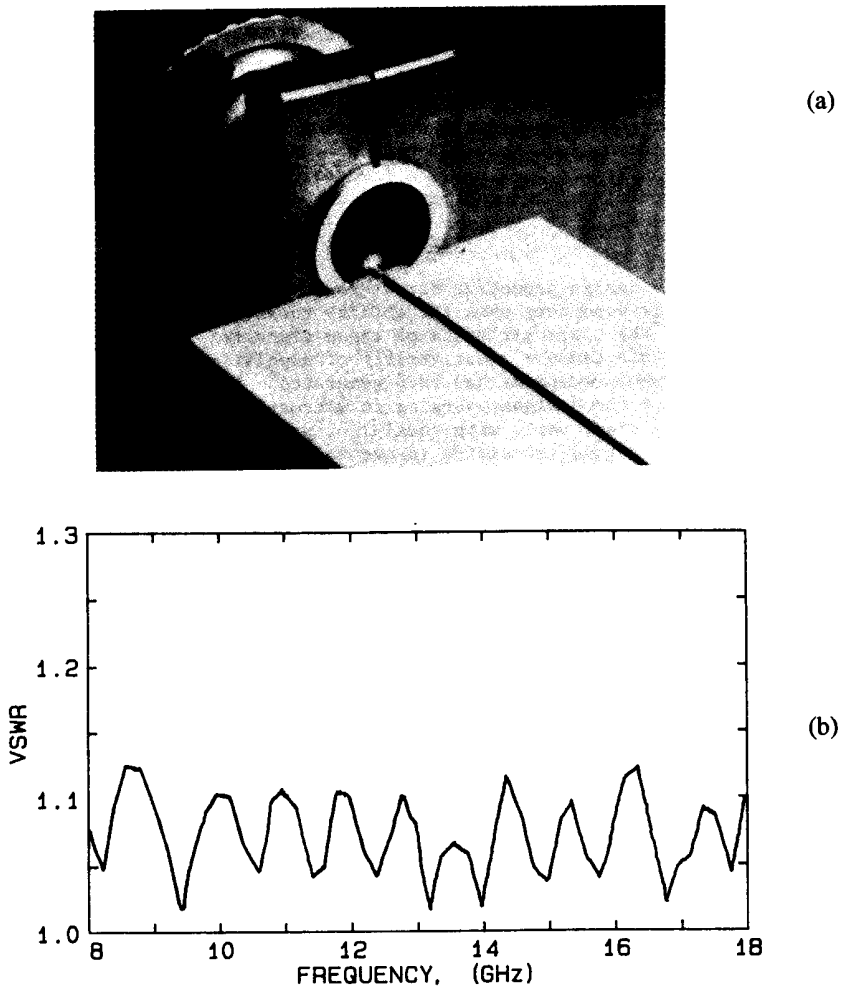


Figure 1.22 (a) Eisenhart transition's side view and (b) measured performance by connecting two transitions back-to-back (from [54], © 1978 IEEE. Reprinted with permission.).

is found that four- or five-step $\lambda/4$ transformers occupy a very small space and provide satisfactory performance. A four-step ridged waveguide transformer operating over the 27.5-GHz to 31.3-GHz band was designed connected to the microstrip by a tab as shown in Figure 1.27. The microstrip used was fabricated on a 0.76-mm-thick quartz substrate. The transition measured greater than a 30-dB return loss and less than a 0.1-dB insertion loss over the band. A similar transition was also analyzed using the mode matching method and the cascading procedure using generalized scattering matrices [66].

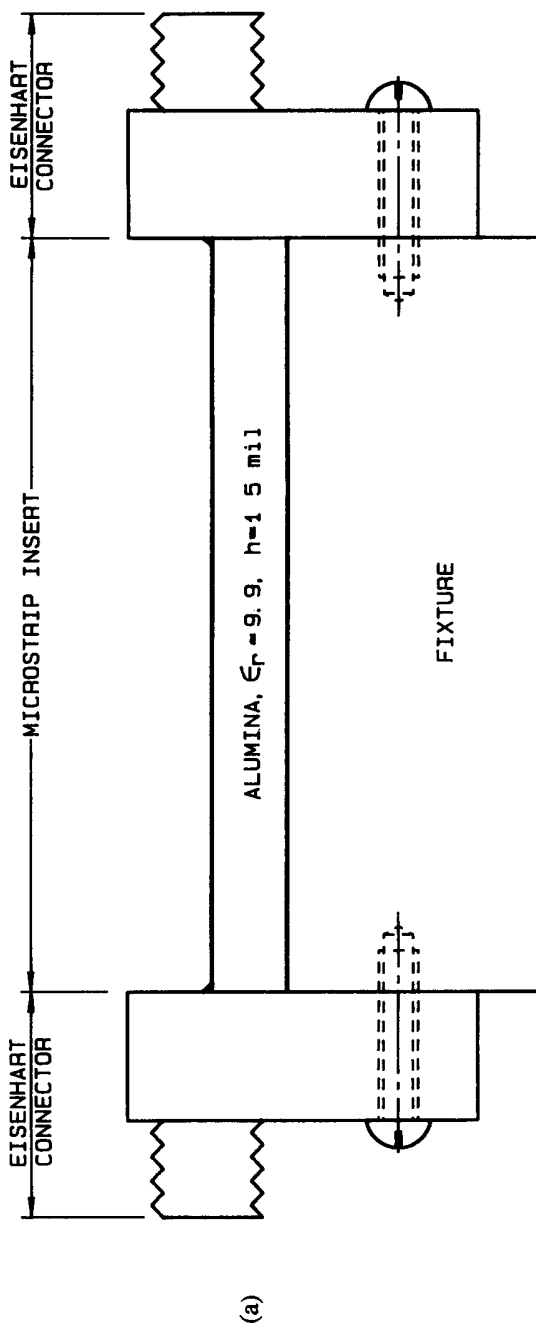


Figure 1.23 (a) Microstrip test assembly with Eisenhart connectors and (b) $|S_{21}|$ and $|S_{11}|$ for 15-mil-thick substrate.

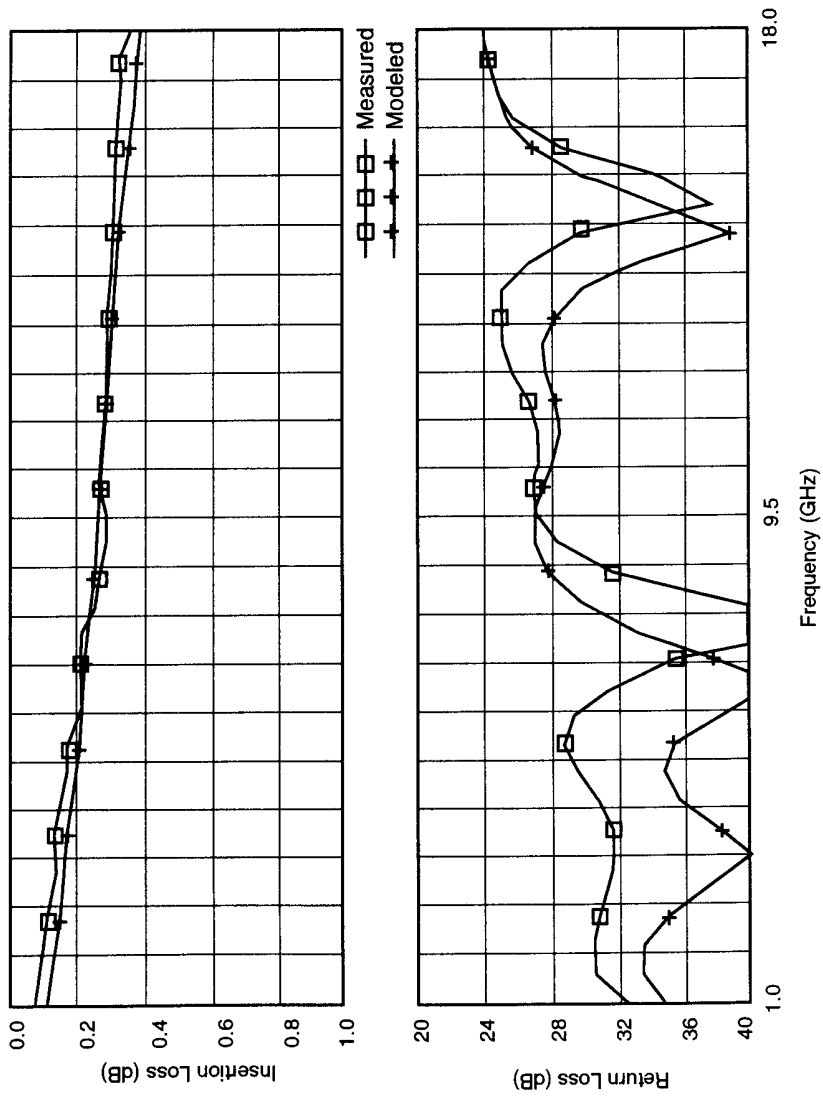


Figure 1.23 (continued).

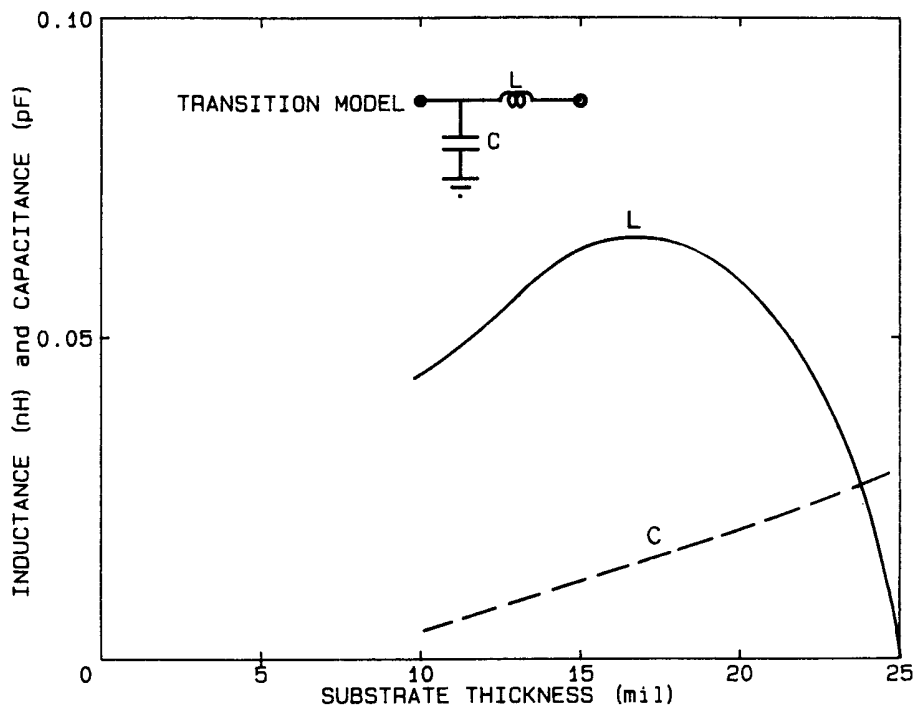


Figure 1.24 Eisenhart connector-to-microstrip transition model values.

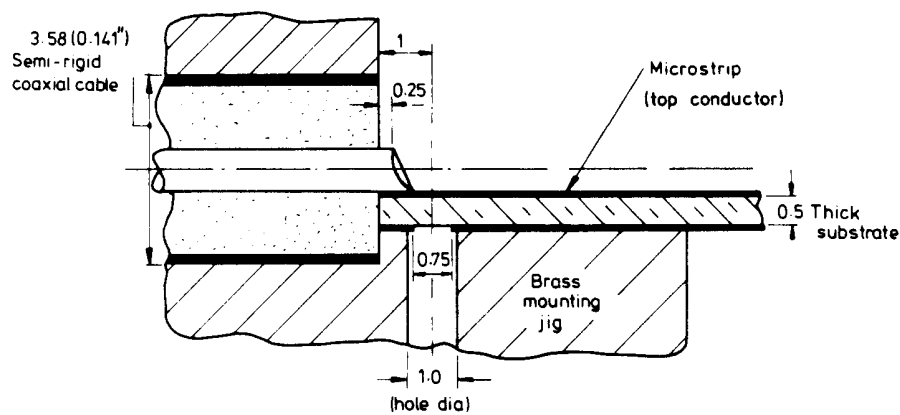


Figure 1.25 Compensated coaxial-to-microstrip transition (all dimensions in millimeters) (from [53], © 1976 IEEE. Reprinted with permission.).

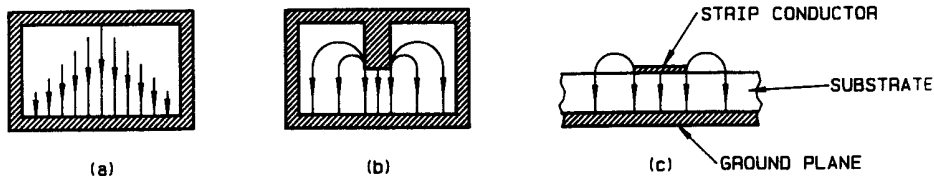


Figure 1.26 Electric field configurations in (a) a waveguide, (b) a ridged waveguide, and (c) an open microstrip.

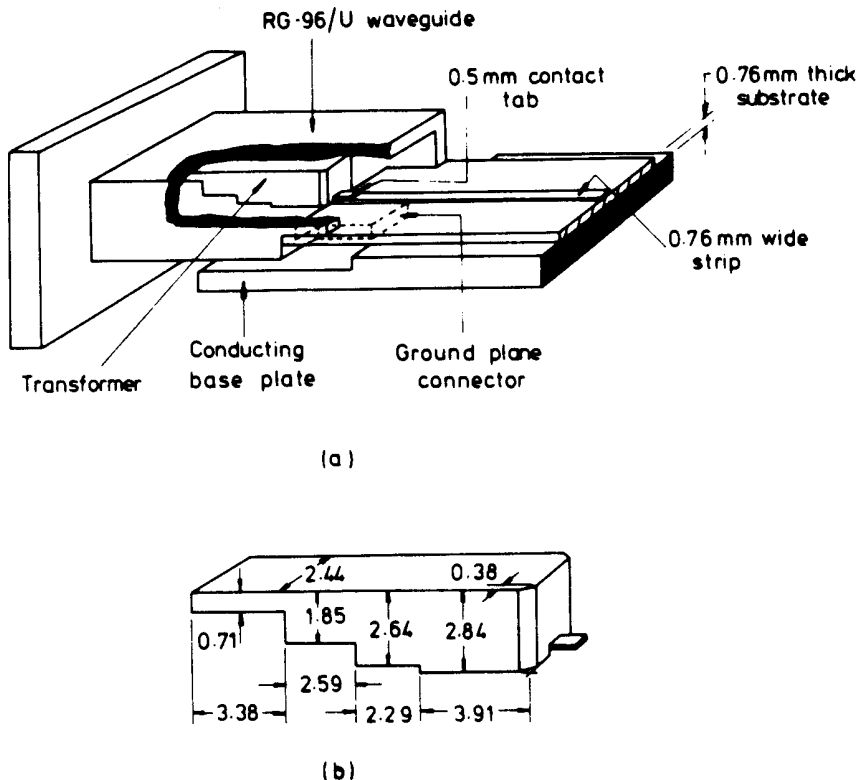


Figure 1.27 Rectangular waveguide-to-microstrip transition using a ridgeline transformer for the 27.5-GHz to 31.8-GHz Band: (a) complete mechanical structure and (b) ridgeline transformer dimensions (all in millimeters) (from [57], © 1969 *The Bell System Technical Journal*, the American Telephone and Telegraph Company. Reprinted with permission.).

However, at higher frequencies, the accuracy limitations of achieving the small dimensions required dictates the performance possible, and the fabrication of such a transition poses serious problems. Tapered ridged waveguide transformers, as shown in Figure 1.28, were also investigated. It was found that a cosine-shaped taper over about three-guide wavelengths long at midband resulted in excellent performance and was considerably less critical in terms of mechanical problems.

Several other waveguide-to-microstrip transitions have been described in the literature [58–60, 62–65]. The simple probe-type waveguide-to-microstrip transition [63] shown in Figure 1.29 is very suitable for combining MIC/MMIC components with waveguide components. As shown in Figure 1.29, the transition consists of a microstrip integrated circuit that is partially extended into the waveguide through an aperture in the broad wall. The substrate fits the full height to facilitate precise alignment. The probe conductor couples the energy from the waveguide; and its input impedance, which is about 75Ω , is matched to 50Ω by using a $\lambda/4$ transformer.

The critical dimensions shown in Figure 1.29 are optimized and summarized in Table 1.2 [63]. An RT5880/Duroid ($\epsilon_r = 2.2$) substrate was used for microstrip lines. The transition was characterized by connecting two transitions back-to-back by a 1.524-cm-long microstrip line. The measured performance for several transitions is also given in Table 1.2.

1.5 MICROSTRIP MEASUREMENTS

As in the case of other transmission structures the important characteristics that need be measured for a microstrip are: (i) characteristic impedance, (ii) phase

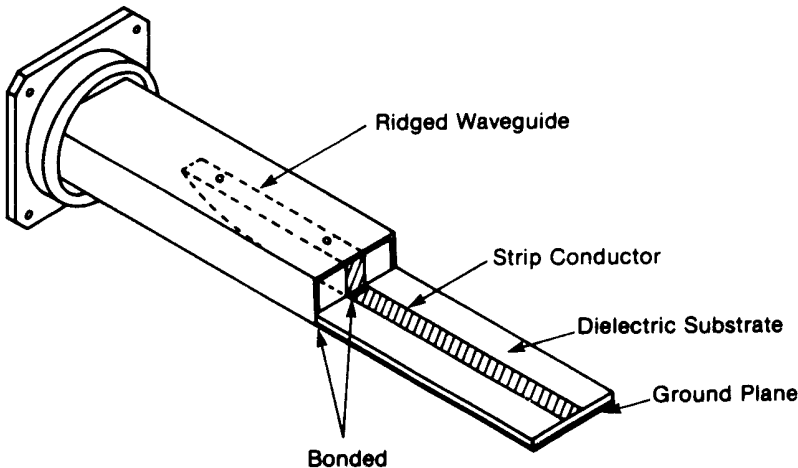


Figure 1.28 Waveguide-to-microstrip transition.

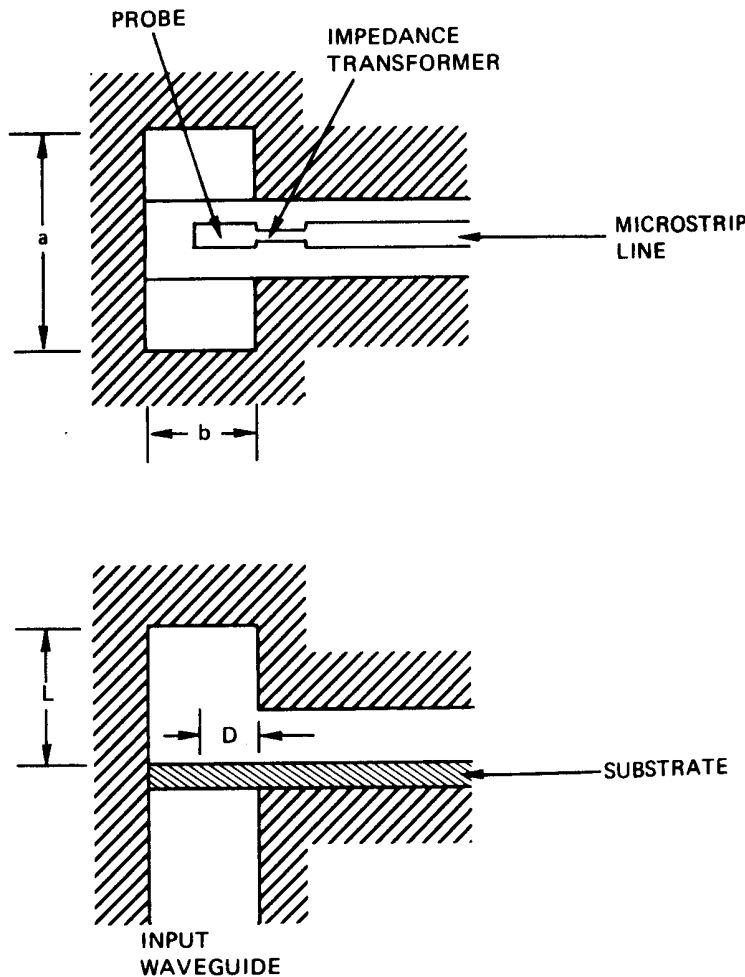


Figure 1.29 Cross-sectional view of a waveguide-to-microstrip transition (from [63], © 1988 IEEE. Reprinted with permission.).

velocity, and (iii) attenuation constant. Also, in several cases, the dielectric constant of the substrate material is not known accurately. Since this information is required for microstrip circuit design, methods have been devised for quick determination of the dielectric constant of metallized substrates [67–69].

In this section we will briefly outline the methods for measuring the substrate dielectric constant and microstrip line characteristics.

Table 1.2
Critical Dimensions for Waveguide-to-Microstrip Transitions and Measured Data for Two
Transitions Connected Back-to-Back by 1.524-cm-long Microstrip Line

Waveguide			Substrate Thickness (mm)	D (mm)	L (mm)	Measured Performance (dB)	
Type	Band	Inside Dimensions ($a \times b$) mm				Return Loss	Insertion Loss
WR 28	Ka	7.112 × 3.556	0.254	2.032	2.032	15	0.4
WR 22	Q	5.69 × 2.845	0.254	1.524	1.524	10	1.0
WR 15	V	3.759 × 1.88	0.127	1.143	1.270	10	2.0
WR 10	W	2.54 × 1.27	0.127	0.711	0.762	14	2.0

1.5.1 Substrate Dielectric Constant

An accurate knowledge of the relative dielectric constant value of substrates is very important for circuit design because this value is used to determine the characteristic impedance and phase velocity. Dielectric constant values for monocrystalline materials such as quartz, sapphire, and GaAs, are fixed. However, for plastic substrates, amorphous materials such as glass, and polycrystalline materials such as ceramics, the dielectric constant value depends upon the manufacturing process and the composition of the final material. In order to control the process, an accurate and automatic ϵ_r measurement technique is necessary.

Basic requirements of an accurate method of measuring ϵ_r include rapid and nondestructive testing, no machining or metallization of the sample (accept substrate as is), real-time measurement, error less than 1 percent, frequency range of 1 GHz to 20 GHz, and handling capability for substrates 0.2-mm to 2-mm thick and 2.5-cm to 10.0-cm long. Several simple techniques for the dielectric constant measurement of microwave substrates have been reported in the literature and are in common use [67–72]. These techniques incorporate the dielectric specimen in a resonant structure, and the permittivity is calculated from a measurement of the resonant frequencies.

In the normal course of fabricating dielectric substrates for MICs, a dielectric-filled resonator cavity is automatically constructed. The rectangular substrate with its top- and bottom-surface metallization (sides not metallized) becomes a parallel plate dielectric-loaded waveguide resonator. This structure is shown in Figure 1.30(a). For high dielectric constant substrates the fringing field is very small, and the sides of the resonator are good approximations to open circuits. The resonant frequency f_{mn} for this type of resonator is given by

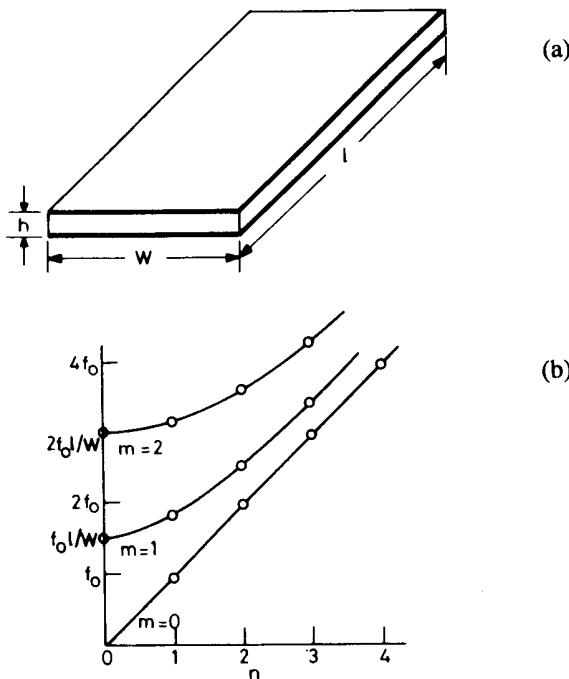


Figure 1.30 (a) Metallized substrate as a parallel plate resonator and (b) resonance frequencies for various modes of a metallized substrate resonator (from [67], © 1971 IEEE. Reprinted with permission.).

$$f_{mn}^2 = \frac{c^2}{\epsilon_r} \left\{ \left(\frac{m}{2W} \right)^2 + \left(\frac{n}{2\ell} \right)^2 \right\} \quad (1.88)$$

where m and n represent the mode of resonance and correspond to the number of half cycle variations along W and ℓ , respectively. Values of f_{mn} are shown in Figure 1.30(b) as dots superimposed on the dispersion curves.

To measure the substrate dielectric constant, the parallel plate resonator is coupled to the measurement system by placing it between two APC-7 type coaxial connectors [67] as shown in Figure 1.31(a). Details of the coupling are shown in Figure 1.31(b). Transmission measurements may be carried out by using a network analyzer or any other suitable system. The modes are identified by referring to Figure 1.30(b).

The accuracy of the above method is limited because of the fringing field and radiation from the open sides of the resonator. A modification has been suggested [68] wherein the substrate is metallized on all sides so that a small microwave cavity is formed. Equation (1.88) for the various resonant frequencies

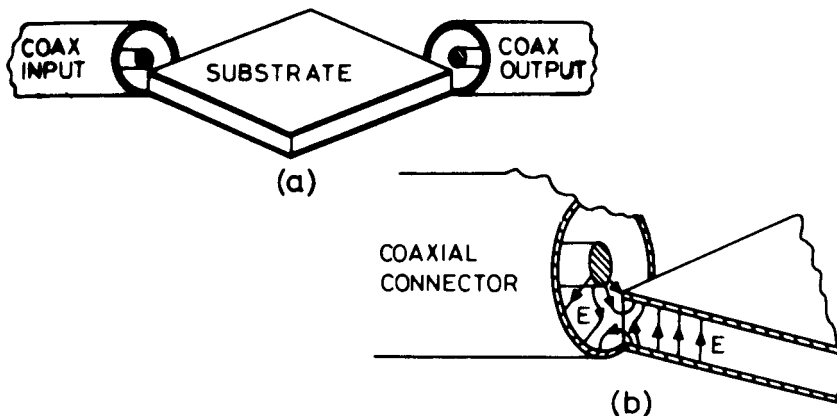


Figure 1.31 Coupling to metallized substrate resonators through coaxial connectors.

is still valid. Resonant frequencies are measured by clearing metallization from the corners of the cavity and positioning the center conductor in APC-7 connectors as shown in Figure 1.31.

Coupling errors in cavity resonance measurements on MIC dielectric substrates are discussed by Ladbrooke et al. [69]. An alternative coupling scheme wherein a coupling aperture is photolithographically cut in the top plane has been suggested. Details of this scheme are shown in Figure 1.32. The broadwall hole with an overlaid strip provides the required coupling, and the energy transfer into and out of the cavity is adequate without having to make the aperture unacceptably large. This type of coupling scheme has been used with substrates that are metallized on the sides also.

Errors because of coupling are analyzed by considering the perturbation of fields. It has been pointed out [69] that the two methods of coupling, namely, corner coupling for resonators with open sides and aperture coupling for resonators with metallized sides, are complementary. As shown in Figures 1.31(b) and 1.32(b), respectively, corner coupling involves the perturbation of electric field lines whereas in the aperture coupling the magnetic field of the resonator is distributed. Errors in the two cases are of opposite natures, and an improved accuracy (≈ 0.5 percent) can be obtained by averaging the results obtained by the two methods.

Although cavity methods are straightforward, they do not lend themselves readily to automated measurements. On the other hand, transmission line methods [73, 74] are particularly well suited to automated measurements. In these methods, the sample is placed in a waveguide and the dielectric constant value is extracted from the two-port scattering parameter measurement using an automatic vector network analyzer. The unmetallized sample is centered between the sidewalls of the waveguide as shown in Figure 1.33 and is easily inserted or extracted via a

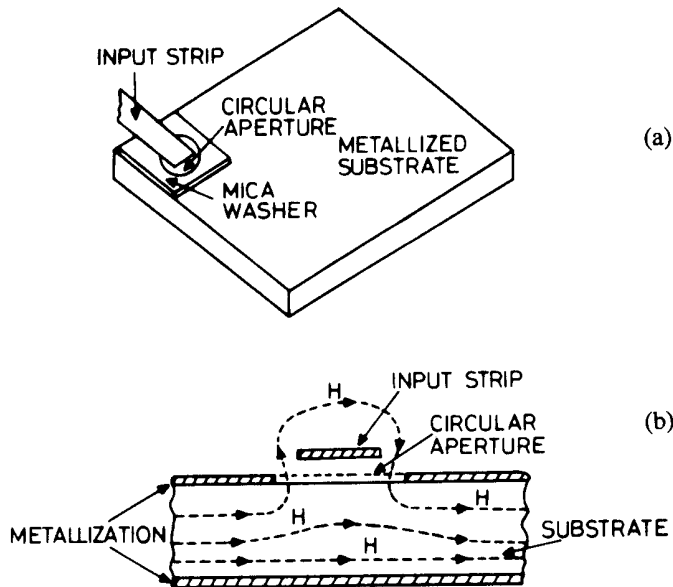


Figure 1.32 Aperture coupling to a substrate resonator metallized on all the sides: (a) configuration and (b) magnetic field distribution (from [69]).

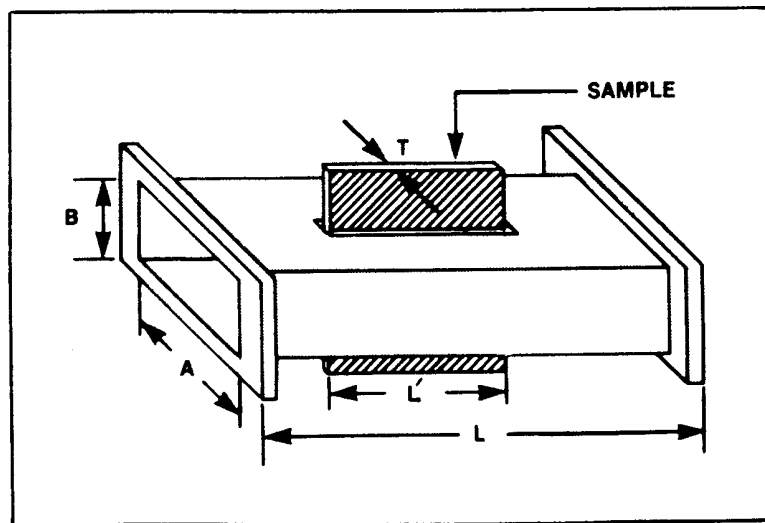


Figure 1.33 A waveguide holder for measuring 2-port S-parameters of a microwave substrate for dielectric constant evaluation (from [74]).

slot. The widespread availability of accurate computer-controlled network analyzers makes this technique attractive. This method of measurement has been described by York and Compton [74].

The dielectric constant can also be determined by measuring the reflection coefficient using an open-ended coaxial line [75] in contact with the unmetallized dielectric substrate. This method has been commercialized by Hewlett-Packard by developing an HP 85070B dielectric probe kit that includes a coaxial probe and the software. The probe is placed in contact with the dielectric substrate and the reflection coefficient is measured using a vector network analyzer. Since the coaxial's open-end fringing fields interact with the dielectric material, ϵ_r and $\tan \delta$ are derived from the reflected signal by solving the boundary value problem. The frequency range of the measurement is from 0.2 GHz to 20 GHz and the accuracy of measurement is about 5 percent. This probe can only be used with thick substrates.

All the above-described transmission and reflection measurement methods require special tools and software to determine the dielectric constant value. The dielectric constant value can also easily be determined by making transmission measurements on a $50\text{-}\Omega$ microstrip line using RF probes [76] or using microstrip transitions as described in the previous section. The effective dielectric constant may be written as

$$\epsilon_{re} = \frac{\epsilon_r + 1}{2} + \frac{\epsilon_r - 1}{2}F$$

or

$$\epsilon_r = [2 \epsilon_{re} + F - 1]/(F + 1) \quad (1.89)$$

where F is obtained from (1.17). For a given $50\text{-}\Omega$ microstrip line length ℓ , if the measured transmission phase ($\angle S_{21}$) in degrees is ϕ , then

$$\epsilon_r = \left[\frac{1}{72} \left(\frac{\phi}{f\ell} \right)^2 + F - 1 \right] / (F + 1) \quad (1.90)$$

where f is in gigahertz and ℓ is in centimeters. Thus, by calculating F as described in Chapter 2, the ϵ_r value can easily be determined. In these measurements, either dispersion effects are kept at a minimum or taken into account in the calculations.

1.5.2 Characteristic Impedance

Since fairly good coaxial-to-microstrip transitions are available, impedance measurement methods are identical to those employed for other transmission lines.

The characteristic impedance can be measured by terminating the microstrip in a matched load and measuring the maximum and minimum VSWR values as functions of frequency. If the impedance to be measured is Z_{0m} Ω using a 50- Ω reference line, then

$$\left(\frac{Z_{0m}}{50}\right)^{\pm 1} = \sqrt{\text{VSWR}_{\max} \cdot \text{VSWR}_{\min}} \quad (1.91)$$

where the exponent +1 is associated with high impedance lines and -1 with low impedance lines. An approximate value of Z_{0m} can be obtained from time domain reflectometry (TDR), and thus the ambiguity between the exponents +1 and -1 can be resolved very easily. It may be noted that this method assumes the frequency insensitivity of Z_{0m} , which is a good approximation for the frequency range of interest.

The above method of measurement has been described by Caulton et al. [77] and by Seckelmann [78]. Several other methods of measuring the characteristic impedance of microstrip lines have been discussed by Getsinger [79].

1.5.3 Phase Velocity or Effective Dielectric Constant

The effective dielectric constant of a microstrip can be measured quite accurately by using resonance techniques. Both the ring and the linear type resonators have been used.

Use of Ring Resonators

A microstrip ring resonator is a microstrip line bent in a circular shape to close in upon itself (Figure 1.34(a)). The main advantage of using ring resonators for dispersion measurements [80] is that, in contrast to the linear resonators, no end effects need to be considered. The resonant frequencies of this type of resonator could be calculated assuming that the mean length of the strip forming the resonator is a multiple of the guide wavelength on the microstrip.

For ring resonators, the curvature of the ring influences the resonance frequencies, so only large resonators can be used. The influence of the curvature becomes large if substrate materials with small relative permittivities and lines with small impedances are used. Under these conditions, the width of the lines becomes large and a mean radius cannot be well defined. When short resonators are used, an accurate analysis of ring resonators is needed. A magnetic wall model of microstrip ring resonators has been discussed by Wolff and Knoppik [81].

The eigenvalue equation resulting from the boundary conditions of a magnetic wall ring resonator model may be written as

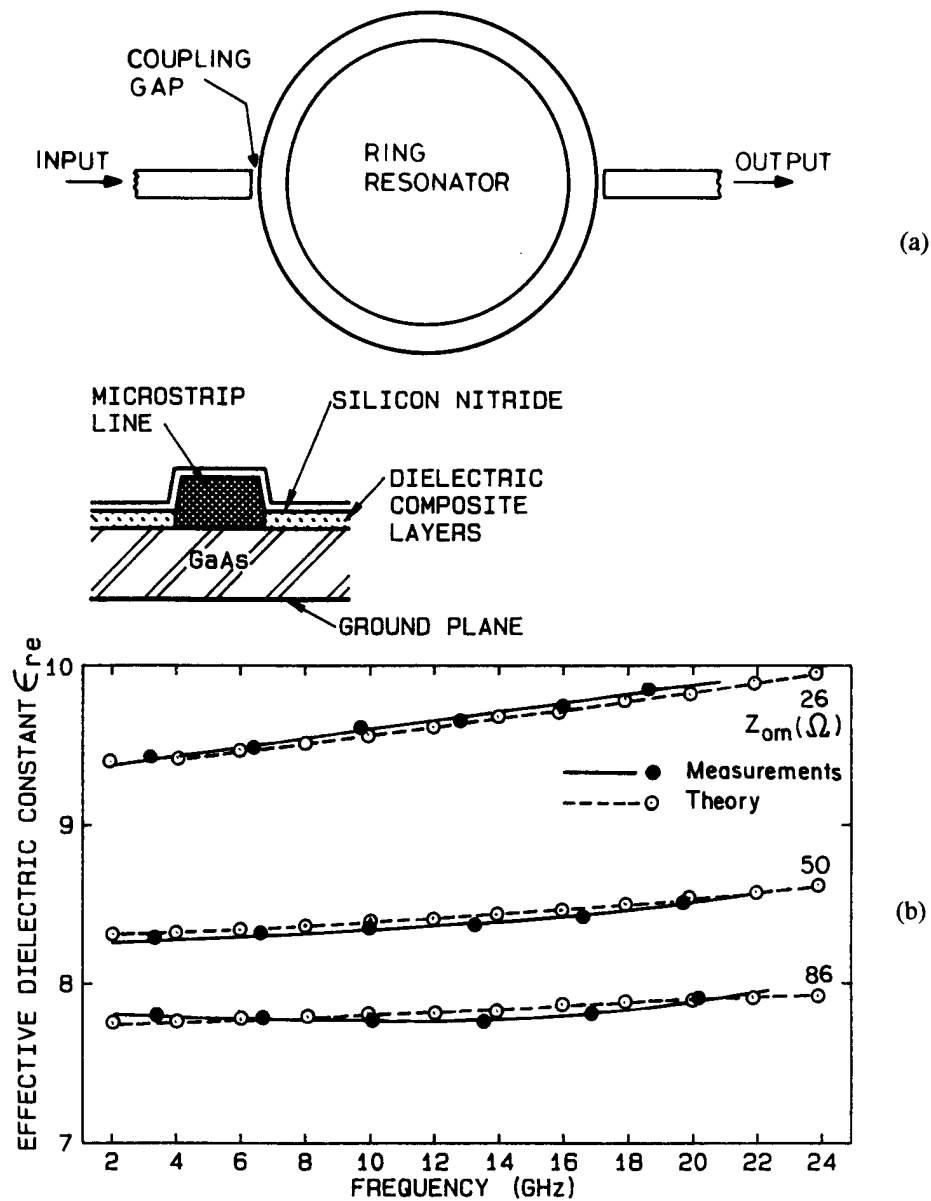


Figure 1.34 (a) A ring resonator set-up for microstrip dispersion measurements and (b) simulated and measured effective dielectric constant versus frequency for a line on 200- μm -thick GaAs substrate (from [83], © 1988 IEEE. Reprinted with permission.).

$$\frac{J'_n(kr_a)}{J'_n(kr_i)} - \frac{N'_n(kr_a)}{N'_n(kr_i)} = 0 \quad (1.92)$$

where k is the wave number in unbounded dielectric and r_a and r_i represent outer and inner radii, respectively. $J'_n(x)$ and $N'_n(x)$ represent derivatives of Bessel functions of the first and the second kind, respectively. Some results based on the solution of (1.92) are described in [81]. It is shown that curvature effects are more pronounced for wider lines (impedances smaller than 50Ω).

More accurate calculations for curvature effect in microstrip ring resonators are presented by Owens [82]. In this method a planar waveguide model is used for the microstrip. Equation (1.92) still holds provided the width of the strip is replaced by the effective width given by this model. Since the effective width is frequency dependent, the frequency variation of the fringing field at the edges of the microstrip is also taken into account.

Extensive measurements were made using ring resonators realized with characteristic impedances in the range of 20Ω to 86Ω on $200\text{-}\mu\text{m}$ -thick GaAs substrate ($\epsilon_r = 12.9$). In these measurements the microstrip configuration uses the composite dielectric structure shown in Figure 1.34 [83]. Here the thicknesses of silicon nitride and dielectric composite layers are very small compared to the substrate thickness. Simulated and measured effective dielectric constant versus frequency are shown in Figure 1.34(b). Note that dispersion effects are negligible up to 18 GHz for microstrip lines of $Z_{0m} \geq 50 \Omega$ on $200\text{-}\mu\text{m}$ -thick substrate.

Linear Resonator Method

The main difficulty with the use of a linear resonator is caused by the end effects. When a linear resonator is coupled to the measurement system at one end, as shown in Figure 1.35(a), the reactances at the two ends are different. The open

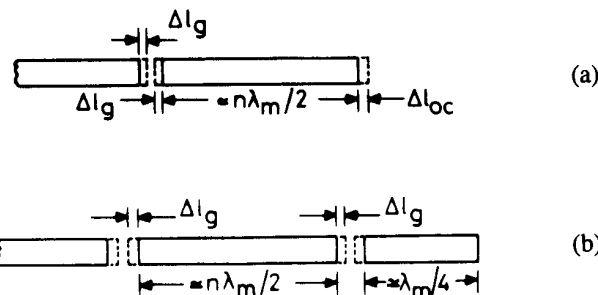


Figure 1.35 (a) A linear microstrip resonator and (b) a modified linear resonator configuration.

end can be represented either by a shunt capacitance or by an incremental line length $\Delta\ell_{oc}$. On the other hand, the gap between the input line and the resonator is represented by a π -network of capacitances, and the incremental length $\Delta\ell_g$ shown in the figure is different from $\Delta\ell_{oc}$. Measurement of the discontinuity reactances will be discussed in detail in Chapter 4. For the purposes of the present discussion, one requires incorporating the effect of these reactances for the accurate measurement of resonant frequencies. A method suitable for this purpose has been described by Richings [84] and by Easter [85]. This method suggests the use of a modified resonator set up as shown in Figure 1.35(b). A $\lambda_m/4$ section at the other end of the resonator ensures that the reactances at two ends of the resonator are identical. Thus, there are only two unknowns now, and these (ϵ_{re} and $\Delta\ell_g$) can be evaluated if measurements are carried out for two different lengths of the resonator.

Alternatively, the effective dielectric constant can be measured by the substitution method using two resonators [6, 51]. Here it is assumed that the two resonant frequencies f_1 and f_2 are very close and that the two structures as shown in Figure 1.36 are identical except for the physical lengths L_1 and L_2 of the resonators. In this configuration, the resonators are loosely coupled, and from the n th-order $\lambda/2$ resonance frequency

$$\epsilon_{re} = \left[\frac{nc}{2f_{1,2}(L_{1,2} + \ell_e)} \right]^2 \quad (1.93)$$

where subscripts 1 and 2 denote resonators 1 and 2, respectively, and c is the velocity of light. The term ℓ_e represents the sum of the coupling-gap end effect $\Delta\ell_g$ and the open-end effect $\Delta\ell_{oc}$. When ϵ_{re} and ℓ_e are constant over the f_2-f_1 range, (1.93) becomes

$$\epsilon_{re} = \left[\frac{nc(f_1 - f_2)}{2f_1 f_2 (L_2 - L_1)} \right]^2 \quad (1.94)$$

where

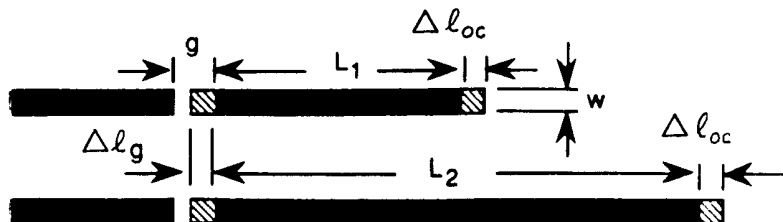


Figure 1.36 Linear resonator pair for dispersion measurements. By measuring the resonant frequency of the two resonators, end effects can be canceled.

$$\ell_e = \frac{f_2 L_2 - f_1 L_1}{f_1 - f_2} \quad (1.95)$$

This method provides ϵ_{re} as a function of frequency and can also be used to calculate ϵ_r from ϵ_{re} as described previously in Section 1.5.1.

1.5.4 Attenuation Constant

The most satisfactory method for measuring the attenuation constant for low-loss substrates is from the Q -factor of a resonant section of the line. The attenuation constant and the unloaded quality factor Q_0 are related by the expression

$$\alpha = \frac{27.3 n}{Q_0 \lambda_m} \text{ (dB/cm)} \quad (1.96)$$

where n is the number of half wavelengths and λ_m is the guide wavelength in centimeters.

It has been pointed out that the ring resonator technique is less suitable for the accurate measurement of microstrip losses because of increased surface wave radiation loss [86]. On the other hand, the shielded open-ended linear resonator in a waveguide below cut-off gives a reliable value of the attenuation constant.

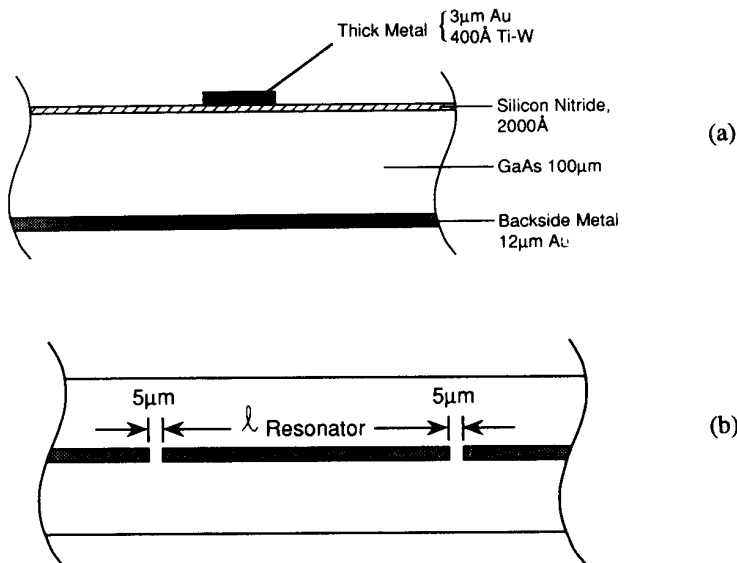


Figure 1.37 Microstrip resonator on GaAs substrate: (a) cross-section view and (b) top view.

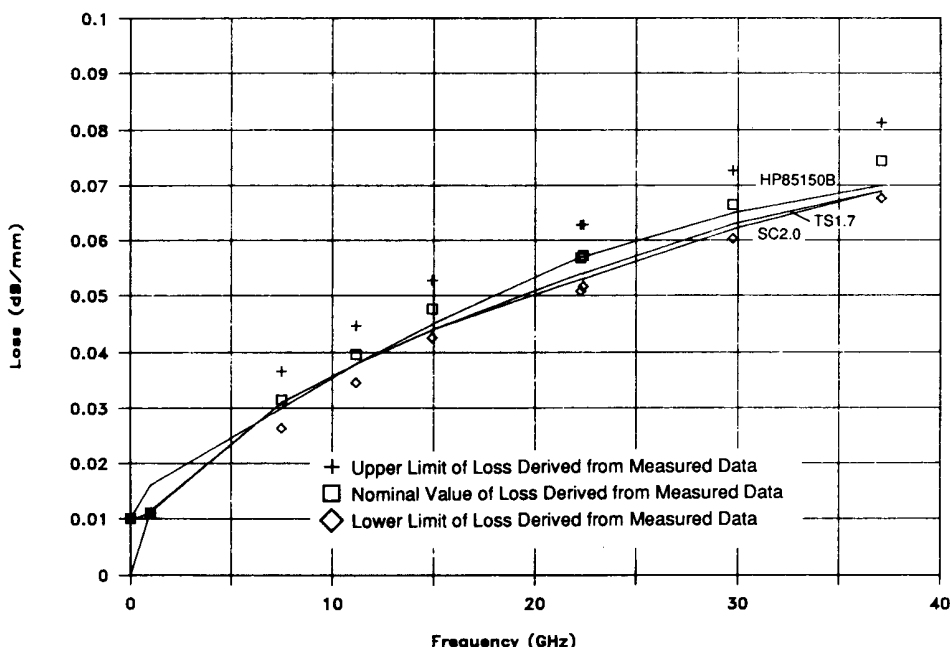


Figure 1.38 Losses in GaAs microstrip for 70- μm width on 100- μm GaAs (from [87], © 1990 IEEE. Reprinted with permission.).

More accurate methods for measuring microstrip line losses have also been described in the literature [87, 88]. Extensive measured data for microstrip loss on GaAs substrates as shown in Figure 1.37, have been given by Goldfarb and Platzker [87]. The results given are for an impedance range of 20 Ω to 90 Ω and for frequencies up to 40 GHz. Figure 1.38 shows a 50- Ω microstrip line loss as a function of frequency. Measured data was also compared with Touchstone (TS1.7), Super Compact (SC2.0), and MDS (HP85150B). The microstrip parameters used for comparison were: unit line length = 1 mm, $\epsilon_r = 12.9$, $h = 100 \mu\text{m}$, $t = 3 \mu\text{m}$, conductor resistivity = 2.44 $\mu\Omega\cdot\text{cm}$, $\tan \delta = 0$, and roughness factor = 0. Figure 1.39 shows measured loss versus line width at several frequencies [87].

An approximate but very simple method for measuring the attenuation constant is based on the comparison technique. In this method two microstrip lines with identical electrical characteristics but different lengths are used. Their insertion losses are measured. The difference between the two values of insertion loss is used to evaluate the attenuation constant. This procedure avoids the systematic errors caused by radiation, coaxial-to-microstrip transition, and so forth. With recent advancements in the de-embedding techniques and RF probes, the attenuation constant of a microstrip line can also be measured accurately using two-port scattering parameter measurements.

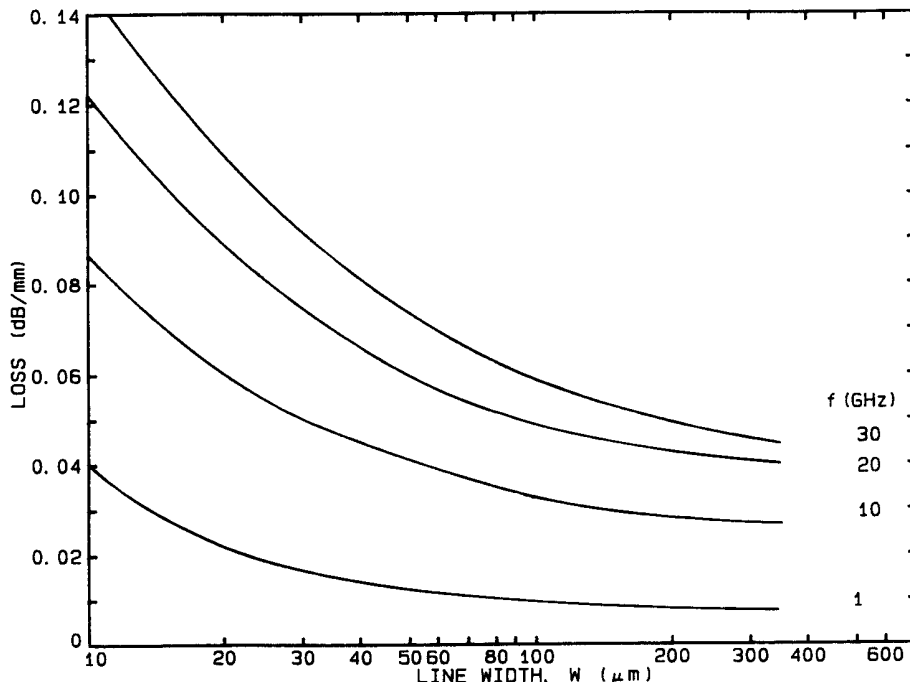


Figure 1.39 Measured microstrip loss versus line width at 1 GHz, 10 GHz, 20 GHz, and 30 GHz; substrate thickness of GaAs: 100 μm .

References

- [1] Gupta, K. C., and A. Singh (Eds.), *Microwave Integrated Circuits*, New York: Halsted Press (John Wiley and Sons), 1974.
- [2] Young, L., and H. Sobol (Eds.), *Advances in Microwaves*, Vol. 8, New York: Academic Press, 1974.
- [3] Frey, J. (Ed.), *Microwave Integrated Circuits*, Dedham, MA: Artech House, 1975. (a reprint volume).
- [4] Hoffman, R. K., *Handbook of Microwave Integrated Circuits*, Norwood, MA: Artech House, 1987.
- [5] Sweet, A. A., *MIC & MMIC Amplifier and Oscillator Circuit Design*, Norwood, MA: Artech House, 1990.
- [6] Edwards, Terry, *Foundations for Microstrip Circuit Design*, 2nd ed., Chichester, U.K.: John Wiley & Sons, 1992.
- [7] Buntschuh, C., "A Study of the Transmission Line Properties of Trapped Inverted Microstrip Line," *Rome Air Development Center-Technical Report-74-311, AD# A-003633*, December 1974.
- [8] Yamashita, E., and K. Atsuki, "Analysis of Microstrip-like Transmission Lines by Non-Uniform Discretization of Integral Equations," *IEEE Trans.*, Vol. MTT-24, 1976, pp. 195–200.
- [9] Schneider, M. V., "Microstrip Lines for Microwave Integrated Circuits," *Bell System Technical Journal*, Vol. 48, 1969, pp. 1421–1444.
- [10] McLevige, W. V., et al., "New Waveguide Structures for Millimeter Wave and Optical Integrated Circuits," *IEEE Trans.*, Vol. MTT-23, 1975, pp. 788–794.
- [11] Howe, H., *Stripline Circuit Design*, Dedham, MA: Artech House, 1974.

- [12] Bahl, I. J., and Ramesh Garg, "A Designer's Guide to Stripline Circuits," *Microwaves*, Vol. 17, 1978, pp. 90–96.
- [13] Wheeler, H. A., "Transmission Line Properties of Parallel Wide Strips by Conformal Mapping Approximation," *IEEE Trans.*, Vol. MTT-12, 1964, pp. 280–289.
- [14] Wheeler, H. A., "Transmission Line Properties of Parallel Strips Separated by a Dielectric Sheet," *IEEE Trans.*, Vol. MTT-13, 1965, pp. 172–185.
- [15] Sobol, H., "Application of Integrated Circuit Technology to Microwave Frequencies," *Proc. IEEE*, Vol. 59, 1971, pp. 1200–1211.
- [16] Svacina, J., "Analysis of Multilayer Microstrip Lines by a Conformal Mapping," *IEEE Trans.*, Vol. MTT-40, No. 4, 1992, pp. 769–782.
- [17] Stinehelfer, H. E., "An Accurate Calculation of Uniform Microstrip Transmission Lines," *IEEE Trans.*, Vol. MTT-16, 1968, pp. 439–444.
- [18] Green, H. E., "The Numerical Solution of Some Important Transmission Line Problems," *IEEE Trans.*, Vol. MTT-13, 1965, pp. 676–692.
- [19] Silvester, P., "TEM Properties of Microstrip Transmission Lines," *Proc. IEE*, Vol. 115, 1968, pp. 42–49.
- [20] Yamashita, E., and R. Mittra, "Variational Method for the Analysis of Microstrip Lines," *IEEE Trans.*, Vol. MTT-16, 1968, pp. 251–256.
- [21] Yamashita, E., "Variational Method for the Analysis of Microstrip-like Transmission Lines," *IEEE Trans.*, Vol. MTT-16, 1968, pp. 529–535.
- [22] Tsai, C.-M., "Field Analysis, Network Modeling and Circuit Applications of Inhomogeneous Multi-Conductor Transmission Lines," Ph.D. Thesis, Dept. of Electrical and Computer Engineering, University of Colorado, Boulder, CO, June 1993.
- [23] Gupta, K. C., and M. D. Abouzahra, "Planar Circuit Analysis," *Numerical Techniques for Microwave and Millimeter-Wave Passive Structures* (ed. T. Itoh), New York: John Wiley & Sons, 1989, pp. 256–260.
- [24] Gupta, K. C., and M. D. Abouzahra, "Segmentation and Desegmentation Techniques," *Analysis and Design of Planar Microwave Components*, Piscataway, NJ: IEEE Press, 1994, pp. 75–86.
- [25] Brebbia, C. A., *The Boundary Element Method for Engineers*, New York: John Wiley & Sons, 1978.
- [26] Banerjee, P. K., and R. Butterfield, *Boundary Element Methods in Engineering Science*, New York: McGraw-Hill, 1981.
- [27] Sano, H., and K. Sadao, "Analysis of Dielectric Waveguide Problem by Boundary Element Method," *Electronics and Communications in Japan*, Part 1, Vol. 70, No. 1, 1987.
- [28] Peaiyoung, S., and S. J. Salon, "Some Technical Aspects of Implementing Boundary Element Equations," *IEEE Trans. on Magnetics*, Vol. 25, No. 4, July 1989.
- [29] Fairweather, G. F., J. Rizzo, D. J. Shippy, and Y. S. Wu, "On the Numerical Solution of Two-Dimensional Potential Problems by an Improved Boundary Integral Equation Method," *J. Computational Physics*, Vol. 31, 1979, pp. 96–112.
- [30] Kellogg, O. D., *Foundations of Potential Theory*, Berlin: Springer, 1929.
- [31] Gupta, K. C., Ramesh Garg, and Rakesh Chadha, *Computer-Aided Design of Microwave Circuits*, Norwood, MA: Artech House, 1981.
- [32] Itoh, T. (Ed.), *Numerical Techniques for Microwave and Millimeter-Wave Passive Structures*, New York: John Wiley & Sons, 1989.
- [33] Davies, J. B., "The Finite Element Method," *Numerical Techniques for Microwave and Millimeter-Wave Passive Structures* (ed. T. Itoh), New York: John Wiley & Sons, 1989.
- [34] Jain, O. P. et al., "Coupled Mode Model of Dispersion in Microstrip," *Electron. Lett.*, Vol. 7, 1971, pp. 405–407.
- [35] Schneider, M. V., "Microstrip Dispersion," *Proc. IEEE*, Vol. 60, 1972, pp. 144–146.
- [36] Getsinger, W. J., "Microstrip Dispersion Model," *IEEE Trans.*, Vol. MTT-21, 1973, pp. 34–39.
- [37] Carlin, H. J., "A Simplified Circuit Model for Microstrip," *IEEE Trans.*, Vol. MTT-21, 1973, pp. 589–591.
- [38] Kompa, G., and R. Mehran, "Planar Waveguide Model for Calculating Microstrip Components," *Electron. Lett.*, Vol. 11, 1975, pp. 459–460.

- [39] Edwards, T. C., and R. R. Owens, "2-18 GHz Dispersion Measurements on 10–100 ohm Microstrip Lines on Sapphire," *IEEE Trans.*, Vol. MTT-24, 1976, pp. 506–513.
- [40] Noble, D. F., and H. J. Carlin, "Circuit Properties of Coupled Dispersive Transmission Lines," *IEEE Trans. on Circuit Theory*, Vol. CT-20, 1973, pp. 56–65.
- [41] Yamashita, E., K. Atsuki, and T. Ueda, "An Approximate Dispersion Formula of Microstrip Lines for Computer-Aided Design of Microwave Integrated Circuits," *IEEE Trans.*, Vol. MTT-27, December 1979, pp. 1036–1038.
- [42] Hammerstad, E., and O. Jensen, "Accurate Models for Microstrip Computer-Aided Design," *IEEE MTT-S Int. Microwave Symp. Digest*, 1980, pp. 407–409.
- [43] Pues, H. F., and A. R. van de Capelle, "Approximate Formulas for Frequency Dependence of Microstrip Parameters," *Electron Lett.*, Vol. 16, No. 23, 1980, pp. 870–872.
- [44] Kirschning, M., and R. H. Jansen, "Accurate Model for Effective Dielectric Constant of Microstrip and Validity up to Millimeter-wave Frequencies," *Electron. Lett.*, Vol. 18, March 18, 1982, pp. 272–273.
- [45] Kobayashi, M., "Frequency Dependent Characteristics of Microstrips on Anisotropic Substrates," *IEEE Trans.*, Vol. MTT-30, November 1982, pp. 2054–2057.
- [46] Kobayashi, M., "Important Role of Inflection Frequency in the Dispersive Property of Microstrip Lines," *IEEE Trans.*, Vol. MTT-30, November 1982, pp. 2057–2059.
- [47] Pramanick, P. and P. Bhartia, "An Accurate Description of Dispersion in Microstrip Lines," *Microwave J.*, Vol. 26, December 1983, pp. 89–92.
- [48] Atwater, H. A., "Tests of Microstrip Dispersion Formulas," *IEEE Trans.*, Vol. MTT-36, March 1988, pp. 619–621.
- [49] Kobayashi, M., "A Dispersion Formula Satisfying Recent Requirements in Microstrip CAD," *IEEE Trans.*, Vol. MTT-36, August 1988, pp. 1246–1250.
- [50] Roy, J. S., et al., "Dispersion Characteristics of Curved Microstrip Transmission Lines," *IEEE Trans.*, Vol. MTT-38, August 1990, pp. 1366–1370.
- [51] York, R. A., and Compton, R. C., "Experimental Evaluation of Existing CAD Models for Microstrip Dispersion," *IEEE Trans.*, Vol. MTT-38, No. 3, March 1990, pp. 327–328.
- [52] Yamashita, E., K. Atsuki, and T. Hirahata, Microstrip Dispersion in a Wide Frequency Range," *IEEE Trans.*, Vol. MTT-29, June 1981, pp. 610–611.
- [53] England, E. H., "A Coaxial to Microstrip Transition," *IEEE Trans.*, Vol. MTT-26, January 1976, pp. 47–48.
- [54] Eisenhart, E. L., "A Better Microstrip Connector," *IEEE MTT-S Int. Microwave Symp. Digest*, 1978, pp. 318–320.
- [55] Majewski, M. L., R. W. Rose, and J. R. Scott, "Modeling and Characterization of Microstrip-to-Coaxial Transitions," *IEEE Trans.*, Vol. MTT-29, August 1981, pp. 799–805.
- [56] Izadian, J. S., and S. M. Izadian, *Microwave Transition Design*, Norwood, MA: Artech House, 1988.
- [57] Schneider, M. V., B. Glance, and W. F. Bodtmann, "Microwave and Millimeter Wave Integrated Circuits for Radio Systems," *Bell Syst. Tech. J.*, Vol. 48, July–Aug. 1969, pp. 1703–1726.
- [58] Van Heuven, J. H. C., "A New Integrated Waveguide-Microstrip Transition," *IEEE Trans.*, Vol. MTT-26, March 1976, pp. 144–147.
- [59] Lavedan, L. J., "Design of Waveguide-to-Microstrip Transitions Specially Suited to Millimeter-wave Applications," *Electron. Lett.*, Vol. 13, September 1977, pp. 81–82.
- [60] Bharj, S. S., and S. Mak, "Waveguide-to-Microstrip Transition Uses Evanescent Mode," *Microwave & RF*, Vol. 23, January 1984, pp. 99–100, 134.
- [61] Moochalla, S. S., and C. An, "Ridge Waveguide Used in Microstrip Transition, *Microwaves & RF*, Vol. 23, March 1984, pp. 149–152.
- [62] Ponchak, G. E., and A. N. Downey, "A New Model for Broadband Waveguide-to-Microstrip Transition Design," *Microwave J.*, Vol. 31, May 1988, pp. 333–343.
- [63] Shih, Y. C., T. N. Ton, and L. Q. Bui, "Waveguide-to-Microstrip Transitions for Millimeter-Wave Applications," *IEEE MTT-S Int. Microwave Symp. Digest*, 1988, pp. 473–475.

- [64] Beaudette, R. G., and L. J. Kushner, "Waveguide-to-Microstrip Transitions," *Microwave J.*, Vol. 32, September 1989, pp. 211–216.
- [65] Gill, H. S., "Transition Links Waveguide and Microstrip Lines," *Microwaves & RF*, Vol. 33, May 1994, pp. 119–120.
- [66] Yao, H. W., et al., "Analysis and Design of Microstrip-to-Waveguide Transitions," *IEEE Trans.*, Vol. MTT-42, December 1994, pp. 2371–2380.
- [67] Napoli, L. S., and J. J. Hughes, "A Simple Technique for the Accurate Determination of the Microwave Dielectric Constant for Microwave Integrated Circuits," *IEEE Trans.*, Vol. MTT-19, 1971, pp. 664–665.
- [68] Howell, J. Q., "A Quick, Accurate Method to Measure the Dielectric Constant of Microwave Integrated Circuit Substrates," *IEEE Trans.*, Vol. MTT-21, 1973, pp. 142–143.
- [69] Ladbrooke, P. H., et al., "Coupling Errors in Cavity Resonance Measurements on MIC Dielectrics," *IEEE Trans.*, Vol. MTT-21, 1973, pp. 560–562.
- [70] Traut, G. R., "Electrical Test Methods for Microwave PCBs," *Microwave J.*, Vol. 24, December 1981, pp. 73–79.
- [71] Kent, G., "Dielectric Resonances for Measuring Dielectric Properties," *Microwave J.*, Vol. 31, October 1988, pp. 99–114.
- [72] Kent, G., "An Evanescent-Mode Tester for Ceramic Dielectric Substrates," *IEEE Trans.*, Vol. MTT-31, October 1988, pp. 1452–1454.
- [73] Kent, G., "A New Method for Measuring the Properties of Dielectric Substrates," *IEEE MTT-Symp. Digest*, 1988, pp. 751–754.
- [74] York, R. A., and R. C. Compton, "An Automated Method for Dielectric Constant Measurements of Microwave Substrates," *Microwave J.*, Vol. 33, March 1990, pp. 115–121.
- [75] Athey, T. W., M. A. Stuchly, and S. S. Stuchly, "Measurement of Radio Frequency Permittivity of Biological Tissues with an Open-Ended Coaxial Line: Part I," *IEEE Trans.*, Vol. MTT-30, January 1982, pp. 82–86.
- [76] Bahl, I., G. Lewis, and J. Jorgenson, "Automatic Testing of MMIC Wafers," *Int. J. Microwave and Millimeter-Wave Computer-Aided Engineering*, Vol. 1, January 1991, pp. 77–89.
- [77] Caulton, M., et al., "Measurements on the Properties of Microstrip Transmission Lines for Microwave Integrated Circuits," *RCA Review*, Vol. 27, 1966, pp. 377–391.
- [78] Seckelmann, R., "On the Measurement of Microstrip Properties," *Microwave J.*, Vol. 11, January 1968, pp. 61–64.
- [79] Getsinger, W. J., "Measurement and Modeling of the Apparent Characteristic Impedance of Microstrip," *IEEE Trans.*, Vol. MTT-31, August 1983, pp. 624–632.
- [80] Troughton, P., "Measurement Technique in Microstrip," *Electron. Lett.*, Vol. 5, 1969, pp. 25–26.
- [81] Wolff, I., and N. Knoppik, "Microstrip Ring Resonator and Dispersion Measurement on Microstrip Lines," *Electron. Lett.*, Vol. 7, 1971, pp. 779–781.
- [82] Owens, R. P., "Curvature Effect in Microstrip Ring Resonators," *Electron. Lett.*, Vol. 12, 1976, pp. 356–357.
- [83] Finlay, H., et al., "Accurate Characterization and Modeling of Transmission Lines for GaAs MMICs," *IEEE Trans.*, Vol. MTT-36, June 1988, pp. 961–967.
- [84] Richings, J. G., "An Accurate Experimental Method for Determining the Important Properties of Microstrip Transmission Lines," *Marconi Review*, 1974, pp. 210–216.
- [85] Easter, B., "The Equivalent Circuit of Some Microstrip Discontinuities," *IEEE Trans.*, Vol. MTT-23, 1975, pp. 655–660.
- [86] Van Heuven, J. H. C., "Conduction and Radiation Losses in Microstrip," *IEEE Trans.*, Vol. MTT-22, 1974, pp. 841–844.
- [87] Goldfarb, M., and A. Platzker, "Losses in GaAs Microstrip," *IEEE Trans. on Microwave Theory Tech.*, Vol. MTT-38, December 1990, pp. 1957–1963.
- [88] Carroll, J., M. Li, and K. Chang, "New Technique to Measure Transmission Line Attenuation," *IEEE Trans. on Microwave Theory Tech.*, Vol. MTT-43, January 1995, pp. 219–222.

CHAPTER 2

Microstrip Lines II: Fullwave Analyses, Design Considerations, and Applications

2.1 METHODS OF FULLWAVE ANALYSIS

As pointed out in Chapter 1, the microstrip configuration is not capable of supporting a pure TEM mode, and small longitudinal components of both the electric and magnetic fields need to be present to satisfy boundary conditions at the dielectric-air interface. These hybrid modes supported by the microstrip cannot be fully described in terms of static capacitances and inductances only. Therefore, one has to consider time-varying electric and magnetic fields and solve the wave equation subject to appropriate boundary conditions. Field analysis of the microstrip (or any other structure, for that matter) without invoking any quasi-static approximations is known as fullwave analysis. Fullwave analysis is carried out to determine the propagation constant instead of the capacitance evaluated in quasi-static analysis.

Methods of studying wave propagation along a microstrip line without making any quasi-static assumption will now be discussed. These methods may be divided into two groups. In one group, the microstrip is considered with a rectangular enclosure, and the other group deals with open microstrip lines. This grouping becomes convenient since different types of mathematical tools are needed to handle closed and open geometries. For example, a Fourier series representation can be used to express the fields in a closed rectangular structure whereas a Fourier integral representation is suited for an open structure.

From the arguments given in Section 1.1.2, it can be seen that the microstrip modes cannot be pure TM or TE waves either. Longitudinal components of both the electric and the magnetic fields are needed. These hybrid modes may be

considered as superposition of TE and TM fields that may, in turn, be expressed in terms of two scalar potentials ψ^h and ψ^c , respectively. Referring to the microstrip configuration of Figure 2.1, the longitudinal and transverse components of the electric and magnetic fields may be written as

$$E_z = j[(k^2 - \beta^2)/\beta] \psi^c(x, y) \exp(-j\beta z) \quad (2.1)$$

$$H_z = j[(k^2 - \beta^2)/\beta] \psi^h(x, y) \exp(-j\beta z) \quad (2.2)$$

$$E_t = [\nabla_t \psi^c(x, y) - (\omega\mu/\beta)(\hat{z} \times \nabla_t) \psi^h(x, y)] \exp(-j\beta z) \quad (2.3)$$

$$H_t = [(\omega\epsilon/\beta)(\hat{z} \times \nabla_t) \psi^c(x, y) + \nabla_t \psi^h(x, y)] \exp(-j\beta z) \quad (2.4)$$

where β is the unknown propagation constant along the z -direction and $k = \omega(\epsilon_0\epsilon_r\mu_0)^{1/2}$. Subscript t refers to transverse coordinates (x, y), and \hat{z} is a unit vector in the z -direction. These relations hold good for both regions 1 and 2, shown in Figure 2.1, when a suitable value of ϵ_r is used in the wavenumber k . Appropriate expressions for ψ^c and ψ^h are chosen for regions 1 and 2. It has been assumed that the structure is lossless and the substrate is nonmagnetic. The field representation of (2.1) to (2.4) is also valid for an enclosed microstrip structure.

The modes of propagation can be divided into two orthogonal sets of modes because the structure is symmetrical about the y - z -plane. One of these sets has a symmetric E_z component and an antisymmetric H_z component (E_z even – H_z odd), while the other set is designated as E_z odd – H_z even. The dominant mode is the

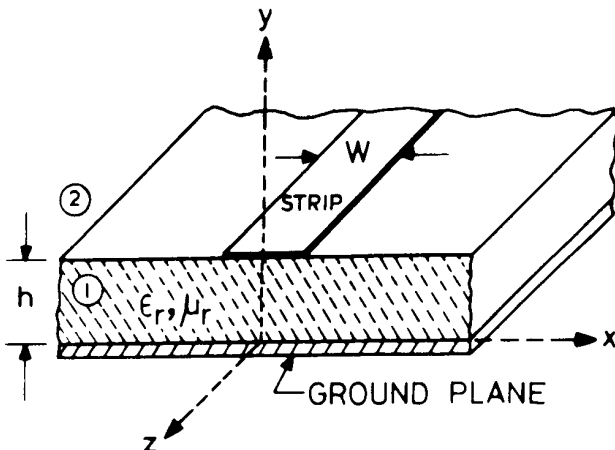


Figure 2.1 Open microstrip configuration.

lowest order E_z even – H_z odd mode and approaches the quasi-TEM solution at low frequencies.

2.2 ANALYSIS OF AN OPEN MICROSTRIP

Fullwave analysis of an open microstrip may be carried out by using a Fourier transformation along the x -direction (parallel to the substrate and perpendicular to the strip). The two methods for analysis described in this section employ such a transformation and, to that extent, resemble the variational method in the Fourier transform domain used for quasi-static analysis of microstrip lines in Chapter 1.

As illustrated in the previous section, various components of the \mathbf{E} and \mathbf{H} fields are expressed in terms of two potentials ψ^h and ψ^e . Fourier transformation is taken along the x -direction. Solutions for the transforms of ψ^e and ψ^h are obtained by matching the boundary conditions in the transform domain. The interface condition in the $y = h$ plane is written in terms of longitudinal and transverse electric currents on the strip conductor. The two methods described in this section differ mainly with regard to the manner in which the boundary conditions at the dielectric-air interface ($y = h$) are applied.

In the Fourier transform domain, potentials $\tilde{\psi}^e$ and $\tilde{\psi}^h$ may be written as

$$\tilde{\psi}_i^e(\alpha, y) = \int_{-\infty}^{\infty} \psi_i^e(x, y) e^{j\alpha x} dx \quad (2.5)$$

and a similar relation holds for $\tilde{\psi}_i^h$. The subscript $i = 1, 2$ designates the regions 1 (substrate) and 2 (air), respectively. $\tilde{\psi}_i$'s satisfy the transformed wave equation, which may be written as

$$(d^2/dy^2 - \gamma_i^2) \tilde{\psi}_i(\alpha, y) = 0 \quad (2.6)$$

where

$$\gamma_i^2 = \alpha^2 + \beta^2 - k_i^2 \quad i = 1, 2$$

$$k_1^2 = \omega^2 \epsilon_r \mu_r \epsilon_0 \mu_0 \quad k_2^2 = \omega^2 \epsilon_0 \mu_0$$

The next step is to write expressions for $\tilde{\psi}_i$ in the two regions such that boundary conditions at $y = 0$ and at $y \rightarrow \infty$ are satisfied. These may be written as

$$\tilde{\psi}_1^e(\alpha, y) = A(\alpha) \sinh(\gamma_1 y) \quad (2.7)$$

$$\tilde{\psi}_2^e(\alpha, y) = B(\alpha) \exp[-\gamma_2(y - h)] \quad (2.8)$$

$$\tilde{\psi}_1^h(\alpha, y) = C(\alpha) \cosh(\gamma_1 y) \quad (2.9)$$

$$\tilde{\psi}_2^h(\alpha, y) = D(\alpha) \exp[-\gamma_2(y - h)] \quad (2.10)$$

The coefficients A , B , C , and D are determined by applying continuity conditions across the interface $y = h$. These conditions are

$$\tilde{E}_{z1}(\alpha, h) = \tilde{E}_{z2}(\alpha, h) \quad (2.11)$$

$$\tilde{E}_{x1}(\alpha, h) = \tilde{E}_{x2}(\alpha, h) \quad (2.12)$$

$$\tilde{H}_{z1}(\alpha, h) - \tilde{H}_{z2}(\alpha, h) = -\tilde{J}_z(\alpha) \quad (2.13)$$

$$\tilde{H}_{x1}(\alpha, h) - \tilde{H}_{x2}(\alpha, h) = \tilde{J}_x(\alpha) \quad (2.14)$$

where $\tilde{J}_x(\alpha)$ and $\tilde{J}_z(\alpha)$ are the Fourier transforms of the unknown current components on the strip and the second subscript (1 or 2) indicates the region 1 or 2. In addition, the boundary condition that must be satisfied on the strip may be written as

$$E_{z2}(x, h) = 0 \quad |x| < W/2 \quad (2.15a)$$

$$(d/dy) H_{z2}(x, h) = 0 \quad |x| < W/2 \quad (2.15b)$$

We now describe two methods of analyzing open microstrip lines by using the aforementioned formulation. These methods differ because of the manner in which the boundary conditions (2.15) are applied. In one of the methods, called the integral equation method by Denlinger [1], boundary conditions (2.15) are applied in the space domain ((x - y)-plane). In the other method, called Galerkin's method in FTD [2, 3], the boundary conditions (2.15) are applied in the Fourier transform domain ((α - y)-plane).

2.2.1 Integral Equation Method in the Space Domain

Equation (2.7) to (2.15) lead to a set of coupled integral equations for the currents $\tilde{J}_x(\alpha)$ and $\tilde{J}_z(\alpha)$. These integral equations are derived to be [1]

$$I_{x0} \int_{-\infty}^{\infty} G_{11}(\alpha, \beta) \tilde{J}_x(\alpha) e^{-j\alpha x} d\alpha + I_{z0} \int_{-\infty}^{\infty} G_{12}(\alpha, \beta) \tilde{J}_z(\alpha) e^{-j\alpha x} d\alpha = 0 \quad (2.16a)$$

and

$$I_{x0} \int_{-\infty}^{\infty} G_{21}(\alpha, \beta) \tilde{J}_x(\alpha) e^{-j\alpha x} d\alpha + I_{z0} \int_{-\infty}^{\infty} G_{22}(\alpha, \beta) \tilde{J}_z(\alpha) e^{-j\alpha x} d\alpha = 0 \quad (2.16b)$$

where $-W/2 < x < W/2$, $\mu_r = 1$, $k_0 = k_2$,

$$G_{11}(\alpha, \beta) = \frac{1}{\det} \left[F_1 b_{22} + \frac{\alpha\beta}{k_1^2 - \beta^2} b_{12} \right] \quad (2.17)$$

$$G_{12}(\alpha, \beta) = b_{12}/\det \quad (2.18)$$

$$G_{21}(\alpha, \beta) = \frac{\gamma_2}{\det} \left[F_1 b_{21} + \frac{\alpha\beta}{k_1^2 - \beta^2} b_{11} \right] \quad (2.19)$$

$$G_{22}(\alpha, \beta) = \gamma_2 b_{11}/\det \quad (2.20)$$

$$b_{11} = -b_{22} = j\alpha \left\{ \frac{k_0^2 - \beta^2}{k_1^2 - \beta^2} - 1 \right\} \quad (2.21)$$

$$b_{12} = \frac{\omega\mu_0\gamma_1}{\beta} \left[\frac{\gamma_2}{\gamma_1} + \frac{k_0^2 - \beta^2}{k_1^2 - \beta^2} \tanh \gamma_1 h \right] \quad (2.22)$$

$$b_{21} = \frac{\omega\epsilon_0\gamma_1}{\beta} \left[\frac{\gamma_2}{\gamma_1} + \epsilon_r \frac{k_0^2 - \beta^2}{k_1^2 - \beta^2} \coth \gamma_1 h \right] \quad (2.23)$$

$$\det = b_{11}b_{22} - b_{12}b_{21} \quad (2.24)$$

$$F_1 = \omega\mu_0\gamma_1 \tanh(\gamma_1 h) / [j(k_0^2 - \beta^2)] \quad (2.25)$$

In deriving (2.16), a one-term approximation has been used for the unknown current distributions $\tilde{J}_x(\alpha)$ and $\tilde{J}_z(\alpha)$. These approximations are given as

$$\tilde{J}_x(\alpha) = I_{x0} \tilde{J}_x(\alpha) \quad (2.26a)$$

$$\tilde{J}_z(\alpha) = I_{z0} \tilde{J}_z(\alpha) \quad (2.26b)$$

It has been assumed that \tilde{J}_x and \tilde{J}_z have known forms, and the only unknowns in their representation are the amplitude coefficients I_{x0} and I_{z0} .

The unknown propagation constant β can now be solved by equating the determinant of the coefficient matrix for the unknowns I_{x0} and I_{z0} to zero.

The current distributions I_x and I_z , chosen by Denlinger [1], are

$$I_z(x) = \begin{cases} 1 + |2x/W|^3 & |x| \leq W/2 \\ 0 & \text{otherwise} \end{cases} \quad (2.27a)$$

$$I_x(x) = \begin{cases} \sin(\pi x/0.7W) & |x| \leq 0.8 W/2 \\ \cos(\pi x/0.2W) & 0.8 W/2 < |x| \leq W/2 \\ 0 & \text{otherwise} \end{cases} \quad (2.27b)$$

It may be pointed out that because of the one-term approximation used here, the results are critically dependent on the choice of the form of the current distribution. This is a disadvantage of this method.

A considerable simplification in the above analysis results from neglecting the transverse current component J_x . This is a good approximation when the strip width is small as compared to the wavelength (i.e., $W/\lambda_0 < 0.1$) and when the lowest order mode is being considered. This approximation reduces the coupled pair of integral equations to a single integral equation containing β as a parameter. The computer time requirement is therefore considerably reduced.

The dispersion curves based on this method will be discussed along with the results of the second method described next.

2.2.2 Galerkin's Method in the Spectral Domain [2, 3]

In this method, the formulation of the problem is similar to that in the above method, but the boundary conditions on the strip, given by Equations (2.15), are now applied in the spectral domain (or Fourier Transform Domain, FTD) rather than in the space domain. In place of integral equations (2.16), one now obtains

$$G_{11}(\alpha, \beta)\tilde{J}_x(\alpha) + G_{12}(\alpha, \beta)\tilde{J}_z(\alpha) = \tilde{U}_1(\alpha) + \tilde{U}_2(\alpha) \quad (2.28a)$$

$$G_{21}(\alpha, \beta)\tilde{J}_x(\alpha) + G_{22}(\alpha, \beta)\tilde{J}_z(\alpha) = \tilde{V}_1(\alpha) + \tilde{V}_2(\alpha) \quad (2.28b)$$

where

$$\tilde{U}_1(\alpha) = \int_{-\infty}^{-W/2} u(x) e^{j\alpha x} dx \quad \tilde{U}_2(\alpha) = \int_{W/2}^{\infty} u(x) e^{j\alpha x} dx \quad (2.29)$$

$$\tilde{V}_1(\alpha) = \int_{-\infty}^{-W/2} v(x) e^{j\alpha x} dx \quad \tilde{V}_2(\alpha) = \int_{W/2}^{\infty} v(x) e^{j\alpha x} dx \quad (2.30)$$

Functions such as G_{11} are defined in (2.17) to (2.20) and $u(x)$, $v(x)$ are defined by

$$E_{z2}(x, h) = \begin{cases} 0 & -W/2 < x < W/2 \\ j[(k_z^2 - \beta^2)/\beta]u(x) & \text{otherwise} \end{cases} \quad (2.31)$$

$$\frac{d}{dy}H_{z2}(x, h) = \begin{cases} 0 & -W/2 < x < W/2 \\ j[(k_z^2 - \beta^2)/\beta]v(x) & \text{otherwise} \end{cases} \quad (2.32)$$

Equations (2.28) are solved by the method of moments using Galerkin's approach. As a first step \tilde{J}_x and \tilde{J}_z are expanded in terms of known basis functions \tilde{J}_{xn} and \tilde{J}_{zn} as follows:

$$\tilde{J}_x(\alpha) = \sum_{n=1}^M c_n \tilde{J}_{xn}(\alpha) \quad \tilde{J}_z(\alpha) = \sum_{n=1}^N d_n \tilde{J}_{zn}(\alpha) \quad (2.33)$$

The basis functions $\tilde{J}_{xn}(\alpha)$ and $\tilde{J}_{zn}(\alpha)$ are chosen such that their inverse Fourier transforms are nonzero only on the strip $-W/2 < x < W/2$. After substituting (2.33) into (2.28) and taking the inner product with the basis functions \tilde{J}_{zn} and \tilde{J}_{xn} for different values of n , we obtain the matrix equation

$$\sum_{n=1}^M K_{m,n}^{1,1} c_n + \sum_{n=1}^N K_{m,n}^{1,2} d_n = 0 \quad m = 1, 2, \dots, N \quad (2.34a)$$

$$\sum_{n=1}^M K_{m,n}^{2,1} c_n + \sum_{n=1}^N K_{m,n}^{2,2} d_n = 0 \quad m = 1, 2, \dots, M \quad (2.34b)$$

where

$$K_{m,n}^{1,1} = \int_{-\infty}^{\infty} \tilde{J}_{zm}(\alpha) G_{11}(\alpha, \beta) \tilde{J}_{xn}(\alpha) d\alpha \quad (2.35)$$

and similar relations hold for other $K_{m,n}$'s. The simultaneous equations (2.34a) and (2.34b) are solved for the propagation constant β by setting the determinant of this set of equations equal to zero. In this method also, the results depend on the choice of basis functions and the values of M and N selected, and the accuracy of the results can be increased by selecting higher values of M and N .

Galerkin's method in FTD has several advantages as compared with the space domain integral equation method discussed in the previous subsection.

1. The method is simpler since the solution is extracted from algebraic equations and not from the coupled integral equations.
2. The physical nature of the mode for each solution can easily be recognized via the corresponding selection made for the basis functions.

Galerkin's method in the spectral domain as discussed earlier for an open microstrip line is also applicable to a shielded microstrip line (with a metallic cover shield but no side walls), to a line with two layers of dielectric substrates, to a microstrip line with a dielectric layer on the strip and substrate, and to similar generalized printed transmission lines that contain several dielectric layers and conductors appearing at several dielectric interfaces. This generalized method is known as the spectral domain immittance approach [4, 5]. A solution of the equations for the transforms of currents in the spectral domain (such as (2.28a, b)) are solved by deriving the dyadic Green's functions (for example, G_{11} , G_{12} , in (2.28) based on the transverse equivalent circuit concept applied in the spectral domain in conjunction with a simple coordinate transformation rule.

2.2.3 Discussion of Results

The results for the effective dielectric constant found from Galerkin's method in the spectral domain by considering two different sets of M and N are shown in Figure 2.2. The basis functions chosen are also shown in this figure. The results (effective dielectric constant versus frequency) are compared with Denlinger's results [1] based on the method described in Section 2.2.1. It may be noted that the first-order solution ($N = M = 1$) does not give satisfactory values since J_{x1} shown in Figure 2.2(a) is not a good choice for J_x .

Fullwave analysis of an open microstrip has been extended for the calculation of characteristic impedance by Knorr and Tufekcioglu [3]. Galerkin's approach in the spectral domain, as discussed in Section 2.2.2, is used for this computation.

When the transverse component of the current is ignored, we can define the characteristic impedance Z_{0i} as

$$Z_{0i} = 2P_{\text{avg}}/I_z^2 \quad (2.36)$$

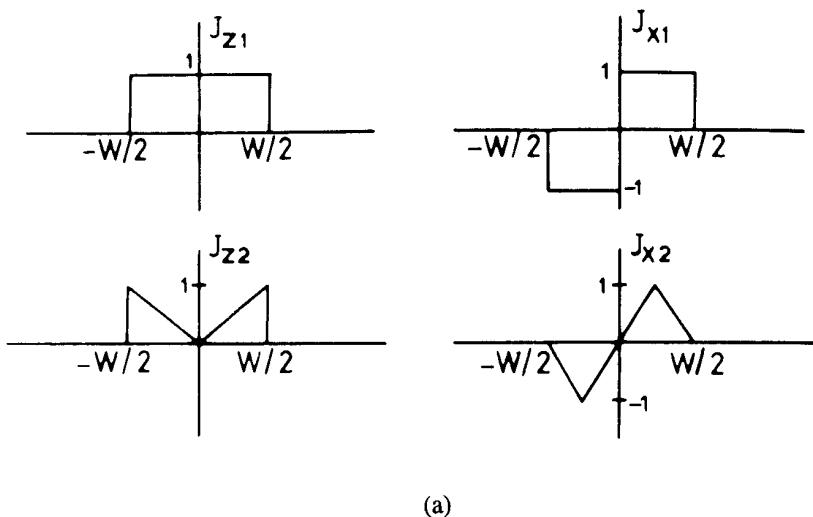
where I_z is the total z -directed strip current. The average power is calculated as

$$P_{\text{avg}} = \frac{1}{2} \text{Re} \int \int (E_x H_y^* - E_y H_x^*) dx dy \quad (2.37)$$

This relation can be written in the spectral domain, using Parseval's theorem, as

$$P_{\text{avg}} = \frac{1}{4\pi} \text{Re} \int_{-\infty}^{\infty} \int_{-\infty}^{\infty} [\tilde{E}_x(\alpha, y) \tilde{H}_y^*(\alpha, y) - \tilde{E}_y(\alpha, y) \tilde{H}_x^*(\alpha, y)] dy d\alpha \quad (2.38)$$

Integration with respect to y can be carried out analytically. This yields an equation of the form



Analysis by using Galerkin's Method in FTD)

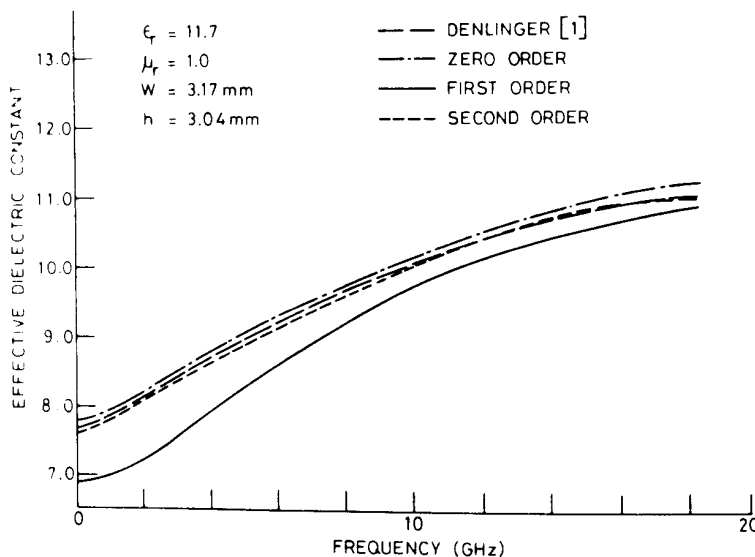


Figure 2.2 (a) Basis functions for currents in a microstrip (used for analysis by using Galerkin's method in FTD) and (b) variation of effective dielectric constant with frequency for an open microstrip (from [2], © 1973 IEEE. Reprinted with permission.).

$$P_{\text{avg}} = \frac{1}{4\pi} \int_{-\infty}^{\infty} g(\alpha) d\alpha \quad (2.39)$$

which is evaluated numerically in each of the two regions.

As in the case of waveguides, alternative definitions of characteristic impedance are possible. One can write

$$Z_{\text{ov}} = \frac{V^2(0)}{2P_{\text{avg}}} \quad (2.40)$$

where $V(0)$ is given by

$$V(0) = - \int_0^h E_x(0, y) dy \quad (2.41)$$

and denotes the voltage between the center of the strip and the ground plane.

Results based on these two definitions are shown in Figure 2.3(a). The quasi-static value of the impedance is also shown. We note that the impedance based on current (i.e., Z_{oi}) converges to the quasi-static value whereas Z_{ov} does not. This is perhaps due to the fact that $V(0)$ is a sensitive function of the assumed current distribution whereas the total current used in (2.36) is not.

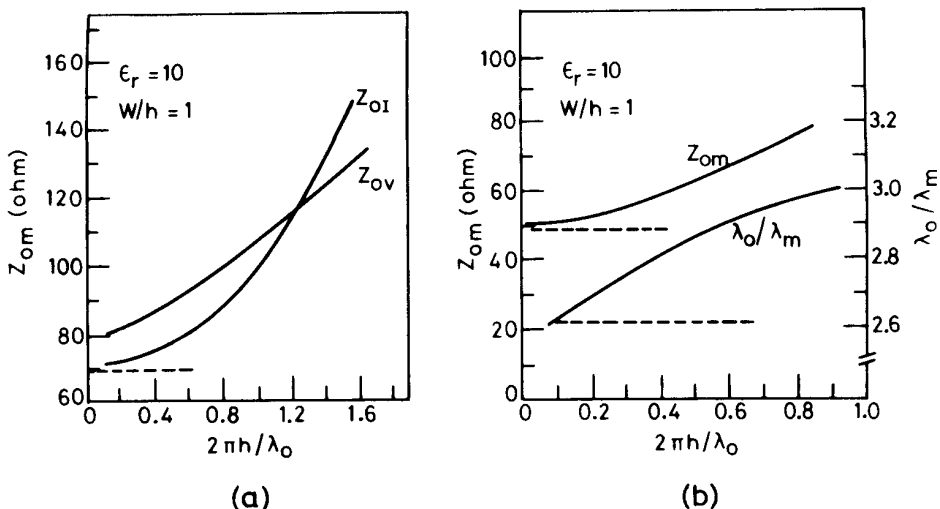


Figure 2.3 Variation of microstrip impedance and wavelength with frequency: (---) quasi-static values (from [3], © 1975 IEEE. Reprinted with permission.).

The results in Figure 2.3(b) show that the characteristic impedance increases with frequency. It may be added that for a 1-mm-thick substrate $h/\lambda_0 = 0.4$ corresponds to 120 GHz, and at this frequency the impedance increases by about 16 percent above the quasi-static value.

The increase in the characteristic impedance with frequency can be interpreted qualitatively as follows. When the frequency increases, the effective dielectric constant for the microstrip increases. This has been observed from the results based on fullwave analysis. An increase in the effective dielectric constant implies that the fields are getting concentrated below the strip, which also amounts to a decrease in the effective width of the microstrip. The characteristic impedance of a microstrip should decrease with the increase of ϵ_{re} . On the other hand, a decrease in the effective strip width should increase the characteristic impedance. The fullwave analysis described above shows that the latter effect is more pronounced. The results based on the planar waveguide model discussed in Chapter 1 agree with this interpretation.

The results for the characteristic impedance and effective dielectric constant for the dominant mode of propagation in open microstrip lines may also be obtained from the results for enclosed microstrips discussed in Section 2.3. The simplest approach for this purpose is to make the enclosure dimensions much larger (typically 10 times) than strip width and substrate height so that the presence of walls do not affect the microstrip line characteristics.

2.3 ANALYSIS OF AN ENCLOSED MICROSTRIP

Three different methods of fullwave analysis for an enclosed microstrip structure were illustrated in Figure 1.6. Of these, the finite difference method is conceptually the simplest. The other methods involved forming and solving integral equations. Since the integral equation methods are used most frequently, we discuss them first in Section 2.3.1. The configuration of the enclosed microstrip is shown in Figure 2.4.

2.3.1 Integral Equation Methods [6–10]

The most commonly used methods for the fullwave analysis of enclosed microstrip lines use integral equation formulation. The features of these methods are as follows: Expressions for potentials ψ^e and ψ^h , in regions 1 and 2, are written in the form of series expansions such that the boundary conditions on the metallic periphery of the enclosure are satisfied. Also, since the main interest lies in the dominant mode, which is E_z even – H_z odd, the total magnetic field is made to vanish at the plane of symmetry $x = 0$. The appropriate expressions are

$$\psi_1^e = \sum_{n=1}^{\infty} A_n^e \sinh \alpha_n^{(1)} y \cos k_n x \quad (2.42)$$

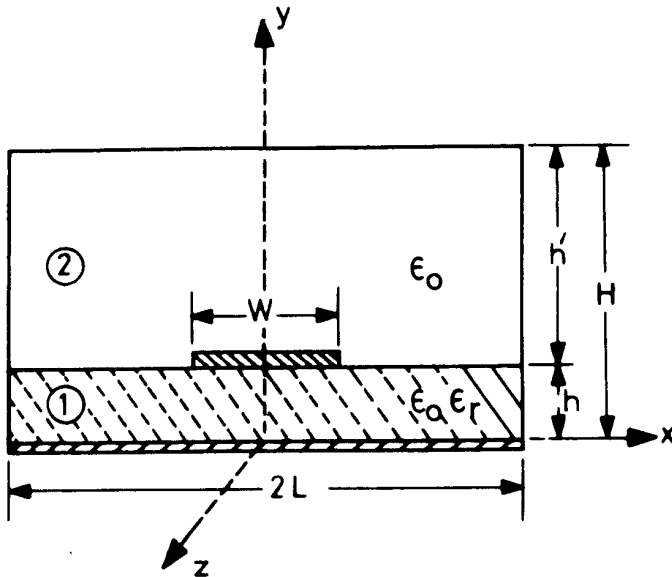


Figure 2.4 Enclosed microstrip configuration.

$$\psi_2^e = \sum_{n=1}^{\infty} B_n^e \sinh \alpha_n^{(2)} (H - y) \cos k_n x \quad (2.43)$$

$$\psi_1^h = \sum_{n=1}^{\infty} A_n^h \cosh \alpha_n^{(1)} y \sin k_n x \quad (2.44)$$

$$\psi_2^h = \sum_{n=1}^{\infty} B_n^h \cosh \alpha_n^{(2)} (H - y) \sin k_n x \quad (2.45)$$

where

$$k_n = [n - (1/2)] \pi / L \quad (2.46)$$

$$\alpha_n^{(1)} = (k_n^2 + \beta^2 - \epsilon_r k_0^2)^{1/2} \quad (2.47)$$

$$\alpha_n^{(2)} = (k_n^2 + \beta^2 - k_0^2)^{1/2} \quad (2.48)$$

where k_0 is the free-space wavenumber and the coefficients A_n 's and B_n 's are yet unknown. L is the width and H is the height of the enclosure as shown in Figure 2.4.

Interface conditions in the plane $y = h$ are applied to the field components derived from (2.42) to (2.45). This results in relations that equate the series of infinite terms. These equations are converted to an infinite set of homogeneous simultaneous equations for coefficients A_n 's and B_n 's by taking scalar products with a complete set of functions appropriate to the various ranges of x . The resulting equations may be written either in terms of integral equations or in terms of a matrix equation and solved for β . The various methods differ in the manner in which the interface conditions are applied and in the method of solving the resulting equations. As for open microstrip lines, both space domain and spectral domain formulations have been developed, and the spectral domain approach is used more frequently.

Space Domain Approach [6]

This method by Zysman and Varon [6] is a straightforward implementation of the steps outlined above. Four mutually independent interface conditions at $y = h$ are written as (Figure 2.4)

$$E_{x1} = E_{x2}, \quad 0 < |x| < L \quad (2.49)$$

$$E_{z1} = E_{z2}, \quad 0 < |x| < L \quad (2.50)$$

$$E_{x1} = 0, \quad 0 < |x| < W/2 \quad (2.51)$$

$$H_{x1} = H_{x2} \quad W/2 < |x| < L$$

$$E_{z1} = 0 \quad 0 < |x| < W/2 \quad (2.52)$$

$$H_{z1} = H_{z2} \quad W/2 < |x| < L$$

These conditions are now imposed on the field components derivable from (2.42) to (2.45). One obtains a pair of coupled homogeneous Fredholm integral equations of the first kind [6] as

$$\sum_{n=1}^{\infty} \left[G_n^{(1)} \int_0^{W/2} h_1(\xi) \cos k_n \xi d\xi + G_n^{(2)} \int_{W/2}^L h_2(\xi) \sin k_n \xi d\xi \right] \sin k_n x = 0 \quad (2.53)$$

$$\sum_{n=1}^{\infty} \left[G_n^{(3)} \int_0^{W/2} h_1(\xi) \cos k_n \xi d\xi + G_n^{(4)} \int_{W/2}^L h_2(\xi) \sin k_n \xi d\xi \right] \cos k_n x = 0 \quad (2.54)$$

Here the G_n 's are known functions of β and $h_1(\xi)$, $h_2(\xi)$ are unknown functions of ξ . These equations may be transformed into a matrix equation algorithm. The roots of the determinantal equation of the resulting matrix can be obtained numerically and yield the phase constant values for propagating waves.

Other variations of the space domain integral equation formulations are discussed in [7–9].

Galerkin's Method in FTD [10]

This method is similar to Galerkin's method in FTD used for open microstrip lines in Section 2.2.2. The bounded nature of the geometry (Figure 2.4) requires the use of the finite Fourier transform instead of the conventional Fourier transform over an infinite range. The latter type of transform was used for open microstrip analysis in Section 2.2.2. The transform used in the present analysis is defined as

$$\tilde{\psi}_i(\alpha_n, y) = \int_{-L}^L \psi_i(x, y) \exp(j\alpha_n x) dx \quad (2.55)$$

where $\alpha_n = (n - 1/2)\pi/L$ for E_z even– H_z odd modes and $\alpha_n = (n\pi/L)$ for E_z odd– H_z even modes ($n = 1, 2, \dots$). The next step is to transform all the field components and to apply boundary and interface conditions in the transform domain. This leads to [10]

$$G_{11}(\alpha_n, \beta) \tilde{J}_x(\alpha_n) + G_{12}(\alpha_n, \beta) \tilde{J}_z(\alpha_n) = K_z \tilde{E}_z(\alpha_n) \quad (2.56a)$$

$$G_{21}(\alpha_n, \beta) \tilde{J}_x(\alpha_n) + G_{22}(\alpha_n, \beta) \tilde{J}_z(\alpha_n) = K_x \tilde{E}_x(\alpha_n) \quad (2.56b)$$

where

$$G_{11} = G_{22} = \alpha_n \beta (\gamma_{n,2} \tanh \gamma_{n,2} h' + \gamma_{n,1} \tanh \gamma_{n,1} h) / \det \quad (2.57a)$$

$$G_{12} = [(\epsilon_r k_0^2 - \beta^2) \gamma_{n,2} \tanh \gamma_{n,2} h' + (k_0^2 - \beta^2) \gamma_{n,1} \tanh \gamma_{n,1} h] / \det \quad (2.57b)$$

$$G_{21} = [(\epsilon_r k_0^2 - \alpha_n^2) \gamma_{n,2} \tanh \gamma_{n,2} h' + (k_0^2 - \alpha_n^2) \gamma_{n,1} \tanh \gamma_{n,1} h] / \det \quad (2.57c)$$

$$\det = (\gamma_{n,1} \tanh \gamma_{n,1} h + \epsilon_r \gamma_{n,2} \tanh \gamma_{n,2} h') (\gamma_{n,1} \coth \gamma_{n,1} h + \gamma_{n,2} \coth \gamma_{n,2} h') \quad (2.57d)$$

and K_z and K_x are known constants. Also

$$\gamma_{n,1}^2 = \alpha_n^2 + \beta^2 - k_0^2 \epsilon_r \quad \gamma_{n,2}^2 = \alpha_n^2 + \beta^2 - k_0^2 \quad h' = H - h$$

$\tilde{J}_x(\alpha_n)$ and $\tilde{J}_z(\alpha_n)$ represent transforms of strip currents $J_x(x)$ and $J_z(x)$, respectively, and $\tilde{E}_z(\alpha_n)$ and $\tilde{E}_x(\alpha_n)$ are transforms of electric field components in the plane $y = h$. The electric field components are unknown for $W/2 < |x| < L$, though they are zero on the strip. These two unknowns are eliminated by applying Galerkin's

method. For this purpose, the currents are written in terms of known basis functions \tilde{J}_{xm} and \tilde{J}_{zm} as

$$\tilde{J}_x(\alpha_n) = \sum_{m=1}^M c_m \tilde{J}_{xm}(\alpha_n) \quad (2.58a)$$

$$\tilde{J}_z(\alpha_n) = \sum_{m=1}^N d_m \tilde{J}_{zm}(\alpha_n) \quad (2.58b)$$

where c_m and d_m are unknown coefficients. These expressions for the currents are substituted into (2.56). Taking inner products of both sides of (2.56) with the basis functions \tilde{J}_{zi} and \tilde{J}_{xi} for different values of i , one obtains

$$\sum_{m=1}^M K_{im}^{1,1} c_m + \sum_{m=1}^N K_{im}^{1,2} d_m = 0 \quad i = 1, 2, \dots, N \quad (2.59a)$$

$$\sum_{m=1}^M K_{im}^{2,1} c_m + \sum_{m=1}^N K_{im}^{2,2} d_m = 0 \quad i = 1, 2, \dots, M \quad (2.59b)$$

The coefficients K_{im}^{pq} , obtained by the inner products, are written as

$$K_{im}^{1,1} = \sum_{n=1}^{\infty} \tilde{J}_z(\alpha_n) G(\alpha_n, \beta) \tilde{J}_{xm}(\alpha_n) \quad (2.60)$$

It is seen that the right-hand sides of (2.56) are eliminated through the use of Parseval's theorem, because the currents $J_z(x)$, $J_x(x)$ and the field components $E_z(x, h)$, $E_x(x, h)$ are zero in the complementary regions of x .

The simultaneous equations (2.59) are solved for the propagation constant β at each frequency ω by setting the determinant of the coefficient matrix equal to zero and by seeking the root of the resulting equation. The dispersion characteristics of microstrip are derived from the values of β .

The choice of the basis functions is important for the numerical efficiency of the method. The accuracy can be improved systematically by increasing the number of basis functions M or N . However, if the first few basis functions approximate the actual unknown current reasonably well, the necessary size of the matrix can be held small for a given accuracy of the solution. For the dominant mode, the following forms for J_{zl} and J_{xl} are suitable:

$$J_{zl}(x) = \begin{cases} \frac{1}{W} \left[1 + \left| \frac{2x}{W} \right|^3 \right] & |x| \leq W/2 \\ 0 & W/2 < |x| < L \end{cases} \quad (2.61)$$

$$J_{xl}(x) = \begin{cases} \frac{2}{W} \sin \frac{2\pi x}{W} & |x| \leq W/2 \\ 0 & W/2 < |x| < L \end{cases} \quad (2.62)$$

The Fourier transforms of the above current distributions are given by

$$\begin{aligned} \tilde{J}_{zl}(\alpha_n) &= \frac{2 \sin(\alpha_n W/2)}{\alpha_n W/2} + \frac{3}{(\alpha_n W/2)^3} \\ &\quad \left\{ \cos(k_n W/2) - \frac{2 \sin(\alpha_n W/2)}{\alpha_n W/2} + \frac{2[1 - \cos(\alpha_n W/2)]}{(\alpha_n W/2)^2} \right\} \end{aligned} \quad (2.63)$$

and

$$\tilde{J}_{xl}(\alpha_n) = \frac{2\pi \sin(\alpha_n W/2)}{(\alpha_n W/2)^2 - \pi^2} \quad (2.64)$$

Results based on this analysis [10] have been compared with the results of the space domain integral equation method discussed earlier, and the agreement is good.

2.3.2 Finite Difference Method

In this method the microstrip cross section is divided into small rectangles by means of a rectangular net. Wave equations for ψ^e and ψ^h are solved for values of the potentials at the net points, and for this purpose the wave equations for ψ^e and ψ^h may be written in finite difference form as [11]

$$\lambda \psi_{m,n}^e = 2(1 + R^2) \psi_{m,n}^e - \psi_{m+1,n}^e - \psi_{m-1,n}^e - R^2 \psi_{m,n+1}^e - R^2 \psi_{m,n-1}^e \quad (2.65)$$

$$\lambda \psi_{m,n}^h = 2(1 + R^2) \psi_{m,n}^h - \psi_{m+1,n}^h - \psi_{m-1,n}^h - R^2 \psi_{m,n+1}^h - R^2 \psi_{m,n-1}^h \quad (2.66)$$

where $\lambda = (k^2 - \beta^2)(\Delta x)^2$, $\psi_{m,n}^e = \psi^e(m\Delta x, n\Delta y)$, $\psi_{m,n}^h = \psi^h(m\Delta x, n\Delta y)$, and $R = \Delta x/\Delta y$. Integers m and n in subscripts refer to the coordinates of the grid point. The configuration and the coordinate system are shown in Figure 2.4. After applying boundary and interface conditions, the finite difference equations (2.65) and (2.66) may be written in the form of the matrix equation

$$[\mathbf{A}][\boldsymbol{\phi}] = \lambda[\boldsymbol{\phi}] \quad (2.67)$$

where $[\mathbf{A}]$ is the coefficient matrix, which is sparse and has the size $2(MN - 1)$ by $(MN - 1)$ with $M\Delta x = L$ and $N\Delta y = H$ (as shown in Figure 2.4). Potentials $\psi_{m,n}^e$

and $\psi_{m,n}^h$ are elements of vector Φ . It may be pointed out that λ has different values in regions 1 and 2.

There are several methods of solving (2.67), and a discussion of these techniques is given in [11] and [12]. It may be pointed out that the relaxation method used for quasi-static analysis becomes prohibitively slow in the present case. A method suitable for the present case has been described by Martin and Wilkinson [13]. Also, the matrix resulting from (2.65) and (2.66) is asymmetric, whereas efficient methods are available for the solution of symmetric matrix eigenvalue problems. A symmetric matrix can be obtained by using the variational method [12]. Another advantage of the variational method is that a graded mesh (with closer spacings near the strip and wider spacings near the enclosure walls) can be used. This permits the analysis of structures of realistic dimensions without prohibitively large computer storage requirements.

The derivation of a variational expression suitable for finite difference equations proceeds from a general variational formulation for an inhomogeneously filled structure. The general expression is obtained directly from Maxwell's curl equations [14] and can be written in terms of the longitudinal field components as

$$\iint \left[\frac{1}{\epsilon_r} \frac{1}{k_0^2} (\omega \epsilon_0 \epsilon_r E_z \nabla_t^2 E_z + \omega \mu_0 H_z \nabla_t^2 H_z) + \omega \epsilon_0 \epsilon_r E_z^2 + \omega \mu_0 H_z^2 \right] dS = 0 \quad (2.68)$$

Applying the divergence theorem, one may obtain a variational expression for the surface integral J of (2.68) as [12]

$$J = \iint_S \left\{ A\tau \epsilon_r |\nabla_t \psi^e|^2 + \tau |\nabla_t \psi^h|^2 + 2A\tau \left\{ \frac{\partial \psi^e}{\partial x} \frac{\partial \psi^h}{\partial y} - \frac{\partial \psi^h}{\partial x} \frac{\partial \psi^e}{\partial y} \right\} - k_0^2 [(\psi^h)^2 + A\epsilon_r (\psi^e)^2] \right\} dS \quad (2.69)$$

where

$$\psi^h = H_z, \quad \psi^e = \frac{\omega \epsilon_0}{\beta} E_z$$

$$\tau = \frac{\omega^2 \mu_0 \epsilon_0 - \beta^2}{\omega^2 \mu_0 \epsilon_0 \epsilon_r - \beta^2} \quad A = (\beta c / \omega)^2$$

where c is the velocity of electromagnetic waves in free space. Since (2.69) does not involve derivatives higher than the first order, it can be put in finite difference form using the following formulas (refer to Figure 2.5 with $\Delta_1 = \Delta_2 = \Delta$)

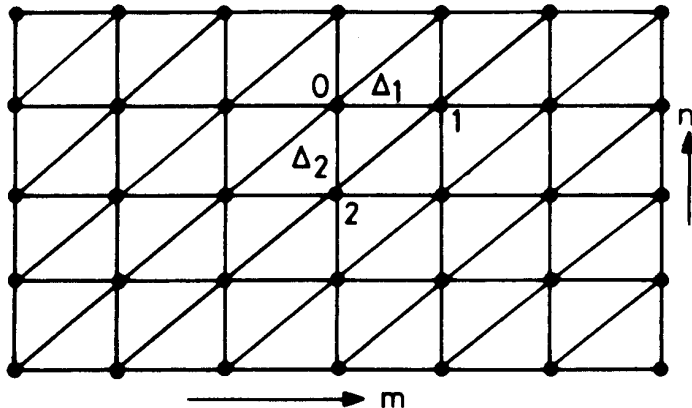


Figure 2.5 A typical region within the finite difference mesh.

$$\iint_S |\nabla_t \phi|^2 dS \approx \left\{ \left[\frac{\phi_1 - \phi_0}{\Delta} \right]^2 + \left[\frac{\phi_2 - \phi_0}{\Delta} \right]^2 \right\} \frac{\Delta^2}{2} \quad (2.70)$$

and

$$\iint_S \phi^2 dS \approx \frac{1}{3} (\phi_0^2 + \phi_1^2 + \phi_2^2) \frac{\Delta^2}{2} \quad (2.71)$$

where ϕ_0, ϕ_1, \dots represent values of potential ψ^e or ψ^h at points 0, 1, \dots . Using approximations described by (2.70) and (2.71), it is possible to arrive at an approximation for the contribution from the elementary triangular region of Figure 2.5 to the integral of (2.69). The surface integral J of (2.69) is then computed as the sum of such approximations for each elemental region in the structure. The stationary property of J is utilized after differentiating with respect to each of the variables $\psi_1^h, \psi_2^h, \dots, \psi_i^h, \psi_1^e, \psi_2^e, \dots, \psi_i^e$. In this way N linear equations are derived for the system where N is the total number of variables ψ^h and ψ^e . These relations are put in the form of a matrix equation (2.67), which now becomes a symmetric band structure matrix. The solution of such a matrix may be found by the following three steps: (i) $[A]$ is reduced to a tridiagonal form [15]; (ii) the eigenvalues of the tridiagonal matrix are found by the method of bisection [16]; and (iii) the eigenvector associated with a specific eigenvalue is found by the method of inverse iterations [17]. References [15–17] give details of these three steps.

A disadvantage of the finite difference method is the large size of the matrix to be handled and the resulting computer storage requirement.

Equation (2.69) can also be solved by the finite element method in place of the finite difference method discussed above. Corr and Davies [12] have tried this technique and found that there are no advantages to be gained by using the finite element method.

2.3.3 Discussion of Results

Methods for fullwave analysis of a microstrip provide information about two aspects of wave propagation along the microstrip, namely, dispersion and higher order modes. The principal features of these results are discussed in this section.

Dispersion

Information regarding the dispersive nature of propagation in a microstrip can be expressed in different ways. Figures (2.6) and (2.7) indicate two ways of representing dispersion. In Figure (2.6), the frequency is plotted against the phase constant β leading to the traditional ω - β diagram. This figure also includes a ω - β curve based on a quasi-static analysis (which is a straight line). Results of the fullwave analysis based on two different methods are shown. These two curves are not straight but lie between the two straight lines, one corresponding to a quasi-static analysis and the other for a homogeneously filled line. At lower frequencies (less than 5 GHz) results given by both methods coincide with the quasi-static results.

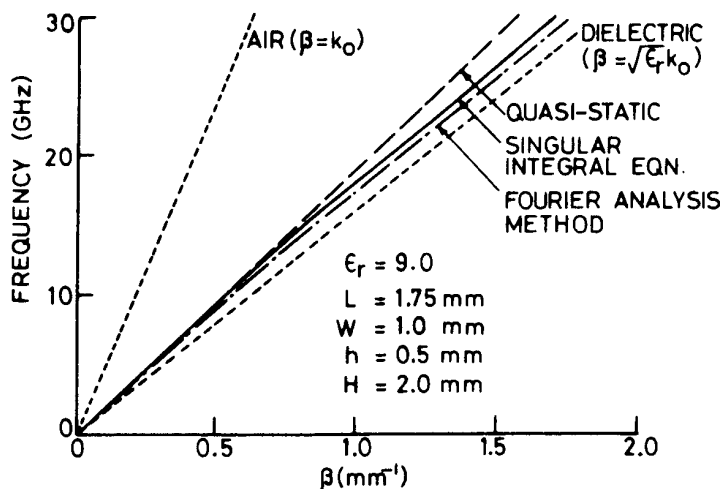


Figure 2.6 Dispersion behavior of a microstrip as computed by different methods (from [8], © 1971 IEEE. Reprinted with permission.).

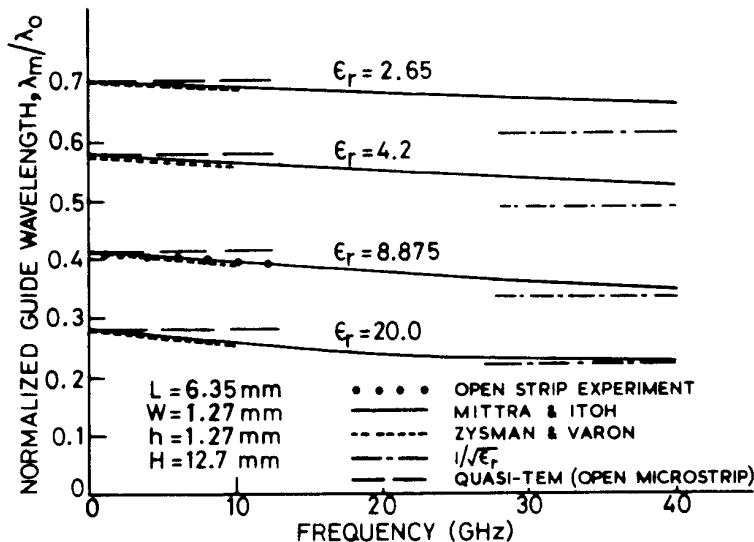


Figure 2.7 Variation of microstrip guide wavelength with frequency (from [8], © 1971 IEEE. Reprinted with permission.).

Figure (2.7) presents the same results in a different manner. Here the normalized guide wavelength λ_m/λ_0 is plotted as a function of frequency. Two different methods (the integral equation method and the singular integral equation method [8]) are compared. Experimental results for an open microstrip are also included. It is observed that λ_m/λ_0 decreases with an increase in frequency and tends to $1/\sqrt{\epsilon_r}$. It implies that at higher frequencies more and more energy propagates inside the substrate and below the strip.

Higher Order Modes

Plotting the $\omega\beta$ diagram for higher order modes requires considerable computation time. Thus only limited results are available.

The singular integral equation method has been used to investigate higher order modes [8]. The results for a substrate of dielectric constant 8.875 (alumina) are shown in Figure 2.8. Similar results are available [8] for three other dielectric constant values (2.62, 4.2, and 20.0). The existence of a number of higher order modes is evident in these plots. It should be noted that this mode spectrum is not complete since only the E_z even– H_z odd type of modes are shown. Comparison with similar curves for other values of ϵ_r indicates that the frequency at which the first higher order mode begins to appear is lower for higher values of ϵ_r .

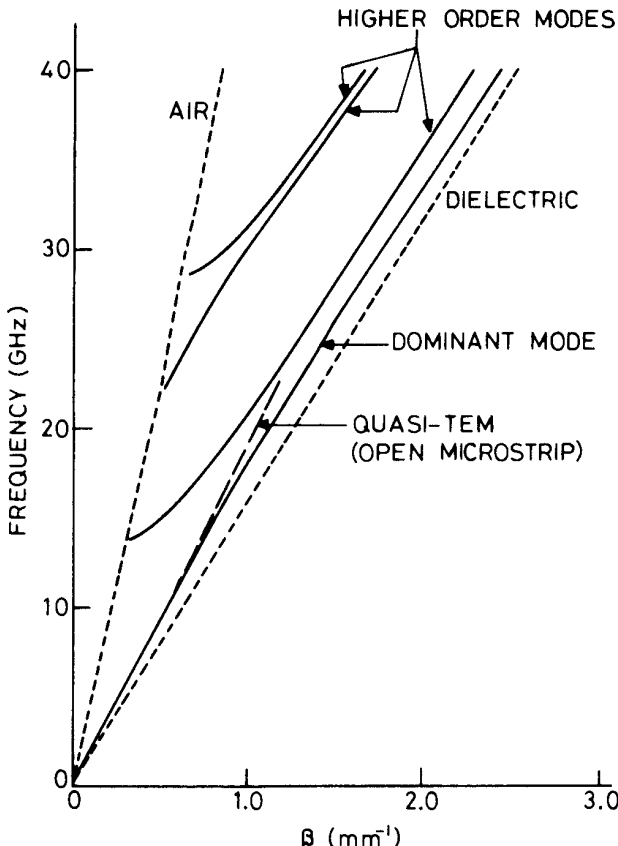


Figure 2.8 Higher order modes in a microstrip (computed by using the singular integral equation method) $\epsilon_r = 8.875$, $L = 6.35$ mm, $W = 1.27$ mm, $h = 1.27$ mm, and $H = 12.7$ mm (from [8], © 1971 IEEE. Reprinted with permission.).

Dispersion curves for higher order modes have also been calculated by Corr and Davies [12] using the finite difference method discussed earlier. Their results are presented in Figure 2.9(b) for the microstrip configuration shown in Figure 2.9(a). This plot includes E_z odd– H_z even type of modes also. It is seen that the dispersion curves tend to group in pairs of E_z even and E_z odd modes of the same order. The difference between the static limiting value of ϵ_{re} for the lowest mode and the TEM value is attributed entirely to discretization errors in the finite difference method.

Higher order microstrip modes have been compared with LSM and LSE modes of the slab line structure formed by the removal of the microstrip conductor

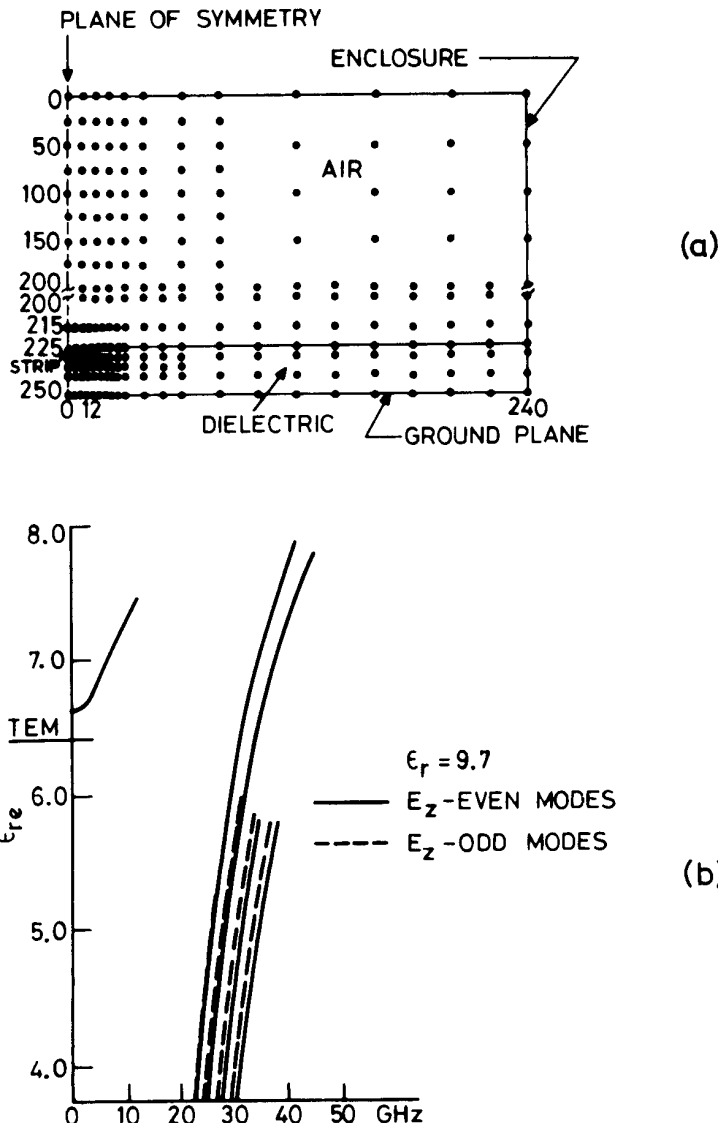


Figure 2.9 (a) Mesh points for microstrip analysis by using the finite difference method (scale 1 unit = 0.002 in) and (b) higher order modes, computed by using the finite difference method (from [12], © 1972 IEEE. Reprinted with permission.).

[12]. A very close similarity between the power density distributions of E_z odd and LSM modes is noted. Also higher order E_z even and E_z odd modes have very similar power density distributions. It is concluded that because the plane of symmetry makes so little difference to the higher order modes with the same subscript, these modes are strongly associated not with the strip but with the dielectric-air interface. In view of their close similarity to the LSM modes, they can be considered as distorted LSM modes. The specific type of mode correspondences may be grouped together. Using the notation E for E_z even and M for E_z odd modes, it can be said that modes E_1 , M_1 , and LSM_{12} are similar; modes E_2 , M_2 , and LSM_{14} are similar; and so on. Thus, for an enclosed microstrip, the approximate cut-off frequency for higher order modes may be obtained from the cut-off frequency of LSM modes.

Considerable information about higher order modes can also be obtained from the planar waveguide model for a microstrip as discussed in Chapter 1. Cut-off frequencies and guide wavelengths for various modes are given by (1.85) and (1.86), respectively.

2.4 DESIGN CONSIDERATIONS

In this section various important design parameters of microstrip lines are discussed. These include attenuation constant, power handling capability, effect of tolerances, and dielectric anisotropy. Various expressions, useful for microstrip design, are summarized in the last subsection.

2.4.1 Microstrip Losses

Attenuation in a microstrip structure is caused by two loss components: conductor loss and dielectric loss. If a magnetic substrate is used, a magnetic loss component will also be present. We will discuss losses for nonmagnetic substrates in this subsection.

Conductor Loss

A comprehensive treatment of conductor loss in a microstrip structure is given by Pucel et al. [18] and by Schneider [19]. Both of these analyses are based on the “incremental inductance rule” of Wheeler [20]. In this method the series surface resistance R per unit length is expressed in terms of that part of the total inductance L_i per unit length that is attributable to the skin effect, that is, the inductance L_i produced by the magnetic field within the conductors.

It is well known that for a conductor the surface impedance, $Z_s (=R + jX)$, has a real part R (surface resistance per unit length) that is equal to the imaginary part X . That is,

$$R = X = \omega L_i \quad (2.72)$$

According to Wheeler, L_i can be found from the external inductance L per unit length. L_i is obtained as the incremental increase in L caused by an incremental recession of all metallic walls due to the skin effect. This situation is shown in Figure 2.10. The amount of recession is equal to half the skin depth $\delta = (2/\omega\mu_0\sigma)^{1/2}$. An assumption underlying this rule is that the radius of curvature and the thickness of the conductors exposed to the electromagnetic fields are greater than the skin depth, preferably several skin depths. According to Wheeler [20], we have

$$L_i = \sum_m \frac{\mu_m}{\mu_0} \frac{\partial L}{\partial n_m} \frac{\delta_m}{2} \quad (2.73)$$

$$R = \sum_m \frac{R_{sm}}{\mu_0} \frac{\partial L}{\partial n_m} \quad (2.74)$$

where $\partial L/\partial n_m$ denotes the derivative of L with respect to incremental recession of wall m , n_m is the normal direction to this wall, and $R_{sm} = \omega\mu_m \delta_m/2$ is the surface resistance of the wall m .

The attenuation constant because of conductor (ohmic) loss is defined as

$$\alpha_c \approx \frac{P_c}{2P(z)} = \frac{\text{Power loss in conductors}}{2 \text{ (Power transmitted)}} \text{ (nepers/unit length)} \quad (2.75)$$

In terms of R and Z_{0m} (characteristic impedance), α_c may be written as

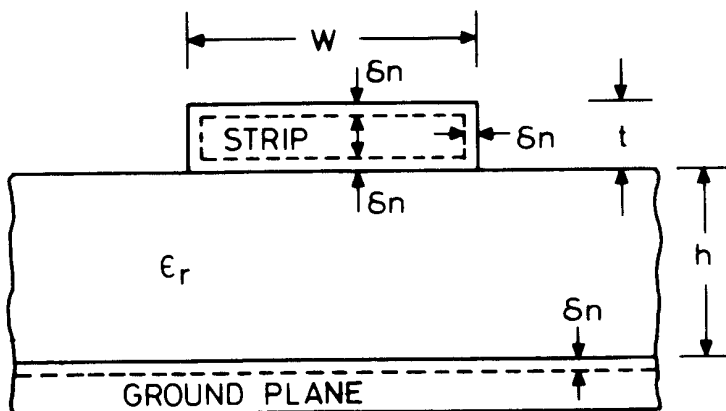


Figure 2.10 Recession of conducting walls of a microstrip for loss calculation using "incremental inductance rule."

$$\alpha_c = \frac{|I|^2 R}{2 |I|^2 Z_{0m}} = \frac{1}{2\mu_0 Z_{0m}} \sum_m R_{sm} \frac{\partial L}{\partial n_m} \quad (2.76)$$

Inductance L of the microstrip structure can be expressed in terms of the characteristic impedance for the microstrip with the substrate replaced by air (Z_{0m}^a) and is given as

$$L = Z_{0m}^a / c \quad (2.77)$$

where c is the velocity of electromagnetic waves in free space.

Wheeler's incremental inductance rule requires the thickness of the conductors to be greater than about four times the skin depth. The effect of using smaller thicknesses has also been reported [21–23]. It is observed that the conductor losses are reduced by about 9 percent when the conductor thickness is $\pi/2$ times the skin depth.

An expression for the attenuation constant based on (2.76) is presented later in Section 2.4.5 where all other design information is also summarized.

Dielectric Loss

For a uniformly filled transmission line the dielectric loss α_{du} is independent of the geometry of the line and may be written as

$$\alpha_{du} = \frac{gZ_0}{2} = \frac{\omega}{2} \sqrt{\frac{\mu}{\epsilon'}} \epsilon'' = \frac{\omega}{2} \sqrt{\mu\epsilon'} \tan \delta \quad (2.78)$$

where g is the shunt conductance per unit length of the line, ϵ' is the real part, and ϵ'' is the imaginary part of the permittivity of the dielectric. However, when the dielectric is not uniform over the cross section of the line, the above expression does not apply. Calculation of the loss for the mixed dielectric case has been considered by Welch and Pratt [21] and by Schneider [24]. In both of these analyses, an effective loss tangent ($\tan \delta_e$) is derived. The results obtained in these two analyses can be shown to be identical when the difference in the definition of filling factor q in the two cases is taken into account.

When the upper dielectric (air) is assumed to be lossless, the following expression for α_d (attenuation constant considering mixed dielectrics) is obtained [21]

$$\begin{aligned} \alpha_d &= \frac{\omega}{2} \sqrt{\mu\epsilon_{re}} (\tan \delta)_e \\ &= \frac{\omega}{2} \sqrt{\mu\epsilon_{re}} \frac{\sigma_e}{\omega\epsilon_{re}} \end{aligned} \quad (2.79)$$

If σ is the conductivity of the dielectric and σ_0 the conductivity of air, we can write

$$\sigma_e = q\sigma + (1 - q) \sigma_0 \approx q\sigma \quad (\text{since } \sigma_0 \ll \sigma)$$

Also,

$$\epsilon_0 \epsilon_{re} = q\epsilon + (1 - q)\epsilon_0 \quad \text{with } \epsilon = \epsilon_0 \epsilon_r$$

Therefore, (2.79) becomes

$$\alpha_d = q \left\{ \frac{\epsilon}{q\epsilon + (1 - q)\epsilon_0} \right\}^{1/2} \alpha_{du} = \left(\frac{\epsilon_r}{\epsilon_{re}} \right)^{1/2} q\alpha_{du} \quad (2.80)$$

where q is the dielectric filling fraction (see Section 1.2.1) and α_{du} is the attenuation constant for a line uniformly filled with the dielectric ϵ_r , given by (2.78). Since

$$q = \frac{\partial \epsilon_{re}}{\partial \epsilon_r} = \frac{\epsilon_{re} - 1}{\epsilon_r - 1}$$

the attenuation constant α_d may be written as

$$\alpha_d = 27.3 \frac{\epsilon_r}{\sqrt{\epsilon_{re}}} \frac{\epsilon_{re} - 1}{\epsilon_r - 1} \frac{\tan \delta}{\lambda_0} \quad \text{dB/unit length} \quad (2.81)$$

For microstrip lines on alumina substrate the dielectric loss α_d is negligible compared to the total loss α . But for microstrip lines utilizing semiconductor substrates such as Si, the dielectric loss factor is dominant. For example, a 50- Ω line on a silicon substrate ($\epsilon_r = 11.7$) with a resistivity of 10³- Ω cm has a dielectric loss on the order of 0.36 dB/cm while the conductor loss is about 0.19 dB/cm [21]. For these substrates the dielectric conductivity σ is nonzero. In this case, (2.81) can be used with some modification; the final expression is given [21] as

$$\alpha_d = 4.34 \frac{1}{\sqrt{\epsilon_{re}}} \frac{\epsilon_{re} - 1}{\epsilon_r - 1} \left(\frac{\mu_0}{\epsilon_0} \right)^{1/2} \sigma \quad \text{dB/unit length} \quad (2.82)$$

Dielectric loss in a microstrip has also been computed numerically using the moment method [25]. In this case, α_d is written as

$$\alpha_d = \frac{(\sigma/2) \int E^2 ds}{2P} = \frac{\sigma \int E^2 ds}{2V^2/Z_{0m}} \quad (2.83)$$

Equations (2.81) and (2.82) give a value of α_d , which is about 1 percent higher than that predicted by the numerical method of Simpson and Tseng [25]. Values of the conductor and the dielectric losses per unit length in 50- Ω microstrip lines on various substrates have been calculated using results given in [26] and are shown in Figure 2.11 as function of frequency. Attenuation for lines on quartz substrate has been discussed by Van Heuven [27].

2.4.2 Power Handling Capability [28]

There is a widespread impression that microstrip lines are suitable only for low-power components. Although microstrip lines are not as well suited for high-power applications as are waveguides or coaxial lines of comparable cross section, they

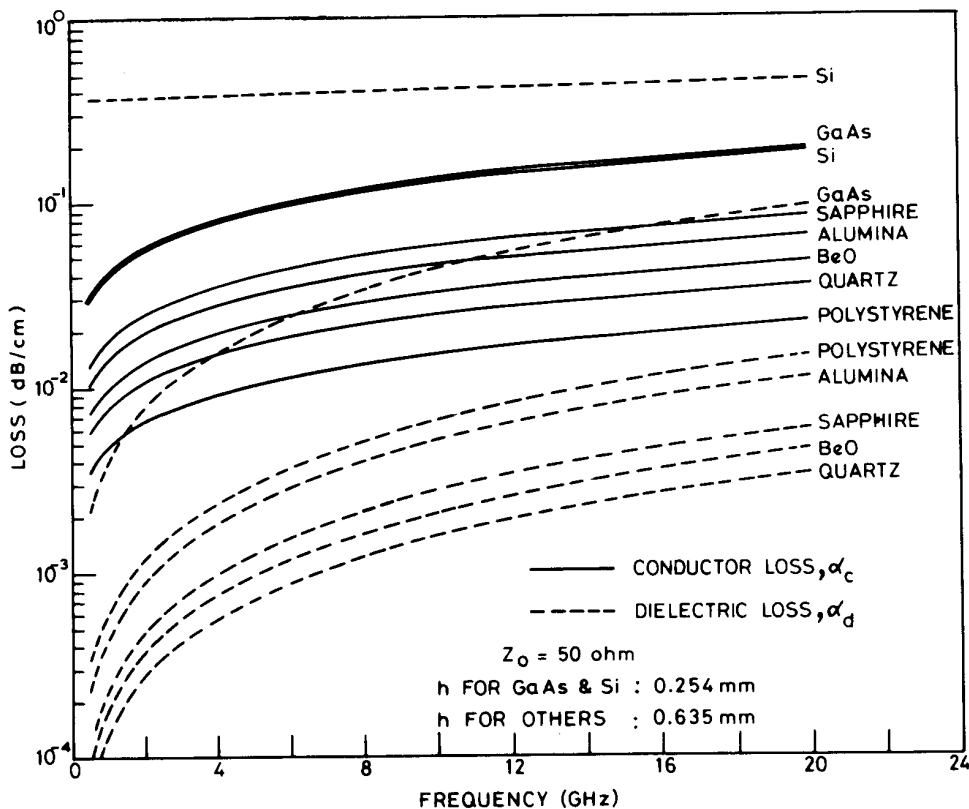


Figure 2.11 Conductor and dielectric losses as a function of frequency for microstrip lines on various substrates.

could certainly be used for several medium-power applications. A $50\text{-}\Omega$ microstrip on a 25-mil-thick alumina substrate can handle a few kilowatts of power.

The power handling capacity of a microstrip, like that of any other dielectric filled transmission line, is limited by heating caused because of ohmic and dielectric losses and by dielectric breakdown. An increase in temperature due to conductor and dielectric losses limits the average power of the microstrip line, while the breakdown between the strip conductor and ground plane limits the peak power.

Average Power

The *average power handling capability* (APHC) of a microstrip is determined by the temperature rise of the strip conductor and the supporting substrate. The parameters that play major roles in the calculation of average power capability are: (i) transmission line losses; (ii) thermal conductivity of the substrate material; (iii) surface area of the strip conductor; and (iv) ambient temperature; that is, temperature of the medium surrounding the microstrip. Therefore, dielectric substrates with low-loss tangent and large thermal conductivity will increase the average power handling capability of microstrip lines.

The temperature rise of the strip conductor can be calculated from the heat flow field in the cross section. An analogy between the heat flow field and the electric field is described in Table 2.1. The heat generated by the conductor loss and the dielectric loss is discussed separately in the following paragraphs.

Density of Heat Flow Due to Conductor Loss

A loss of electromagnetic power in the strip conductor generates heat in the strip. Because of the good heat conductivity of the strip metal, heat generation is uniform along the width of the conductor. Since the ground plane is held at ambient

Table 2.1
Analogy Between Heat Flow Field and Electric Field

<i>Heat Flow Field</i>	<i>Electric Field</i>
1. Temperature, T ($^{\circ}\text{C}$)	Potential, V (V)
2. Temperature gradient, T_g ($^{\circ}\text{C}/\text{m}$)	Electric field, \mathbf{E} (V/m)
3. Heat flow rate, Q (W)	Flux, ϕ (coulomb)
4. Density of heat flow, q (W/m^2)	Flux density, D (coulomb/ m^2)
5. Thermal conductivity, K ($\text{W}/(\text{m}/^{\circ}\text{C})$)	Permittivity, ϵ (coulomb/ m/V)
6. Density of heat generated, ρ_h (W/m^3)	Charge density, ρ (coulomb/ m^3)
7. $q = -K \nabla T$	$D = -\epsilon \nabla V$
8. $\nabla \cdot q = \rho_h$	$\nabla \cdot D = \rho$

temperature (i.e., acts as a heat sink), this heat flows from the strip conductor to the ground plane through the substrate. The heat flow can be calculated by considering the analogous electric field distribution. The heat flow field in the microstrip structure corresponds to the electrostatic field (without any dispersion) of the microstrip. From Figure 1.4 we note that the electric field lines (the thermal field in the case of heat flow) spread near the ground plane.

To account for the increase in area normal to heat flow lines, the parallel plate model of a microstrip is used. For these calculations ϵ_r (in electrical analog) is assumed to be equal to the ratio of the thermal conductivity of the substrate (Table 2.2) to that of the air. The equivalent width of the strip (W_e) in the parallel plate model is calculated from the electrical analog as

$$W_e = \frac{120 \pi h}{Z'_{0m} \sqrt{\epsilon'_{re}}} \quad (2.84a)$$

where h is the thickness of the substrate and Z'_{0m} is the characteristic impedance of the microstrip (in ohms). Microstrip parameters Z'_{0m} and ϵ'_{re} are calculated with ϵ_r replaced by K_d/K_a (the ratio of thermal conductivity of the dielectric to that of the air). When the impedance of a microstrip with air as the dielectric is written as Z_{0m}^a ($= Z'_{0m} \sqrt{\epsilon'_{re}}$), (2.84a) becomes

$$W_e = \frac{120 \pi h}{Z_{0m}^a} \quad (2.84b)$$

Table 2.2
Properties of Various Dielectric Substrates Used for Microstrip Characteristics
in Section 2.4

Material	ϵ_r	Loss Tangent at 10 GHz	K (W/cm/ $^{\circ}$ C)	Dielectric Strength (kV/cm)
Sapphire	11.7	10^{-4}	0.4	4×10^3
Alumina	9.7	2×10^{-4}	0.3	4×10^3
Quartz (fused)	3.8	10^{-4}	0.01	10×10^3
Polystyrene	2.53	4.7×10^{-4}	0.0015	280
Beryllium oxide (BeO)	6.6	10^{-4}	2.5	—
GaAs ($\rho = 10^7 \Omega \text{ cm}$)	12.3	16×10^{-4}	0.3	350
Si ($\rho = 10^3 \Omega \text{ cm}$)	11.7	50×10^{-4}	0.9	300
Air	1	≈ 0	0.00024	30

Consider a unit length of the line. The power absorbed (ΔP) in the line, due to conductor loss in the strip when one watt of power is incident, is given by

$$\Delta P = 0.2303 \alpha_c \quad (\text{W/m}) \quad (2.85)$$

where α_c (dB/m), the attenuation coefficient due to loss in the strip conductor, is assumed small. The density of heat flow due to the conductor loss may be written as

$$q_c = \frac{0.2303 \alpha_c}{W_e} \quad (\text{W/m}^2) \quad (2.86)$$

Density of Heat Flow Due to Dielectric Loss

In addition to the conductor loss, heat is generated by dielectric loss in the substrate. The density of the heat generated is proportional to the square of the electric field. However, we can consider a parallel plate model wherein the electric field is uniform and the density of the heat generated can also be considered uniform. This assumption ignores the increased dielectric loss in regions of high electric field near the strip edges. However, since the dielectric loss is a small fraction of the total loss (except for semiconductor substrates like Si), the above assumption should hold. The effective width for this parallel plate model depends on the spread of electric field lines and is a function of frequency. The effective width, $W_{\text{eff}}(f)$, is given by [29, 30]

$$W_{\text{eff}}(f) = W + \frac{W_{\text{eff}}(0) - W}{1 + (f/f_p)^2} \quad (2.87)$$

where

$$f_p = \frac{Z_{0m}}{2\mu_0 h}$$

and $W_{\text{eff}}(0)$ is equal to W_e of (2.84). μ_0 is the permeability of free space, ϵ_{re} is the static value of the effective dielectric constant [31], and Z_{0m} is the characteristic impedance of the microstrip (in ohms).

The heat flow in the y -direction caused by a sheet of heat sources can be evaluated by considering the configuration in Figure 2.12.

The heat conducted away by air is negligible, and the air-dielectric boundary can be considered as an insulating wall (corresponding to a magnetic wall in the electric analog). Therefore, the configuration is modified by removing the insulat-

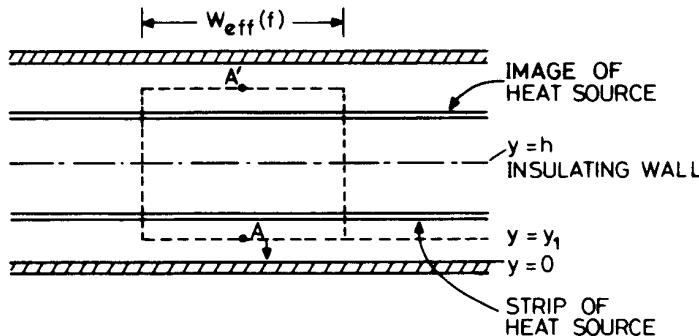


Figure 2.12 Geometry for calculating the density of heat flow due to dielectric loss in microstrip lines.

ing wall and incorporating an image source of heat and an image of the ground plane as shown. The space between the two ground planes is filled homogeneously by the dielectric medium. Now the heat flow at a point A is obtained by applying the divergence theorem (for heat flow field) to the volume shown by the dotted lines, that is,

$$\iiint (\nabla \cdot q_d) dv = \oint_s q_d \cdot ds = \iiint \rho_h dv \quad (2.88)$$

where s is the enclosed area. The total q_d at $y = y_1$ is contributed by the heat sources lying between $y = y_1$ and $y = h$ (and their images). It may be noted that sources located at $y < y_1$ (and their images) do not contribute to the heat flow at $y = y_1$. Thus,

$$q_d(y) = -(h - y) \rho_h \quad (2.89)$$

The negative sign implies that the heat flow is in the $-y$ direction (for $y < h$). If α_d (dB/m) is the attenuation coefficient due to dielectric loss, the density of heat generated, ρ_h , may be written as

$$\rho_h = \frac{0.2303 \alpha_d}{W_{\text{eff}}(f) h} \quad (2.90)$$

From (2.89) and (2.90)

$$q_d(y) = -\frac{0.2303 \alpha_d}{W_{\text{eff}}(f)} (1 - y/h) \quad (2.91)$$

Temperature Rise

The total density of the heat flow due to conductor and dielectric losses may be expressed in terms of a temperature gradient as

$$q = q_c + q_d(y) = -K \frac{\partial T}{\partial y} \quad (2.92)$$

where K is the thermal conductivity of the substrate. Therefore, the temperature at $y = h$ (i.e., at the strip conductor) is given by

$$T = \frac{0.2303}{K} \int_0^h \left\{ \frac{\alpha_c}{W_e} + \frac{\alpha_d}{W_{\text{eff}}(f)} (1 - y/h) \right\} dy + T_{\text{amb}} \quad (2.93)$$

The corresponding rise in temperature is

$$\Delta T = \frac{0.2303}{K} \frac{h}{2} \left\{ \frac{\alpha_c}{W_e} + \frac{\alpha_d}{W_{\text{eff}}(f)} \right\} \quad (\text{°C/W}) \quad (2.94)$$

This relation is used for calculating the average power handling capability of the microstrip line.

The properties of various substrates are given in Table 2.2. Strip conductors, except in the case of polystyrene substrates, are of gold ($t = 0.01$ mm) while in the case of polystyrene substrates copper ($t = 0.035$ mm) is used. Conductor loss in the ground plane does not contribute to APHC limitation. However, as the ground plane loss is very small compared to the strip loss [32], formulas for the total loss could be used to calculate APHC. Results shown in Figure 2.13 for variations of ΔT with frequency are based on this assumption. The following interesting observations are noted from this figure. (i) The temperature rise ΔT increases with frequency. (ii) The beryllium oxide (BeO) substrate has a smaller temperature rise due to its higher value of thermal conductivity. Alumina and sapphire have nearly the same ΔT variation, although alumina has about 25 percent lower thermal conductivity compared to sapphire. This is due to the fact that sapphire line has slightly more loss due to a higher dielectric constant. Also W_e and W_{eff} in the case of sapphire are smaller. Therefore, the combined effect of these parameters on ΔT is almost equal in sapphire and alumina. (iii) We note that for frequencies less than 2.6 GHz, ΔT for Si ($1000 \Omega\text{cm}$) is larger than that for GaAs ($10^7 \Omega\text{cm}$). At 2.6 GHz the two ΔT 's are equal, and for frequencies above 2.6 GHz ΔT is smaller for Si. (iv) Plastic substrates (polystyrene etc.) have higher values of ΔT due to poor thermal conductivity, although the losses are smaller (Figure 2.11).

It may be pointed out that the effects of any thermal resistance barriers that may exist between the bonding of the strip and the microstrip dielectric, between

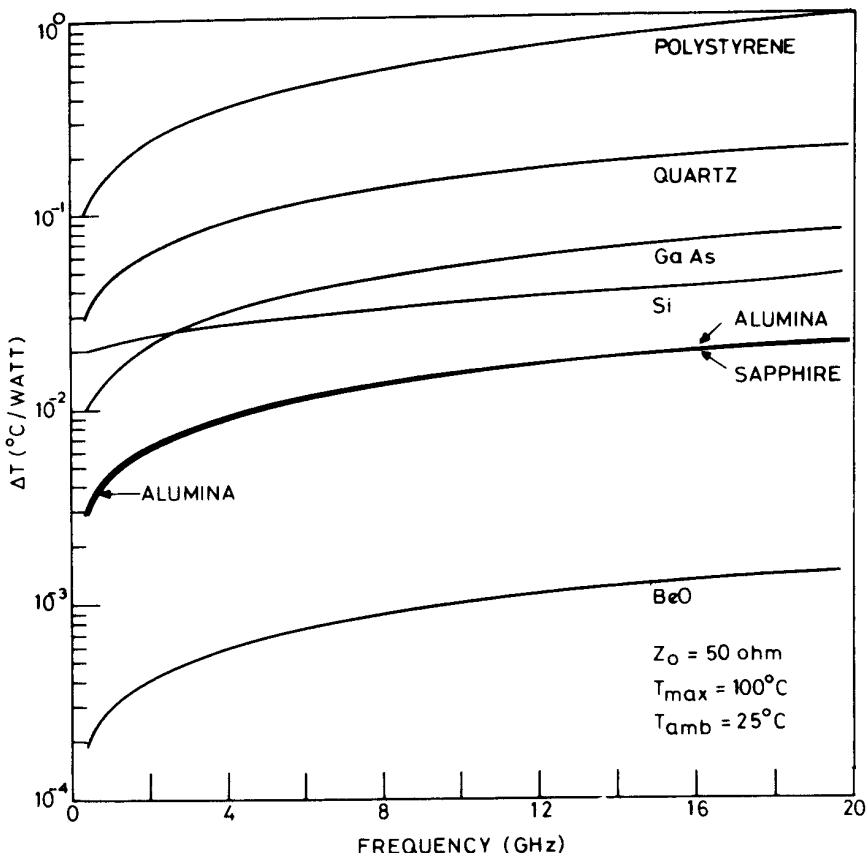


Figure 2.13 Rise in temperature of the strip conductor as a function of frequency for various substrates.

the microstrip dielectric and the ground plane, and between the ground plane and any heat sink have not been taken into account in this analysis. This effect can limit the average power handling capability of microstrip.

Average Power Handling Capability

The maximum average power for a given line may be calculated from

$$P_{\text{avg}} = (T_{\max} - T_{\text{amb}})/\Delta T \quad (2.95)$$

where ΔT denotes rise in temperature per watt and T_{\max} is the maximum operating temperature. For polystyrene, the maximum operating temperature is 100°C ,

whereas for the rest of the dielectrics (in Table 2.2) it is much more than 100°C. The maximum operating temperature of microstrip circuits is limited due to (i) change of substrate properties with temperature, (ii) change of physical dimensions with temperature, and (iii) connectors. One can assume the maximum operating temperature of microstrip circuits to be the one where its electrical and physical characteristics remain unchanged. Circuits on alumina and glass fiber-reinforced teflon substrates have been tested up to 150°C for about 2000 hours. It has been found [33] that the electrical and physical characteristics remain unchanged.

For $T_{\max} = 100^\circ\text{C}$, $T_{\text{amb}} = 25^\circ\text{C}$, and $Z_{0m} = 50 \Omega$, values of APHC for various substrates at 2 GHz, 10 GHz, and 20 GHz are calculated and given in Table 2.3. Among the dielectrics considered, APHC is the lowest for polystyrene and it is maximum for BeO. At lower frequencies, GaAs microstrip lines have better APHC than Si microstrip lines, but at higher frequencies (> 2.6 GHz) APHC is better in the case of Si. For commonly used alumina (or sapphire) substrates, a 50- Ω microstrip can carry about 5.14 kW of CW power at 10 GHz.

Peak Power Handling Capability

The calculation of peak power handling capability of microstrip lines is more complicated. The peak voltage that can be applied without causing dielectric breakdown determines the peak power handling capability (PPHC) of the microstrip. If Z_{0m} is the characteristic impedance of the microstrip and V_0 is the maximum voltage the line can withstand, the maximum peak power is given by

$$P_p = \frac{V_0^2}{2Z_{0m}} \quad (2.96)$$

Table 2.3
Comparison of APHC for Various Substrates

Substrate	Maximum Average Power (kW)		
	2.0 GHz	10 GHz	20 GHz
Polystyrene	0.321	0.124	0.075
Quartz	1.200	0.523	0.357
Si	3.19	2.23	1.64
GaAs	3.55	1.47	0.934
Sapphire	11.65	5.10	3.46
Alumina	12.12	5.17	3.40
BeO	174.5	75.7	51.5

Thick substrates can support higher voltages (for the same breakdown field). Therefore, low impedance lines and lines on thick substrates have higher peak power handling capability.

The sharp edges of the strip conductor serve as field concentrators. The electric field tends to a large value at the sharp edges of the conductor if it is a flat strip and decreases as the edge of the conductor is rounded off more and more. Therefore, thick and rounded strip conductors will increase breakdown voltage.

The dielectric strengths of the substrate material as well as of the air play important roles. The breakdown strength of dry air is approximately 30 kV/cm. Thus the maximum (tangential) electric field near the strip edge should be less than 30 kV/cm. To avoid air breakdown near the strip edge, the edge of the strip conductor can be painted with a dielectric paint that has the same dielectric constant as that of the substrate and is lossless. The dielectric strength of various dielectrics is also given in Table 2.2. This table shows that, among the dielectrics considered, fused quartz has the maximum dielectric strength while polystyrene has the minimum.

In some cases connectors or launchers decide the PPHC of the microstrip line. The 3-mm subminiature connectors and their transitions will breakdown before the line [34] itself. *N*-type connectors and transitions have higher PPHC. An additional factor, which may reduce PPHC, is the effect of internal mismatches. Experimental data for PPHC are not readily available. Howe [34] has reported successful operation of microstrip lines up to 10 kW at S-band and 4 kW at X-band.

2.4.3 Effect of Tolerances [35]

Characteristics of microstrip lines (namely, Z_{0m} and ϵ_{re}) are primarily functions of strip width W and substrate parameters ϵ_r and h . These are also influenced by factors such as strip thickness, frequency of operation (dispersion), and size of enclosure. Any changes in the values of W , ϵ_r , or h give rise to corresponding changes in Z_{0m} and ϵ_{re} .

Substrate properties, like surface finish, metallization thickness, and the fabrication process, determine the accuracy of fabrication of the strip width. In addition to the error in fabrication of the strip width, the thickness and the dielectric constant of the substrate have some manufacturing tolerances. All these factors contribute to variations in Z_{0m} and ϵ_{re} of the microstrip. Since it is very difficult to incorporate arrangements for post-fabrication adjustments in MICs, it is necessary to take into account the effect of tolerances at the design stage itself. However, unlike the effects of deterministic parameters like dispersion and strip thickness, the effect of tolerances cannot be incorporated exactly because of the uncertainty in Z_{0m} and ϵ_{re} arising from tolerances.

The effect of tolerances on the performance of a microstrip can be analyzed using the sensitivity approach. This approach is the easiest method of predicting

the worst case behavior corresponding to a given set of tolerances. It does not require the actual statistical distribution of tolerances. Only their maximum absolute values are needed. Sensitivity analysis is useful in situations where deviations in parameters can be considered incremental. This implies that the circuit characteristics should be slowly varying functions in the domain of parameter variation around the exact parameter values.

It has been observed that the maximum change in the characteristics of a microstrip due to tolerances can be evaluated using the equations

$$\frac{|\Delta Z_{0m}|_{\max}}{Z_{0m}} = \left| \frac{\Delta W}{W} S_W^{Z_{0m}} \right| + \left| \frac{\Delta h}{h} S_h^{Z_{0m}} \right| + \left| \frac{\Delta \epsilon_r}{\epsilon_r} S_{\epsilon_r}^{Z_{0m}} \right| \quad (2.97)$$

and

$$\frac{|\Delta \epsilon_{rel}|_{\max}}{\epsilon_{re}} = \left| \frac{\Delta W}{W} S_W^{\epsilon_{re}} \right| + \left| \frac{\Delta h}{h} S_h^{\epsilon_{re}} \right| + \left| \frac{\Delta \epsilon_r}{\epsilon_r} S_{\epsilon_r}^{\epsilon_{re}} \right| \quad (2.98)$$

where ΔW , Δh , and $\Delta \epsilon_r$ are the tolerances in W , h , and ϵ_r , respectively. The sensitivity S_B^A is defined as

$$S_B^A = \frac{B}{A} \frac{\partial A}{\partial B} \quad (2.99)$$

The influence of tolerances can be reduced by using improved fabrication techniques and using substrates with better tolerances. The required fabrication accuracy for the strip width will be a function of the specified accuracy in transmission line characteristics and given tolerances in substrate parameters.

It can be determined from the equations

$$\left| S_W^{Z_{0m}} \right| \frac{|\Delta W|}{W} = \frac{|\Delta Z_{0m}|}{Z_{0m}} - \left| \frac{\Delta h}{h} S_h^{Z_{0m}} \right| - \left| \frac{\Delta \epsilon_r}{\epsilon_r} S_{\epsilon_r}^{Z_{0m}} \right| \quad (2.100)$$

$$\left| S_W^{\epsilon_{re}} \right| \frac{|\Delta W|}{W} = \frac{|\Delta \epsilon_{rel}|}{\epsilon_{re}} - \left| \frac{\Delta h}{h} S_h^{\epsilon_{re}} \right| - \left| \frac{\Delta \epsilon_r}{\epsilon_r} S_{\epsilon_r}^{\epsilon_{re}} \right| \quad (2.101)$$

The required fabrication accuracy for the strip width is the minimum of the two values of ΔW obtained from the above equations. The fabrication accuracy of h or tolerance in ϵ_r can be determined in a similar manner provided that the tolerances for the other two parameters are known.

Expressions for the sensitivity of microstrip characteristics (Z_{0m} and ϵ_{re}) with respect to various parameters (for example, W , h , and ϵ_r) can be calculated using the

closed-form expressions for Z_{0m} and ϵ_{re} given by Schneider [19] and the definition of sensitivity given in (2.99). Various sensitivities may thus be written as

$$S_W^{Z_{0m}} = -S_h^{Z_{0m}} = \frac{-1}{Z_{0m} \sqrt{\epsilon_{re}}} \left\{ \frac{60(8h/W - W/4h)}{8h/W + W/4h} + 1.25 Z_{0m} \frac{\epsilon_r - 1}{\sqrt{\epsilon_{re}}} \frac{h/W}{(1 + 10h/W)^{3/2}} \right\} \quad \text{for } (W/h \leq 1) \quad (2.102)$$

$$S_W^{Z_{0m}} = -S_h^{Z_{0m}} = - \left[\frac{Z_{0m} \sqrt{\epsilon_{re}}}{120\pi} \left\{ \frac{W}{h} + 0.44 \frac{h}{W} + 6 \frac{h}{W} \left(1 - \frac{h}{W}\right)^5 \right\} + 1.25 \frac{\epsilon_r - 1}{\epsilon_{re}} \frac{h/W}{(1 + 10h/W)^{3/2}} \right] \quad \text{for } (W/h \geq 1) \quad (2.103)$$

$$S_W^{\epsilon_{re}} = -S_h^{\epsilon_{re}} = \frac{2.5}{W/h} \frac{\epsilon_r - 1}{\epsilon_{re}} (1 + 10h/W)^{-3/2} \quad (2.104)$$

$$S_{\epsilon_r}^{Z_{0m}} = -0.25 \frac{\epsilon_r}{\epsilon_{re}} [1 + (1 + 10h/W)^{-1/2}] \quad (2.105)$$

$$S_{\epsilon_r}^{\epsilon_{re}} = 0.5 \frac{\epsilon_r}{\epsilon_{re}} [1 + (1 + 10h/W)^{-1/2}] \quad (2.106)$$

The sensitivity curves for impedance and effective dielectric constants are shown in Figure 2.14 and Figure 2.15, respectively, for $\epsilon_r = 9.7$.

The sensitivity values thus obtained are used in (2.97) to determine the maximum change in Z_{0m} . From $(\Delta Z_{0m})_{\max}$ the maximum value of VSWR is obtained using the relation

$$\text{VSWR} = \left[1 - \frac{|\Delta Z_{0m}|_{\max}}{Z_{0m}} \right]^{-1} \quad (2.107)$$

The VSWR values are plotted in Figure 2.16 for the set of tolerances mentioned therein. The alternative problem of determining the fabrication accuracy of the strip width is evaluated using (2.100). It is plotted in Figure 2.17 for a VSWR value of 1.05.

It may be observed from (2.97) that there is a tradeoff between tolerances; that is, the tolerance value for one parameter can be increased or decreased at the cost of other parameters. This helps in the optimum use of fabrication technologies.

The effect of tolerances on the characteristics of a microstrip has been compared with the effects of finite thickness of metal strip, dispersion, discontinuity, and an imperfect measurement system and is detailed later in Section 2.4.5.

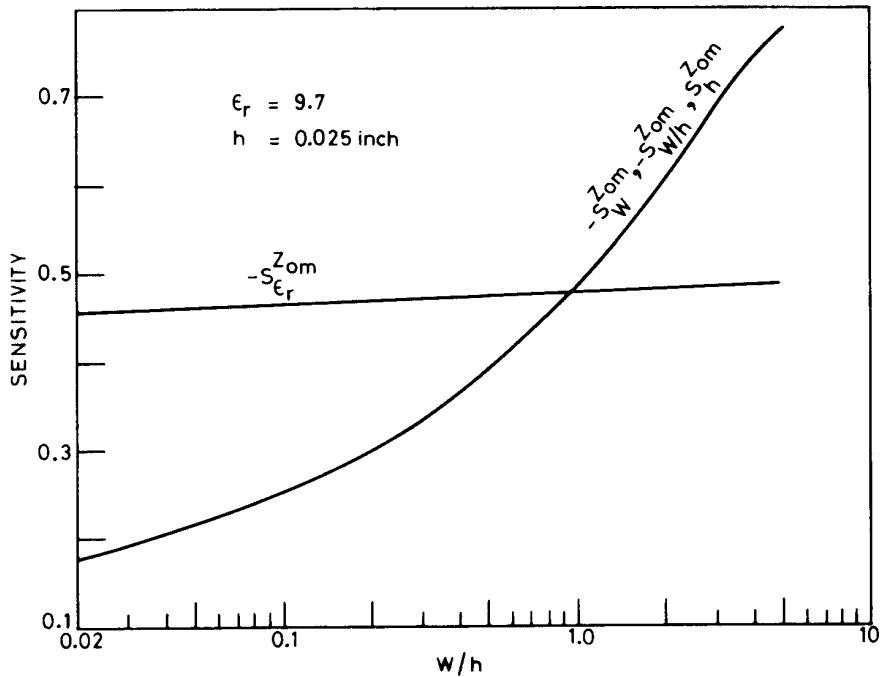


Figure 2.14 Sensitivity of microstrip impedance with respect to W , h , and ϵ_r (from [35], © 1978 IEEE. Reprinted with permission.).

2.4.4 Effect of Dielectric Anisotropy

Some of the dielectric substrates used for microstrip circuits exhibit anisotropy in permittivity. The most common examples are sapphire (especially when single crystal) and Epsilam-10 (trade name for a ceramic loaded resin). In both these cases, the substrates are manufactured such that one of the principal axes of the permittivity tensor is perpendicular to the dielectric interface $y = h$. If there were no fringing electric fields (in microstrip configuration) all the field lines would coincide with this axis, and the capacitance is determined by the value of permittivity in this direction. In such a case there is no effect of anisotropy.

If the line parameters are to be independent of line orientation in the xz -plane, the permittivity tensor in the x - and z -directions must be equal. For sapphire we take $\epsilon_x = \epsilon_z = 11.6$ and $\epsilon_y = 9.4$, whereas for Epsilam-10 $\epsilon_x = \epsilon_z = 15.0$ and $\epsilon_y = 10.0$.

Quasi-static analysis of a microstrip on anisotropic substrates has been carried out by using the finite difference method [36] and also by using a transformation

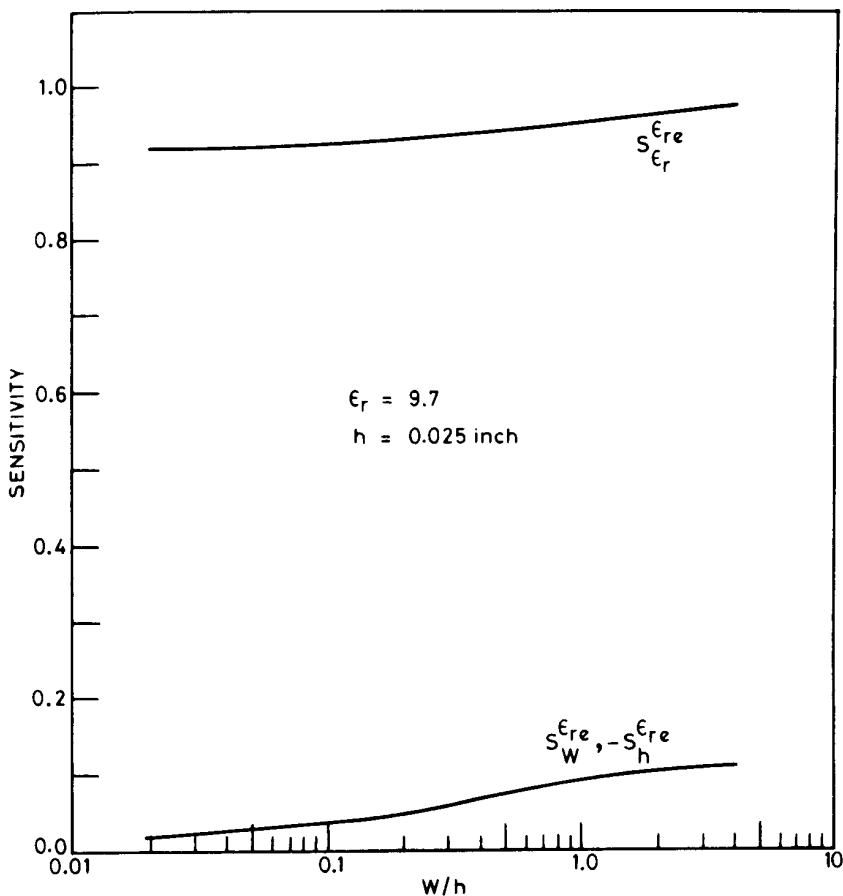


Figure 2.15 Sensitivity of the effective dielectric constant of a microstrip with respect to W , h , and ϵ_r (from [35], © 1978 IEEE. Reprinted with permission.).

[37] that enables the capacitance for anisotropic substrates to be derived from microstrip formulas for isotropic substrates.

Finite Difference Method [36]

This method is a straightforward solution of the Laplace equation by finite difference techniques. When the dielectric is anisotropic, the Laplace equation may be written as

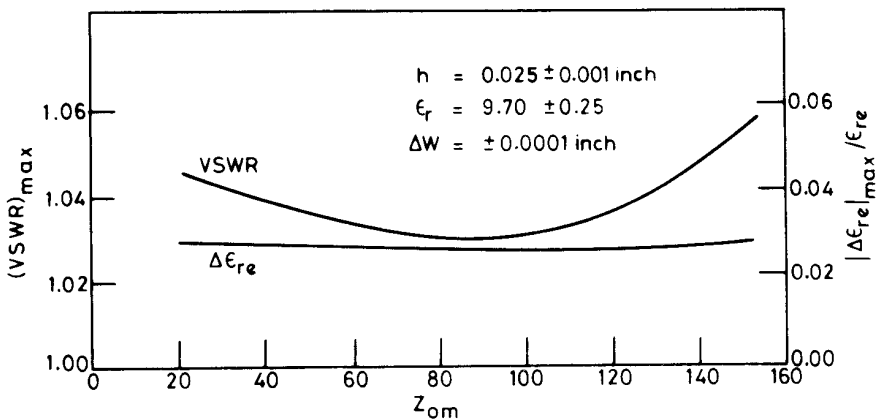


Figure 2.16 VSWR and change in effective dielectric constant because of tolerances in microstrip parameters (from [35], © 1978 IEEE. Reprinted with permission.).

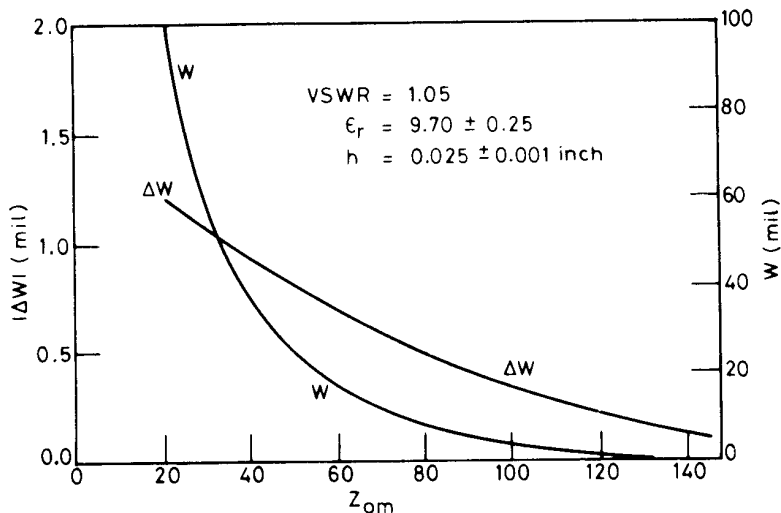


Figure 2.17 Tolerance in microstrip width allowed for a VSWR value of 1.05 (from [35], © 1978 IEEE. Reprinted with permission.).

$$\epsilon_x \frac{\partial^2 \phi(x, y)}{\partial x^2} + \epsilon_y \frac{\partial^2 \phi(x, y)}{\partial y^2} = 0 \quad (2.108)$$

In finite difference form this may be written as follows for all net points in the dielectric material (see Figure 1.9)

$$\epsilon_x(\phi_B + \phi_A) + \epsilon_y(\phi_D + \phi_C) - 2(\epsilon_x + \epsilon_y)\phi_P = 0 \quad (2.109)$$

and when the point P lies on the dielectric-air interface

$$1/2(1 + \epsilon_x)(\phi_B + \phi_A) + \phi_D + \epsilon_y\phi_C - (2 + \epsilon_x + \epsilon_y)\phi_P = 0 \quad (2.110)$$

The rest of the procedure for evaluating capacitances is the same as outlined in Section 1.2.2.

Transform Method [37]

A simple, but rigorous transformation that converts the anisotropic electrostatic field into an isotropic one with similar shape has been reported by Szentkuti [37]. This transformation may be described as follows.

For the substrate ($y \leq h$) let

$$\bar{x} = x, \bar{y} = y\sqrt{(\epsilon_x/\epsilon_y)} \quad \text{that is, } \bar{h} = h\sqrt{(\epsilon_x/\epsilon_y)} \quad (2.111)$$

$$\bar{\epsilon}_r = \bar{\epsilon}_x = \bar{\epsilon}_y = \sqrt{(\epsilon_x\epsilon_y)} \quad (2.112)$$

Potentials and their derivatives at the original and transformed points (P and \bar{P}) are related by

$$\phi_P = \bar{\phi}_{\bar{P}} \quad (2.113)$$

$$\partial\phi_P/\partial y = \sqrt{\epsilon_x/\epsilon_y}(\partial\bar{\phi}_{\bar{P}}/\partial\bar{y}) \quad (2.114)$$

Expressing (2.108) in terms of \bar{x} and \bar{y} leads to an isotropic Laplace equation for $\phi(\bar{x}, \bar{y})$. Also

$$E_x = -\partial\bar{\phi}/\partial\bar{x} = \bar{E}_{\bar{x}} \quad D_y = -\bar{\epsilon}_r\epsilon_0\partial\bar{\phi}/\partial\bar{y} = \bar{D}_{\bar{y}} \quad (2.115)$$

Thus we note that: (i) values of the tangential component of \mathbf{E} and the normal component of flux at the interface $y = h$ are not affected by the transformation, (ii) all potential and charges are not altered within the region $y \leq h$, and (iii) the potential of the transformed ground plane is conserved. Therefore, capacitances of the original anisotropic and the transformed isotropic structures are equal.

Effective dielectric constants for anisotropic substrates are compared with the corresponding values for isotropic substrates ($\epsilon_r = \epsilon_y$) as a function of W/h in Figure 2.18. We note that considerable difference exists for thin lines (small W/h), whereas

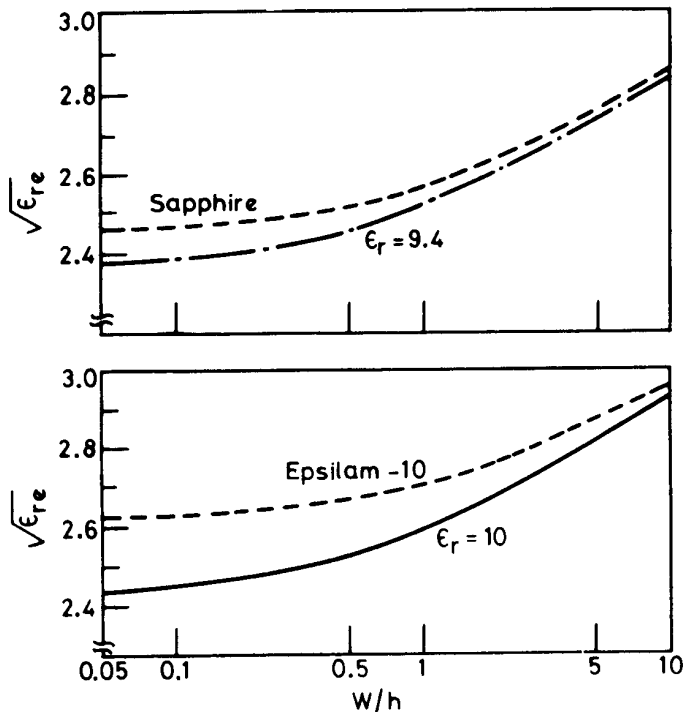


Figure 2.18 Effect of dielectric anisotropy on effective dielectric constants of microstrip lines on sapphire ($\epsilon_x = \epsilon_z = 11.6$, $\epsilon_y = 9.9$) and Epsilam-10 substrates (from [37], © 1976 IEE (U.K). Reprinted with permission.).

the two results tend to identical values as W/h increases. This can be explained by noting that the fringing field values are larger for narrow strips, and it is only the E_x component of the fringing field that is affected by ϵ_x .

2.4.5 Design Equations

The numerical methods for the characterization of microstrip lines discussed so far involve extensive computations. Closed-form expressions are necessary for the optimization and computer-aided-design of microstrip circuits. A complete set of design equations for a microstrip is presented in this section. This includes closed-form expressions for the characteristic impedance and effective dielectric constant and their variation with metal strip thickness, enclosure size, and dispersion. Expressions for microstrip loss and quality factor Q are also described.

Characteristic Impedance and Effective Dielectric Constant

Closed-form expressions for Z_{0m} and ϵ_{re} have been reported by Wheeler [38], Schneider [19], and Hammerstad [39]. Wheeler and Hammerstad have also given synthesis expressions for Z_{0m} . The closed-form expressions based on the works of Wheeler and Schneider are given [39] as

$$Z_{0m} = \frac{\eta}{2\pi\sqrt{\epsilon_{re}}} \ell_n \left(\frac{8h}{W} + 0.25 \frac{W}{h} \right) \quad \left(\frac{W}{h} \leq 1 \right) \quad (2.116a)$$

$$Z_{0m} = \frac{\eta}{\sqrt{\epsilon_{re}}} \left\{ \frac{W}{h} + 1.393 + 0.667 \ell_n \left(\frac{W}{h} + 1.444 \right) \right\}^{-1} \quad (W/h \geq 1) \quad (2.116b)$$

where $\eta = 120\pi \Omega$

$$\epsilon_{re} = \frac{\epsilon_r + 1}{2} + \frac{\epsilon_r - 1}{2} F(W/h) \quad (2.117)$$

$$F(W/h) = \begin{cases} (1 + 12h/W)^{-1/2} + 0.04(1 - W/h)^2 & (W/h \leq 1) \\ (1 + 12h/W)^{-1/2} & (W/h \geq 1) \end{cases}$$

Hammerstad noted [40] that the maximum relative error in ϵ_{re} and Z_{0m} is less than 1 percent. The expressions for W/h in terms of Z_{0m} and ϵ_r are as follows. For $Z_{0m}\sqrt{\epsilon_{re}} > 89.91$, that is, $A > 1.52$

$$W/h = \frac{8 \exp(A)}{\exp(2A) - 2} \quad (2.118a)$$

for $Z_{0m}\sqrt{\epsilon_{re}} \leq 89.91$, that is, $A \leq 1.52$

$$W/h = \frac{2}{\pi} \left\{ B - 1 - \ell_n(2B - 1) + \frac{\epsilon_r - 1}{2\epsilon_r} \left[\ell_n(B - 1) + 0.39 - \frac{0.61}{\epsilon_r} \right] \right\} \quad (2.118b)$$

where

$$A = \frac{Z_{0m}}{60} \left\{ \frac{\epsilon_r + 1}{2} \right\}^{1/2} + \frac{\epsilon_r - 1}{\epsilon_r + 1} \left\{ 0.23 + \frac{0.11}{\epsilon_r} \right\}$$

$$B = \frac{60\pi^2}{Z_{0m}\sqrt{\epsilon_r}}$$

These expressions also provide an accuracy better than one percent.

A more accurate expression for the characteristic impedance Z_{0m}^a of a microstrip for $t = 0$ and $\epsilon_r = 1$ is given by [41]

$$Z_{0m}^a = \frac{\eta}{2\pi} \ell_n \left[\frac{f(u)}{u} + \sqrt{1 + \left(\frac{2}{u} \right)^2} \right] \quad (2.119)$$

where

$$f(u) = 6 + (2\pi - 6) \exp \left[- \left(\frac{30.666}{u} \right)^{0.7528} \right] \quad (2.120)$$

and $u = W/h$ and $\eta = 120\pi \Omega$. The accuracy of this expression is better than 0.01 percent for $u \leq 1$ and 0.03 percent for $u \leq 1000$. The effective dielectric constant ϵ_{re} may be expressed as

$$\epsilon_{re} = \frac{\epsilon_r + 1}{2} + \frac{\epsilon_r - 1}{2} \left(1 + \frac{10}{u} \right)^{-a(u)b(\epsilon_r)} \quad (2.121)$$

$$a(u) = 1 + \frac{1}{49} \ell_n \left(\frac{u^4 + (u/52)^2}{u^4 + 0.432} \right) + \frac{1}{18.7} \ell_n \left[1 + \left(\frac{u}{18.1} \right)^3 \right] \quad (2.122a)$$

$$b(\epsilon_r) = 0.564 \left(\frac{\epsilon_r - 0.9}{\epsilon_r + 3} \right)^{0.053} \quad (2.122b)$$

The accuracy of this model is better than 0.2 percent for $\epsilon_r \leq 128$ and $0.01 \leq u \leq 100$. Finally, the characteristic impedance is

$$Z_{0m} = \frac{Z_{0m}^a}{\sqrt{\epsilon_{re}}} \quad (2.123)$$

The results discussed above are based on the assumption that the thickness of the strip conductor is negligible. But, in practice, the strip has a finite thickness t that affects the characteristics.

Effect of Strip Thickness

The effect of strip thickness on Z_{0m} and ϵ_{re} of microstrip lines has been reported by a number of investigators [19, 31, 38, 41–54]. Simple and accurate formulas for Z_{0m} and ϵ_{re} with finite strip thickness are [31]

$$Z_{0m} = \frac{\eta}{2\pi\sqrt{\epsilon_{re}}}\ell_n\left\{\frac{8h}{W_e} + 0.25\frac{W_e}{h}\right\} \quad (W/h \leq 1) \quad (2.124a)$$

$$Z_{0m} = \frac{\eta}{\sqrt{\epsilon_{re}}}\left\{\frac{W_e}{h} + 1.393 + 0.667\ell_n\left(\frac{W_e}{h} + 1.444\right)\right\}^{-1} \quad (W/h \geq 1) \quad (2.124b)$$

where

$$\frac{W_e}{h} = \frac{W}{h} + \frac{1.25}{\pi}\frac{t}{h}\left(1 + \ell_n\frac{4\pi W}{t}\right) \quad (W/h \leq 1/2\pi) \quad (2.125a)$$

$$\frac{W_e}{h} = \frac{W}{h} + \frac{1.25}{\pi}\frac{t}{h}\left(1 + \ell_n\frac{2h}{t}\right) \quad (W/h \geq 1/2\pi) \quad (2.125b)$$

$$\epsilon_{re} = \frac{\epsilon_r + 1}{2} + \frac{\epsilon_r - 1}{2}F(W/h) - C \quad (2.126)$$

in which

$$C = \frac{\epsilon_r - 1}{4.6} \frac{t/h}{\sqrt{W/h}} \quad (2.127)$$

It can be observed that the effect of thickness on Z_{0m} and ϵ_{re} is insignificant for small values of t/h . This agrees with the experimental results reported in [42] for $t/h \leq 0.005$, $2 \leq \epsilon_r \leq 10$, and $W/h \geq 0.1$. However, the effect of strip thickness is significant on conductor loss in the microstrip line.

Effect of Enclosure

Most microstrip circuit applications require a metallic enclosure for hermetic sealing, mechanical strength, electromagnetic shielding, mounting connectors, and ease of handling. The effect of the top cover alone [55–57] as well as of the top cover and side walls [51, 58] has been reported in the literature. Both the top cover and side walls tend to lower impedance and effective dielectric constant. This is because the fringing flux lines are prematurely terminated on the enclosure walls. This increases the electric flux in air. The closed-form equations for a microstrip with top cover (without side walls) are obtained as [56, 57]

$$Z_{0m}^a = Z_{0\infty}^a - \Delta Z_{0m}^a \quad (2.128a)$$

$$\alpha_T = \alpha_c + \alpha_d \quad (2.132)$$

The two components α_c and α_d are given by

$$\alpha_c = \begin{cases} 1.38 A \frac{R_s}{h Z_{0m}} \frac{32 - (W_e/h)^2}{32 + (W_e/h)^2} & \text{dB/unit length } (W/h \leq 1) \\ 6.1 \times 10^{-5} A \frac{R_s Z_{0m} \epsilon_{re}(f)}{h} \left[W_e/h + \frac{0.667 W_e/h}{W_e/h + 1.444} \right] & \text{dB/unit length } (W/h \geq 1) \end{cases} \quad (2.133)$$

and

$$\alpha_d = \begin{cases} 4.34 \eta \sigma \frac{\epsilon_{re}(f) - 1}{\sqrt{\epsilon_{re}(f)} (\epsilon_r - 1)} & \text{dB/unit length} \\ 27.3 \frac{\epsilon_r}{\epsilon_r - 1} \frac{\epsilon_{re}(f) - 1}{\sqrt{\epsilon_{re}(f)}} \frac{\tan \delta}{\lambda_0} & \text{dB/unit length} \end{cases} \quad (2.134)$$

where

$$A = 1 + \frac{h}{W_e} \left\{ 1 + \frac{1.25}{\pi} \ell \alpha \frac{2B}{t} \right\}$$

$R_s = \sqrt{\pi f \mu_0 \rho_c}$; ρ_c = resistivity of the strip conductor

$\sigma = \omega \epsilon_0 \epsilon_r \tan \delta$ = conductivity of the dielectric substrate;

and

$$B = \begin{cases} h & \left(W/h \geq \frac{1}{2\pi} \right) \\ 2\pi W & \left(W/h \leq \frac{1}{2\pi} \right) \end{cases}$$

The dielectric loss is normally very small compared with the conductor loss for dielectric substrates. The dielectric loss in silicon substrates (used for monolithic MICs), however, is usually of the same order or even larger than the conductor loss. This is because of the lower resistivity available in silicon wafers. However, higher resistivity can be obtained in GaAs, and therefore the dielectric loss is lower for this material. Values of conductor and dielectric losses per unit length for

50- Ω microstrip lines on various substrates (dielectric as well as semiconductor) are plotted in Figure 2.11 (in Section 2.4.1) as functions of frequency. At a given frequency the total loss can be obtained by adding the two values.

Figure 2.19 compares the total loss for 50- Ω microstrip lines on RT/duroid, quartz, and alumina substrates. At the same h/λ_0 ratio, high dielectric constant substrates result in greater loss.

Microstrip loss data presented above require that the conductor thickness be greater than about four times the skin depth. The microstrip conductor loss calculation for any metalization thickness has been reported by Lee and Itoh [65] based on the phenomenological loss equivalence method and by Faraji-Dana and Chow [66, 67] based on ac resistance. Faraji-Dana and Chow's calculated conductor loss data for thick conductors agree very well with the calculated results obtained using expressions reported by Pucel et al. [18]. Aksun and Morkoc [68] have reported dielectric loss results for microstrip substrates consisting of different GaAs layer thicknesses on an Si substrate.

Quality Factor- Q

The quality factor, Q , of a microstrip can be related to the total loss in the line by [69]

$$Q_T = \frac{\beta}{2\alpha_T} \quad (2.135)$$

where Q_T is the total Q of the resonator (quarter wavelength), α_T is the total loss in the resonator, and $\beta = 2\pi/\lambda_m$. When losses in a resonant line are considered, another loss factor, α_r , due to radiation at the open-end discontinuities must also be taken into account [69, 70]. The corresponding radiation Q -factor is given by [69]

$$Q_r = \frac{Z_{0m}}{480\pi(h/\lambda_0)^2 R} \quad (2.136)$$

where

$$R = \frac{\epsilon_{re}(f) + 1}{\epsilon_{re}(f)} - \frac{[\epsilon_{re}(f) - 1]^2}{2[\epsilon_{re}(f)]^{3/2}} \ell_n \left\{ \frac{\sqrt{\epsilon_{re}(f)} + 1}{\sqrt{\epsilon_{re}(f)} - 1} \right\} \quad (2.137)$$

Note that the effect of dispersion is considered, as described by (2.131).

The total Q of the resonator can be expressed by

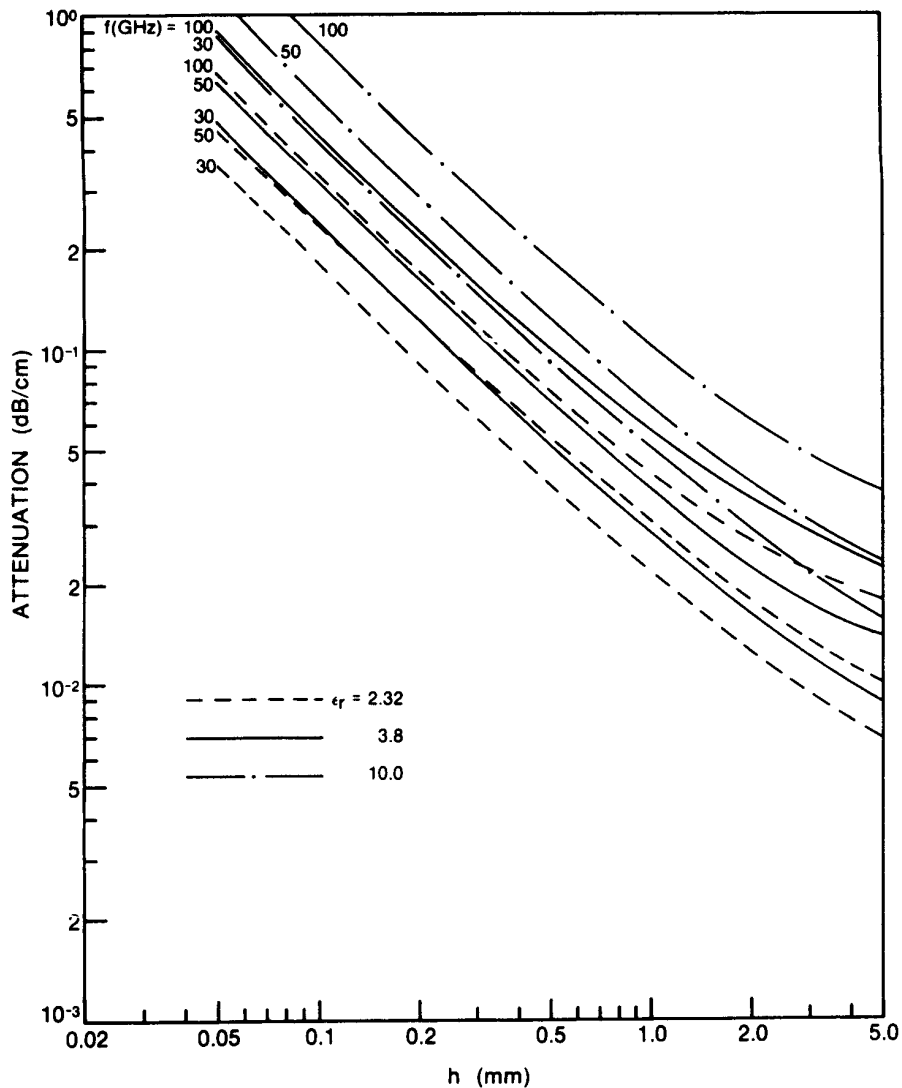


Figure 2.19 Total loss versus substrate thickness (h) for RT/Duroid ($\epsilon_r = 2.32$), Quartz ($\epsilon_r = 3.8$), and Alumina ($\epsilon_r = 10.0$) at various frequencies.

$$\frac{1}{Q_T} = \frac{1}{Q_c} + \frac{1}{Q_d} + \frac{1}{Q_r} \quad (2.138)$$

Here, Q_c , Q_d , and Q_r are the quality factors corresponding to conductor, dielectric, and radiation losses, respectively. Finally, the circuit quality factor, Q_0 , is defined as

$$\frac{1}{Q_0} = \frac{1}{Q_c} + \frac{1}{Q_d} = \frac{\lambda_0(\alpha_c + \alpha_d)}{\pi\sqrt{\epsilon_{re}(f)}} \quad (2.139)$$

The variation with frequency of Q_0 , Q_r , and Q_T for a quarter-wave resonator on GaAs, alumina, and quartz substrates is shown in Figure 2.20. A quarter-wave 50- Ω resonator on a 25-mil-thick alumina substrate has a Q_0 of about 240 at 2.0 GHz and 550 at 10.0 GHz, whereas Q_T is 230 at 2.0 GHz and nearly 160 at 10.0 GHz. This is due to the fact that the radiation losses are higher than conductor and dielectric losses at higher frequencies. On the other hand, a quarter-wave 50- Ω resonator on a 10-mil GaAs substrate has Q_0 of about 82 at 2.0 GHz and 160 at 10.0 GHz, whereas Q_T is 82 at 2.0 GHz and nearly 145 at 10.0 GHz. This is explained by smaller radiation losses for thin substrates. Thus, the commonly accepted rule that thick substrates should be used for high Q circuits does not apply to microstrip lines because of high radiation losses incurred under this condition.

The variation, with substrate thickness, of the total Q for half-wave resonators on RT/duroid, quartz, and alumina is shown in Figure 2.21 for $f = 30$ GHz, 50 GHz, and 100 GHz. For a given frequency, there is an optimum substrate thickness at which the Q is maximum. This optimum value of h decreases with increasing frequency and decreasing dielectric constant value, mainly because of radiation.

Comparison of Various Factors Affecting Microstrip Characteristics

The effect of tolerances on the characteristics of a microstrip has been compared in [71] with the effects of finite thickness of a metal strip, dispersion, discontinuities, and an imperfect measurement system. These are included here as Table 2.4 and Table 2.5 for a 50- Ω microstrip on alumina and polystyrene substrates, respectively.

It may be observed from the tables that the change in Z_{0m} is relatively higher due to the dimensional tolerances and the imperfect measurement system. For a microstrip on polystyrene substrate, the change in characteristics due to dimensional tolerances dominates the change due to other factors. However, at 10 GHz and for microstrip on alumina substrate, dispersion gives rise to the largest change in ϵ_{re} .

2.4.6 Frequency Range of Operation

The maximum frequency of operation of a microstrip is limited due to several factors such as excitation of spurious modes, higher losses, pronounced discontinu-

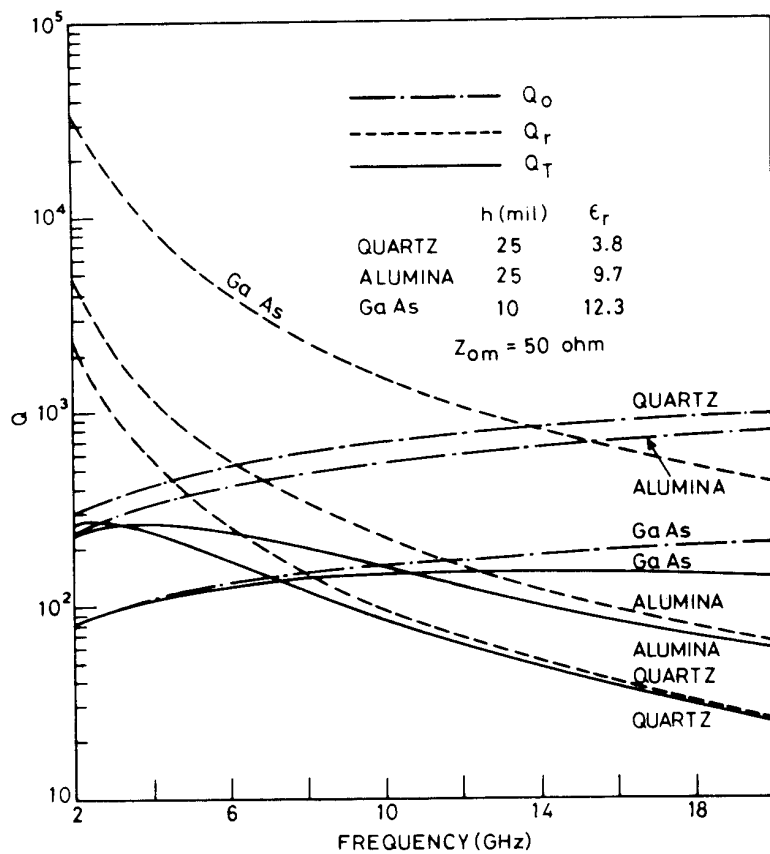


Figure 2.20 Variation of Q -factors with frequency for quarterwave microstrip resonators on Quartz, Alumina, and GaAs substrates.

ity effects, low Q due to radiation from discontinuities, effect of dispersion on pulse distortion, tight fabrication tolerances, handling fragility, and, of course, technological processes. The frequency at which significant coupling occurs between the quasi-TEM mode and the lowest order surface wave spurious mode is given below [72].

$$f_T = \frac{150}{\pi h} \sqrt{\frac{2}{\epsilon_r - 1}} \tan^{-1}(\epsilon_r) \quad (2.140)$$

where f_T is in gigahertz and h is in millimeters. Thus the maximum thickness of the quartz substrate ($\epsilon_r \approx 3.8$) for microstrip circuits designed at 100 GHz is less than 0.5 mm.

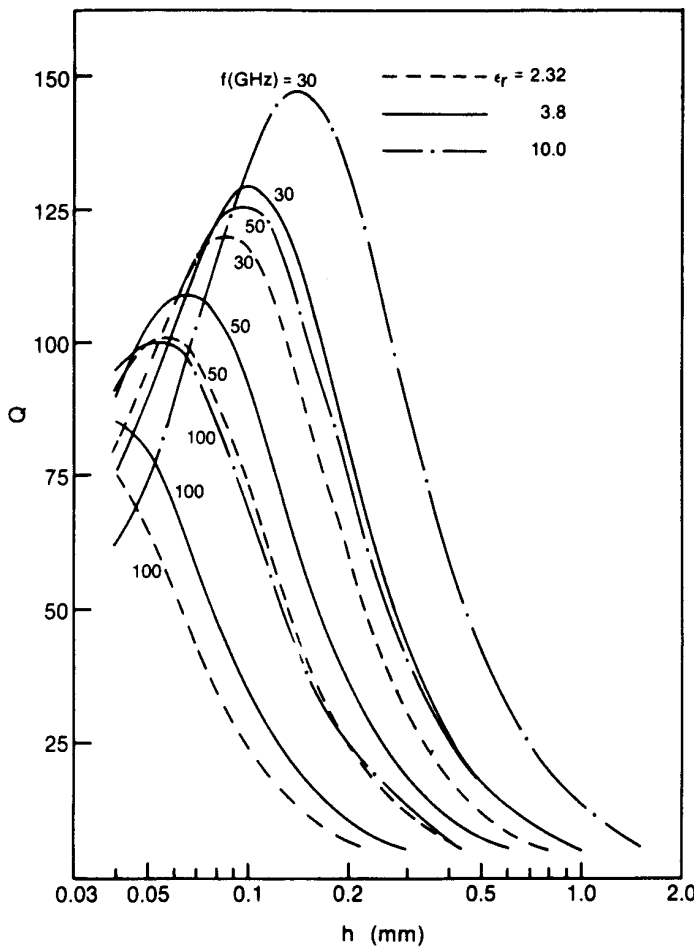


Figure 2.21 Total Q for a half-wave resonator on RT/Duroid ($\epsilon_r = 2.32$), Quartz ($\epsilon_r = 3.8$) and Alumina ($\epsilon_r = 10.0$) versus substrate thickness.

The excitation of higher order modes in a microstrip can be avoided by operating it below the cut-off frequency of the first higher order mode, which is given approximately by [72]

$$f_c \equiv \frac{300}{\sqrt{\epsilon_r(2W + 0.8h)}} \quad (2.141)$$

Table 2.4
 Change in the Characteristics of Microstrip on Alumina Substrate
 $(Z_{0m} = 50 \Omega, \epsilon_r = 9.7, h = 0.025 \text{ in})$

<i>Effect of Various Factors</i>		<i>VSWR (due to change in Z_{0m})</i>	$\Delta\epsilon_r$
Effect of thickness (compared with $t = 0$ case)	$t/h = 0.004$ $t/h = 0.040$	1.013 1.029	-0.029 -0.075
Effect of dispersion (compared to quasi-static value)	$f = 3 \text{ GHz}$ $f = 10 \text{ GHz}$	1.003 1.03	+0.033 +0.303
Effect of dimensional tolerances ($\Delta\epsilon_r = \pm 0.25$, $\Delta h = \pm 0.001 \text{ in}$)	$\Delta W = \pm 0.0002 \text{ in}$ $\Delta W = \pm 0.0020 \text{ in}$	≤ 1.037 ≤ 1.076	$\leq \pm 0.1919$ $\leq \pm 0.2347$
Effect of step discontinuity $W_2/W_1 = 2.0$ ($W_1 = 0.025 \text{ in}$) $C_{\text{step}} = 8.9 \times 10^{-3} \text{ pF}$	$f = 3 \text{ GHz}$ $f = 10 \text{ GHz}$	1.008 1.028	—
Launchers, connectors, or transitions	$f = 3 \text{ GHz}$ $f = 10 \text{ GHz}$	1.065 1.100	—

Table 2.5
 Change in the Characteristics of a Microstrip on Polystyrene Substrate
 $(Z_{0m} = 50 \Omega, \epsilon_r = 2.55, h = 0.0625 \text{ in})$

<i>Effect of Various Factors</i>		<i>VSWR (due to change in Z_{0m})</i>	$\Delta\epsilon_r$
Effect of thickness (compared with $t = 0$ case)	$t/h = 0.022$ $t/h = 0.044$	1.009 1.017	-0.004 -0.009
Effect of dispersion (compared to quasi-static value)	$f = 2 \text{ GHz}$ $f = 4 \text{ GHz}$	1.007 1.027	+0.011 +0.043
Effect of dimensional tolerances ($\Delta\epsilon_r = \pm 0.2$, $\Delta h = \pm 0.005 \text{ in}$)	$\Delta W = \pm 0.0001 \text{ in}$ $\Delta W = \pm 0.0030 \text{ in}$	≤ 1.097 ≤ 1.110	$\leq \pm 0.1596$ $\leq \pm 0.1619$
Effect of step discontinuity $W_2/W_1 = 2.0$ $C_{\text{step}} = 2.66 \times 10^{-2} \text{ pF}$	$f = 2 \text{ GHz}$ $f = 4 \text{ GHz}$	1.016 1.032	— —
Launchers, connectors, or transitions	$f = 2 \text{ GHz}$ $f = 4 \text{ GHz}$	1.060 1.070	— —

where f_c is in gigahertz and W and h are in millimeters. This limitation is mostly applicable to low impedance lines that have wide microstrip conductors and/or thick substrates commonly used for microstrip patch antenna elements.

An infinitely long microstrip does not radiate as there is no coupling between the dominant mode and the higher order radiating modes. However, whenever there is some discontinuity in the line, namely an open end, slit, step in width, bend, or a gap, higher order radiating modes are excited, which depend upon the substrate thickness and frequency of operation. The operating frequency at which the radiation becomes significant may be calculated from the radiation Q factor of a $\lambda/2$ resonator, approximately given by

$$Q_r = \frac{3\epsilon_r Z_{0m}\lambda_0^2}{32\eta h^2} \quad (2.142)$$

where $\eta = 120\pi$. Thus for thicker substrates, where $Q \approx Q_r$, the variation of Q is proportional to $1/(fh)^2$. For example, a 50Ω resonator on a quartz substrate has a $Q_r \approx 0.4252 \times 10^4/(fh)^2$ where f is in gigahertz and h is in millimeters. At 100 GHz, the substrate thickness is less than 0.065 mm for Q_r greater than 100. A substrate thickness of this order results in attenuation on the order of 1 dB/cm. Thus not only do thin substrates give rise to high losses, but they are also difficult to handle and result in narrow conducting strips. Fabrication tolerances and technological processes such as photoetching limit the minimum strip width and the spacing between two adjacent strips in the case of coupled lines. High impedance lines of about 120Ω require strip widths on the order of 0.02 mm on a 0.065-mm-thick quartz substrate, thereby also setting a limit on the frequency of operation of microstrip lines because of low radiation Q_r .

On a microstrip, phase and group velocities are frequency dependent. Therefore, a digital pulse signal is distorted due to different velocities of the signals' frequency components. To minimize distortion, the dispersion effects must be minimized by keeping the fh product as small as possible.

2.5 OTHER TYPES OF MICROSTRIP LINES

There are several derivatives of microstrip lines being used in MICs. These include inverted and suspended microstrip lines, a multilayered microstrip, a thin film microstrip, and valley microstrip. These structures are briefly described in this section.

2.5.1 Suspended and Inverted Microstrip Lines

Suspended and inverted microstrip lines (shown in Figure 2.22) provide a higher Q (500 to 1500) than the conventional microstrip lines. The wide range of achievable

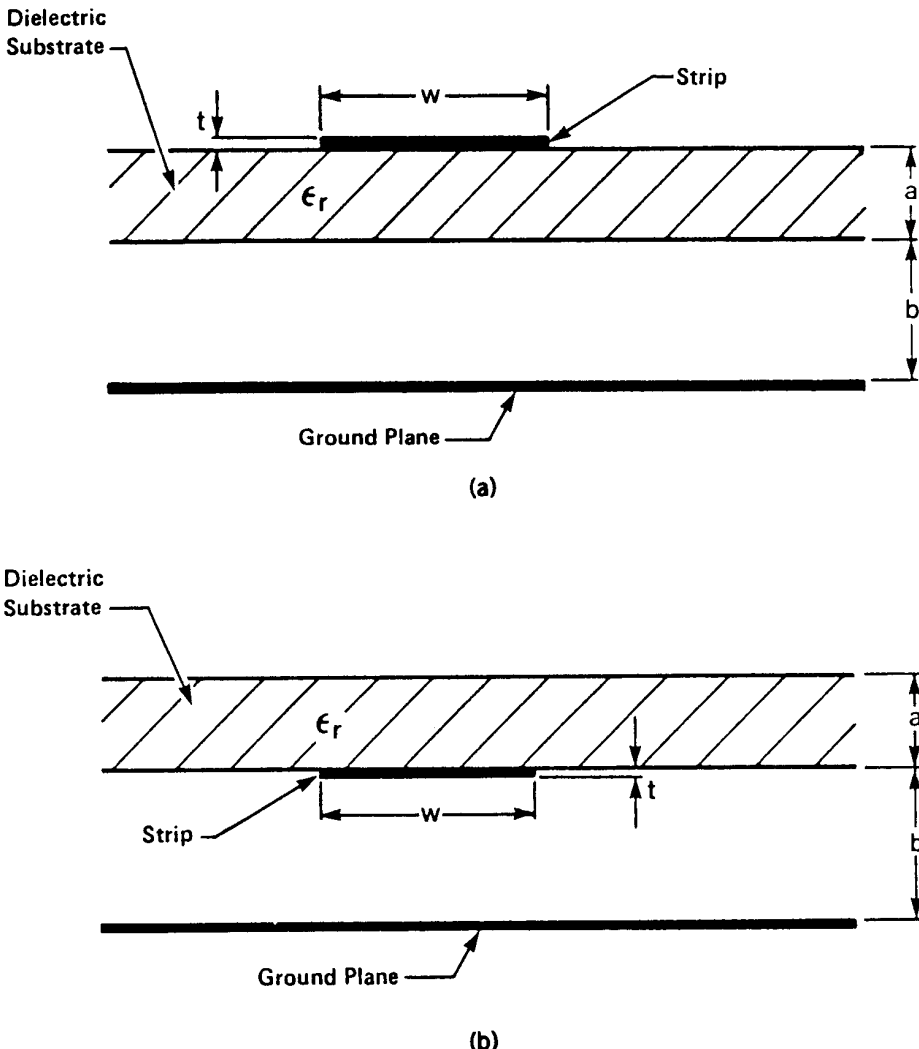


Figure 2.22 Suspended-substrate microstrip line configurations: (a) suspended and (b) inverted.

impedance values makes these media particularly suitable for filters. Expressions for the characteristic impedance and effective dielectric constant for $t/h \ll 1$ are given as [73]

$$Z_0 = \frac{60}{\sqrt{\epsilon_{re}}} \ell_n \left[\frac{f(u)}{u} + \sqrt{1 + \left(\frac{2}{u} \right)^2} \right] \quad (2.143)$$

where

$$f(u) = 6 + (2\pi - 6) \exp\left[-\left(\frac{30.666}{u}\right)^{0.7528}\right]$$

For the suspended microstrip $u = w/(a + b)$ and for the inverted microstrip $u = w/b$, where all the variables are defined in Figure 2.22.

For a suspended microstrip the effective dielectric constant ϵ_{re} is obtained from

$$\sqrt{\epsilon_{re}} = \left[1 + \frac{a}{b} \left(a_l - b_l \ell_n \frac{w}{b} \right) \left(\frac{1}{\sqrt{\epsilon_r}} - 1 \right) \right]^{-1} \quad (2.144)$$

where

$$a_l = \left(0.8621 - 0.1251 \ell_n \frac{a^4}{b} \right)$$

$$b_l = \left(0.4986 - 0.1397 \ell_n \frac{a^4}{b} \right)$$

and for an inverted microstrip the effective dielectric constant is given by

$$\sqrt{\epsilon_{re}} = 1 + \frac{a}{b} \left(\bar{a}_l - \bar{b}_l \ell_n \frac{w}{b} \right) (\sqrt{\epsilon_r} - 1) \quad (2.145)$$

where

$$\bar{a}_l = \left(0.5173 - 0.1515 \ell_n \frac{a^2}{b} \right)^2$$

$$\bar{b}_l = \left(0.3092 - 0.1047 \ell_n \frac{a^2}{b} \right)^2$$

The accuracy of (2.144) and (2.145) is within ± 1 percent for $1 < w/b \leq 8$, $0.2 \leq a/b \leq 1$, and $\epsilon_r \leq 6$. For $\epsilon_r \approx 10$, the error is less than ± 2 percent.

2.5.2 Multilayered Dielectric Microstrip

Multilayered dielectric microstrip lines are becoming an integral part of GaAs ICs. Several applications of such structures include circuit passivation or scratch

protection, high-speed digital circuit crossover interconnects, MMIC crossover interconnects, metal-insulator-metal capacitors, high directivity couplers [74, 75] tightly coupled structures [76–78], improving pulse characteristic propagation [79], and many others. Analysis of multilayered dielectric microstrip lines has been performed using quasi-static analyses such as the variational method [80–82], the potential theory method, and full wave spectral domain methods [83, 84].

Multilayered structures are generally fabricated in MMICs using very thin dielectric layers of insulating materials such as silicon nitride ($\epsilon_r \approx 6.7$) and polyimide ($\epsilon_r \approx 3.0$). The dielectric constant of these materials might vary from foundry to foundry depending upon the composition used. The characteristic impedance and effective dielectric constant of a multilayered structure using polyimide are calculated utilizing the variational method, and the results are plotted in Figures 2.23 and 2.24 for several values of dielectric thicknesses. It may be noted from these figures that the lower polyimide dielectric layer has a significant effect on these characteristics as compared to that of the upper layer. Figure 2.25 shows the calculated capacitance per unit length of a microstrip line for various values of the lower dielectric layer thickness and fixed value of upper layer thickness. Even thin layers of low dielectric constant under the microstrip conductors reduce its capacitance significantly. This feature can be used to reduce the parasitic capacitance of a lumped inductor realized in this configuration in order to extend its maximum operating frequency to higher values. The effects of uncertainties in the polyimide layer's thickness and dielectric constant values on the effective dielectric constant and characteristic impedance are given in Table 2.6.

Figure 2.26 shows the calculated capacitance and inductance per unit length of a microstrip as a function of strip width for various values of air thickness under the conductor. The capacitance reduces significantly even for small thicknesses, while the inductance is almost constant.

2.5.3 Thin Film Microstrip (TFM)

In order to make MMICs compact and low cost, a *thin film microstrip* (TFM) structure has also been used [85–89]. Both active and passive miniature circuits have been successfully realized with TFM employing a narrow-width microstrip conductor on thin low-dielectric constant materials, fabricated on semi-insulating GaAs substrate. As shown in Figure 2.27, a ground plane is placed between a thin dielectric layer and the GaAs substrate. The GaAs substrate provides support as well as a semiconductor medium for active devices. Due to the thin microstrip conductors, TFM has relatively high insertion loss as compared to a conventional microstrip.

The loss characteristics of a TFM and a conventional microstrip on GaAs are compared [85] in Figure 2.28. The metal thickness t of the TFM is assumed to be one-third of the thin film thickness ($H/3$). The thin film dielectric is SiON, having a dielectric constant value of 5. Three micron-thick conductors were used in the

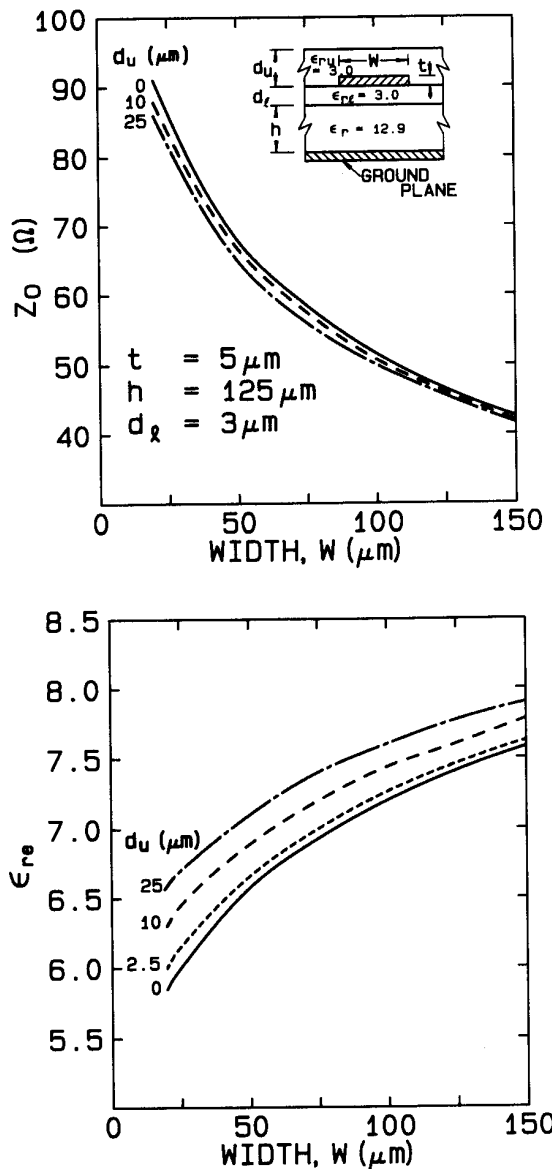


Figure 2.23 Calculated Z_0 and $\epsilon_{r\text{e}}$ for various values of d_u and W . $\epsilon_r = 12.9$, $t = 5 \mu\text{m}$, and $h = 125 \mu\text{m}$.

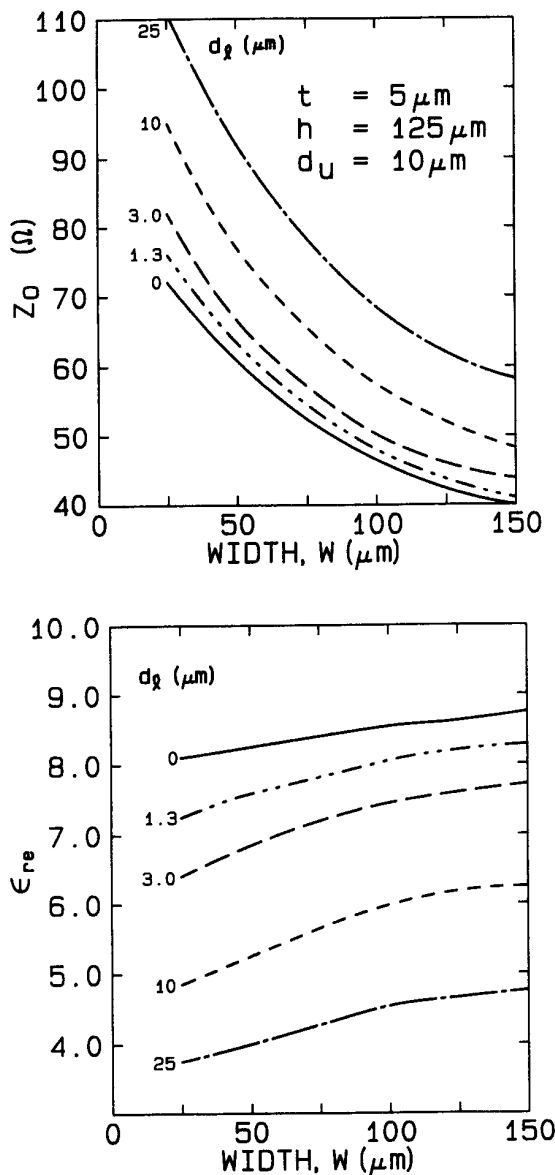


Figure 2.24 Calculated Z_0 and ϵ_{re} for various values of d_i and W : $\epsilon_r = 12.9$, $t = 5 \mu\text{m}$, and $h = 125 \mu\text{m}$.

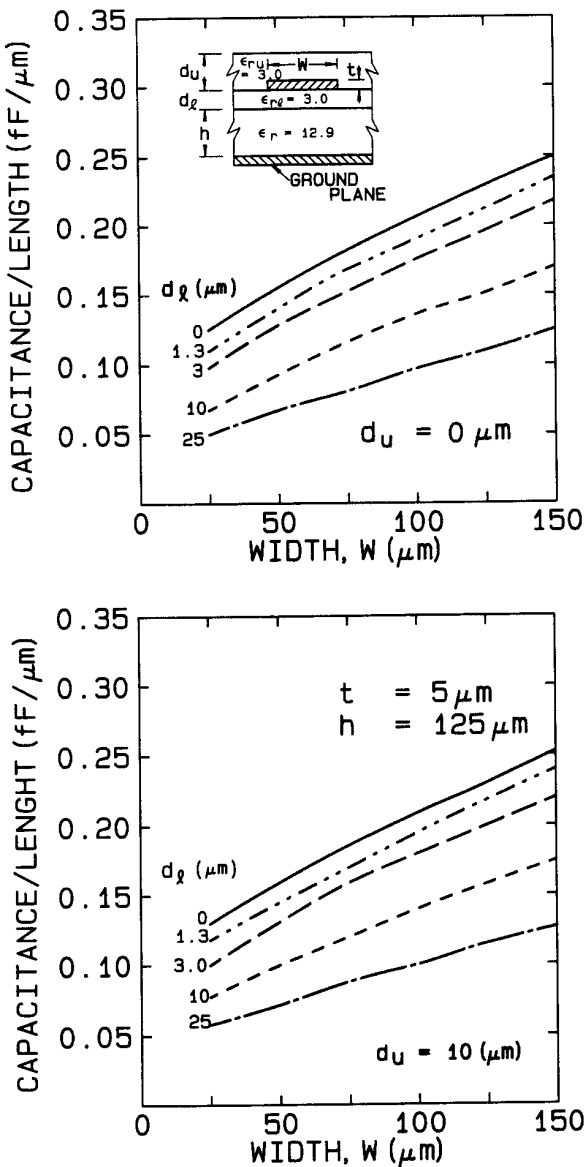


Figure 2.25 Calculated capacitance per unit length of a multilayered microstrip.

Table 2.6
 Sensitivity Analysis of a Multilayered Microstrip Line $\epsilon_{rl}(\text{GaAs}) = 12.9$,
 Substrate Thickness, $h = 125 \mu\text{m}$

<i>Microstrip Parameter Change (%)</i>	<i>Uncertainty in Polyimide Layers</i>			
	<i>Line Width (μm)</i>	$\Delta\epsilon_{ru} = +10\%$	$\Delta d_l = +10\%$	$\Delta d_u = +10\%$
		$\Delta\epsilon_{rl} = +10\%$ (Dielectric Constant)	(Under layer)	(Over layer)
$\Delta\epsilon_{re}$	20	+3.3	-1.9	+0.4
$\Delta Z_{0m}(\Omega)$	20	-1.5	+1.0	-0.2
$\Delta\epsilon_{re}$	90	+1.8	-1.2	+0.2
$\Delta Z_{0m}(\Omega)$	90	-0.9	+0.7	-0.1

calculation of conventional microstrip line characteristics. Loss calculations were performed for 50Ω lines. Figure 2.29 shows measured data obtained at 10 GHz for the TFM lines. Here the thin film dielectric is polyimide ($\epsilon_{rd} \approx 3$, $H \approx 3 \mu\text{m}$). TFM lines can readily be realized to achieve very low characteristic impedances 3Ω to 4Ω , by using microstrip conductor widths on the order of $100 \mu\text{m}$, without exciting higher order modes. Thus TFM overcomes the low characteristic impedance limit problem of a conventional microstrip and has an important application in the design of power amplifier matching networks where very low characteristic impedance is required to match very low device input impedance.

2.5.4 Valley Microstrip Lines

Valley microstrip lines have been used to realize low-loss and miniature MMIC components using multilayer techniques. Figure 2.30 shows cross sections of valley microstrip lines with and without slits. These lines have lower insertion loss than TFM [90–94]. These structures have been analyzed using quasi-TEM techniques [93–94]. The calculated value of the characteristic impedance of a valley microstrip as a function of strip width for several values of slit widths is shown in Figure 2.31 [92]. The thin film dielectric is polyimide ($\epsilon_{rd} = 3.3$), having a thickness of $10 \mu\text{m}$. The insertion loss is about 0.5 dB/mm at 10 GHz.

2.6 MICROSTRIP APPLICATIONS

Satellite, airborne communications, and EW systems have requirements for small size, light weight, and low-cost microwave passive components. Microstrip line-based filters, impedance transformers, hybrids, couplers, power dividers/combiners, delay lines, baluns, circulators, and antennas are used extensively in microwave systems,

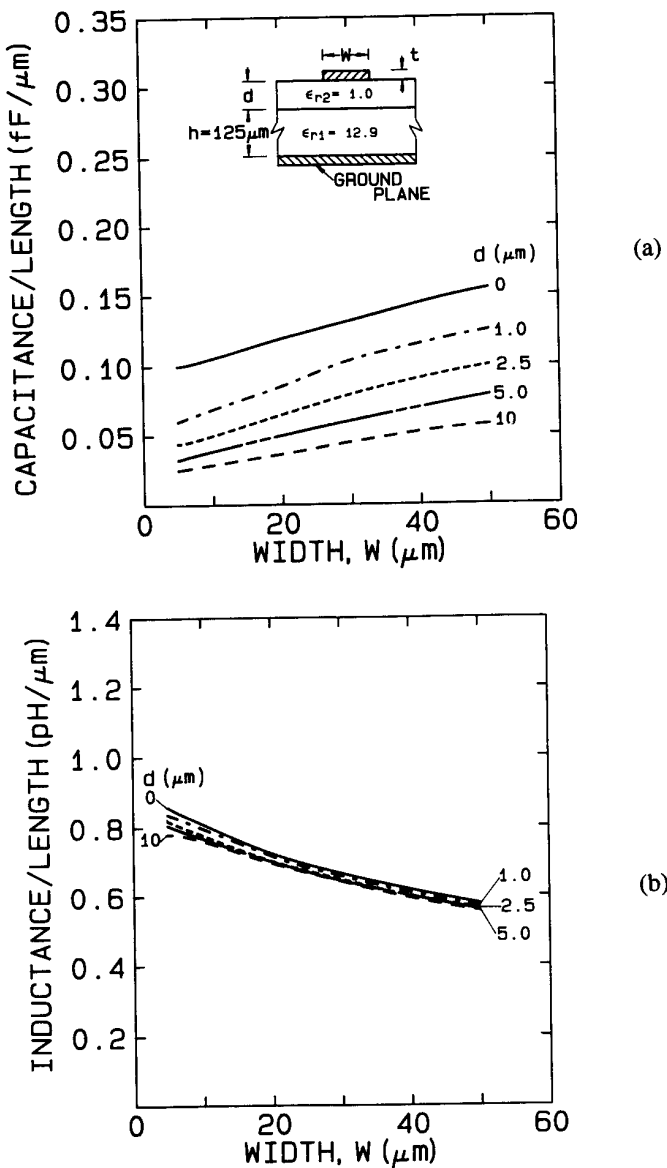


Figure 2.26 (a) Calculated capacitance per unit length of a multilayered microstrip and (b) calculated inductance per unit length of a multilayered microstrip.

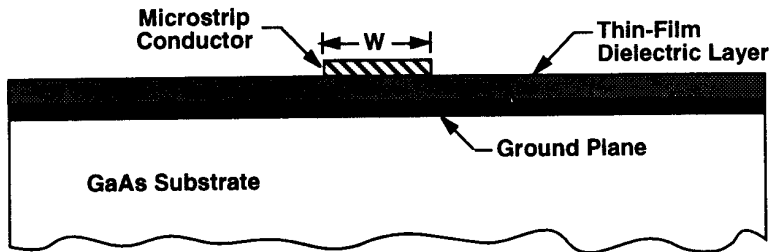


Figure 2.27 Cross section of a low impedance thin film microstrip transmission line (TFMS).

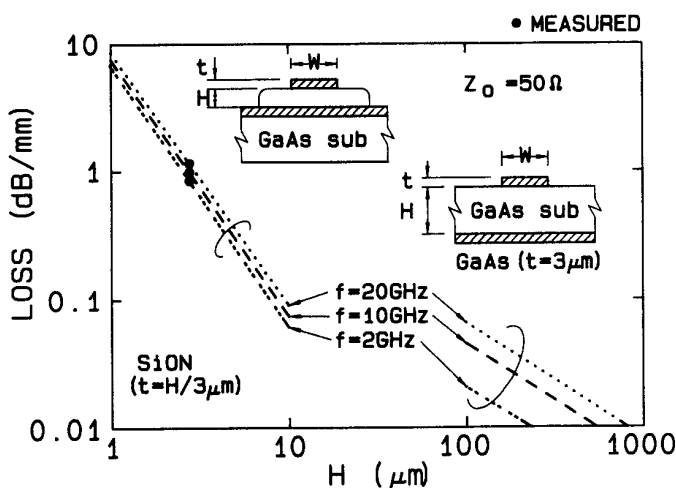


Figure 2.28 Characteristics of TFMS and conventional microstrip lines (from [85], © 1989 IEEE. Reprinted with permission.).

including measurement instruments where the demand on low-loss and high-power characteristics is not severe. The suspended microstrip provides a higher Q than the microstrip, as most of the energy is propagating in air. This results in lower loss passive components.

Sections of microstrip lines constitute the basic building blocks of microwave integrated circuits. When the size of the microstrip section is reduced to dimensions much smaller than the wavelength, it can be used as a lumped element. Examples of lumped microstrip elements are spiral inductors, thin film resistors, interdigital capacitors, metal-insulator-metal (MIM) capacitors, via holes, and airbridges as shown in Figure 2.32. Microstrip sections in lumped and distributed forms are commonly used in passive and active hybrid and monolithic integrated circuits. Examples of

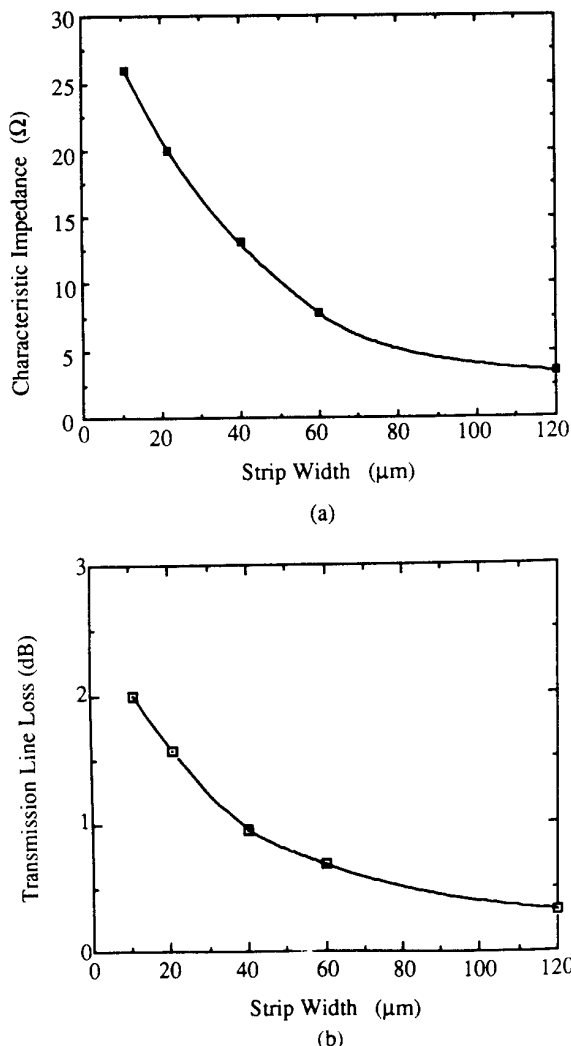


Figure 2.29 (a) Characteristic impedance and (b) transmission loss (per millimeter) at 10 GHz for various widths of TFM lines (from [88], © 1993 IEEE. Reprinted with permission.).

passive circuits include filters, impedance transformers, hybrids, couplers, power dividers/combiners, delay lines, and baluns. Amplifiers, oscillators, mixers, and control circuits employing solid state devices constitute the other class. Microwave packages and assembly techniques frequently use microstrip transmission medium

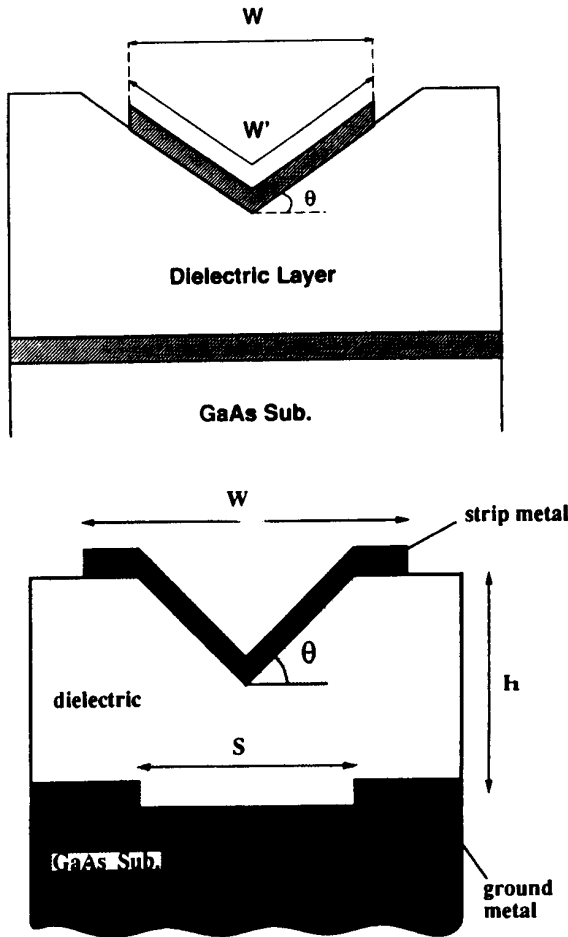


Figure 2.30 Cross section of the valley microstrip line with and without slit.

in the feedthroughs and interconnects. Another important application of microstrip lines is in high-temperature superconducting microwave integrated circuits. This section provides a brief introduction to the design of microstrip elements for the above-mentioned applications.

2.6.1 Lumped Elements

Lumped-element circuits that have lower Q than distributed circuits have the advantage of smaller size, lower cost, and wide-band characteristics. These are

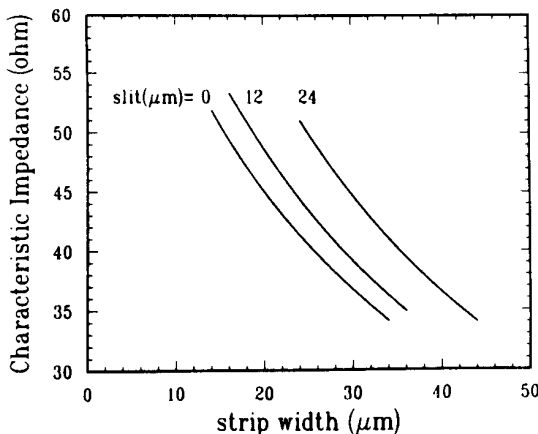


Figure 2.31 Calculated value of the characteristic impedance of a valley microstrip line as a function of the strip width for slit widths = 0, 12 μm , and 24 μm . The dielectric film thickness, H , is 10 μm , and the valley taper, θ , is 35° (from [92], © 1992 IEEE. Reprinted with permission.).

especially suitable for monolithic MICs and for broadband hybrid MICs where real estate requirements are of prime importance. Impedance transformations on the order of 20:1 can be easily accomplished using the lumped-element approach. Therefore, high-power devices that have very low impedance values can easily be tuned with large impedance transformers using lumped elements. Consequently, lumped elements find applications in high-power oscillators, power amplifiers, and broadband circuits.

With the advent of new photolithographic techniques, the fabrication of lumped elements that was limited to X-band frequencies can now be extended to about 60 GHz. The three basic building blocks for circuit design—inductors, capacitors, and resistors—are available in lumped form. Computer-aided design of circuits using lumped elements requires a complete and accurate characterization of lumped elements at microwave frequencies. This necessitates the development of comprehensive mathematical models that take into account the presence, for example, of ground planes, proximity effect, fringing fields, and parasitics. In this section we describe briefly the design of inductors, capacitors, and resistors [95–98].

Design of Inductors

Inductors are used as RF chokes, matching elements, and reactive terminations; and they can also be found in filters, couplers, dividers and combiners, and resonant circuits. A lumped inductor may be realized using a high-impedance microstrip section or a spiral conductor as shown in Figure 2.32a. Inductors in MICs are

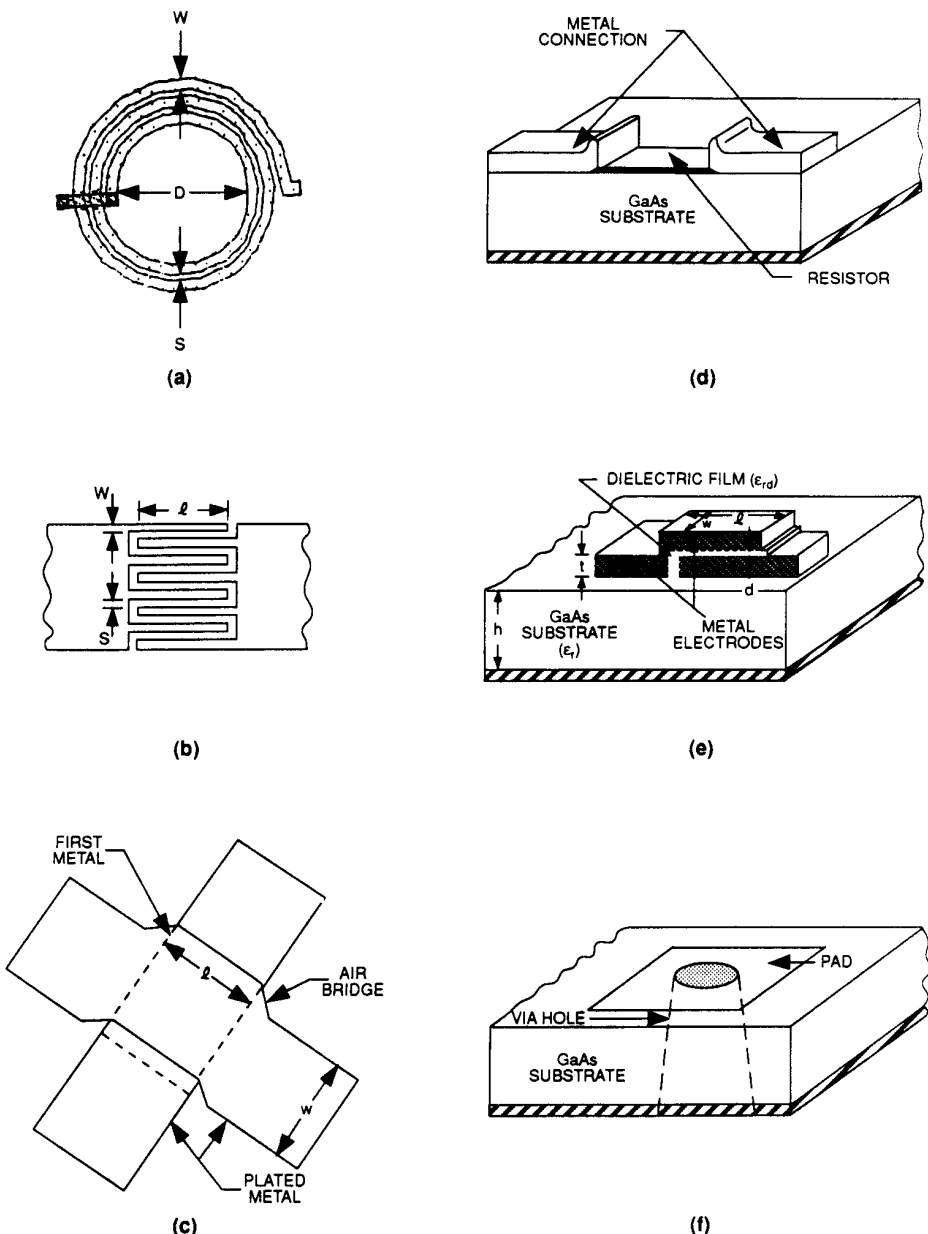


Figure 2.32 MMIC circuits use passive lumped elements: (a) spiral inductor; (b) interdigital capacitor; (c) airbridge crossover; (d) thin film resistor; (e) MIM capacitor; and (f) via hole.

fabricated using a standard IC process with no additional process steps. The innermost turn of the spiral inductor is connected to other circuitry through a conductor that passes under airbridges in MMICs, whereas a wire bond connection is made in hybrid MICs. The width and thickness of the conductor under the airbridges determine the current-carrying capacity of the inductor. Typically the thickness is 0.5 μm to 1.0 μm and the airbridge separates it from the upper conductors by 1.5 μm to 3.0 μm . Typical inductance values for monolithic microwave circuits operating above L-band fall in the range of 0.5 nH to 10 nH. In order to realize high Q inductors, the conductor thickness must be greater than 4 times the skin depth at the operating frequency. Silver-plated inductors have much higher Q than gold plated inductors.

Straight sections of microstrip are used for low inductance values typically up to 2 nH to 3 nH. Spiral inductors (circular or rectangular) have higher Q and can provide higher inductance values. These inductors are commonly used for high-density circuits. The presence of a ground plane also affects the inductance value, which decreases as the ground plane is brought nearer. This decrease can be taken into account by means of a correction factor K_g . With this correction, the effective inductance L may be written as

$$L = K_g L_0 \quad (2.146)$$

where L_0 is the free-space inductance value. A closed-form expression for K_g for a ribbon is given by [96]

$$K_g = 0.57 - 0.145 \ell_n \frac{W}{h}, \quad \frac{W}{h} > 0.05 \quad (2.147)$$

where W is the conductor width and h is the substrate thickness. To a first-order approximation, the above expression can also be used with other types of inductors.

Table 2.7 gives approximate expressions for inductances and resistances of various types of inductors. In the case of spirals n is the number of turns and S is the spacing between the turns, R_s is the sheet resistance of the conductor per square, ℓ is the length of the conductor, and K is a correction factor that takes into account the crowding of the current at the corners of the conductor. Expressions for K for various structures are

$$K = 1.4 + 0.217 \ell_n \left(\frac{W}{5t} \right) \quad 5 < \frac{W}{t} < 100 \quad \text{for a ribbon} \quad (2.148a)$$

$$K = 1 + 0.333 \left(1 + \frac{S}{W} \right) \quad \text{for a spiral} \quad (2.148b)$$

Table 2.7
Expressions for Lumped Inductors

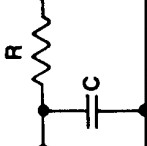
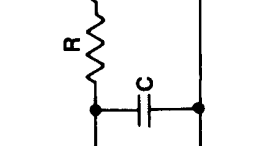
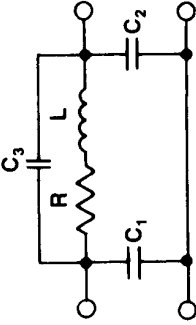
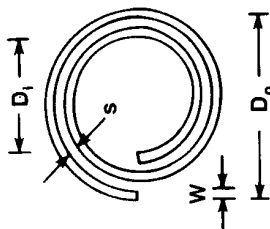
Inductors	Equivalent Circuit	Expressions
Strip		$L(\text{nH}) = 2 \times 10^{-4} \ell \left[\ln\left(\frac{\ell}{W+t}\right) + 1.193 + 0.2235 \frac{W+t}{\ell} \right] \cdot K_s$ $R(\Omega) = \frac{KR\ell}{2(W+t)}$
Loop		$L(\text{nH}) = 1.257 \times 10^{-3} a \left[\ln\left(\frac{a}{W+t}\right) + 0.078 \right] \cdot K_s$ $R(\Omega) = \frac{KR_s}{W+t \pi a}$

Table 2.7 (continued)
Expressions for Lumped Inductors

Inductors	Equivalent Circuit	Expressions
Spiral		$L(nH) = 0.03937 \frac{\alpha^2 n^2}{8a + 11c} \cdot K_s$ $a = \frac{D_0 + D_o}{4}, \quad c = \frac{D_0 - D_o}{2}$ $R(\Omega) = \frac{K\pi a n R_s}{W}$ $C_3 (\text{pF}) = 3.5 \times 10^{-5} D_0 + 0.06$



where t is the thickness of the conductors. The unloaded Q of an inductor may be calculated from

$$Q = \frac{\omega L}{R} \quad (2.149)$$

More accurate models for MMIC spiral inductors with 1.5, 2.5, and 3.5 turns have been published in the literature [98].

Design of Capacitors

Lumped-element capacitors are commonly used in matching circuits, filters, dividers, and couplers and for RF by-passing and dc blocking. Basically there are two types of passive capacitors generally used in microwave and millimeter wave circuits: interdigital, shown in Figure 2.32b, and *metal-insulator-metal* (MIM), depicted in Figure 2.32e. The choice between the interdigital and MIM capacitors depends on the capacitance value to be realized, the processing technology available, size requirements, and the frequency of operation. Usually for values less than 1 pF interdigital capacitors can be used, while for higher values MIM techniques are generally used to minimize the overall size.

The analysis of interdigital capacitors has been reported by Alley [95]. These capacitors can be fabricated employing an interdigital microstrip conductor pattern, by the technique used in the fabrication of MICs, and do not require any additional processing step. The series capacitance is a strong function of the number of fingers and the gap between the fingers and increases with the length of the fingers. An approximate closed-form expression for circuit elements is given in Table 2.8. Here n is the number of fingers, ϵ_{re} is the effective dielectric constant of microstrip line of width W , h is the substrate thickness, and R_s is the surface resistance of the microstrip conductors. All dimensions are in microns. The elliptic functions $K(k)$ and $K'(k)$ are defined in Section 7.2.1. Unfortunately, this model has limitations as it does not accurately represent the capacitor's characteristics. Table 2.9 provides more accurate interdigital capacitor equivalent circuit model values extracted from accurately measured "on-wafer" Sparameters [98].

MIM capacitors are constructed by using a thin layer of a low-loss dielectric between two metal plates. In MMICs, the bottom plate of the capacitor uses first metal, a thin unplated metal, and typically the dielectric material is silicon nitride (Si_3N_4). The top plate uses a thick plated conductor to reduce the loss in the capacitor. Typically the bottom plate and the top plate have sheet resistances of 0.06 Ω/sq and 0.01 Ω/sq , respectively, and a typical dielectric thickness is 0.2 μm . The dielectric constant of silicon nitride is about 6.8, which yields a capacitance of about 300 pF/mm². The top plate is generally connected to other circuitry by using an air bridge that provides higher breakdown voltages.

Table 2.8
Expressions for Lumped Capacitors

 	$C \text{ (pF)} = \frac{\epsilon_0 10^{-3}}{18\pi} \frac{K(k)}{K'(k)} (n - 1) \ell$ $k = \tan^2\left(\frac{n\pi}{4b}\right), \quad a = \frac{W}{2} \quad \text{and} \quad b = \frac{W + S}{2}$
	$R \text{ (\Omega)} = \frac{4}{3} \frac{R\ell}{Wn}$
	$C \text{ (pF)} = \frac{10^{-3} \epsilon_d W \ell}{36\pi d}$ $R_u \text{ (\Omega)} = \frac{R\ell}{W}$ $G \text{ (S)} = \omega C \tan \delta$
	$C_1 \text{ (pF)} = 1.11 \times 10^{-3} (\sqrt{\epsilon_r}/Z_{0m} - 0.034 W/h) \ell$

Table 2.9

Physical Dimensions and Equivalent Circuit Model Values for Interdigital Capacitors (XX in designations INDIGXX indicates the finger length in μm)

<i>Physical Dimensions</i>	<i>INDIG80</i>	<i>INDIG180</i>	<i>INDIG300</i>	<i>INDIG400</i>	<i>UNITS</i>
ℓ Finger length	80	180	300	400	μm
W Finger width	12	12	12	12	μm
S Finger spacing, side	8	8	8	8	μm
SE Finger spacing, end	12	12	12	12	μm
t Finger thickness	5	5	5	5	μm
n Number of fingers	20	20	20	20	μm
h Substrate thickness	125	125	125	125	μm

<i>Equivalent Circuit Values</i>	<i>INDIG80</i>	<i>INDIG180</i>	<i>INDIG300</i>	<i>INDIG400</i>	<i>UNITS</i>
C Capacitance	0.126	0.252	0.405	0.527	pF
L Inductance	0.000	0.025	0.064	0.101	nH
R Resistance	1.89	0.850	0.500	0.441	Ω
G Shunt capacitance	0.028	0.052	0.080	0.104	pF

The microstrip transmission line-based model of an MIM capacitor is given in Table 2.8, where the top conductor is assumed to be connected to the left-hand side port. This model uses a microstrip transmission line of the same width, W , and length, ℓ , as the dimensions of the capacitor to represent the distributed effects and Z_{0m} is the characteristic impedance. ϵ_{rd} is the dielectric constant of the dielectric film of thickness d . The shunt conductance, G , represents the dielectric film loss of the capacitor. The series resistance R_0 accounts for the conductor loss in the metallization of the bottom plate whose thickness is much less than the skin depth. The fringing capacitance associated with the top plate, C_1 , can be calculated from the total microstrip capacitance [98]. All dimensions are in microns. Table 2.10 summarizes the model parameters of various MIM capacitors.

Design of Thin Film Resistors

Thin film resistors are used in several applications including terminations, isolation resistors, feedback networks, biasing elements, attenuators, and gain-equalizing elements, and as stabilizing resistors that prevent parasitic oscillations. The design of these resistors requires a knowledge of (i) sheet resistance, (ii) thermal resistance, (iii) current-handling capacity, (iv) nominal tolerances, and (v) temperature coefficient of the film. Planar resistors can be realized either by depositing thin films of lossy material on a dielectric base or by employing semiconductor films on a semi-

Table 2.10
Distributed Model Values of the MIM Capacitors

C (pF)	W (μm)	ℓ (μm)	ϵ_{re}	Z_{0m}	C_1 (pF) (for $h = 125 \mu\text{m}$)
0.5	42	42	7.68	67.05	0.0014
2.0	82	82	8.08	52.3	0.0029
5.0	130	130	8.44	42.08	0.0049
10.0	182	182	8.75	35.51	0.0068
15.0	223	223	8.95	31.68	0.0084
20.0	258	258	9.13	28.63	0.0101

insulating substrate. Nichrome and tantalum nitride are the most popular and useful film materials for thin film resistors (thickness $0.05 \mu\text{m}$ to $0.2 \mu\text{m}$).

MMICs use both the metal film resistors and active semiconductor layer (e.g., n+ ion implanted) resistors. Typical values for the sheet resistance of thin film (TiWN) and n+ resistors are approximately $9.5 \Omega/\text{sq}$ and $135 \Omega/\text{sq}$, respectively [98]. Thin film resistors may be characterized by microstrip transmission line theory in which the thin film resistor consists of several sections of an ideal resistor in series with transmission line sections as shown in Figure 2.33. The total sum of all the transmission line sections is equal to the length of the thin film resistor.

The number of sections n required to model a resistor accurately is dictated by the L/λ ratio where L is the total length of the resistor and λ is the guide wavelength for the microstrip transmission line at the highest operating frequency. The ideal resistor has a value of $R' = R/n$ where R is the total dc resistance of the resistor. As a general rule of thumb, the number of sections n can be calculated from the relation

$$n = 1 \quad \text{for } L/\lambda \leq 0.02$$

and

$$n \geq 50 \frac{L}{\lambda} \quad \text{for } L/\lambda \geq 0.02 \quad (2.150)$$

2.6.2 Passive Components

Microstrip passive components are fabricated using both hybrid and monolithic microwave integrated circuit techniques. Most commonly used substrate materials are RT Duroid, alumina, and GaAs. Use of a high dielectric constant substrate $\epsilon_r \approx 10$ is highly desirable. However, the substrate thickness is limited by modal

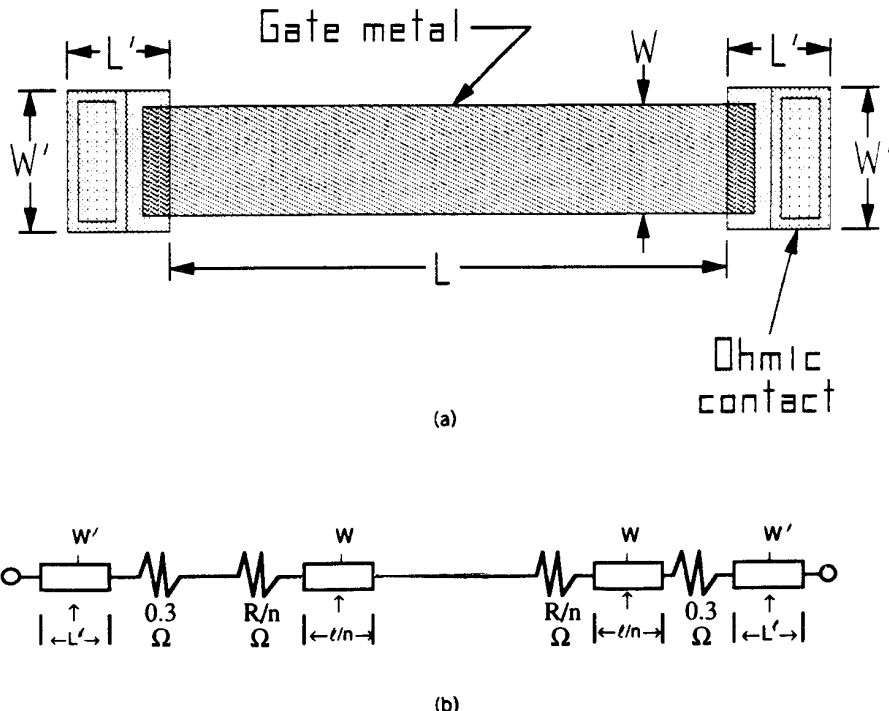


Figure 2.33 (a) A physical layout of the thin film resistor—each end of the resistor has an ohmic contact pad with the shaded section representing the resistor metal—and (b) the distributed model of the thin film resistor consists of a number, n , of microstrip lines and resistors.

problems. High-impedance lines on thin substrates require very narrow conductors, which become lossy, and the fabrication of narrow conductors can be difficult. For low frequencies up to about 4 GHz to 6 GHz for circuits and up to and beyond 20 GHz for microstrip antennas, plastic substrates ($\epsilon_r \approx 2$ to 4) are often used. Alumina (Al_2O_3) is one of the most suitable substrate materials for use up to 20 GHz. The grade of the Al_2O_3 used depends upon the fabrication technology employed: thin or thick film. The dielectric constant of alumina may be high for millimeter-wave circuits because high impedance lines with required tolerances are difficult to fabricate and are lossy. Quartz with a dielectric constant of 4 is more suitable and widely used for high-frequency (>20 GHz) microwave and millimeter-wave integrated circuits. Beryllia is a good conductor of thermal energy and is suitable for power applications where heat dissipation is large and a low thermal resistance substrate is required. GaAs is one of the most suitable substrates for MMICs, since most of the active devices, such as low-noise MESFETs, power MESFETs, and Schot-

thy diodes, are fabricated on a semi-insulating GaAs substrate along with the passive components.

In many microwave filter designs, a length of transmission line terminated in either an open circuit or a short circuit is often used as a resonator. Figure 2.34 illustrates four such resonators with their equivalent LRC networks, which were

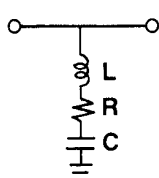
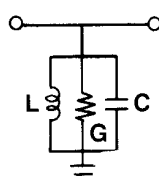
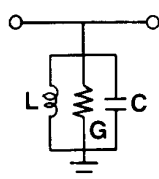
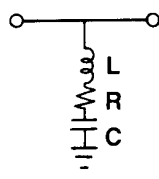
<u>Stub Configuration</u>	<u>Equivalent LRC Network</u>	<u>Element Values</u>
$\lambda/4$ Open Circuited		$\omega_0 L = \frac{\pi}{4} Z_0$ $Z_0 = \frac{4}{\pi} \sqrt{\frac{L}{C}}$ $R = Z_0 \alpha l$ $Q = \frac{\omega_0 L}{R} = \frac{\pi}{4 \alpha l}$ $\omega_0 = \frac{1}{\sqrt{LC}}$
$\lambda/4$ Short Circuited		$\omega_0 C = \frac{\pi}{4} Y_0$ $Z_0 = \frac{\pi}{4} \sqrt{\frac{L}{C}}$ $G = Y_0 \alpha l$ $Q = \frac{\omega_0 C}{G} = \frac{\pi}{4 \alpha l}$
$\lambda/2$ Open Circuited		$\omega_0 C = \frac{\pi}{2} Y_0$ $Z_0 = \frac{\pi}{2} \sqrt{\frac{L}{C}}$ $G = Y_0 \alpha l$ $Q = \frac{\pi}{2 \alpha l}$
$\lambda/2$ Short Circuited		$\omega_0 L = \frac{\pi}{2} Z_0$ $Z_0 = \frac{2}{\pi} \sqrt{\frac{L}{C}}$ $R = Z_0 \alpha l$ $Q = \frac{\pi}{2 \alpha l}$

Figure 2.34 Equivalent circuits for microstrip line resonators.

determined by equating slope parameters for both of these configurations at resonance $\omega = \omega_0$. Figures 2.35, 2.36, and 2.37 show many popular microstrip passive components. The design of such components has been thoroughly discussed in references [96, 99–103]. To predict the performance of microstrip passive components, the effects of junction and layout discontinuities and interaction effects between circuit elements due to close proximity must be included in the circuit analysis.

2.6.3 Active Components

Over the past two decades microwave active circuits have evolved from individual solid-state transistors, diodes, and passive elements housed in conventional waveguides and/or coaxial lines to integrated fully planar assemblies, fabricated using the microstrip medium. A hybrid microwave integrated circuit (MIC) consists of

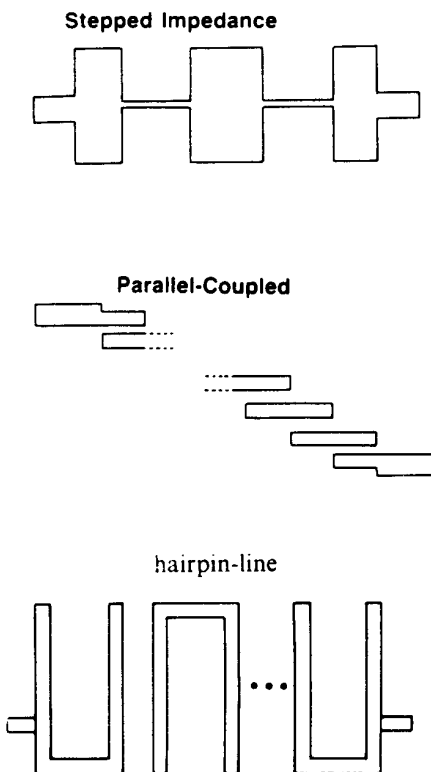


Figure 2.35 Microstrip filter configurations.

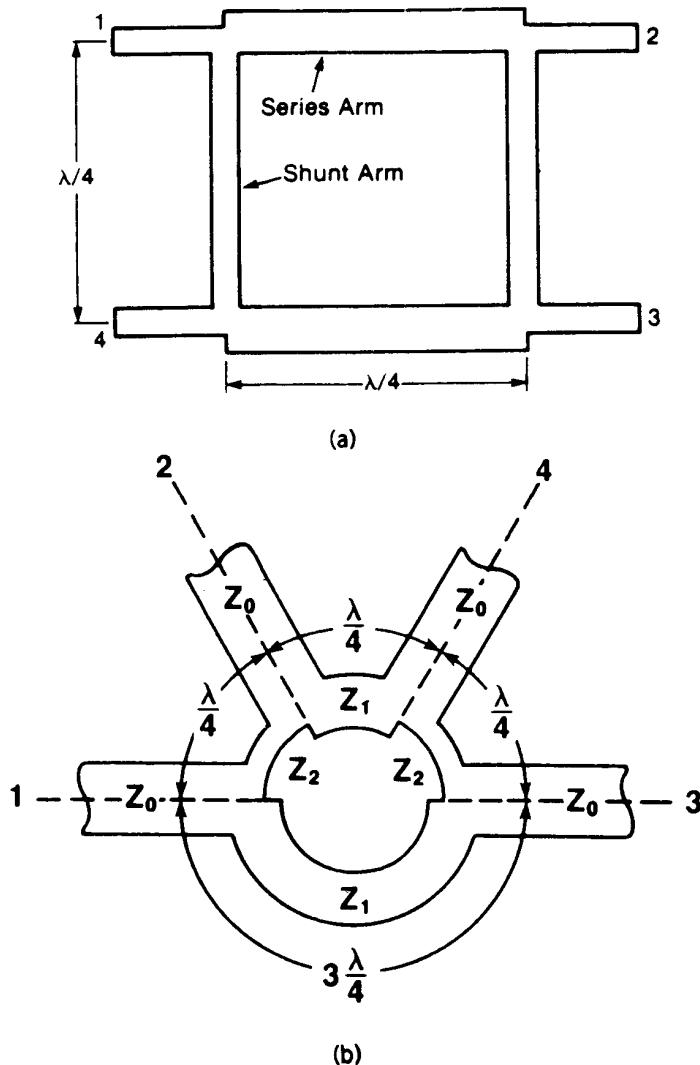


Figure 2.36 Microstrip hybrids: (a) branch line and (b) ring.

a microstrip interconnect pattern and microstrip distributed circuit components printed on a suitable substrate with active and lumped circuit components (in packaged or chip form) attached individually to the printed interconnect circuit by using soldering and wire bonding techniques. Solid-state active elements are either silicon or gallium arsenide (or other III-V compound) devices. More recently,

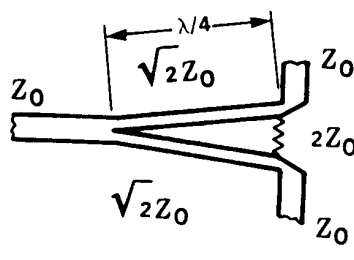
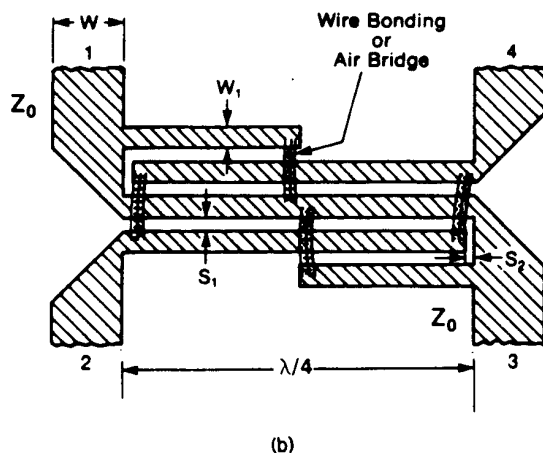
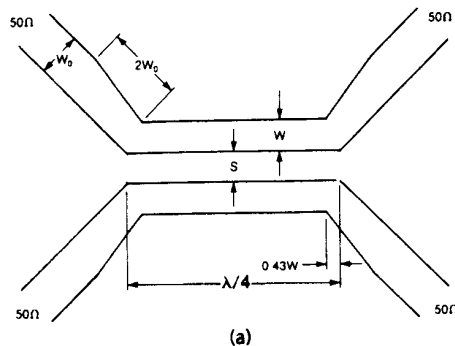


Figure 2.37 Microstrip couplers and combiner: (a) coupled line; (b) Lange coupler; and (c) Wilkinson.

the solid state monolithic microwave integrated circuit (MMIC) approach is becoming commonplace. In MMICs all interconnections and components, both active and passive, are fabricated simultaneously on a semi-insulating semiconductor substrate (usually gallium arsenide (GaAs)) using deposition and etching processes, thereby eliminating discrete components and wire bond interconnects. Microstrip is commonly used for passive components. The term MMIC is used for circuits operating in the microwave (1 GHz to 30 GHz) region of the frequency spectrum as well as the millimeter wave (30 GHz to 300 GHz) region. Major advantages of MMICs include low cost, small size, low weight, circuit design flexibility, broadband performance, elimination of circuit tweaking, high-volume manufacturing capability, package simplification, improved reproducibility, improved reliability, and multi-function performance on a single chip.

Microwave integrated circuits use two types of active devices: two-terminal devices referred to as diodes such as Schottky, Gunn, tunnel, impact avalanche and transit time (IMPATT), varactor, and PIN; and three-terminal devices referred to as transistors such as the bipolar junction transistor (BJT), metal semiconductor field effect transistor (MESFET), high electron mobility transistor (HEMT), and heterojunction bipolar transistor (HBT). Microwave circuits using these devices include amplifiers, oscillators, multipliers, mixers, switches, phase shifters, attenuators, modulators, and many others used for receiver or transmitter applications covering microwave and millimeter-wave frequency bands. The theory and performance of most of these circuits have been well documented [96, 99, 103–110]. Examples of some active circuits using the microstrip medium are shown in Figure 2.38. Solid-state circuits are extensively used in applications such as radar, communication, navigation, electronic warfare (EW), smart weapons, consumer electronics, and microwave instruments.

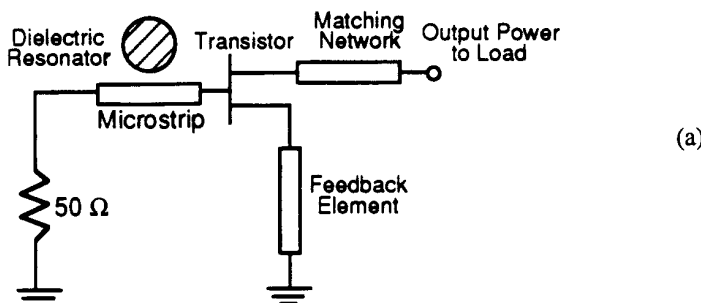


Figure 2.38 (a) Basic configuration of a dielectric resonator oscillator. The feedback element is used to make the active device unstable, the matching network allows the transfer of maximum power to the load, and the dielectric resonator provides frequency stability. (b) Photograph of a 10-W power amplifier using MMIC chips (Courtesy ITT). (c) Balanced microstrip mixer layout.

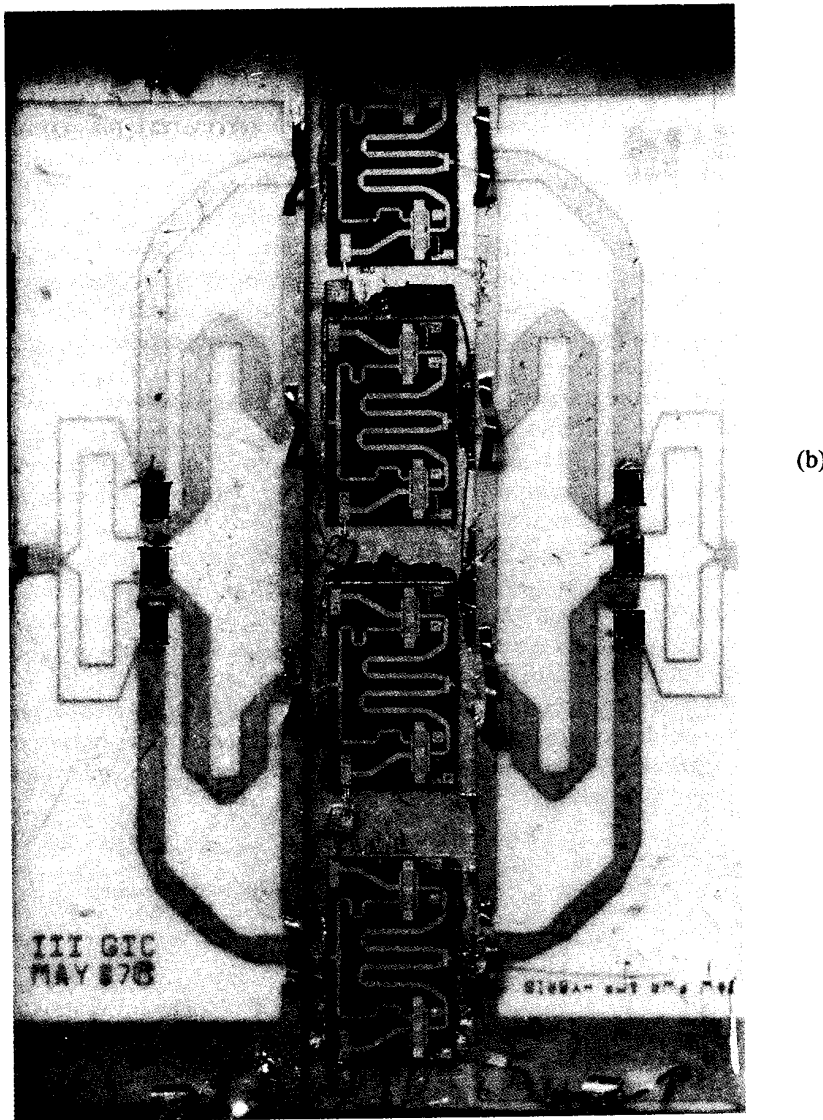


Figure 2.38 (continued).

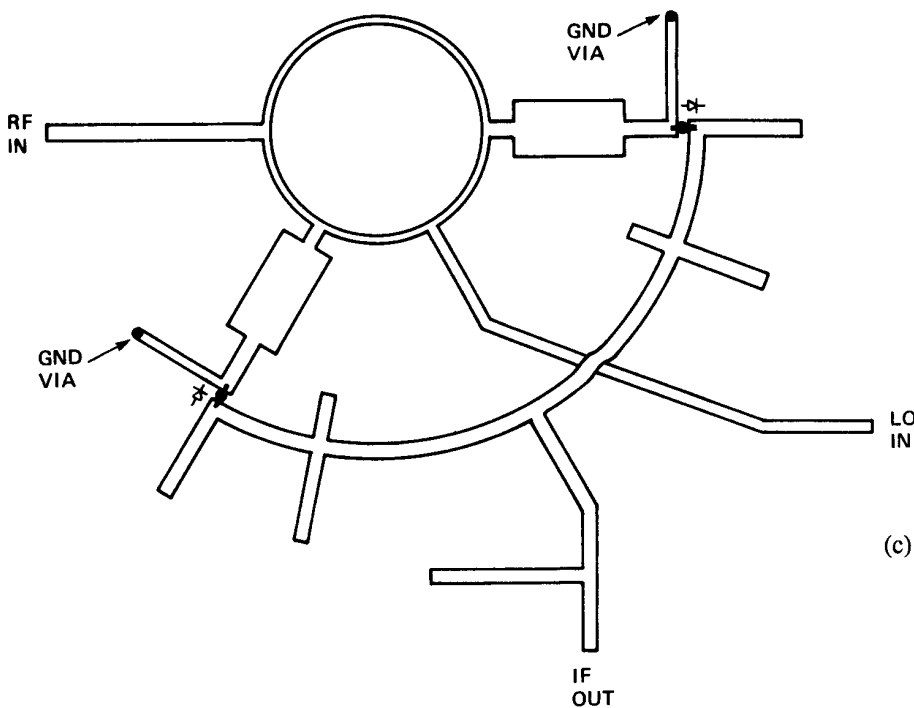


Figure 2.38 (continued).

2.6.4 Packages and Assemblies

Microwave packaging and assembly techniques play a very important role in the performance, cost, and reliability of packaged monolithic microwave integrated circuits. MMIC packages provide the necessary support structure and a protective enclosure without affecting its electrical and thermal characteristics appreciably. The affordability requirements on packages mandate that their complexity be minimized.

The microstrip is the commonly used transmission medium in MICs and MMICs. It also provides excellent layout flexibility. Therefore, in order to provide a good interface between the MMIC and other circuitry in the package or between the MMIC and subsystem, a microstrip line is desired as an interconnect medium in microwave packages. The design of microwave packages has been treated extensively in the literature [111–122]. The most important electrical characteristics of microwave packages are low insertion loss, high return loss and isolation, and no cavity or feedthrough resonance over the operating frequency range. When a chip set is placed in the cavity of a microwave package, there should be minimum

degradation in the chip's performance. Generally this cannot be accomplished without accurate electrical and electromagnetic modeling of the critical package elements. Microwave design principles must be applied to three parts of the package: RF feedthrough, cavity, and dc bias lines. Of the three, the design of the RF feedthrough is the most critical in determining the performance of packaged MMIC chips.

The selection of the substrate material and thickness for packages depends on the electrical performance requirements, cost, and frequency range of interest. The substrate thickness is selected to match its height with MMIC thickness, otherwise a pedestal for mounting MMIC chips is required as MMIC chips are about 4-mil-thick. Microwave packages generally use 10-mil to 20-mil-thick alumina substrate, while millimeter-wave packages use 4-mil to 5-mil-thick quartz. A low dielectric constant is generally preferred because it makes the package interconnects electrically small, more tolerant to variations in microstrip dimensions, broadband, and results in a high yield. The microstrip width and thickness determines the characteristic impedance and the DC resistance, whereas the spacing between the two conductors on the same plane controls the cross talk due to coupling. The coupling magnitude decreases with the increase of separation between two conductors. However, if a ground plane is placed between the two lines as shown in Figure 2.39 the coupling is reduced to an acceptable level. In this case the effect of the ground plane on the characteristics of the microstrip line must be taken into account. Generally, sufficient space between the microstrip circuit, the package walls, and the lid is provided to prevent any interactions. The effect of package lid on the MIC/MMIC characteristics is kept to a minimum by keeping the lid above the MIC/MMIC surface about 5 times the package substrate thickness.

MMIC packaging can be performed at three levels. These are: ICs can be mounted in individual packages; ICs can be packaged with support circuitry in a housing; or ICs can be packaged at the subsystem level. The packaging requirements depend upon the application at hand. However, in compact packages, the

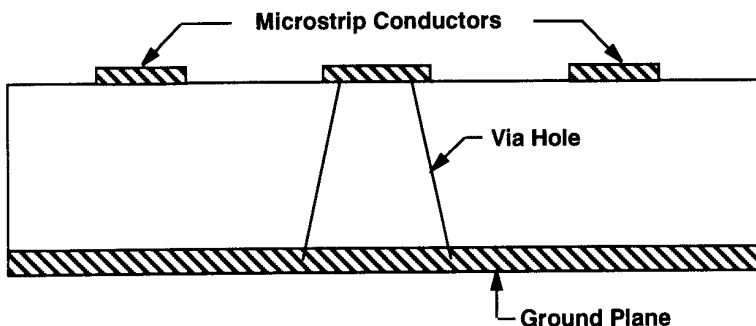


Figure 2.39 A ground plane between two microstrip conductors improves cross talk.

effect of side walls on the circuit performance must be included. The effect of the side wall on the microstrip characteristics can be calculated either from the analysis of the odd-mode propagation in a coupled microstrip line or by using a fullwave analysis method. Table 2.11 lists the relationship of the microstrip line's impedance and effective dielectric constant as a function of the spacing between the package wall and the microstrip line width on a 0.38-mm-thick alumina substrate [78]. Figure 2.40 shows a microstrip line in proximity with the side wall of a package. Figures 2.41 and 2.42 show some of the typical packages used for microstrip circuits.

2.6.5 Superconducting Microstrip Circuits

Most planar transmission lines are lossy (due to high conductor loss) to varying degrees when compared with coaxial lines and waveguides, which precludes their use for the realization of narrow-band filters and low-loss delay lines. The low surface resistance of superconducting materials at microwave frequencies is attractive to

Table 2.11
The Effect of the Package Side Wall on the Characteristic Impedance
and Effective Dielectric Constant of a Microstrip Line
($h = 0.38$ mm, $\epsilon_r = 9.9$)

<i>Distance from Wall, H</i>	<i>W = 1.05 mm</i>		<i>W = 0.38 mm</i>	
	Z_{0m}	ϵ_{re}	Z_{0m}	ϵ_{re}
10h	26.4	7.8	49.6	6.9
3h	26.2	7.7	49.2	6.8
2h	25.9	7.6	48.7	6.7
1h	25.2	7.3	47.1	6.4
0.5h	23.8	6.9	42.9	6.1
0.33h	22.7	6.7	40.1	5.9

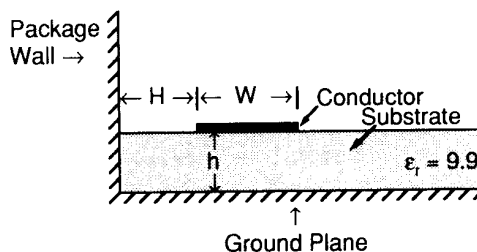


Figure 2.40 A cross-sectional view that shows the relationship of the microstrip line to the package wall and the ground plane.

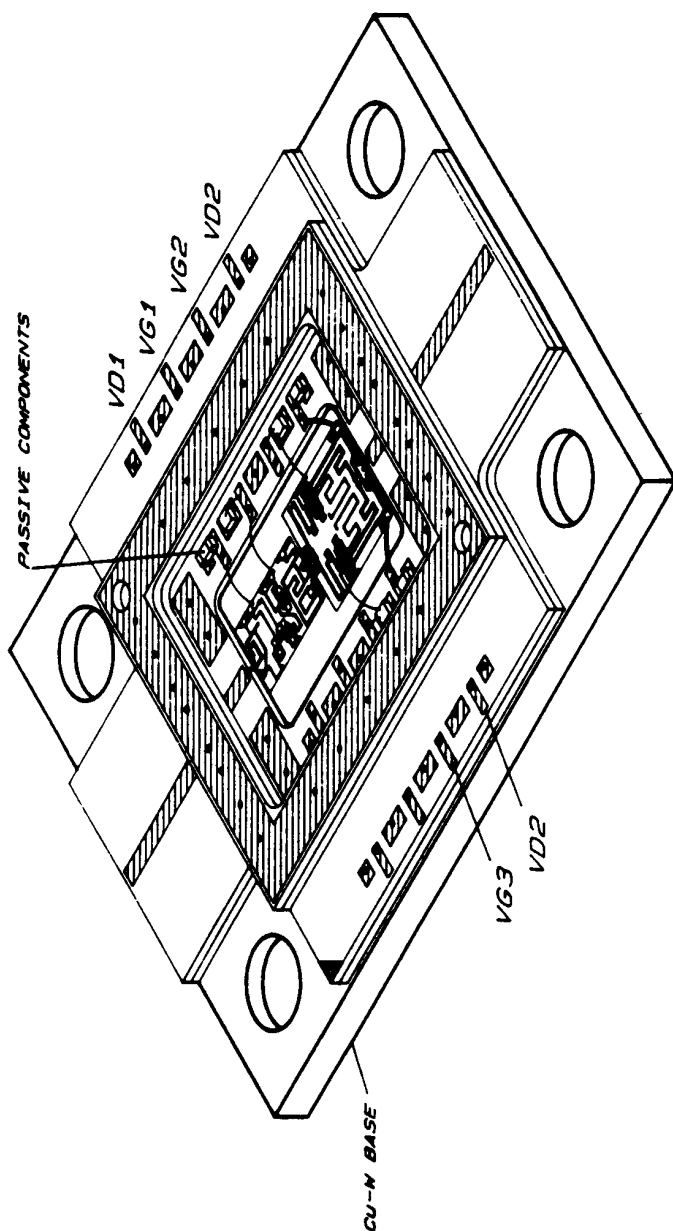


Figure 2.41 Multichip ceramic package.

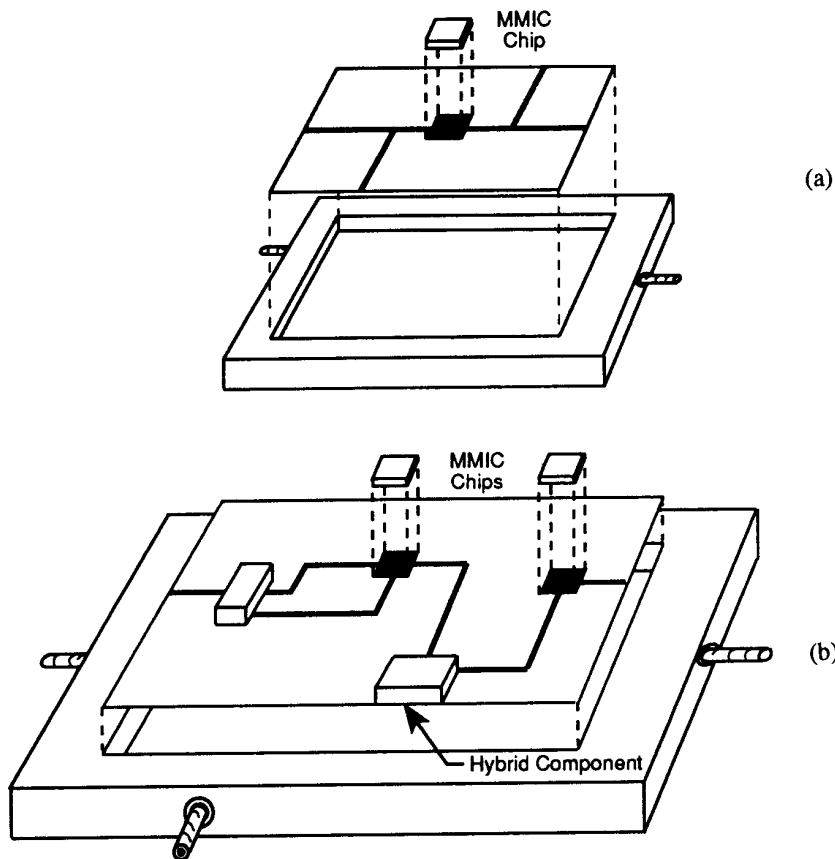


Figure 2.42 Package assemblies: (a) single MMIC chip with support circuitry and (b) MMICs with hybrid circuitry.

realize nearly lossless planar passive components. Materials exhibiting superconducting behavior at temperatures as high as 125K have generated a great deal of interest in microwave circuitry for the realization of low-loss passive components. The high-temperature superconducting materials are referred to as HTS, and the temperature at which the materials exhibit this property is referred to as the transition temperature, T_c , and is commonly measured in Kelvin (K). The growth of good quality HTS films compatible with hybrid and monolithic microwave integrated circuits has made HTS readily usable. Several HTS materials are listed in Table 2.12. Yttrium barium copper oxide (YBCO) has the lowest T_c . In order to maintain stable circuit operation, the material should be selected to have a T_c substantially higher than the operating temperature. The materials shown in Table

Table 2.12
**Material Parameters for High-Temperature
 Superconductors**

Material	$T_c(K)$	$\lambda(\mu m)$
$YBa_2Cu_3O_7$	95	0.150
$Bi_2Sr_2CaCu_2O_8$	85	0.300
$Bi_2Sr_2Ca_2Cu_3O_{10}$	110	
$Tl_2Ba_2CaCu_2O_8$	108	
$Tl_2Ba_2Ca_2Cu_3O_{10}$	125	0.200

Note: Here λ is the zero-temperature penetration depth of the fields into superconductors.

2.12 have a T_c higher than liquid nitrogen (77K) and also have larger energy gaps that make them usable at liquid nitrogen and at high power levels, respectively. HTS films can easily be deposited on low-loss tangent ($\tan \delta \leq 0.0001$ at microwave frequencies) substrates such as sapphire, silica, MgO, lithium nitrate, and lanthanum aluminate ($LaAlO_3$) with good lattice match to realize low-loss HTS microstrip lines. Sapphire is one of the most commonly used materials for depositing HTS films. At room temperature the dielectric constant along its c -optic axis is $\epsilon_{||} = 11.6$ and perpendicular to this axis (z -axis) the dielectric constant is $\epsilon_{\perp} = 9.4$. The planar surface lies in the optic axis called the c -plane. At 77K the values are slightly lower, but for a first-order approximation one can still use these values.

Superconductor Technologies [123, 124] have characterized HTS microstrip using thin films of thallium barium calcium copper oxide ($TlBaCaCuO$) grown on lanthanum aluminate ($LaAlO_3$) substrate. Typical specifications for such substrates are given in Table 2.13. Figure 2.43 shows the surface resistance measured at 10 GHz as a function of temperature. The sample used was 1-cm² and was much thicker than the penetration depth. Figure 2.44 shows the loaded Q of microstrip resonators measured at 5 GHz as a function of input power for 6-mil- and 40-mil-wide microstrip conductors. The loaded Q for HTS microstrip resonators at small power levels are 25 to 100 times more than that for conventional microstrip resonators.

For a superconductor, the conductivity based on a two-fluid theory is given by

$$\sigma = \sigma_1 - j\sigma_2 = \sigma_n \left(\frac{T}{T_c} \right)^4 - j \frac{1 - (T/T_c)^4}{2\pi f \mu_0 \lambda^2} \quad \text{for } T < T_c \quad (2.151)$$

where σ_n is the normal part of the conductivity, f is the operating frequency, μ_0 is the free-space permeability, λ is the penetration depth, T is the temperature, and T_c is the critical temperature of the HTS. The real and imaginary parts of the conductivity correspond to the normal electrons and superconducting electron

Table 2.13
Typical Substrate and HTS Film Specifications

Substrate

TYPE: Lanthanum Aluminate (LaAlO_3)
 DIELECTRIC CONSTANT: 24 typical
 DIELECTRIC LOSS TANGENT: 3×10^{-5} typical
 THICKNESS: $0.010'' \pm 0.0005''$
 $0.020'' \pm 0.0005''$
 DIMENSIONS: $1.00 \text{ cm} \pm 0.01 \text{ cm}$
 $2.00'' \pm 0.0005''$

HTS Film

COMPOSITION: TiBaCaCuO
 THICKNESS: $0.75 \mu\text{m} \pm 0.1 \mu\text{m}$, typical
 PENETRATION DEPTH: $0.3 \mu\text{m}$, typical @ 77 K
 CRITICAL CURRENT: $5 \times 10^5 \text{ A/cm}^2$, typical @ 77 K
 R_s (at 10 GHz): 0.25 mohm, typical @ 77 K
 T_c : 100 K, minimum
 Q_0 (at 5 GHz): 10,000 minimum

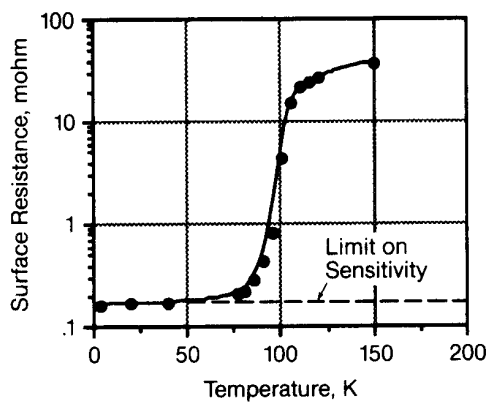


Figure 2.43 R_s versus temperature of TiCaBaCuO HTS measured at 10 GHz (from [124]).

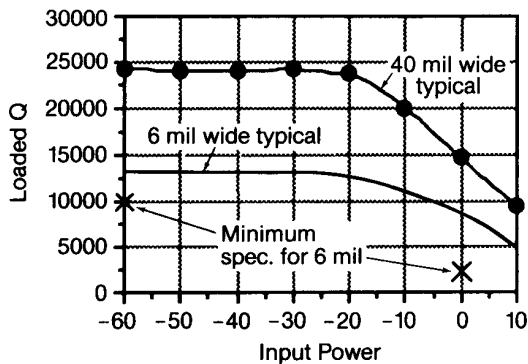


Figure 2.44 Loaded Q of microstrip resonators measured at 5 GHz [124].

pairs, respectively [125]. Using (2.151) one can modify the surface impedance and calculate approximately the microstrip characteristics. The analysis of the superconducting microstrip line has been described in the literature [125–130]. Antsos et al. [125] reported closed-form expressions for the characteristic impedance, effective dielectric constant, and attenuation constant based on quasi-TEM analysis of HTS. Lee et al. [131] described fullwave analysis of HTS microstrip lines on anisotropic substrates using an equivalent surface impedance approach. A superconducting microstrip line with a perfectly conducting ground plane on an anisotropic substrate for which the optic axis is the (x - y)-plane is shown in Figure 2.45. In this case, high-quality $\text{YBa}_2\text{Cu}_3\text{O}_7$ (YBCO) films have been deposited on m -plane sapphire (the angle between the c -plane and the m -plane is 90°). The characteristic impedance, effective dielectric constant, and attenuation constant, calculated using the fullwave

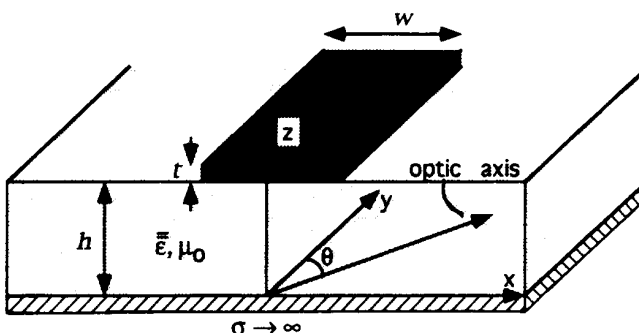


Figure 2.45 Superconducting microstrip line with a perfectly conducting ground plane on an anisotropic substrate.

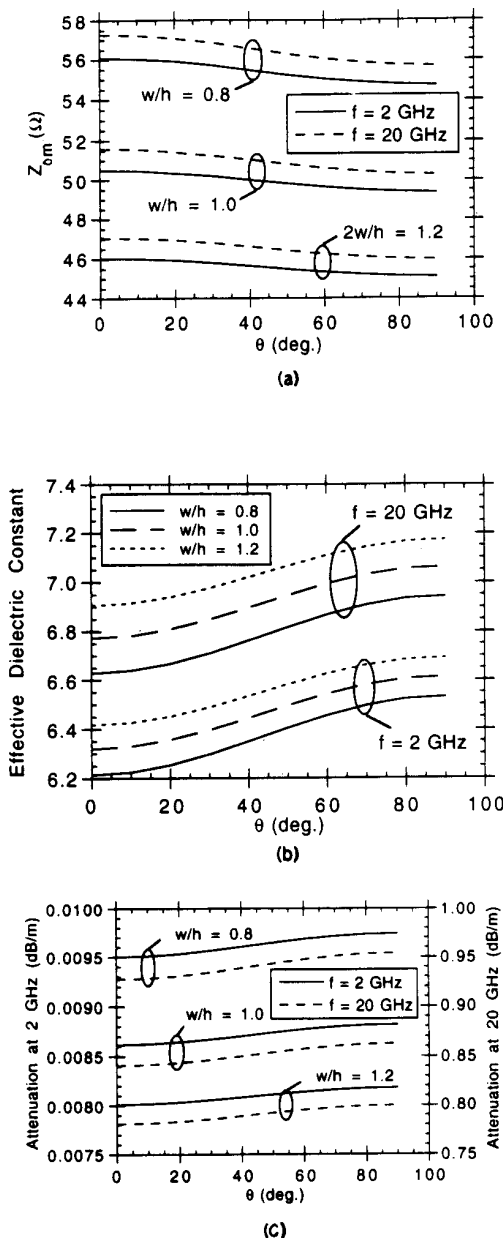


Figure 2.46 Calculated HTS microstrip line characteristics as a function of the rotation angle of the optic axis using the fullwave method: (a) characteristic impedance; (b) effective dielectric constant; and (c) attenuation constant (from [131], © 1993 IEEE. Reprinted with permission.).

method for YBCO microstrip lines on a 430- μm -thick *m*-plane sapphire substrate, are shown in Figure 2.46 as a function of the rotation angle θ of the optic axis. Other parameters used in the calculations are the zero-temperature penetration depth of the fields into the superconductor $\lambda = 0.323 \mu\text{m}$, the real part of conductivity $\sigma = 3.5\text{S}/\mu\text{m}$, conductor thickness $t = 0.4 \mu\text{m}$, transition temperature $T_c = 90\text{K}$, and operating temperature $T = 77\text{K}$. The characteristic impedance and effective dielectric constant values shown in Figure 2.46 for an HTS microstrip are very close to the conventional microstrip results on a sapphire substrate. Thus approximate expressions for the microstrip on an anisotropic substrate in Section 2.4.4 may be used to calculate HTS microstrip characteristics.

Microwave circuits including filters, delay lines, resonators, dividers, combiners, and Lange couplers have been developed using an HTS microstrip [123, 132–140]. Specific applications of HTS microstrip lines include narrow-band filters, low-loss delay lines, high Q resonators, and a low-loss receiver front end consisting of a microstrip antenna, a low-noise amplifier, and a mixer for improved sensitivity.

References

- [1] Denlinger, E. J., "A Frequency Dependent Solution for Microstrip Transmission Lines," *IEEE Trans.*, Vol. MTT-19, 1971, pp. 30–39.
- [2] Itoh, T., and R. Mittra, "Spectral-Domain Approach for Calculating Dispersion Characteristics of Microstrip Lines," *IEEE Trans.*, Vol. MTT-21, 1973, pp. 496–498.
- [3] Knorr, J. B., and A. Tufekcioglu, "Spectral-Domain Calculation of Microstrip Characteristics Impedance," *IEEE Trans.*, Vol. MTT-23, 1975, pp. 725–728.
- [4] Itoh, T., "Spectral Domain Approach for Dispersion Characteristics of Generalized Printed Transmission Lines," *IEEE Trans.*, Vol. MTT-28, No. 7, July 1980, pp. 733–736.
- [5] Uwano, T., and T. Itoh, "Spectral Domain Analysis," *Numerical Techniques in Microwaves and Millimeterwave Passive Structures* (ed. T. Itoh) New York: John Wiley and Sons, 1989, pp. 334–380.
- [6] Zysman, G. I., and D. Varon, "Wave Propagation in Microstrip Transmission Lines," *IEEE G-MTT Int. Microwave Symp. Digest*, 1969, pp. 2–9.
- [7] Hornsby, J. S., and A. Gopinath, "Fourier Analysis of a Dielectric-Loaded Waveguide with a Microstrip," *Electron. Lett.*, Vol. 5, 1969, pp. 265–267.
- [8] Mittra, R., and T. Itoh, "A New Technique for the Analysis of the Dispersion Characteristics of Microstrip Lines," *IEEE Trans.*, Vol. MTT-19, 1971, pp. 47–56.
- [9] Lewin, L., "The Use of Singular Integral Equations in the Solution of Waveguide Problems," *Advances in Microwaves*, Vol. 1, (ed. L. Young), New York: Academic Press, 1966, pp. 211–284.
- [10] Itoh, T., and R. Mittra, "A Technique for Computing Dispersion Characteristics of Shielded Microstrip Lines," *IEEE Trans.*, Vol. MTT-22, 1974, pp. 896–898.
- [11] Hornsby, J. S., and A. Gopinath, "Numerical Analysis of a Dielectric Loaded Waveguide with a Microstrip Line—Finite Difference Methods," *IEEE Trans.*, Vol. MTT-17, 1969, pp. 684–690.
- [12] Corr, D. G., and J. B. Davies, "Computer Analysis of the Fundamental and Higher Order Modes in Single and Coupled Microstrip," *IEEE Trans.*, Vol. MTT-20, 1972, pp. 669–678.
- [13] Martin, R. S., and J. H. Wilkinson, "Reduction of the Symmetric Eigenproblem $Ax = \lambda Bx$ and Related Problems to Standard Form," *Numer. Math.*, Vol. 11, 1968, pp. 99–110.
- [14] Berk, A. D., "Variational Principles for Electromagnetic Resonators and Waveguides," *IRE Trans.*, Vol. AP-4, 1956, pp. 104–111.
- [15] Schwartz, H. R., "Tridiagonalization of a Symmetric Band Matrix," *Numer. Math.*, Vol. 12, 1968, pp. 231–241.

- [16] Barth, W., et al., "Calculation of the Eigenvalues of a Symmetric Tridiagonal Matrix by the Method of Bisection," *Numer. Math.*, Vol. 9, 1967, pp. 336–393.
- [17] Wilkinson, J. H., "Calculation of the Eigenvectors of a Symmetric Tridiagonal Matrix by Inverse Iteration," *Numer. Math.*, Vol. 4, 1962, pp. 368–376.
- [18] Pucel, R. A., et al., "Losses in Microstrip," *IEEE Trans.*, Vol. MTT-16, 1968, pp. 342–350. Correction in *IEEE Trans.*, Vol. MTT-16, 1968, p. 1064.
- [19] Schneider, M. V., "Microstrip Lines for Microwave Integrated Circuits," *Bell System Technical Journal*, Vol. 48, 1969, pp. 1422–1444.
- [20] Wheeler, H. A., "Formulas for the Skin Effect," *Proc. IRE*, Vol. 30, 1942, pp. 412–424.
- [21] Welch, J. D., and H. J. Pratt, "Losses in Microstrip Transmission Systems for Integrated Microwave Circuits," *NEREM Rec.*, Vol. 8, 1966, pp. 100–101.
- [22] Horton, R., et al., "Variation of Microstrip Losses with Thickness of Strip," *Electron. Lett.*, Vol. 7, 1971, p. 490.
- [23] Garg, R., et al., "Optimum Thickness of Metal in Waveguiding Structures, Ground Planes and Reflectors," *Int. J. Electron.*, Vol. 39, 1975, pp. 525–527.
- [24] Schneider, M. V., "Dielectric Loss in Integrated Microwave Circuits," *Bell System Technical Journal*, Vol. 48, 1969, pp. 2325–2332.
- [25] Simpson, T. L., and B. Tseng, "Dielectric Loss in Microstrip Lines," *IEEE Trans.*, Vol. MTT-24, 1976, pp. 106–108.
- [26] Bahl, I. J., and D. K. Trivedi, "A Designer's Guide to Microstrip Line," *Microwaves*, Vol. 16, May 1977, pp. 174–182.
- [27] Van Heuven, J., "Properties of Microstrip Lines on Fused Quartz," *IEEE Trans.*, Vol. MTT-18, 1970, pp. 113–114.
- [28] Bahl, I. J., and K. C. Gupta, "Average Power Handling Capability of Microstrip Lines," *IEE Journal on Microwaves, Optics and Acoustics*, January 1979, pp. 1–4.
- [29] Owens, R. P., "Predicted Frequency Dependence of Microstrip Characteristic Impedance Using the Planar-Waveguide Model," *Electron. Lett.*, Vol. 12, 1976, pp. 269–270.
- [30] Bianco, B., et al., "Frequency Dependence of Microstrip Parameters," *Alta Freq.*, Vol. 43, 1974, pp. 413–416.
- [31] Bahl, I. J., and R. Garg, "Simple and Accurate Formulas for Microstrip with Finite Strip Thickness," *Proc. IEEE*, Vol. 65, 1977, pp. 1611–1612.
- [32] Frey, J., "Hybrid and Monolithic Microwave Integrated Circuits," *Microwave Integrated Circuits*, (ed. J. Frey), Dedham, MA: Artech House, 1975, pp. xvii–xxi.
- [33] Heckl, H., and O. Schweiger, "Evaluation and Space Qualification of MIC on Alumina and Glass Fiber Reinforced Teflon Substrates," ESA session on "Space Qualified MIC" at *6th European Microwave Conf.*, 1976, Rome.
- [34] Howe, Jr., H., "Stripline is Alive and Well—," *Microwave J.*, Vol. 14, July 1971, p. 25.
- [35] Garg R., "The Effect of Tolerances on Microstrip Line and Slotline Performance," *IEEE Trans.*, Vol. MTT-26, 1978, pp. 16–19.
- [36] Owens, R. P., et al., "Quasi-static Characteristics of Microstrips on an Anisotropic Sapphire Substrate," *IEEE Trans.*, Vol. MTT-24, 1976, pp. 499–505.
- [37] Szentkuti, B. T., "Simple Analysis of Anisotropic Microstrip Lines by a Transform Method," *Electron. Lett.*, Vol. 12, 1976, pp. 672–673.
- [38] Wheeler, H. A., "Transmission Line Properties of Parallel Strips Separated by a Dielectric Sheet," *IEEE Trans.*, Vol. MTT-13, 1965, pp. 172–185; "Transmission Line Properties of a Strip on a Dielectric Sheet on a Plane," *IEEE Trans.*, Vol. MTT-25, 1977, pp. 631–647.
- [39] Hammerstad, E. O., "Equations for Microstrip Circuit Design," *Proc. European Microwave Conf.*, 1975, pp. 268–272.
- [40] Hammerstad, E. O., Private communication.
- [41] Hammerstad, E., and O. Jensen, "Accurate Models for Microstrip Computer-Aided Design," *IEEE MTT-S Int. Microwave Symp. Dig.*, 1980, pp. 407–409.

- [42] Gunston, M. A. R., and J. R. Weale, "Variation of Microstrip Impedances with Strip Thickness," *Electron. Lett.*, Vol. 5, 1969, pp. 697–698.
- [43] Kaupp, H. P., "Characteristics of Microstrip Transmission Lines," *IEEE Trans.*, Vol. EC-16, 1967, pp. 185–193.
- [44] Schwarzmüller, A., "Microstrip Plus Equations Add Up to Fast Designs," *Electronics*, Vol. 40, October 1967, pp. 109–112.
- [45] John, S., and P. Arlett, "Simple Method for the Calculation of the Characteristic Impedance of Microstrip," *Electron. Lett.*, Vol. 10, 1974, pp. 188–190.
- [46] Kumar, A., et al., "A Method for the Calculation of the Characteristic Impedance of Microstrip," *Int. J. Electron.*, Vol. 40, 1976, pp. 45–47.
- [47] Ross, R. F. G., and M. J. Howes, "Simple Formulas for Microstrip Lines," *Electron. Lett.*, Vol. 12, 1976, p. 410.
- [48] Gunston, M. A. R., and J. R. Weale, "The Transmission Characteristics of Microstrip," *The Marconi Review*, 1969, pp. 226–244.
- [49] Gunston, M. A. R., *Microwave Transmission-line Impedance Data*, London: Van Nostrand, 1972, p. 48.
- [50] Yamashita, E., and R. Mittra, "Variation Method for the Analysis of Microstrip Lines," *IEEE Trans.*, Vol. MTT-16, 1968, pp. 251–256.
- [51] Stinehelfer, H. E., "An Accurate Calculation of Uniform Microstrip Transmission Lines," *IEEE Trans.*, Vol. MTT-16, 1968, pp. 439–444.
- [52] Kowalski, G., and R. Pregla, "Dispersion Characteristics of Shielded Microstrips with Finite Thickness," *Arch. Elekt. Übertr.*, Vol. 25, 1971, pp. 193–196.
- [53] Pregla, R., and S. Nokes, "Calculation of the Capacitance of Thick Microstrip Using a Variational Expression," *Arch. Elekt. Übertr.*, Vol. 29, 1975, pp. 125–128.
- [54] Silvester, P., "TEM Wave Properties of Microstrip Transmission Lines," *Proc. IEEE*, Vol. 115, 1968, pp. 43–48.
- [55] Yamashita, E., "Variation Method for the Analysis of Microstrip Line Transmission Lines," *IEEE Trans.*, Vol. MTT-16, 1968, pp. 529–539.
- [56] Bahl, I. J., "Easy and Exact Methods for Shielded Microstrip Design" *Microwaves*, Vol. 17, December 1978, pp. 61–62.
- [57] March, S. L., "Empirical Formulas for the Impedance and Effective Dielectric Constant of Covered Microstrip for Use in the Computer-Aided Design of Microwave Integrated Circuits," *Proc. European Microwave Conf.*, Microwave Exhibitors & Publishers Ltd., Kent, United Kingdom, 1981, pp. 671–676.
- [58] Gish, D. L., and O. Graham, "Characteristic Impedance and Phase Velocity of a Dielectric Supported Air Strip Transmission Line with Side Walls," *IEEE Trans.*, Vol. MTT-18, 1970, pp. 131–148.
- [59] Getsinger, W. J., "Microstrip Dispersion Model," *IEEE Trans.*, Vol. MTT-21, 1973, pp. 34–39.
- [60] Edwards, T. C., and R. P. Owens, "2-18 GHz Dispersion Measurements on 10-100 ohm Microstrip Line on Sapphire," *IEEE Trans.*, Vol. MTT-24, 1976, pp. 506–513.
- [61] Kirschning, M., and R. H. Jansen, "Accurate Model for Effective Dielectric Constant of Microstrip and Validity up to Millimeter-wave Frequencies," *Electron. Lett.*, Vol. 25, 18 March 1982, pp. 272–273.
- [62] Kobayashi, M., "A Dispersion Formula Satisfying Recent Requirements in Microstrip CAD," *IEEE Trans.*, Vol. MTT-36, August 1988, pp. 1246–1250.
- [63] Krage, M. K., and G. I. Haddad, "Frequency Dependent Characteristics of Microstrip Transmission Lines," *IEEE Trans.*, Vol. MTT-20, 1972, pp. 678–688.
- [64] Denlinger, E. J., "Losses in Microstrip Lines," *IEEE Trans. on Microwave Theory Tech.*, Vol. MTT-28, June 1980, pp. 513–522.
- [65] Lee, H. Y., and T. Itoh, "Wideband Conductor Loss Calculation of Planar Quasi-TEM Transmission Lines with Thin Conductors Using Phenomenological Loss Equivalence Method," *IEEE MTT-S Int. Microwave Symp. Digest*, 1989, pp. 367–370.

- [66] Faraji-Dana, R., and Y. Chow, "Edge Condition of the Field and A.C. Resistance of a Rectangular Strip Conductor," *IEE Proc.*, Vol. 137, Pt. H., April 1990, pp. 133–140.
- [67] Faraji-Dana, R., and Y. Chow, "The Current Distribution and AC Resistance of a Microstrip Structure," *IEEE Trans.*, Vol. MTT-38, September 1990, pp. 1268–1277.
- [68] Aksun, M. I., and H. Morkoc, "GaAs on Si as Substrate for Microwave and Millimeter-Wave Monolithic Integration," *IEEE Trans.*, Vol. MTT-36, January 1988, pp. 160–162.
- [69] Belohoubek, E., and E. J. Denlinger, "Loss Considerations for Microstrip Resonators," *IEEE Trans.*, Vol. MTT-23, 1975, pp. 522–526.
- [70] Denlinger, E., "Radiation from Microstrip Resonators," *IEEE Trans.*, Vol. MTT-16, 1969, pp. 235–236.
- [71] Garg, Ramesh, "A Microstrip Design Guide," *Int. J. Electron.*, Vol. 46, 1979, pp. 187–192.
- [72] Vendelin, G. D., "Limitations on Stripline Q," *Microwave J.*, Vol. 13, May 1970, pp. 63–69.
- [73] Pramanick, P., and P. Bhartia, "CAD Models for Millimeter-wave Finlines and Suspended-Substrate Microstrip Lines," *IEEE Trans.*, Vol. MTT-33, December 1985, pp. 1429–1435.
- [74] Buntschuh, C., "High Directivity Microstrip Couplers Using Dielectric Overlays," *IEEE G-MTT Symp. Digest*, 1975.
- [75] Houpt, G., and H. Delys, "High Directivity Microstrip Directional Couplers," *Electron. Lett.*, Vol. 10, May 2, 1974, pp. 142–143.
- [76] Izadian, J. S., "A New 6–18 GHz, -3 dB Multisection Hybrid Coupler Using Asymmetric Broadside, and Edge Coupled Lines," *IEEE MTT-S Int. Microwave Symp. Digest*, 1989, pp. 243–247.
- [77] Nakajima, M. and E. Yamashita, "A Quasi-TEM Design Method for 3 dB Hybrid Couplers Using a Semi-Reentrant Coupling Section," *IEEE Trans.*, Vol. MTT-38, November 1990, pp. 1731–1736.
- [78] Willems, D., and I. Bahl, "A MMIC Compatible Tightly Coupled Line Structure Using Embedded Microstrip," *IEEE Trans.*, Vol. MTT-41, December 1993, pp. 2303–2310.
- [79] Quian, Y., and E. Yamashita, "Low-Distortion and Low-Crosstalk Characteristics of Picosecond Pulses in a Dual-Plane Coupled Microstrip Lines Structure," *IEEE Microwave and Guided Wave Letters*, Vol. 3, August 1993, pp. 273–275.
- [80] Yamashita, E., "Variational Method for the Analysis of Microstrip Like Transmission Lines," *IEEE Trans.*, Vol. MTT-16, August 1968, pp. 529–535.
- [81] Yamashita, E., and R. Mittra, "Variational Method for the Analysis of Transmission Lines," *IEEE Trans.*, Vol. MTT-16, April 1968, pp. 251–256.
- [82] Bahl, I. J., and S. S. Stuchly, "Analysis of Microstrip Covered with Lossy Dielectric," *IEEE Trans. on Microwave Theory Tech.*, Vol. MTT-28, February 1980, pp. 104–109.
- [83] Das, N. K., and D. M. Pozar, "Generalized Spectral Domain Green's Function for Multilayer Dielectric Substrates with Applications to Multilayer Transmission Lines," *IEEE Trans.*, Vol. MTT-35, March 1987, pp. 326–335.
- [84] Finlay, H. J., et al., "Accurate Characterization and Modeling of Transmission Lines for GaAs MMICs," *IEEE Trans.*, Vol. MTT-36, June 1988, pp. 961–967.
- [85] Hiraoka, T., T. Tokumitsu, and M. Akaike, "Very Small Wide-band MMIC Magic-Ts Using Microstrip Lines on a Thin Dielectric Film," *IEEE Trans.*, Vol. MTT-37, October 1989, pp. 1569–1575.
- [86] Tokumitsu, T., et al., "Multilayer MMIC Using a 3 μm \times 3-layer Dielectric Film Structure," *IEEE MTT-S Int. Microwave Symp. Digest*, 1990, pp. 831–834.
- [87] Gillick, M., and I. D. Robertson, "An X-band Monolithic Power Amplifier Using Low Characteristic Impedance Thin-Film Microstrip Transformers," *IEEE Microwave and Guided Wave Lett.*, August 1992, pp. 328–330.
- [88] Gillick, M., and I. D. Robertson, "Ultra Low Impedance CPW Transmission Lines for Multilayer MMICs," *IEEE Microwave and Millimeter-wave Monolithic Circuits Symp. Digest*, 1993, pp. 127–130.
- [89] Banba, S., and H. Ogawa, "Small-Sized MMIC Amplifiers Using Thin Dielectric Layers," *IEEE Trans. on Microwave Theory Tech.*, Vol. 43, March 1995, pp. 485–492.
- [90] Ogawa, H., et al., "MMIC Transmission Lines for Multi-Layered MMICs," *IEEE MTT-S Int. Microwave Symp. Digest*, 1991, pp. 1067–1070.

- [91] Hasegawa, T., et al., "Characteristics of Valley Microstrip Lines for Use in Multilayer MMICs," *IEEE Microwave and Guided Wave Lett.*, Vol. 1, October 1991, pp. 275–277.
- [92] Hasegawa, T., S. Banda, and H. Ogawa, "A Branchline Hybrid Using Valley Microstrip Lines," *IEEE Microwave and Guided Wave Lett.*, Vol. 2, February 1992, pp. 76–78.
- [93] Rong, A. S., and Z. L. Sun, "A Novel Quasi-TEM Analysis of Valley Microstrip Lines with Slit for Use in Multilayered MMICs," *IEEE MTT-S Int. Microwave Symp. Digest*, Vol. 2, 1993, pp. 955–958.
- [94] Rong, A. S., and Z. L. Sun, "Packaging and Metallization Effects of Valley Microstrip Line with Slit for Use in Very Small Multilayer MMICs," *IEEE MTT-S Int. Microwave Symp. Digest*, 1994, pp. 1723–1726.
- [95] Alley, G. D., "Interdigital Capacitors and Their Application to Lumped-Element Microwave Integrated Circuits," *IEEE Trans.*, Vol. MTT-18, 1970, pp. 1028–1033.
- [96] Bahl, I. J., and P. Bhartia, *Microwave Solid State Circuit Design*, New York: John Wiley, 1988.
- [97] Pettenpaul, E., et al., "CAD Models of Lumped Elements on GaAs Up to 18 GHz," *IEEE Trans.*, Vol. MTT-36, February 1988, pp. 294–304.
- [98] Sadhir, V. K., I. J. Bahl, and D. A. Willems, "CAD Compatible Accurate Models of Microwave Passive Lumped Elements for MMIC Applications," *Int. J. Microwave and Millimeter-Wave Computer-Aided Engineering*, Vol. 4, April 1994, pp. 148–162.
- [99] Bhartia, P., and I. J. Bahl, *Millimeter Wave Engineering and Applications*, New York: John Wiley, 1984.
- [100] Rizzi, P. A., *Microwave Engineering Passive Circuits*, Englewood Cliffs, NJ: Prentice Hall, 1988.
- [101] Chang, K. (ed.), *Handbook of Microwave and Optical Components*, Vol. 1, New York: John Wiley, 1989.
- [102] Pozar, D. M., *Microwave Engineering*, Reading, PA: Addison-Wesley, 1990.
- [103] Chang, K., *Microwave Solid-State Circuits and Applications*, New York: John Wiley & Sons, 1994.
- [104] Kollberg, E. L. (ed.), *Microwave and Millimeter-Wave Mixers*, New York: IEEE Press, 1984.
- [105] Pucel, R. A. (ed.), *Monolithic Microwave Integrated Circuits*, New York: IEEE Press, 1985.
- [106] Goyal, R. (ed.), *Monolithic Microwave Integrated Circuits: Technology and Design*, Norwood, MA: Artech House, 1989.
- [107] Chang, K. (ed.), *Handbook of Microwave and Optical Components*, Vol. 2, New York: John Wiley, 1990.
- [108] Vendelin, G. D., A. M. Pavio, and U. L. Rohde, *Microwave Circuit Design Using Linear and Nonlinear Techniques*, New York: John Wiley, 1990.
- [109] Ali, F., and A. Gupta (eds.), *HEMTs and HBTs: Devices, Fabrication and Circuits*, Norwood, MA: Artech House, 1991.
- [110] Bahl, I. J., "Solid State Circuits," in *The Electrical Engineering Handbook* (R. C. Dorf, Editor-in-Chief), Boca Raton, FL: CRC Press, 1993.
- [111] Pengelly, R., and P. Schumacher, "High-Performance 20 GHz Package for GaAs MMICs," *MSN & Comm. Tech.*, Vol. 18, January 1988, pp. 10–19.
- [112] Ishitsuka, F., and N. Sato, "Low-cost, High Performance Package for a Multi-Chip MMICs Module," *IEEE IC Symp. Digest*, 1988, pp. 221–224.
- [113] Berson, B., "Strategies for Microwave and Millimeter Wave Packaging Today," *19th European Microwave Conf. Proc.*, 1989, pp. 89–95.
- [114] Tomimuro, H., et al., "A New Packaging Technology for GaAs MMICs Modules," *IEEE GaAs IC Symp. Dig.*, 1989, pp. 307–310.
- [115] Berson, B., F. Rosenbaum, and R. A. Sparks, "MMIC Packaging," *Monolithic Microwave Integrated Circuits* (ed. R. Goyal), Norwood, MA: Artech House, 1989.
- [116] Tummala, R. R., and E. J. Rayaszewski (Eds.), *Microelectronic Packaging Handbook*, New York: Van Nostrand Reinhold, 1989.
- [117] Chai, S., et al., "Low-Cost Package Technology for Advanced MMIC Applications," *IEEE Int. Microwave Symp. Digest*, 1990, pp. 625–628.
- [118] Shih, Y. C., et al., "A High Performance Quartz Package for Millimeter Wave Applications," *IEEE Int. Microwave Symp. Digest*, 1991, pp. 1063–1066.

- [119] Smith, S. R., and M. T. Murphy, "Electrical Characterization of Packages for Use with GaAs MMIC Amplifiers," *IEEE MTT-S Int. Microwave Symp. Digest*, 1993, pp. 131–134.
- [120] Ndagijimana, F., et al., "The Inductive Connection Effects of a Mounted SPDT in a Plastic S08 Package," *IEEE MTT-S Int. Microwave Symp. Digest*, 1993, pp. 91–94.
- [121] Wein, D., et al., "Microwave and Millimeter-Wave Packaging and Interconnection Methods for Single and Multiple Chip Modules," *IEEE GaAs IC Symp. Digest*, 1993, pp. 333–336.
- [122] Strauss, G., and W. Menzel, "A Novel Concept for mm-Wave Interconnects and Packaging," *IEEE MTT-S Int. Microwave Symp. Digest*, 1994, pp. 1141–1144.
- [123] Madden, J., and N. Fenzi, "HTS Filters and Delay Lines Suit EW Systems," *Microwaves & RF*, Vol. 33, May 1994, pp. 79–84.
- [124] Superconductor Technologies Data Sheet, 460 Ward Dr., Santa Barbara, CA, 1994.
- [125] Antsos, D., et al., "Modeling of Planar Quasi-TEM Superconducting Transmission Lines," *IEEE Trans.*, Vol. MTT-40, June 1992, pp. 1128–1132.
- [126] Lee, H. Y., and T. Itoh, "Phenomenological Loss Equivalence Method for Planar Quasi-TEM Transmission Lines with a Thin Normal Conductor or Superconductor," *IEEE Trans.*, Vol. MTT-37, December 1989, pp. 1904–1909.
- [127] Ekholm, E. B., and S. W. McKnight, "Attenuation and Dispersion for High-Tc Superconducting Microstrip Lines," *IEEE Trans.*, Vol. MTT-38, April 1990, pp. 387–395.
- [128] van Deventer, T. E., et al., "High Frequency Characterization of High-Temperature Superconducting Thin Film Lines," *IEEE MTT-S Int. Microwave Symp. Digest*, 1990, pp. 285–288.
- [129] Vendik, I. B., et al., "A CAD Model for Microstrips on r-cut Sapphire Substrates," *Int. J. Microwave and Millimeter-Wave Computer-Aided Engineering*, Vol. 4, October 1994, pp. 274–383.
- [130] Vendik, O., and E. Kollberg, "Software Models HTSC Microstrip and Coplanar Lines," *Microwaves & RF*, Vol. 32, July 1993, pp. 118–120.
- [131] Lee, L. H., et al., "Full-Wave Analysis of Superconducting Microstrip Lines on Anisotropic Substrates Using Equivalent Surface Impedance Approach," *IEEE Trans.*, Vol. MTT-41, December 1993, pp. 2359–2367.
- [132] Bybokas, J., and B. Hammond, "High Temperature Superconductors," *Microwave J.*, Vol. 23, February 1990, pp. 127–138.
- [133] Williams, J. T., and S. A. Long, "High Temperature Superconductors and Their Application in Passive Antenna System," *IEEE Antenna Propagation Mag.*, August 1990, pp. 7–18.
- [134] Agarwal, K. K., "Superconductors and MMICs in Microwave Systems," *Appl. Microwave*, Vol. 4, Spring 1992, pp. 72–81.
- [135] Hammond, R. B., G. L. Hey-Shipton, and G. L. Matthaei, "Designing with Superconductors," *IEEE Spectrum*, April 1993, pp. 34–39.
- [136] Delin, K. A., and T. P. Orlando, "Superconductivity," *The Electrical Engineering Handbook* (R. C. Dorf, Editor-in-Chief), Boca Raton, FL: CRC Press, 1993.
- [137] Shen, Z. Y., et al., "High-Temperature Superconductor/II-V Hybrid Microwave Circuits," *Microwave Opt. Tech Letts.*, Vol. 6, October 1993, pp. 732–736.
- [138] Liang, G. C., et al., "High-Power HTS Microstrip Filters for Wireless Communication," *IEEE MTT-S Int. Microwave Symp. Digest*, 1994, pp. 183–186.
- [139] Shen, Z. Y., *High-Temperature Superconducting Microwave Circuits*, Norwood, MA: Artech House, 1994.
- [140] Madden, J., "Microwave HTS Application Notes," Superconductor Technologies, Santa Barbara, CA, 1994.

CHAPTER 3

Microstrip Discontinuities I: Quasi-Static Analysis and Characterization

3.1 INTRODUCTION

Microstrip circuits invariably incorporate transmission line discontinuities of one type or another. Some of the most common forms of microstrip discontinuities are open ends, gaps, steps in width, right-angled bends, T junctions, and cross junctions. These are shown in Figure 3.1. Examples of circuits or circuit elements, wherein these discontinuities occur frequently, are also listed in this figure. A complete understanding and design of microstrip circuits require characterization of various discontinuities included in the circuit. Since discontinuity dimensions are usually much smaller than the wavelength in microstrip, they may be modelled by lumped-element equivalent circuits. A more complete characterization involves determination of frequency-dependent scattering matrix coefficients associated with the discontinuity. Various methods of characterization of microstrip discontinuities are discussed in this and the next chapter.

Discontinuities appear in conventional microwave circuits (using coaxial lines and waveguides) also. However, it may be pointed out that it is much more important to characterize discontinuities in microstrip circuits accurately. This is because of the fact that the microstrip circuits do not lend themselves to easy adjustments or tuning after the fabrication of the circuit is completed. If a provision is made for adjustments, the main advantages of compactness and reliability gained by the use of microstrip circuits are lost (at least partially). In monolithic circuits the first-pass success of design is heavily dependent on accurate characterization of microstrip and other discontinuities. Recent developments in microwave CAD have emphasized the introduction of accurate models for microstrip discontinuities.

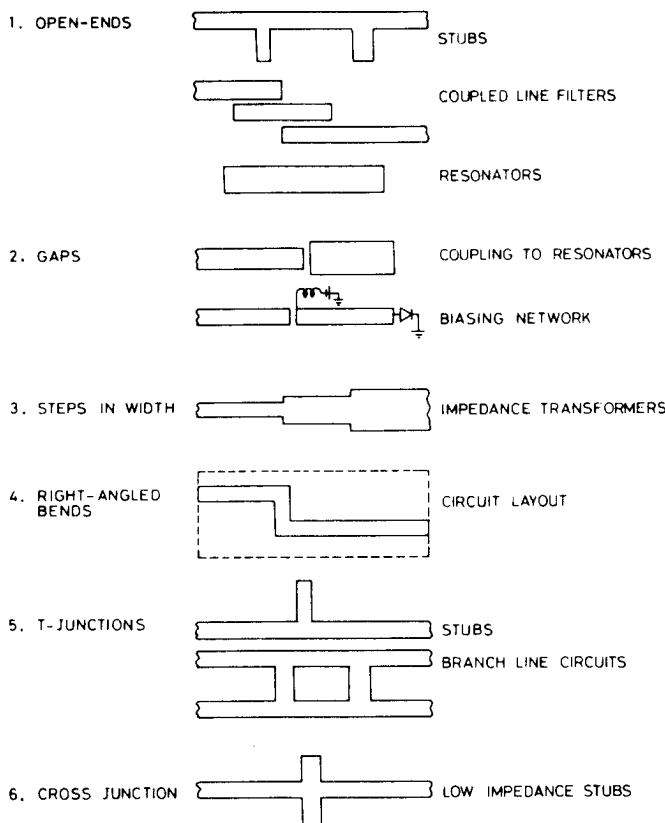


Figure 3.1 Various types of microstrip discontinuities and their typical applications.

A discontinuity in a microstrip is caused by an abrupt change in the geometry of the strip conductor. Therefore, electric and magnetic field distributions are modified near the discontinuity. The altered electric field distribution gives rise to a change in capacitance, and the changed magnetic field distribution can be expressed in terms of an equivalent inductance. The analysis of a microstrip discontinuity involves the evaluation of these capacitances and inductances and can either be based on quasi-static considerations or carried out more rigorously by fullwave analysis.

Quasi-static analysis involves calculations of static capacitances and low-frequency inductances. Equivalent circuits for discontinuities may be derived from these results. Alternatively, a waveguide type dynamic analysis taking dispersion (and possibly higher order modes) into account may be carried out. This can be based on the planar waveguide model of the microstrip line or one of the more rigorous full-wave electromagnetic analyses. Such a dynamic analysis leads to a

frequency-dependent scattering matrix. Again, equivalent circuits for discontinuities can be based on these results. Methods for the calculation of quasi-static capacitances and inductances for a discontinuity will be discussed in this chapter. Methods of dynamic analysis of the discontinuities are included in Chapter 4.

3.2 DISCONTINUITY CAPACITANCE EVALUATION

The static values of capacitances associated with discontinuities can be evaluated by finding the excess charge distribution near the discontinuity. The quasi-static methods for the evaluation of discontinuity capacitance have been treated by Farrar and Adams [1–3], Maeda [4], Itoh et al. [5, 6], Silvester and Benedek [7, 8], Benedek and Silvester [9], and Horton [10, 11]. The different methods used for these calculations are:

1. Matrix inversion method [1–3];
2. Variational method [4];
3. Galerkin's method in the spectral domain [5, 6];
4. Use of line sources with charge reversal [7–9].

These methods are discussed briefly in the following subsections. In all these methods, the following assumptions are implied: (i) the size of the discontinuity is small compared to the wavelength so that the phase variation across the discontinuity can be neglected; (ii) the current on the strip has zero divergence; and (iii) the strip conductor is infinitely thin.

3.2.1 Matrix Inversion Method

The matrix inversion method [3] is a very general approach for determining the static capacitance of a conductor of any arbitrary shape on the top surface of the microstrip substrate. The total conductor area is divided into small subsections over which the charge density can be assumed to be uniform. This subdivision for a microstrip rectangular section of length L and width W is shown in Figure 3.2. The typical subsection Δs_j , of sides Δx_j and Δz_j , is assumed to bear a uniform surface charge density σ_j . The potential at subsection Δs_i due to n number of subsections may be written as

$$V_i = \sum_{j=1}^n \sigma_j D_{ij} \quad (3.1)$$

where D_{ij} is a function representing the potential at subsection Δs_i , due to a uniform charge density of magnitude unity on Δs_j . One can write a Green's function express-

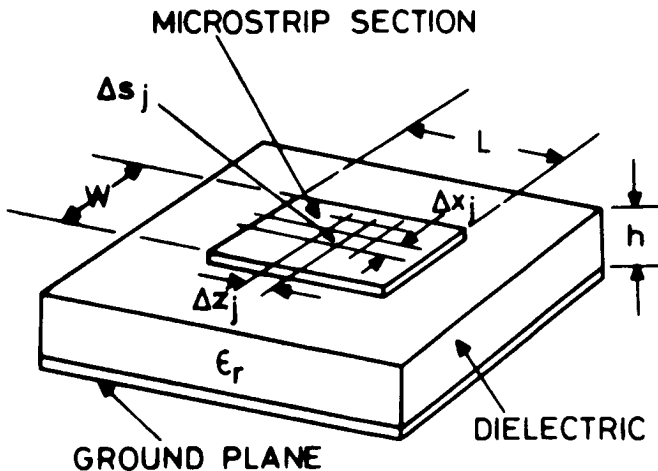


Figure 3.2 A typical microstrip discontinuity area divided into small sections.

ing potential due to a unit charge at Δs_j . Since the potential varies in all three directions, the Green's function becomes three-dimensional. Values of D_{ij} correspond to values of this Green's function at $y = h$. Equation (3.1) may be put in matrix form as

$$[\mathbf{V}] = [\mathbf{D}] [\boldsymbol{\sigma}] \quad (3.2)$$

The unknown charge densities $[\boldsymbol{\sigma}]$ are obtained by matrix inversion

$$[\boldsymbol{\sigma}] = [\mathbf{D}]^{-1} [\mathbf{V}] \quad (3.3)$$

If the voltage over the conductor with respect to the ground plane is taken as unity, the total capacitance of the conductor may be written as

$$C = \sum_{j=1}^n \sigma_j = \sum_{i=1}^n \sum_{j=1}^n D'_{ij} \quad (3.4)$$

where D'_{ij} represents an element of matrix $[\mathbf{D}]^{-1}$.

In order to implement this method, an expression for D_{ij} is needed. D_{ij} for a rectangular subsection is derived by using the theory of images [3]. A rectangular subsection has been selected because of its frequent occurrence in discontinuity problems. For evaluation of D_{ij} , the potential due to a uniformly charged plate in free space is obtained first. D_{ij} for the microstrip section is then evaluated by using the principle of multiple images. The resulting expression is a series, each term of

which is contributed by an image of the charge. This series expression may be written as

$$\begin{aligned}
 D_{ij} = & \sum_{n=1}^{\infty} \frac{K^{n-1}}{2\pi\epsilon_0(1+\epsilon_r)} \\
 & \cdot \left\{ (z_j - z_i) \ell_n \frac{(c+A)(d+B)(d+G)(c+H)}{(d+C)(c+D)(c+E)(d+F)} \right. \\
 & + \frac{\Delta z_j}{2} \ell_n \frac{(d+B)(d+C)(c+E)(c+H)}{(c+D)(c+A)(d+G)(d+F)} \\
 & + (x_j - x_i) \ell_n \frac{(a+A)(b+B)(b+H)(a+G)}{(b+D)(a+C)(a+E)(b+F)} \\
 & + \frac{\Delta x_j}{2} \ell_n \frac{(b+B)(b+D)(a+E)(a+G)}{(a+C)(a+A)(b+G)(b+F)} \\
 & - (2n-2) h \left[\tan^{-1} \frac{ac}{(2n-2)hA} \right. \\
 & \left. + \tan^{-1} \frac{bd}{(2n-2)hB} \right] + (2n-2) h \\
 & \cdot \left[\tan^{-1} \frac{ad}{(2n-2)hC} + \tan^{-1} \frac{bc}{(2n-2)hD} \right] \\
 & + 2nh \left[\tan^{-1} \frac{ac}{2nhE} + \tan^{-1} \frac{bd}{2nhF} \right] \\
 & \left. - 2nh \left[\tan^{-1} \frac{ad}{2nhG} + \tan^{-1} \frac{bc}{2nhH} \right] \right\} \quad (3.5)
 \end{aligned}$$

where

$$\begin{aligned}
 A &= \sqrt{a^2 + c^2 + (2n-2)^2 h^2} & E &= \sqrt{a^2 + c^2 + (2nh)^2} \\
 B &= \sqrt{b^2 + d^2 + (2n-2)^2 h^2} & F &= \sqrt{b^2 + d^2 + (2nh)^2} \\
 C &= \sqrt{a^2 + d^2 + (2n-2)^2 h^2} & G &= \sqrt{a^2 + d^2 + (2nh)^2} \\
 D &= \sqrt{b^2 + c^2 + (2n-2)^2 h^2} & H &= \sqrt{b^2 + c^2 + (2nh)^2}
 \end{aligned}$$

and

$$a = z_j - \frac{\Delta z_j}{2} - z_i \quad b = z_j + \frac{\Delta z_j}{2} - z_i$$

$$c = x_j - \frac{\Delta x_j}{2} - x_i \quad d = x_j + \frac{\Delta x_j}{2} - x_i$$

$$K = \frac{1 - \epsilon_r}{1 + \epsilon_r}$$

Slow convergence of the series in (3.5) is a drawback of this method. About 40 terms of the series have been used in the computation of discontinuity capacitances [3].

The method has been used for finding capacitances associated with microstrip open ends, steps, and gaps. The capacitance associated with an open end (shown in Figure 3.3) may be written as

$$C_{oc} = \frac{1}{2} \lim_{L \rightarrow \infty} [C_t(L) - CL] \quad (3.6)$$

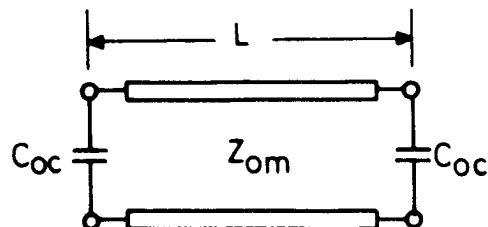
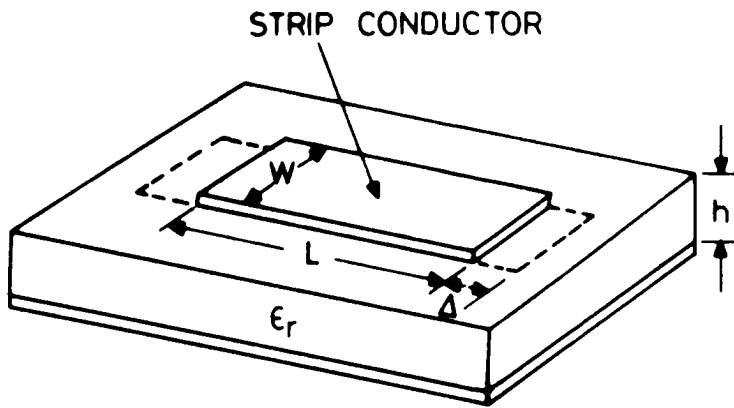


Figure 3.3 Configuration for calculating the microstrip open-end capacitance and its equivalent circuit.

$C_t(L)$ is the total capacitance of a microstrip section of total length L and C is the capacitance per unit length of an infinite line of the same width. In order to find the limit in (3.6), the length L is increased iteratively and the total capacitance is computed until the open-end capacitance given by (3.6) converges. A difficulty with this procedure is that (3.6) involves subtraction of two nearly equal large numbers, and therefore very accurate computations of $C_t(L)$ and CL are necessary.

The configuration for calculating the capacitance associated with a step in the width of a microstrip is shown in Figure 3.4. Its equivalent circuit is also shown in this figure. The capacitance associated with the step is evaluated as

$$C_s = \lim_{L \rightarrow \infty} [C_t(L) - C_{oc}(W_1) - C_{oc}(W_2) - C_1 L - C_2 L] \quad (3.7)$$

where $C_{oc}(W_1)$ and $C_{oc}(W_2)$ are open-end capacitances of lines of width W_1 and W_2 , respectively, and C_1 and C_2 are capacitances per unit length for these lines.

In the case of a microstrip gap, the equivalent circuit consists of three capacitances in a π -configuration as shown in Figure 3.5.

To evaluate these capacitances, a capacitance matrix $[\mathbf{C}(L)]$ is computed as

$$[\mathbf{C}(L)] = \begin{bmatrix} C_{11}(L) & C_{12}(L) \\ C_{21}(L) & C_{22}(L) \end{bmatrix} \quad (3.8)$$

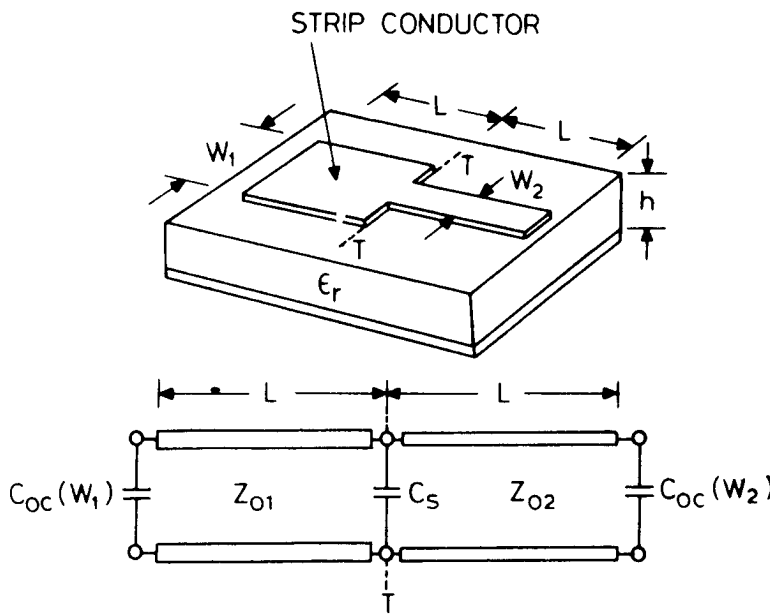


Figure 3.4 Geometry for calculating the capacitance of a step discontinuity and its equivalent circuit.

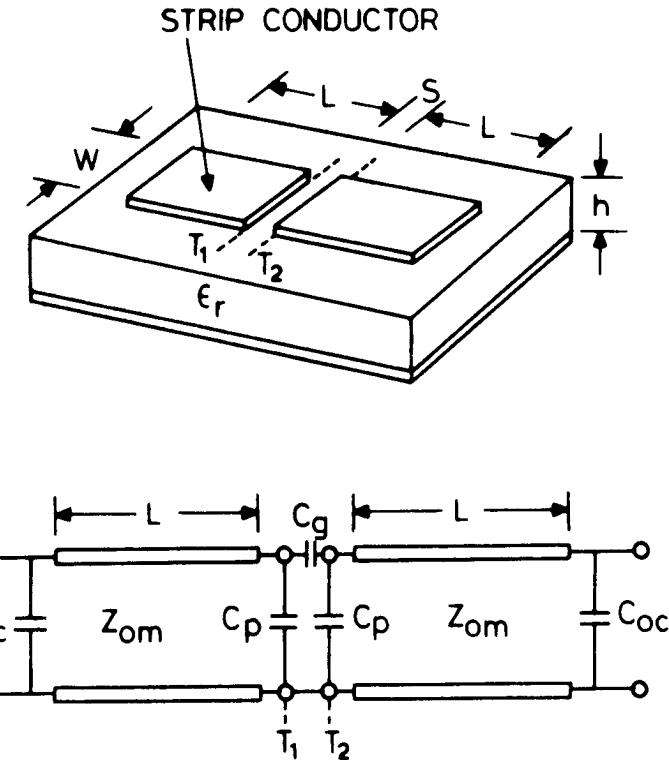


Figure 3.5 Configuration for characterizing a microstrip gap and its equivalent circuit.

where $C_{ij}(L)$ are related to the elements of the admittance matrix of the two-port network (shown in Figure 3.5) by

$$C_{ij}(L) = Y_{ij}/j\omega \quad (3.9)$$

Capacitances C_p and C_g are then computed by using

$$C_p = \lim_{L \rightarrow \infty} [C_{11}(L) - CL - C_{oc}] \quad (3.10a)$$

$$C_g = \lim_{L \rightarrow \infty} C_{12}(L) \quad (3.10b)$$

It may be noted that the subtraction of two nearly equal large numbers is involved in (3.7) and (3.10a). But such a subtraction is not involved in the computation of C_g , and thus an accurate computation of C_g is much less time consuming.

One can conclude that the method described above is a general one and can be used to compute the excess capacitance of any microstrip discontinuity. The difficulties faced in this method are: slow convergence of infinite series in the three-dimensional Green's function and the subtraction of two nearly equal large numbers. The accuracy of capacitance results can be improved at the expense of increased computer time.

3.2.2 Variational Method

This method [4] uses the variational principle to formulate the capacitance problem. It is known that the capacitance can be expressed by a variational expression that is stationary with respect to arbitrary first-order variations in the charge distribution on the strip conductor [12]. If the charge distribution is $\rho(r)$, the capacitance C may be expressed as

$$\frac{1}{C} = \frac{\iint \rho(r) G(r; r') \rho(r') dv' dv}{[\int \rho(r') dv']^2} \quad (3.11)$$

where the integrals are over all the volume in which the charge is distributed. Source and observation point coordinates are shown in Figure 3.6. Since (3.11) is a lower bound type of expression, the capacitance can be obtained by maximizing with a suitable choice of charge distribution as a trial function.

Therefore, the charge distribution does not need to be known exactly when using this method. G is a three-dimensional Green's function for potential and satisfies the relation

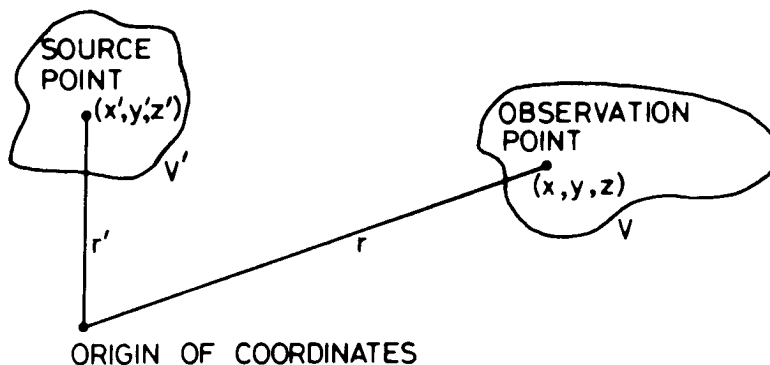


Figure 3.6 Coordinate system for source and observation points.

$$\nabla^2 G(x, y, z; x', y', z') = -\frac{1}{\epsilon_0 \epsilon_r} \delta(x - x') \delta(y - y') \delta(z - z') \quad (3.12)$$

where δ indicates a Dirac's delta function. Green's functions for the case $y = h$ are adequate for the evaluation of excess capacitance of a discontinuity using the variational expression (3.11).

The variational method has been used to characterize two types of discontinuities: an open end and a gap, for which suitable Green's functions have been developed. As shown in Figure 3.7(a), a gap in the strip conductor of a microstrip line, which is represented by a π equivalent circuit, can be analyzed by placing an electric wall and a magnetic wall successively along the plane of symmetry A. This corresponds to a short circuit and an open circuit, respectively, in the equivalent circuit representation. The capacitances between the microstrip end and the plane A are denoted C_e for electric wall and C_m for magnetic wall. The parameters of the equivalent π circuit, C_p (shunt gap capacitance) and C_g (coupling capacitance between the adjacent strip conductors), may be written in terms of C_e and C_m as

$$C_e = C_p + 2C_g \quad \text{and} \quad C_m = C_p \quad (3.13)$$

The capacitances C_e and C_m can be evaluated using (3.11) with suitable G and ρ . The configuration considered for evaluation of G for the two cases is shown in Figure 3.7(b). The portion of the microstrip between the planes of symmetry located at $z = 0$ and $z = -c$ is enclosed in a box as shown in this figure. Two Green's functions G_e and G_m are evaluated for electric wall and magnetic wall cases by writing the solution of (3.12) as a linear combination of hyperbolic sinusoidal functions and applying boundary and continuity conditions. The expressions obtained for G_e and G_m may be written as [4]

$$G_e(x, y, z; x', h, z') = \begin{cases} \sum_{m=1}^{\infty} \sum_{n=1}^{\infty} P Q \sinh(\gamma_{mn}y) \sinh[\gamma_{mn}(b - h)] & (0 \leq y \leq h) \\ \sum_{m=1}^{\infty} \sum_{n=1}^{\infty} P Q \sinh[\gamma_{mn}(b - y)] \sinh(\gamma_{mn}h) & (h \leq y \leq b) \end{cases} \quad (3.14a)$$

$$G_m(x, y, z; x', h, z') = \begin{cases} \sum_{m=1}^{\infty} \sum_{n=0}^{\infty} \sigma_n P R \sinh(\gamma_{mn}y) \sinh[\gamma_{mn}(b - h)] & (0 \leq y \leq h) \\ \sum_{m=1}^{\infty} \sum_{n=0}^{\infty} \sigma_n P R \sinh[\gamma_{mn}(b - y)] \sinh(\gamma_{mn}h) & (h \leq y \leq b) \end{cases} \quad (3.15b)$$

and

$$G_m(x, y, z; x', h, z') = \begin{cases} \sum_{m=1}^{\infty} \sum_{n=0}^{\infty} \sigma_n P R \sinh(\gamma_{mn}y) \sinh[\gamma_{mn}(b - h)] & (0 \leq y \leq h) \\ \sum_{m=1}^{\infty} \sum_{n=0}^{\infty} \sigma_n P R \sinh[\gamma_{mn}(b - y)] \sinh(\gamma_{mn}h) & (h \leq y \leq b) \end{cases} \quad (3.15a)$$

$$G_m(x, y, z; x', h, z') = \begin{cases} \sum_{m=1}^{\infty} \sum_{n=0}^{\infty} \sigma_n P R \sinh(\gamma_{mn}y) \sinh[\gamma_{mn}(b - h)] & (0 \leq y \leq h) \\ \sum_{m=1}^{\infty} \sum_{n=0}^{\infty} \sigma_n P R \sinh[\gamma_{mn}(b - y)] \sinh(\gamma_{mn}h) & (h \leq y \leq b) \end{cases} \quad (3.15b)$$

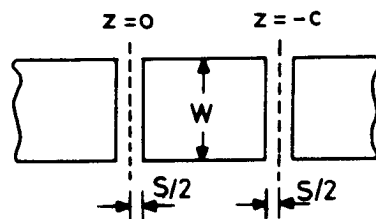
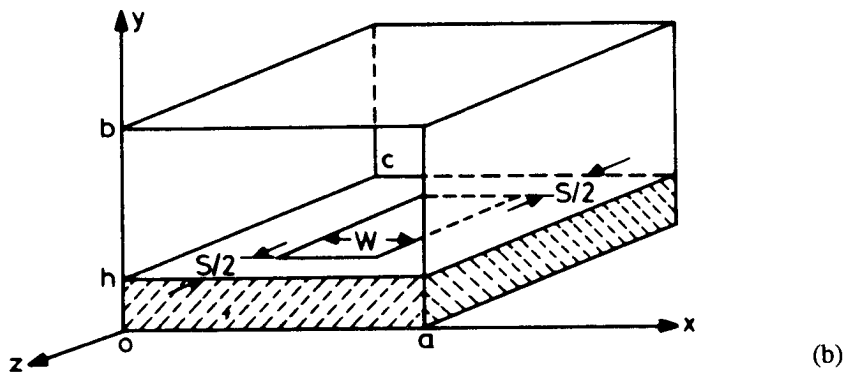
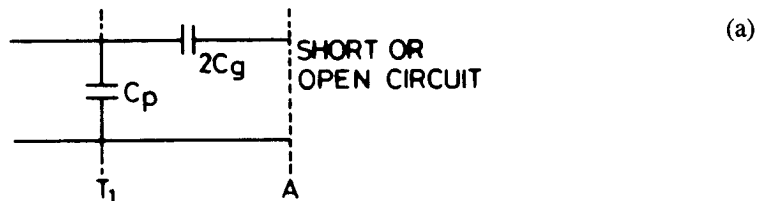
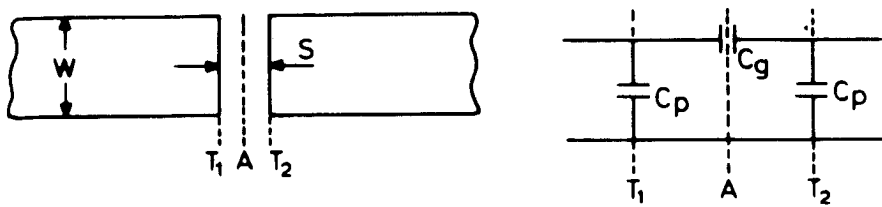


Figure 3.7 (a) Representation of a gap in microstrip and its equivalent circuit and (b) configuration for evaluating Green's functions for gap capacitances.

where

$$P = \frac{4}{ac\gamma_{mn}\Gamma_{mn}} \sin\left(\frac{m\pi x}{a}\right) \sin\left(\frac{m\pi x'}{a}\right)$$

$$Q = \sin\left(\frac{n\pi z}{c}\right) \sin\left(\frac{n\pi z'}{c}\right)$$

$$R = \cos\left(\frac{n\pi z}{c}\right) \cos\left(\frac{n\pi z'}{c}\right)$$

$$\gamma_{mn} = \left[\left(\frac{m\pi}{a} \right)^2 + \left(\frac{n\pi}{c} \right)^2 \right]^{1/2}$$

$$\Gamma_{mn} = \epsilon_r \cosh(\gamma_{mn}h) \sinh[\gamma_{mn}(b-h)] + \sinh(\gamma_{mn}h) \cosh[\gamma_{mn}(b-h)]$$

and σ_n is $\frac{1}{2}$ for $n = 0$ and is 1 for $n \neq 0$. The only additional information required to solve (3.11) is an estimate for the charge distribution ρ . If it is assumed that $\rho(x, z)$ is separable in the x - and z -directions we can write

$$\rho(x, z) = f(x) g(z) \quad (3.16)$$

where $f(x)$ corresponds to the charge distribution of a uniform microstrip and may be written as [13]

$$f(x) = \begin{cases} 1 + \left| \frac{2}{W} \left(x - \frac{a}{2} \right) \right|^3 & \text{for } \left| x - \frac{a}{2} \right| \leq \frac{W}{2} \\ 0 & \text{elsewhere} \end{cases} \quad (3.17)$$

Charge density in the longitudinal direction also increases near the edge of the strip conductor, and $g(z)$ may be assumed to be of the form

$$g(z) = \begin{cases} 0 & \frac{c}{2} - \frac{S}{2} \leq \left| z - \frac{c}{2} \right| \leq \frac{c}{2} \\ 1 + \frac{K}{h} \left\{ \left| z - \frac{c}{2} \right| - \frac{c}{2} + \frac{S}{2} + h \right\} & \frac{c}{2} - \frac{S}{2} - h \leq \left| z - \frac{c}{2} \right| \leq \frac{c}{2} - \frac{S}{2} \\ 1 & \left| z - \frac{c}{2} \right| \leq \frac{c}{2} - \frac{S}{2} - h \end{cases} \quad (3.18)$$

The coefficient K is determined so as to maximize the capacitance. A table of optimum values of coefficient K for the electric and magnetic walls for various values of ϵ_r and S/h is given by Maeda [4]. When S/h is large (or in the case of an open-circuit discontinuity), K becomes unity for the electric as well as the magnetic walls.

This method has been used to characterize gaps and open ends. The open-end capacitance is evaluated as a limit of the gap capacitance C_g when the gap width becomes very large. A fairly good agreement with experimental results is reported in [4].

3.2.3 Galerkin's Method in the Fourier Transform Domain [5, 6]

This method is similar to Galerkin's method in FTD used for fullwave analysis of microstrip lines discussed in Chapter 2 and the variational method in FTD used for quasi-static analysis in Chapter 1. The microstrip configuration and the coordinate system are shown in Figure 3.8.

In this case a two-dimensional Fourier transform in the $(x-z)$ -plane is used. Transforms of potential and charge are defined by

$$\tilde{\phi}(\alpha, y, \beta) = \int_{-\infty}^{\infty} \int_{-\infty}^{\infty} \phi(x, y, z) \exp(j[\alpha x + \beta z]) dx dz \quad (3.19)$$

$$\tilde{\rho}(\alpha, \beta) = \int_{-\ell/2}^{\ell/2} \int_{-W/2}^{W/2} \rho(x, z) \exp(j[\alpha x + \beta z]) dx dz \quad (3.20)$$

In the spectral domain, Poisson's equation is written as

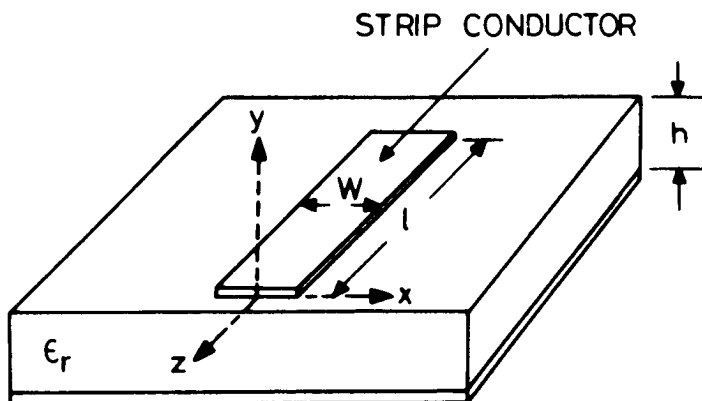


Figure 3.8 Microstrip geometry and the coordinate system used for Galerkin's method in spectral domain.

$$\left[\frac{\partial^2}{\partial y^2} - (\alpha^2 + \beta^2) \right] \tilde{\phi}(\alpha, y, \beta) = -\frac{1}{\epsilon_0} \rho(\alpha, \beta) \delta(y) \quad (3.21)$$

Boundary conditions at $y = -h$ and $y \rightarrow \infty$ and the interface conditions across $y = 0$ are written in the spectral domain. When these conditions are applied to (3.21), we obtain

$$G(\alpha, \beta) \tilde{\rho}(\alpha, \beta) = \tilde{\phi}_i(\alpha, 0, \beta) + \tilde{\phi}_0(\alpha, 0, \beta) \quad (3.22)$$

where

$$G(\alpha, \beta) = \frac{1}{\epsilon_0 \sqrt{(\alpha^2 + \beta^2)} [1 + \epsilon_r \coth\{\sqrt{(\alpha^2 + \beta^2)} h\}]} \quad (3.23)$$

and $\tilde{\phi}_i$ and $\tilde{\phi}_0$ are the transforms of the potential functions on the strip and outside the strip at $y = 0$, respectively. We assume that the potentials on the strip and the ground plane are 1 and 0 V, respectively. Using (3.19),

$$\tilde{\phi}_i = \frac{4}{\alpha \beta} \sin \frac{\alpha W}{2} \sin \frac{\beta \ell}{2} \quad (3.24)$$

Now (3.22) contains two unknowns: the transforms of charge on the strip $\tilde{\rho}$ and the potential outside the strip $\tilde{\phi}_0$.

At this stage Galerkin's method is applied, which eliminates one of the unknowns $\tilde{\phi}_0$ and converts (3.22) into a small-sized matrix equation. This is subsequently solved for the unknown coefficients. The matrix equation is

$$\sum_{n=1}^N K_{mn} d_n = f_m \quad m = 1, 2, \dots, N \quad (3.25)$$

where

$$K_{mn} = \int_{-\infty}^{\infty} \int_{-\infty}^{\infty} \tilde{\zeta}_m(\alpha, \beta) G(\alpha, \beta) \tilde{\zeta}_n(\alpha, \beta) d\alpha d\beta$$

$$f_m = \int_{-\infty}^{\infty} \int_{-\infty}^{\infty} \tilde{\zeta}_m(\alpha, \beta) \tilde{\phi}_i(\alpha, 0, \beta) d\alpha d\beta$$

and $\tilde{\zeta}_m$'s are the basis functions for $\tilde{\rho}$. Equation (3.25) is solved for d_n . Finally, the charge distribution in the space domain is expressed in terms of the superposition of the inverse transforms of the basis functions weighted by the coefficients d_n .

The choice of the basis functions is arbitrary as long as they satisfy the required condition that they are zero in the appropriate range. The basic functions chosen are transforms of the following:

$$\zeta_m(x, z) = \begin{cases} |x|^{k-1} |z|^{j-1} & \text{on the strip} \\ 0 & \text{otherwise} \end{cases} \quad (3.26)$$

where $m = 1$ for $k = 1, j = 1$; $m = 2$ for $k = 2, j = 1$ and so on. In actual numerical computations one or two terms in ζ_m are sufficient. Total capacitance for the strip is obtained from the expression

$$C = \int_{-\ell/2}^{\ell/2} \int_{-W/2}^{W/2} \rho(x, z) dx dz = (2\pi)^2 \sum_{n=1}^N d_n f_n \quad (3.27)$$

The fringing capacitance at the end of the open-circuited microstrip may again be evaluated using (3.6).

Comparing with the variational method of the last subsection, one notes that Green's function in the transform domain is a closed-form expression in contrast to a slowly converging series in the space domain.

Although this method could, in principle, be applied to other discontinuities also, the results are available for microstrip open ends only.

3.2.4 Use of Line Sources with Charge Reversal

All three methods for the evaluation of discontinuity capacitance discussed so far involve subtraction of two nearly equal large quantities. This factor limits the computational accuracy. A method using line sources with charge reversal [7–9] overcomes this difficulty. This method uses line sources (not subareas) to develop Green's functions suitable for discontinuity problems. The basic element common to all the discontinuities considered using this method is a semi-infinite line charge. Formulation of Green's function for a semi-infinite line charge is shown in Figure 3.9. Here, the semi-infinite line charge (c) is considered as a superposition of two line charges (a) and (b). Figure 3.9(a) shows a uniform and infinitely long line charge such as present in the case of an infinite microstrip. This charge distribution can be obtained by solving

$$\phi_e(x) = \int_{-\infty}^{\infty} \sigma_{\infty}(\xi) G_e(x, \xi) d\xi \quad (3.28)$$

where G_e is the two-dimensional Green's function of the microstrip problem discussed in Section 1.2.3 and σ_{∞} is the charge density on an infinitely extended

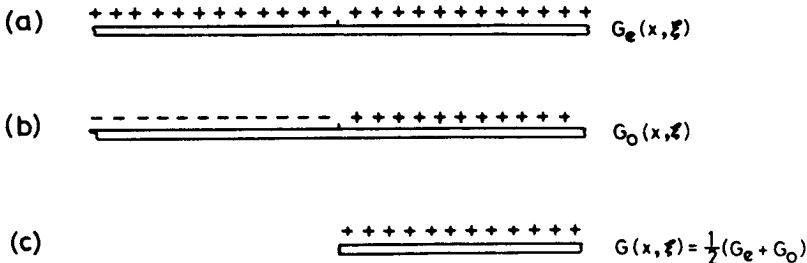


Figure 3.9 Formulation of Green's functions for a semi-infinite line source.

microstrip line. We also consider a charge distribution shown in Figure 3.9(b) that is exactly similar to $\sigma_{\infty}(\xi)$ on half the infinite strip and exactly $-\sigma_{\infty}(\xi)$ on the other half. While this situation is physically difficult to realize, there is no mathematical objection to it, and the potential distribution in this case may be written as

$$\phi_0(x) = \int_{-\infty}^{\infty} \sigma_{\infty}(\xi) G_0(x, \xi) d\xi \quad (3.29)$$

where $G_0(x, \xi)$ is the appropriate Green's function. When the charge distributions given by (3.28) and (3.29) are combined, we obtain the configuration of a semi-infinite line charge, Figure 3.9(c), and the potential distribution is now given by

$$\phi_{si} = \frac{1}{2} \{ \phi_e + \phi_0 \} = \frac{1}{2} \int \sigma_{\infty}(\xi) \{ G_e(x, \xi) + G_0(x, \xi) \} d\xi \quad (3.30)$$

where ϕ_{si} is the potential associated with a charge distribution exactly like that of an infinite microstrip but terminating at the origin. The potential ϕ_{si} cannot satisfy the requirement of constant potential everywhere on the semi-infinite strip. To obtain a constant potential, a certain amount of extra charge, say σ_e , must be placed on half the strip. This excess charge σ_e may be obtained from the equation

$$\phi - \phi_{si} = \int \sigma_e(\xi) G(x; \xi) d\xi \quad (3.31)$$

where ϕ is a constant potential ($= \phi_e$) over the semi-infinite length and $G = 1/2(G_e + G_0)$. It may be noted that the excess charge $\sigma_e(\xi)$ is responsible for the discontinuity capacitance C , which may now be written as

$$C = \frac{1}{\phi} \int \sigma_e dx \quad (3.32)$$

Using the concepts outlined above, computing the capacitance associated with a microstrip open end involves:

1. Constructing G_e and G_0 ;
2. Evaluating ϕ_{si} from (3.30);
3. Solving integral equation (3.31) for σ_e ;
4. Finding the capacitance from (3.32).

Although the integration (3.31) is over a semi-infinite length, it may be noted that both the potential residual and the excess charge approach zero asymptotically (and rather rapidly) for points at increasing distances from the strip end. Also, (3.31) and (3.32) permit the solution for excess charge density and excess capacitance directly, and the subtraction of two equally large quantities is not involved.

Green's functions G_e and G_0 are obtained [7] by considering the multiple images of a line charge when placed parallel to a dielectric slab. Green's function G_e for a microstrip is given by (1.36) of Chapter 1, and G_0 may be written as

$$G_0(x, h, z; x_0) = \frac{1 - K}{4\pi\epsilon_0\epsilon_r} \left[f(0) - (1 - K) \sum_{n=1}^{\infty} K^{n-1} f(n) \right] \quad (3.33)$$

where $K = (1 - \epsilon_r)/(1 + \epsilon_r)$ and

$$f(n) = \ell_n \frac{\sqrt{z^2 + 4n^2h^2 + (x - x_0)^2} + z}{\sqrt{z^2 + 4n^2h^2 + (x - x_0)^2} - z}$$

The line source configuration used is shown in Figure 3.10 and h is the height of the dielectric substrate.

This method is very general and is used for all types of microstrip discontinuities [8, 9] shown in Figure 3.1. The formulation for a microstrip gap is sketched in Figure 3.11. Green's functions G_{even} and G_{odd} are used in equations similar to (3.31) to calculate the residual potentials which lead to excess charges and discontinuity capacitances. Similar formulations may be carried out for other discontinuities also.

3.3 DISCONTINUITY INDUCTANCE EVALUATION

The calculation of capacitances associated with microstrip discontinuities has been discussed in the above section. However, in several cases, for example, bends, steps, and T-junctions, inductive effects also become significant. Evaluation of inductive reactances in the equivalent circuit of microstrip discontinuities using the quasi-static method [14, 15] will be discussed in this section. These inductive components are frequency dependent, and quasi-static calculations can only provide their low-frequency values.

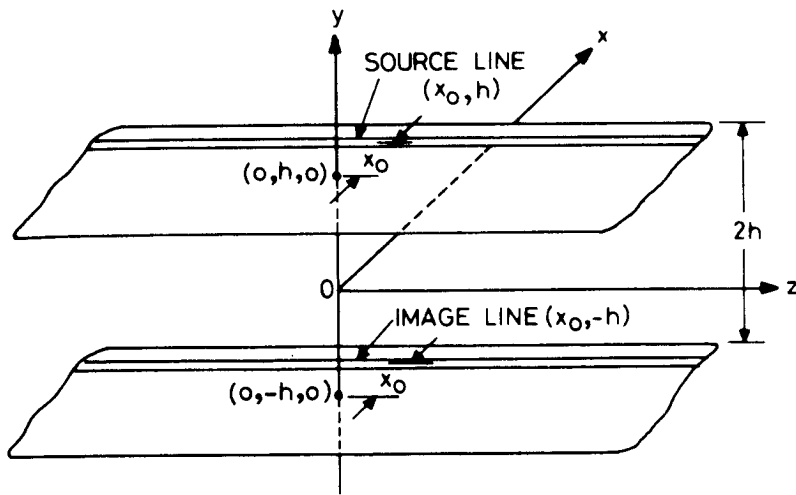


Figure 3.10 Configuration for calculating G_e and G_0 of Figure 3.9.

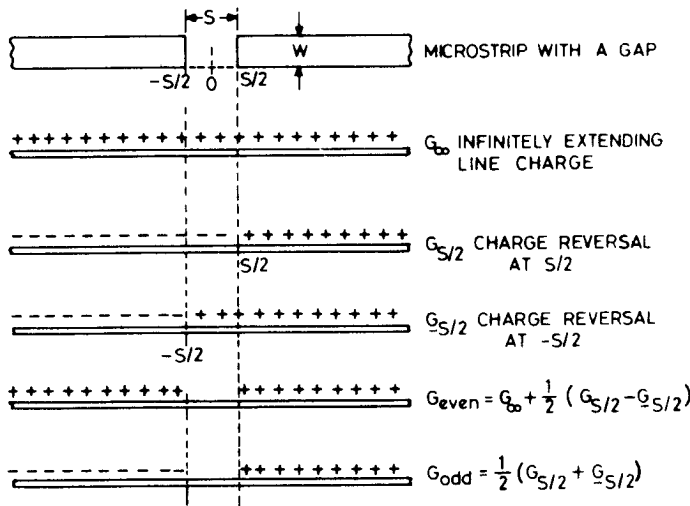


Figure 3.11 Representation of a microstrip gap in terms of line charges.

When inductances are being calculated, the presence of the dielectric substrate (provided it is nonmagnetic) may be disregarded, and only the discontinuity structure and its image in the ground plane are considered. For magnetic substrates it will be necessary to consider the multiple images formed.

The magnetic vector potential A due to the current density J on any section of the line or discontinuity can be written as

$$A = \mu_0 \int G J \, dV \quad (3.34)$$

where G is Green's function given by

$$G = \frac{1}{4\pi[(x - x_0)^2 + (y - y_0)^2 + (z - z_0)^2]^{1/2}} \quad (3.35)$$

From Maxwell's equation, the electric field may be written as

$$\mathbf{E} = -\frac{\partial \mathbf{A}}{\partial t} - \nabla \phi \quad (3.36)$$

where ϕ is the impressed voltage on the strip that causes current to flow. Also from Ohm's law we have

$$\mathbf{J} = \sigma \mathbf{E} \quad (3.37)$$

where σ is the strip conductivity. Combining (3.34), (3.36), and (3.37) we may write

$$\mathbf{J} + \mu_0 \sigma \frac{\partial}{\partial t} \int G J \, dV = -\sigma \nabla \phi \quad (3.38)$$

For good conductors $\sigma \rightarrow \infty$ and (3.38) may be rewritten as

$$\mu_0 \frac{\partial}{\partial t} \int G J \, dV \approx -\nabla \phi \quad (3.39)$$

Divergence of (3.39) yields (under quasi-static assumptions)

$$\nabla^2 \phi = 0 \quad (3.40)$$

which implies that the impressed potential satisfies Laplace's equation on the strip conductor. The current density distribution on the microstrip structure can be found by solving (3.40) for ϕ (or $\nabla \phi$) and then (3.39) for J . Knowledge of current density distribution J enables the inductance L of the microstrip structure to be obtained from the relation

$$\int (\bar{A} \cdot \bar{J}) \, dV = I^2 L \quad \text{where } I = \int \bar{J} \cdot \bar{dS} \quad (3.41)$$

A straightforward implementation of the procedure indicated above will yield a value of discontinuity inductance as the difference between two large numbers corresponding to the inductance of the total structure including the discontinuity and the inductance contributed by the uniform line portion of the discontinuity structure. In this procedure it becomes difficult to obtain accurate values of L . This can be overcome using an excess current technique [14] similar to the excess charge formulation [7] used in Section 3.2.4. We will discuss this technique for the case of a right-angled bend.

For the purpose of inductance calculation, the configuration of the right-angled bend is divided into five sections (S1 to S5) as shown in Figure 3.12. The planes PP' and QQ' are located such that the currents in S1 and S5 are practically the same as for infinitely long lines, that is, J_{∞} or J_{∞} , respectively. In S2 and S4, the current distribution is considered to consist of two components J_{e1} or J_{e2} and J_{e3} or J_{e4} , the latter being excess circulating current because of the discontinuity. In S3 the only current component present is the excess circulating current J_{e5} . The

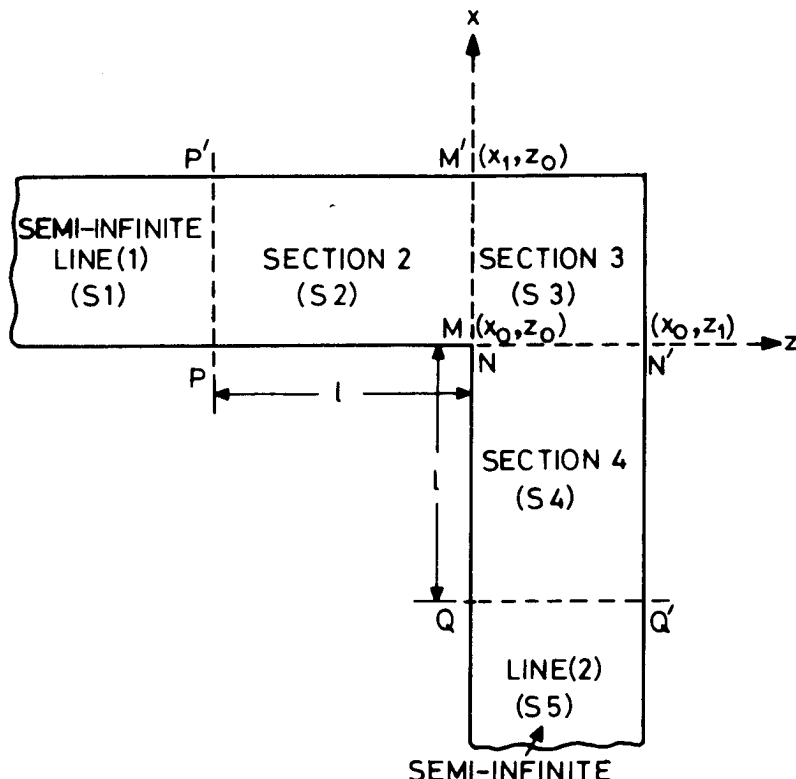


Figure 3.12 Subdivision of a right-angled bend structure for calculating the discontinuity inductance.

magnitude and the distribution of excess circulating currents J_{e2} , J_{e3} , and J_{e4} are to be determined. Equation (3.39) becomes (for the configuration in Figure 3.12),

$$\int_{S1} G_i J_{\infty} dS + \int_{S2} G_i (J_{\infty} + J_{e2}) dS + \int_{S3} G_i J_{e3} dS + \int_{S4} G_i (J_{\infty} + J_{e4}) dS + \int_{S5} G_i J_{\infty} dS = \frac{-1}{\mu_0} \nabla \Phi \quad (3.42)$$

where $\Phi = \phi / (j t \omega)$, t is the thickness of the strip conductor, and ω is the angular frequency. J_{∞} and J_{∞} are current distributions for infinite lines and vary only along x and z , respectively. Thus, they can be integrated analytically with respect to x and z , respectively. G_i is Green's function for the line current element and its image and may be written as

$$G_i = \frac{1}{4\pi[(x - x_0)^2 + (z - z_0)^2]^{1/2}} - \frac{1}{4\pi[(x - x_0)^2 + (2h)^2 + (z - z_0)^2]^{1/2}} \quad (3.43)$$

When Green's functions for semi-infinite line currents (along with their images in the ground plane) are introduced, (3.42) may be rewritten as

$$\int_{S2+S3+S4} G_i J_e dS = \frac{-1}{\mu_0} \nabla \Phi - \int_{z_0}^{z_1} G_2 J_{\infty} dz - \int_{x_0}^{x_1} G_1 J_{\infty} dx \quad (3.44)$$

Green's functions G_1 and G_2 are given by

$$G_1 = \ell_n \left[\frac{(x_0 - x) + \{(x_0 - x)^2 + (2h)^2 + (z_0 - z)^2\}^{1/2}}{(x_0 - x) + \{(x_0 - x)^2 + (z_0 - z)^2\}^{1/2}} \right] \quad (3.45)$$

and

$$G_2 = \ell_n \left[\frac{(z_0 - z) + \{(x_0 - x)^2 + (2h)^2 + (z_0 - z)^2\}^{1/2}}{(z_0 - z) + \{(x_0 - x)^2 + (z_0 - z)^2\}^{1/2}} \right] \quad (3.46)$$

Equation (3.44) is solved by Galerkin's method, and the solution for J_e in each region is used to calculate the excess inductance.

This method has also been used for a T-junction [14], a step discontinuity, and a cross junction [15].

3.4 CHARACTERIZATION OF VARIOUS DISCONTINUITIES

Quasi-static techniques for evaluating discontinuity capacitances and inductances were described in the previous section. The results of these types of analyses for

various microstrip discontinuities will be presented now. Closed-form expressions for these discontinuities (wherever available) and the ranges of their validity are included here. Some of these closed-form expressions are based on the fullwave analysis data, methods for which are discussed in Chapter 4. Techniques of compensation of the reactive effects of these discontinuities to obtain better circuit performance are also described in this section.

3.4.1 Open Ends

An open-end discontinuity occurs frequently in a number of circuits such as resonators, matching stubs, parallel coupled filters, and in microstrip antennas. The equivalent circuit of an open end is represented by an excess capacitance C_{oc} , which can be transformed into an equivalent length of transmission line, $\Delta\ell_{oc}$, as shown in Figure 3.13. The equivalent capacitance shown in Figure 3.13(b) is what is usually calculated, whereas the equivalent line length representation (Figure 3.13(c)) is more convenient for circuit design.

The most extensive data set on the microstrip open circuit has been obtained by Silvester and Benedek [7] using the method of line sources with charge reversal. Their results are presented in Figure 3.14. Also they have given an empirical expression that is very useful for computational purposes and may be written as

$$\frac{C_{oc}}{W} = \exp \left\{ 2.3026 \sum_{i=1}^5 C_i(\epsilon_r) \left[\log \frac{W}{h} \right]^{i-1} \right\} \quad (\text{pF/m}) \quad (3.47)$$

where C_i 's are numerical constants tabulated in [7] for $\epsilon_r = 1.0, 2.5, 4.2, 9.6, 16.0$, and 51.0. For example, for $\epsilon_r = 9.6$, values of C_i are 1.738, -0.2538, 0.1308, -0.0087, -0.0113 for $i = 1, \dots, 5$ respectively.

The equivalent additional line length $\Delta\ell_{oc}$ for an open-circuit discontinuity may be obtained from C_{oc} by using the relation

$$\frac{\Delta\ell_{oc}}{h} = \frac{C_{oc}}{W} \frac{cZ_{0m} W/h}{\sqrt{\epsilon_{re}}} \quad (3.48)$$

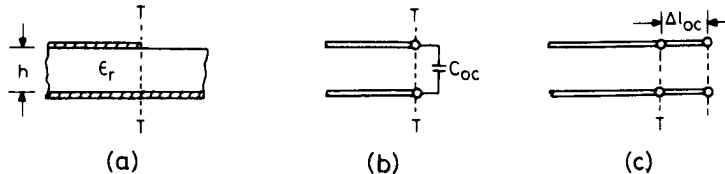


Figure 3.13 (a) Microstrip open-end discontinuity, (b) equivalent capacitance representation, and (c) equivalent line length representation.

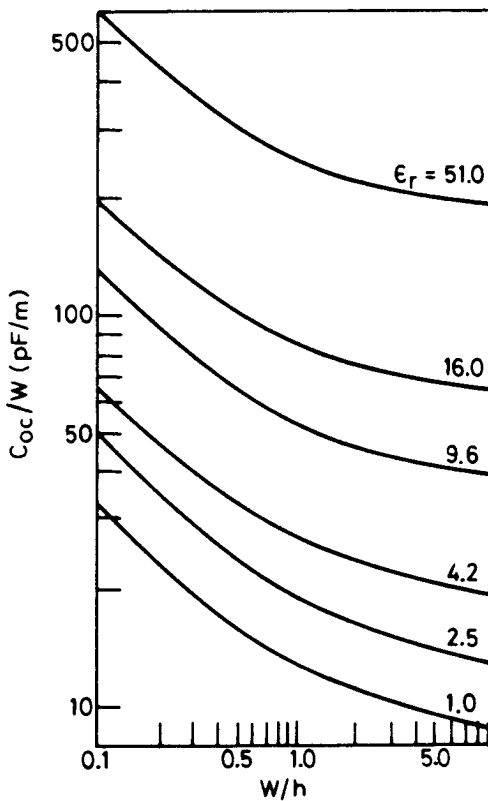


Figure 3.14 Capacitance associated with an open-end discontinuity (from [7], © 1972 IEEE. Reprinted with permission.).

where c is the velocity of wave propagation in free space. An empirical expression for $\Delta\ell_{oc}/h$ has been obtained by modifying the expression derived by Hammerstad and Bekkadal [16]. The expression is given [17] as

$$\frac{\Delta\ell_{oc}}{h} = 0.412 \frac{\epsilon_{re} + 0.3}{\epsilon_{re} - 0.258} \left[\frac{W/h + 0.264}{W/h + 0.8} \right] \quad (3.49)$$

Maximum relative error in this expression, as compared to (3.47), is less than 4 percent for $W/h \geq 0.2$ and $2 \leq \epsilon_r \leq 50$. However, the result above is not valid [18] for wide microstrip lines (say $W/h > 3$) used extensively for microstrip antennas.

A more accurate expression, with accuracy better than 0.2 percent for the range of normalized widths $0.01 \leq W/h \leq 100$ and $\epsilon_r \leq 128$, has been derived [19] by curve fitting the numerical results based on hybrid-mode fullwave analysis [20, 21]. According to this,

$$\frac{\Delta\ell_{oc}}{h} = \xi_1 \xi_3 \xi_5 / \xi_4 \quad (3.50)$$

where

$$\begin{aligned}\xi_1 &= 0.434907 \frac{\epsilon_{re}^{0.81} + 0.26 (W/h)^{0.8544} + 0.236}{\epsilon_{re}^{0.81} - 0.189 (W/h)^{0.8544} + 0.87} \\ \xi_2 &= 1 + \frac{(W/h)^{0.371}}{2.358 \epsilon_r + 1} \\ \xi_3 &= 1 + \frac{0.5274 \arctan[0.084(W/h)^{1.9413/\xi_2}]}{\epsilon_{re}^{0.9236}} \\ \xi_4 &= 1 + 0.0377 \arctan[0.067(W/h)^{1.456}] \cdot \{6 - 5 \exp[0.036(1 - \epsilon_r)]\} \\ \xi_5 &= 1 - 0.218 \exp(-7.5W/h)\end{aligned}$$

and the expressions for effective dielectric constant ϵ_{re} given in [22] are used.

The effect of dispersion on $\Delta\ell_{oc}$ has been analyzed by Itoh [23]. At millimeter wavelengths the value of $\Delta\ell_{oc}$ is considerably smaller than that computed by using the quasi-static approximation. However, for frequencies up to about 10 GHz, the quasi-static approach gives reasonably good results.

For thicker substrates and for wider microstrip lines, radiation from an open-end discontinuity becomes significant [24, 25]. Rigorous fullwave analyses based on the method of moments [26, 27] and spectral domain [28] for characterization of a microstrip open end have also been reported. Figure 3.15 is a typical example of the very few results available from such analyses. We note that as frequency increases, the radiation conductance associated with the open end increases while the capacitance decreases. Closed-form expressions for a microstrip open-end discontinuity model shown in Figure 3.16 are given as [28]

$$C_1 \left(\frac{25Z_{0m}}{h} \right) = 1.125 \tanh \left(1.358 \frac{W}{h} \right) - 0.315 \quad (\text{pF} \cdot \Omega) \quad (3.51a)$$

$$C_2 \left(\frac{25Z_{0m}}{h} \right) = 6.832 \tanh \left(0.0109 \frac{W}{h} \right) + 0.910 \quad (\text{pF} \cdot \Omega) \quad (3.51b)$$

$$L \left(\frac{25}{h Z_{0m}} \right) = 0.008285 \tanh \left(0.5665 \frac{W}{h} \right) + 0.0103 \quad (\text{nH}/\Omega) \quad (3.51c)$$

$$R/Z_{0m} = 1.024 \tanh \left(2.025 \frac{W}{h} \right) \quad (3.51d)$$

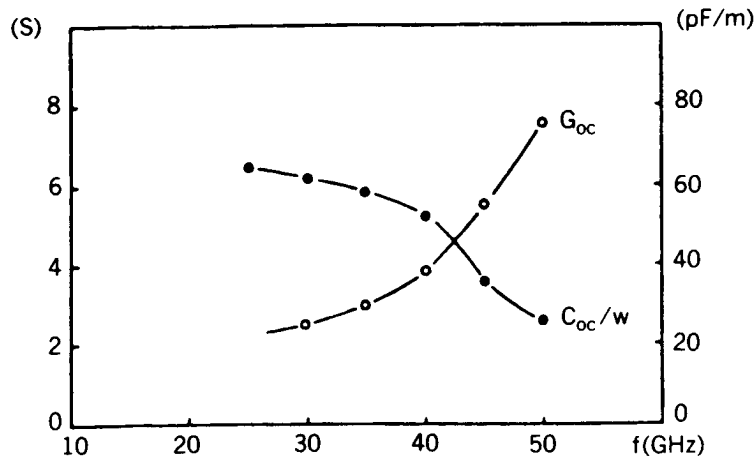


Figure 3.15 Normalized capacitance and radiation conductance of an open-ended microstrip line: $\epsilon_r = 9.6$, $W/h = 1$, and $h = 0.6$ mm (from [26], © 1985 IEEE. Reprinted with permission.).

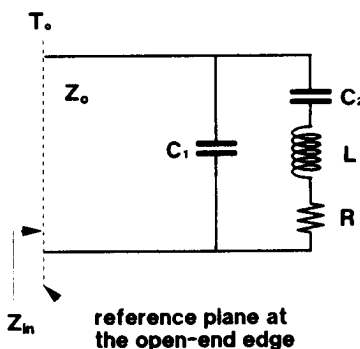


Figure 3.16 Equivalent circuit model for a microstrip open-end discontinuity (from [28], © 1994 IEEE. Reprinted with permission.).

where both h and W are in milli-inches and Z_{0m} is the characteristic impedance of the microstrip line.

3.4.2 Gaps in a Microstrip

The characterization of a gap in a microstrip is useful in the design of, for example, dc blocks, end coupled filters, and coupling elements to resonators. A microstrip gap and its equivalent circuits are shown in Figure 3.17. There are three sets of published data for gap capacitance [1, 4, 9]. Perhaps the results of Benedek and

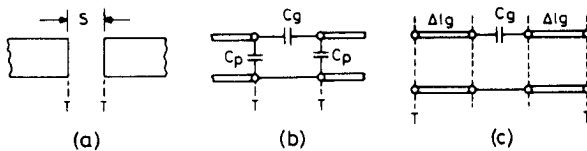


Figure 3.17 (a) A microstrip gap and (b, c) its equivalent circuits.

Silvester are the most accurate as the other two involve the subtraction of nearly equal large numbers. The available results are shown in Figure 3.18. The two sets of points shown in Figure 3.18(b) correspond to results of Maeda [4] and Farrar and Adam [1]. The capacitances C_{odd} and C_{even} are related to C_p and C_g by

$$C_{\text{even}} = 2 C_p$$

$$C_{\text{odd}} = 2 C_g + C_p \quad (3.52)$$

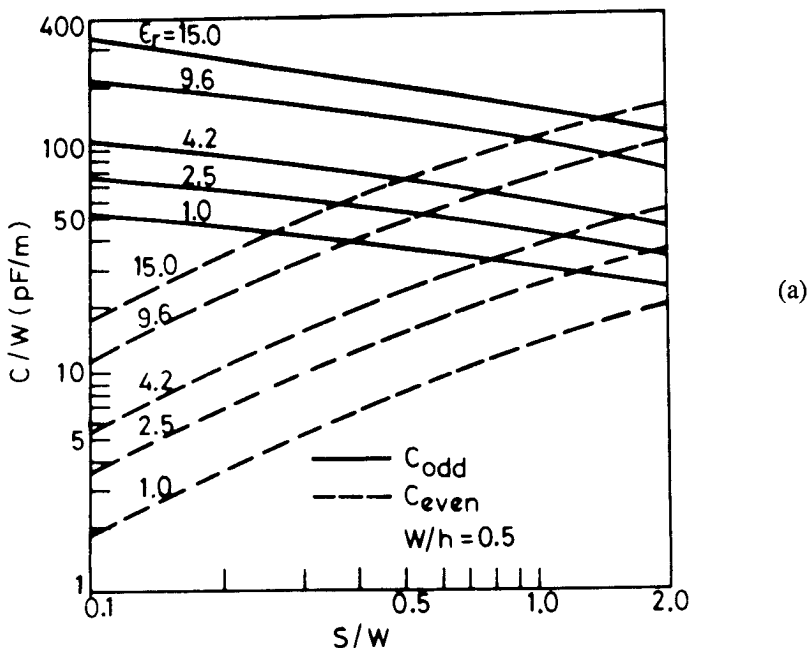


Figure 3.18 (a) Capacitances for a microstrip gap evaluated by using line sources with charge reversal ($W/h = 0.5$), (b) capacitances for a microstrip gap evaluated by using line sources with charge reversal ($W/h = 1.0$), and (c) capacitances for a microstrip gap evaluated by using line sources with charge reversal ($W/h = 2.0$) (from [8], © 1972 IEEE. Reprinted with permission.).

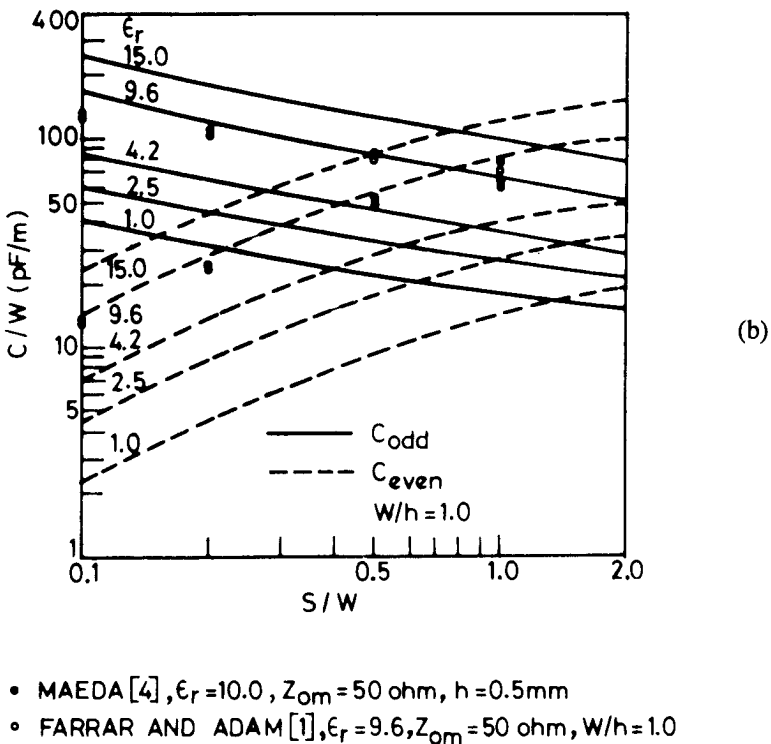


Figure 3.18 (continued).

Equivalent line length $\Delta\ell_g$ of Figure 3.17 may be calculated as

$$\frac{\Delta\ell_g}{h} = \frac{C_p}{W} \frac{c Z_{0m} W/h}{\sqrt{\epsilon_{re}}} \quad (3.53)$$

A comparison of computed and experimental results given by Maeda [4] is shown in Figure 3.19. Experimental results for C_g are derived from [29]. The agreement between the experimental results and computed values is reasonably good.

It may be noted that the curves of Figure 3.18 are well suited for polynomial approximation as has been done for the open-end capacitance discussed in the previous section. The closed-form expressions for C_{even} and C_{odd} for $\epsilon_r = 9.6$ and $0.5 \leq W/h \leq 2$ have been determined [17] by curve fitting the available numerical results [9]. The expressions are

$$C_{odd}/W \text{ (pF/m)} = \left(\frac{S}{W} \right)^{m_0} \exp(k_0) \quad (3.54)$$

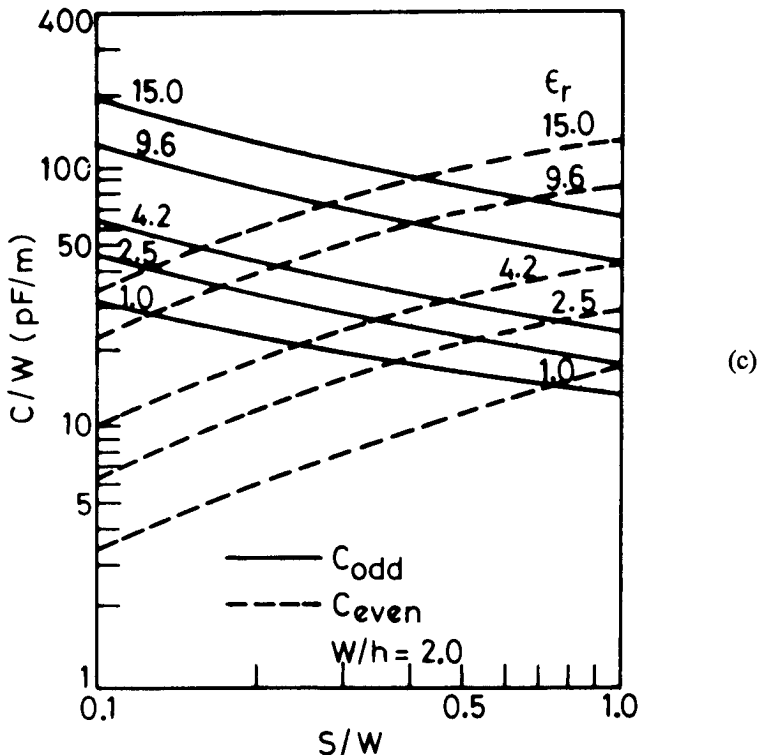


Figure 3.18 (continued).

$$C_{\text{even}}/W \text{ (pF/m)} = 12 \left(\frac{S}{W} \right)^{m_e} \exp(k_e) \quad (3.55)$$

where

$$\left. \begin{aligned} m_0 &= \frac{W}{h} (0.619 \log W/h - 0.3853) \\ k_0 &= 4.26 - 1.453 \log W/h \end{aligned} \right\} \quad (0.1 \leq S/W \leq 1.0)$$

$$m_e = 0.8675 \quad k_e = 2.043 \left(\frac{W}{h} \right)^{0.12} \quad (0.1 \leq S/W \leq 0.3)$$

$$m_e = \frac{1.565}{(W/h)^{0.16}} - 1 \quad k_e = 1.97 - \frac{0.03}{W/h} \quad (0.3 \leq S/W \leq 1.0)$$

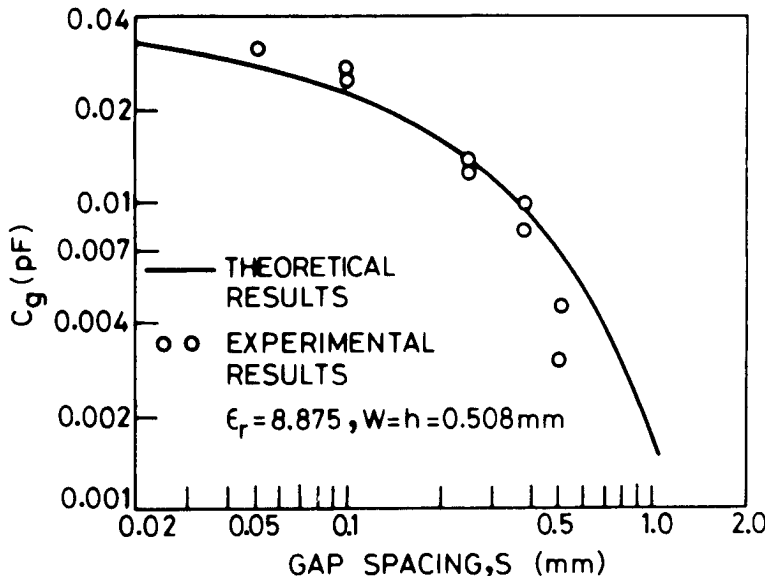


Figure 3.19 Comparison of theoretical and experimental results for gap capacitance (from [4], © 1972 IEEE. Reprinted with permission.).

The values of C_{odd} and C_{even} for other values of ϵ_r in the range $2.5 \leq \epsilon_r \leq 15$ can be calculated by scaling according to the relations

$$C_{\text{odd}}(\epsilon_r) = C_{\text{odd}}(9.6)(\epsilon_r/9.6)^{0.8} \quad (3.56)$$

$$C_{\text{even}}(\epsilon_r) = C_{\text{even}}(9.6)(\epsilon_r/9.6)^{0.9} \quad (3.57)$$

The accuracy of these expressions is within 7 percent for the above-mentioned set of parameters.

Closed-form expressions for a microstrip gap discontinuity based on the spectral domain method have been reported by Alexopoulos and Wu [28]. The model parameters shown in Figure 3.20 are evaluated for $\epsilon_r = 9.9$ using the following equations:

$$\begin{aligned}
 R_l/Z_{0m} &= 1.024 \tanh\left(2.025 \frac{W}{h}\right) \\
 &\cdot \tanh\left[\left(0.01584 + 0.0187 \frac{h}{W}\right) \frac{S}{h}\right. \\
 &\left. + \left(0.1246 + 0.0394 \sinh\left(\frac{W}{h}\right)\right)\right] \quad (3.58a)
 \end{aligned}$$

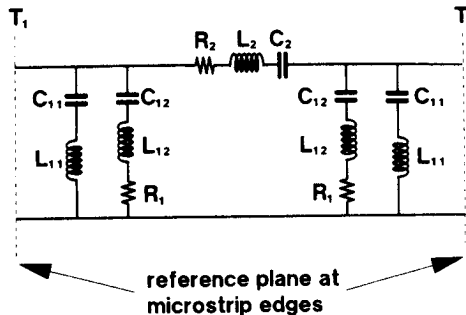


Figure 3.20 Equivalent circuit model for a microstrip gap discontinuity (from [28], © 1994 IEEE. Reprinted with permission.).

$$\begin{aligned}
 C_2\left(\frac{25Z_{0m}}{h}\right) = & \left[0.1776 + 0.05104 \ell_n\left(\frac{W}{h}\right) \right] \frac{h}{S} \\
 & + \left[0.574 + 0.3615 \frac{h}{W} + 1.156 \ell_n\left(\frac{W}{h}\right) \right] \\
 & \cdot \operatorname{sech}\left(2.3345 \frac{S}{h}\right) \quad (\text{pF} \cdot \Omega)
 \end{aligned} \tag{3.58b}$$

$$\begin{aligned}
 L_2\left(\frac{25}{hZ_{0m}}\right) = & \left[0.00228 + \frac{0.0873}{7.52W/h + \cosh(W/h)} \right] \\
 & \cdot \sinh\left(2.3345 \frac{S}{h}\right) \quad (\text{nH}/\Omega)
 \end{aligned} \tag{3.58c}$$

$$\begin{aligned}
 R_2/Z_{0m} = & \left[-1.78 + 0.749 \frac{W}{h} \right] \frac{S}{h} \\
 & + \left[1.196 - 0.971 \ell_n\left(\frac{W}{h}\right) \right] \cdot \sinh\left(2.3345 \frac{S}{h}\right)
 \end{aligned} \tag{3.58d}$$

$$\begin{aligned}
 C_{11}\left(\frac{25Z_{0m}}{h}\right) = & \left[1.125 \tanh\left(1.358 \frac{W}{h}\right) - 0.315 \right] \\
 & \cdot \tanh\left[\left(0.0262 + 0.184 \frac{h}{W}\right)\right] \\
 & + \left(0.217 + 0.0619 \ell_n\left(\frac{W}{h}\right)\right) \frac{S}{h} \quad (\text{pF} \cdot \Omega)
 \end{aligned} \tag{3.59a}$$

$$\begin{aligned}
 C_{12} \left(\frac{25Z_{0m}}{h} \right) = & \left[6.832 \tanh \left(0.0109 \frac{W}{h} \right) + 0.910 \right] \\
 & \cdot \tanh \left[\left(1.411 + 0.314 \frac{h}{W} \right) \right. \\
 & \left. + \left(\frac{S}{h} \right)^{1.248+0.360\tan^{-1}(W/h)} \right] \quad (\text{pF} \cdot \Omega) \tag{3.59b}
 \end{aligned}$$

$$\begin{aligned}
 L_{11} \left(\frac{25}{hZ_{0m}} \right) = & \left[0.134 + 0.0436 \ell_n \frac{h}{W} \right] \\
 & \cdot \exp \left[- \left(3.656 + 0.246 \frac{h}{W} \right) \right. \\
 & \left. + \left(\frac{S}{h} \right)^{1.739+0.390\ell_n(W/h)} \right] \quad (\text{nH}/\Omega) \tag{3.59c}
 \end{aligned}$$

$$\begin{aligned}
 L_{12} \left(\frac{25}{hZ_{0m}} \right) = & \left[0.008285 \tanh \left(0.5665 \frac{W}{h} \right) + 0.0103 \right] \\
 & + \left[0.1827 + 0.00715 \ell_n \frac{W}{h} \right] \\
 & \cdot \exp \left[- \left(5.207 + 1.283 \tanh \left(1.656 \frac{h}{W} \right) \right) \right. \\
 & \left. + \left(\frac{S}{h} \right)^{0.542+0.873\tan^{-1}(W/h)} \right] \quad (\text{nH}/\Omega) \tag{3.59d}
 \end{aligned}$$

3.4.3 Steps in Width

Steps in width exist at junctions of two microstrip lines that have different impedances. This type of discontinuity is encountered when designing matching transformers, couplers, filters, and transitions. The configurations of a step discontinuity and its equivalent circuit are shown in Figure 3.21. Results for excess capacitance C_s have been given by Farrar and Adams [1], Benedek and Silvester [9], and Gupta and Gopinath [30]. Data for C_s given by Gupta and Gopinath are most extensive and are presented in Figure 3.22 for $\epsilon_r = 2.3$ and 9.6. The small dotted curve in Figure 3.22(b) corresponds to [9] and has been inserted to compare the two sets

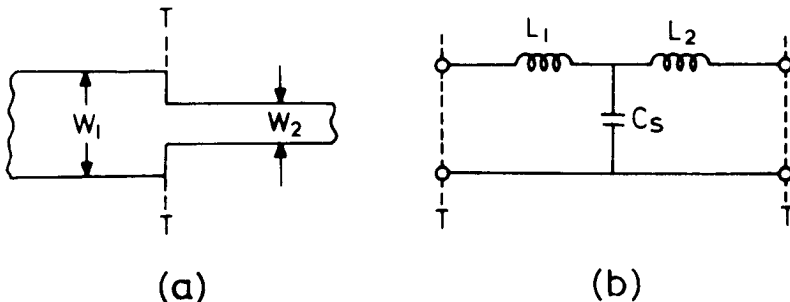


Figure 3.21 (a) A microstrip step discontinuity and (b) its equivalent circuit.

of results. In terms of distributed elements, the discontinuity capacitance C_s has the effect of an increase in the wide line's length and an equal decrease in the narrow line's length. As these effects are small, the change in lengths may be approximated by $\Delta\ell_{oc}(1 - W_2/W_1)$ [16] where $\Delta\ell_{oc}$ is the open-circuit line extension calculated from (3.48) for line width W_1 . A more accurate expression for the change in lengths that is applicable for a wide range of ϵ_r values is given by Rizzoli et al. [31] as $\Delta\ell_{oc}f(\epsilon_r)[1 - W_2/W_1]$, where the function $f(\epsilon_r)$ has the form

$$f(\epsilon_r) = 1.25 + 0.19 \tan^{-1}(6.16 - \epsilon_r) \quad (3.60)$$

Measurement of the step capacitance has been reported by Easter et al. [32]. A comparison with the results in Figure 3.22 is difficult because of insufficient information about the experimental data.

Some results for the inductance associated with a step discontinuity in a microstrip are also available [15]. These are based on the method of quasi-static computation of inductance discussed in Section 3.3. Inductance L_s plotted in Figure 3.23 is the total of inductances L_1 and L_2 shown in Figure 3.21 and has been normalized with respect to $(L_{w1}h)$ where L_{w1} is the inductance per unit length of microstrip of width W_1 given by

$$L_{w1} = \frac{Z_{0m}\sqrt{\epsilon_{re}}}{c} \quad (\text{H/m}) \quad (3.61)$$

where Z_{0m} and ϵ_{re} correspond to width W_1 and $c = 3 \times 10^8 \text{ m/s}$. A comparison of theoretical and experimental results is also available [15] and is shown in Figure 3.24. The experiments were carried out in the frequency range of 6.5 GHz to 10 GHz. It may be pointed out that inductance values are in the range of $1.4 \times 10^{-11} \text{ H}$ to $9.6 \times 10^{-11} \text{ H}$.

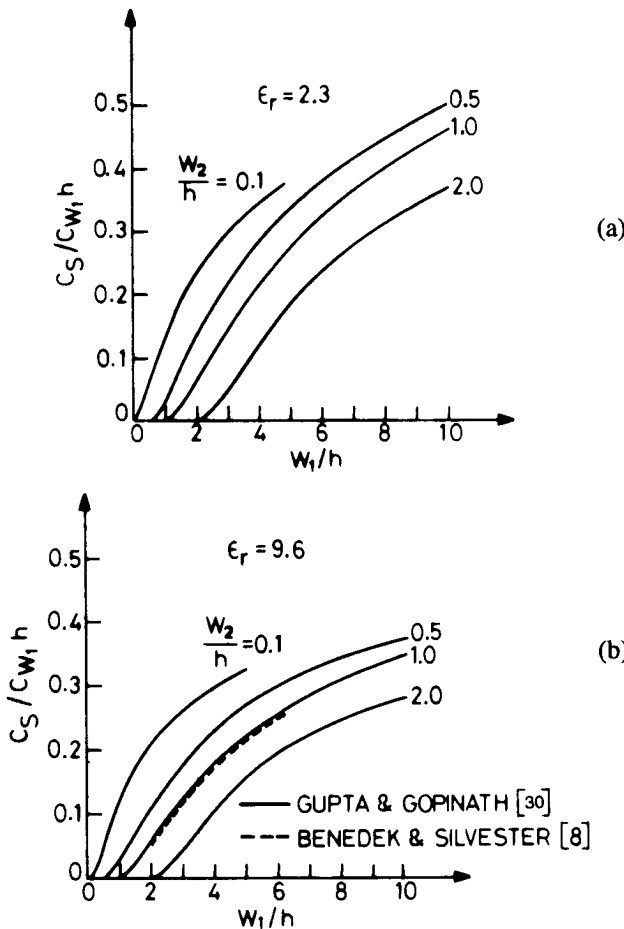


Figure 3.22 Shunt capacitance for a step discontinuity. C_{w1} ($= \sqrt{\epsilon_r}/cZ_{0m}$) denotes capacitance per unit length of the line of width W_1 (from [30], © 1977 IEEE. Reprinted with permission.).

To factor in the effect of discontinuity inductances in the circuit design, the total inductance L_s may be separated into L_1 and L_2 (as a first-order approximation) as follows:

$$L_1 = \frac{L_{w1}}{L_{w1} + L_{w2}} L_s \quad (3.62a)$$

$$L_2 = \frac{L_{w2}}{L_{w1} + L_{w2}} L_s \quad (3.62b)$$

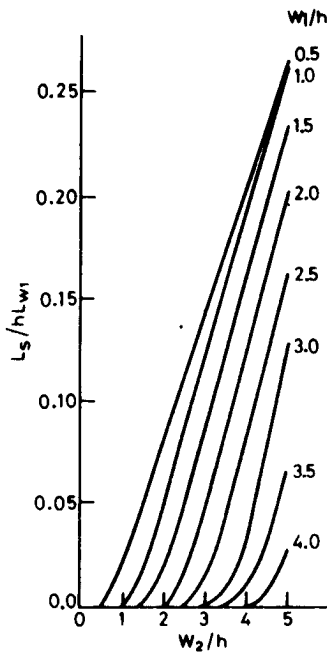


Figure 3.23 Calculated inductance values for a microstrip step discontinuity. L_{w1} ($= \sqrt{\epsilon_r} Z_{0m}/c$) denotes inductance per unit length of the line of width W_1 (from [15], © 1976 IEEE. Reprinted with permission.).

and corresponding additional line lengths may be written as

$$\frac{\Delta\ell_1}{h} = \frac{\Delta\ell_2}{h} = \frac{L_s}{(L_{w1} + L_{w2})h} \quad (3.63)$$

The closed-form expressions for C_s and L_s have been derived by curve fitting the numerical results. The expressions are given as

$$\frac{C_s}{\sqrt{W_1 W_2}} \text{ (pF/m)} = (10.1 \log \epsilon_r + 2.33) \frac{W_1}{W_2} - 12.6 \log \epsilon_r - 3.17 \quad (3.64)$$

(for $\epsilon_r \leq 10$; $1.5 \leq W_1/W_2 \leq 3.5$)

This expression yields a percentage error of less than 10 percent. A more accurate expression can be written for alumina substrates ($\epsilon_r = 9.6$) as

$$\frac{C_s}{\sqrt{W_1 W_2}} \text{ (pF/m)} = 130 \log \left(\frac{W_1}{W_2} \right) - 44 \quad (\text{for } 3.5 \leq W_1/W_2 \leq 10) \quad (3.65)$$

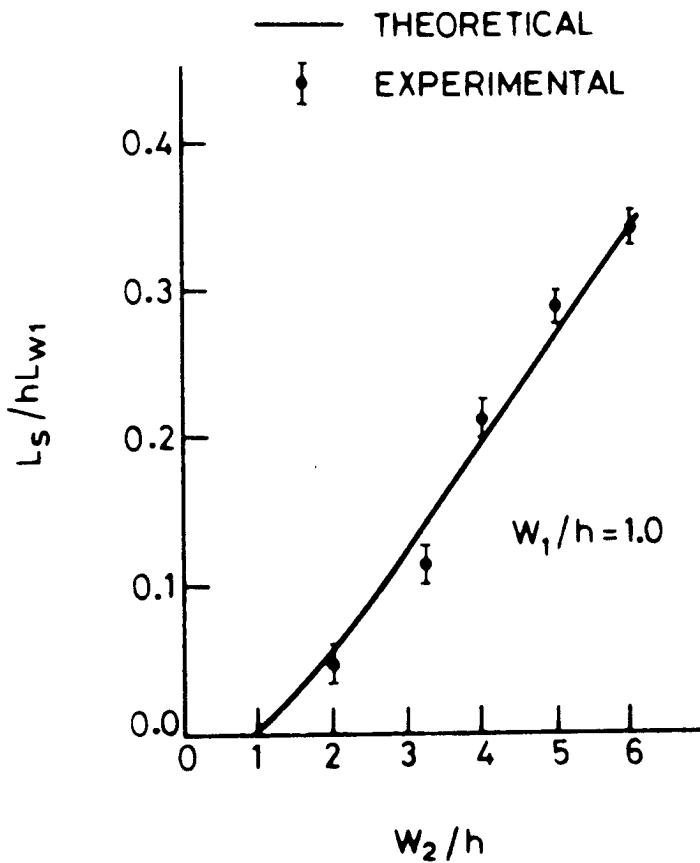


Figure 3.24 Comparison of theoretical and experimental results for step discontinuity inductance. Bars indicate the experimental error range (from [15], © 1976 IEEE. Reprinted with permission.).

The above relation is accurate to within 0.5 percent. The expression for inductance is given by

$$\frac{L_s}{h} \text{ (nH/m)} = 40.5 \left(\frac{W_1}{W_2} - 1.0 \right) - 75 \log \frac{W_1}{W_2} + 0.2 \left(\frac{W_1}{W_2} - 1 \right)^2 \quad (3.66)$$

Equation (3.66) has an error of less than 5 percent for $W_1/W_2 \leq 5$ and $W_1/h = 1.0$. More general expressions for C_s and L_s are given as

$$C_s = 0.00137 \frac{\sqrt{\epsilon_{\text{rel}}}}{Z_{0m1}} \left(1 - \frac{W_2}{W_1}\right) h \left[\frac{\epsilon_{\text{rel}} + 0.3}{\epsilon_{\text{rel}} - 0.258} \right] \left[\frac{W_1/h + 0.264}{W_1/h + 0.8} \right] \quad (\text{pF}) \quad (3.67\text{a})$$

$$L_s = 0.000987 h \left(1 - \frac{Z_{0m1}}{Z_{0m2}} \sqrt{\frac{\epsilon_{\text{rel}}}{\epsilon_{\text{rel}}^2}}\right)^2 \quad (\text{nH}) \quad (3.67\text{b})$$

where Z_{0m} and ϵ_{re} are the microstrip line characteristic impedance and effective dielectric constant, respectively, and the substrate thickness h is in micrometers.

3.4.4 Bends

A microstrip bend may be formed by two lines of equal or unequal impedances and is normally used for introducing flexibility in the layout of the circuit design. The equivalent circuit of a microstrip bend with lines of equal impedances is shown in Figure 3.25. The most common form of microstrip bend used in circuits and investigated analytically is a right-angled bend ($\phi_b = 90^\circ$).

Silvester and Benedek [8] have computed the electrostatic value of the excess capacitance of right-angled bends; their results are shown in Figure 3.26. Experimental results given by Easter [33] are shown as three small circles in this figure. It is observed that the agreement between the theoretical and experimental results is reasonably good only for microstrips with $50\text{-}\Omega$ impedance.

Inductance for right-angled bends has been computed by Thomson and Gopinath [14], and their results are shown in Figure 3.27, wherein the normalized inductance ($L_b/L_w h$) is plotted for different width: height ratios. A comparison to the experimental results of Easter [33] is also shown, but the agreement is not very good.

Closed-form expressions for right-angled bend discontinuities are given [17] as

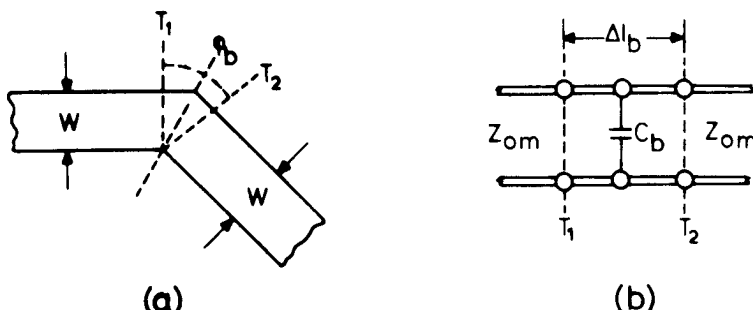


Figure 3.25 (a) Geometry and (b) equivalent circuit of a microstrip bend.

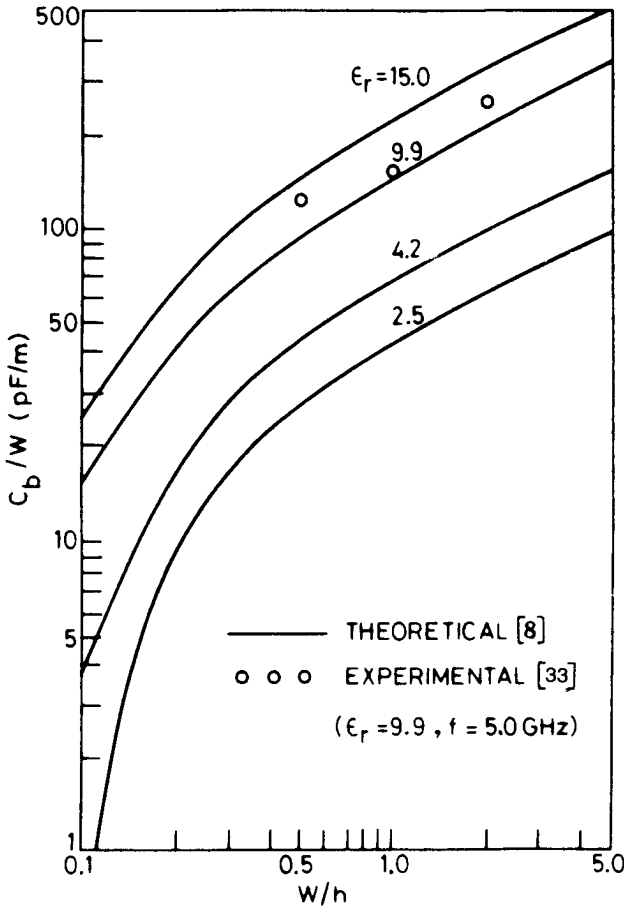


Figure 3.26 Discontinuity capacitance of a microstrip right-angled bend (from [8], © 1973 IEEE. Reprinted with permission.).

$$\frac{C_b}{W} \text{ (pF/m)} = \begin{cases} \frac{(14 \epsilon_r + 12.5) W/h - (1.83 \epsilon_r - 2.25)}{\sqrt{W/h}} + \frac{0.02 \epsilon_r}{W/h} & (W/h < 1) \\ (9.5 \epsilon_r + 1.25) W/h + 5.2 \epsilon_r + 7.0 & (W/h \geq 1) \end{cases} \quad (3.68a)$$

$$\frac{L_b}{h} \text{ (nH/m)} = 100(4\sqrt{W/h} - 4.21) \quad (3.69)$$

Equations (3.68) are accurate to within 5 percent for $2.5 \leq \epsilon_r \leq 15$ and $0.1 \leq W/h \leq 5$. The accuracy of (3.69) is about 3 percent for $0.5 \leq W/h \leq 2.0$.

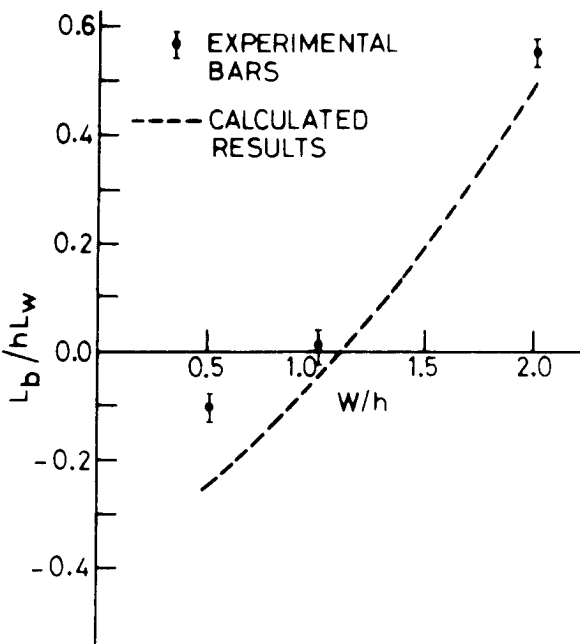


Figure 3.27 Discontinuity inductance of a microstrip right-angled bend. Bars indicate the experimental error range (from [14], © 1968 IEEE. Reprinted with permission.).

3.4.5 T-Junctions

The T-junction is perhaps the most important discontinuity in a microstrip as it is found in most circuits such as impedance networks, stub filters, and branch-line couplers. A microstrip T-junction and its equivalent circuit are shown in Figure 3.28. The discontinuity capacitance C_T for this structure has been calculated by Silvester and Benedek [8]. Their results are shown in Figure 3.29. Capacitances shown in this figure are for per-unit main-line width. The inductance calculation for T-junctions have been carried out by Thomson and Gopinath [14]. Their results are shown in Figure 3.30. A comparison with the experimental results of Easter [33] is also shown. The agreement between the experimental and theoretical results for L_2 is not as good as for L_1 .

Closed-form expressions for the discontinuity reactances of the equivalent circuit shown in Figure 3.28(b) with a main-line impedance of 50Ω and for $\epsilon_r = 9.9$ have also been derived [17] as follows:

$$\frac{C_T}{W_1} \text{ (pF/m)} = \frac{100}{\tanh(0.0072 Z_0)} + 0.64 Z_0 - 261 \quad (25 \leq Z_0 \leq 100) \quad (3.70)$$

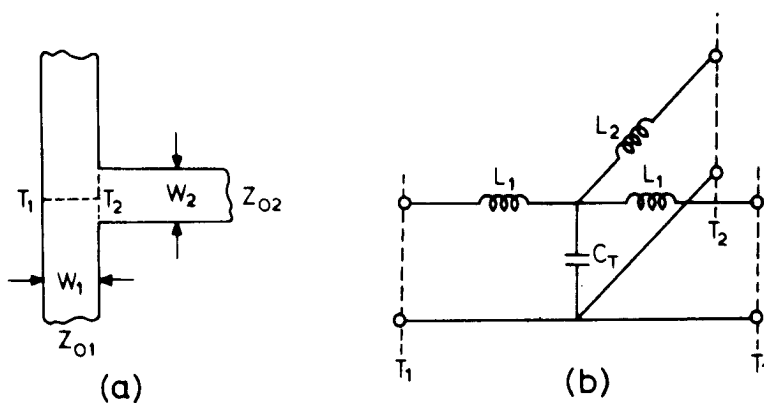


Figure 3.28 (a) A microstrip T-junction and (b) its equivalent circuit.

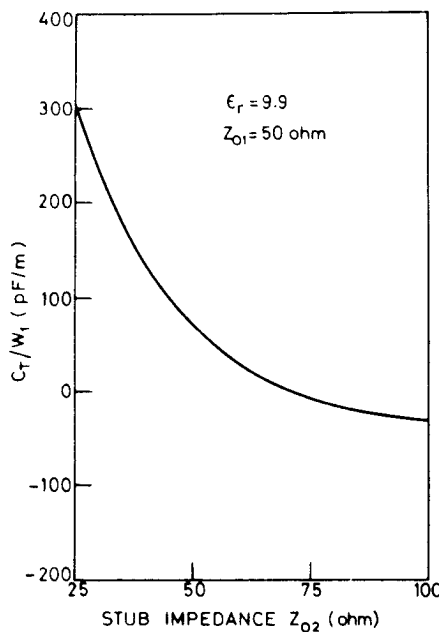


Figure 3.29 Discontinuity capacitance of a microstrip T-junction (from [8], © 1973 IEEE. Reprinted with permission.).

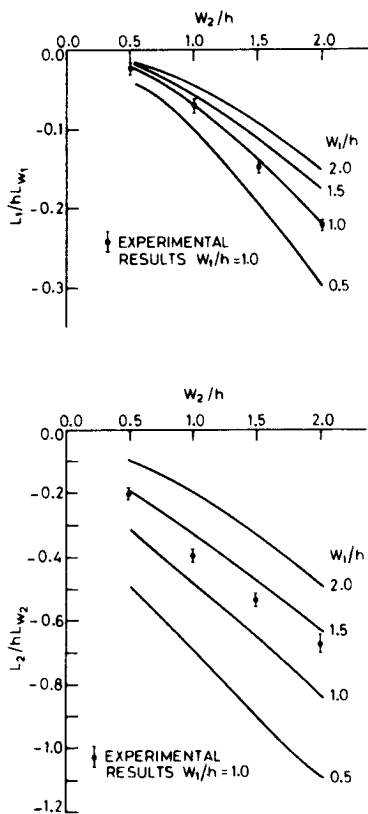


Figure 3.30 Discontinuity inductances of a microstrip T-junction (from [14], © 1968 IEEE. Reprinted with permission.).

where Z_0 is the characteristic impedance of the stub

$$\frac{L_1}{h} \text{ (nH/m)} = -\frac{W_2}{h} \left\{ \frac{W_2}{h} \left(-0.016 \frac{W_1}{h} + 0.064 \right) + \frac{0.016}{W_1/h} \right\} L_{w1} \quad (3.71)$$

$$(0.5 \leq (W_1/h, W_2/h) \leq 2.0)$$

$$\frac{L_2}{h} \text{ (nH/m)} = \left\{ \left(0.12 \frac{W_1}{h} - 0.47 \right) \frac{W_2}{h} + 0.195 \frac{W_1}{h} - 0.357 \right. \\ \left. + 0.0283 \sin \left(\pi \frac{W_1}{h} - 0.75\pi \right) \right\} L_{w2} \quad (1 \leq W_1/h \leq 2.0; 0.5 \leq W_2/h \leq 2) \quad (3.72)$$

where L_w is the inductance per unit length for a microstrip of width W . The equations have an error of less than 5 percent.

Equations (3.70) to (3.72) hold for the symmetric T-junction shown in Figure 3.28(a). For a nonsymmetrical T-junction (Figure 3.31a), an equivalent circuit like that shown in Figure 3.31(b) has been proposed [18]. It has been suggested that for moderate nonsymmetry, the results for the symmetrical case may be extended to the nonsymmetrical case as follows. For the main arm turns ratio, use the main-line impedance of the side being calculated. For the sidearm reference plane displacement and the shunt susceptance, use the main line impedance equal to the geometric mean of the two actual ones. The expressions for the symmetric case are

$$\frac{d_1}{D_2} = 0.055 \left[1 - 2 \frac{Z_1}{Z_2} \left(\frac{f}{f_{pl}} \right)^2 \right] \frac{Z_1}{Z_2} \quad (3.73)$$

$$\frac{d_2}{D_1} = 0.5 - \left[0.05 + 0.7 \exp \left(-1.6 \frac{Z_1}{Z_2} \right) + 0.25 \frac{Z_1}{Z_2} \left(\frac{f}{f_{pl}} \right)^2 - 0.17 \ell_n \frac{Z_1}{Z_2} \right] \frac{Z_1}{Z_2} \quad (3.74)$$

$$n^2 = 1 - \pi \left(\frac{f}{f_{pl}} \right)^2 \left[\frac{1}{12} \left(\frac{Z_1}{Z_2} \right)^2 + \left(0.5 - \frac{d_2}{D_1} \right)^2 \right] \quad (3.75)$$

$$\frac{B_T \lambda_1}{Y_2 D_1} = 5.5 \frac{\epsilon_r + 2}{\epsilon_r} \left[1 + 0.9 \ell_n \frac{Z_1}{Z_2} + 4.5 \frac{Z_1}{Z_2} \left(\frac{f}{f_{pl}} \right)^2 \right. \\ \left. - 4.4 \exp \left(-1.3 \frac{Z_1}{Z_2} \right) - 20 \left(\frac{Z_2}{\eta_0} \right)^2 \right] n^{-2} \frac{d_1}{D_2} \quad (3.76)$$

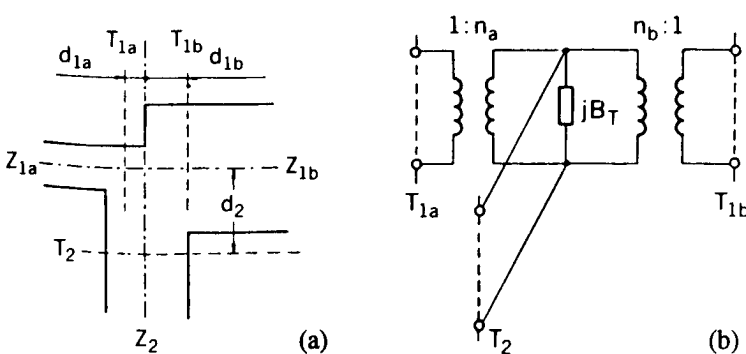


Figure 3.31 Equivalent circuit for modeling a nonsymmetric T-junction in microstriplines (from [18], © 1981 IEEE. Reprinted with permission.).

where D , f_p , Z , and λ are the equivalent parallel plate line width, first higher order mode cut-off frequency, characteristic impedance, and guide wavelength of the microstrip line. The subscripts 1 and 2 represent series and shunt lines. Expressions for D and f_p are given as

$$D = \eta_0 h / (\sqrt{\epsilon_{\text{re}}} Z) \quad (3.77)$$

$$f_p \text{ (GHz)} = 0.4Z/h \quad (3.78)$$

where $\eta_0 = 377 \Omega$ and h is in millimeters.

3.4.6 Cross Junctions

One of the most common applications of a cross junction is for the realization of low impedance stubs. When a low impedance stub has a strip width large enough to sustain transverse resonance modes, one of the possible solutions is to employ two stubs in parallel, connected on either side of the main line. The impedance of each of the equivalent stubs is equal to twice the impedance of the simulated stub.

The geometry of a microstrip cross junction and its equivalent circuit are shown in Figure 3.32. Capacitance C_+ has been calculated by Silvester and Benedek [8], and their results are shown in Figure 3.33. Inductances associated with a cross junction have been computed by Gopinath et al. [15] but are expressed in terms of a somewhat different equivalent circuit (shown in Figure 3.34). Inductance results

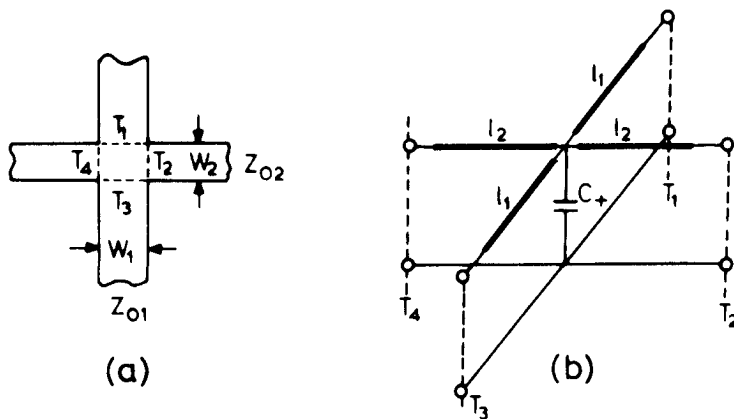


Figure 3.32 (a) Geometry and (b) equivalent circuit of a microstrip cross junction.

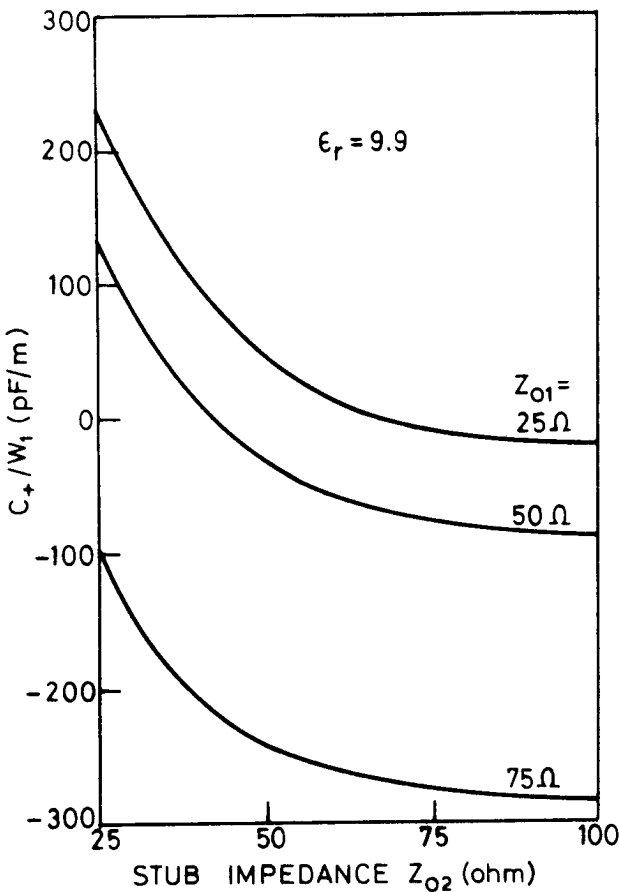
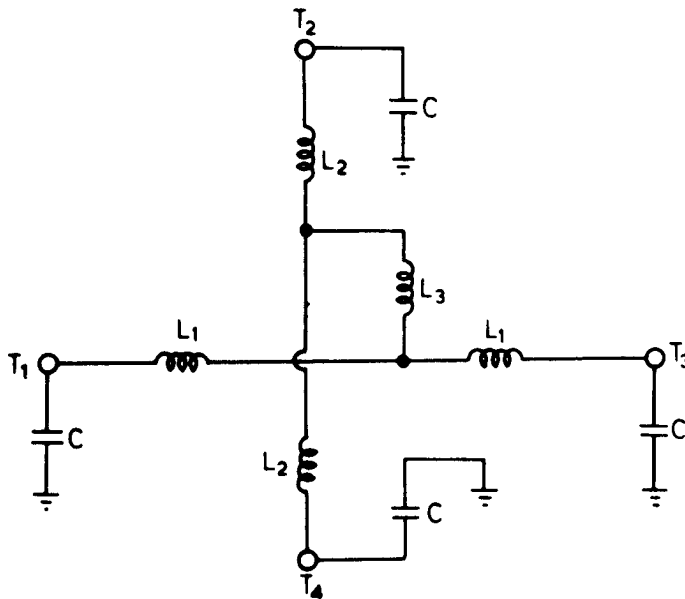


Figure 3.33 Discontinuity capacitance of a microstrip cross junction (from [8], © 1973 IEEE. Reprinted with permission.).

are shown in Figure 3.35(a, b). Figure 3.35(a) presents calculated values of L_1 normalized to $L_{w1}h$ of the cross junction for different W_1/h and W_2/h . This same set of curves is to be used to estimate normalized L_2 by interchanging W_1 and W_2 . Calculated values of L_3 normalized to $L_{w1}h$ are shown in Figure 3.35(b). Only one experimental point due to Easter [33] is available for comparison and is shown in these figures. The agreement is good for L_1 and L_2 but not for L_3 .

Closed-form expressions for cross-junction discontinuities have been derived [17] by curve fitting the available numerical results for capacitances and inductances for $\epsilon_r = 9.9$. The expressions are accurate to within 5 percent and are given as



$$C = C_+/4$$

Figure 3.34 An equivalent circuit for a microstrip cross junction using lumped inductors (from [15]. © 1976 IEEE. Reprinted with permission.).

$$\begin{aligned} \frac{C_+}{W_1} \text{ (pF/m)} &= \left[\log \frac{W_1}{h} \left\{ 86.6 \frac{W_2}{h} - 30.9 \left(\frac{W_2}{h} \right)^{1/2} + 367 \right\} + \left(\frac{W_2}{h} \right)^3 \right. \\ &\quad \left. + 74 \frac{W_2}{h} + 130 \right] \left(\frac{W_1}{h} \right)^{-1/3} \\ &\quad - 240 + \frac{2}{W_2/h} - 1.5 \frac{W_1}{h} \left(1 - \frac{W_2}{h} \right) \end{aligned} \quad (3.79)$$

$$(0.3 \leq W_1/h \leq 3.0 \text{ and } 0.1 < W_2/h \leq 3.0)$$

$$\begin{aligned} \frac{L_1}{h} \text{ (nH/m)} &= \left\{ \frac{W_1}{h} \left[165.6 \frac{W_2}{h} + 31.2 \sqrt{\frac{W_2}{h}} - 11.8 \left(\frac{W_2}{h} \right)^2 \right] \right. \\ &\quad \left. - 32 \frac{W_2}{h} + 3 \right\} \left(\frac{W_1}{h} \right)^{-3/2} \end{aligned} \quad (3.80)$$

$$\begin{aligned} - \frac{L_3}{h} \text{ (nH/m)} &= 337.5 + \left(1 + \frac{7}{W_1/h} \right) \frac{1}{W_2/h} - 5 \frac{W_2}{h} \cos \left[\frac{\pi}{2} \left(1.5 - \frac{W_1}{h} \right) \right] \end{aligned} \quad (3.81)$$

$$(0.5 \leq (W_1/h, W_2/h) \leq 2.0)$$

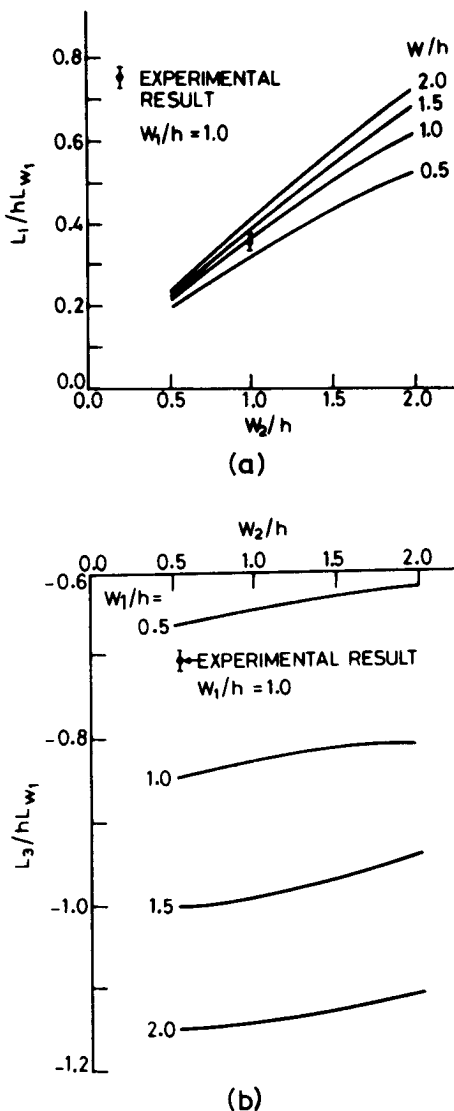


Figure 3.35 Discontinuity inductances L_1 , shown in (a), and L_3 , in (b), for a cross junction (from [15], © 1976 IEEE. Reprinted with permission.).

where $C = C_+/4$. The unsymmetric cross junction has been studied experimentally [34] and compared with the T-junction. This comparison indicates that the T-junction data may be used as a first step to estimate the properties of the cross junction. An approximate value of C_+ may be calculated by using $C_+ = 0.75 C_m$ where

C_m is the capacitance of the uniform microstrip line of widest width in the cross junction.

3.4.7 Notch

A notch or a narrow transverse slit in the strip conductor of a microstrip line can be introduced to realize a series inductance. The configuration of this discontinuity and that of its equivalent circuit are shown in Figure 3.36. The value of the series inductance L_N can be obtained from the approximate relation [35]

$$\frac{L_N}{h} \text{ (nH/mm)} = 2 \left(1 - \frac{Z_{0m}}{Z'_{0m}} \sqrt{\frac{\epsilon_{re}}{\epsilon'_{re}}} \right)^2 \quad (3.82)$$

where ϵ_{re} and ϵ'_{re} are the effective dielectric constants for microstrip lines with widths W and $(W - b)$, respectively, and Z_{0m} and Z'_{0m} are the corresponding impedances. The substrate thickness h is measured in millimeters. The expression for L_N above is valid for $0 \leq b/W \leq 0.9$ and $a \leq h$.

3.5 COMPENSATED MICROSTRIP DISCONTINUITIES

In microwave integrated circuit designs, the reactances introduced by microstrip discontinuities should either be taken into account or microstrip structures with compensated discontinuities should be used. In general, compensated discontinuities improve the circuit performance as well as the bandwidth. Usually chamfered bends or rounded corners are used in MICs and MMICs. The chamfered discontinuity technique is also known as the discontinuity compensation in which the discontinuity reactances are minimized by removing appropriate portions of the microstrip conductor near the discontinuity location. In this section we describe briefly the step in width, right-angled bend, and T-junction compensated microstrip discontinuities.

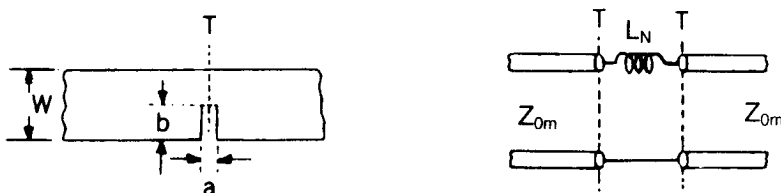


Figure 3.36 Notch discontinuity and its equivalent circuit.

3.5.1 Step in Width

The compensation of a step discontinuity using appropriate tapers has been reported [36–39]. In this case the effect of discontinuity reactances is reduced by chamfering the large width. The taper length depends upon the step ratio, dielectric constant value, and the substrate thickness (h). For $h/\lambda \leq 0.01$ and a step ratio less than 3, the step discontinuity reactance is negligible and generally no compensation technique is needed. Figure 3.37 shows three types of tapers. The taper shown in Figure 3.37(a) has been studied using a planar waveguide model and is described in Section 4.1.2. For a gradual taper, as shown in Figure 3.37(b), closed form expressions for the contour of taper compensating step discontinuities in microstrip lines are given by Raicu [39]. For a partial taper, as shown in Figure 3.37(c), discontinuity compensation on the 75- μm -to 125- μm -thick GaAs substrate has been arrived at by using a commercial fullwave analysis CAD tool. For a step-width ratio ranging from 3 to 13, the step discontinuity reactance is negligible when $L = W_1/8$ and $W'_1 = 0.33W_1$.

3.5.2 Bends

In practical circuits, microstrip bends are chamfered (see Figure 3.38) to compensate for the excess capacitance. Measurements by Easter et al. [32] indicate that a chamfer of approximately 72 percent as defined in Figure 3.38 is needed for a bend in a 50- Ω line on alumina substrate. This figure includes variation of normalized discontinuity susceptance (B/Y_0) as a function of percentage chamfer and shows that 72 percent chamfering will increase the length correction in the equivalent circuit to approximately 0.3 of the substrate thickness. The length of the chamfer (W_c) is approximately $1.8W$. Groll and Weidmann [40] have also found the optimum length of the chamfer using TDR measurements for a 50- Ω line on alumina substrate. They observed that $W_c = 1.83W$ gives a VSWR less than 1.11 up to 12 GHz. Hammerstad and Bekkadal [16] have found optimum lengths of the chamfer for

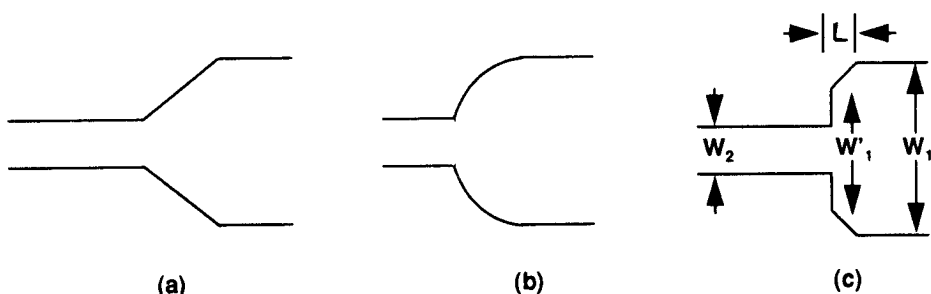


Figure 3.37 Three different kinds of compensated step-in-width discontinuity configurations with (a) linear taper, (b) curved taper, and (c) partial linear taper.

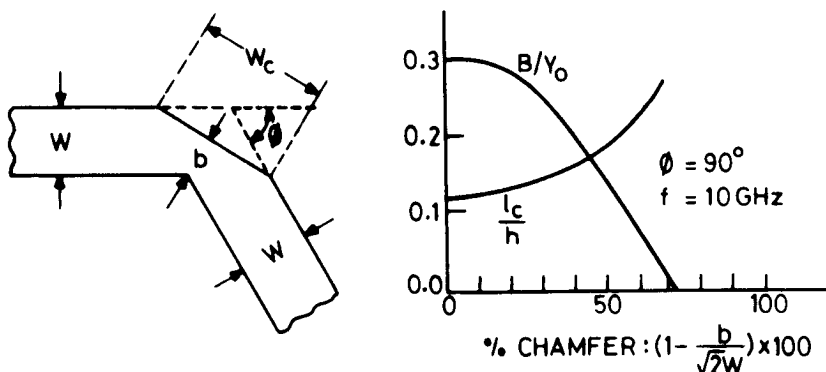


Figure 3.38 A chamfered bend and variations of shunt susceptance and series equivalent length of a chamfered right-angled bend as a function of percentage chamfer (from [32], © 1973 Microwave Exhibitions & Publishers (U.K.). Reprinted with permission.).

50- Ω microstrips on rexolite substrates having various bend angles ($\phi = 30^\circ, 60^\circ, 90^\circ$, and 120°). The value of W_c comes out to be about $1.8W$ in all of these cases.

Data on the optimum amount of chamfering have been given in [41] as

$$M = 52 + 65 \exp(-1.35 W/h) \quad (3.83)$$

for $W/h \geq 0.25$ and $\epsilon_r \leq 25$, where M is the percentage chamfer given by $(X/d) \times 100\%$ with X and d as shown in Figure 3.39. For a chamfered bend, the reflection coefficient $S_{11} \sim 0$, when the transmission line is terminated by an impedance equal to its characteristic impedance, but the discontinuity reactances cause a reduction Δb in length compared to that measured along the centerlines of the microstrip lines. A closed-form expression for this reduction in length may be written as [18]

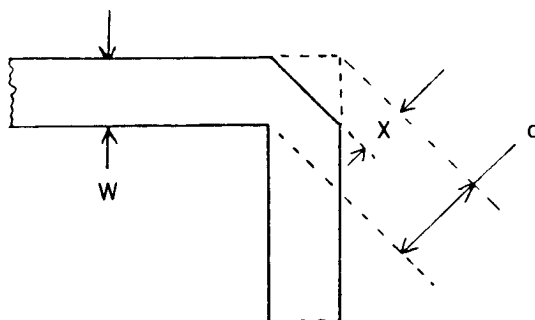


Figure 3.39 Geometry of a chamfered bend.

$$\Delta b/D = 0.16\{2 - (f/f_p)^2\} \quad (3.84)$$

where D and f_p are given by (3.77) and (3.78), respectively.

Several other types of chamfering, as shown in Figure 3.40, have been studied. Figure 3.41 compares calculated S_{11} for an uncompensated right-angled bend

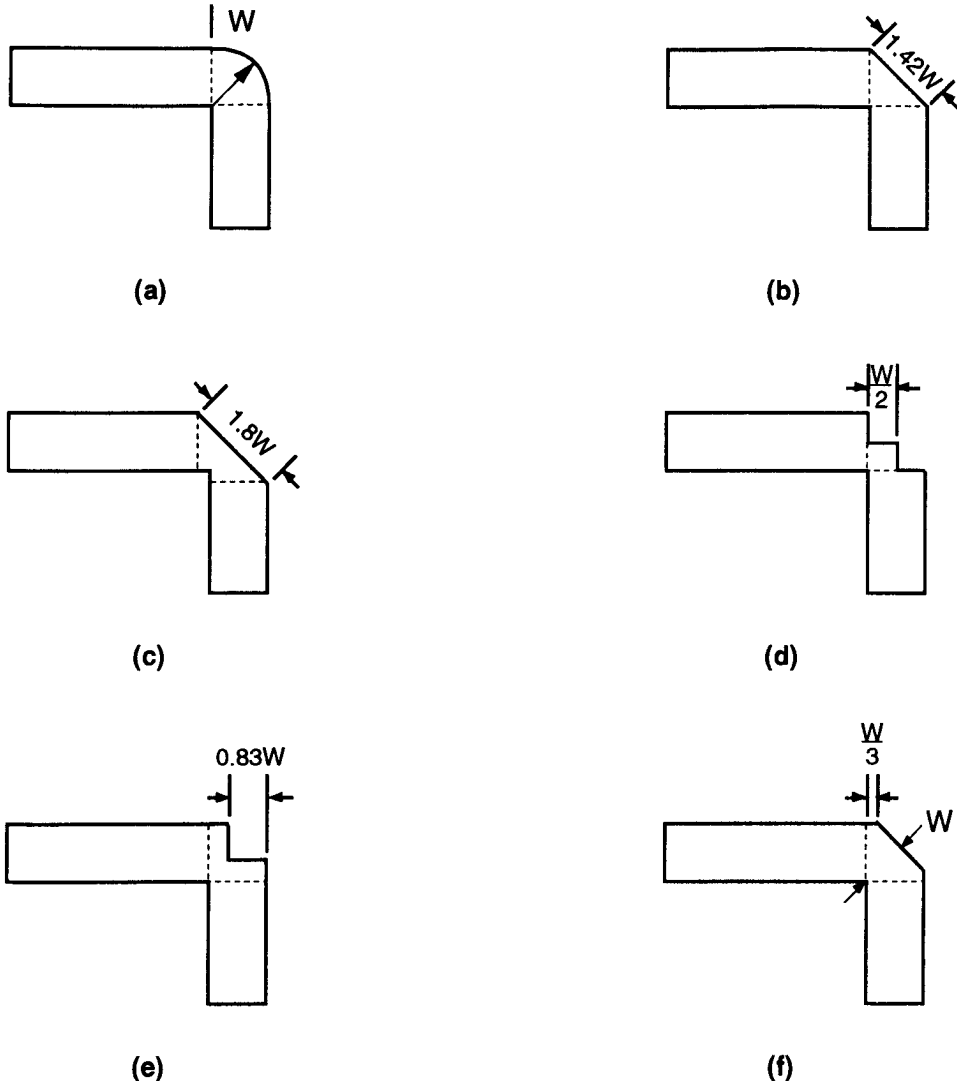


Figure 3.40 Six different configurations for compensated right-angled bends: (a, b, c, d, e, f).

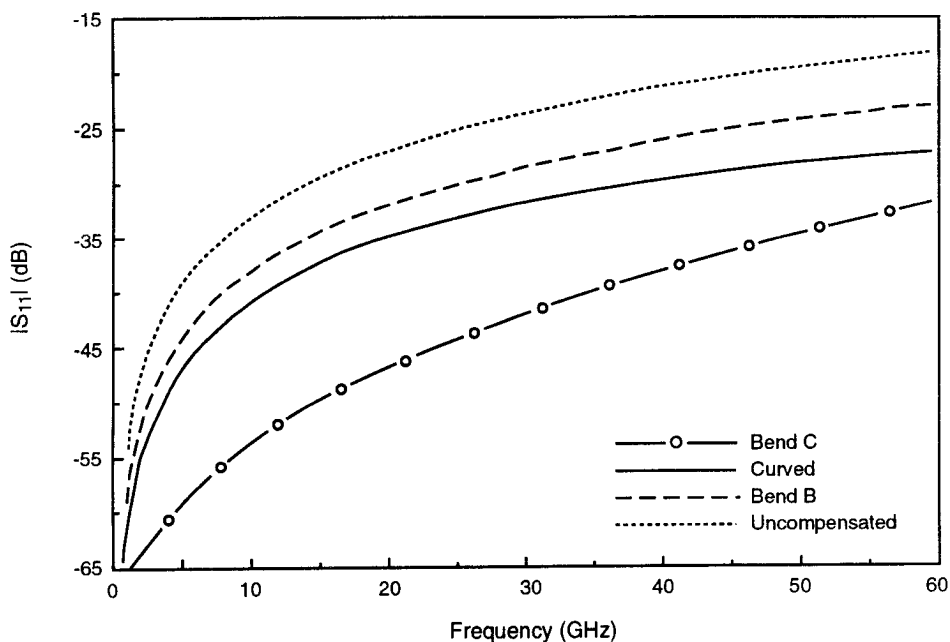


Figure 3.41 Magnitude of the reflection coefficient as a function of frequency for several compensated and uncompensated right-angled bends: $W = 73 \mu\text{m}$, $h = 100 \mu\text{m}$, $\epsilon_r = 12.9$, and the curved line has a mean radius = $2W$.

discontinuity with different compensated topologies. The configuration of Figure 3.40(c) provides the best compensation for this example.

3.5.3 T-Junction

The T-junction discontinuity compensation is much more difficult than the step-in width and right-angled bend discontinuity compensation techniques described in the previous subsections. Figure 3.42(a) shows T-junction compensation configurations using rectangular and triangular notches and their approximate dimensions for $h/\lambda \ll 1$. However, accurate dimensions of the compensated configuration depend upon the line widths, dielectric constant, and the substrate thickness. Figure 3.42(b) illustrates T-junction discontinuity minimization configurations in which the line widths are tapered to minimize the junction effect. In this case the taper length is about twice the line width or substrate thickness, whichever is larger.

T-junction discontinuities can also be compensated for by adjusting the lengths of the three microstrip lines forming the junction. The effect of the shunt susceptance can be compensated for by changing the microstrip widths near the junction

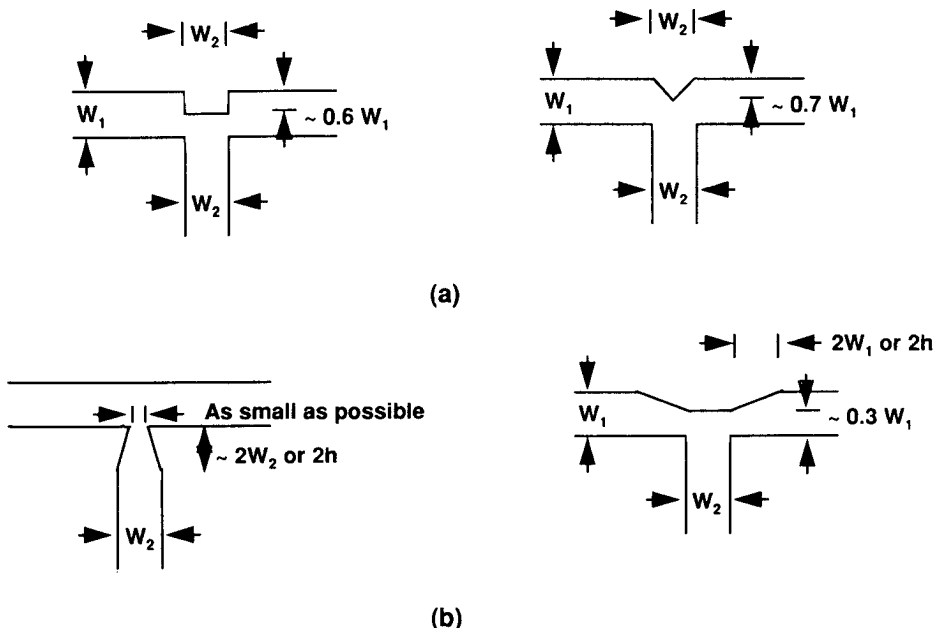


Figure 3.42 (a) T-junction discontinuity compensation configurations and (b) minimized T-junction discontinuity effect configuration.

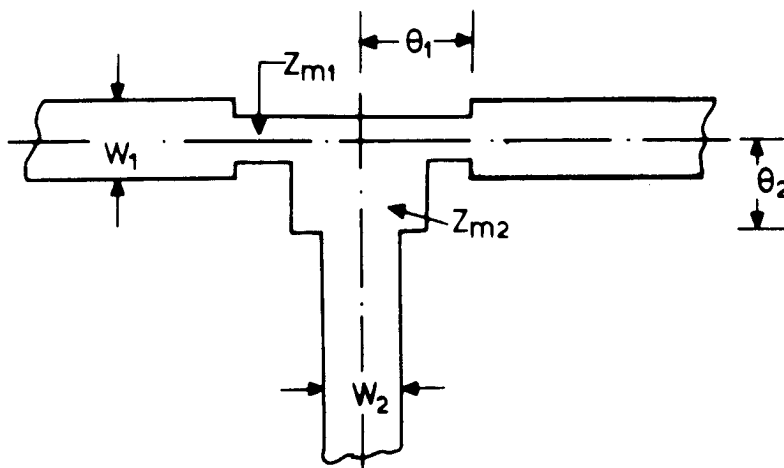


Figure 3.43 A T-junction with compensation for junction discontinuity reactances.

as shown in Figure 3.43. The lengths θ_1 , θ_2 and the characteristic impedances (Z_{m1} , Z_{m2}) of the modified portions near the junctions can be derived from the values of the discontinuity reactances [42].

The discussion on microstrip discontinuities is continued in Chapter 4, where fullwave analyses for discontinuities and the techniques for experimental measurements of discontinuity parameters are discussed.

References

- [1] Farrar, A., and A. T. Adams, "Matrix Methods for Microstrip three-dimensional Problems," *IEEE Trans.*, Vol. MTT-20, 1972, pp. 497–504.
- [2] Farrar, A., and A. T. Adams, "Computation of Static Capacitance Data for Single, Double and Triple Microstrip Line," *IEEE-GMTT Int. Microwave Symp. Digest*, 1970, pp. 257–261.
- [3] Farrar, A., and A. T. Adams, "Computation of Lumped Microstrip Capacities by Matrix Methods: Rectangular Sections and End Effect," *IEEE Trans.*, Vol. MTT-19, 1971, pp. 495–497; Also see correction *IEEE Trans.*, Vol. MTT-20, 1972, p. 294.
- [4] Maeda, M., "An Analysis of Gap in Microstrip Transmission Lines," *IEEE Trans.*, Vol. MTT-20, 1972, pp. 390–396.
- [5] Itoh, T., R. Mittra, and R. D. Ward, "A New Method for Solving Discontinuity Problems in Microstrip Lines," *1972 IEEE-GMTT Int. Microwave Symp. Digest*, pp. 68–70.
- [6] Itoh, T., R. Mittra, and R. D. Ward, "A Method for Computing Edge Capacitance of Finite and Semi-Finite Microstrip Lines," *IEEE Trans.*, Vol. MTT-20, 1972, pp. 847–849.
- [7] Silvester, P., and P. Benedek, "Equivalent Capacitance of Microstrip Open Circuits," *IEEE Trans.*, Vol. MTT-20, 1972, pp. 511–516.
- [8] Silvester, P., and P. Benedek, "Microstrip Discontinuity Capacitances for Right-angle Bends, T-junctions and Crossings," *IEEE Trans.*, Vol. MTT-21, 1973, pp. 341–346; see correction *IEEE Trans.*, Vol. MTT-23, 1975, p. 456.
- [9] Benedek, P., and P. Silvester, "Equivalent Capacitance for Microstrip Gaps and Steps," *IEEE Trans.*, Vol. MTT-20, 1972, pp. 729–733.
- [10] Horton, R., "The Electrical Characterization of a right-angled Bend in Microstrip Line," *IEEE Trans.*, Vol. MTT-21, 1973, pp. 427–429.
- [11] Horton, R., "Equivalent Representation of an Abrupt Impedance Step in Microstrip Line," *IEEE Trans.*, Vol. MTT-21, 1973, pp. 562–564.
- [12] Collin, R. E., *Field Theory of Guided Waves*, New York: McGraw-Hill, 1960, p. 148.
- [13] Yamashita, E., "Variational Method for the Analysis of Microstrip-like Transmission Lines," *IEEE Trans.*, Vol. MTT-16, 1968, pp. 529–535.
- [14] Thompson, A. F., and A. Gopinath, "Calculation of Microstrip Discontinuity Inductances," *IEEE Trans.*, Vol. MTT-23, 1975, pp. 648–655.
- [15] Gopinath, A., et al., "Equivalent Circuit Parameters of Microstrip Step Change in Width and Cross Junctions," *IEEE Trans.*, Vol. MTT-24, 1976, pp. 142–144.
- [16] Hammerstad, E. O., and F. Bekkadal, *Microstrip Handbook*, ELAB report STF 44 A74169, The University of Trondheim, The Norwegian Institute of Technology, 1975.
- [17] Garg, R., and I. J. Bahl, "Microstrip Discontinuities," *Int. J. Electron.*, Vol. 45, July 1978, pp. 81–87.
- [18] Hammerstad, E., "Computer-Aided Design of Microstrip Couplers with Accurate Discontinuity Models," *IEEE MTT-S Int. Microwave Symp. Digest*, 1981, pp. 54–56.
- [19] Kirschning, M., R. H. Jansen, and N. H. L. Koster, "Accurate Model for Open End Effect of Microstrip Lines," *Electron Lett.*, Vol. 17, February 1981, pp. 123–125.
- [20] Jansen, R. H., and N. H. L. Koster, "Accurate Results on the End Effect of Single and Coupled Microstrip Lines for Use in Microwave Circuit Design," *Arch. Elektr. Ubertr.*, Vol. 34, 1980, pp. 453–459.

- [21] Jansen, R. H., "Hybrid Mode Analysis of End Effects of Planar Microwave and Millimeter Wave Transmission Lines," *Proc. Inst. Electr. Eng.*, Vol. 128, Part H, 1981, pp. 77–86.
- [22] Hammerstad, E., and O. Jansen, "Accurate Models for Microstrip Computer-Aided Design," *IEEE MTT-S Int. Microwave Symp. Digest*, 1980, pp. 407–409.
- [23] Itoh, T., "Analysis of Microstrip Resonators," *IEEE Trans.*, Vol. MTT-22, November 1974, pp. 946–952.
- [24] James, J. R., and A. Henderson, "High Frequency Behavior of Microstrip Open-End Terminations," *IEE J. Microwaves, Opt. Acoust.*, Vol. 3, 1979, pp. 205–211.
- [25] Boukamp, J., and R. H. Jansen, "The High-Frequency Behavior of Microstrip Open Ends in Microwave Integrated Circuits Including Energy Leakage," *Proc. 14th European Microwave Conf.*, 1984, pp. 142–147.
- [26] Katehi, P. B., and N. G. Alexopoulos, "Frequency-Dependent Characteristics of Microstrip Discontinuities in Millimeter-Wave Integrated Circuits," *IEEE Trans.*, Vol. MTT-33, October 1985, pp. 1029–1035.
- [27] Jackson, R. W., and D. M. Pozar, "Full-Wave Analysis of Microstrip Open-End and Gap Discontinuities," *IEEE Trans.*, Vol. MTT-33, 1985, pp. 1036–1042.
- [28] Alexopoulos, N. G., and S.-C. Wu, "Frequency-Independent Equivalent Circuit Model for Microstrip Open-end and Gap Discontinuity," *IEEE Trans.*, Vol. MTT-42, July 1994, pp. 1268–1272.
- [29] *The Microwave Engineer's Handbook and Buyers Guide*, Dedham, MA: Horizon House, 1969, p. 72.
- [30] Gupta, C., and A. Gopinath, "Equivalent Circuit Capacitance of Microstrip Step Change in Width," *IEEE Trans.*, Vol. MTT-25, 1977, pp. 819–822.
- [31] Rizzoli, V., F. Mastri, and D. Masotti, "Modeling the Microstrip Impedance Step from Direct Measurements in the 1–27 GHz Band," *Microwave and Opt. Tech. Lett.*, Vol. 4, December 1991, pp. 562–566.
- [32] Easter, B., et al., "Resonant Techniques for the Accurate Measurement of Microstrip Properties and Equivalent Circuits," *Proc. 1973 European Microwave Conf.*, paper B. 7.5.
- [33] Easter, B., "The Equivalent Circuit of some Microstrip Discontinuities," *IEEE Trans.*, Vol. MTT-23, 1975, pp. 655–660.
- [34] Akello, R. J., et al., "Equivalent Circuit of the Asymmetric Cross Over Junction," *Electron. Lett.*, Vol. 13, 1977, pp. 117–118.
- [35] Hoefer, W. J. R., "Equivalent Series Inductivity of a Narrow Transverse Slit in Microstrip," *IEEE Trans.*, Vol. MTT-25, October 1977, pp. 822–824.
- [36] Malherbe, J. A. G., "The Compensation of Step Discontinuities in TEM-Mode Transmission Lines," *IEEE Trans.*, Vol. MTT-26, November 1978, pp. 883–885.
- [37] Chadha, R., and K. C. Gupta, "Compensation of Discontinuities in Planar Transmission Lines," *IEEE Trans. on Microwave Theory Tech.*, Vol. MTT-30, December 1982, pp. 2151–2156.
- [38] Hoefer, W. J. R., "A Contour Formula for Compensated Microstrip Steps and Open Ends," *IEEE MTT-S Int. Microwave Symp. Digest*, Boston, 1983, pp. 524–526.
- [39] Raicu, D., "Universal Taper for Compensation of Step Discontinuities in Microstrip Lines," *IEEE Microwave Guided Lett.*, Vol. 1, September 1991, pp. 249–251.
- [40] Groll, H., and W. Weidmann, "Measurement of Equivalent Circuit Elements of Microstrip Discontinuities by a Resonant Method," *Nachrichtentechnische Zeitschrift*, Vol. 28, 1975, pp. 74–77.
- [41] Douville, R. J. P., and D. J. James, "Experimental Study of Symmetric Microstrip Bends and Their Compensation," *IEEE Trans. on Microwave Theory Tech.*, Vol. MTT-26, 1978, pp. 175–182.
- [42] Dydyk, M., "Master the T-junction and Sharpen Your MIC Designs," *Microwaves*, Vol. 16, May 1977, pp. 184–186.

CHAPTER 4

Microstrip Discontinuities II: Fullwave Analysis and Measurements

The quasi-static characterization of capacitances and inductances associated with microstrip discontinuities was discussed in Chapter 3. Results based on quasi-static analysis are valid, with sufficient accuracy, only up to frequencies of a few gigahertz. For a complete characterization of discontinuities, the frequency dependence of various parameters must be determined. This information is obtained from dynamic analyses, which are discussed in this chapter. Two-dimensional analysis, based on a planar waveguide model of a microstrip line, is presented in Section 4.1. Methods for more rigorous fullwave analysis are described in Section 4.2. Techniques for measuring microstrip discontinuities are also included in this chapter.

4.1 PLANAR WAVEGUIDE ANALYSIS

4.1.1 Discontinuity Characterization

The planar waveguide model [1–3] for the microstrip line discussed in Section 1.3 is a very powerful technique for analyzing a number of microstrip discontinuities. Steps in width, T-junctions, bends, and cross junctions have been analyzed using this method and are discussed in this section. The equivalent circuits of these discontinuities can be obtained by using the derived scattering parameters and the theory of linear networks.

Step in Width [4]

The planar waveguide model of a step discontinuity is shown in Figure 4.1. Dimensions a and b are widths of planar waveguides corresponding to the microstrip lines

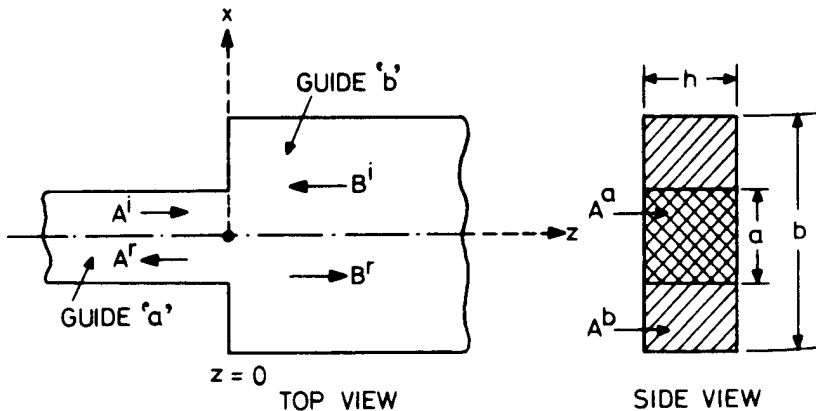


Figure 4.1 Top and side views of a step (in width) discontinuity.

“a” and “b,” respectively. The cross-sectional areas of these guides are denoted by A^a ($= a \times h$) and A^b ($= b \times h$).

Since the height of the substrate, h , is much less than the wavelength in the microstrip, the fields are uniform along the y -direction in the equivalent planar waveguide model. Under this condition only TEM and TE_{m0} modes can be excited. (TM_{mn} modes do not exist because a small value of the substrate height requires $n = 0$ whereas the lowest value of n for TM modes is unity.) For TE_{m0} modes, the transverse fields in the planar waveguide model can be expressed in terms of orthogonal series expansions as

$$E_t = \sum_{m=0}^{\infty} U_{m0} \{ \hat{z} \times \nabla_t \psi_{m0}(x, y) \} \quad (4.1)$$

$$H_t = \sum_{m=0}^{\infty} I_{m0} \{ -\nabla_t \psi_{m0}(x, y) \} \quad (4.2)$$

where U_{m0} and I_{m0} are the expansion coefficients and ψ_{m0} are the scalar potentials for TE modes. The unit vector along the z -axis is denoted by \hat{z} , and $m = 0$ corresponds to the dominant mode (TEM). The symbol ∇_t designates the transverse component of the gradient.

In the discontinuity plane ($z = 0$) the following boundary and interface conditions must be satisfied:

$$H_t^b = 0 \quad \text{in region } (A^b - A^a) \quad (4.3a)$$

$$H_t^a = H_t^b \quad \text{in region } A^a \quad (4.3b)$$

$$E_t^a = E_t^b \quad \text{in region } A^a \quad (4.3c)$$

It can be shown that the conditions given by (4.3) can only be satisfied if the transverse magnetic field of guide "a" is expanded in terms of the modes of guide "b." While expanding the magnetic field H_t^a in terms of the modes of guide "b," the expansion coefficients I^b are chosen in such a way that $H_t^b = 0$ in region $A^b - A^a$ and will be equal to H_t^a in the discontinuity plane. On the other hand, no special boundary condition exists for the transverse electric field in the region $A^b - A^a$, so that the electric field E_t^b in the discontinuity cross section can be expanded in terms of the modes of guide "a."

Multiplying (4.3c) by $(\hat{z} \times \nabla_t \psi_{M0}^a)$ for various values of $M (= 0, 1, 2 \dots)$ and integrating over the aperture A^a leads to the equation

$$U_{M0}^a = \iint_{A^a} E_t^b \cdot (\hat{z} \times \nabla_t \psi_{M0}^a) dA \quad (4.4)$$

Due to the orthogonality property of the employed functions only coefficients U_{M0}^a will be nonzero. Similarly the following expression is found for the expansion coefficients I^b :

$$I_{P0}^b = \iint_{A^a} H_t^a \cdot (-\nabla_t \psi_{P0}^b) dA \quad (4.5)$$

Substituting the expansions of E_t^b and H_t^a from (4.1) and (4.2), respectively, one gets the following expressions for U_{M0}^a and I_{P0}^b :

$$U_{M0}^a = \sum_{p=0}^{\infty} U_{p0}^b K_{(M0)(p0)} \quad (4.6)$$

$$I_{P0}^b = \sum_{m=0}^{\infty} I_{m0}^a K_{(m0)(p0)} \quad (4.7)$$

where M , m and P , p correspond to the modes in the guides "a" and "b" respectively. K 's are called the coupling integrals, and the evaluation of these integrals provides information about the degree of interaction between the modes in the two guides. The coupling integrals are given by

$$K = K_{(M0)(p0)} = \iint_{A^a} (\hat{z} \times \nabla_t \psi_{p0}^b) \cdot (\hat{z} \times \nabla_t \psi_{M0}^a) dA \quad (4.8a)$$

$$K^T = K_{(m0)(p0)} = \iint_{A^a} (\nabla_t \psi_{m0}^a) \cdot (\nabla_t \psi_{p0}^b) dA \quad (4.8b)$$

The expansion coefficients U and I can be replaced by the normal modes coefficients A^i , A^r and B^i , B^r (see Figure 4.1). The resulting equations are

$$\sqrt{Z_{M0}^a} (A_{M0}^i + A_{M0}^r) = \sum_{p=0}^{\infty} \sqrt{Z_{p0}^b} K_{(M0)(p0)} (B_{p0}^i + B_{p0}^r) \quad (4.9a)$$

$$\sqrt{Y_{P0}^b} (B_{P0}^i - B_{P0}^r) = \sum_{m=0}^{\infty} \sqrt{Y_{m0}^a} K_{(m0)(P0)} (A_{m0}^i - A_{m0}^r) \quad (4.9b)$$

where $m, M, p, P = 0, 1, 2, \dots$ and $Z (= 1/Y)$ is the wave impedance for TE mode given by

$$Z = \frac{\omega\mu}{\beta_z}$$

Here β_z is the propagation constant along the z -axis. For compactness, (4.9) may be written as

$$\sqrt{Z^a} (A^i + A^r) = \sqrt{Z^b} K (B^i + B^r) \quad (4.10a)$$

$$\sqrt{Y^b} (B^i - B^r) = \sqrt{Y^a} K^T (A^i - A^r) \quad (4.10b)$$

The incident and the reflected modes may be related by an **S**-matrix as

$$\begin{bmatrix} A^r \\ B^r \end{bmatrix} = [\mathbf{S}] \begin{bmatrix} A^i \\ B^i \end{bmatrix} \quad (4.11)$$

By knowing K , K^T , Z^a , and Z^b one can calculate the Sparameters of the step discontinuity.

Results and Equivalent Circuit

Numerical results of the scattering parameters of a symmetric step discontinuity have been reported by Kompa [4]. Typical results for frequency-dependent scattering matrix coefficients are shown in Figure 4.2. The incident mode considered here is the dominant TEM mode, while only even modes with $m = 0, 2, 4$ are assumed to be excited by the discontinuity. Figure 4.2 shows that, at frequencies well below the cut-off frequency of the first higher order mode ($m = 2$), the transmission and reflection coefficients are fairly constant. At the cut-off frequency of the TE_{20} mode (f_{c1}) the incident TEM mode is rejected and no transmission is possible. Assuming the step to be lossless, the reflection coefficient becomes equal to unity. For frequencies greater than the cut-off frequency, a part of the power is transmitted by the TE_{20} mode due to mode conversion, so that the transmission coefficient S_{21} for the dominant mode is always smaller than that for $f = 0$ (quasi-static case).

The equivalent circuit of a step discontinuity is determined from the known **S**-matrix by converting it into the **Y**-matrix. The **Y**-matrix elements y_{ik} , which are normalized with respect to the characteristic admittance of guide "a," can be obtained from the relation

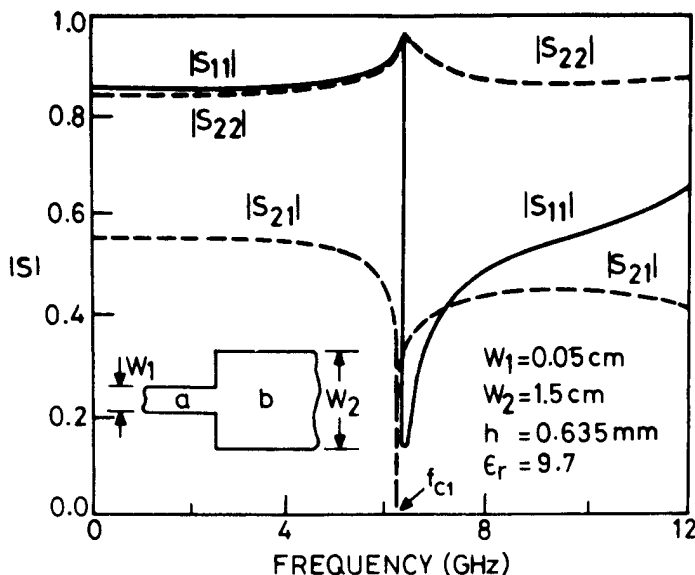


Figure 4.2 Computed scattering coefficients for a step discontinuity as a function of frequency (from [4], © 1976 S. Hirzel Verlag. Reprinted with permission.).

$$\mathbf{Y} = (\bar{\mathbf{I}} + \mathbf{S})^{-1} (\bar{\mathbf{I}} - \mathbf{S}) \quad (4.12)$$

where $\bar{\mathbf{I}}$ is the identity matrix. The equivalent circuit is shown in Figure 4.3(a). Ports 1-1' and 2-2' refer to the TEM mode, while the port 3-3' corresponds to the first higher order mode. The characteristic impedance Z_{03} for this mode is defined by the axial power flow of the first higher order mode in guide "b," that is,

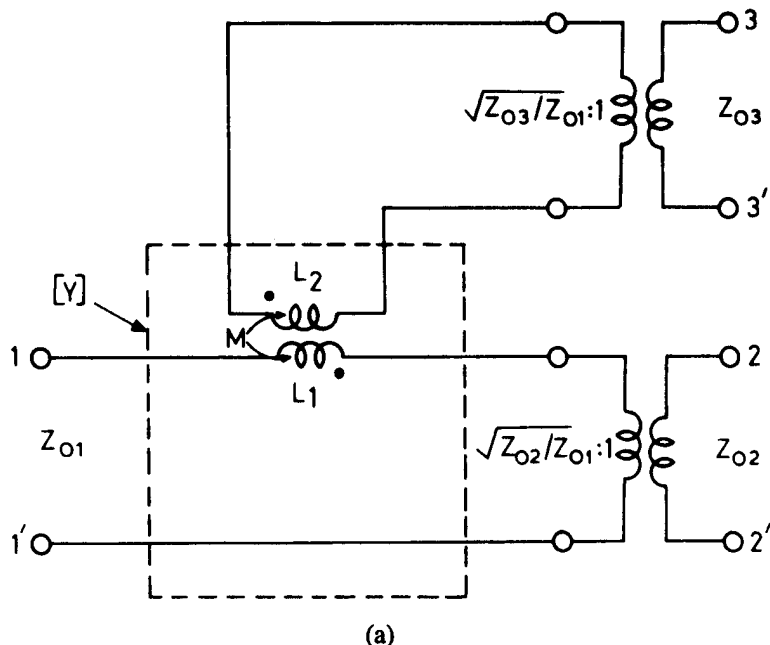
$$Z_{03} = \frac{h^2 |E_{\max}|^2}{2 P_{p0}} \quad (4.13)$$

where P_{p0} is the axial power flowing in the ($p0$) mode.

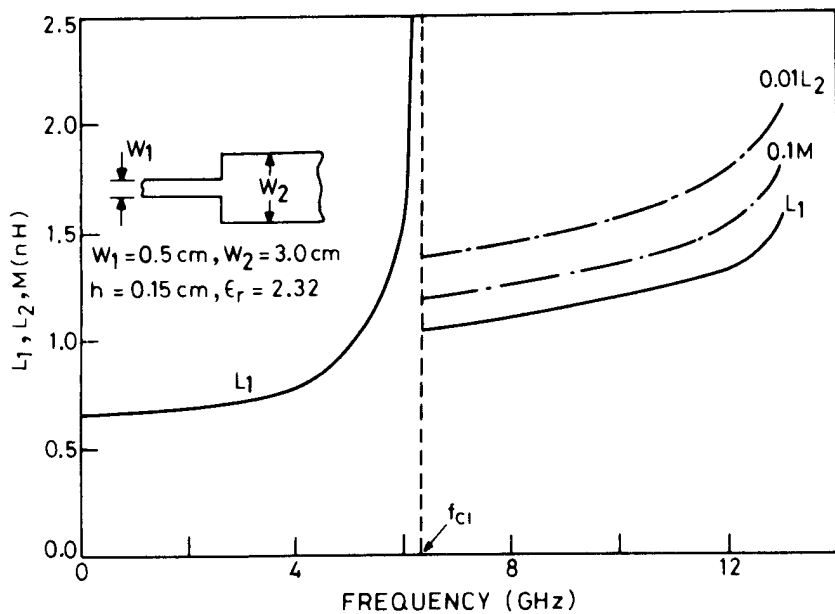
Figure 4.3(b) shows computed results for the equivalent circuit parameters. It can be seen that under single-mode propagation conditions, the discontinuity can be represented by a simple series inductance.

T-Junction [5]

The fullwave analysis of a T-junction using the planar waveguide model has been reported by Mehran [5]. The other two discontinuities (the right-angled bend and the cross junction) can be considered in terms of the T-junction by making use of



(a)



(b)

Figure 4.3 (a) Frequency-dependent equivalent circuit for a step discontinuity and (b) variations of equivalent circuit parameters of a step discontinuity with frequency (from [4], © 1976 S. Hirzel Verlag. Reprinted with permission.).

symmetry considerations. Therefore the T-junction will be considered in detail for formulating the boundary value problem.

The T-junction geometry (shown in Figure 4.4) is subdivided into regions "a" and "b" wherein the transverse fields are expressed in terms of an orthogonal series expansion. The fields are matched at the discontinuity interface $z = 0$, which results in an infinite system of linear equations. The wave amplitudes in region "a," for arbitrary excitation, can be calculated by truncating the system of linear equations. To obtain the scattering parameters of the T-junction, the wave amplitudes of the transmitted waves in region "b" are evaluated.

The height of the substrate, h , is again much less than the wavelength in the microstrip, and the magnetic field does not have a component in the y -direction. Therefore, as was the case for step discontinuity, the description of the total field is complete in terms of an expansion using TE_{m0} modes only ($m = 0$ corresponds to the TEM-mode).

In region "a," the transverse field components may be written in terms of the series of the scalar potentials used in (4.1) and (4.2) as

$$E_i^a = U_{00} \nabla_i \psi_{00}^a + \sum_{m=1}^{\infty} U_{m0} (\hat{z} \times \nabla_i \psi_{m0}^a) \quad (4.14)$$

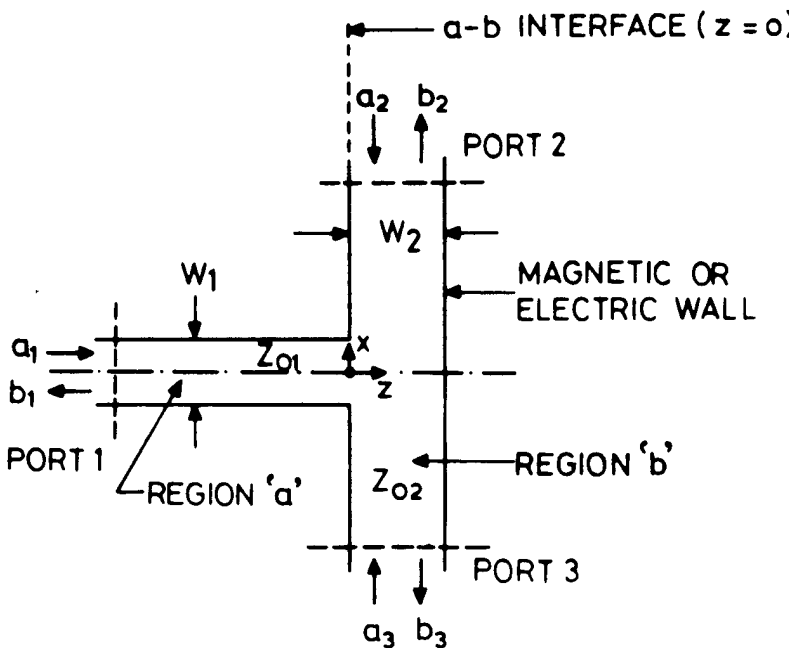


Figure 4.4 Configuration for analyzing a T-junction.

$$H_t^a = I_{00} (\hat{z} \times \nabla_t \psi_{00}^a) + \sum_{m=1}^{\infty} I_{m0} (-\nabla_t \psi_{m0}^a) \quad (4.15)$$

These field components satisfy the boundary conditions on the guide walls. ψ_{00}^a represents the scalar potential for the TEM mode and is given by

$$\psi_{00}^a = \frac{1}{\sqrt{W_1 h}} y \quad (4.16a)$$

The scalar potentials ψ_{m0}^a (which are also known as the orthonormalized vector mode functions of guide "a") are given by

$$\psi_{m0}^a = \frac{1}{m\pi} \sqrt{\frac{2W_1}{h}} \sin \left\{ \frac{m\pi}{W_1} \left(x + \frac{W_1}{2} \right) \right\} \quad m \neq 0 \quad (4.16b)$$

Further, the expansion coefficients U_{m0} and I_{m0} for the field components E_t^a and H_t^a , respectively, are related to wave amplitudes $a_{1(m0)}$ and $b_{1(m0)}$ by

$$\sqrt{Y_{m0}^a} U_{m0} = a_{1(m0)} \exp(-j\beta_z^a z) + b_{1(m0)} \exp(j\beta_z^a z) \quad (4.17)$$

$$\sqrt{Z_{m0}^a} I_{m0} = a_{1(m0)} \exp(-j\beta_z^a z) - b_{1(m0)} \exp(j\beta_z^a z) \quad (4.18)$$

where Z_{m0}^a and Y_{m0}^a are wave impedances and admittances, respectively, for TE modes in region "a" and are given by

$$Z_{m0}^a = \frac{1}{Y_{m0}^a} = \frac{\omega\mu}{\beta_z^a} \quad (4.19)$$

where β_z^a is the propagation constant along the z -axis in region "a." The fields in region "b" may also be expanded by writing relations analogous to (4.14) and (4.15). However, by using an expansion of this type, matching of the fields at the interface cannot be achieved because the functions ψ_{m0}^b of guide "b" will vanish in the ($z = 0$)-plane. Hence an additional continuous spectrum is taken into account in region "b." This yields

$$E_t^b = E_t^{eb} + \int_{-\infty}^{\infty} F(\beta_x^b) \sqrt{\frac{\omega\mu}{\beta_x^b}} \begin{Bmatrix} \cos[\beta_x^b(z - W_2)] \\ \sin[\beta_x^b(z - W_2)] \end{Bmatrix} [\hat{z} \times \nabla_t \psi^b(\beta_x)] d\beta_x^b \quad (4.20)$$

$$H_t^b = H_t^{eb} + j \int_{-\infty}^{\infty} F(\beta_x^b) \sqrt{\frac{\beta_x^b}{\omega \mu}} \begin{Bmatrix} \sin[\beta_x^b(z - W_2)] \\ -\cos[\beta_x^b(z - W_2)] \end{Bmatrix} [\nabla_t \psi^b(\beta_x)] d\beta_x^b \quad (4.21)$$

where β_x^b is the propagation constant in the x -direction in region "b." The superscript e denotes a set of discrete incident modes, and $F(\beta_x^b)$ is a weighting function to be determined. The function $\psi^b(\beta_x)$ is defined by

$$\psi^b(\beta_x) = \frac{\exp(j\beta_x^b x)}{\beta_x^b \sqrt{h}} \quad (4.22)$$

In (4.20) and (4.21), and also in the equations appearing later in this section, the upper functions are used if a T-junction with a magnetic side wall opposite to guide "a" is analyzed. For an electric wall, the lower functions are valid. The latter configuration is useful for extending the results of a T-junction discontinuity to the case of a cross junction.

The boundary condition that must be fulfilled by the transverse field components given by (4.14), (4.15) and (4.20), (4.21) is the continuity relation at the interface ($z = 0$)-plane. However, the unknown weighting function $F(\beta_x^b)$ must be derived first. This is done by choosing the magnetic field components at the interface $a - b$ in the following way

$$H_t^b(z = 0) = \begin{cases} H_t^a(z = 0) & \text{for } W_1/2 \geq x \geq -W_1/2 \\ 0 & \text{for } W_1/2 \leq x \leq -W_1/2 \end{cases} \quad (4.23)$$

When (4.23) is multiplied by $\nabla_t \psi^{b*}(\beta_x)$ and integrated with respect to y from 0 to h , the weighting function $F(\beta_x^b)$ is obtained through the orthogonality of the employed functions. This results in

$$F(\beta_x^b) = \frac{j\sqrt{\omega \mu / \beta_x^b}}{2\pi} \int_{-W_1/2}^{W_1/2} \int_0^h H_t^a(z = 0) \{\nabla_t \psi^{b*}(\beta_x)\} dx dy \quad (4.24)$$

where the asterisk * denotes the complex conjugate.

Finally, expressions for E_t^a and E_t^b , (4.14) and (4.20), at the interface $a - b$ are equated. The resulting equation is solved by projecting the series in (4.14) and (4.20) into the function space spanned by the elements $\{\nabla_t \psi^{b*}(\beta_x)\}$. The integration is performed with respect to the strip $-\infty \leq x \leq \infty$, $0 \leq y \leq h$. This procedure results in an infinite system of linear equations. The wave amplitudes $a_{1(m0)}$ and $b_{1(m0)}$ of

region "a" for arbitrary excitation can be calculated by truncating the infinite system of linear equations. Thus the field component $H_t^a(z=0)$ is known and (4.24) yields the weighting function $F(\beta_x^b)$.

To obtain the scattering parameters of the T-junction, the wave amplitude of the transmitted wave in region "b" is calculated. It is known that the integral representation of E_t^b has to decompose into the discrete modes of waveguide "b" for $|x| \geq W_1/2$. This decomposition is achieved by inserting the known function $F(\beta_x^b)$ in (4.20) and evaluating the resulting integral. The field amplitudes can then be recognized as the coefficients of the constituent modal terms.

For TE_{m0} modes the expansion coefficients for guide "a" are related by the equation

$$U_{M0} = \frac{-j\omega\mu}{\beta_{z(M0)}^b} \begin{cases} \cot(\beta_{z(M0)}^b W_2) \\ -\tan(\beta_{z(M0)}^b W_2) \end{cases} I_{M0} + \sum_{m=0}^{\infty} \sum_{p=0}^{\infty} \frac{j\omega\mu \left\{ \frac{\epsilon_{0p}}{2} \right\} \sqrt{\epsilon_{0m}\epsilon_{0M}} \exp(-j\beta_x^b W_1/2)}{W_1 W_2 \left\{ [\beta_{x(p0)}^b]^2 - \left(\frac{m\pi}{W_1} \right)^2 \right\}} \cdot H(M, \beta_x^b) I_{m0} + R_{M0} \quad (4.25a)$$

$$\text{with } \epsilon_{0i} = \begin{cases} 2 & \text{for } i \neq 0 \\ 1 & \text{for } i = 0 \end{cases}$$

$$H(M, \beta_x^b) = \begin{cases} \frac{2 \beta_{x(p0)}^b \sin(\beta_{x(p0)}^b W_1/2)}{(\beta_{x(p0)}^b)^2 - (M\pi/W_1)^2} & \text{for } \frac{M\pi}{W_1} \neq \beta_{x(p0)}^b \\ \frac{1}{2} W_1 \cos \frac{M\pi}{2} & \text{for } \frac{M\pi}{W_1} = \beta_{x(p0)}^b \end{cases} \quad (4.25b)$$

$$R_{M0} = \begin{cases} \int_0^h \int_{-W_1/2}^{W_1/2} E_t^b(z=0) (\hat{z} \times \nabla_t \psi_{M0}^a) dx dy & \text{for } M \neq 0 \\ \int_0^h \int_{-W_1/2}^{W_1/2} E_t^b(z=0) (\hat{z} \times \nabla_t \psi_{00}^a) dx dy & \text{for } M = 0 \end{cases} \quad (4.25c)$$

where $M = 0, 2, 4, \dots$ and M and p denote modes present in regions "a" and "b," respectively. Since the amplitudes of the incident waves are known, the amplitudes of the reflected waves in region "a" can be computed from (4.17), (4.18), and (4.25). The amplitudes of the waves transmitted into region "b" can also be calculated. For the waves transmitted in region "b," the amplitudes are described by

$$b_{2(p0)} = \exp[-j\beta_{x(p0)}^b W_1] \begin{Bmatrix} 1 \\ 0 \end{Bmatrix} a_{3(p0)} + \sum_{m=0}^{\infty} I_{m0} \cdot \frac{\omega \mu (-1)^p \begin{Bmatrix} \sqrt{\epsilon_{0p} \epsilon_{0m}} \\ \sqrt{2 \epsilon_{0m}} \end{Bmatrix} \sin[\beta_{x(p0)}^b W_1 / 2]}{\sqrt{W_1 W_2} \sqrt{Z_{p0}^b} \left[(\beta_{x(p0)}^b)^2 - \left(\frac{m\pi}{W_1} \right)^2 \right]} \exp[-j\beta_{x(p0)}^b W_1 / 2] \quad (4.26a)$$

and

$$b_{3(p0)} = \exp[-j\beta_{x(p0)}^b W_1] \begin{Bmatrix} 1 \\ 0 \end{Bmatrix} a_{2(p0)} + \sum_{m=0}^{\infty} I_{m0} \cdot \frac{\omega \mu (-1)^p \begin{Bmatrix} \sqrt{\epsilon_{0p} \epsilon_{0m}} \\ \sqrt{2 \epsilon_{0m}} \end{Bmatrix} \sin[\beta_{x(p0)}^b W_1 / 2]}{\sqrt{W_1 W_2} \sqrt{Z_{p0}^b} \left[(\beta_{x(p0)}^b)^2 - \left(\frac{m\pi}{W_1} \right)^2 \right]} \exp[j\beta_{x(p0)}^b W_1 / 2] \quad (4.26b)$$

with $p = 0, 1, 2, \dots$ and $m = 0, 2, 4, \dots$

In the above equations also, the upper functions are used when a T-junction is analyzed with a magnetic side wall opposite to guide "a." For an electric wall, the lower functions are valid.

For odd values of m and M the expression $\sin[\beta_{x(p0)}^b W_1 / 2]$ in (4.25) and (4.26) must be replaced by $-j\cos[\beta_{x(p0)}^b W_1 / 2]$. Using (4.25) and (4.26), the scattering parameters of a T-junction can be calculated.

Results and Equivalent Circuit

Numerical results for the scattering parameters have been reported by Mehran [5]. If the incident wave is the dominant TEM mode, at least four modes should be considered in region "b" and at least two modes in region "a" when the transmission coefficient is to be calculated with an accuracy of 1 percent. The two modes in region "a" describe the total field and account for the reflected wave also.

Typical results for frequency-dependent scattering matrix coefficients of a T-junction are shown in Figure 4.5. We note that $|S_{11}^T|$, and therefore the power reflected by the T-junction discontinuity at $z = 0$ increases with frequency in the range $0 \leq f \leq f_{c1}$, where f_{c1} is the cut-off frequency of the first higher order (TE_{10}) mode in region "b." Correspondingly, the power transmitted into region "b" decreases with frequency (Figure 4.5(b)). For frequencies greater than f_{c1} , a part of the power is transmitted by the TE_{10} mode, so that the transmission coefficient

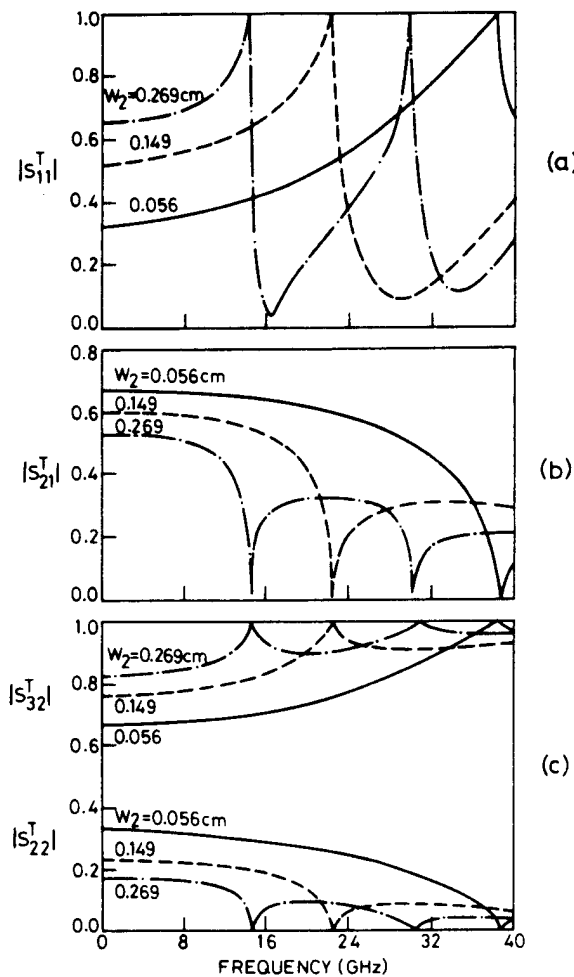


Figure 4.5 Numerical results for scattering coefficients of a T-junction: $\epsilon_r = 9.7$, $h = 0.0635$ cm, $W_1 = 0.056$ cm (from [5], © 1975 S. Hirzel Verlag. Reprinted with permission.).

$|S_{21}^T|$ for the TEM mode is always smaller than that for $f = 0$. Figure 4.5(c) indicates that if the TEM mode is incident at port 2, the power reflected into guide "b" decreases with increasing frequency. Also the power transmitted into guide "a" decreases, whereas the power transmitted into port 3 behaves in the opposite manner. It may be pointed out that the information contained in Figure 4.5 provides Sparameters for the TEM-mode since the incident power has been assumed to propagate in the dominant TEM-mode. For frequencies greater than f_{c1} (cut-off for the TE_{10} -mode) a part of the power is transmitted in the TE_{10} mode also. Therefore,

Sparameters for the TEM-mode do not describe the circuit completely for frequencies greater than f_{cl} .

A comparison between theoretical and experimental results is shown in Figure 4.6. Small circles show the experimental points. Discrepancies near the cut-off frequencies of higher order modes in microstrip of width W are attributed to the radiation effects.

The frequency-dependent equivalent circuit of a discontinuity can be derived from the scattering parameters. The equivalent circuits of a T-junction with a magnetic wall and an electric wall at $z = W_2$ can be represented as shown in Figure 4.7(a) and 4.7(b), respectively.

The impedances Z_{im}^T of the equivalent circuit elements can be determined using the relation between the short-circuit admittance matrix and the scattering matrix. These impedances may be written in terms of Sparameters as [6]

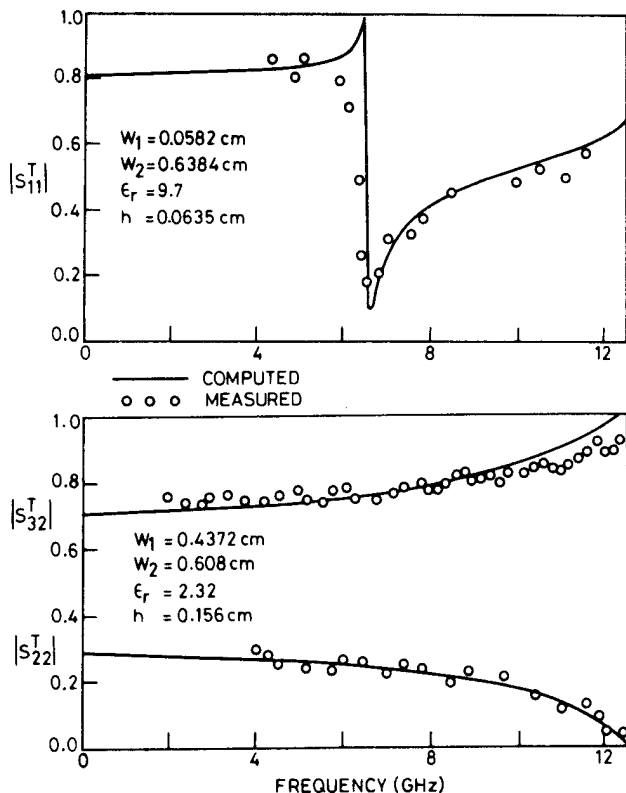


Figure 4.6 Comparison of computed results of fullwave analysis of a T-junction with experimental results (from [5], © 1975 S. Hirzel Verlag. Reprinted with permission.).

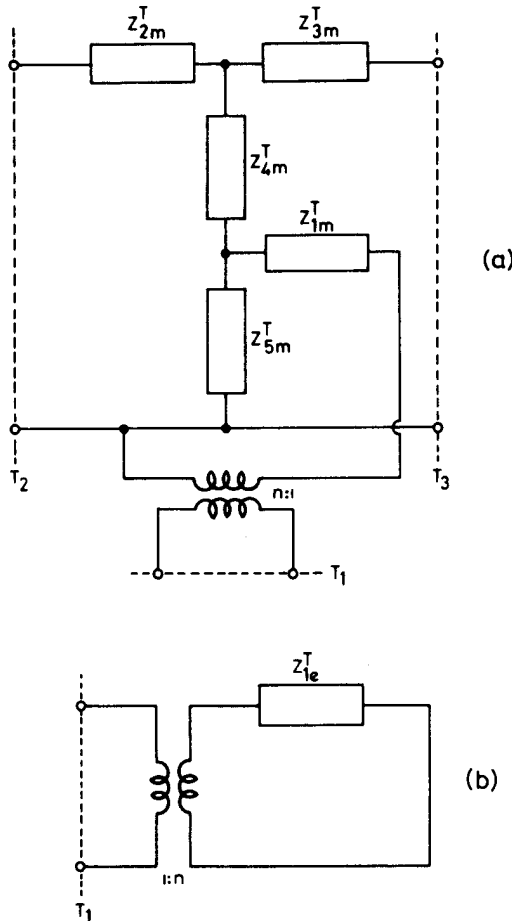


Figure 4.7 Frequency-dependent equivalent circuit for a microstrip T-junction: (a) with magnetic wall and (b) with electric wall (from [6], © 1975 S. Hirzel Verlag. Reprinted with permission.).

$$\begin{aligned}
 Z_{1m}^T &= \frac{n[(1 - S_{22}^T + S_{32}^T)\{2S_{12}^T(nS_{12}^T - 1) + n(1 + S_{11}^T)(1 - S_{22}^T - S_{23}^T)\}]}{D^T} \\
 Z_{3m}^T = Z_{2m}^T &= \frac{(1 + S_{22}^T - S_{23}^T)[(1 - S_{11}^T)(1 - S_{22}^T - S_{23}^T) - 2(S_{12}^T)^2]}{D^T} \\
 Z_{4m}^T &= 2 \frac{(S_{12}^T)^2 - 2nS_{12}^T(1 - S_{22}^T + S_{23}^T) + S_{23}^T(1 - S_{11}^T)}{D^T} \\
 Z_{5m}^T &= \frac{2nS_{12}^T(1 - S_{22}^T + S_{23}^T)}{D^T} \quad (4.27)
 \end{aligned}$$

where

$$D^T = (1 - S_{22}^T + S_{23}^T) [(1 - S_{11}^T)(1 - S_{22}^T - S_{23}^T) - 2(S_{12}^T)^2]$$

$$n^2 = Z_{01}/Z_{02}$$

In the above equation, the subscript m denotes a magnetic wall. The impedances Z_{im}^T are normalized with respect to Z_{02} . For frequencies lower than the cut-off frequency of the first higher order mode, all elements of the equivalent circuit are reactances (capacitive or inductive). The reactance representation of the equivalent circuit is shown in Figure 4.8(a). For a typical set of T-junction parameters the variations of these reactances with frequency are shown in Figure 4.8(b). This figure shows that except for C_{4t} , other capacitances and inductances of the equivalent circuit do not vary much with frequency up to about 10 GHz.

For a T-junction with electric wall, Z_{le}^T is given by the expression for Z_{lm}^T when S-parameters corresponding to a T-junction with electric wall (Figure 4.4) are used.

Right-Angled Bend and Cross Junction [5]

The scattering parameters for right-angled bends and cross junctions can be derived from those for the T-junction. This is achieved by an even- and odd-mode excitation at the opposite ports (ports 2 and 3 in Figure 4.4). Right-angled bends and cross junctions are discussed in the following paragraphs.

The scattering parameters of a right-angled bend can be arrived at from the analysis of a T-junction with a magnetic wall at $z = W_2$. When the T-junction is excited symmetrically at ports 2 and 3 ($a_2 = a_3 = v_2$ as shown in Figure 4.9), the symmetry plane $x = 0$ (which bisects the T-junction into two identical right-angled bends) can be replaced by a magnetic wall. Using the symmetry and reciprocity properties of the structure, the relationship between the scattering parameters of the T-junction and the bend may be written as

$$\begin{aligned} S_{12}^B &= \sqrt{2} S_{12m}^T \\ S_{21}^B &= \sqrt{2} S_{21m}^T \\ S_{11}^B &= S_{11m}^T \\ S_{22}^B &= S_{23m}^T + S_{22m}^T \end{aligned} \quad (4.28)$$

The superscripts B and T denote the bend and the T-junction, respectively. The subscript m indicates a T-junction with a magnetic wall at $z = W_2$. Equations (4.28) constitute a correspondence between a right-angled bend and a T-junction whose W_1 is chosen such that

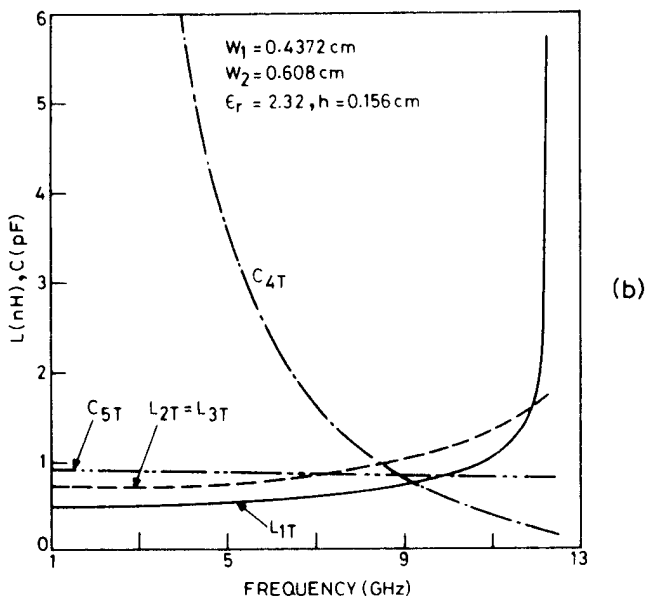
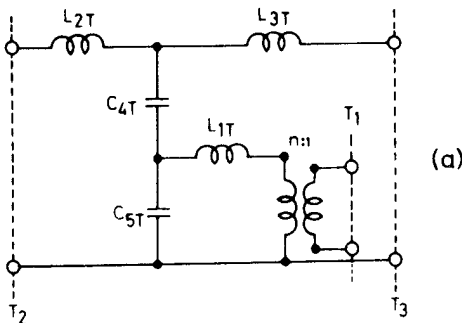


Figure 4.8 (a) Microstrip T-junction discontinuity capacitances and inductances and (b) variations of equivalent circuit parameters with frequency (from [6], © 1975 S. Hirzel Verlag. Reprinted with permission.).

$$Z_{01}^T = Z_{01}^B / 2$$

or

$$W_{e1}^T(f) = 2W_{e1}^B(f) \quad (4.29)$$

The *S*-parameters of a cross junction are calculated in the following manner. Any arbitrary excitation v at port 1 can be considered as a superposition of a symmetric

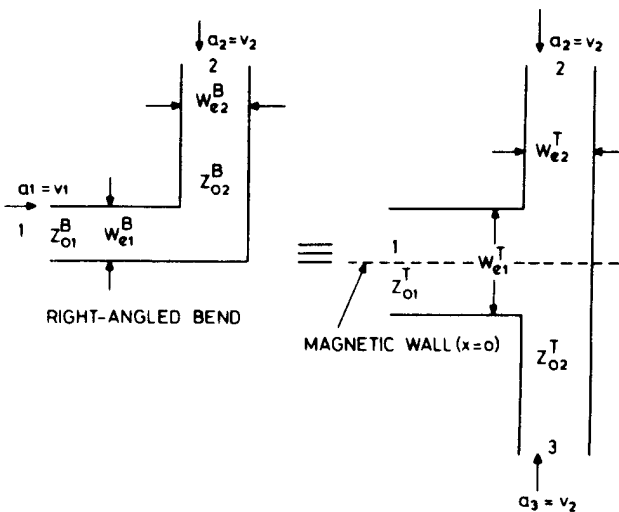


Figure 4.9 Derivation of right-angled bend from symmetrically excited T-junction.

($a_1 = v/2$, $a_3 = v/2$) excitation and an antisymmetric excitation ($a_1 = v/2$, $a_3 = -v/2$) at ports 1 and 3. This situation is shown in Figure 4.10. The cross junction with symmetric excitation is a combination of two T-junctions with magnetic walls placed back to back. Similarly, for antisymmetric excitation, a cross junction corresponds to two T-junctions with an electric wall as shown in Figure 4.10. These T-junctions have the effective width of the through arm equal to $W_{e2}^C/2$. The above considerations allow us to write the S-parameters of a cross junction as

$$\begin{aligned} S_{11}^C &= (S_{11m}^T + S_{11c}^T)/2 \\ S_{13}^C &= (S_{11m}^T - S_{11c}^T)/2 \\ S_{12}^C &= (1/\sqrt{2}) S_{12m}^T \quad S_{22}^C = S_{22m}^T \quad S_{24}^C = S_{23m}^T \end{aligned} \quad (4.30)$$

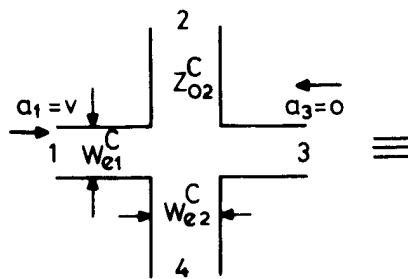
The effective width of the T-junction has to be determined so that

$$Z_{02}^C = Z_{02}^T/2 \quad \text{or} \quad W_{e2}^C(f) = 2 W_{e2}^T(f) \quad (4.31)$$

The superscript C denotes cross junction.

Results and Equivalent Circuit

S-parameters for right-angled bends are calculated using (4.28) and (4.29). For cross junctions, (4.30) and (4.31) are used. The equivalent circuits for these discontinuities are derived from the equivalent circuit impedances Z_{im}^T of the T-junction.



CROSS JUNCTION

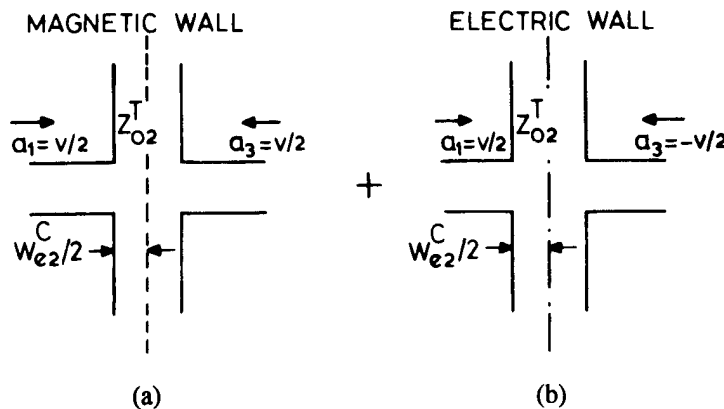


Figure 4.10 Derivation of a cross junction from superposition of (a) symmetrically and (b) antisymmetrically excited T-junctions.

The frequency-dependent equivalent circuit of the right-angled bend, based on the conversion procedure from the T-junction (with magnetic wall at $z = W_2$) to the right-angled bend discussed above is shown in Figure 4.11(a). The equivalent circuit element impedances are obtained from the relations (see also Figure 4.7a)

$$\begin{aligned} Z_1^B &= Z_{2m}^T + 2Z_{4m}^T \\ Z_2^B &= 2Z_{5m}^T \\ Z_3^B &= 2Z_{1m}^T \end{aligned} \quad (4.32)$$

The superscript B denotes a right-angled bend, while subscript m denotes a magnetic wall. The variations of capacitive and inductive components of an equivalent circuit

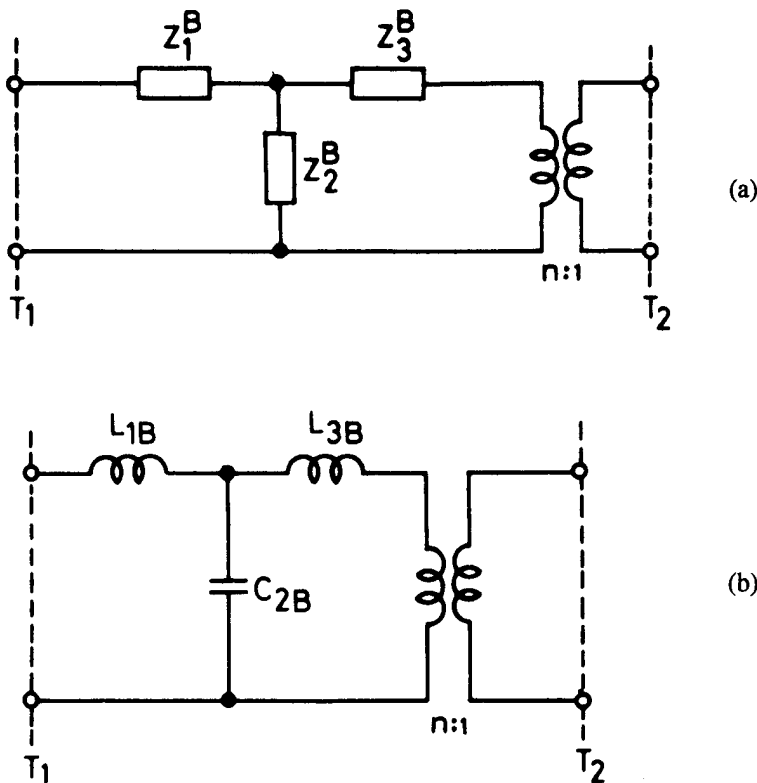


Figure 4.11 (a) and (b) Equivalent circuits of a right-angled bend based on fullwave analysis and (c) variations of computed results for capacitance and inductances as a function of frequency (from [6], © 1975 S. Hirzel Verlag. Reprinted with permission.).

(shown in Figure 4.11(b)) with frequency are shown in Figure 4.11(c). This figure shows that the capacitive and inductive values are almost constant up to 10 GHz.

The frequency-dependent equivalent circuit of the cross junction, derived from the T-junctions (with magnetic and electric walls at $z = W_2/2$), is shown in Figure 4.12(a). The relations between the elements of the equivalent circuit of the T-junction and the cross junction can be written as (see also Figure 4.7)

$$Z_1^C = 2 Z_{le}^T$$

$$Z_2^C = Z_{2m}^T$$

$$Z_3^C = Z_{4m}^T (Z_{lm}^T - Z_{le}^T) \left\{ \frac{1}{Z_{4m}^T} + \frac{1}{Z_{lm}^T - Z_{le}^T} + \frac{1}{Z_{5m}^T} \right\}$$

$$Z_4^C = Z_{5m}^T \cdot Z_3^C / Z_{4m}^T$$

$$Z_5^C = Z_{5m}^T \cdot Z_3^C / (Z_{lm}^T - Z_{le}^T) \quad (4.33)$$

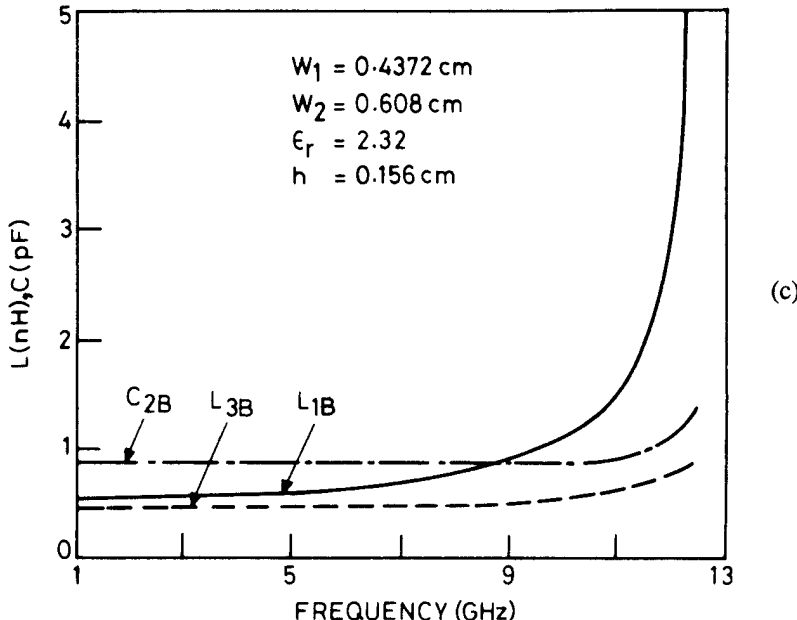


Figure 4.11 (continued).

with superscript C denoting the cross junction. The subscript e indicates electric wall at $z = W_2/2$ opposite to guide "a" of the T-junction. The equivalent circuit in terms of capacitances and inductances, based on the results of (4.33), is shown in Figure 4.12(b). The variations of these components with frequency are shown in Figure 4.12(c). In this case also, the variation of inductances with frequency is small, up to 10 GHz.

The planar waveguide model of a microstrip can also be used to analyze more general unsymmetrical discontinuities [7]. An example of an unsymmetrical crossing is shown in Figure 4.13(a). The microstrip lines are replaced by the equivalent planar waveguides, and the connecting field region is treated as a rectangular disc resonator. The fields of the rectangular disc resonator can also be approximated by a magnetic wall model. The magnetic fields in various regions are matched at the subareas A_i ($i = 1, 2, 3, 4$), all other boundaries being magnetic walls. By superposition of the fields of the four subproblems and matching the electric fields in the area A_i , the scattering matrix of the discontinuity can be calculated, taking into account the influence of dispersion effects and higher order modes. Figure 4.13(b) shows some other types of discontinuities that can be analyzed using this method.

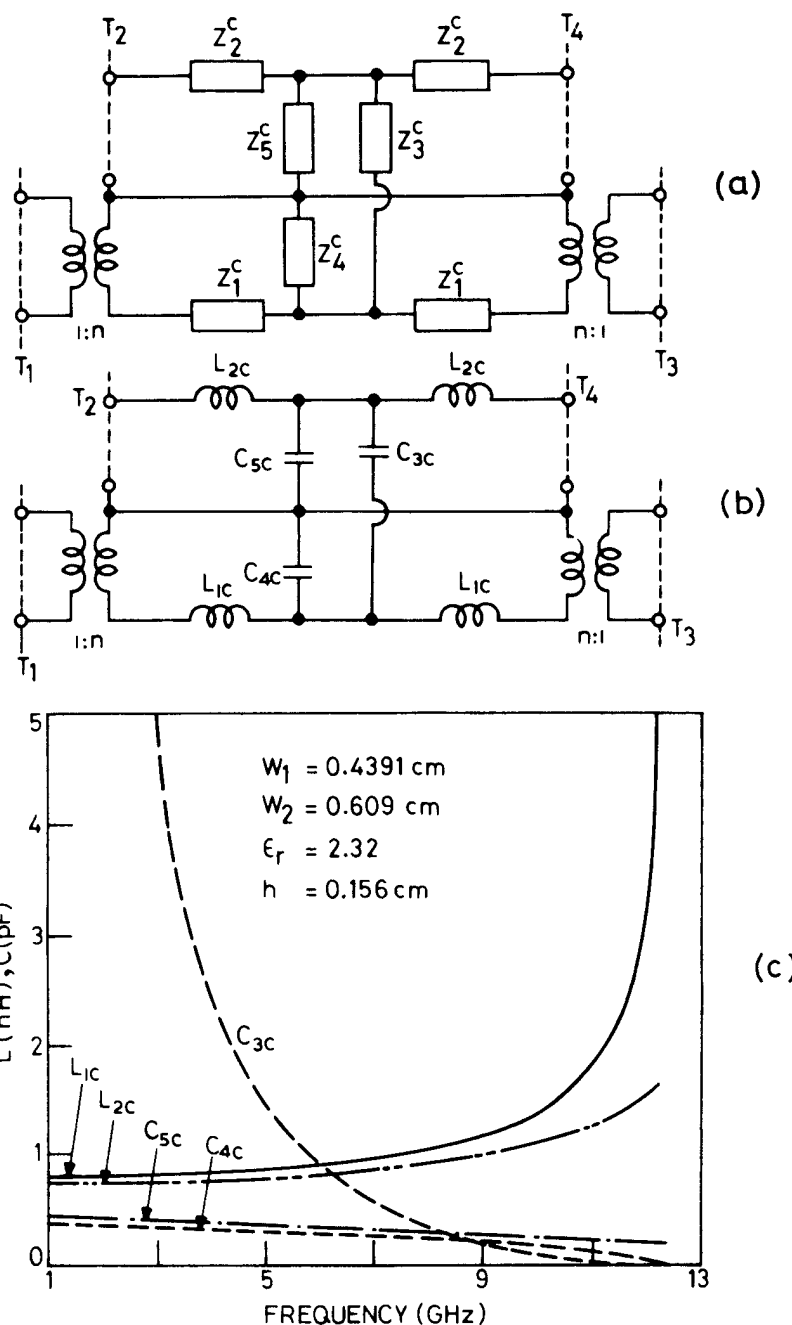


Figure 4.12 (a) and (b) Frequency-dependent equivalent circuits of a cross junction and (c) discontinuity capacitances and inductances as a function of frequency (from [6], © 1975 S. Hirzel Verlag. Reprinted with permission.).

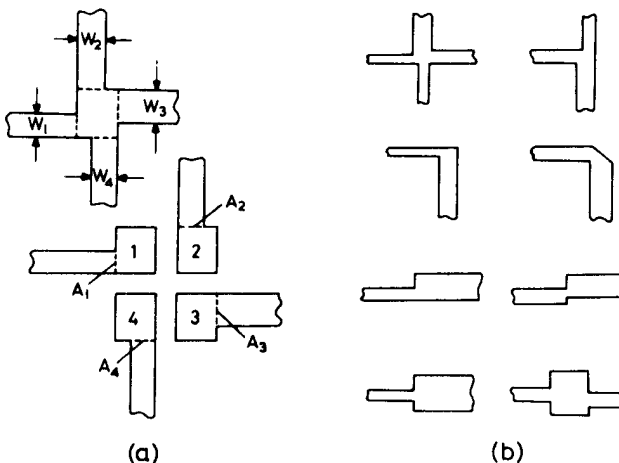


Figure 4.13 (a) Configuration for calculation of dynamic properties of an unsymmetric cross junction and (b) other types of discontinuities that could be analyzed by the parallel plate waveguide model.

4.1.2 Compensation of Discontinuity Reactances

The planar waveguide analysis approach discussed in Section 4.1.1 has been used not only for characterizing microstrip discontinuities but also for the compensation of microstrip discontinuity reactances. The compensation of discontinuity reactances [8] involves a modification of the discontinuity's geometrical configuration so as to minimize its adverse effects on the performance of microstrip circuits. This compensation has been reported [8] for three types of discontinuities: step junctions, right-angled bends, and T-junctions. A combination of the segmentation and desegmentation methods [3] has been used in these cases. The computed results for these three types of compensated discontinuities are shown in Figure 4.14 to 4.16. For the sake of comparison, the characteristics of the uncompensated discontinuities are also shown in these three cases.

4.1.3 Radiation and Parasitic Coupling

Because of the open nature of the microstrip configuration, hybrid and monolithic microwave circuits suffer from radiation originating at various geometrical discontinuities. Two consequences of this radiation phenomenon are additional signal loss in the circuit and undesired interactions between different parts of the circuit due to external electromagnetic coupling. These phenomena can become significant in three different situations. First, when attempts are made to increase circuit density in monolithic microwave circuits, more bends and other discontinuities are

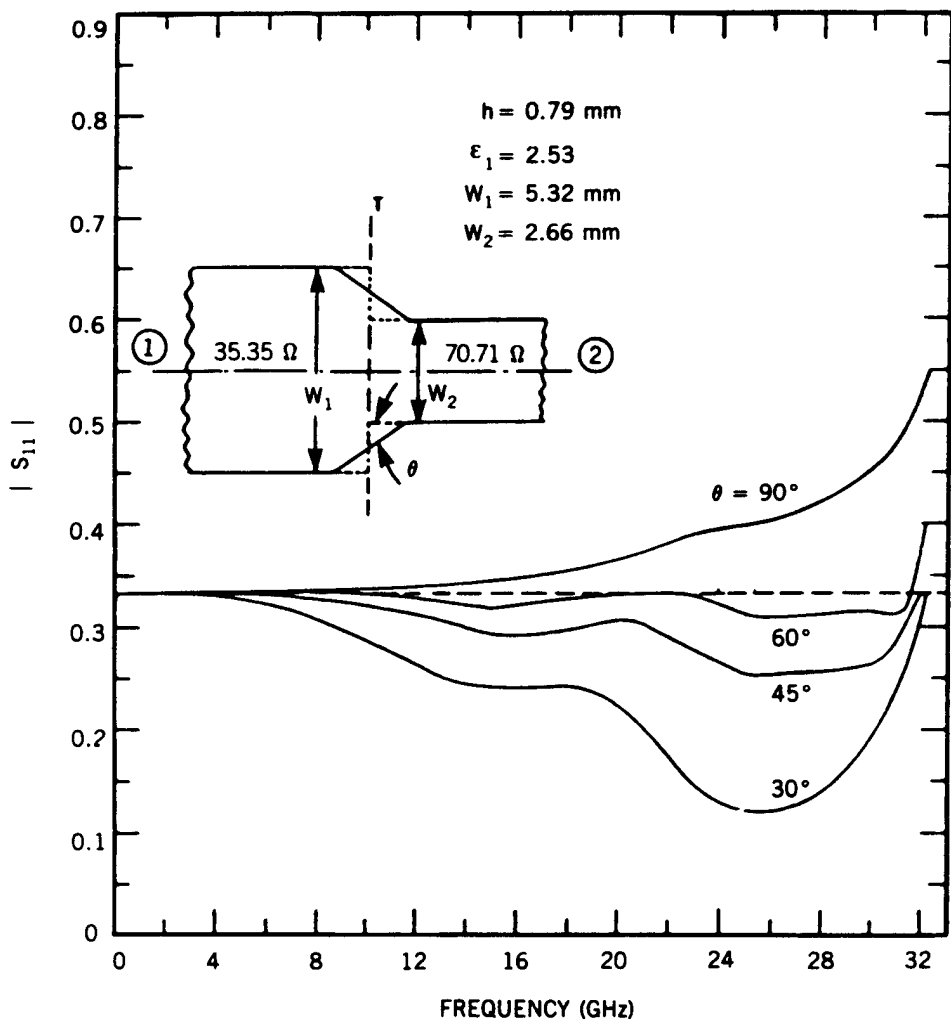


Figure 4.14 Reflection coefficients for the uncompensated and compensated step discontinuities with 1:2 impedance ratio (from [8], © 1982 IEEE. Reprinted with permission.).

introduced and spurious electromagnetic coupling increases considerably. Second, in microstrip antenna arrays, relatively thicker substrates are used and the feed networks printed on these substrates can result in substantial spurious radiation. Third, in multichip modules, microstrip interconnects that have bends and junction discontinuities introduce EM coupling between various parts of the module, which degrades RF performance.

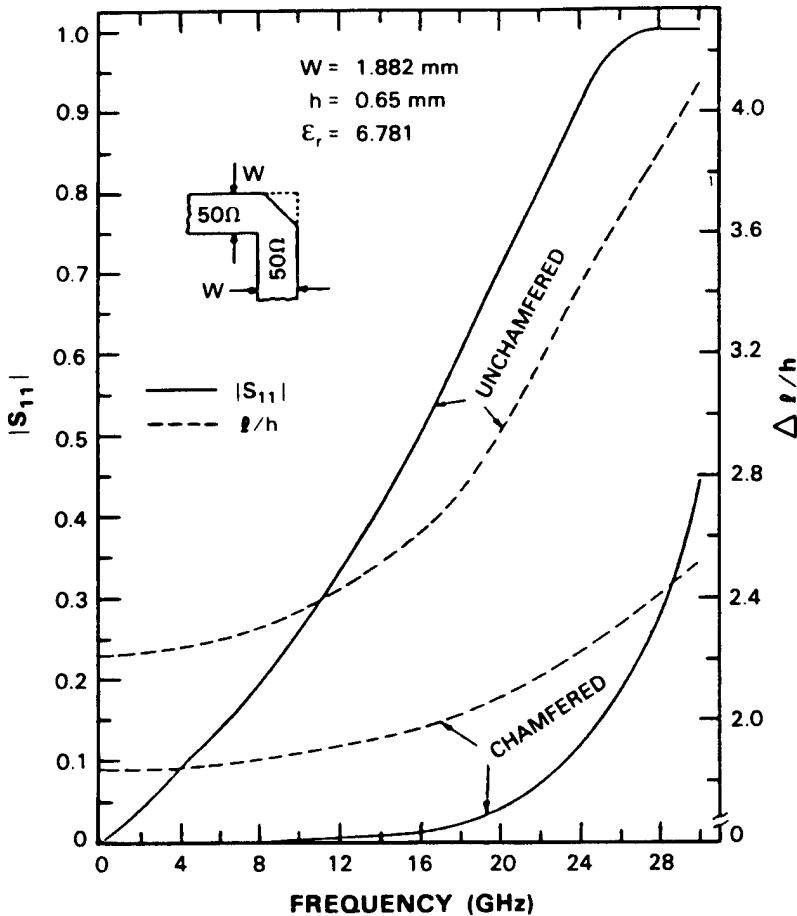


Figure 4.15 Reflection coefficients and normalized electrical lengths for uncompensated and optimally compensated right-angled bends (from [8], © 1982 IEEE. Reprinted with permission.).

Radiation from Microstrip Discontinuities

Three different approaches for addressing the issue of radiation from microstrip discontinuities have been reported in the literature. These are:

1. The Poynting vector method based on longitudinal electric currents and polarization currents associated with discontinuities [9–12];
2. The equivalent magnetic current formulation based on two-dimensional planar analysis [13, 14];
3. Fullwave analysis methods incorporating radiation phenomenon [15].

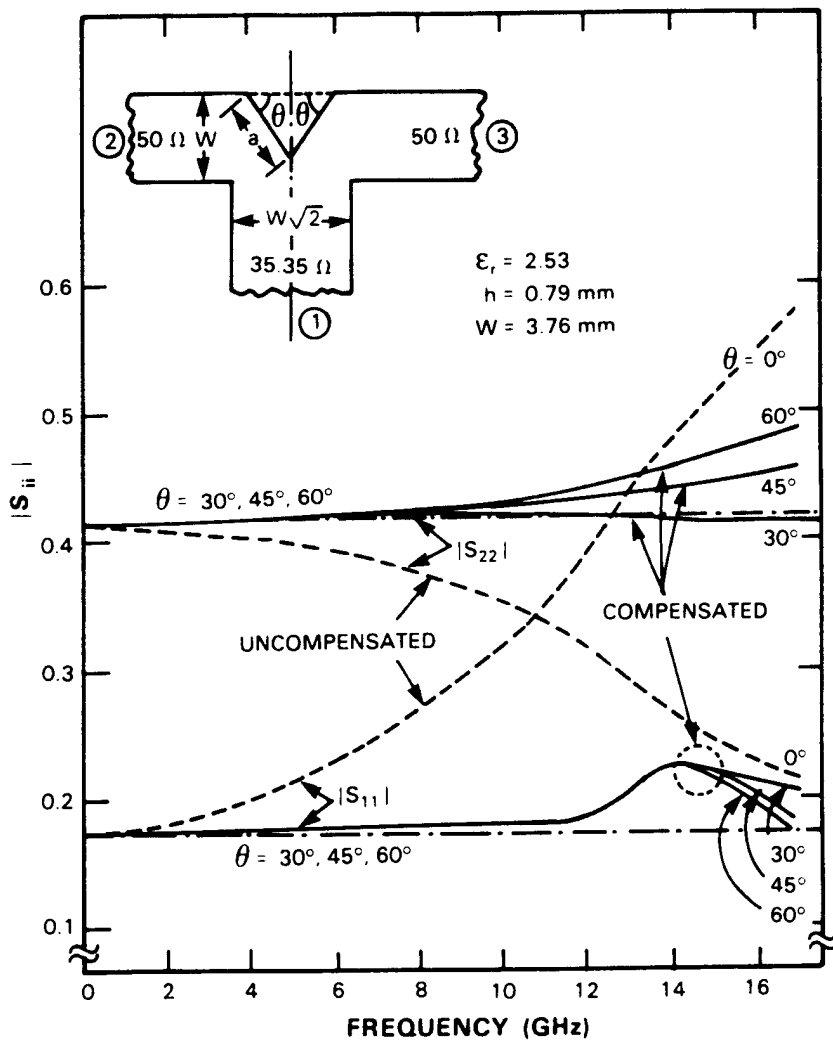


Figure 4.16 Main line and branch line reflection coefficients for uncompensated and compensated T-junctions (impedance ratio $1/\sqrt{2}:1:1$) (from [8], © 1982 IEEE. Reprinted with permission.).

Poynting Vector Method

In this approach, the source of radiation is described as a line current in the middle of the strip conductor, and, in the case of a microstrip open circuit, a polarization current flowing perpendicular to it. For other discontinuities, different polarization effects are associated with the longitudinal currents. The Poynting vector is

calculated in the far field, and the total radiated power is calculated therefrom. The method is limited to narrow strip transmission lines with $W \ll \lambda_0$ and thin substrates with $h \ll \lambda_0$ having discontinuities of small extent. The air-substrate layers are represented by a homogeneous dielectric with a relative dielectric constant equal to ϵ_{re} of the microstrip line. Using this approach, the ratio of the radiated power to the incident power can be expressed as

$$P_{\text{rad}}/P_{\text{inc}} = 2\pi\eta_0 \cdot (h/\lambda_0)^2 \cdot F_i/Z_{0m} \quad (4.34)$$

where F_i is the dimensionless radiation factor that characterizes the specific radiation properties of the discontinuity and is dependent only on ϵ . The expressions for F_i for various discontinuities are summarized in [12]. The microstrip line is described by its characteristic impedance Z_{0m} . The power radiated by surface waves is ignored (as $h/\lambda_0 \ll 1$) as compared with the free-space power. It is important to note that the radiated power is proportional to $(h/\lambda_0)^2$, a result that is consistent with the behavior of narrow-width rectangular microstrip patch antennas [16].

Equivalent Magnetic Current Formulation [13, 14]

This approach is an extension of the planar waveguide mode used for characterization of microstrip discontinuities discussed in Section 4.1.1. To evaluate the radiation field produced by microstrip discontinuities, the multiport network model is used to find the voltage distribution around the edges of the discontinuity configuration. This voltage distribution is expressed as an equivalent magnetic current distribution, which is used to compute the resultant radiation fields.

The procedure is similar to that developed earlier [17, 18] for microstrip patch antennas. To implement this method, we add a number of open ports at the edges of the discontinuity structure from which the radiation (or spurious external coupling) is being evaluated. This is shown in Figure 4.17 (a, b) for a right-angled bend and a compensated right-angled bend, respectively.

Lengths of transmission lines on two sides of the junction are made large enough so that the higher order evanescent modes produced by the discontinuities decay out at the locations of external ports 1 and 2. The circuit behavior is simulated by terminating port 2 in a matched load and adding a matched source to port 1. Voltages at the N ports at the edges are computed by using the following procedure.

1. The configuration is broken down in elementary regular segments, connected at the interfaces by a discrete number of interconnections.
2. Z-matrices for each of these elementary segments are evaluated by using the Green's function approach for individual geometries.
3. Individual Z-matrices obtained in step 2 are combined by using the segmentation formula.

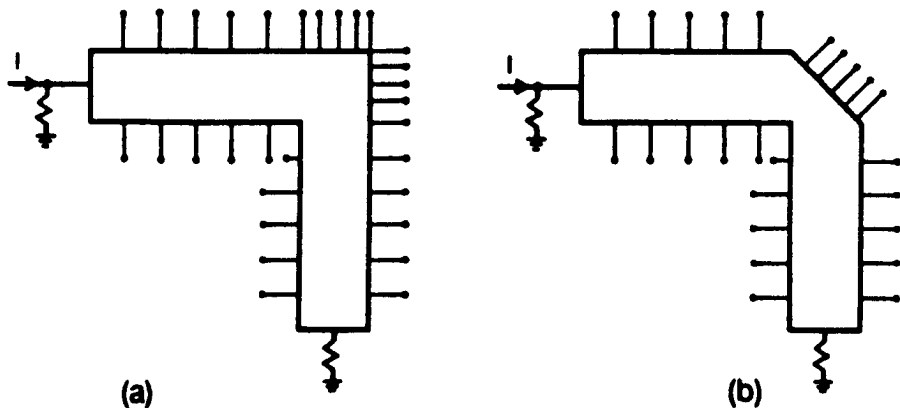


Figure 4.17 Multiple ports located at the edges of the microstrip discontinuities for (a) a right-angled bend and (b) a compensated right-angled bend. Voltages at these ports are expressed as an equivalent magnetic current distribution.

4. The overall multiport Z-matrix is used to calculate voltages at the N edge ports for a unit current input at port 1.

As mentioned earlier, a similar procedure has been used for the design of microstrip path antennas [17] also. The only distinction in the latter case is the use of edge admittance networks (containing equivalent radiation conductances) that are connected to the edge ports. Because of the nonresonant nature of the microstrip discontinuity structures, the radiated power is small and the edge voltages may be assumed to be unaffected by radiation conductances involved. However, for a more accurate assessment of the radiated power, radiation conductance networks may be added to edge ports and iterative computations may be carried out to evaluate radiation fields.

Voltages at the discontinuity edges are represented by equivalent magnetic current sources as shown in Figure 4.18(a, b). Each of the magnetic current line sources is divided into small sections over which the field may be assumed to be uniform. The amplitude M of each of the magnetic current elements is twice that of the edge voltage at that location, and the phase of M is equal to the phase of the corresponding voltage. The total radiation is computed using the superposition of the far field radiated by each section. Referring to the coordinate system, shown in Figure 4.19, the far-field pattern may be written in terms of voltages at the various elements. With the voltage at the i th element expressed as $V(i)e^{j\alpha(i)}$, we have

$$F(\theta, \phi) = \sum_{i=1}^N V(i) W(i) \exp\{j(k_0 \gamma_0(i)) + \alpha(i)\} F_i(\theta, \phi) \quad (4.35)$$

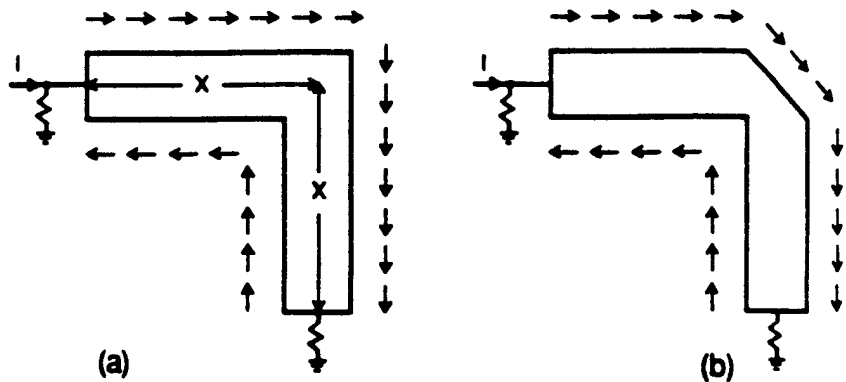


Figure 4.18 Equivalent magnetic current distribution at discontinuity edges: (a) for a sharp bend and (b) for a chamfered bend.

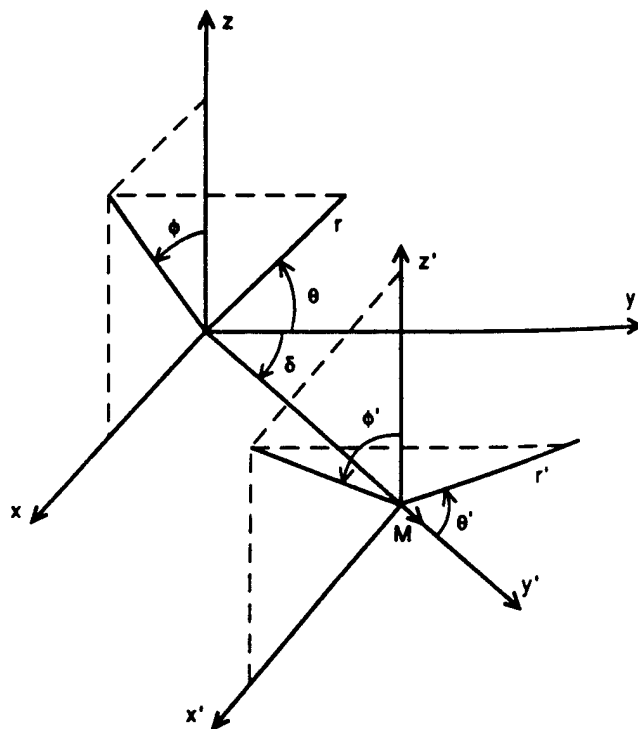


Figure 4.19 Coordinate system for external field calculations.

where

$$F_i(\theta, \phi) = \frac{\sin \{(k_0 W(i)/2) \cos \theta\}}{(k_0 W(i)/2) \cos \theta} \sin \theta \quad (4.36)$$

$$\gamma_0(i) = X_0(i) \sin \theta \cos \phi + Y_0(i) \cos \theta \quad (4.37)$$

N is the number of ports, $X_0(i)$, $Y_0(i)$ specify the location of the i th magnetic current element, and $W(i)$ is the width of the i th element.

The radiated power is calculated by integrating the Poynting vector over the half-space and may be written as

$$P_r = \frac{1}{240\pi} \int_{-\pi/2}^{\pi/2} \int_0^\pi (|E_\theta|^2 + |E_\phi|^2) r^2 \sin \theta \, d\theta \, d\phi \quad (4.38)$$

The fields E_θ and E_ϕ are expressed in terms of $F(\theta, \phi)$ as

$$E_\theta = \hat{a}_\theta (-jkF(\theta, \phi)) F_\theta / 4\pi r \quad (4.39)$$

$$E_\phi = \hat{a}_\phi (-jkF(\theta, \phi)) F_\phi / 4\pi r \quad (4.40)$$

where

$$F_\phi = \sin \phi' \sin \phi + \cos \delta \cos \phi \cos \phi' \quad (4.41)$$

$$F_\theta = -\sin \phi' \cos \theta \cos \phi + \cos \delta \cos \theta \sin \phi + \sin \delta \cos \phi' \sin \theta \quad (4.42)$$

and

$$\begin{aligned} \cos \theta' &= \sin \theta \sin \phi \sin \delta + \cos \theta \cos \delta \\ \cos \phi' &= \sin \theta \cos \phi / \sqrt{1 - \cos^2 \theta'} \end{aligned} \quad (4.43)$$

The radiation loss may be expressed as

$$\text{Power loss (dB)} = 10 \log_{10} \left(1 - \frac{P_r}{P_i} \right) \quad (4.44)$$

where P_i is the input power at port 1.

To identify the regions of the discontinuity configuration that contribute dominantly to the radiated power, several computations were performed by taking different regions around the discontinuity. These computations show that in most of the cases the biggest contribution to the radiated power is due to ports in the

region of the discontinuity itself. The results for a 50Ω right-angled bend, as shown in Table 4.1, illustrate this point.

Radiation from a Right-Angled Microstrip Bend. Results for the power radiated by a 90° bend normalized with respect to the input power are shown in Figure 4.20 for frequency ranges from 10 GHz to 40 GHz. These results are in good agreement with results based on the complex Poynting vector method, which are also plotted in Figure 4.20. The radiation loss at 40 GHz is a 0.0062 dB for a 50Ω line bend on a GaAs ($\epsilon_r = 12.9$) substrate. The values for radiation loss from a 90° bend in a 50Ω line on a substrate with $\epsilon_r = 2.2$ at 30 GHz and 40 GHz are 0.1 dB and 0.17 dB, respectively.

Table 4.1
Radiated Power as a Function of Microstrip Line Length
($\epsilon_r = 12.9$, $h = 127.1 \mu\text{m}$, $f = 10 \text{ GHz}$)

Length X (shown in Figure 4.18)	$P_r/P_i (\text{dB})$
$(0.4 \times 0.4) \lambda$	-40.64
$(0.35 \times 0.35) \lambda$	-40.67
$(0.3 \times 0.3) \lambda$	-40.77
$(0.25 \times 0.25) \lambda$	-40.84
$(0.2 \times 0.2) \lambda$	-41.1
Ports on bend only	-41.1

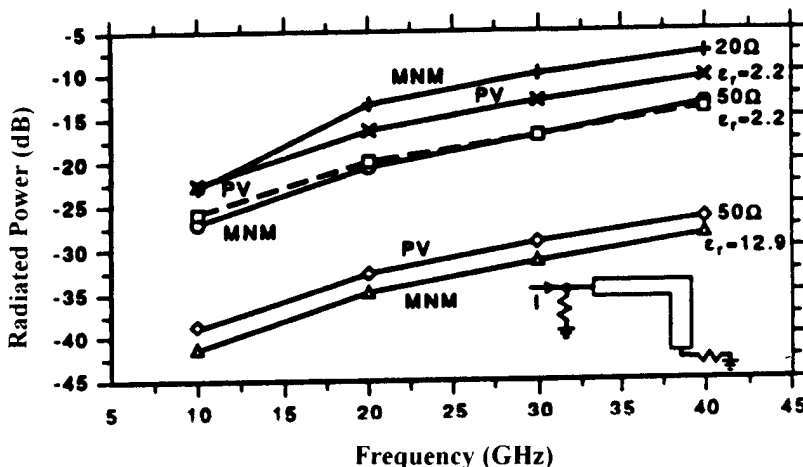


Figure 4.20 Normalized radiated power from a right-angled bend (MNM: Multiport Network Model and PV: Poynting Vector method).

Radiation from a Microstrip Step Junction. The power radiated from a step junction discontinuity, with a change in impedance from $50\ \Omega$ to $10\ \Omega$, on a $\epsilon_r = 2.2$ substrate with a thickness of 0.79 mm is plotted in Figure 4.21. A similar computation for a $50\ \Omega$ to $70.7\ \Omega$ junction (at 30 GHz, $\epsilon_r = 2.2$, thickness 0.02 in) yields the normalized radiated power to be -24.8 dB when the input power is fed from the $50\text{-}\Omega$ line and -33 dB when the power is fed from the $70.7\text{-}\Omega$ line.

Radiation from a T-Junction Discontinuity. Computed results for power radiated from a T-junction ($50\text{-}\Omega$ main line with $35.35\text{-}\Omega$ branch line on a substrate, thickness $1/32$ in, $\epsilon_r = 2.2$) are shown in Figure 4.22. The radiation loss at 12 GHz is 0.18 dB . It is found that for such a T-junction most of the contribution to the radiation loss originates from the region of the junction.

Radiation Evaluated from Fullwave Analysis

Fullwave analysis methods for the characterization of microstrip discontinuities are discussed in Section 4.2. When these analyses are conducted without using any enclosure or shield above the microstrip structure [15], the radiation effect gets incorporated in the discontinuity characterization. However, the computation of power radiated by discontinuities based on fullwave analysis has not been reported extensively. A general consensus is that for thin substrates used for microwave hybrid and monolithic circuit applications, radiation loss from microstrip discontinuities can be neglected.

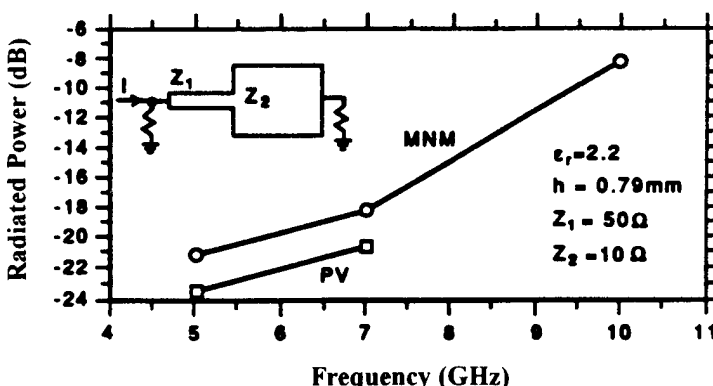


Figure 4.21 Normalized radiated power from a step (MNM: Multiport Network Model and PV: Poynting Vector method).

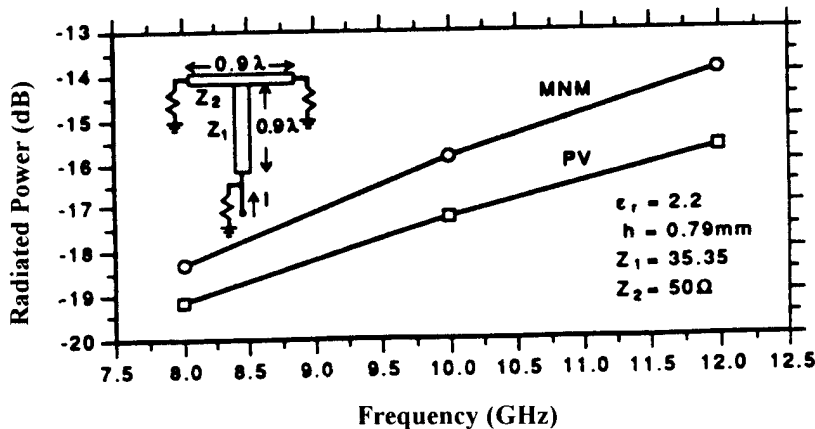


Figure 4.22 Normalized radiated power from a T-junction (MNM: Multiport Network Model and PV: Poynting Vector method).

Spurious Coupling Among Discontinuities

Parasitic coupling among different parts of a microstrip circuit caused by external fields produced by discontinuities is considered a more significant phenomenon than the radiation loss discussed above.

The spurious coupling between two discontinuities (due to the external fields) may be incorporated in the planar waveguide model-based analysis by connecting an additional multiport network between the two discontinuities as shown in Figure 4.23. The *multiport coupling network* (MCN) is characterized in terms of an admittance matrix Y_m . Elements of this matrix represent mutual admittances between various sections of the edges of the two discontinuities. The elements of the matrix Y_m are obtained by representing the edge fields by small sections of length, $d\ell$, of equivalent magnetic current and by computing the magnetic field components H_θ and H_r produced at the j th subsection of the nearby discontinuity. We have

$$H_\theta = j \frac{k_0 M d\ell \sin \theta}{4 \pi \eta_0 r} \left(1 + \frac{1}{jk_0 r} - \frac{1}{(k_0 r)^2} \right) e^{-jk_0 r} \quad (4.45)$$

$$H_r = \frac{M d\ell \cos \theta}{2 \pi \eta_0 r^2} \left(1 + \frac{1}{jk_0 r} \right) e^{-jk_0 r} \quad (4.46)$$

The induced current in the j th element is calculated from the magnetic field as

$$J_j = (\hat{z} \times \bar{H}) \cdot \hat{j} \quad (4.47)$$

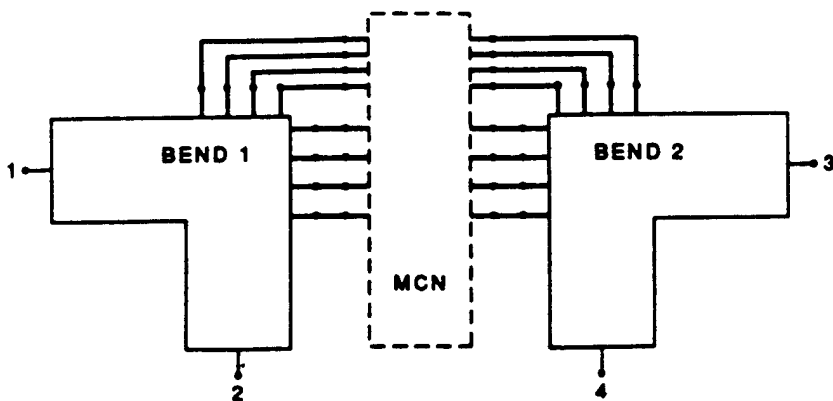


Figure 4.23 A multiport coupling network (MCN) incorporated for modeling spurious coupling between discontinuities.

where \hat{j} is a unit vector normal to the j th element. The value of Y_{ji} is obtained from the current induced in the j th subsection as a result of voltage, V_i , at the i th subsection.

$$Y_{ji} = J_j d\ell_j / V_i \quad (4.48)$$

The **Z** matrix of the mutual coupling network is the inverse of Y_m . The segmentation method is used to combine the **Z** matrix representations of the discontinuities and the coupling network to yield the overall **Z** matrix. The **Z** matrix is converted to **S** parameters. The effect of the coupling on the circuit performance is obtained from these **S** parameters.

It may be noted that a similar procedure has been employed successfully to model the mutual coupling between patches of a microstrip antenna array [18].

In addition to the above-mentioned approach, the spurious coupling among microstrip discontinuities can be derived from the fullwave electromagnetic analysis discussed in the next section.

4.2 FULLWAVE ANALYSIS OF DISCONTINUITIES

As the operating frequency of microwave and millimeter-wave integrated circuits increases, the surface wave and radiation effects become more significant. To account for these phenomena and to accurately characterize various discontinuities, fullwave solutions (without making any assumptions) become essential. A number of electromagnetic analysis software packages based on fullwave analysis are now available commercially [19–22] for analyzing microstrip discontinuities and circuits.

The development of fullwave simulation techniques has enabled microwave designers and software vendors to characterize microstrip discontinuities accurately by using rigorous numerical methods with minimum analytical and numerical approximations.

One of the earliest fullwave analyses reported for microstrip discontinuities is Galerkin's Method in Spectral Domain [23], which is an extension of the spectral domain analysis procedure discussed for a uniform microstrip line in Chapter 2. More recently the integral equation approach based on the moment method solution in space domain [24, 25] has been more popular. Other fullwave numerical electromagnetic methods (such as the finite difference time domain technique [26]) have also been used to characterize microstrip discontinuities. These fullwave analysis methods are reviewed in this section.

4.2.1 Galerkin's Method in the Spectral Domain [23]

Galerkin's method in the spectral domain has been used for the fullwave analysis of microstrip open ends and gaps. The characterization of these two discontinuities can be carried out by analyzing suitably designed linear resonators. For an open end, one can consider a section of microstrip with open ends on each side, as shown in Figure 4.24. By carrying out a fullwave analysis for the resonance frequency of this structure, one can obtain the equivalent line length contributed by the open end. The extent of the substrate can be finite in either one or both of the dimensions x and z . In the analysis reported in [23] the substrate is considered to be infinite along z and finite along the x -direction. In the x -direction two conducting planes ($2L$ apart) are placed symmetrically with respect to the microstrip. A cover plate is located at $y = H$. The analysis of such a structure in the spectral domain requires a Fourier transform along the z -direction and a finite Fourier transform along x .

Details of Galerkin's method in the spectral domain were discussed in Chapter 2. The choice of the basis functions for currents on the strip is important for the numerical efficiency of the method. For the dominant mode of resonance, the following forms for J_z and J_x are suitable:

$$J_z(x, z) = J_1(x)J_2(z) \quad (4.49)$$

$$J_x(x, z) = J_3(x)J_4(z) \quad (4.50)$$

where

$$J_1(x) = \begin{cases} \frac{1}{W} \left[1 + \left| \frac{2x}{W} \right|^3 \right] & |x| \leq W/2 \\ 0 & \text{elsewhere} \end{cases} \quad (4.51a)$$

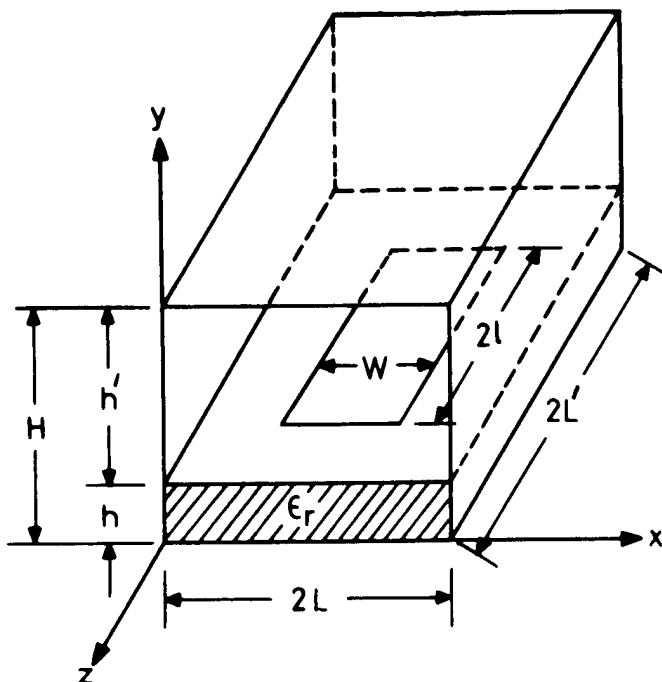


Figure 4.24 Geometry for analysis of microstrip open ends and gaps.

$$J_2(z) = \begin{cases} \frac{1}{\ell} \cos\left(\frac{\pi z}{2\ell}\right) & |z| \leq \ell \\ 0 & \text{elsewhere} \end{cases} \quad (4.51b)$$

$$J_3(x) = \begin{cases} \frac{2}{W} \sin\left(\frac{2\pi x}{W}\right) & |x| \leq W/2 \\ 0 & \text{elsewhere} \end{cases} \quad (4.51c)$$

$$J_4(z) = \begin{cases} \frac{z}{2\ell^2} & |z| \leq \ell \\ 0 & \text{elsewhere} \end{cases} \quad (4.51d)$$

After performing various steps of Galerkin's method in the spectral domain discussed in Section 2.3.1, a dispersion relation for the microstrip resonator is developed. This dispersion relation is solved for the resonant frequency. The microstrip open-end and gap discontinuities can be characterized by calculating the

effective increase in length, $\Delta\ell$, of suitably designed microstrip resonators. For resonance one can write

$$2(\ell + \Delta\ell) = \lambda_m/2 \quad (4.52)$$

where

$$\lambda_m = \lambda_0/\sqrt{\epsilon_{re}} = c/(\sqrt{\epsilon_{re}} f_{res})$$

Open End

The effective increase in length, $2\Delta\ell_{oc}$, for a microstrip resonator is determined from the method described above. From $\Delta\ell_{oc}$ one can find the open-end discontinuity capacitance, C_{oc} , by using (3.48). The frequency-dependent behavior of C_{oc} can be found by calculating the resonant frequencies of microstrip resonators of different lengths.

It may be pointed out that for frequencies up to about 10 GHz the quasi-static approach gives reasonably reliable results. At 8 GHz, for $h = 0.66$ mm, $W/h = 1.0$, and $\epsilon_r = 9.8$, the measured value of $\Delta\ell_{oc}$ is 0.021 ± 0.001 mm [27], whereas the corresponding quasi-static value of $\Delta\ell_{oc}$ calculated using (3.49) is 0.0206 mm.

Gap

Fullwave analysis of a gap discontinuity can also be carried out by using Galerkin's method in the spectral domain. In this case, one considers two types of resonators. First, an analysis is carried out with conducting planes (electric walls) at $z = 0$ and $z = 2L'$. The latter dimension is chosen such that $(2L' - 2\ell)$ is equal to the gap spacing. A second computation is carried out for magnetic walls at $z = 0$ and $z = 2L'$. For both of these computations, finite Fourier transforms are used along the x - and z -directions. Equivalent lengths, $\Delta\ell_e$ and $\Delta\ell_m$, for electric and magnetic walls, respectively, are determined from the respective resonance frequencies of resonators. From $\Delta\ell_e$ and $\Delta\ell_m$ two equivalent capacitances, C_e and C_m , are calculated. These capacitances are related to the discontinuity capacitances of π equivalent circuits of a gap (Figure 3.7a) by the following equations:

$$C_g = (C_e - C_m)/2 \quad (4.53a)$$

$$C_p = C_m \quad (4.53b)$$

The spectral domain approach has also been used for discontinuities in open microstrips (without any shield or enclosing box). Again, open-end and gap discontinuities have received more detailed attention [28–33].

The spectral domain approach is best suited for treating microstrip discontinuities of simple shape, where the current distribution can be expanded using a set of basis functions having closed-form Fourier transform counterparts. Analysis involving semi-infinite long lines are ideal for this method since the current on these lines can be represented by a pair of forward and backward travelling waves, which in the Fourier transform plane are simple delta functions. Therefore, semi-infinite lines have been used as standard feeds in analyzing discontinuities in [30, 33]. However, since the current in and near the discontinuity region is not uniform, a different set of subsectional basis functions is needed to capture the junction effect. This hybrid use of basis functions implies that each set of basis functions must be carefully defined over the structure, and different algorithms are needed to evaluate the moment integrals associated with each type of basis function. Also, to obtain accurate results, the spectral domain approach requires the precomputation of the propagation constant and/or transverse distribution of the current on each distinct feed strip [30, 33, 34].

4.2.2 Integral Equation Solution in the Space Domain

As mentioned earlier, the space domain solution of the integral equation for discontinuity structures is a very versatile alternative to the spectral domain method. Spatial domain evaluation provides more physical insight since the problem remains in the physical domain. For this approach, Green's functions are numerically evaluated first and treated as known functions in the integral equation. This implies that the selection of the expansion functions for the current is arbitrary, which renders the approach very versatile. Moreover, subsectional basis functions of simple form can be implemented with straightforward numerical algorithms using the spatial domain approach. Therefore, this approach provides an ideal base for a general solver and has been used in several electromagnetic simulators for microwave circuits. The groundwork for a mixed potential integral equation MPIE-based, spatial domain microstrip solver can be attributed to Mosig and Gardiol [24, 35].

The use of potentials is generally preferred in the spatial domain approach because the associated Green's functions are better suited for numerical evaluations. Using an $e^{j\omega t}$ time convention, the MPIE can be expressed as

$$\begin{aligned} \vec{E}^s &= \frac{-j\omega\mu_0}{4\pi} \int_S \left[G_m(\bar{x}, \bar{x}') \vec{J}(\bar{x}') ds' \right. \\ &\quad \left. - \frac{1}{k_0^2} \nabla \nabla' G_e(\bar{x}, \bar{x}') \vec{J}(\bar{x}') \right] dS' \\ &= -\vec{E}^{\text{inc}}(\bar{x}) \quad \bar{x} \text{ on } S \end{aligned} \quad (4.54)$$

where \vec{J} is the unknown current density on the microstrip discontinuity surface S and \vec{E}^s and \vec{E}^{inc} denote the scattered and incident fields, respectively. The scalar

Green's functions, G_m and G_e , are associated with the potentials produced by a unit source on top of the grounded substrate. They are identified as Green's functions of the magnetic and electric types, respectively. By evoking the continuity equation

$$\nabla \cdot \vec{J} + j\omega q = 0$$

it can be shown that G_m is related to the surface current density while G_e is related to the surface charge density q . Thus, (4.54) can also be expressed in terms of the surface current and charge densities. For a single-layer grounded dielectric slab in open space, these Green's functions can be expressed in terms of Sommerfeld integrals as [36, 37]

$$G_m(R) = \int_0^{\infty} 2J_0(\xi R) \frac{\xi}{D_{TE}} d\xi \quad (4.55)$$

$$G_e(R) = \int_0^{\infty} 2J_0(\xi R) \frac{\xi[u_0 + u \tanh(ut)]}{D_{TE}D_{TM}} d\xi \quad (4.56)$$

for $R = |\bar{x} - \bar{x}'|$, where

$$\begin{aligned} D_{TE} &= u_0 + u \coth(ut) \\ D_{TM} &= \epsilon_r u_0 + u \tanh(ut) \end{aligned} \quad (4.57)$$

$$u_0 = \sqrt{\xi^2 - 1} \quad u = \sqrt{\xi^2 - \epsilon_r} \quad (4.58)$$

R is the distance between the source and observation points, t is the slab thickness, and k_0 is the free-space propagation constant. Since these kernels are a function of R , they can be precomputed for a given range of R . Once they are known, the integral equation (4.54) can be solved readily in the spatial domain.

Several results for discontinuities' characterizations based on this method are available in [24, 25]. Electromagnetic simulators based on this approach have been used by several microwave circuit CAD software developers to derive models for microstrip discontinuities.

4.2.3 Time Domain Methods for Microstrip Discontinuity Characterization

In addition to the frequency domain methods discussed so far, time domain techniques for electromagnetic analysis can be used for the characterization of microstrip discontinuities and, in general, for the characterization of microstrip circuits. The *finite-difference time domain* (FDTD) approach [26, 38] is most popular among

the various time domain methods available. The *transmission line matrix* (TLM) approach could be used as well for this purpose [39].

The key feature of the time domain analysis results from the fact that an impulse response contains all the information of a system for the whole frequency range. Thus, a wide frequency range characterization of discontinuities can be obtained by using a pulse excitation in the time domain and evaluating the Fourier transform of the time domain pulse response.

Among various time domain methods, FDTD is the most direct from a mathematical point of view and is based on time and space discretizations of Maxwell's equations:

$$\frac{\partial \vec{E}}{\partial t} = \frac{1}{\epsilon_i} \nabla \times \vec{H} \quad (4.59)$$

$$\frac{\partial \vec{H}}{\partial t} = -\frac{1}{\mu_0} \nabla \times \vec{E} \quad (4.60)$$

where the subscript i emphasizes different values of ϵ_r to be used in substrate and air regions. To simulate the wave propagation in three dimensions, the spatial node points where different values of \mathbf{E} and \mathbf{H} are to be calculated are arranged in a mesh configuration. A unit cell of this mesh is shown in Figure 4.25. A repetitive arrangement of such cells fills the computational domain. Every component of the magnetic field \mathbf{H} can be obtained by the loop integral of the electric field \mathbf{E} using the four surrounding nodal \mathbf{E} values according to Maxwell's curl equation for \mathbf{E} . A similar approach is used for the calculation of \mathbf{H} . As a result of this procedure, not only the placements of the \mathbf{E} and \mathbf{H} nodes are off in space by half a space step, but the time instants when the \mathbf{E} or \mathbf{H} field are calculated are also off by half a time step. This gives rise to a "leap frog" algorithm with components of \mathbf{E} being calculated at $n\Delta t$ and components of \mathbf{H} being calculated at $(n + 1/2)\Delta t$, where Δt is the discretization unit in time. The resulting finite difference equations are of central difference form and of second-order accuracy. They are given by

$$E_x^{n+1}(i, j, k) = E_x^n(i, j, k) + \frac{\Delta t}{\epsilon \Delta h} (H_z^{n+1/2}(i, j, k) - H_z^{n+1/2}(i, j - 1, k) \\ - H_y^{n+1/2}(i, j, k) + H_y^{n+1/2}(i, j, k - 1))$$

$$E_y^{n+1}(i, j, k) = E_y^n(i, j, k) + \frac{\Delta t}{\epsilon \Delta h} (H_x^{n+1/2}(i, j, k) - H_x^{n+1/2}(i, j, k - 1) \\ - H_z^{n+1/2}(i, j, k) + H_z^{n+1/2}(i - 1, j, k))$$

$$E_z^{n+1}(i, j, k) = E_z^n(i, j, k) + \frac{\Delta t}{\epsilon \Delta h} (H_y^{n+1/2}(i, j, k) - H_y^{n+1/2}(i - 1, j, k) \\ - H_x^{n+1/2}(i, j, k) + H_x^{n+1/2}(i, j - 1, k))$$

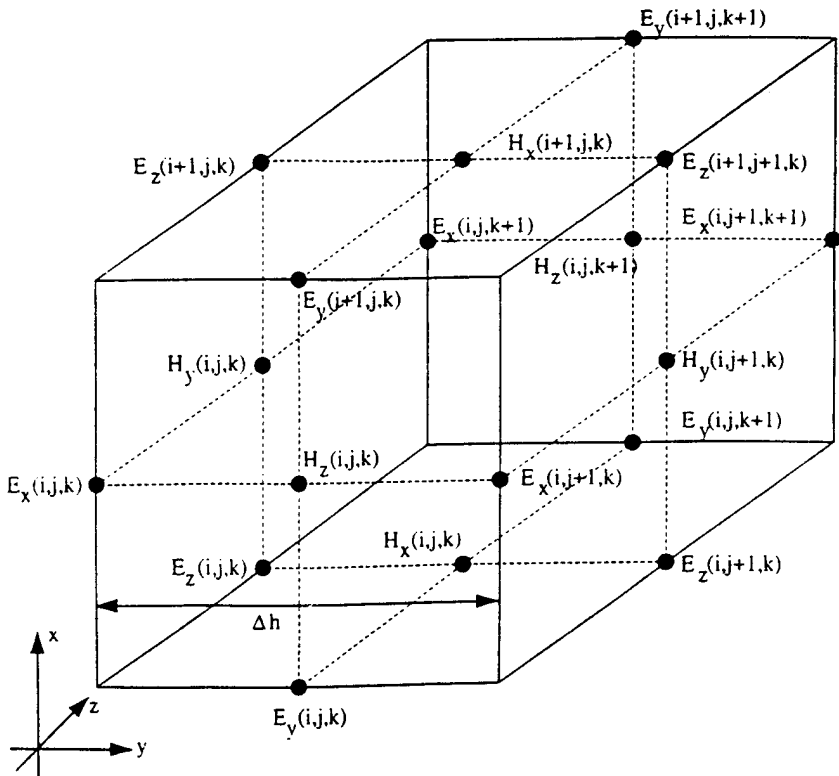


Figure 4.25 One cell of a typical mesh used for FDTD computations.

$$\begin{aligned}
 H_x^{n+1/2}(i, j, k) &= H_x^{n-1/2}(i, j, k) - \frac{\Delta t}{\mu \Delta h} (E_z^n(i, j + 1, k) - E_z^n(i, j, k) \\
 &\quad - E_y^n(i, j, k + 1) + E_y^n(i, j, k)) \\
 H_y^{n+1/2}(i, j, k) &= H_y^{n-1/2}(i, j, k) - \frac{\Delta t}{\mu \Delta h} (E_x^n(i, j, k + 1) - E_x^n(i, j, k) \\
 &\quad - E_z^n(i + 1, j, k) + E_z^n(i, j, k)) \\
 H_z^{n+1/2}(i, j, k) &= H_z^{n-1/2}(i, j, k) - \frac{\Delta t}{\mu \Delta h} (E_y^n(i + 1, j, k) - E_y^n(i, j, k) \\
 &\quad - E_x^n(i, j + 1, k) + E_x^n(i, j, k))
 \end{aligned} \tag{4.61}$$

The indices i , j , and k define the positions of the field nodes. Distances between the nodes are $\Delta x = \Delta y = \Delta z = \Delta h$. For any finite-difference scheme, a stability

condition must be found that guarantees that the numerical error generated in one step of the calculation does not accumulate and grow. The stability condition for the “leap frog” algorithm is given by

$$v_{\max} \cdot \Delta t \leq \frac{1}{\sqrt{1/\Delta x^2 + 1/\Delta y^2 + 1/\Delta z^2}} \quad (4.62)$$

For the special case of $\Delta x = \Delta y = \Delta z = \Delta h$, the above condition becomes

$$v_{\max} \cdot \Delta t \leq \frac{1}{\sqrt{3}} \cdot \Delta h \quad (4.63)$$

where v_{\max} is the maximum signal phase velocity in the configuration being considered.

The excitation pulse most commonly used for FDTD computations is Gaussian in shape. It has a smooth waveform in time, and its Fourier transform is also a Gaussian pulse centered at zero frequency. This property makes a Gaussian pulse a perfect choice for investigating the frequency-dependent characteristics of microstrip discontinuities.

Another important consideration in implementing a FDTD algorithm is the use of an “absorbing boundary condition” to confine the computational space and thus keep the computer memory requirements to a reasonable size. Until recently, approximations in the absorbing boundary were the principal bottleneck, responsible for the limited accuracy of FDTD results. However, the introduction of the *perfectly matched layer* (PML) by Berenger [40, 41] is a major breakthrough in reducing the FDTD errors due to the absorbing boundary condition. The basic concept of this PML can be considered as an extension of the well-known fact that the condition

$$\sigma/\epsilon_0 = \sigma^*/\mu_0 \quad (4.64)$$

provides for the reflectionless transmission of a plane wave propagating normally across the interface between free space ($\epsilon_0, \mu_0, \sigma = 0$) and the outer boundary layer (with σ and σ^* as electric conductivity and magnetic conductivity, respectively.)

Let us consider the extension of (4.64) to PML for a two-dimensional transverse electric (TE to z -direction) case with field components E_x, E_y , and H_z and with the computation grid in the (x - y)-plane. The PML technique splits the H_z field into two components, H_{zx} and H_{zy} , and introduces (σ_x, σ_x^*) and (σ_y, σ_y^*) pairs both of which satisfy the relation (4.64). Under these conditions, it can be shown that the wave in the PML medium propagates with exactly the speed of light but decays exponentially along x and y . Also, the wave impedance of the PML medium exactly equals that of vacuum, regardless of the angle of propagation or frequency. The

TM case can be treated by duality by splitting E_z into E_x and E_y . In the three-dimensional case, all six components of the field vectors are split and the resulting PML modification of Maxwell's equations yields 12 equations. PML matching conditions are analogous.

Figure 4.26 shows the finite-difference computational domain used for the microstrip open-end discontinuity characterization problem [26]. Due to symmetry, only half of the structure is placed in the mesh domain with a magnetic wall at the plane of symmetry. These computations yield the total E -field at the open end. For S_{11} calculations, the incident field is obtained from that of an infinitely long micro-

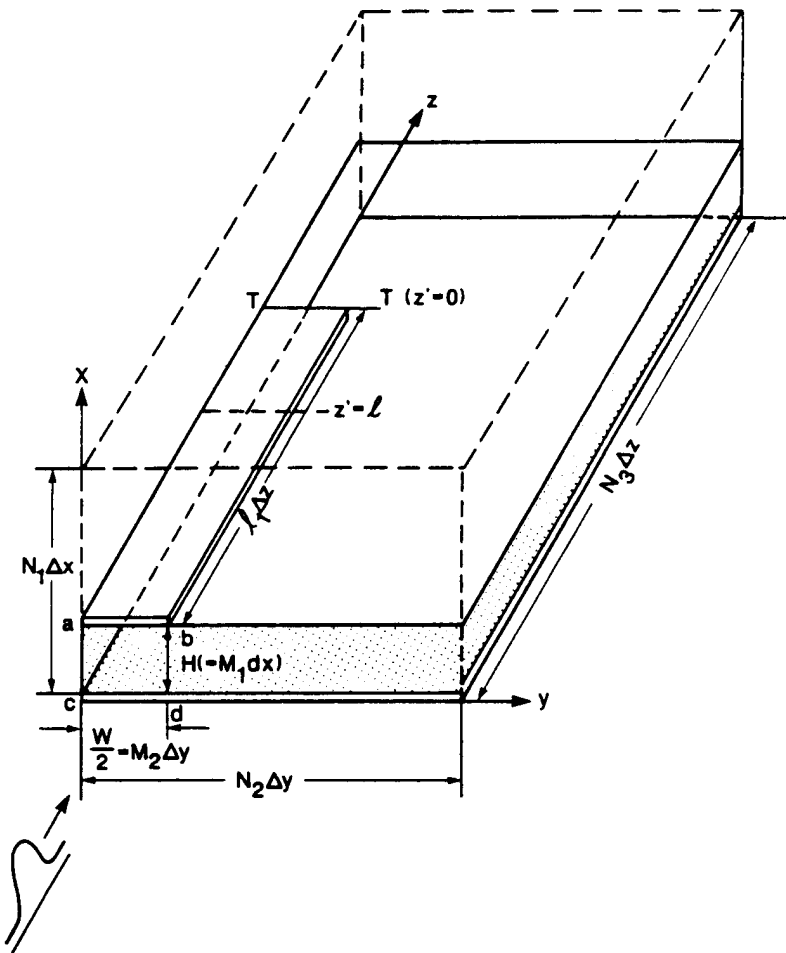


Figure 4.26 Configuration for characterization of a microstrip open end by FDTD (from [26], © 1988 IEEE. Reprinted with permission.).

strip, and the reflected field from the open end is obtained from the difference between the total open-end field and the incident field. When an equivalent circuit (a parallel combination of $G(f)$ and $C(f)$) is used to model the microstrip open end, the resulting values are plotted in Figure 4.27 [26]. Spectral domain analysis results of [31] are also shown in the figure. The amount of discrepancy seen, especially for higher frequencies, raises question about both sets of results. $G(f)$ values given in [31] do not exhibit a trend to go down smoothly to zero as the frequency goes to dc. The major difference in $C(f)$ behavior is in the increase in $C(f)$ value with frequency (before ultimately going down) seen in time domain analysis results. Such a behavior has also been seen in some other frequency domain analysis [42, 43]. Perhaps, refinements in implementation of both of these approaches are needed before any comparative conclusions can be drawn.

4.3 DISCONTINUITY MEASUREMENTS

Often experimental validation of microstrip discontinuities becomes necessary to test the accuracy of numerical results. Methods for accurately measuring microstrip discontinuities are based on the technique of incorporating discontinuities in microstrip resonators and measuring the change in the resonance frequency. Since these resonators are coupled very loosely to the test equipment, the measurements are not affected by the uncertain characteristics of coaxial-to-microstrip transitions. Both linear and ring resonators have been used for discontinuity measurements.

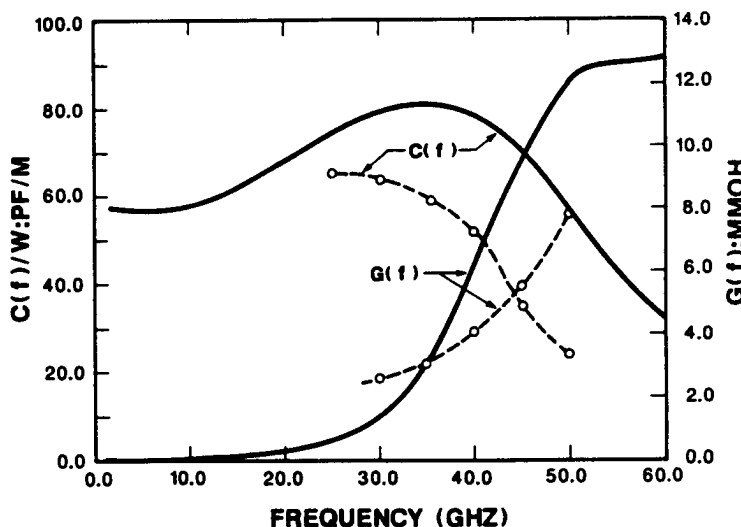


Figure 4.27 Wide frequency range modeling of a microstrip open end as obtained from FDTD: (—) and spectral domain (---) methods (from [26], © 1988 IEEE. Reprinted with permission.).

Two (or more) resonators need to be fabricated and tested for complete discontinuity characterization. The use of these resonators to measure the phase velocity in a microstrip was discussed in Section 1.5.3. The effect of microstrip discontinuities can also be determined accurately by measuring the scattering parameters. Measurements of discontinuities using resonators and scattering parameters methods are discussed in this section.

4.3.1 Linear Resonator Method

This method [27, 44, 45] uses a linear microstrip resonator that incorporates the discontinuity to be tested and is lightly coupled to the measuring instrumentation through a microstrip gap. The linear resonator is obtained by a $n\lambda_m/2$ length of a microstrip section open at the two ends. Thus the microstrip open end and the microstrip gap constitute essential parts of this measuring arrangement and must be calibrated before measurements on any other discontinuity may be carried out.

To minimize significant effects due to the change in substrate properties and fabrication, it is necessary to measure the effective dielectric constant ϵ_{re} for each circuit either by adding a linear resonator alongside each test configuration or by etching the test configuration to a suitable form and making a second measurement of the resonant frequency. The careful use of the latter strategy realizes the advantages of a substitutional method and will be illustrated in the method for characterization of microstrip gaps discussed in the following paragraph.

Open Ends and Gaps

An arrangement for characterization of the open end and the gap is shown in Figure 4.28(a). The length ℓ is chosen so that the effective length of this section at the frequency of measurement is $n\lambda_m/2$, where n is an integer and λ_m the microstrip wavelength. The length ℓ' should have an effective length of $\lambda_m/4$. The

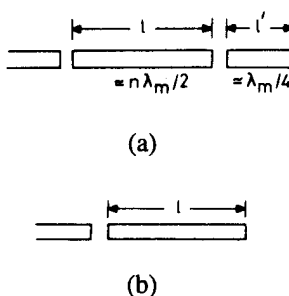


Figure 4.28 Arrangements for experimental characterization of an open end and a gap: (a) with two gaps and (b) with one gap and one open end.

free-space wavelength for the resonance of the structure, as shown in Figure 4.28(a), is then given by

$$(\ell + 2\Delta\ell_g) = \frac{n}{2} \frac{\lambda_0}{\sqrt{\epsilon_{re}}} \quad (4.65)$$

where $\Delta\ell_g$ is the extra length contributed by the microstrip gap. The equivalent circuit used for the gap is shown in Figure 3.17. The next step involves selective etching of length ℓ' . The resonance wavelength is measured again after ℓ' is removed (Figure 4.28(b)). Equation (4.65) can now be modified as

$$(\ell + \Delta\ell_{oc} + \Delta\ell_g) = \frac{n}{2} \frac{\lambda_0}{\sqrt{\epsilon_{re}}} \quad (4.66)$$

where $\Delta\ell_{oc}$ is the equivalent line length associated with an open end. There are three unknowns appearing in (4.65) and (4.66), namely, $\Delta\ell_g$, $\Delta\ell_{oc}$, and ϵ_{re} . So an additional measurement is required. If two values of ℓ are chosen to give resonance frequencies for different n close to the normal frequency of measurement, then one measurement with ℓ' present, together with two measurements (for different values of ℓ) with the extra section ℓ' removed, are sufficient to give ϵ_{re} , $\Delta\ell_{oc}$, and $\Delta\ell_g$. Suitable choices of resonant mode, n , and lengths ℓ have to be made such that various resonant frequencies are close together and ϵ_{re} can be taken as constant over this frequency range.

It has been mentioned [27] that this method has an experimental uncertainty of $\pm 10 \mu\text{m}$, which is largely attributable to substrate variations. This uncertainty corresponds to about $\pm 0.005 Y_0$ at 10 GHz.

Right-Angled Bends and Steps in Width

Variations of the procedure described above may also be used for other discontinuities. The arrangement for characterization of a right-angled bend [27, 44] and its equivalent circuit are shown in Figure 4.29. Two resonators of different lengths are needed to determine the two unknowns (B and $\Delta\ell_b$) in the equivalent circuit. These resonators will either have a voltage minimum or a voltage maximum at the corner, according to whether the effective overall length ($2\ell_1 + 2\Delta\ell_b + \Delta\ell_{oc} + \Delta\ell_g$) or ($2\ell_2 + 2\Delta\ell_b + \Delta\ell_{oc} + \Delta\ell_g$) at resonance is an odd or an even number of half wavelengths. For example, in the case of a half-wave resonator, there will be a voltage minimum at the corner of the bend and the effective increase in length will be $2\Delta\ell_b$. On the other hand, for a fullwave resonator the presence of a voltage maximum at the corner will cause the shunt susceptance B to increase the effective length of the fullwave resonator by an amount $(\lambda_m/\pi) \cdot \tan^{-1}(B/2Y_0)$. The relation for resonance frequency may now be written as

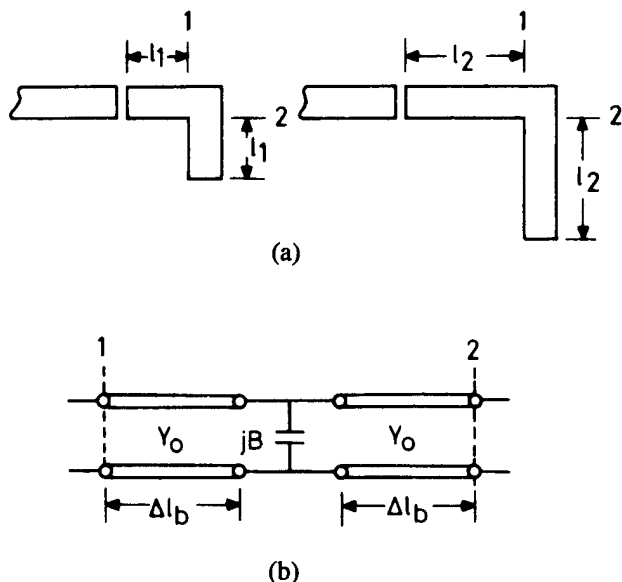


Figure 4.29 (a) An arrangement of experimental characterization of a right-angled bend and (b) equivalent circuit of the right-angled bend.

$$\ell_2 + \Delta\ell_{oc} + \frac{\Delta\ell_{oc} + \Delta\ell_g}{2} + \frac{\lambda_m}{2\pi} \tan^{-1}\left(\frac{B}{2Y_0}\right) = (2n+1)\frac{\lambda_m}{2} \quad (4.67)$$

Thus the series and the shunt components of the equivalent circuit can be separated. Since ϵ_{re} , $\Delta\ell_{oc}$, and $\Delta\ell_g$ are known from previous measurements, the parameters of the equivalent circuit shown in Figure 4.29(b) may be determined from the two frequencies of resonance.

A similar arrangement can be used to determine equivalent circuit parameters of a step continuity. The circuit arrangement is shown in Figure 4.30. Two resonators are used. Their lengths are adjusted so that in one case (i) we have a voltage

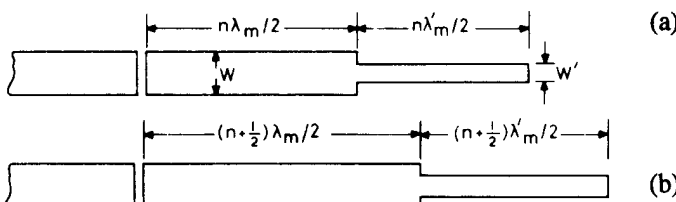


Figure 4.30 Circuit layouts for measuring the equivalent circuit of a step discontinuity: (a) with voltage maximum at the step and (b) with voltage minimum at the step.

maximum at the step while in the other case (ii) we have a voltage minimum at the step. Note that microstrip wavelengths λ_m and λ'_m correspond to microstrip lines of widths W and W' , respectively, and are not equal. Also in this case, we need the previous characterization of ϵ_{re} , $\Delta\ell_{oc}$, and $\Delta\ell_g$ for two widths W and W' .

TJunctions

A T-junction, its equivalent circuit, and circuit arrangement for its characterization [27] are shown in Figure 4.31. Only a symmetrical T-junction, with its through arm having the same impedance on either side of the branch, is considered.

The circuit of Figure 4.31(b) enables an accurate determination of the line length ℓ_a by determining the resonance of the half wavelength along the through arm before and after removing the stub. It may be pointed out that the susceptance B is ineffective because of the presence of a voltage minimum at the location of B . The length ℓ_b may be obtained from the frequency of peak attenuation when the

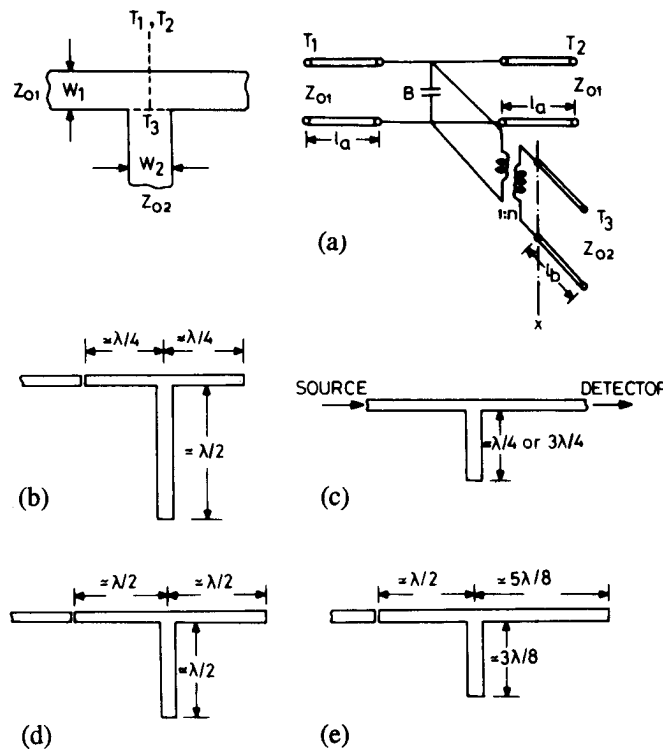


Figure 4.31 Circuit arrangement required for characterization of a T-junction: (a) discontinuity geometry and equivalent circuit, (b) set-up for determination of ℓ_a , (c) set-up for obtaining ℓ_b , (d) set-up for determination of B , and (e) set-up for determination of n^2 (from [27], © 1975 IEEE. Reprinted with permission.).

stub arm of Figure 4.31(c) is an odd number of quarter wavelengths long. Due to the shunt resonance of the stub, peak attenuation is a strong function of stub length. The end effect of the open end of the stub is assumed to be known from previous measurements. The configuration of Figure 4.31(d) enables B to be determined. The impedance ratio n^2 is measured by using the configuration shown in Figure 4.31(e). Values of B and n^2 depend on previous measurements, but some cancellation in the uncertainty can be obtained if the stub in Figure 4.31(d) is etched off and measurements carried out to obtain ϵ_{re} from resonance of the "through arm." The accuracy of determining n^2 has been estimated [27] as ± 2 percent. It may be noted that the transformation ratio n does not affect the resonance frequency for the configurations (b) to (d) because of the presence of an open or short circuit at plane XX (Figure 4.31(a)).

Measurements for a symmetrical cross junction may also be made by using circuits of Figures 4.31(b, c, d, and e) and taking advantage of the symmetry of the junction. Similar measurement techniques may also be designed for other discontinuity structures.

The main advantage of the linear resonator method is that it involves shorter lengths that result in better accuracy. Since this method uses the open ends of the resonator, it is necessary to characterize the open ends accurately. This is one of the disadvantages associated with this method. The other disadvantage of this method is the need for fabricating a set of resonators for each frequency of interest. These problems are overcome in the ring resonator method, which is discussed in the next section.

4.3.2 Ring Resonator Method

Ring resonators were described in Section 1.5 during the discussion of measurement of microstrip phase velocities. When a ring resonator is used in place of a linear resonator as discussed above, the open-end and gap reactances need not be calibrated and taken into account. This method is convenient particularly for symmetrical two-port discontinuities (with $S_{11} = S_{22}$).

A microstrip ring structure resonates if its electrical length is an integral multiple of the guide wavelength. When a discontinuity is introduced into the ring, each resonance degenerates into two distinct modes. This splitting is conveniently interpreted in terms of even and odd excitations of the discontinuity [46]. The even mode corresponds to the incidence of two waves of equal magnitude and phase upon the discontinuity; while in the odd mode, waves of equal magnitude but opposite phase are incident from two sides. Any one of these resonances can be excited by an appropriate choice of the point of excitation along the ring. In an experimental setup [46], this is achieved by shifting the position of the launcher along the ring as shown in Figure 4.32.

A symmetrical discontinuity may be represented in terms of a T-network as shown in Figure 4.33(a). Parameters of the T-network can be evaluated from the

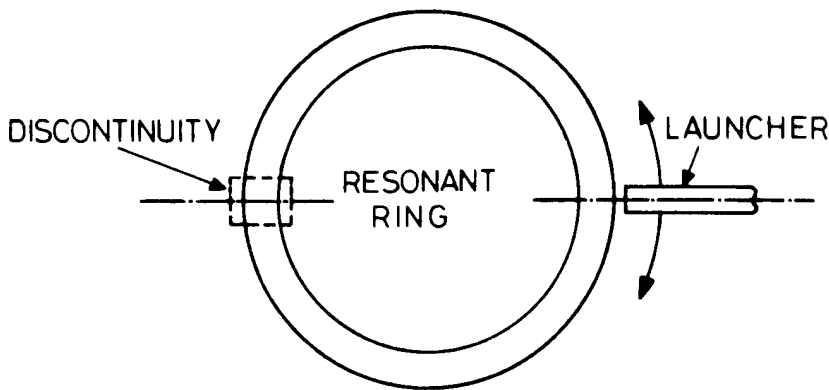


Figure 4.32 Ring resonator method for measurement on a two-port symmetrical discontinuity.

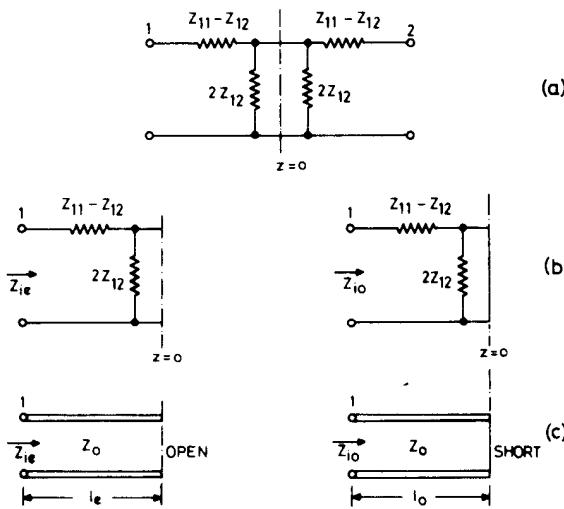


Figure 4.33 (a) Representation of a symmetrical discontinuity by a T-network, (b) equivalent circuits for even and odd modes and (c) equivalent line lengths for these modes.

two impedances Z_{ie} and Z_{io} shown in Figure 4.33(b) and obtained by introducing an open circuit and a short circuit, respectively, at the $z=0$ plane. These impedances can be expressed in terms of two fictitious electrical lengths ℓ_e and ℓ_o (shown in Figure 4.33(c)) as

$$Z_{ie} = Z_{11} + Z_{12} = -j \cot k\ell_e \quad (\text{even case}) \quad (4.68a)$$

$$Z_{io} = Z_{11} - Z_{12} = j \tan k\ell_o \quad (\text{odd case}) \quad (4.68b)$$

where $k = 2\pi/\lambda_m$ is the propagation constant along the ring resonator and all the impedances have been normalized to the characteristic impedance of the microstrip ring. These equivalent lengths ℓ_e and ℓ_o add to the total length of the ring for even and odd excitations, respectively, as shown in Figure 4.34(a, b). Resonance conditions for the two cases may be written as

$$\ell_{\text{ring}} + 2\ell_e = n\lambda_{me} \quad (4.69)$$

and

$$\ell_{\text{ring}} + 2\ell_o = n\lambda_{mo} \quad (4.70)$$

where λ_{me} and λ_{mo} are guide wavelengths corresponding to the even and odd mode resonance frequencies, respectively. ℓ_{ring} is the physical length of the ring resonator

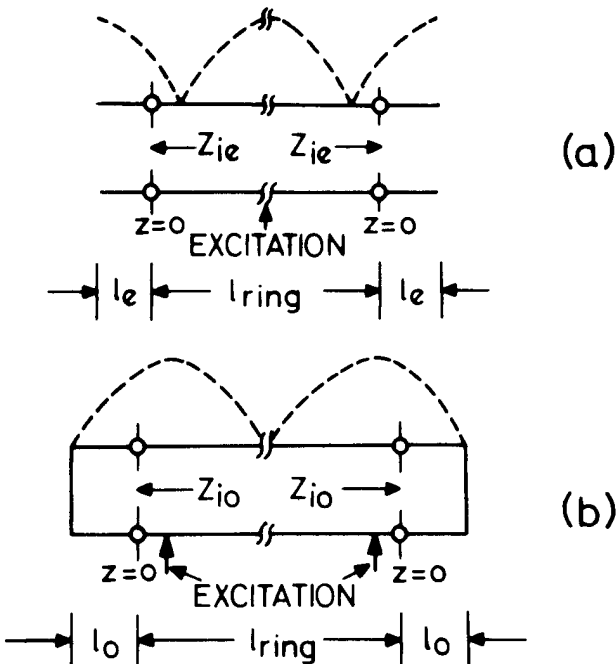


Figure 4.34 Standing wave patterns on the ring for (a) even and (b) odd modes of excitation.

along the mean circumference. Equations (4.68) to (4.70) may be used to evaluate Z_{l1} and Z_{l2} and hence the equivalent circuit.

This method can also be extended for unsymmetrical discontinuities. An example of characterization of impedance steps in a ring resonator is given in reference [47]. The circuit arrangement used is shown in Figure 4.35. Two steps are located such that lengths ℓ_1 and ℓ_2 are electrically equal. A voltage maximum or minimum can be arranged to appear at the discontinuity locations successively by changing the point of excitation. Shunt and series parts of equivalent circuits are thus separated.

4.3.3 Scattering Parameters Measurement Method

With recent advancements in de-embedding techniques and RF probes, the discontinuity equivalent circuit model parameters can also be determined accurately from 1-port or 2-port scattering parameter measurements. The model parameters are extracted by computer optimization, which correlates the calculated and measured Sparameters. The model parameter values can be obtained to the same accuracy as the measurement accuracy by using recently developed on-wafer sapphire substrate calibration standards and the *thru-reflect-line* (TRL) calibration method. The TRL calibration method is based on the transmission line calibration standards, which include nonzero thru, a reflect (open or short), and delay line standards (one or more dictated by the frequency range over which the calibration is performed). The advantage of the TRL calibration lies in simple standards that can be placed on the same substrate as the components ensuring a common transmission medium.

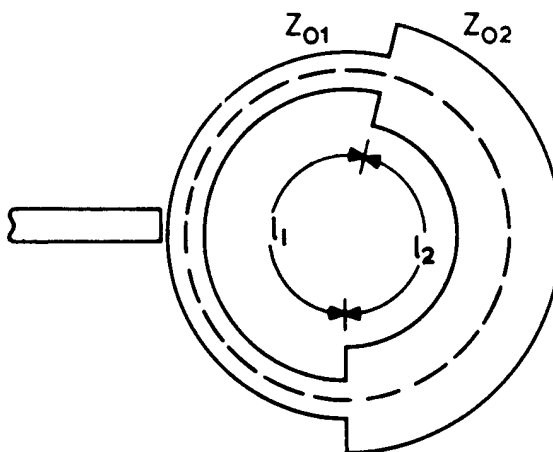


Figure 4.35 An arrangement for the characterization of step discontinuity by ring resonator method.

Figure 4.36 shows examples of structures that can be tested for 2-port S-parameters to characterize right-angle bend, step-in-width, and T-junction microstrip discontinuities. The minimum distance between the two discontinuities (right-angle bend and step-in width) must be kept to 2 to 3 line widths or substrate thicknesses, whichever is greater, so that the interaction effects between the discontinuities due to evanescent modes are negligible. Figures 4.37 and 4.38 show a comparison between the numerical and measured S-parameters for the step-in-width and T-junction discontinuities, respectively [48]. The measured results were obtained using RF probes and agrees very well with the fullwave analysis values.

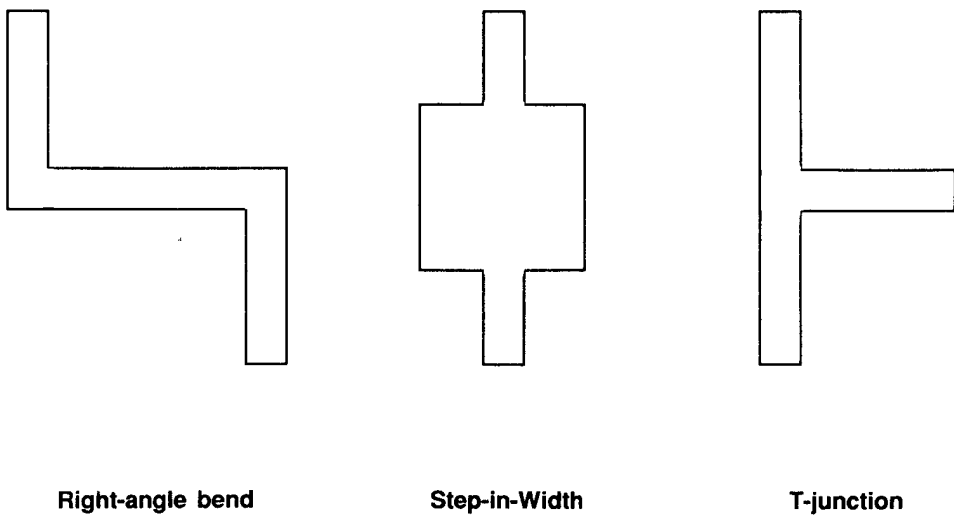


Figure 4.36 Examples of microstrip discontinuity measurement structures.

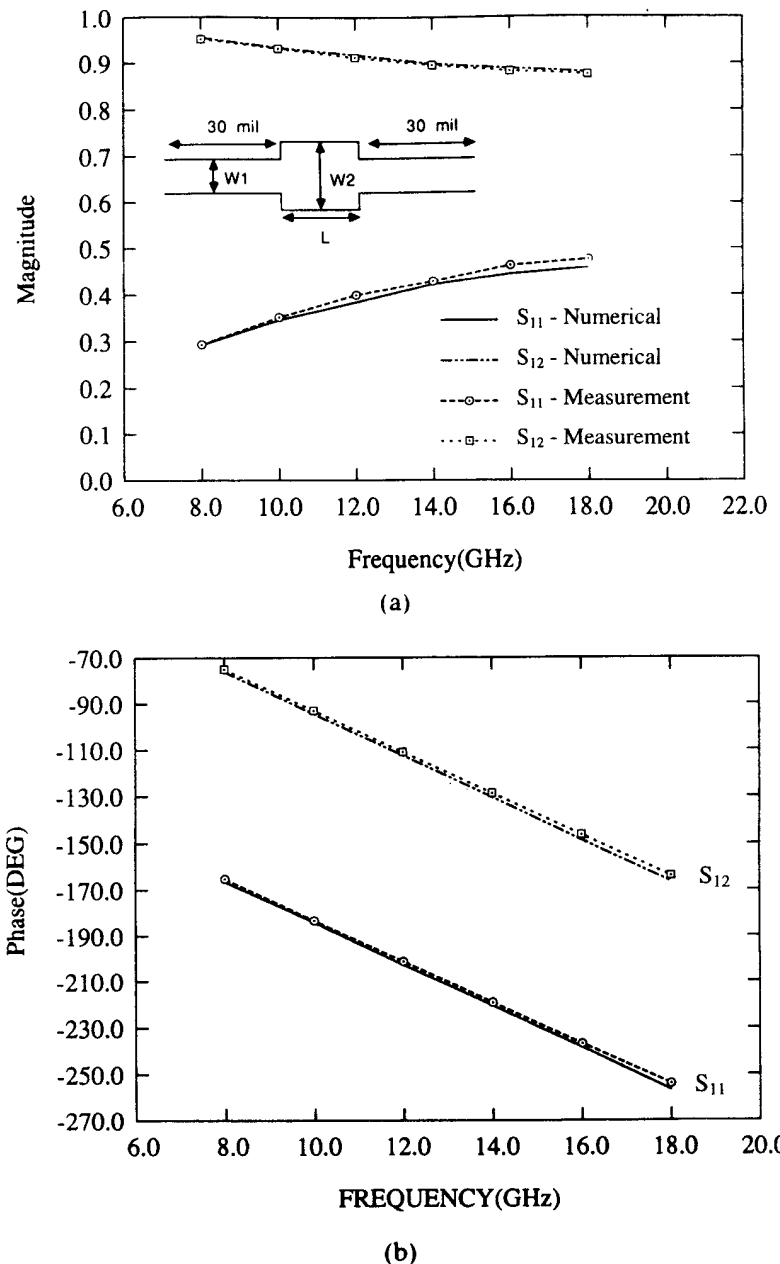


Figure 4.37 Scattering parameters of the two-step configuration shown. Numerical (experimental) dimensions: $W_1 = 9.2$ (9.2) mil, $W_2 = 23$ (23.1) mil, $L = 50.6$ (50.0) mil, $\epsilon_r = 9.9$, $h = 10$ mil. (a) Magnitude and (b) phase (from [48], © 1989 IEEE. Reprinted with permission.).

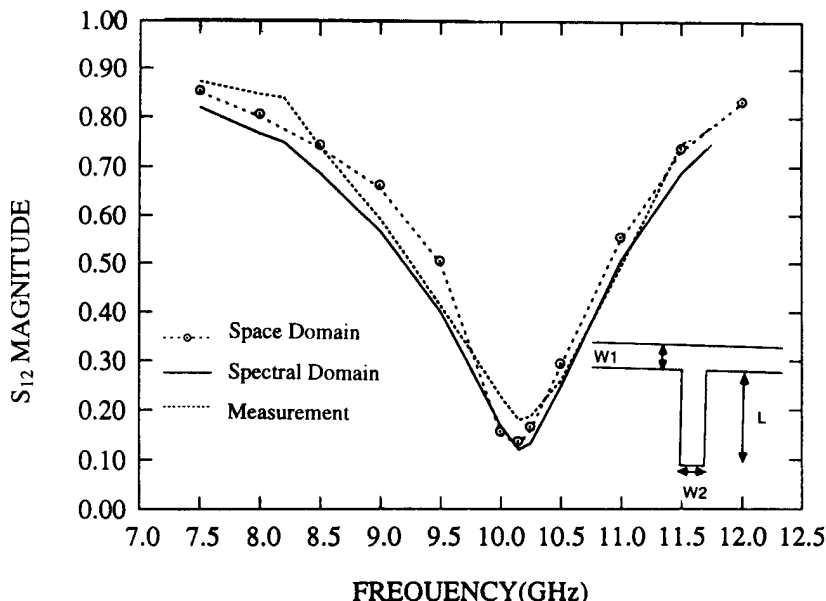


Figure 4.38 Scattering parameters S_{12} for microstrip stub. Parameters for space (spectral) domain analysis: $W_1 = 1.44$ (1.40), $W_2 = 1.44$ (1.40); $L = 2.16$ (2.16), $\epsilon_r = 10.65$, $h = 1.27$. All dimensions are in millimeters (from [48], © 1989 IEEE. Reprinted with permission.).

References

- [1] Wolff, I., G. Kompa, and R. Mehran, "Calculation Method for Microstrip Discontinuities and T-Junctions," *Electron. Lett.*, Vol. 8, 1972, pp. 177–179.
- [2] Kompa, G., and R. Mehran, "Planar Waveguide Model for Calculating Microstrip Components," *Electron. Lett.*, Vol. 11, 1975, pp. 459–460.
- [3] Gupta, K. C., and M. D. Abouzahra, "Planar Circuit Analysis," *Numerical Technique for Microwave and Millimeter-Wave Passive Structures* (ed. T. Itoh), New York: John Wiley & Sons, 1989, pp. 273–278.
- [4] Kompa, G., "S-matrix Computation of Microstrip Discontinuities with a Planar Waveguide Model," *Archiv. Elektr. Übertr.*, Vol. 30, 1976, pp. 58–64.
- [5] Mehran, R., "The Frequency-dependent Scattering Matrix of Microstrip Right-Angle Bends, T-Junctions and Crossings," *Archiv. Elektr. Übertr.*, Vol. 29, 1975, pp. 454–460.
- [6] Mehran, R., "The Frequency-dependent Equivalent Circuits for Microstrip Right-Angle Bends, T-Junctions and Crossings," *Archiv. Elektr. Übertr.*, Vol. 30, 1976, pp. 80–82.
- [7] Menzel, W., and I. Wolff, "A Method for Calculating the Frequency Dependent Properties of Microstrip Discontinuities," *IEEE Trans.*, Vol. MTT-25, 1977, pp. 107–112.
- [8] Chadha, R., and K. C. Gupta, "Compensation of Discontinuities in Planar Transmission Lines," *IEEE Trans.*, Vol. MTT-30, December 1982, pp. 2151–2156.
- [9] Lewin, L., "Radiation from Discontinuities in Stripline," *Proc. IEE*, Vol. 107C, 1960, pp. 163–170.
- [10] Abouzahra, M. D., and L. Lewin, "Radiation from Microstrip Discontinuities," *IEEE Trans.*, Vol. MTT-27, 1979, pp. 722–723.
- [11] Abouzahra, M. D., "On the Radiation from Microstrip Discontinuities," *IEEE Trans.*, Vol. MTT-29, 1981, pp. 666–668.

- [12] Hoffman, K., "Radiation from Microwave Circuits," *Handbook of Microwave Integrated Circuits*, Norwood, MA: Artech House, 1987, pp. 311–324.
- [13] Sabban, A., and K. C. Gupta, "Multiport Network Model for Evaluating Radiation Loss and Spurious Coupling between Discontinuities in Microstrip Circuits," *IEEE MTT-S Int. Microwave Symp. Digest*, 1989, pp. 707–710.
- [14] Sabban, A., and K. C. Gupta, "Characterization of Radiation Loss from Microstrip Discontinuities Using a Multiport Network Modeling Approach," *IEEE Trans.*, Vol. MTT-39, April 1991, pp. 705–712.
- [15] Gardiol, F. E., "Radiation from Microstrip Circuits: an Introduction," *Intl. J. MIMICAE*, Vol. 1 (2), 1991, pp. 225–235.
- [16] James, J. R., et al., *Microstrip Antennas, Theory and Design*, Stevenage, UK: Peter Peregrinus, Ltd., 1981, p. 90.
- [17] Benalla, A., and K. C. Gupta, "Multiport Network Model and Transmission Characteristics of Two Port Rectangular Microstrip Antennas," *IEEE Trans. on Antennas Propagation*, Vol. AP-36, October 1988, pp. 1337–1342.
- [18] Benalla, A., and K. C. Gupta, "Multiport Network Approach for Modeling the Mutual Coupling Effects in Microstrip Patch Antennas and Arrays," *IEEE Trans. on Antennas Propagation*, Vol. AP-37, February 1989, pp. 148–152.
- [19] "HP Momentum," HP85158A/85184A, Hewlett-Packard Company, HP-EEsof, Santa Rosa Systems Division, Santa Rosa, California.
- [20] "IE3D," Version 2.0, Zeland Software, Inc., Fremont, California.
- [21] "Em," Sonnett Software, Inc., Liverpool, New York.
- [22] "Explorer," Compact Software, Inc., Paterson, New Jersey.
- [23] Itoh, T., "Analysis of Microstrip Resonators," *IEEE Trans.*, Vol. MTT-22, 1974, pp. 946–952.
- [24] Mosig, J. R., and F. E. Gardiol, "Integral Equation Techniques for Dynamic Analysis of Microstrip Discontinuities," *Alta Freq.*, Vol. LVII, June 1988, pp. 171–181.
- [25] Wu, D. I., D. C. Chang, and B. L. Brim, "Accurate Numerical Modeling of Microstrip Junctions and Discontinuities," *Intl. J. MIMICAE*, Vol. 1, 1991, pp. 48–58.
- [26] Zhang, X., and K. K. Mei, "Time-Domain Finite Difference Approach to the Calculation of Frequency-Dependent Characteristics of Microstrip Discontinuities," *IEEE Trans.*, Vol. MTT-36, December 1988, pp. 1775–1786.
- [27] Easter, B., "The Equivalent Circuits of Some Microstrip Discontinuities," *IEEE Trans.*, MTT-23, 1975, pp. 655–660.
- [28] Jansen, R. H., "Hybrid Mode Analysis of End Effects of Planar Microwave and Millimeter Wave Transmission Lines," *Proc. Inst. Elec. Engr.*, Vol. 128, Part H, April 1978, pp. 77–86.
- [29] Boukamp, J., and R. H. Jansen, "The High Frequency Behavior of Microstrip Open Ends in Microwave Integrated Circuits Including Energy Leakage," *Proc. 14th European Microwave Conf.*, 1984, pp. 142–147.
- [30] Jackson, R. W., and D. M. Pozar, "Microstrip Open-End and Gap Discontinuities," *IEEE Trans.*, Vol. MTT-33, October 1985, pp. 1036–1042.
- [31] Katehi, P. B., and N. C. Alexopoulos, "Frequency-Dependent Characteristics of Microstrip Discontinuities in Millimeter-Wave Integrated Circuits," *IEEE Trans.*, Vol. MTT-33, October 1985, pp. 1029–1035.
- [32] Koster, N. H. L., and R. H. Jansen, "The Microstrip Step Discontinuity: A Revised Description," *IEEE Trans.*, Vol. MTT-34, February 1986, pp. 213–223.
- [33] Jackson, R. W., "Full-wave, Finite Element Analysis of Irregular Microstrip Discontinuities," *IEEE Trans.*, Vol. MTT-37, 1989, pp. 81–89.
- [34] Jansen, R. H., "The Spectral-domain Approach for Microwave Integrated Circuits," *IEEE Trans.*, Vol. MTT-33, 1985, pp. 1043–1056.
- [35] Mosig, J. R., and F. E. Gardiol, "A Dynamic Radiation Model for Microstrip Structures," *Advances in Electronics and Electron Physics* (ed. P. W. Hawkes), Vol. 59, New York: Academic Press, 1982.

- [36] Mosig, J. R., "Arbitrarily Shaped Microstrip Structures and Their Analysis with a Mixed Potential Integral Equation," *IEEE Trans.*, Vol. MTT-36, 1988, pp. 314–323.
- [37] Chang, D. C., and J. X. Zheng, "Electromagnetic Modeling of Passive Circuit Elements in MMIC," *IEEE Trans.*, Vol. MTT-40, September 1992, pp. 1741–1747.
- [38] Wolff, I., "Finite Difference Time-domain Simulation of Electromagnetic Fields and Microwave Circuits," *Intl. J. Numerical Modeling: Electronic Networks, Devices and Fields*, Vol. 5, 1992, pp. 163–182.
- [39] Eswarappa, C., and W. J. R. Hoefer, "Time Domain Analysis of Via Holes and Shorting Pins in Microstrip Using 3-D SCN TLM," *IEEE MTT-S Symp. Digest*, Vol. 2, June 1993, pp. 917–920.
- [40] Berenger, J., "A Perfectly Matched Layer for the Absorption of Electromagnetic Waves," *J. Comp. Phys.*, Vol. 114, October 1994, pp. 185–200.
- [41] Katz, D., E. Thiele, and A. Taflove, "Validation and Extension to Three Dimensions of the Berenger PML Absorbing Boundary Condition for FDTD Meshes," *IEEE Microwave & Guided Wave Lett.*, Vol. 4, August 1994, pp. 268–270.
- [42] James, J. R., and A. Henderson, "High-Frequency Behavior of Microstrip Open-End Terminations," *IEE J. Microwave Opt. Acoustics*, Vol. 3, September 1979, pp. 205–211.
- [43] James, D. S., and S. H. Te, "Microstrip End Effects," *Electron. Lett.*, Vol. 8, January 27, 1972, pp. 46–47.
- [44] Easter, B., et al., "Resonant Techniques for the Accurate Measurement of Microstrip Properties and Equivalent Circuits," *Proc. 1973 European Microwave Conf.*, paper B 7.6.
- [45] Stephenson, I. W., and B. Easter, "Resonant Techniques for Establishing the Equivalent Circuits of Small Discontinuities in Microstrip," *Electron. Lett.*, Vol. 7, 1971, pp. 582–584.
- [46] Hoefer, W. J. R., and A. Chattopadhyay, "Evaluation of the Equivalent Circuit Parameters of Microstrip Discontinuities Through Perturbation of a Resonant Ring," *IEEE Trans.*, Vol. MTT-23, 1975, pp. 1067–1071.
- [47] Groll, H., and W. Weidmann, "Measurement of Equivalent Circuit Elements of Microstrip Discontinuities by a Resonant Method," *Nachr. Zeit.*, Vol. 28, 1975, pp. 74–77.
- [48] Harokopus, Jr., W. P., and P. B. Ketehi, "Characterization of Microstrip Discontinuities on Multilayer Dielectric Substrates Including Radiation Losses," *IEEE Trans. on Microwave Theory Tech.*, Vol. MTT-37, December 1989, pp. 2058–2066.

CHAPTER 5

Slotlines

5.1 INTRODUCTION

A slotline is a planar transmission structure proposed for use in MICs by Cohn in 1968 [1]. The basic slotline configuration is shown in Figure 5.1. It consists of a dielectric substrate with a narrow slot etched in the metallization on one side of the substrate. The other side of the substrate is without any metallization. The geometry is planar and, as mentioned earlier in Chapter 1, is well suited for its usage in microwave integrated circuits.

Slotlines can be included in microstrip circuits by etching the slotline circuit in the ground plane of the substrate for microstrip circuits. This type of hybrid combination allows flexibility in the design of microwave circuits and has led to some new types of circuits such as hybrid branchline directional couplers. Also, some of the circuit elements, which cannot easily be achieved in microstrip configuration, can be incorporated in the slotline part of the circuit. These, for example, could be short circuits, high impedance lines, series stubs, and baluns. Slotlines can also be employed as a resonant or nonresonant antenna.

In a slotline, the wave propagates along the slot with the major electric field component oriented across the slot in the plane of metallization on the dielectric substrate. The mode of propagation is non-TEM and almost transverse electric in nature. However, unlike conventional waveguides, there is no low-frequency cutoff because the slotline is a two-conductor structure. The approximate field distribution in a slotline is shown in Figure 5.2. This near-field distribution has been discussed by Cohn [2].

The various methods used for the analysis of a slotline are described in the following section. Design considerations for the slotline, short-end and open-end discontinuities, transitions from slotline to microstrip and coaxial line, and some circuit applications of slotlines are discussed in this chapter.

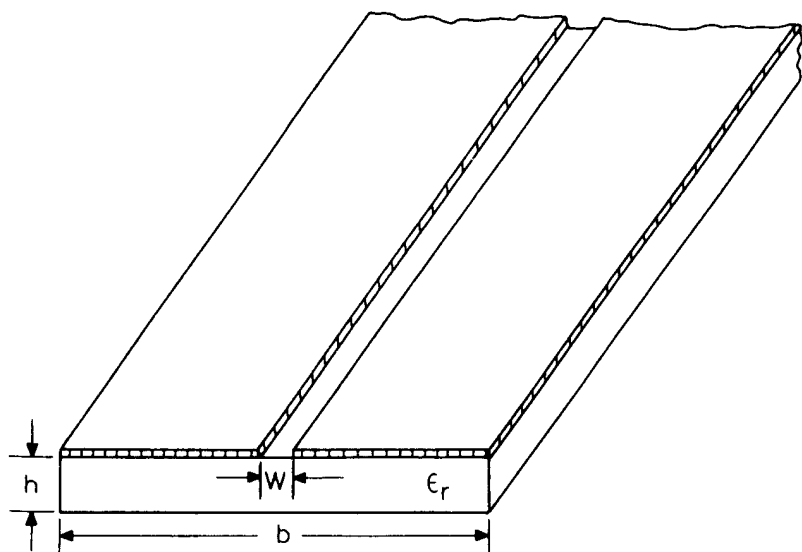


Figure 5.1 Slotline configuration.

----- MAGNETIC FIELD LINES
— ELECTRIC FIELD LINES

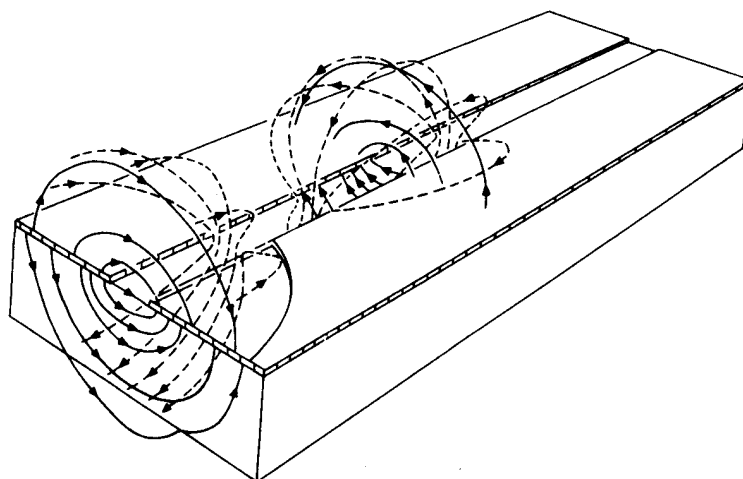


Figure 5.2 Field distribution in a slotline.

5.2 SLOTLINE ANALYSIS

The slotline was first analyzed by Cohn [1]. He employed the transverse resonance approach after converting the slotline into a waveguide configuration. Since then, a number of other techniques have been employed. Some of these analytical techniques are:

1. Approximate analysis [1];
2. The transverse resonance approach [1];
3. Galerkin's method in Fourier transform domain [3–7];
4. Finite-difference time domain technique [8].

The first three methods are discussed in the following sections.

5.2.1 Approximate Analysis

Before attempting a rigorous analysis, it is worthwhile to look at an approximate solution for slotline characteristics. This has the advantage of mathematical simplicity and provides a better qualitative picture. An approximate analysis for the field distribution, polarization of magnetic field, and expression for slot wavelength are presented below.

Field Distribution

For a waveguiding structure to be useful as a transmission line or a circuit element, it is necessary to confine the fields near the structure. An analysis of the field distribution of the transmission line structure is helpful in determining the parameters necessary to prevent the spreading of the fields.

The slotline field contains six components: three electric field components and three magnetic field components. The longitudinal component of the electric field is very weak since the energy propagates between the two conductors. If the slot width W is much smaller than the free-space wavelength λ_0 , the electric field across the slot may be represented by an equivalent line source of magnetic current, and then the far-field contains only three components: H_x , H_r , and E_ϕ . At a distance r ($\gg W$) in the air region above the slot (Figure 5.3), these may be written as [1]

$$H_x = AH_0^{(1)}(k_c r) \quad (5.1)$$

$$H_r = -\frac{\gamma_x}{k_c^2} \frac{\partial H_x}{\partial r} = \frac{A}{\sqrt{1 - (\lambda_s/\lambda_0)^2}} H_1^{(1)}(k_c r) \quad (5.2)$$

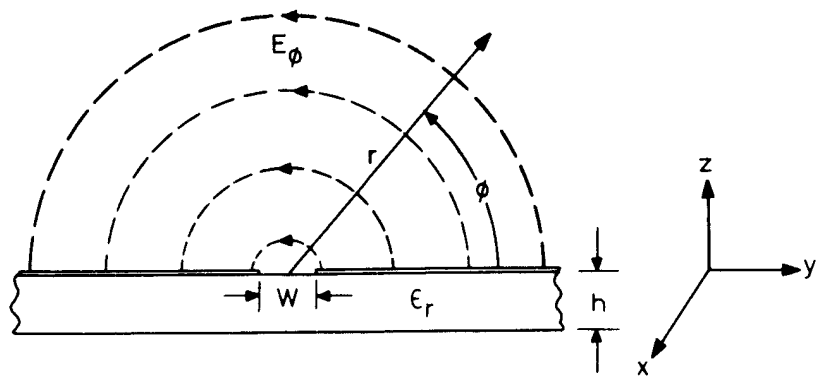


Figure 5.3 Cylindrical coordinates configuration for the approximate analysis of slotline.

$$E_\phi = \frac{j\omega\mu}{k_c^2} \frac{\partial H_x}{\partial r} = -\eta H_r \lambda_s / \lambda_0 \quad (5.3)$$

where γ_x is the propagation constant along the x -direction, which is the direction of propagation, and k_c is related to the slot wavelength λ_s by the equation

$$k_c = j \frac{2\pi}{\lambda_0} \sqrt{\left(\frac{\lambda_0}{\lambda_s}\right)^2 - 1} \quad (5.4)$$

From the above expressions for the field components the following information may be obtained.

Rate of Decay of Field

For large values of r , $H_0^{(1)}(j|r|)$ and $H_1^{(1)}(j|r|)$ may be expressed as

$$H_n^{(1)}(j|r|) = \frac{2}{\sqrt{j\pi|r|}} \exp\left(-|r| - j\frac{n\pi}{2} - j\frac{\pi}{4}\right) \quad (5.5)$$

Therefore, if $k_c r$ is imaginary, the field will decay with distance r . Equation (5.4) shows that $k_c r$ is imaginary for $\lambda_s/\lambda_0 < 1$. Hence a relative wavelength ratio less than unity is a sufficient condition to ensure transverse decay of the field. To a zero-order approximation, λ_s/λ_0 is equal to $\sqrt{2}/(\epsilon_r + 1)$. As λ_s/λ_0 is decreased, that is, ϵ_r increased, the rate of decay becomes faster and fields become more tightly bound to the slot. For example, the ratio of voltage $V(r)$ at a distance r equal to one inch (2.54 cm) to the voltage V directly across the slot on a substrate with $\epsilon_r = 16$ is calculated (at 3 GHz) to be

$$V(r)/V = \frac{\pi}{2} \left| k_c r H_1^{(1)}(k_c r) \right| = 0.038 \quad (5.6)$$

Information regarding the rate of decay of fields is also helpful in determining the size of the enclosure needed for the slotline.

Polarization of the Magnetic Field

The polarization of the magnetic field in a slotline can be obtained from the ratio $|H_x/H_r|$. Equations (5.1) and (5.2) give

$$\left| \frac{H_x}{H_r} \right| = \left| \frac{H_0^{(1)}(k_c r)}{H_1^{(1)}(k_c r)} \right| \sqrt{1 - (\lambda_s/\lambda_0)^2} \quad (5.7)$$

From the mathematical tables it is evident that $H_1^{(1)}(j|r|)$ is always greater than $H_0^{(1)}(j|r|)$ and also $\lambda_s < \lambda_0$. Therefore, $|H_x|$ is always less than $|H_r|$, and the magnetic field cannot have circular polarization. Nevertheless elliptical polarization exists for all values of r .

The field configuration shown in Figure 5.2 indicates that the magnetic field has regions of elliptical polarization both in the air region above the slot and on the conducting surface constituting the slot. These regions of elliptical polarization can be utilized for the construction of nonreciprocal ferrite components. Robinson and Allen [9] have used slotline in the construction of ferrite devices.

Slot Wavelength

As shown in Figure 5.2, slotline field components are not confined to the substrate alone. They extend into the air regions above the slot and below the substrate also. Therefore, the energy is distributed between the substrate and the air regions. Consequently, the effective dielectric constant for a slotline (ϵ_{re}) is less than the substrate permittivity ϵ_r . Galejs [10] has shown that the zeroth-order value of ϵ_{re} for a slot on an infinitely thick substrate is the average dielectric constant of the two media, that is,

$$\epsilon_{re} = \frac{\epsilon_r + 1}{2} \quad (5.8)$$

and therefore,

$$\frac{\lambda_s}{\lambda_0} = \sqrt{\frac{2}{\epsilon_r + 1}} \quad (5.9)$$

It has been observed by Garg and Gupta [11] that for slotline on a finite thickness substrate, the above value of λ_s/λ_0 is approached for the cutoff thickness for the TE₀ surface wave mode. The cutoff thickness $(h/\lambda_0)_c$ is given by

$$(h/\lambda_0)_c = 0.25/\sqrt{\epsilon_r - 1} \quad (5.10)$$

The approximate analysis discussed above gives a good physical picture of the field configuration of the slotline. But it does not lead to an evaluation of the characteristic impedance of the slotline. Moreover, the variation of slot wavelength λ_s with different geometrical parameters of the slotline, that is, h , W , and b , is not provided by this analysis. To overcome these shortcomings, several rigorous analyses of slotline have been carried out [1–8, 12–15]. These analyses take into account the effects of various parameters on the slotline impedance Z_{0s} and the wavelength λ_s . Some of these analyses are described next.

5.2.2 Transverse Resonance Method

In this method, a slotline is analyzed as a rectangular waveguide configuration. The key feature of this analysis is the introduction of boundary walls such that a rectangular waveguide configuration with a capacitive iris is obtained. It is then analyzed in terms of waveguide modes propagating perpendicular to the slotline plane.

Development of Waveguide Model

A waveguide model for a slotline is obtained by introducing (i) conducting planes normal to the slot and the substrate at $x = 0$ and $x = a$ such that $a = \lambda_s/2$ as shown in Figure 5.4(a). Since the spacing between the two planes is $\lambda_s/2$, the introduction of these planes does not disturb the field variations. A standing wave field configuration with E_y and E_z equal to zero at $x = 0$ and $x = a$ is obtained. (ii) Next, electric walls or magnetic walls are inserted in planes parallel to the slot and perpendicular to the substrate at $y = \pm b/2$ as shown in Figure 5.4(b, c). Since the fields are tightly bound to the slot, the walls at $y = \pm b/2$ will have a negligible effect when the distance b is sufficiently large. Introduction of electric walls creates a configuration of a capacitive iris in a rectangular waveguide as shown in Figure 5.4(d). The two cases of electric walls and magnetic walls are analyzed separately.

Slot Wavelength

Having developed the capacitive iris waveguide model the method of transverse resonance is applied to determine the slot wavelength. In this method the sum of susceptances at the iris plane is equated to zero.

This sum includes the susceptances of the TE₁₀ mode looking in the +z and -z directions and the capacitive iris susceptance due to higher order modes on

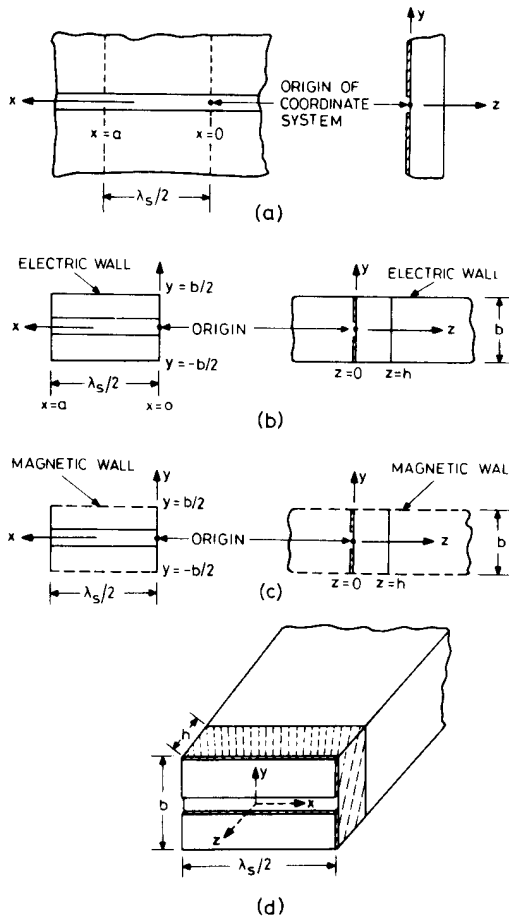


Figure 5.4 Development of the rectangular waveguide model for slotline analysis using the transverse resonance method: (a) The configuration, (b) model with electric walls, (c) model with magnetic walls, and (d) resulting configuration of an iris in a waveguide.

both sides of the iris (the TE_{10} mode cannot exist for the magnetic wall case). The introduction of magnetic walls or electric walls at $y = \pm b/2$ gives rise to different sets of modes. These sets are $TE_{1,2n}$ and $TM_{1,2m}$ where n is an integer ≥ 0 and $m \geq 1$ for electric walls, and n or $m = 1/2, 3/2, 5/2$ for magnetic walls.

Two separate expressions for the total susceptance ηB_t for the electric wall and magnetic wall cases are obtained. These are given in Appendix 5.A.

Evaluation of Slot Wavelength

Roots of the equation $\eta B_t = 0$, with ηB_t given by (A.1) or (A.2) for the electric wall case or magnetic wall case, respectively, give the slot wavelength λ_s . It is a function

of λ_0 also, unlike in a microstrip because the mode of propagation in the slotline is hybrid in nature.

Numerical computations by Cohn [1] show that, for large values of b , identical results are obtained for both the electric wall and magnetic wall models. In the specific case when $\epsilon_r = 20$, $h = 3.48$ mm, $W = 0.625$ mm, $\lambda_0 = 10.67$ cm, and $\lambda_s = 3.45$ cm, the solutions for electric and magnetic walls approach each other for $b > 38.1$ mm and are only slightly different for $b = 25.4$ mm.

Slotline Impedance

Because of the non-TEM nature of the mode in a slotline, the characteristic impedance Z_{0s} cannot be defined uniquely. The definition based on the power-voltage relationship is used more frequently and may be written as [6]

$$Z_{0s} = |V|^2/2P \quad (5.11)$$

where V is the peak voltage across the slot. The average power P can be expressed in terms of energy storage W_t , which may be related to the rate of change of total susceptance B_t with frequency. For resonant cavities [16]

$$W_t = \left(\frac{V^2}{4} \right) \left(\frac{\partial B_t}{\partial \omega} \right) \quad (5.12)$$

and also since

$$W_t = \frac{\pi P}{2\omega} \frac{v}{v_g} \quad (5.13)$$

we can write

$$Z_{0s} = (v/v_g) \pi / (\omega \partial B_t / \partial \omega)$$

With $p = \lambda_0/\lambda_s$, it may be also expressed as

$$Z_{0s} = \eta \frac{v}{v_g} \frac{\pi}{p} \left\{ \frac{\Delta p}{-\Delta(\eta B_t)} \right\} \quad (5.14)$$

The ratio of the phase velocity v to the group velocity v_g can be evaluated from the sensitivity of (λ_0/λ_s) with respect to frequency f . It is given by

$$\frac{v}{v_g} = 1 - \frac{f}{\lambda_s/\lambda_0} \frac{\Delta(\lambda_s/\lambda_0)}{\Delta f} \quad (5.15)$$

Evaluation of Slotline Impedance

For the given set of slotline parameters ϵ_r , W , h , and b choose a small frequency interval Δf centered around f , the frequency of operation. The value of $\Delta(\lambda_s/\lambda_0)$ is computed from two separate solutions of $\eta B_t = 0$ for the two values of h/λ_0 corresponding to the ends of the frequency interval. Using the value of $\Delta(\lambda_s/\lambda_0)$ in (5.15) gives the value of v/v_g . The change in susceptance $\Delta(\eta B_t)$ (needed for evaluating Z_{0s}) is computed from (A.1) or (A.2) with λ_s held constant (λ_s is obtained from the value of λ_s/λ_0 at the frequency f) and p incremented slightly plus and minus from the value $p = \lambda_0/\lambda_s$ at $\eta B_t = 0$. (The two values of p are obtained from the two end values of λ_0 for the frequency interval Δf selected.)

Computations of slot wavelength and impedance, based on the above method, have been carried out. They are shown in Figure 5.5 for $\epsilon_r = 9.7$. Mariani et al. [17] have also reported slotline characteristics for $\epsilon_r = 9.6, 11.0, 13.0, 16.0$, and 20.0 .

The method of transverse resonance is valid for the following range of parameters

$$W < 0.25 \lambda_0 / \sqrt{\epsilon_r} \quad (5.16a)$$

$$W/h \leq 1 \quad (5.16b)$$

$$b \geq 7W \quad (5.16c)$$

Condition (5.16a) is necessary to avoid resonance across the slot. Although this method can also be used to determine the effect of the finite size of metal sheets enclosing the slot, it cannot be employed for wide slots ($W/h > 1$). The method described next does not suffer from this limitation.

5.2.3 Galerkin's Method in the Spectral Domain

An accurate analysis of the slotline is based on the use of Galerkin's method in the Fourier transform domain. This method is very popular and is similar to those used for fullwave analysis of microstrip lines (in Section 2.3.1) and for analysis of microstrip discontinuities (in Section 3.2.3).

Field components in a slotline are expressed in terms of two scalar potentials $\psi^e(x, y)$ and $\psi^h(x, y)$. The longitudinal components are proportional to these potentials and are written as

$$E_z = k_c^2 \psi^e(x, y) \exp(\pm j\beta z) \quad (5.17)$$

$$H_z = k_c^2 \psi^h(x, y) \exp(\pm j\beta z) \quad (5.18)$$

where β is the propagation constant and

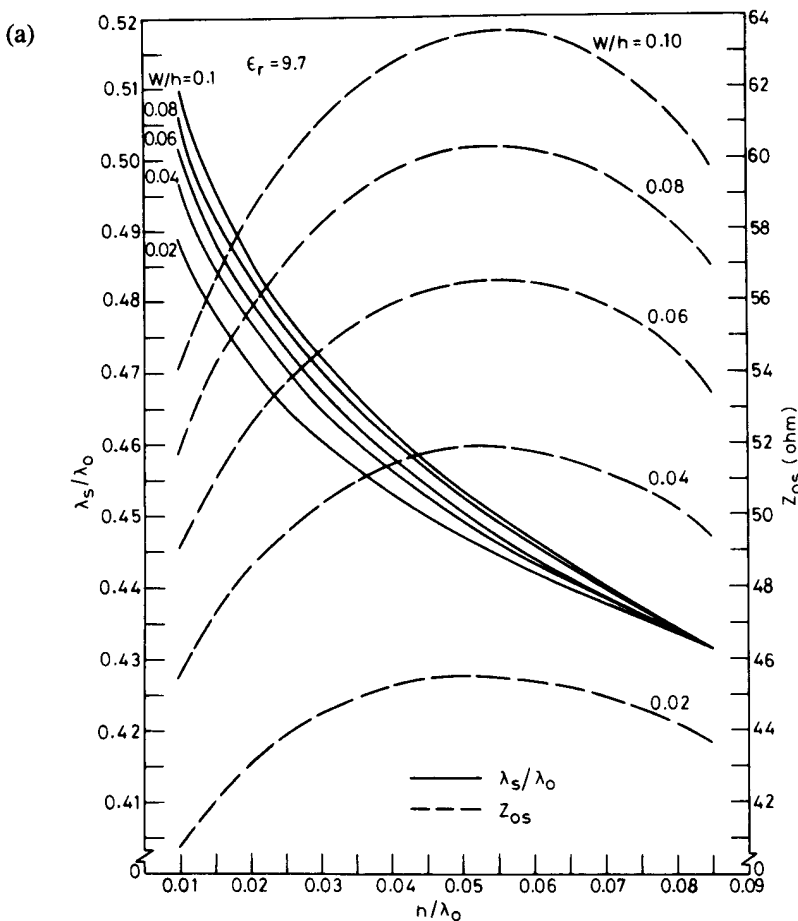


Figure 5.5 (a) Characteristics of slotline ($\epsilon_r = 9.7$, $W/h = 0.02$ to 0.1 , $h/\lambda_0 = 0.01$ to 0.085) and (b) characteristics of slotline ($\epsilon_r = 9.7$, $W/h = 0.2$ to 1.0 , $h/\lambda_0 = 0.01$ to 0.085).

$$k_c^2 = k_i^2 - \beta^2$$

$$k_i = (\epsilon_i \mu_i)^{1/2} \quad i = 1, 2, 3 \quad (5.19)$$

Values of i specify the three regions of the slotline cross section as shown in Figure 5.6. The next step is the Fourier transformation of the scalar wave equation along x . This transformation converts the second-order partial differential equation into an ordinary differential equation that can be solved easily. The solutions for transforms of scalar potentials in the three regions may be written as

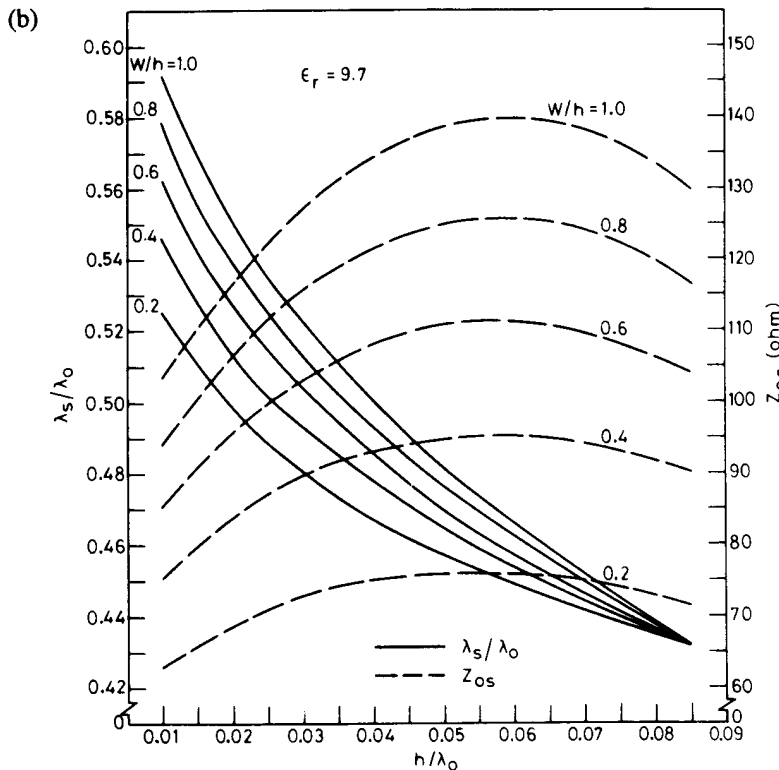


Figure 5.5 (continued).

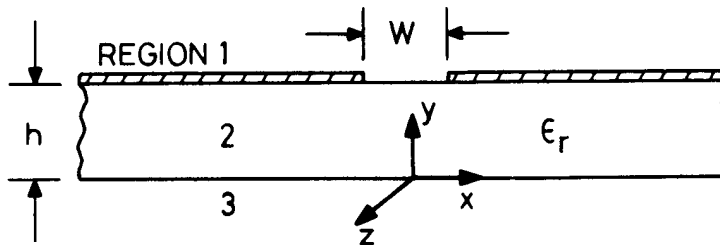


Figure 5.6 Configuration of slotline for analysis using Galerkin's method in FTD.

$$\begin{aligned}
 \psi_1^e(\alpha, y) &= A^e(\alpha) \exp[-\gamma_1(y - h)] \\
 \psi_2^e(\alpha, y) &= B^e(\alpha) \sinh \gamma_2 y + C^e(\alpha) \cosh \gamma_2 y \\
 \psi_3^e(\alpha, y) &= D^e(\alpha) \exp(\gamma_1 y)
 \end{aligned} \tag{5.20}$$

and

$$\begin{aligned}\psi_1^h(\alpha, y) &= A^h(\alpha) \exp[-\gamma_1(y - h)] \\ \psi_2^h(\alpha, y) &= B^h(\alpha) \sinh \gamma_2 y + C^h(\alpha) \cosh \gamma_2 y \\ \psi_3^h(\alpha, y) &= D^h(\alpha) \exp(\gamma_1 y)\end{aligned}\quad (5.21)$$

where

$$\gamma_i^2 = \alpha^2 + \beta^2 - k_i^2$$

The eight unknown coefficients A^e through D^h are related to the tangential electric and magnetic field components at the interfaces $y = 0$ and $y = h$ by the continuity conditions and can also be related to the surface current density on the metal and the electric fields in the slot at $y = h$. If the Fourier transforms of the x - and z -directed current densities are denoted by $\tilde{J}_x(\alpha)$ and $\tilde{J}_z(\alpha)$ and electric field components by $\tilde{E}_x(\alpha)$ and $\tilde{E}_z(\alpha)$, one obtains a set of coupled equations of the form

$$\begin{bmatrix} M_1(\alpha, \beta), M_2(\alpha, \beta) \\ M_3(\alpha, \beta), M_4(\alpha, \beta) \end{bmatrix} \begin{bmatrix} \tilde{J}_x(\alpha) \\ \tilde{J}_z(\alpha) \end{bmatrix} = \begin{bmatrix} \tilde{E}_x(\alpha) \\ \tilde{E}_z(\alpha) \end{bmatrix} \quad (5.22)$$

The matrix \mathbf{M} is now inverted to express transforms of current densities in terms of electric field transforms. If the \mathbf{N} -matrix is the inverse of the \mathbf{M} -matrix, (5.22) gives

$$\begin{bmatrix} N_1(\alpha, \beta), N_2(\alpha, \beta) \\ N_3(\alpha, \beta), N_4(\alpha, \beta) \end{bmatrix} \begin{bmatrix} \tilde{E}_x(\alpha) \\ \tilde{E}_z(\alpha) \end{bmatrix} = \begin{bmatrix} \tilde{J}_x(\alpha) \\ \tilde{J}_z(\alpha) \end{bmatrix} \quad (5.23)$$

The matrix elements N_1, \dots, N_4 are known functions of α and β . Now $\tilde{E}_x(\alpha)$ and $\tilde{E}_z(\alpha)$ are expanded in terms of the Fourier transforms of basis functions, and Galerkin's method is applied to yield a homogeneous system of linear equations. The determinant of the coefficient matrix, corresponding to this set of linear equations, equated to zero gives the dispersion relation. An iteration scheme for β can be used to find a nontrivial solution of this dispersion relation.

The rate of convergence of this series representation depends upon the choice of basis functions. A frequently used choice [6] is

$$E_x = \sum_{n=0}^N a_n E_{xn} \quad (5.24)$$

$$E_{xn} = \begin{cases} \frac{2}{\pi W} \frac{T_{2n}(2x/W)}{\sqrt{1 - (2x/W)^2}} & n = 0, 1, 2, \dots ; |x| \leq W/2 \\ 0 & \text{elsewhere} \end{cases} \quad (5.25)$$

$$E_z = \sum_{m=1}^M b_m E_{zm} \quad (5.26)$$

$$E_{zm} = \begin{cases} \frac{2}{\pi W} \sqrt{1 - (2x/W)^2} U_{2m-1}(2x/W) & m = 1, 2, \dots; |x| \leq W/2 \\ 0 & \text{elsewhere} \end{cases} \quad (5.27)$$

where $T_n(\bullet)$ and $U_n(\bullet)$ are Chebyshev polynomials of the first and second kind, respectively. The Fourier transforms of the above basis functions can be found readily in closed form as

$$\tilde{E}_{xn} = (-1)^n J_{2n}\left(\frac{\alpha W}{2}\right) \quad n = 0, 1, \dots \quad (5.28)$$

and

$$\tilde{E}_{zm} = j(-1)^{m+1} 2m \frac{J_{2m}(\alpha W/2)}{(\alpha W/2)} \quad m = 1, 2, \dots \quad (5.29)$$

The computations involved can be simplified by assuming $E_z = 0$. A comparison of the magnitudes of the x and z components of the electric field shows that E_z is about one-tenth of E_x and can therefore be neglected [4].

This method has also been used to evaluate the characteristic impedance of slotlines [6]. In the definition of characteristic impedance (5.11) the voltage across the slot is obtained by integrating the transverse electric field component E_x as

$$V = \int_{-W/2}^{W/2} E_x(x) dx = \tilde{E}_x(\alpha)|_{\alpha=0} = \tilde{E}_x(0) \quad (5.30)$$

The time-averaged power flow P along the slotline can be obtained as in (2.37). Again the computations involved can be simplified by neglecting $E_z(x)$.

A comparison of results obtained by Galerkin's method in the spectral domain with Cohn's method [1] indicates that the transverse resonance method used by Cohn yields accurate results for a slotline within the limits prescribed in (5.16). However, for wider slots one should use Galerkin's method in the spectral domain.

Higher order modes in a slotline can also be determined using the above method. Citerne et al. [13] and Kitazawa et al. [14] have determined the propagation constant for the first higher order mode in a slotline using different techniques. Figure 5.7 shows the dispersion characteristics of the normalized propagation constant β/k_0 for the dominant and first higher order mode [14]. Computations show that one basis function is sufficient for the dominant mode, while two basis functions

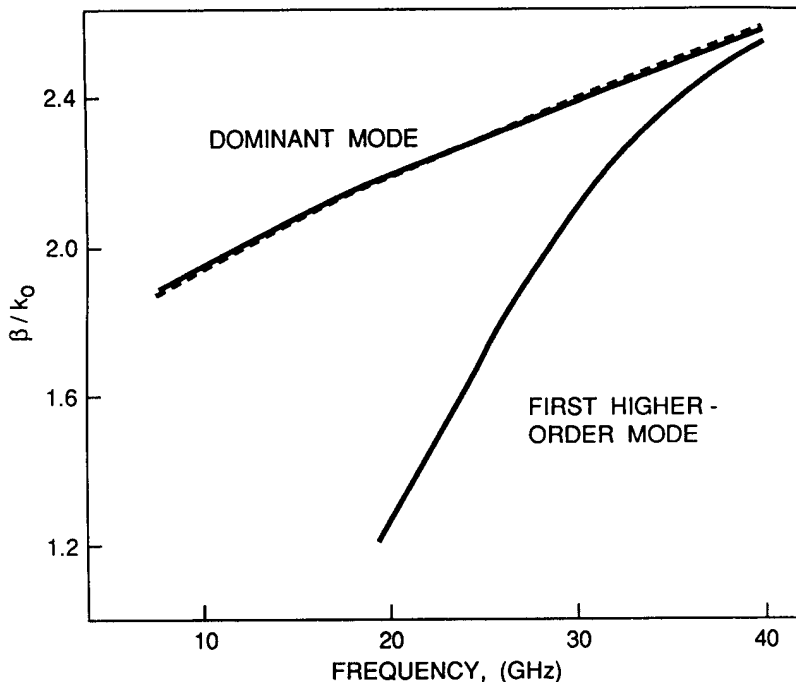


Figure 5.7 Normalized propagation constant for the dominant and first higher order mode in a slotline: $\epsilon_r = 9.6$, $h = 1$ mm, $W = 1$ mm. A broken line represents Cohn's method [1] (from [14], © 1980 IEEE. Reprinted with permission.).

are necessary for the first higher order mode. The numerical data are compared with the results of Cohn [1], and the agreement is quite good.

5.3 DESIGN CONSIDERATIONS

5.3.1 Closed-Form Expressions

The various methods of analysis discussed above do not lead to any closed-form expressions for slotline wavelength and impedance. This becomes a serious handicap for circuit analysis and design especially when computer-aided design techniques are used. Some attempts to overcome this difficulty have been reported [11]. Closed-form expressions given below have been obtained by curve fitting the result based on Cohn's analysis. These expressions have an accuracy of about 2 percent for the following range of parameters

$$\begin{aligned} 9.7 \leq \epsilon_r &\leq 20 \\ 0.02 \leq W/h &\leq 1.0 \\ 0.01 \leq h/\lambda_0 &\leq (h/\lambda_0)_c \end{aligned} \quad (5.31)$$

where $(h/\lambda_0)_c$ is the cutoff value for the TE_0 surface-wave mode on the grounded substrate and is given by (5.10).

The expressions obtained are:

- For $0.02 \leq W/h < 0.2$

$$\begin{aligned} \lambda_s/\lambda_0 &= 0.923 - 0.448 \log \epsilon_r + 0.2 W/h \\ &\quad - (0.29 W/h + 0.047) \log(h/\lambda_0 \times 10^2) \end{aligned} \quad (5.32)$$

$$\begin{aligned} Z_{0s} &= 72.62 - 35.19 \log \epsilon_r + 50 \frac{(W/h - 0.02)(W/h - 0.1)}{W/h} \\ &\quad + \log(W/h \times 10^2)[44.28 - 19.58 \log \epsilon_r] \\ &\quad - [0.32 \log \epsilon_r - 0.11 + W/h(1.07 \log \epsilon_r + 1.44)] \\ &\quad \cdot (11.4 - 6.07 \log \epsilon_r - h/\lambda_0 \times 10^2)^2 \end{aligned} \quad (5.33)$$

- For $0.2 \leq W/h \leq 1.0$

$$\begin{aligned} \lambda_s/\lambda_0 &= 0.987 - 0.483 \log \epsilon_r + W/h(0.111 - 0.0022 \epsilon_r) \\ &\quad - (0.121 + 0.094 W/h - 0.0032 \epsilon_r) \log(h/\lambda_0 \times 10^2) \end{aligned} \quad (5.34)$$

$$\begin{aligned} Z_{0s} &= 113.19 - 53.55 \log \epsilon_r + 1.25 W/h(114.59 - 51.88 \log \epsilon_r) \\ &\quad + 20(W/h - 0.2)(1 - W/h) \\ &\quad - [0.15 + 0.23 \log \epsilon_r + W/h(-0.79 + 2.07 \log \epsilon_r)] \\ &\quad \cdot [10.25 - 5 \log \epsilon_r + W/h(2.1 - 1.42 \log \epsilon_r) \\ &\quad - h/\lambda_0 \times 10^2]^2 \end{aligned} \quad (5.35)$$

It is possible to derive more accurate expressions for the slotline wavelength when the dielectric constant of the substrate is fixed. Expressions with 1 percent accuracy for dielectric constant values of 9.7 and 20.0 are

1. $\epsilon_r = 9.7, 0.01 \leq h/\lambda_0 \leq (h/\lambda_0)_c$

- (i) $0.02 \leq W/h \leq 0.1$

$$\begin{aligned} \lambda_s/\lambda_0 &= -(0.29 W/h + 0.057) \log(h/\lambda_0 \times 10^2) + 0.283 W/h \\ &\quad + 0.485 \end{aligned} \quad (5.36)$$

(ii) $0.1 < W/h \leq 1.0$

$$\begin{aligned}\lambda_s/\lambda_0 = & -(0.11W/h + 0.077)\log(h/\lambda_0 \times 10^2) + 0.104W/h \\ & + 0.507\end{aligned}\quad (5.37)$$

2. $\epsilon_r = 20, 0.01 \leq h/\lambda_0 \leq (h/\lambda_0)_c$ (i) $0.02 \leq W/h \leq 0.1$

$$\begin{aligned}\lambda_s/\lambda_0 = & -(0.269W/h + 0.047)\log(h/\lambda_0 \times 10^2) + 0.2W/h \\ & + 0.345\end{aligned}\quad (5.38)$$

(ii) $0.1 < W/h \leq 1.0$

$$\begin{aligned}\lambda_s/\lambda_0 = & -(0.094W/h + 0.072)\log(h/\lambda_0 \times 10^2) + 0.075W/h \\ & + 0.362\end{aligned}\quad (5.39)$$

The logarithms in expressions (5.32) through (5.39) are to the base 10.

High ϵ_r substrates are used for circuit applications to confine the field near the slot. Slotlines on low ϵ_r substrates have interesting applications in antennas. Janaswamy and Schaubert [6] have obtained closed-form expressions for low ϵ_r substrates by curve fitting the numerical results obtained from Galerkin's method in FTD. These expressions are as follows and are valid for the range of parameters [6]

$$\begin{aligned}2.22 \leq \epsilon_r \leq 9.8 \\ 0.0015 \leq W/\lambda_0 \leq 1.0 \\ 0.006 \leq h/\lambda_0 \leq 0.06\end{aligned}$$

1. For $0.0015 \leq W/\lambda_0 \leq 0.075$ and $2.22 \leq \epsilon_r \leq 3.8$

$$\begin{aligned}\lambda_s/\lambda_0 = & 1.045 - 0.365\ell_n\epsilon_r + \frac{6.3(W/h)\epsilon_r^{0.945}}{(238.64 + 100W/h)} \\ & - \left[0.148 - \frac{8.81(\epsilon_r + 0.95)}{100\epsilon_r} \right] \cdot \ell_n(h/\lambda_0) \\ av = & 0.37 \text{ percent, max} = 2.2 \text{ percent (at one point)}\end{aligned}\quad (5.40)$$

$$\begin{aligned}
Z_{0S} = & 60 + 3.69 \sin \left[\frac{(\epsilon_r - 2.22) \pi}{2.36} \right] + 133.5 \ell_n(10\epsilon_r) \sqrt{W/\lambda_0} \\
& + 2.81 [1 - 0.011\epsilon_r(4.48 + \ell_n\epsilon_r)] (W/h) \ell_n(100h/\lambda_0) \\
& + 131.1 (1.028 - \ell_n\epsilon_r) \sqrt{h/\lambda_0} \\
& + 12.48 (1 + 0.18\ell_n\epsilon_r) \frac{W/h}{\sqrt{\epsilon_r - 2.06 + 0.85(W/h)^2}} \\
av = & 0.67 \text{ percent, max} = 2.7 \text{ percent (at one point)} \tag{5.41}
\end{aligned}$$

2. For $0.0015 \leq W/\lambda_0 \leq 0.075$ and $3.8 \leq \epsilon_r \leq 9.8$

$$\begin{aligned}
\lambda_S/\lambda_0 = & 0.9217 - 0.277\ell_n\epsilon_r + 0.0322(W/h) \left[\frac{\epsilon_r}{(W/h + 0.435)} \right]^{1/2} \\
& - 0.01\ell_n(h/\lambda_0) \left[4.6 - \frac{3.65}{\epsilon_r^2 \sqrt{W/\lambda_0} (9.06 - 100W/\lambda_0)} \right] \\
av = & 0.6 \text{ percent, } |\max| = 3 \text{ percent (at three points, occurs for} \\
& W/h > 1 \text{ and } \epsilon_r > 6.0) \tag{5.42}
\end{aligned}$$

$$\begin{aligned}
Z_{0S} = & 73.6 - 2.15\epsilon_r + (638.9 - 31.37\epsilon_r)(W/\lambda_0)^{0.6} \\
& + (36.23\sqrt{\epsilon_r^2 + 41} - 225) \frac{W/h}{(W/h + 0.876\epsilon_r - 2)} \\
& + 0.51(\epsilon_r + 2.12)(W/h)\ell_n(100h/\lambda_0) \\
& - 0.753\epsilon_r(h/\lambda_0)/\sqrt{W/\lambda_0} \\
av = & 1.58 \text{ percent, max} = 5.4 \text{ percent (at three points, occurs for} \\
& W/h > 1.67) \tag{5.43}
\end{aligned}$$

3. For $0.075 \leq W/\lambda_0 \leq 1.0$ and $2.22 \leq \epsilon_r \leq 3.8$

$$\begin{aligned}
\lambda_S/\lambda_0 = & 1.194 - 0.24\ell_n\epsilon_r - \frac{0.621\epsilon_r^{0.835}(W/\lambda_0)^{0.48}}{(1.344 + W/h)} \\
& - 0.0617 \left[1.91 - \frac{(\epsilon_r + 2)}{\epsilon_r} \right] \ell_n(h/\lambda_0) \\
av = & 0.69 \text{ percent, max} = -2.6 \text{ percent (at two points, for} \\
& W/\lambda_0 > 0.8) \tag{5.44}
\end{aligned}$$

$$Z_{0S} = 133 + 10.34(\epsilon_r - 1.8)^2 + 2.87[2.96 + (\epsilon_r - 1.582)^2] \\ \cdot [\{W/h + 2.32\epsilon_r - 0.56\} \\ \cdot \{(32.5 - 6.67\epsilon_r)(100h/\lambda_0)^2 - 1\}]^{1/2} \\ - (684.45h/\lambda_0)(\epsilon_r + 1.35)^2 \\ + 13.23[(\epsilon_r - 1.722)W/\lambda_0]^2$$

av = 1.9 percent, |max| = 5.4 percent (at three points, for
 $W/\lambda_0 > 0.8$)

(5.45)

4. For $0.075 \leq W/\lambda_0 \leq 1.0$ and $3.8 \leq \epsilon_r \leq 9.8$

$$\lambda_S/\lambda_0 = 1.05 - 0.04\epsilon_r + 1.411 \times 10^{-2}(\epsilon_r - 1.421) \\ \cdot \ell_n\{W/h - 2.012(1 - 0.146\epsilon_r)\} \\ + 0.111(1 - 0.366\epsilon_r)\sqrt{W/\lambda_0} \\ + 0.139(1 + 0.52\epsilon_r)\ell_n(14.7 - \epsilon_r)(h/\lambda_0)\ell_n(h/\lambda_0)$$

av = 0.75 percent, |max| = 3.2 percent (at two points, occurs for
 $W/\lambda_0 = 0.075, h/\lambda_0 > 0.03$)

(5.46)

$$Z_{0S} = 120.75 - 3.74\epsilon_r + 50[\tan^{-1}(2\epsilon_r) - 0.8] \\ \cdot (W/h)^{[1.11+(0.132(\epsilon_r-27.7)/(100h/\lambda_0+5))]} \\ \cdot \ell_n[100h/\lambda_0 + \sqrt{(100h/\lambda_0)^2 + 1}] \\ + 14.21(1 - 0.458\epsilon_r)(100h/\lambda_0 + 5.1\ell_n\epsilon_r - 13.1) \\ \cdot (W/\lambda_0 + 0.33)^2$$

av = 2.0 percent, |max| = 5.8 percent (at two points, occurs for

$W/\lambda_0 < 0.1$). In the above formula, $\tan^{-1}(\cdot)$ assumes its principal value.

(5.47)

In the expressions (5.40) to (5.47) “av” stands for the average of the absolute percentage error and “max” for the maximum percentage error in a sample of 120 data points.

The values obtained from the closed-form expressions (5.40) to (5.47) have been compared with the numerical data in [12]. The comparison covers the microwave and millimeter-wave frequency range.

5.3.2 Effect of Metal Thickness

It has been assumed in the analysis presented in Section 5.2 that the metal conductors constituting the slot have zero thickness, which does not reflect reality. Kitazawa

et al. [14, 15] have evaluated the effect of finite metal thickness on the phase constant and characteristic impedance. It is observed that λ_s increases and the characteristic impedance decreases with the increase in metal thickness t . For $\epsilon_r = 20$, the increase in λ_s is about 1 percent, and the decrease in characteristic impedance is about 2 percent for a t/W ratio of 0.02.

5.3.3 Effect of Tolerances

The effect of tolerances in various parameters on the performance of a slotline can be carried out using sensitivity analysis, as we did for the microstrip in Section 2.4.3. The worst case behavior for a given set of tolerances is represented by the maximum change in characteristic impedance and slot wavelength. Expressions for these quantities are (for a fixed λ_0)

$$\frac{|\Delta Z_{0s}|_{\max}}{Z_{0s}} = \left| \frac{\Delta W}{W} S_W^{Z_{0s}} \right| + \left| \frac{\Delta h}{h} S_h^{Z_{0s}} \right| + \left| \frac{\Delta \epsilon_r}{\epsilon_r} S_{\epsilon_r}^{Z_{0s}} \right| \quad (5.48)$$

$$\frac{|\Delta \epsilon_{re}|_{\max}}{\epsilon_{re}} = \left| \frac{\Delta W}{W} S_W^{\epsilon_{re}} \right| + \left| \frac{\Delta h}{h} S_h^{\epsilon_{re}} \right| + \left| \frac{\Delta \epsilon_r}{\epsilon_r} S_{\epsilon_r}^{\epsilon_{re}} \right| \quad (5.49)$$

$$\text{where } \epsilon_{re} = (\lambda_0 / \lambda_s)^2 \quad (5.50)$$

The sensitivity expressions can be obtained by using closed-form equations for Z_{0s} and λ_s/λ_0 . These expressions are given in Appendix 5.B for high ϵ_r values and plotted as sensitivity curves in Figure 5.8 and 5.9 [18]. Sensitivity expressions for low ϵ_r values can be similarly derived by using (5.40) to (5.47).

For a given set of slotline parameters the sensitivity values are calculated and substituted in (5.48) to determine $(\Delta Z_{0s})_{\max}$. This value of $(\Delta Z_{0s})_{\max}$ is used to calculate slotline VSWR. It is shown in Figure 5.10 for $\epsilon_r = 9.7$. The inverse problem of determining the fabrication tolerance for a given set of other tolerances can be solved in the same manner as has been done for a microstrip in Section 2.4.3. The required fabrication accuracy in the slot width for a VSWR of 1.05 and a given set of other tolerances is shown in Figure 5.11 [18].

5.3.4 Losses in Slotline

The losses in a slotline, like those in a microstrip, are the result of the lossy dielectric and the conductors with finite conductivity σ . Dielectric loss α_d can be computed by using a complex value for the relative permittivity, ϵ_r , of the substrate in the evaluation of the propagation constant of the slotline. Due to the lossy substrate the propagation constant becomes complex, $\gamma = \beta + j\alpha$, with α representing the

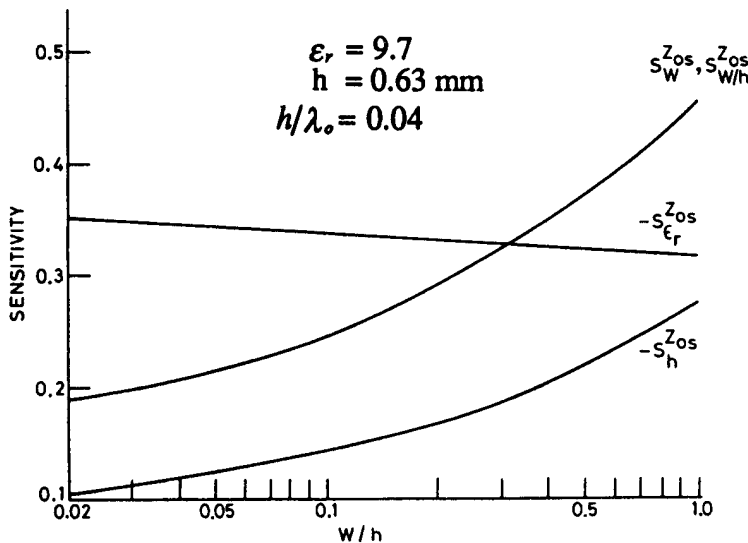


Figure 5.8 Sensitivity of the characteristic impedance of a slotline with respect to its parameters (from [18], © 1978 IEEE. Reprinted with permission.).

dielectric loss α_d in nepers/meter of the line. The dielectric loss in a slotline has been found to be of the same order as the loss tangent of the substrate [12].

Conductor loss α_c cannot be obtained from Wheeler's incremental inductance rule because the mode of propagation in a slotline is non-TEM in nature. In such a case one can follow the classical perturbation approach. In this approach conductor loss is evaluated by means of the energy dissipated by the *lossless fields* while propagating through the conductors with surface resistance $R_s = \sqrt{\omega\mu_0/2\sigma}$. The conductor attenuation constant α_c , expressed in nepers/meter, is defined as

$$\begin{aligned}\alpha_c &= \frac{1}{2} \frac{\text{Power dissipated in the conductors}}{\text{Power transmitted along the guide}} \\ &= \frac{P_c}{2P} \quad (5.51)\end{aligned}$$

The power dissipated in the conductors per unit length of the slotline (Figure 5.6) is given by

$$P_c = \frac{R_s}{2} \int_{W/2}^{\infty} (|H_x^+|^2 + |H_x^-|^2 + |H_z^+|^2 + |H_z^-|^2) dy \quad (5.52)$$

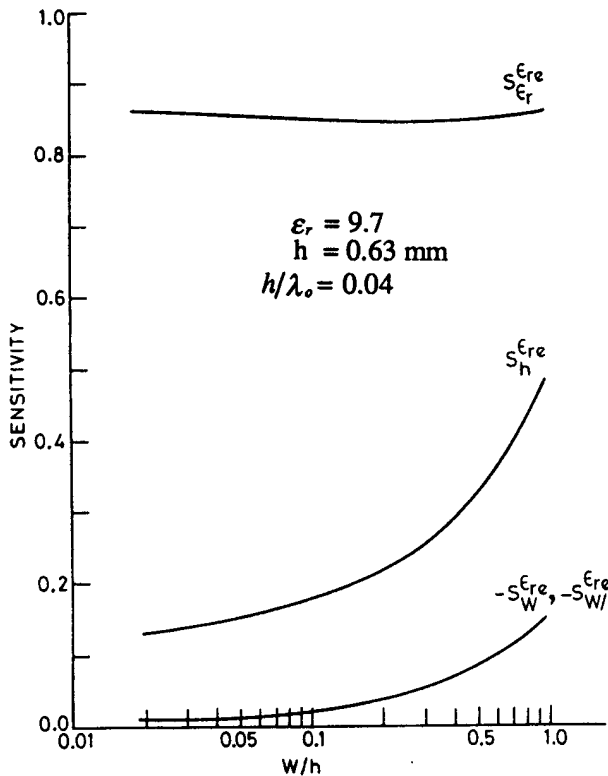


Figure 5.9 Sensitivity of the effective dielectric constant of a slotline with respect to its parameters (from [18], © 1978 IEEE. Reprinted with permission.).

where H_x^\pm, \dots are the magnetic fields just above and below the conductor surface, respectively. The power transmitted along the guide is obtained as

$$P = \frac{1}{2} \operatorname{Re} \int \int_{-\infty}^{\infty} (E_x H_y^* - E_y H_x^*) dx dy \quad (5.53)$$

The field components E_x, H_y, \dots are obtained from an analysis of the slotline for the given set of parameters. The overall attenuation per unit length α is then given by

$$\alpha = \alpha_c + \alpha_d \quad (5.54)$$

The actual evaluation of the integrals in (5.52) does not pose any problem as far as $|H_z|^2$ is concerned, because this field component is regular along the edges

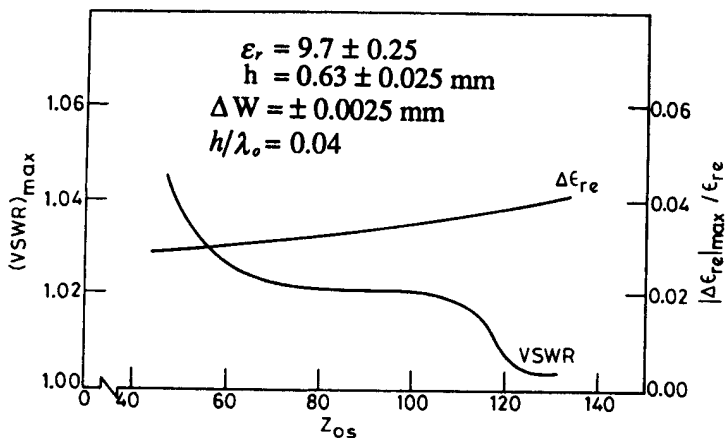


Figure 5.10 Effect of tolerances on the characteristics of a slotline (from [18], © 1978 IEEE. Reprinted with permission.).

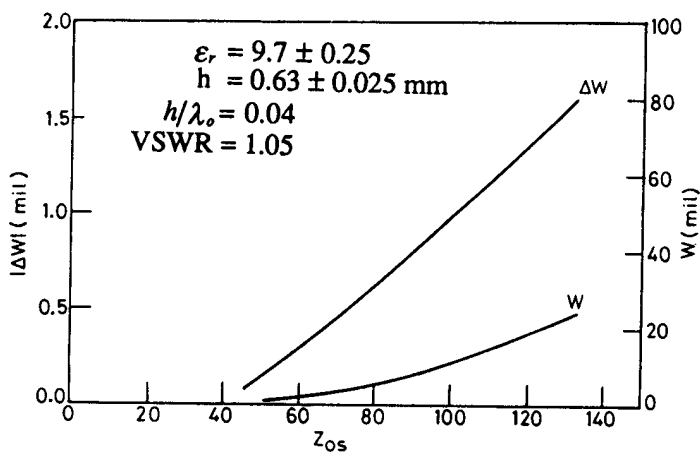


Figure 5.11 Fabrication accuracy requirement for the slot width W for given substrate tolerances in ϵ_r and h , and the required VSWR performance (from [18], © 1978 IEEE. Reprinted with permission.).

$|x| = W/2$. However, $|H_s|^2 = |J_s|^2$ is singular along the edges and diverges as $(x^2 - [W/2]^2)^{-1}$. This is a nonintegrable singularity. Rozzi et al. [12] overcame this difficulty by arguing that due to the effect of the small but finite thickness of the conductors, the actual edge behavior of the longitudinal current falls between the $r^{-1/2}$ type and $r^{-1/3}$ type. They assumed a current distribution of the following type (for $|x| \geq W/2$)

$$J_z \propto \left(\frac{2|x|}{W} - 1 \right)^{-1/3} \cdot e^{-(2|x|/W-1)/2} \quad (5.55)$$

The above current distribution has the required edge behavior and qualitatively correct far-field dependence. Now, the singularity of $|J_z|^2$ is of the type $(x^2 - [W/2]^2)^{-2/3}$, which poses no convergence problem.

Das and Pozar [19] have circumvented the problem of singularity of a current at the slot edges by using the finite conductivity of metal conductors and enforcing the proper impedance boundary conditions and by solving for the complex propagation constant. Results for the conductor loss of a slotline [19, Figure 10] have been compared with the traditional perturbation analysis. The comparison is found to be fairly good except for narrow slots where the conductor loss is found to be relatively smaller.

The conductor and dielectric losses obtained by Rozzi et al. [12] are plotted in Figure 5.12 for a slotline on alumina substrate with $h = 0.635$ mm, $\epsilon_r = 9.8$, $\sigma = 4.1 \times 10^7$ S/m, and $\tan \delta = 2 \times 10^{-4}$. It is seen that the conductor loss is higher than the dielectric loss for all values of slot width and frequency. It increases with frequency but decreases with slot width. Consequently, in the millimetric wave region narrow slots will be very lossy. An increase in the substrate thickness and/or dielectric constant will allow larger slot widths for the same impedance. A limit to the substrate thickness and permittivity is set by the excitation of TM surface waves in the substrate [12].

Experimental results by Kurpis [20] show that the relative value for unloaded Q-factors of microstrip and slotline resonators are 280 and 120, respectively.

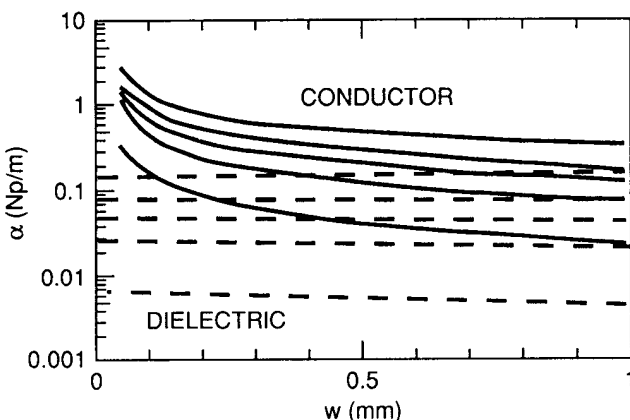


Figure 5.12 Dielectric loss (---) and conductor loss (—) in the slotline as a function of slot width at 2 GHz, 7 GHz, 12 GHz, 18 GHz, and 30 GHz; losses increase with frequency (from [12], © 1990 IEEE. Reprinted with permission.).

5.4 SLOTLINE DISCONTINUITIES

As in the case of microstrip circuits, the characterization of slotline discontinuities is needed for the design of slotline circuits. However, only two types of discontinuities in the slotline have been studied. These are short-end and open-end discontinuities. The experimental data is available for both types of discontinuities, but only short-end discontinuity has been analyzed.

5.4.1 Short End

A short end (shown in Figure 5.13) is created by merely ending the slot or equivalently filling the slot with a conducting surface lying in the plane of the slot. The current flows in the metal surface around the end of the slot, and there is appreciable energy stored beyond the termination. This is illustrated in Figure 5.13. The net result is a predominance of stored magnetic energy, which gives rise to an inductive reactance as seen at a reference plane normal to the slot axis and coincident with the end of the slot.

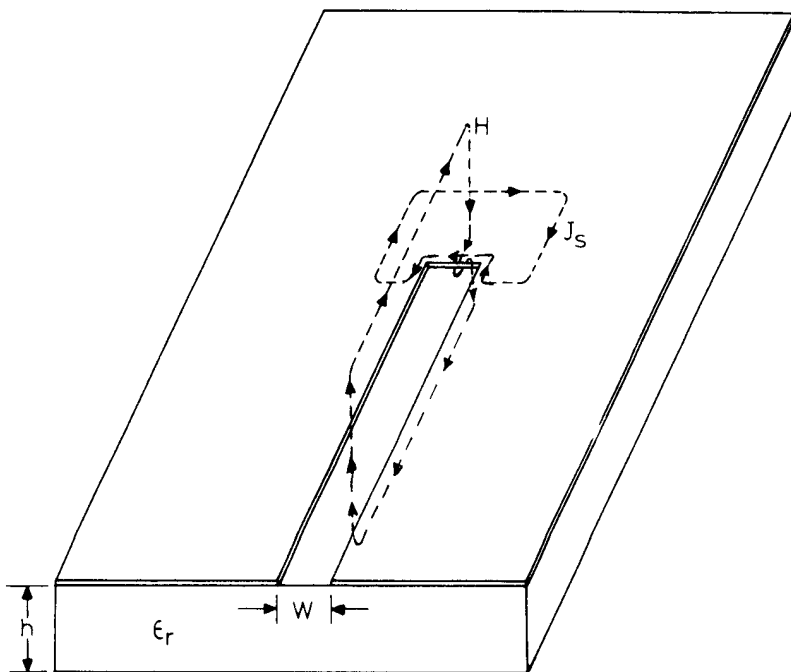


Figure 5.13 Field and current distributions in the vicinity of a slotline short end.

Fullwave analysis of the short end has been carried out in [21, 22]. Experimental characteristics of this discontinuity have been reported by Knorr and Saenz [23] and Chramiec [24]. Yang and Alexopoulos [22] have compared their theoretical results with those of Jansen [21] and measurements of Knorr [23]. This comparison is plotted in Figure 5.14 for the normalized end reactance of the slot. As expected the end reactance of a shorted slot is purely inductive and significant. It increases with the increase in slot width and h/λ_0 ratio. The equivalent length of the short end may be up to 0.1 λ_s . Figure 5.14 also shows good agreement between the theoretical results of two different authors. However, the agreement with the measured values of the end reactance is not so good. Measurement results are subject to various kinds of errors such as tolerances in fabrication, measurement accuracy, substrate tolerances, and coaxial-to-slotline transition.

Like an open end in a microstrip line, the short end in a slotline is not purely reactive. There are losses associated with the short end that are due to the propagation of power in surface waves and radiation in the form of space waves and can be described in terms of an equivalent resistance R presented by the discontinuity to the rest of the circuit. Yang and Alexopoulos [22] have calculated

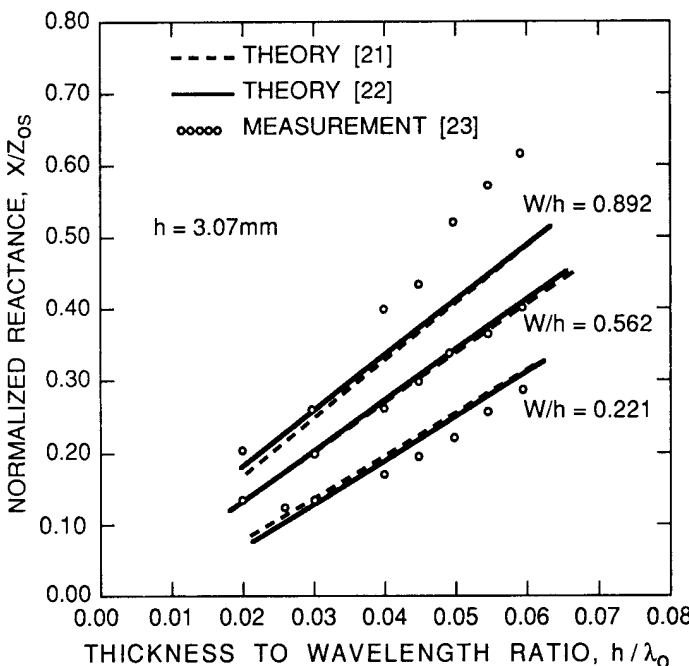


Figure 5.14 Normalized end reactance of a shorted slot, $\epsilon_r = 12$ (from [22], © 1988 IEEE. Reprinted with permission.).

the normalized end resistance for a shorted slot on the $\epsilon_r = 12$ substrate. These results are plotted in Figure 5.15. A comparison of Figure 5.14 for X/Z_0s , and Figure 5.15 for R/Z_0s shows that for the chosen substrate thickness of $h = 3.07$ mm, the resistance and reactance are of the same order, which means that in this case radiated space waves and surface waves are strongly excited. The equivalent circuit of a short end is, therefore, a series combination of an inductor and a resistor. It may be mentioned that a slotline short end is frequently used in slotline circuits and has the same significance as an open end in microstrip circuits.

5.4.2 Open End

For some circuit applications an open end in slotline circuits is required. An open circuit can be achieved by slowly tapering the metallizations constituting the slot. This is shown in Figure 5.16(a). This type of open circuit is impractical because it requires a lot of substrate area and cannot be implemented at any position in the circuit. Moreover, this type of open circuit produces a lot of radiation. In practice, an open circuit in a slotline is simulated by means of a circular disc opening (no

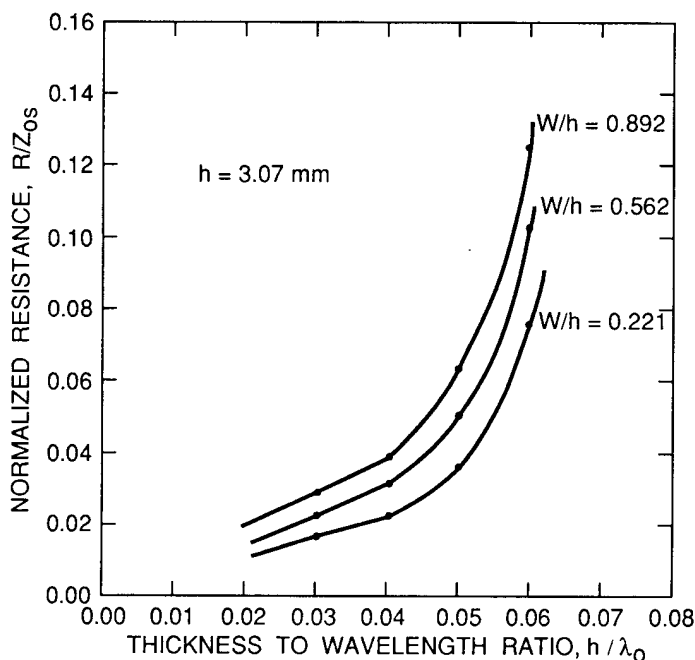


Figure 5.15 Normalized end resistance of a shorted slot, $\epsilon_r = 12$ (from [22], © 1988 IEEE. Reprinted with permission.).

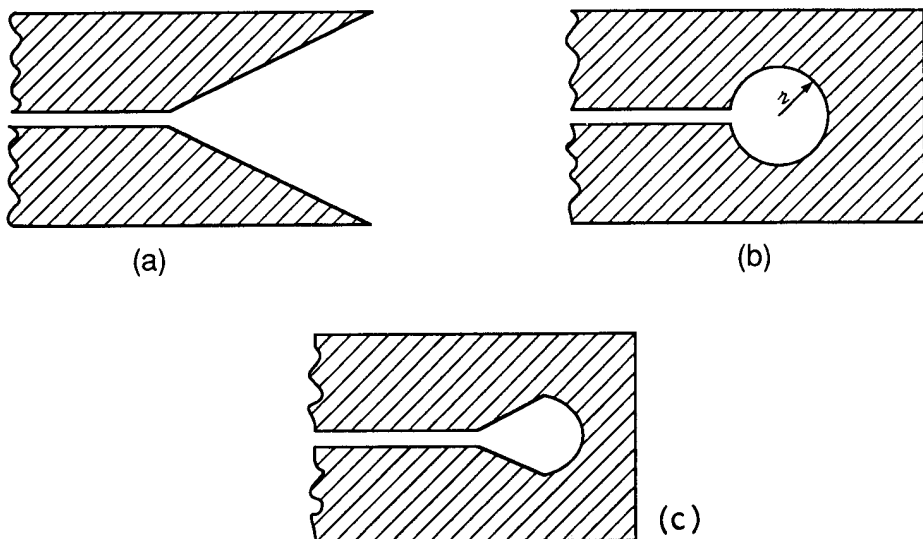


Figure 5.16 Various types of open-end discontinuity in a slotline: (a) a flared open end; (b) circular disc open end; and (c) combination of flared slot and half-disc open end.

metallization) at the end of the slotline. This is shown in Figure 5.16(b). The larger the radius of the disc the better will be the open-circuit behavior. Theoretically, the circular disc will behave like a resonator especially if the width of the connecting slotline is narrow compared to the radius of the disc. Experimental studies carried out by Chramiec [24] on alumina substrate confirm this behavior. It is observed that if the operating frequency is higher than the resonant frequency, the circular disc behaves like an open circuit, that is, it is capacitive in nature. Chramiec has also studied a slotline discontinuity that is a combination of a flared slot and a half disc. This is shown in Figure 5.16(c). This discontinuity has a resonant behavior very similar to the circular slot/disc. But this discontinuity has the advantage that it requires lesser surface area and therefore can be used to minimize the overlap between microstrip and slotline portions of the circuit resulting in reduced proximity effects. Chramiec has used this slotline discontinuity to develop a 1.5-GHz to 6-GHz low VSWR microstrip-to-slotline transition [24].

5.5 OTHER SLOTLINE CONFIGURATIONS

5.5.1 Coupled Microstrip-Slotline

The cross section of a coupled microstrip-slotline is shown in Figure 5.17. It consists of a slot in the ground plane of a microstrip line. This configuration has been used in the hybrid branchline coupler discussed in Section 5.7.1.

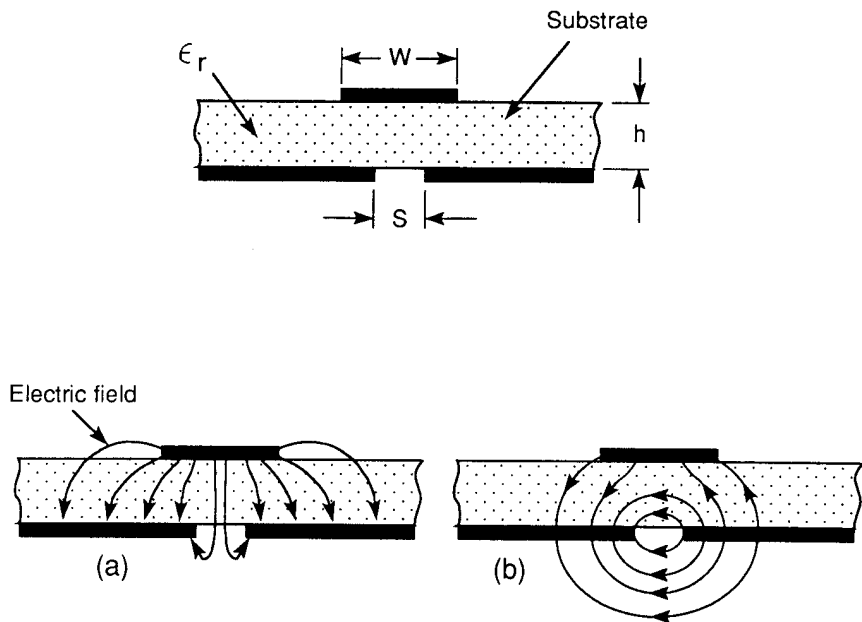


Figure 5.17 Cross section of a coupled microstrip-slotline, and the electric field distributions for (a) even mode and (b) odd mode (from [28], © 1982 IEEE. Reprinted with permission.).

A coupled microstrip-slotline has been analyzed by a number of investigators [25–30]. The method of analysis used most frequently is Galerkin's method in the spectral domain. It was observed that two types of modes propagate in this transmission line: quasi-microstrip mode and the quasi-slotline mode. The electric field distribution for these modes is shown in Figure 5.17. The mode in Figure 5.17(a) has the field distribution similar to that of a microstrip line. Since it has even symmetry, it is also called the even mode. Similarly, the mode in Figure 5.17(b) is called the odd mode, and the field distribution is similar to that in a slotline. Figures 5.18 and 5.19 show the effective dielectric constants and the characteristic impedances of these modes [30]. It is observed from these figures that for the even mode, the effective dielectric constant decreases and the characteristic impedance increases with increasing slot width. This is because the effect of free space below the slot becomes more pronounced [25]. This mode can be used to realize very high impedances, in the order of 200Ω to 300Ω . Quite the opposite is true of the behavior of the odd mode or the slot mode with respect to the increase in strip width. This mode is less sensitive to the presence of the strip. It may be due to the fact that most of the energy in this mode is confined near the slot.

A variation of coupled microstrip-slotline is used in the design of double substrate directional couplers [31]. In this configuration, the slotline is sandwiched between two microstrips by placing another microstrip on the slotline side of the coupled microstrip-slotline. This configuration is discussed later in Section 5.7.3.

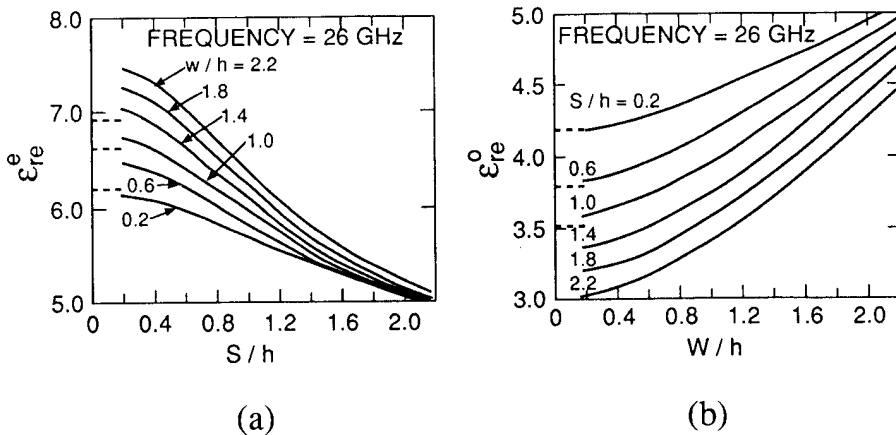


Figure 5.18 Effective dielectric constant of coupled microstrip-slotline ($\epsilon_r = 9.6$): (a) even mode (--- Itoh's result [25]) and (b) odd mode (- - - Cohn's result [1]) (from [30], © 1989 IEEE. Reprinted with permission.).

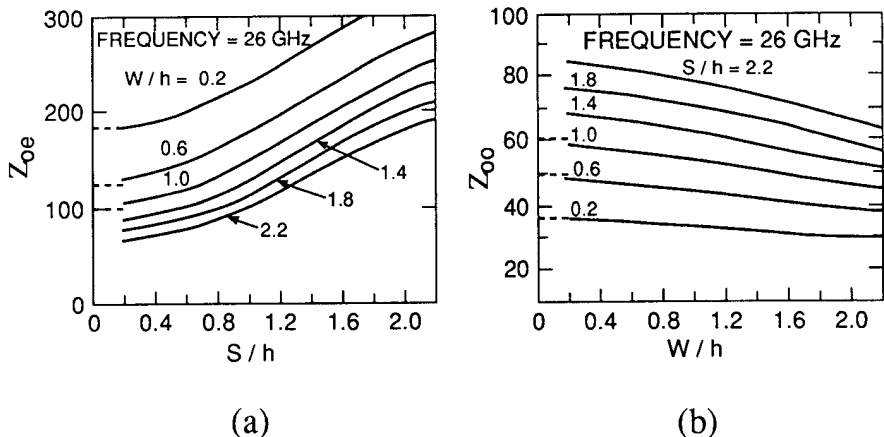


Figure 5.19 Characteristic impedance of coupled microstrip-slotline ($\epsilon_r = 9.6$): (a) even mode (--- Itoh's result [25]) and (b) odd mode (- - - Cohn's result [1]) (from [30], © 1989 IEEE. Reprinted with permission.).

5.5.2 Conductor-Backed Slotline

It is very tempting to introduce a conductor backing to the slotline. Among the many advantages that are envisaged are improved mechanical strength, easier implementation of microstrip-slotline circuits, help in grounding floating regions, convenience in dc biasing, and heat sink.

Shigesawa et al. [32] and Das and Pozar [19] have carried out fullwave analysis of a conductor-backed slotline with a cover plate (see Figure 5.20). The analysis shows that for a conductor-backed slotline of infinite lateral dimension, power leaks into the dielectric-filled parallel plate region away from the slot. The loss of power can be explained by a leaky mode characterized by the complex propagation constant $\gamma = \beta + j\alpha$, the imaginary part α accounting for the power loss. The leakage phenomenon is explained as follows.

Far away from the slot, the conductor-backed slotline resembles a conventional dielectric filled parallel plate waveguide formed by the electric conductors on both sides of the substrate. This waveguide supports a TEM mode for which there is no cut-off frequency. Therefore, there are two modes in the conductor-backed slotline: the slotline mode and the TEM mode. Leakage occurs for that range of parameters for which the propagation constant β of the slot mode is less than that of the parallel plate mode [19]. In the structure under study, the propagation constant β/k_0 for the slot mode lies between $\sqrt{\epsilon_r}$ and 1. The TEM mode for the parallel plate waveguide has the propagation constant $\beta_{TEM}/k_0 = \sqrt{\epsilon_r}$. Since $\beta_{TEM} > \beta$, leakage occurs independent of frequency or parallel plate separation.

Shigesawa et al. [32] have carried out the analysis of a conductor-backed slotline using two different approaches: a mode-matching technique and the transverse equivalent network approach. Das and Pozar [19] used the fullwave spectral domain moment method. Measurements were also carried out to determine the leaky wave aspect of the leakage phenomenon [32]. For this purpose, the electric field distribution was probed across the width of slotline at a distance far away from the point of excitation. A sketch of the measurement set-up and a plot of the leaky wave field across the width of the slotline are shown in Figure 5.21. It was observed that the maximum of the electric field occurred at an angle θ from the slot axis given by $\cos^{-1}(\beta/(k_0\sqrt{\epsilon_r}))$. Das and Pozar [19] have compared the theoretical values of β/k_0 and α/k_0 with the computed and measured values in [32]. This is plotted in Figure 5.22. It is observed that the agreement is very good for wider slots between the measured values of [32] and theoretical calculations in [19]. Also, the attenuation constant is fairly high for the narrow slots. The effect of finite plate widths of

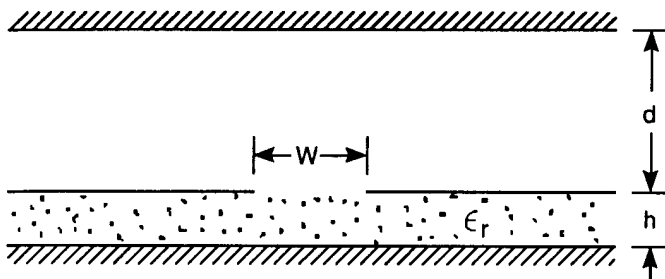


Figure 5.20 Cross section of a conductor-backed slotline.

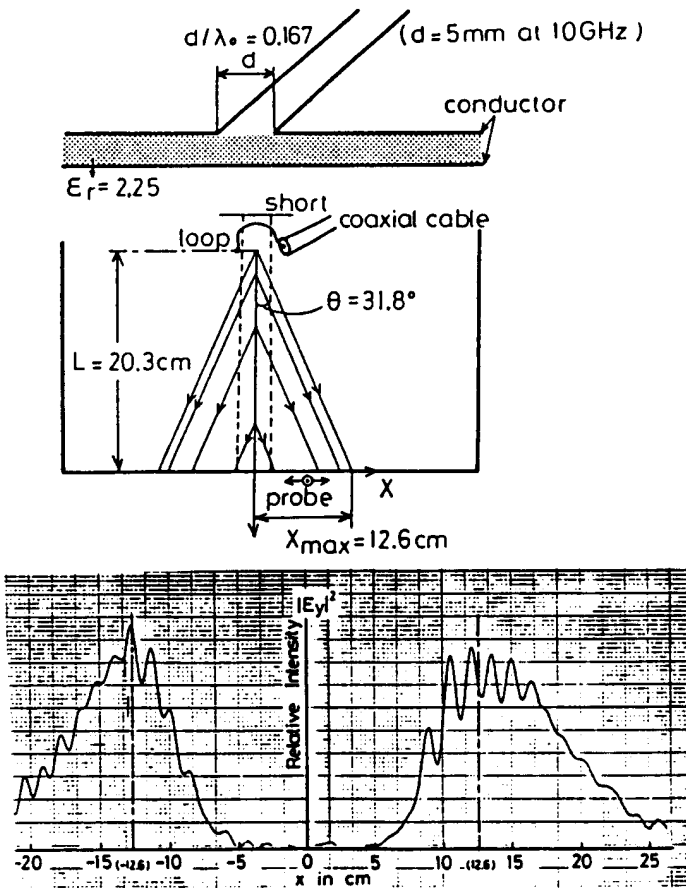


Figure 5.21 Sketch of the measurement set-up, and a plot of the leaky wave field across the width of a slotline ($h = 5 \text{ mm}$, $f = 10 \text{ GHz}$, $\epsilon_r = 2.25$) (from [32], © 1988 IEEE. Reprinted with permission.).

the slotline and the conductor backing is also discussed by the authors [32]. In this case the propagation constant is found to be purely real.

The leaky slotline mode is one of the unwanted features of a conductor-backed slotline. Another aspect of this transmission line becomes important when either the top plates or bottom plate of the structure is finite in the lateral direction but the substrate is thick enough electrically to support a surface wave also. At higher frequencies the value of β for the slotline mode can become lower than the value of β for the surface wave. When this happens the power from the slotline mode will couple to the surface wave, and β for the slotline mode will become

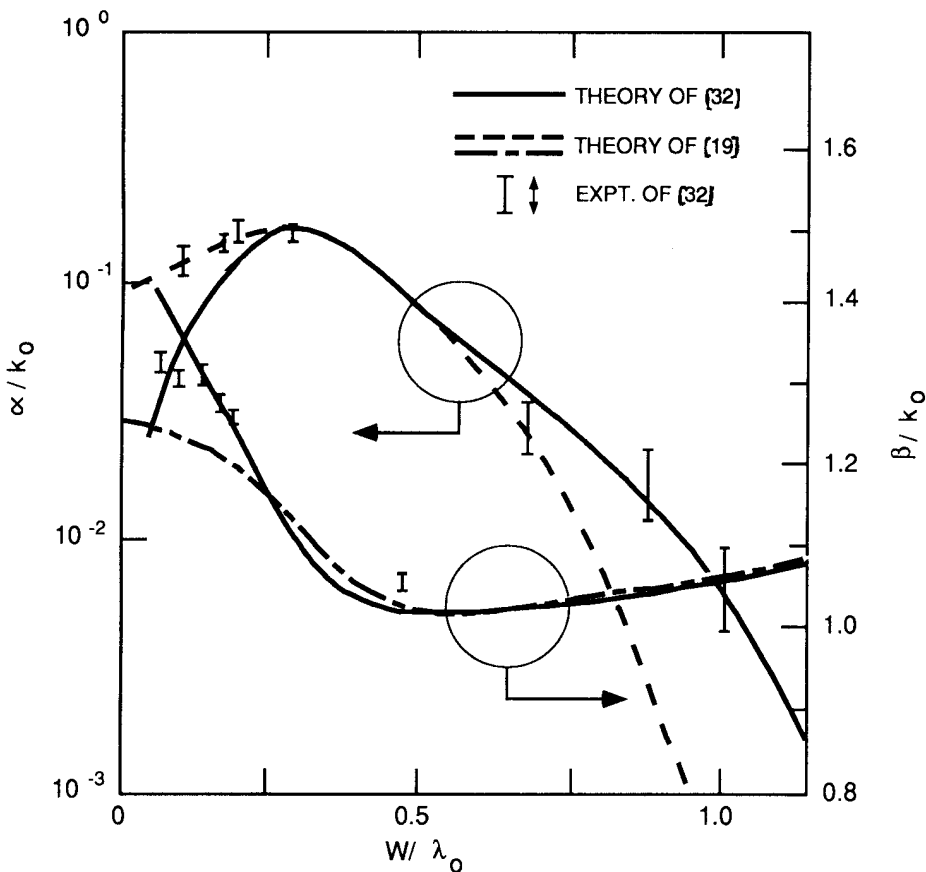


Figure 5.22 Phase constant (β/k_0) and attenuation constant (α/k_0) of a conductor-backed slotline as a function of slot width for $\epsilon_r = 2.55$, $h/\lambda_0 = 0.267$, $f = 10$ GHz (from [19], © 1991 IEEE. Reprinted with permission.).

complex. Surface wave propagation could produce unexpected cross talk with neighboring circuits. Shigesawa et al. [32] have calculated the crossover frequency between the slotline mode and the TM_0 surface wave mode.

In addition to the discrete modes, a slotline also supports a continuum of radiation modes due to its open nature. These modes can get excited at a discontinuity and are utilized to develop slot antennas. Rozzi et al. [33] have studied these modes for a conductor-backed slotline.

5.5.3 Conductor-Backed Slotline with a Superstrate

This modification of the conductor-backed slotline has been suggested by Das [34] to eliminate leakage. The cross section of the conductor-backed slotline with a

superstrate is shown in the inset of Figure 5.23. Here, the superstrate parameters are described by the thickness d and the relative dielectric constant ϵ_{r2} . The substrate parameters are the thickness h and the relative dielectric constant ϵ_{r1} . As described in Section 5.5.2, leakage occurs because the propagation constant of the slotline mode is lower than the propagation constant of the parallel plate TEM mode. The propagation constant β of the slotline mode can be increased by loading the conductor-backed slotline by means of a superstrate. The loading is increased to an extent such that $\beta > \beta_{\text{TEM}} (= k_0 \sqrt{\epsilon_{r1}})$. Loading by the superstrate increases with the increases in its dielectric thickness d and relative dielectric constant ϵ_{r2} , thickness h of the substrate, and frequency. This is shown in Figure 5.23 for the effective dielectric constant ϵ_{re} . The increase in ϵ_{re} is almost linear with d when d is greater than a certain minimum value.

The effect of superstrate on the characteristic impedance Z_{0s} has also been determined by Das [34]. It is plotted in Figure 5.24. This figure shows that for a given set of parameters there is a minimum value of superstrate thickness d below which Z_{0s} decreases sharply to small values. This low value of Z_{0s} is interpreted as indicative of onset of leakage, that is, transition from the bound mode to unbound (leaky) mode. The evaluation of the field distribution as a function of d confirms the corresponding field spreading about the slot. Using such studies on field spreading and/or impedance variation, a suitable set of parameters for a conductor-backed slotline can be chosen so that leakage effects are avoided. For example, for the parameters of curve 1 of Figure 5.24, the value of d should be greater than 0.5 mm.

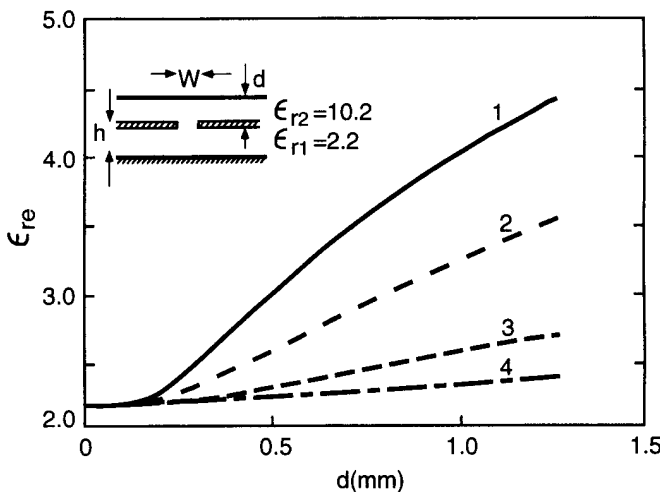


Figure 5.23 Effective dielectric constant of conductor-backed slotline with superstrate with $W = 1$ mm (1 : $h = 0.157$ cm, $f = 10$ GHz; 2 : $h = 0.076$ cm, $f = 10$ GHz; 3 : $h = 0.157$ cm, $f = 3$ GHz; 4 : $h = 0.076$ cm, $f = 3$ GHz) (from [34], © 1973 IEEE. Reprinted with permission.).

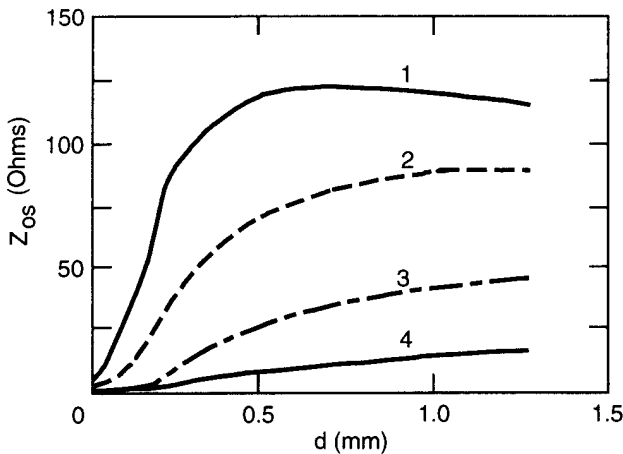


Figure 5.24 Characteristic impedance Z_{0s} for the geometries of Figure 5.23 (from [34], © 1991 IEEE. Reprinted with permission.).

5.6 SLOTLINE TRANSITIONS

To test and design slotline circuits it is necessary to have a transition between a slotline and the measuring equipment. A coaxial-to-slotline transition is commonly used for this purpose. Transitions between slotline and other transmission lines are also useful and increase the applications of slotlines. One such transition is slotline-to-microstrip. These two types of transitions are discussed in this section. Slotline-to-CPW transition is discussed in Chapter 7.

It is also possible to design a transition from a rectangular waveguide to a slotline. This transition can be achieved very easily in the finline configuration. Finline is discussed in the next chapter.

5.6.1 Coaxial-to-Slotline Transition

A commonly used coaxial line-to-slotline transition is shown in Figure 5.25(a). It consists of a miniature coaxial line placed perpendicular to and at the end of an open-circuited slotline. The outer conductor of the cable is electrically connected (with solder or epoxy) to the metallization in the left half of the slot plane. The inner conductor is extended over the slot and connected to the metallization on the opposite side of the slot. This transition has been analyzed in [35] by assuming that the inner conductor of the coaxial line has a semicircular shape over the slot as shown in Figure 5.25(b).

An equivalent circuit suggested in [35] for the coax-slot transition of Figure 5.25 is shown in Figure 5.26. The impedances Z_{0s} and Z_{cl} are the characteristic

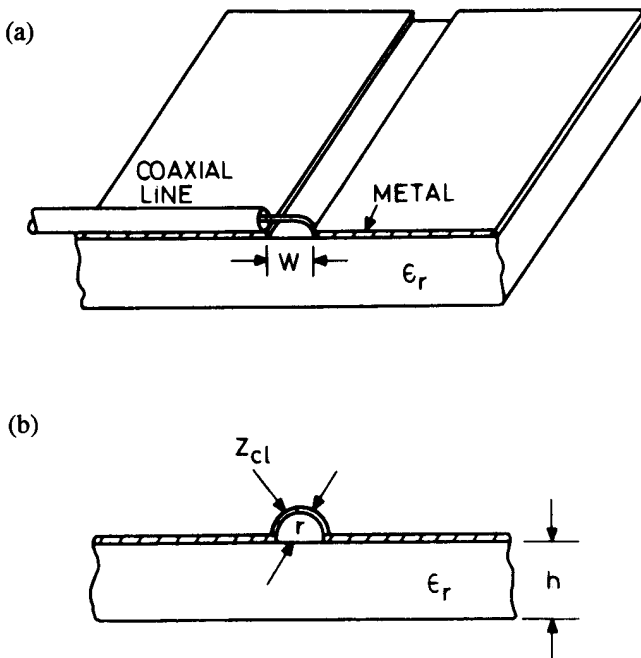


Figure 5.25 A coaxial-to-slotline transition and its analysis model.

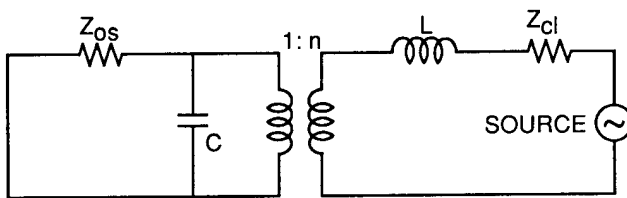


Figure 5.26 Equivalent circuit of the transition shown in Figure 5.25.

impedances of the slotline and coaxial line, respectively. The fringe capacitance at the open end of the slot is represented by the lumped capacitor C . The inductance L represents the self-inductance of the semicircular loop. The transformation ratio n can be evaluated approximately by using (5.6), which gives the ratio of the voltage at a distance r to the voltage across the slot. We have

$$n = \frac{\pi}{2} |k_c r H_1^{(1)}(k_c r)| \quad (5.56)$$

where k_c is defined by (5.4).

From (5.56), it may be noted that the value of the transformer ratio n decreases with increases in frequency. Thus we can expect the performance of the transition to worsen at higher frequencies.

A comparison between experimental VSWR for a coaxial-to-slotline transition and the values based on the above model is shown in Figure 5.27. This transition has been constructed with a 50Ω 3.58-mm semirigid coaxial cable that is coupled to a slotline etched from a 3.175-mm-thick substrate with $\epsilon_r = 20$. The slot impedance is about 75Ω ($W/h = 0.55$). The measured value of L is found to be 0.61nH , and the capacitance C has a typical value of 0.2 pF . It is seen that the experimental curve is in reasonable agreement with the theoretical curve for $C = 0\text{ pF}$. Also, to achieve this agreement, the value of r used is 2.54 mm, which is about 50 percent greater than the actual height of the inner conductor of the coaxial line above the slot. There are two possible reasons for the lack of any better agreement between the model and the actual performance. First, the inner conductor of the coaxial line does not form a loop of exactly semicircular shape. Second, the Hankel function approximation does not describe accurately the variations of the electric field near the slot [2].

The transition described above has been successfully used in the S-band as it presents a good VSWR (less than 1.15) in the frequency range of 1.65 GHz to 4.0 GHz. A lower VSWR value over a narrow frequency range can be obtained by using a movable short as shown in Figure 5.28. This transition is very useful for feeding and testing slotline circuits.

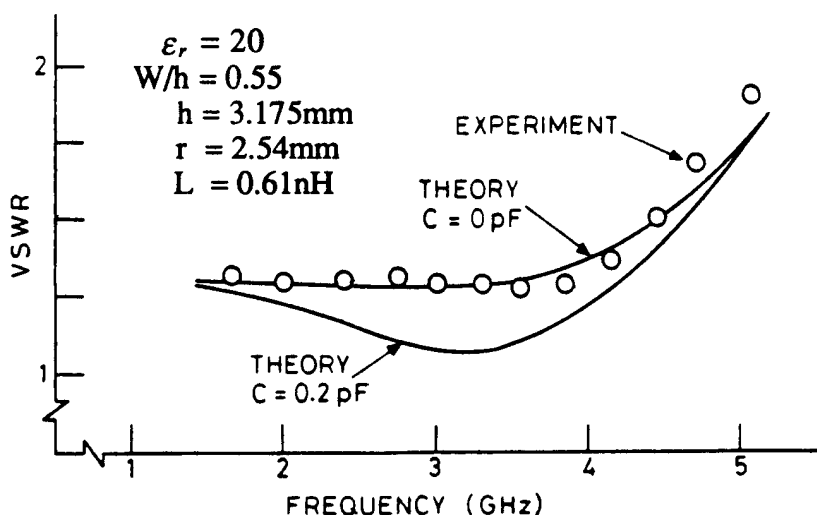


Figure 5.27 Comparison of theoretical and experimental VSWR for coaxial-to-slotline transition (from [35], © 1974 IEEE. Reprinted with permission.).

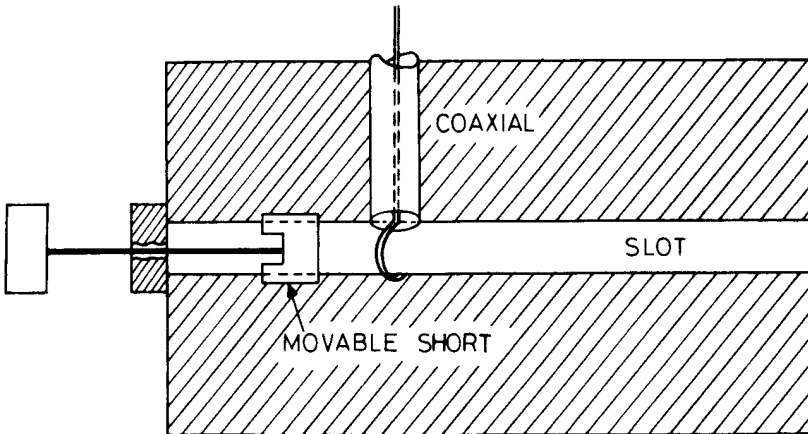


Figure 5.28 Coaxial-to-slotline transition with a movable short.

5.6.2 Microstrip-to-Slotline Cross-Junction Transition

Most of the circuits, wherein a slotline is used, also incorporate microstrip lines. Thus a microstrip-to-slotline transition is desired. Also the fabrication of the microstrip-to-slotline transition can easily be included in the MIC fabrication routine when an arrangement is made for etching the substrate on both sides. This transition has been comprehensively analyzed by many investigators [35–42]. A layout of this transition is shown in Figure 5.29.

The slotline, which is etched on one side of the substrate, is crossed at a right angle by a microstrip conductor on the opposite side. The microstrip extends about one quarter of a wavelength beyond the slot. The transition can be fabricated using the usual photoetching process and is thus easily reproducible. Also, as the microstrip part of the circuit can be placed on one side of the substrate and the slotline part on the other side, this transition makes two-level circuit design possible. Coupling between the slotline and microstrip line occurs by means of the magnetic field (see Figures 1.4(d) and 5.2).

A transmission line equivalent circuit of the transition (Figure 5.29(a)) proposed by Chambers et al. [36] is shown in Figure 5.29(b). The reactance X_{0s} represents the inductance of a shorted slotline (see Section 5.4.1), and C_{0c} is the capacitance of an open microstrip (see Section 3.4.1). Z_{0s} and Z_{0m} are slotline and microstrip characteristic impedances respectively. θ_s and θ_m represent the electrical lengths (quarter-wave at the center frequency) of the extended portions of the slotline and the microstrip, respectively, measured from the reference planes as shown in Figure 5.29(a). The transformer turns ratio n describes the magnitude of the coupling between the microstrip and slotline.

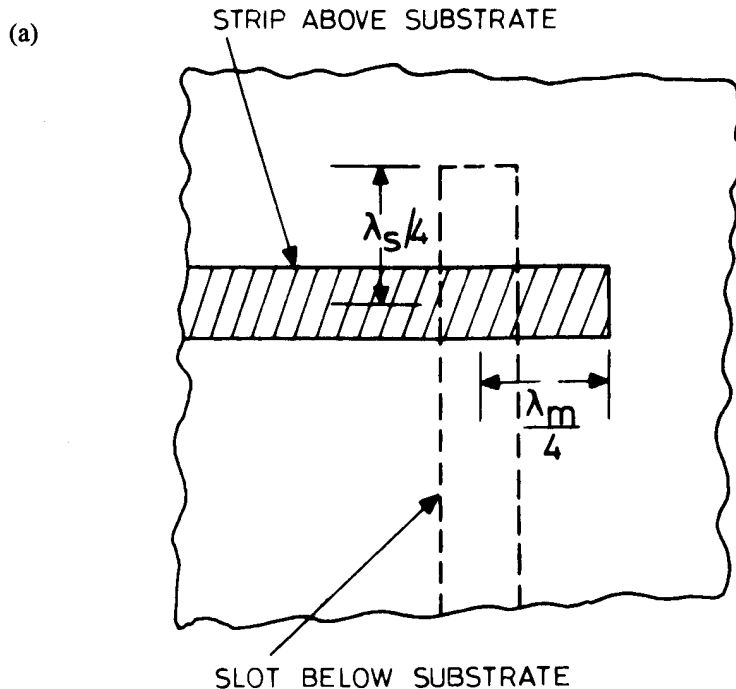


Figure 5.29 (a) Microstrip-to-slotline transition, (b) transmission line equivalent circuit for the transition of (a), (c) reduced equivalent circuit of (b), and (d) transformed equivalent circuit of (c).

For further analysis the equivalent circuit in Figure 5.29(b) may be redrawn as in Figure 5.29(c). Here,

$$jX_s = Z_{0s} \frac{jX_{0s} + jZ_{0s}\tan\theta_s}{Z_{0s} - X_{0s}\tan\theta_s} \quad (5.57)$$

and

$$jX_m = Z_{0m} \frac{1/j\omega C_{0c} + jZ_{0m}\tan\theta_m}{Z_{0m} + \tan\theta_m/\omega C_{0c}} \quad (5.58)$$

After transformation to the microstrip side, the equivalent circuit of Figure 5.29(c) reduces to that shown in Figure 5.29(d). In this circuit,

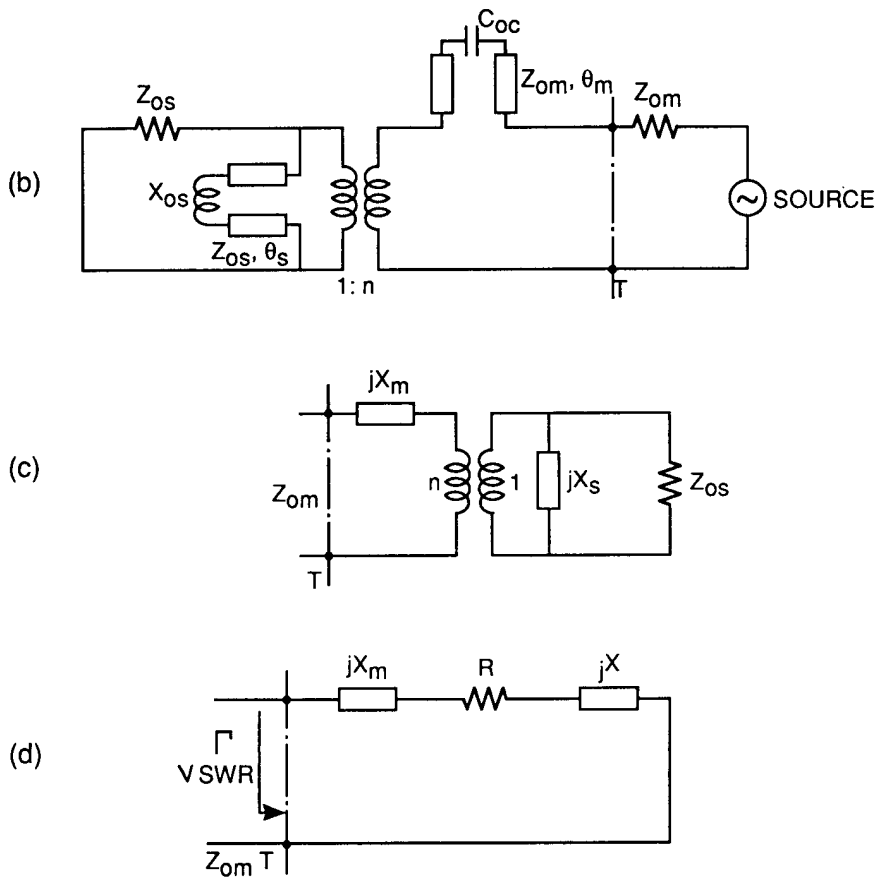


Figure 5.29 (continued).

$$R = n^2 \frac{Z_{0s} X_s^2}{Z_{0s}^2 + X_s^2} \quad (5.59)$$

and

$$X = n^2 \frac{Z_{0s}^2 X_s}{Z_{0s}^2 + X_s^2} \quad (5.60)$$

Finally, the reflection coefficient Γ is given by

$$\Gamma = \frac{R - Z_{0m} + j(X_m + X)}{R + Z_{0m} + j(X_m + X)} \quad (5.61)$$

From the above analysis one can determine the characteristic impedance of the slotline Z_{0s} needed to match the microstrip line impedance Z_{0m} .

In the approximate analysis reported by Knorr [35] the transformer turns ratio n is determined from a knowledge of the slotline field components as

$$n = V(h) / V_0 \quad (5.62)$$

where

$$V(h) = - \int_{-b/2}^{b/2} E_y(h) dy \quad (5.63)$$

V_0 is the voltage across the slot and $E_y(h)$ is the electric field of the slotline on the other surface of the dielectric substrate. Limits of integration in (5.63) correspond to the locations of electric (or magnetic) walls in Cohn's analysis discussed in Section 5.2.2 (see Figure 5.4). From Cohn's analysis $E_y(h)$ may be written as

$$E_y(h) = - \frac{V_0}{b} \left\{ \cos \frac{2\pi u}{\lambda_0} h - \cot q_0 \sin \frac{2\pi u}{\lambda_0} h \right\} \quad (5.64)$$

where

$$q_0 = \frac{2\pi u}{\lambda_0} h + \tan^{-1} (u/v) \quad (5.65)$$

$$u = \{\epsilon_r - (\lambda_0/\lambda_s)^2\}^{1/2} \quad v = \{\lambda_0/\lambda_s\}^2 - 1 \quad (5.66)$$

Yang and Alexopoulos [22], Das [37], and Antar et al. [38] have analyzed the microstrip-to-slotline cross-junction transition comprehensively. The analysis in [22] includes the effects of (i) radiation and surface waves excited by the cross-junction, (ii) the line discontinuities, and (iii) all the mutual couplings due to the dominant and higher order modes of each line. Das [37] has derived a simple closed-form expression for turns ratio n after making a number of approximations in the analysis. This expression is given as

$$n = \frac{J_0(k_{es}W_m/2)J_0(k_{em}W_s/2)}{k_{es}^2 + k_{em}^2} \cdot \left[\frac{k_{em}^2 k_2 \epsilon_r}{k_2 \epsilon_r \cos k_1 h - k_1 \sin k_1 h} + \frac{k_{es}^2 k_1}{k_1 \cos k_1 h + k_2 \sin k_1 h} \right] \quad (5.67)$$

where $J_0(\cdot)$ is the zeroth-order Bessel function and

$$k_1 = \sqrt{|k_0^2 \epsilon_r - k_{es}^2 - k_{em}^2|} = k_0 \sqrt{|\epsilon_r - \epsilon_{res} - \epsilon_{rem}|}$$

$$k_2 = k_0 \sqrt{|\epsilon_{res} + \epsilon_{rem} - 1|}$$

$$k_{es} = k_0 \sqrt{\epsilon_{res}} \quad k_{em} = k_0 \sqrt{\epsilon_{rem}}$$

Here, ϵ_{rem} and ϵ_{res} are the effective dielectric constants and W_m and W_s are the widths of the microstrip line and the slotline, respectively. Expression (5.67) depends on the microstrip parameters (W_m , ϵ_{rem}) as well as the slotline parameters (W_s , ϵ_{res}), whereas the expression (5.62) depends on the slotline parameters only. Das [37] has given an expression for n for a multilayered configuration also in terms of Green's function. The value of n obtained from (5.67) is compared to that obtained from (5.62) in Figure 5.30 for two sets of parameters [37]. It is observed from this figure that the results are comparable at lower frequencies, with $n = 1$ at dc ($f \approx 0$). However, there is a significant deviation at higher frequencies that suggests the inaccuracy of Knorr's analysis for higher frequencies where higher order modes, surface waves, and radiation effects become important.

A comparison of VSWR between the measurements of [35] the transmission line circuit model of Figure 5.29(b) and theoretical values of [22] is shown in Figure 5.31. Again, the agreement is good between the comprehensive analysis and circuit model for lower frequencies and poor for higher frequencies. The reason appears to be the same as discussed earlier for turns ratio n . The measured value of VSWR in Figure 5.31 shows a wider bandwidth than that of either the circuit model or the analytical results in [22]. It is suggested in [22] that the measured value of VSWR is very much influenced by nonideal match load, the coaxial-to-microstrip line transition, and substrate losses. Antar et al. [38] have used a slightly different equivalent circuit for the transition. Their theoretical results are found to have better agreement with the measurements of Knorr [35].

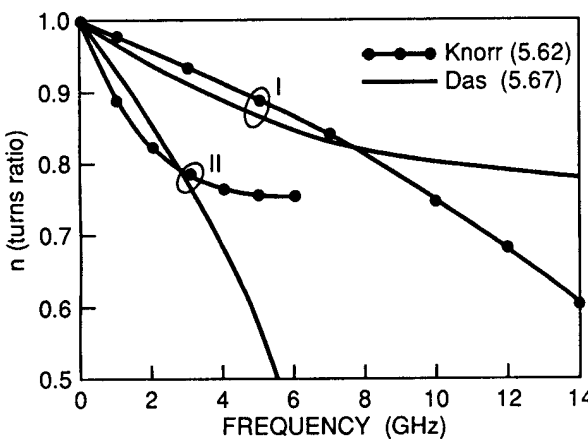


Figure 5.30 Comparison of transformer turns ratio n versus frequency for microstrip-slotline cross-junction obtained from (5.62) and (5.67). Curve I : $h = 0.3175$ cm, $\epsilon_r = 20$, $W_m = 0.157$ cm, $W_s = 0.206$ cm; Curve II : $h = 0.12$ cm, $\epsilon_r = 10.2$, $W_m = 0.12$ cm, $W_s = 0.11$ cm (from [37], © 1993 IEEE. Reprinted with permission.).

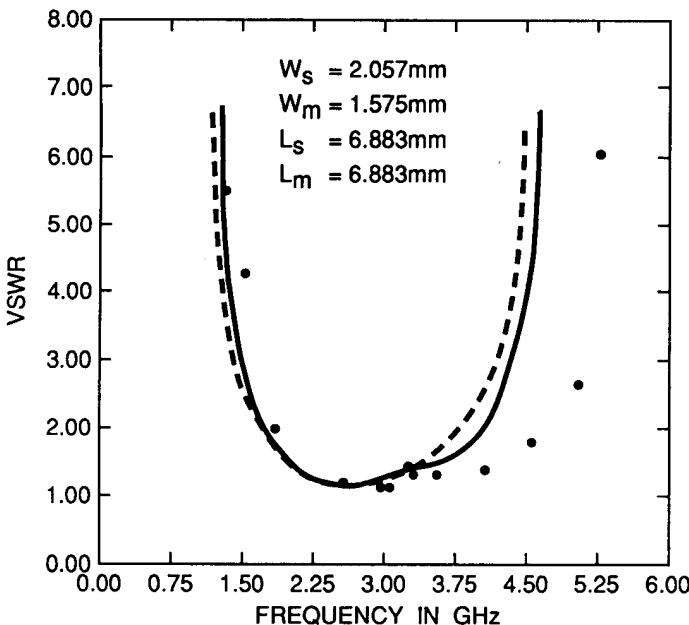


Figure 5.31 Comparison of VSWR versus frequency for microstrip-to-slotline transition, $\epsilon_r = 20$ and $h = 3.175$ mm (— transmission line circuit model, ●●●● measurement [34], - - - theory [22]) (from [22], © 1988 IEEE. Reprinted with permission.).

Bandwidth Improvement. Bandwidth limitation of the cross-junction transition results mainly from the frequency dependence of X and X_m (Figure 5.29(d)). These reactances in turn depend on the stub length and turns ratio. A short-circuited microstrip will minimize X_m , and an open-circuited slotline will minimize X . Alternatively, stub reactances can be so designed that there is a mutual cancellation of X and X_m and $R = Z_{0m}$. To achieve this condition various investigators have tried different approaches. Some of these are described next.

In the transition developed by Robinson and Allen [9] the microstrip is terminated in a quarter-wave radial stub as shown in Figure 5.32(a). For this transition, a VSWR value less than 1.10 is obtained from 8.0 GHz to 10.0 GHz (20 percent bandwidth). Chramiec [24] has terminated the slotline in a radial stub, and the microstrip stub is a combination of a radial section and a rectangular section as shown in Figure 5.32(b). Reactances X and X_m are designed to cancel each other (Figure 5.33) when the transition is developed on a 1.5-mm-thick alumina substrate, with $\alpha = 60^\circ$ for the radial slot line stub, $W/h = 0.2$, $W_r = 7.5$ mm, and $\ell_r = 6.5$ mm. The measured $VSWR = 1.5$ bandwidth of two cascaded transitions separated by a slotline section of 12 mm is found to be two octaves from 1.5 GHz to 6 GHz. This is plotted in Figure 5.34. When this transition was scaled to a 0.7-mm-thick alumina

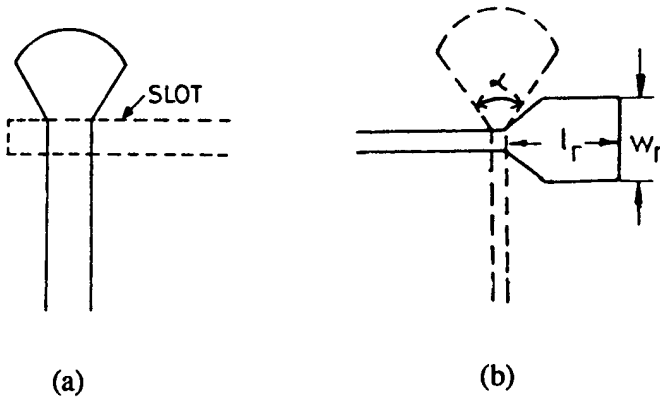


Figure 5.32 Two different types of microstrip-slotline transition with nonuniform stubs: (a) microstrip and (b) microstrip and slotline.

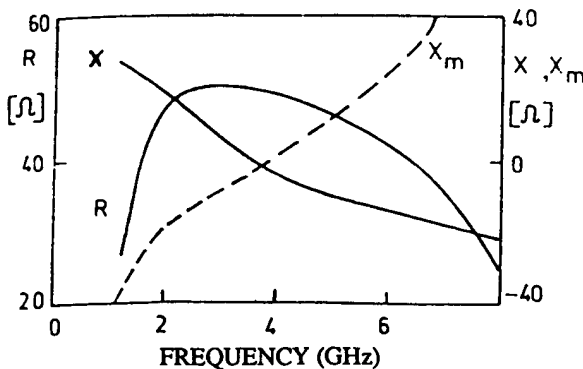


Figure 5.33 Variation of X , X_m and R with frequency for the transition in Figure 5.32(b) (from [24], © 1989 IEEE. Reprinted with permission.).

substrate the VSWR was found to be below 1.45 in the frequency range 2 GHz to 12.7 GHz [24]. The cross-junction transition on an anisotropic substrate has been studied by Podcameni and Coimbra [39].

Schuppert [40] has carried out an extensive study on the transmission line equivalent circuit of the cross-junction. First of all he simplified the equivalent circuit of Figure 5.29 by assuming $n = 1$ and by neglecting the open-circuit and short-circuit discontinuity reactances. Using this simplified equivalent circuit he obtained a simple expression for the insertion loss of the transition as a function of characteristic impedance of the microstrip and slotline stubs assuming that the characteristic impedance of the slotline is the same as that of the microstrip, that

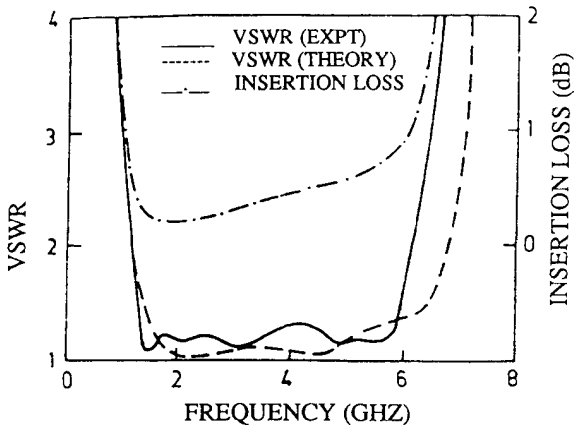


Figure 5.34 Comparison of theoretical VSWR characteristic of a single microstrip-slotline transition and experimental VSWR performance of two cascaded transitions: $h = 1.5 \text{ mm}$, $\epsilon_r = 9.8$ (from [24], © 1989 IEEE. Reprinted with permission.).

is, 50Ω . The simple analysis of the equivalent circuit shows that the bandwidth of the transition increases with increasing characteristic impedance of the slotline stub and decreasing characteristic impedance of the microstrip stub. Moreover, the bandwidth is at a maximum when the characteristic impedance of the microstrip stub is 2.618 times the characteristic impedance of the slotline stub. Experiments were carried out by Schuppert on uniform and nonuniform impedance stubs. The nonuniform stubs were realized in the form of circular geometry of various diameters. Theoretical and measured insertion losses for such a transition on alumina substrate of 0.635-mm thickness are shown in Figure 5.35. The agreement is

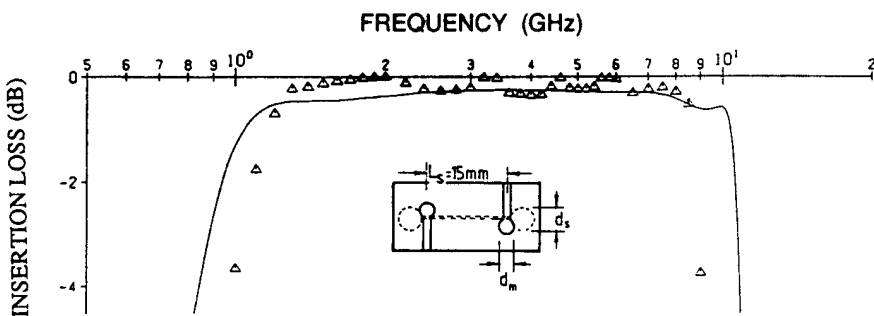


Figure 5.35 Insertion loss of a cascade of two microstrip-to-slotline transitions separated by a slotline of length 15 mm, $d_m = 5 \text{ mm}$, and $d_s = 6 \text{ mm}$ [theoretical (—) and measurements (ΔΔΔ)] (from [40], © 1988 IEEE. Reprinted with permission.).

seen to be fairly good. The cascade connection of two transitions has a bandwidth of approximately one decade. The bandwidth of a single transition will be larger than this. To reduce interaction between the two circular stubs, especially when the diameter increases, it has been suggested that triangular or radial stubs may be used instead [40].

The analysis by Schuppert makes a number of simplifying assumptions that do not appear to be reasonable particularly for a decade bandwidth transition. It appears that mutual cancellation of discontinuity reactances occurs over a broad bandwidth in this case. For example, a circular slot behaves like a resonant circuit [24]. Similarly, a circular microstrip patch will also behave like a resonant circuit, with the resonant frequency adjustable by a proper selection of its diameter. Microstrip-to-slotline cross-junction transition with circular stubs was also studied by de Ronde [43]. The configuration of this transition is different from that in Figure 5.35. In this case, the slotline runs below the microstrip in the form of a spiral. The transition employs a short circuit at the center of a microstrip circular stub. The reported VSWR of this transition is less than 1.1 in the 1.0-GHz to 10-GHz frequency range. A transition with a microstrip short-circuited at the junction has also been studied [40]. It was found to have a larger bandwidth than the open-circuited microstrip stub, but its implementation needs a via-hole grounding that may sometimes be difficult. A microstrip-to-slotline transition using a six-port junction has been described by Schiek and Kohler [44]. Although this transition has good performance between 2 GHz to 9 GHz, it needs more substrate space.

5.7 SLOTLINE APPLICATIONS

It was mentioned in Section 5.1 that slotlines can be incorporated in microstrip circuits by etching the slotline circuit in the ground plane of the microstrip circuit. This type of hybrid combination has a number of advantages. Most of these advantages are due to the balanced (slotline) and unbalanced (microstrip line) natures of the transmission lines used. Many circuit functions that were not possible or easily realizable in microstrip form can now be implemented. These include short circuit, series T-junction, balanced circuits, and tight coupling. In addition to these, flexibility in circuit design is introduced, for example, series and parallel device mounting, wider range of line impedance, elimination of line crossings, and substrate space saving, leading to better integration. These features have given rise to some novel circuits like hybrid branchline couplers, magic-T, and balanced circuits in printed form. The hybrid circuits based on microstrip-slotline, microstrip-CPW, and microstrip-slotline-CPW combinations are also called double-sided MICs [30].

5.7.1 Circuits Using T-Junctions

T-junctions and their variations occur very frequently in slotline-microstrip circuits or double-sided MICs. A slotline-microstrip T-junction can be obtained by allowing

the microstrip line to run indefinitely in the microstrip-to-slotline transition of Figure 5.29. The resulting T-junction will be as shown in Figure 5.36(a). The equivalent circuit of this T-junction can be obtained from the equivalent circuit of Figure 5.29(b) and will be as shown in Figure 5.36(b). Assuming $n = 1$ simplifies this circuit to that given in Figure 5.36(c). This is the equivalent circuit of a power divider with the slotline appearing in series with the two arms of a microstrip line. Therefore, this T-junction behaves like a series-T. Further, if the slotline is terminated in its matched load, the equivalent circuit will reduce to that shown in Figure 5.36(d), where $R_s = n^2 Z_{0s}$.

Another T-junction can be obtained when the slotline of Figure 5.29 is not terminated in an open circuit but is allowed to run indefinitely. In this case the T-junction will behave like a parallel T-junction, that is, the slotline arms and the

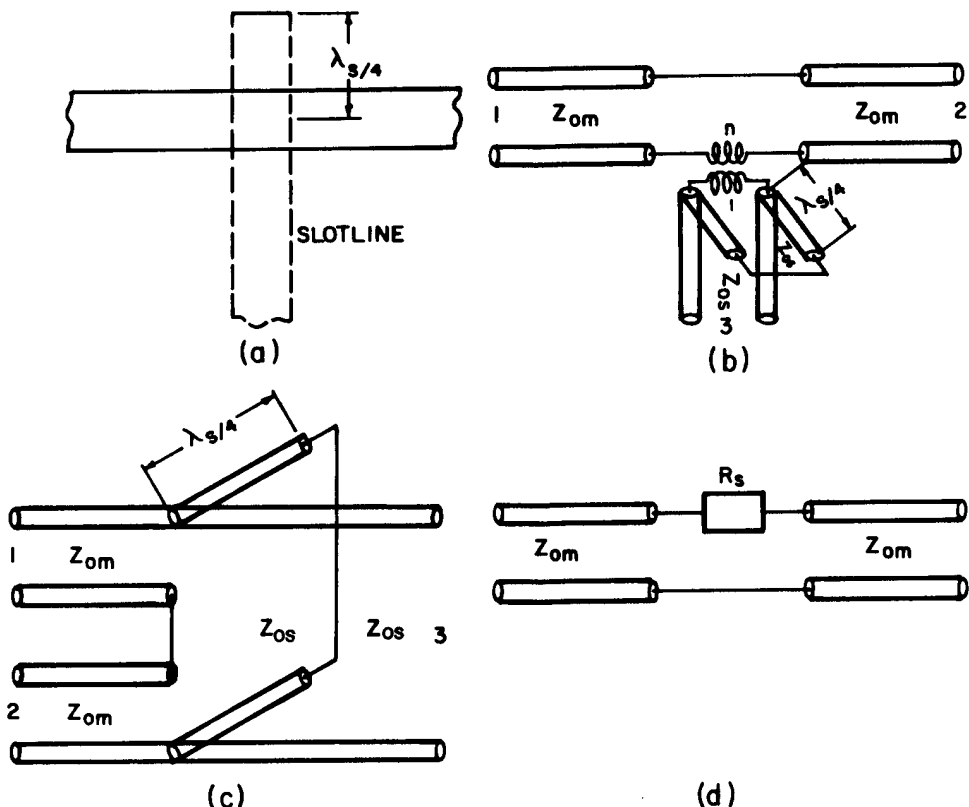


Figure 5.36 Slotline-microstrip series T-junction: (a) schematic; (b) equivalent circuit of (a); (c) equivalent circuit of (a) for $n = 1$; and (d) equivalent circuit of (b) when port 3 is terminated in matched load.

microstrip arm of the T-junction are connected in parallel to each other. A configuration of this T-junction, the electric field distribution in the slotline, and the equivalent circuit are shown in Figure 5.37 [30, 45].

Series and parallel T-junctions can be combined to realize magic-T or 180° hybrids, as is discussed next.

Magic-T/ 180° Hybrid. Magic-T in a microstrip-slotline configuration has been studied by de Ronde [43], Aikawa and Ogawa [30, 45], and Chua [46]. Aikawa and Ogawa have described three different types of magic-T. Two of these magic-T use microstrip lines, slotlines, and coupled slotlines. Another one uses a microstrip line and a slotline only. The three configurations are shown in Figure 5.38. In this figure solid lines represent slotlines and dotted lines represent the microstrip lines on the reverse side of the substrate. Ports \textcircled{E} and \textcircled{H} correspond to the E - and H -arms of a conventional waveguide magic-T, respectively, and ports $\textcircled{1}$, and $\textcircled{2}$ are the remaining ports. Let us call these magic-T as *microstrip type*, *slotline type*, and *T-junction type* based on the kinds of transmission lines connected to the coupled slotlines for (a) and (b) and the use of T-junction only for (c). The slotline type magic-T can be used up to millimeter-wave frequencies because it does not need via-holes for grounding. The coupling behavior of *microstrip* and *slotline-types* magic-T is the same in principle. Therefore, we shall only explain the behavior of magic-T in Figure 5.38(a, c).

Figure 5.39 describes the in-phase coupling and out-of-phase coupling behaviors of a *microstrip-type* magic-T. Here, we have drawn the electric field distribution in the slotlines to explain the coupling. Let us first consider Figure 5.39(a). A signal fed to the microstrip port \textcircled{H} is converted to the slotline mode and gets divided equally into two quarter-wavelength slotlines, and the direction of the electric field is such that the two slotlines are in parallel (very similar to H -plane T-junction in the waveguide). These signals cancel each other while coupling to the microstrip port \textcircled{E} . Therefore, port \textcircled{E} is the uncoupled port. Then, these signals propagate through the coupled slotlines portion as an odd mode. They get further divided at the microstrip junction and appear as in-phase signals out of the microstrip ports $\textcircled{1}$ and $\textcircled{2}$ because of the even symmetry of the structure and the electric fields.

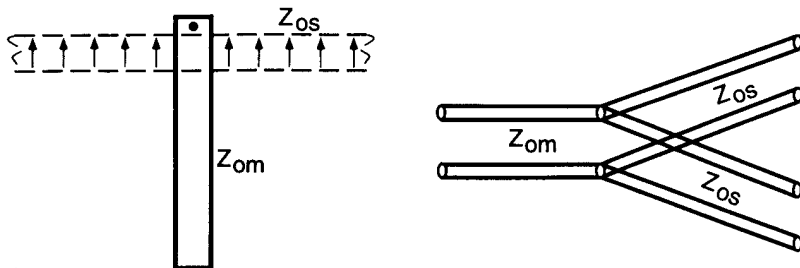


Figure 5.37 Schematic and equivalent circuit of a microstrip-slotline parallel T-junction.

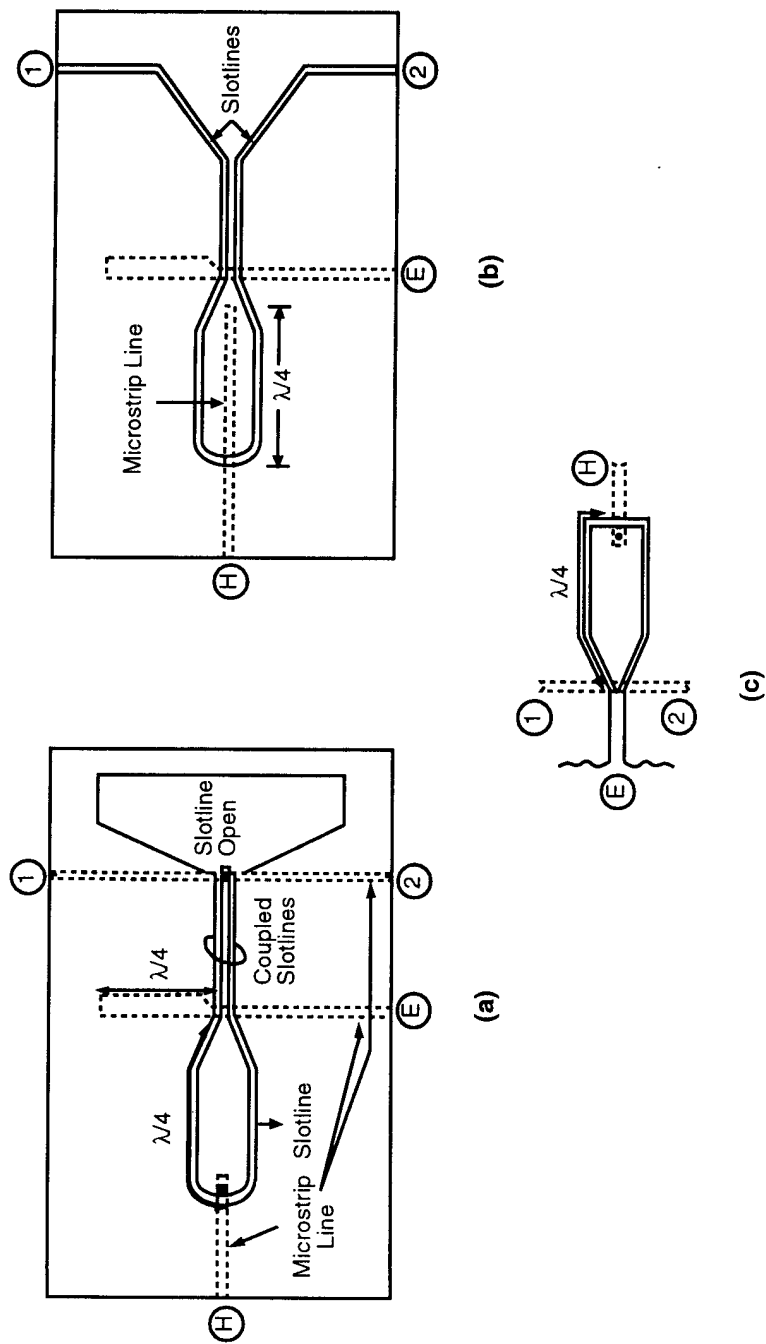


Figure 5.38 Three types of magic-T in a microstrip-slotline configuration: (a) microstrip type; (b) slotline type; and (c) T-junction type (from [30, 45], © 1989, 1980 IEEE. Reprinted with permission.).

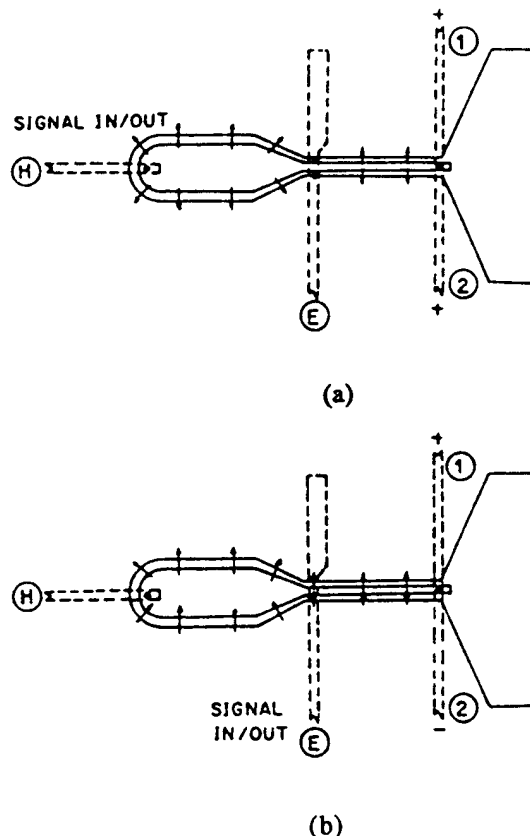


Figure 5.39 Coupling behavior of a microstrip-type magic-T: (a) in-phase coupling and (b) out-of-phase coupling (from [45], © 1980 IEEE. Reprinted with permission.).

In Figure 5.39(b), a signal fed to port **E** is converted to the even mode of the coupled slotlines and thereafter emerges as 180° out-of-phase signals through the ports **①** and **②**. A signal from the **E** port does not couple to the **H** port because the two quarter-wave slotlines are connected in parallel to the microstrip and the electric fields are out-of-phase in these slotline sections.

An equivalent circuit of the microstrip type magic-T is given in Figure 5.40. It is seen that the equivalent circuit is symmetrical with respect to ports **E** and **H**. Consequently, two-port calculations can be used to analyze the four-port circuit. The two-port equivalent circuits for the in-phase and out-of-phase excitations of magic-T are given in Figure 5.41. The analysis of a cascade of two-port circuits can be carried out using the *ABCD* matrix. Theoretical and experimental performances of this magic-T have been calculated. Measured results for a magic-T designed at

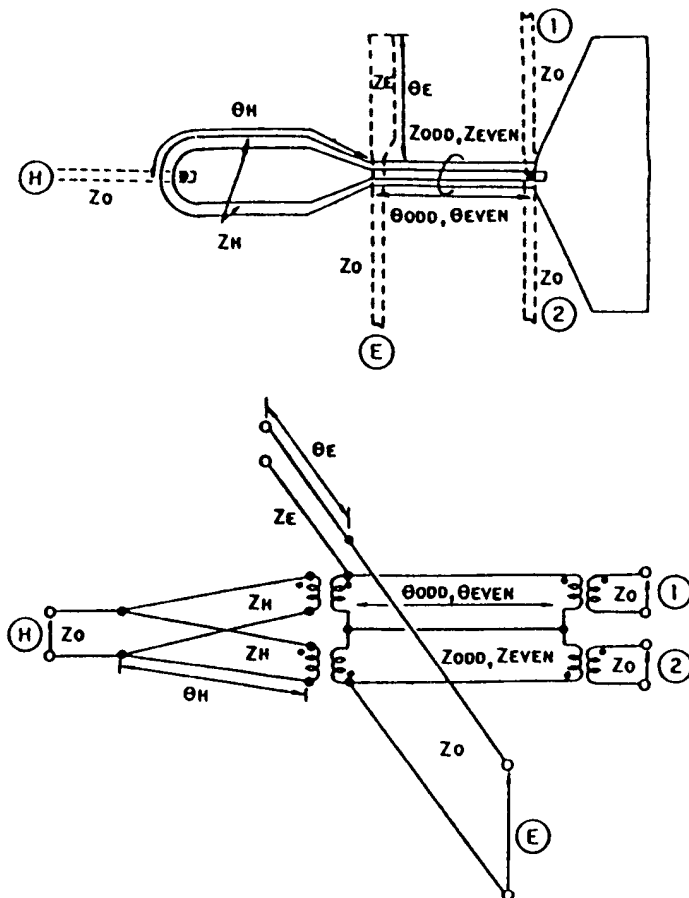


Figure 5.40 Schematic and equivalent circuit of a microstrip-type magic-T (from [45], © 1980 IEEE. Reprinted with permission.).

a center frequency of 6 GHz are plotted in Figure 5.42. The substrate used is alumina with a thickness of 0.635 mm and $\epsilon_r = 9.6$. All the port impedances are 50Ω . The coupled slotline is designed such that $Z_{\text{even}} = 35.4 \Omega (= Z_0/\sqrt{2})$ and $Z_{\text{odd}} = 63.6 \Omega (= Z_H/\sqrt{2})$ because the slotline is designed to be 90Ω . The open microstrip stub impedance Z_E is designed to be 40Ω . It may be observed from the figure that the out-of-phase coupling (E – ①, ②) bandwidth is very wide. The in-phase coupling (H – ①, ②) is almost flat and can transmit even dc signals. The isolation between the ports ① and H is greater than 30 dB and between ports ① and ② is 25 dB at the center frequency. The insertion loss of the in-phase coupling is 0.7 dB and is 0.9 dB for out-of-phase coupling at the center frequency. The insertion

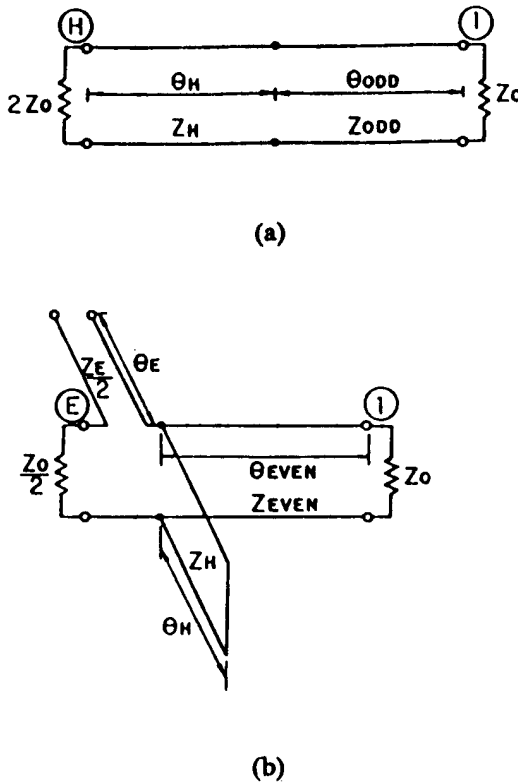


Figure 5.41 Two-port equivalent circuits for the analysis of microstrip type magic-T: (a) in-phase excitation and (b) out-of-phase excitation (from [45], © 1980 IEEE. Reprinted with permission.).

loss is caused mostly by the conductor loss of the transmission lines. The coupling imbalance between ports ① and ② is a maximum 0.3 dB in amplitude and 2.1° in phase over an octave band.

The magic-T described above has a number of practical applications because of the convenient location of the ports. The *E*- and *H*-ports are located on the same side and opposite to the other two ports. This port configuration is quite different from that of a conventional 180° hybrid, such as a rat race. As a result of this, balanced type circuits, such as balanced mixers and balanced modulators, can be implemented with no crossing of transmission lines, which causes signal leakage between the lines and deterioration of the performance.

The magic-T of Figure 5.38(c) can be analyzed in the same manner as the other two. The electric field distributions for out-of-phase excitation and in-phase excitation are shown in Figure 5.43. The theoretical performance can be calculated using the two-port circuit approach described earlier. Theoretical and measured

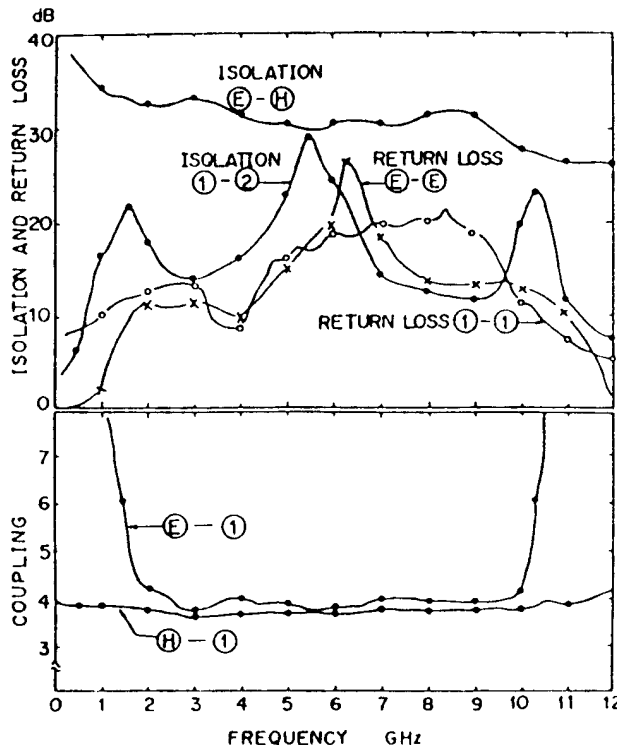


Figure 5.42 Experimental performance of a microstrip-type magic-T designed for the center frequency of 6 GHz (from [45], © 1980 IEEE. Reprinted with permission.).

performances of this type of magic-T are compared in [30]. However, the bandwidth of this magic-T is narrower than that of the microstrip type described earlier.

The configuration of de Ronde's magic-T is shown in Figure 5.44. It consists of a series T-junction and a parallel T-junction. The parallel T-junction is realized in the form of a microstrip T. A linear taper in the microstrip line is introduced in this T to act as an impedance transformer. In an experimental model tested at 2 GHz to 4 GHz on 2.54-cm by 2.54-cm alumina substrate the following performance has been reported [43]:

Isolation between shunt and series arm	≥ 40 dB
Isolation between collinear arms	≥ 20 dB
Imbalance between opposite arms	≤ 0.3 dB
Insertion loss between any two ports	≈ 3.2 dB

A different type of magic-T, studied by Chua [46], is described in Section 5.7.2.

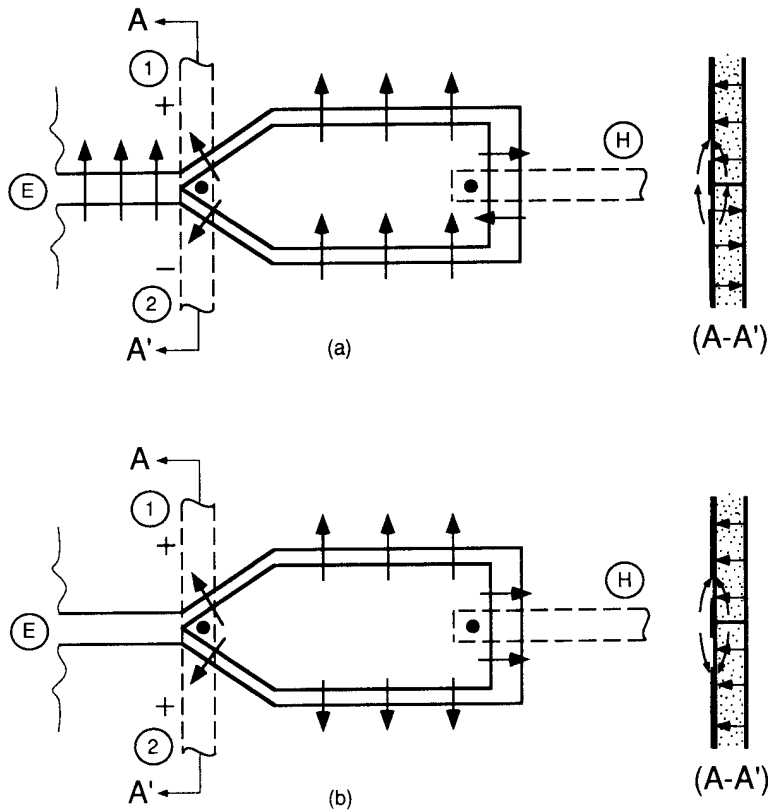


Figure 5.43 Electric field distributions for the T-junction type of magic-T: (a) out-of-phase excitation and (b) in-phase excitation (from [45], © 1980 IEEE. Reprinted with permission.).

Balanced Microstrip-Slotline Circuits [30]. Microstrip-slotline T-junctions have also been used to implement a number of balanced circuits. These include the balanced PSK modulator, phase detector, mixer, ASK modulator, and balanced frequency doubler. The heart of these balanced circuits is the balance-to-unbalance transition or balun between slotline (balanced line) and microstrip line (unbalanced line). A configuration of this balun is shown in Figure 5.45. There are a number of useful features of this balun. These are: (i) very good isolation between the balanced line and the unbalanced line over a wide range of frequency due to the symmetric configuration, (ii) beam-lead devices can easily be mounted in the slotline portion of the balun, and (iii) a dc return path is not required because of the use of the slotline.

The balun, Figure 5.45, consists of a slotline T-junction, two quarter-wave slotlines, and a slotline-to-microstrip T-junction. In the slotline-to-microstrip

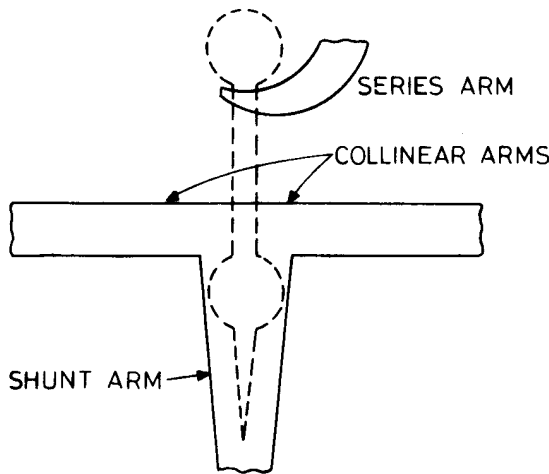


Figure 5.44 Configuration of de Ronde's magic-T (from [43], © 1970 IEEE. Reprinted with permission.).

T-junction the microstrip end is connected to the slotline by means of a through-hole conductor, as shown in the Figure 5.45(a). Alternatively, the microstrip stub can be a quarter-wave long and terminated in an open circuit as shown in Figure 5.45(b). This configuration of a balun is more useful. In this circuit a wire is bonded on the inside conductor of the slotline to supply the modulating signal or to obtain the IF signal. The wire port (or IF port) is isolated from the rf circuit because of the concentration of rf electromagnetic fields in the slotlines and the high series inductance of the wire. The low frequency signals such as the IF and modulating signals do not couple to the microstrip line because (i) a microstrip line does not touch the inside conductor where the wire is bonded and (ii) the quarter-wave open-circuited microstrip line acts as a bandpass filter. Isolation between the rf ports, that is, microstrip line and input slotline, can be understood from the electric field distribution described earlier for the magic-T (Figure 5.43). Consequently, the three ports shown in Figure 5.45 for the balun are isolated from each other without the need for filters.

The equivalent circuit of the balun in Figure 5.45(b) is shown in Figure 5.46. Here, the T-junctions are represented by ideal transformers. It may be observed that the slotline T-junction is represented by a series-T circuit and the slotline-microstrip T-junction by a parallel-T circuit. It should be remembered that the microstrip-slotline T-junction with microstrip through ports, described earlier, behaved like a series-T circuit. Applications of the balun are described next.

Figure 5.47 shows some examples of balanced microwave circuits [30]. The circuit of Figure 5.47(a) can be used as a PSK modulator, phase detector, or a mixer. When it is used as a PSK modulator the carrier propagates along each

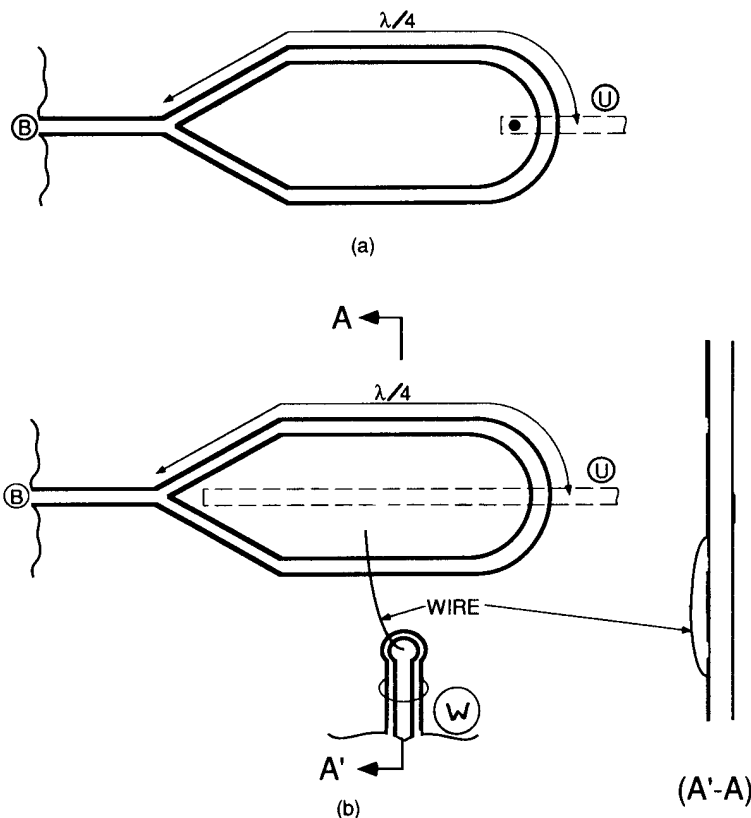


Figure 5.45 Some more configurations of microstrip-slotline balun: (a) balun with a shorted microstrip stub and (b) balun with a wire port and an open microstrip stub (from [30], © 1989 IEEE. Reprinted with permission.).

slotline according to the polarity of the modulating pulse. If it is used as a mixer, an IF signal is obtained at the wire port. The isolation between the RF and LO ports is limited by the mismatch between the characteristics of two diodes. In the frequency doubler circuit of Figure 5.47(b) the diodes are mounted in such a manner that they are forward biased when dc is applied through the wire. The length of the open-circuited microstrip stub is $\lambda/8$ at the input frequency f_0 . When the input signal is applied to the port \textcircled{B} it gets split equally into two parts and is supplied out of phase to the two diodes. The input signal and its odd-harmonics propagate out of phase along the $\lambda/4$ slotlines and nullify each other at the microstrip-slotline junction. Thus, all odd harmonics are decoupled from the output port \textcircled{U} . However, the second harmonic $2f_0$ as well as higher order even harmonics are generated in phase by the diodes. The second harmonic signal is then obtained

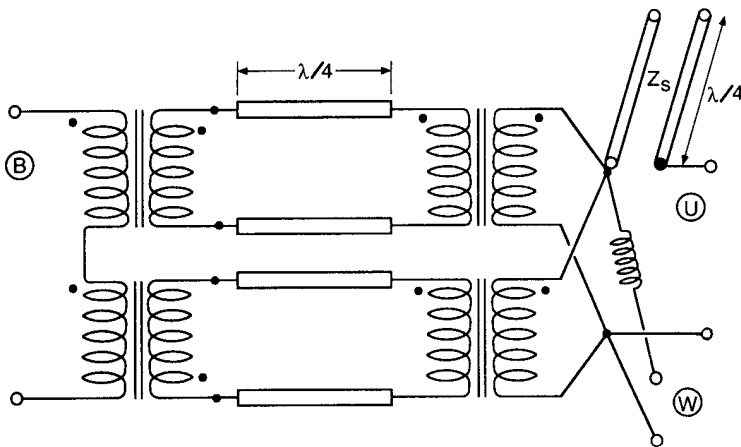


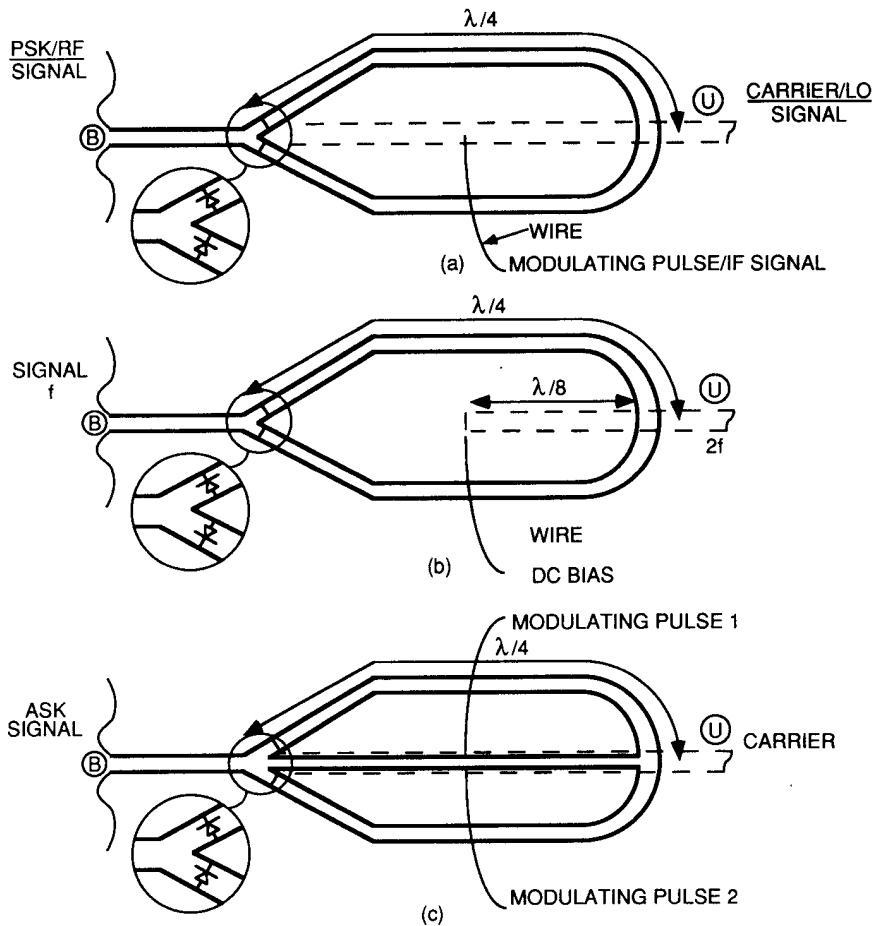
Figure 5.46 Equivalent circuit of the balun in Figure 5.45(b) (from [30], © 1989 IEEE. Reprinted with permission.).

from the output port (U), the $\lambda/8$ microstrip stub playing the role of a bandpass filter at $2 f_0$. The circuit of Figure 5.47(c) can be used as an ASK modulator. In this circuit the inside metallization of the slotlines is divided into two parts so that dc bias to the diodes can be applied independently of each other in order to generate the ASK signal. In principle, other devices such as MESFETs can be used in these circuits in place of diodes.

5.7.2 Circuits Using Wideband 180° Phase Shift

When two microstrip-to-slotline transitions are connected back-to-back as shown in Figure 5.48(a), an additional 180° phase shift is introduced in the signal path. This can be explained qualitatively by considering the **E**-field distribution associated with the microstrip-to-slotline transition. Referring to Figure 5.48(b), we note that the **E**-field in the input microstrip line (near the transition) is in the $-y$ -direction. This produces a slotline wave with the **E**-field in the x -direction. At the second transition an x -directed component of **E** will cause the **E**-field in the output microstrip to lie in the y -direction. Thus, in addition to the phase change introduced by the line length, the **E**-field direction changes from $-y$ to y , which amounts to an equivalent 180° phase change. This phase change is independent of frequency (at least in a first-order analysis) and can thus be used in wide-band circuits. Its application in a rat-race circuit is now discussed.

Rat-Race Hybrid. The usual microstrip rat-race circuit shown in Figure 5.49(a) consists of a $3\lambda/2$ microstrip ring with the four ports located radially as shown. The three adjacent sections are each $\lambda/4$ long, while the fourth section is $3\lambda/4$. Typically this



W78-0316

Figure 5.47 Double-sided balanced microwave circuits: (a) balanced PSK modulator/phase detector/mixer; (b) balanced frequency doubler; and (c) ASK modulator (from [30], © 1989 IEEE. Reprinted with permission.).

circuit will have a bandwidth of 20 percent. A modified version of this circuit [46] involves the replacement of the $3\lambda/4$ microstrip section with a $\lambda/4$ slotline etched on the other side of the substrate as shown in Figure 5.49(b). The remaining 180° electrical length of the microstrip section is compensated for by the two microstrip-slotline junctions required to introduce a slotline in the circuit. Since this phase change is frequency independent, the resulting rat-race circuit has a wider bandwidth. Experimental measurements [46] presented in Figure 5.49(c) show that a bandwidth of greater than an octave can be realized.

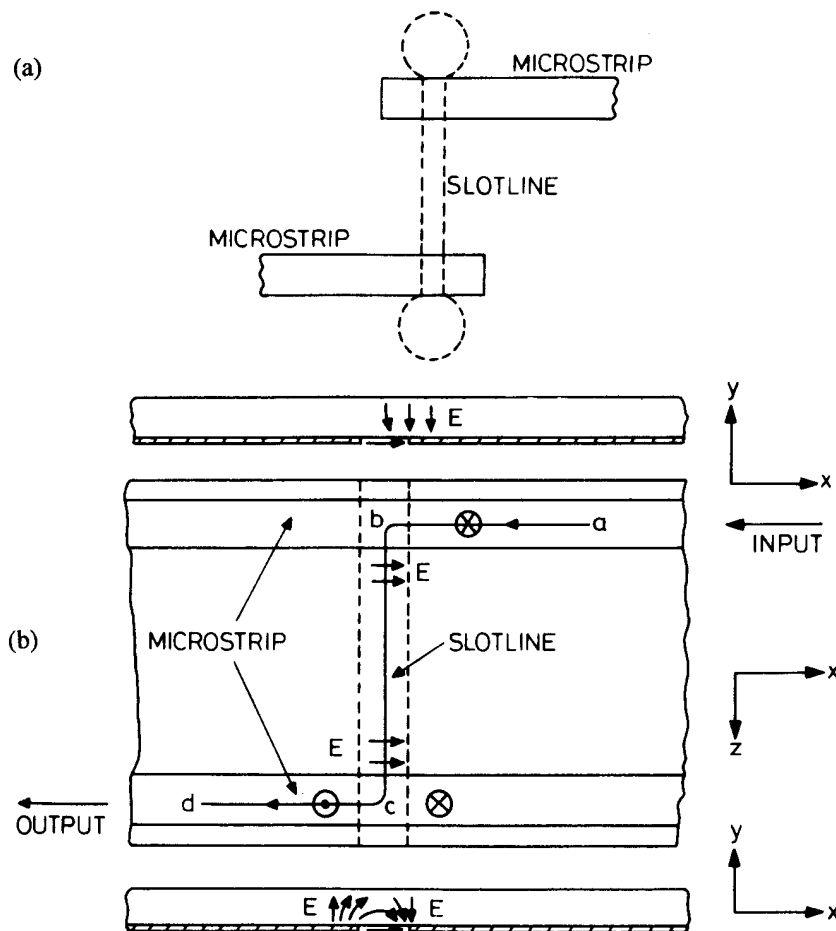


Figure 5.48 (a) Two microstrip-to-slotline transitions connected back-to-back for 180° phase change and (b) mechanism for 180° phase change.

Pulse Inverter. The use of slotline provides a method of obtaining a broadband 180° phase change. This technique can be used successfully in other circuits where a broadband 180° phase shift may be needed. A broadband pulse inverter has also been designed on this principle [47]. The input pulse is fed to one of the microstrip lines (see Figure 5.50(a)), and the inverted pulse output appears at the other microstrip. This pulse inverter was designed using a 0.625-mm thick alumina substrate. The oscilloscope traces of the input and the output pulse trains at 250 MHz are shown in Figure 5.50(b). As seen in this figure, the output pulses are almost identical to the input pulses except for the change in polarity. The bandwidth measurement of the pulse inverter indicates that the circuit works up to 1 GHz.

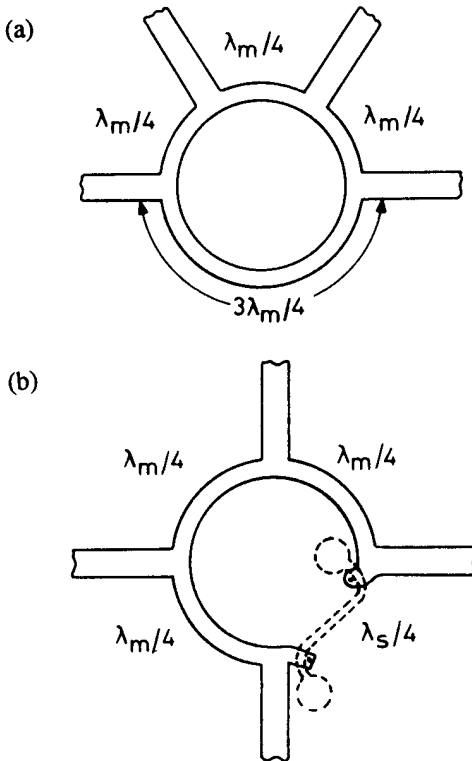


Figure 5.49 (a) A rat-race hybrid using microstrip lines only, (b) rat-race hybrid using slotline in (a), and (c) performance of rat-race hybrid shown in (b) from [46], © 1971 Microwave Exhibitions & Publishers (U.K.). Reprinted with permission.).

Riblet has developed a microstrip-slotline symmetrical ring eight-port comparator circuit [48]. The size of the ring is 3λ at the center frequency. It can be reduced to a wavelength or less by using shunting capacitors across the slotline stubs.

5.7.3 Hybrid/de Ronde's Branchline Couplers

Let us consider the branchline coupler configuration shown in Figure 5.51. A conventional microstrip branchline coupler is shown in Figure 5.51(a) along with its transmission line equivalent circuit (neglecting junction effects). All the branch-lines in this circuit are connected in shunt. Series connections of the branchline are not possible by the use of microstrips. However, the use of slotlines also allows the designer the flexibility of incorporating series-connected branches if desired.

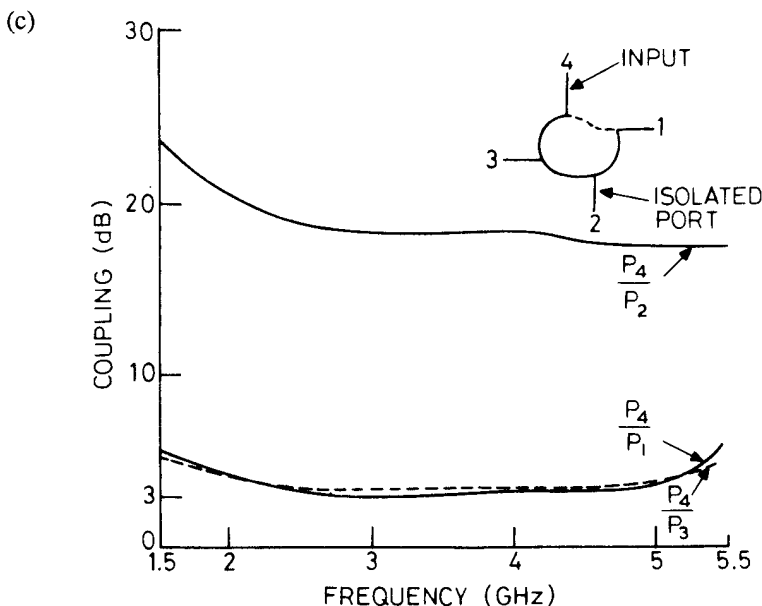


Figure 5.49 (continued).

As shown in Figure 5.51(b), a shunt-connected element can be transformed into an equivalent series-connected element provided two additional quarter-wave sections are included on each side of the series-connected element. If the middle branch of the 3-branch coupler, shown in Figure 5.51(a), is replaced by a series-connected branch in this manner, we obtain the configuration shown in Figure 5.51(c). In this arrangement, there are two half-wave sections between the shunt- and series-connected branches. These half-wave sections can be eliminated and the three branches put together at one place as shown in Figure 5.51(d). This coupler has been analyzed, like any other branchline coupler, using the method of even- and odd-mode excitations.

The modified branchline coupler has two advantages over the conventional microstrip branchline coupler: smaller size and wider bandwidth. Both of these advantages result from the elimination of the two quarter-wave lengths shown in Figure 5.51(a).

The final version of the hybrid branchline coupler, shown in Figure 5.51(d), is very similar to the coupler configuration shown in Figure 5.52, which was suggested earlier empirically by de Ronde [43] and is named after him. One can consider de Ronde's coupler to be derived from the configuration of Figure 5.51(d) in the following manner. Two shunt-connected branches are combined and realized by the microstrip on the top surface of the dielectric substrate. The series-connected branch is realized by the slotline in the ground plane. Performance of a de Ronde

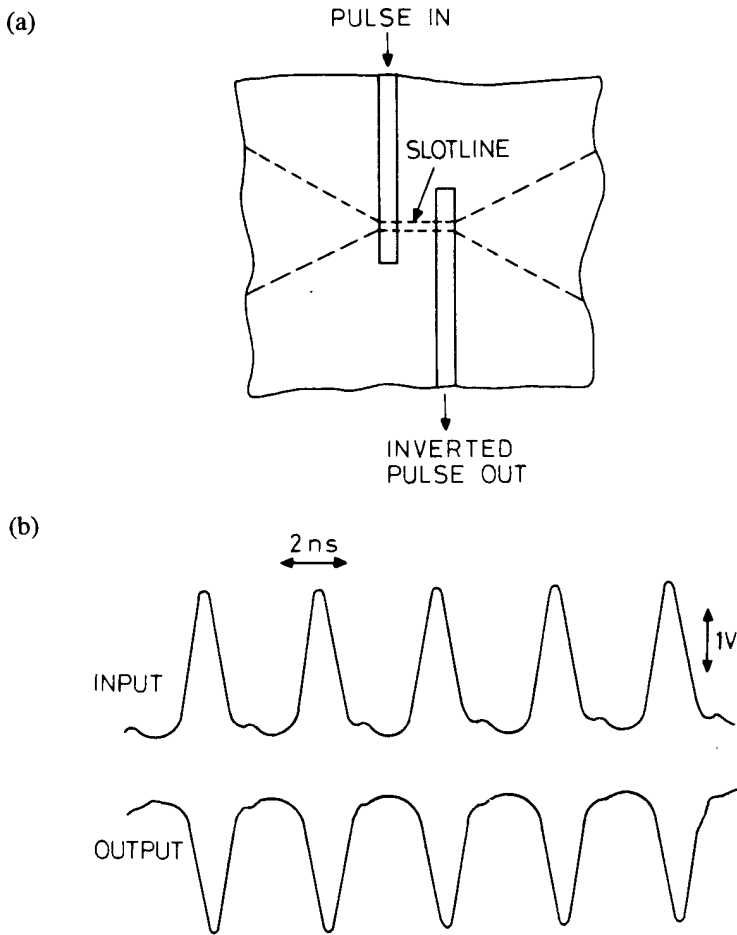


Figure 5.50 (a) Configuration of a microstrip-slotline pulse inverter and (b) oscilloscope trace of the performance of a microstrip-slotline pulse inverter (from [47]).

coupler has been measured [49] and the results are shown in Figure 5.53. The circuit designs are as follows:

Substrate thickness	0.38 mm
Slot width	50 μm
ϵ_r	12
Substrate size	2 cm \times 2 cm
Microstrip impedance	60.4 Ω
Slotline impedance	50 Ω
Frequency range	X-band

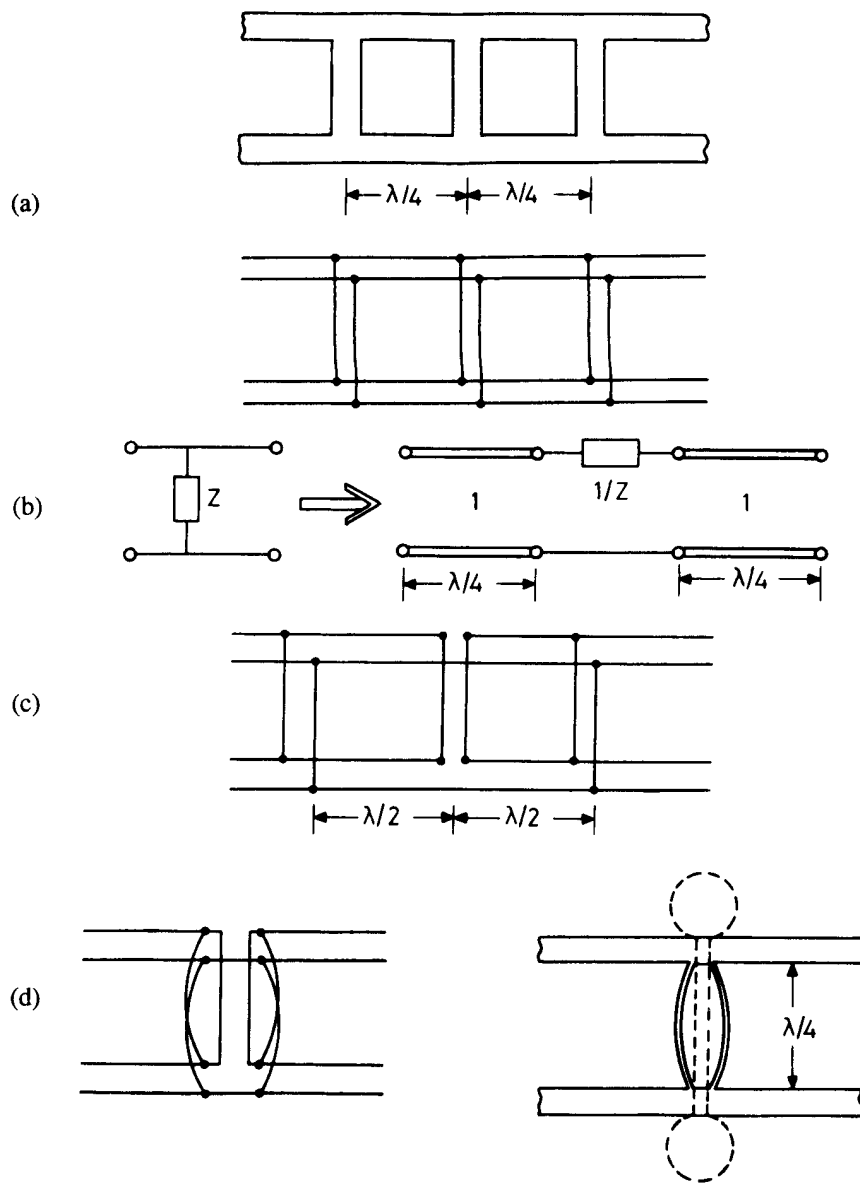


Figure 5.51 (a) Branchline coupler configurations using microstrip lines and two-wire lines, (b) equivalence between a shunt- and a series-connected branch, (c) modified coupler with a series branch, and (d) hybrid branchline coupler.

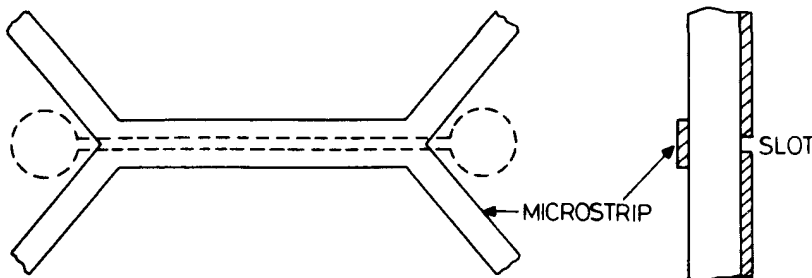


Figure 5.52 Configuration of de Ronde's coupler (from [43], © 1970 IEEE. Reprinted with permission.).

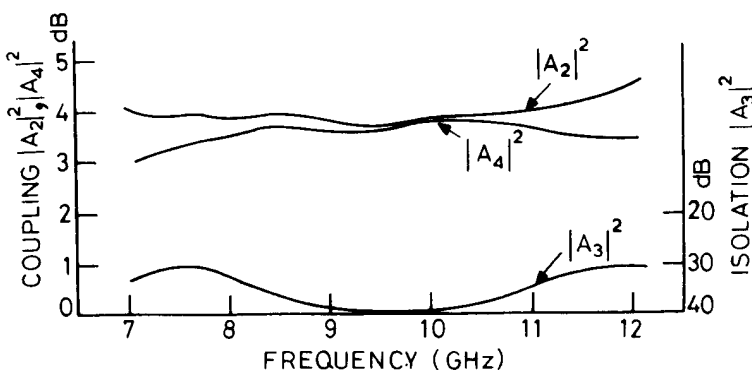


Figure 5.53 Measured performance of de Ronde's coupler (from [49], © 1974 IEEE. Reprinted with permission.).

A thorough analysis of de Ronde's coupler has been carried out by Hoffmann and Siegl [28, 50]. The coupler has been analyzed using the method of even- and odd-mode excitations applied to the coupled microstrip-slotline configuration. Characteristics of this transmission line were described in Section 5.5.1. Let Z_{0e} and ϵ_{re} be the characteristic impedance and effective dielectric constant for the even-mode (quasi-microstrip mode), respectively, and Z_{0o} and ϵ_{ro} be the corresponding quantities for the odd-mode (quasi-slot mode), respectively. Synthesis equations for this coupler are obtained as [28]

$$Z_{0e} = \frac{Z_0}{2} \sqrt{\frac{1+k}{1-k}} \quad (5.68)$$

and

$$Z_{0o} = 2Z_0 \sqrt{\frac{1+k}{1-k}} = \frac{Z_0^2}{Z_{0e}} \quad (5.69)$$

where Z_0 is the characteristic impedance of the feed lines to the coupler and k is the coupling coefficient. From the odd- and even-mode impedances one can determine the strip width and slot width of the coupler. If the length of the coupled section is chosen to be a quarter-wave at the center frequency, the directivity of the coupler is found to be poor because the phase velocities for the even- and odd-modes are different ($\epsilon_{ro} < \epsilon_{re}$). The lower phase for the odd mode can be compensated for, at a particular frequency, by increasing the length of the slotline so that it extends outside the overlapping microstrip [51], as shown in Figure 5.54. The additional slotline leaves the phase associated with the even-mode unchanged, and the total phase of the odd mode can be adjusted such that $\theta_e = \theta_o$. However, this end loading decreases the impedance. To compensate for this the characteristic impedance of the slot mode, Z_{0o} , has to be increased.

Now, let us assume that the phase compensation is to be achieved at the center frequency referenced to the even mode, that is,

$$f_c = \frac{c}{4\ell\sqrt{\epsilon_{re}}} \quad \text{where } \ell \text{ is the length of the coupling section}$$

Further, assuming that a slight increase in Z_{0o} to Z_{0o}^* required for compensation will not alter ϵ_{ro} , that is $\epsilon_{ro}^* = \epsilon_{ro}$, the increased characteristic impedance Z_{0o}^* and the additional slot length ℓ_s on either end of the coupled section are obtained as [28]

$$Z_{0o}^* = \frac{Z_{0o}}{2} \left[\cot\left(\frac{\pi}{4}\sqrt{\frac{\epsilon_{ro}}{\epsilon_{re}}}\right) + \tan\left(\frac{\pi}{4}\sqrt{\frac{\epsilon_{ro}}{\epsilon_{re}}}\right) \right] \quad (5.70)$$

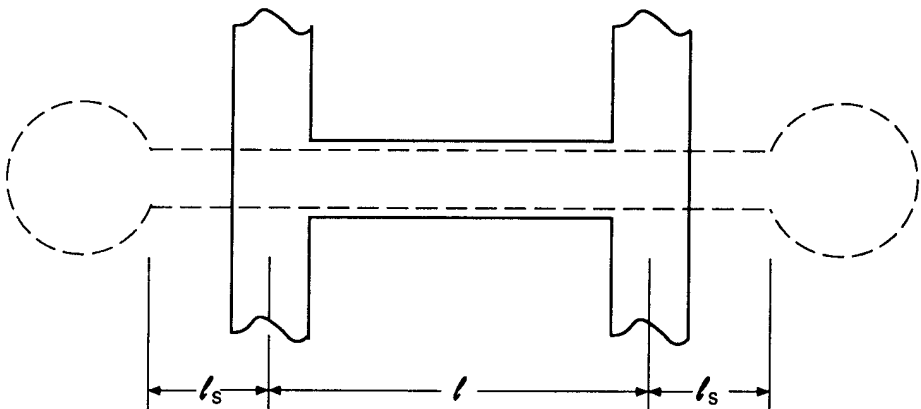


Figure 5.54 de Ronde's coupler with increased length of slotline for improving the isolation (from [50], © 1982 IEEE. Reprinted with permission.).

$$\ell_s = \frac{2\ell}{\pi} \sqrt{\frac{\epsilon_{re}}{\epsilon_{ro}}} \tan^{-1} \left\{ \frac{Z_{0c}^*}{Z_{0o}} \left[1 - 2 \sin^2 \left(\frac{\pi}{4} \sqrt{\frac{\epsilon_{ro}}{\epsilon_{re}}} \right) \right] \right\} \quad (5.71)$$

Another approach for equalizing the even- and odd-mode velocities for the coupled microstrip-slotline is to cover the slotline with a dielectric sheet as shown in Figure 5.55.

Aikawa and Ogawa [30] have designed a de Ronde's coupler in the millimeter wave region at a center frequency of 26 GHz. It was fabricated on 0.3 mm-thick alumina substrate. The insertion loss variation of the coupler was found to be less than 0.5 dB over the frequency range 25 GHz to 28.5 GHz. The isolation was greater than 18 dB over a bandwidth of 6 GHz.

A two-layer slotline-coupled microstrip directional coupler has been reported by Tanaka et al. [31]. The cross-section of the transmission line used in the coupler is shown in Figure 5.56. It consists of two microstrip lines that couple through a slot in a common ground plane of the microstrips. This slot coupler has been designed for both tight coupling (~ 3 dB) as well as loose coupling (such as 10 dB). The design of this coupler is exactly similar to any coupled-line directional coupler,

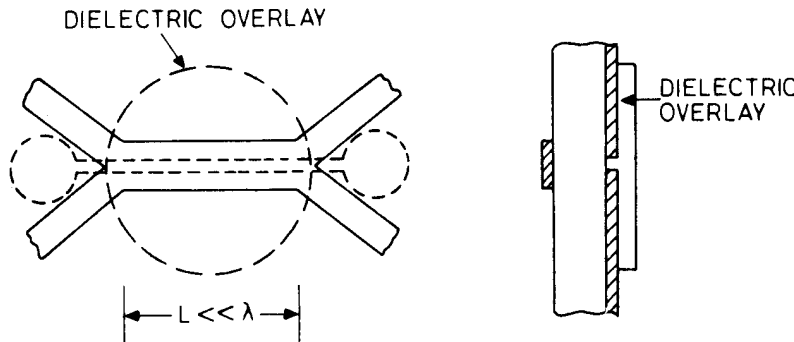


Figure 5.55 de Ronde's coupler with a dielectric overlay for equalizing the even- and odd-mode phase velocities.

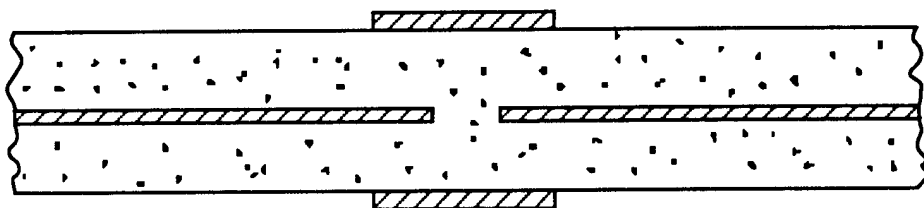


Figure 5.56 Cross-section of slotline-coupled microstrip lines.

which is based on the even- and odd-mode characteristics of the coupled section. A number of couplers were designed for a center frequency of 1.5 GHz. The substrate thickness was 0.8 mm and relative permittivity 2.5. Measurements on these couplers showed more than 25 dB return loss, more than 28 dB isolation, and a coupling variation of 0.2 dB over the 1.2-GHz to 1.8-GHz frequency range [31]. These couplers were then combined to obtain multiport directional couplers avoiding any microstrip line crossover.

5.7.4 Other Types of Slotline Circuits

The circuits mentioned in this section are based on the properties of slotlines only. They do not have the hybrid composition as described in earlier circuits using slotlines. These circuits can be classified into two categories: circuits using slotline resonators (for example, filters) and ferrite devices using slotline.

Circuits Using Slotline Resonators

Slotline resonators have been used for the design of filters, both band-pass and band-reject types [52]. The design procedure for slotline filters is the same as that for any other transmission line; that is, it is based on the coupling coefficient between either two end-coupled or two parallel-coupled sections of transmission line. The experimental results in [52] indicate that the performance of slotline filters is not superior to those using other transmission lines.

Ferrite Devices Using Slotline

When the slotline was introduced as an alternative transmission structure for MICs, it was expected that the slotline would be more suitable than the microstrip line for nonreciprocal ferrite devices. This expectation was based on the existence of an elliptically polarized magnetic field distribution in the slot as discussed in Section 5.2.1. However, the experimental and analytical studies reported so far on circulators and isolators [53–55] have not pointed out any significant advantage of ferrite devices using slotline. A differential phase shifter in a coupled microstrip-slotline configuration (Figure 5.17) holds promise. El-Sharawy and Jackson have reported the analysis and experimental results on this type of phase shifter [29]. A multilayered configuration provides a larger amount of phase shift. A differential phase shift of the order of $45^\circ/\text{cm}$ was measured by them over a 6-GHz to 8.5-GHz frequency range.

References

- [1] Cohn, S. B., "Slotline on a Dielectric Substrate," *IEEE Trans.*, Vol. MTT-17, 1969, pp. 768–778.
- [2] Cohn, S. B., "Slotline Field Components," *IEEE Trans.*, Vol. MTT-20, 1972, pp. 172–174.

- [3] Knorr, J. B., and K. D. Kuchler, "Analysis of Coupled Slots and Coplanar Strips on Dielectric Substrates," *IEEE Trans.*, Vol. MTT-23, 1975, pp. 541–548.
- [4] Itoh, T., and R. Mittra, "Dispersion Characteristics of Slotlines," *Electron. Lett.*, Vol. 7, 1971, pp. 364–365.
- [5] Janaswamy, R., and D. H. Schaubert, "Dispersion Characteristics for Wide Slotlines on Low Permittivity Substrate," *IEEE Trans.*, Vol. MTT-33, 1985, pp. 723–726.
- [6] Janaswamy, R., and D. H. Schaubert, "Characteristic Impedance of a Wide Slotline on Low-Permittivity Substrates," *IEEE Trans.*, Vol. MTT-34, 1986, pp. 900–902.
- [7] Itoh, T. (Ed), *Numerical Techniques for Microwave and Millimeter-wave Passive Structures*, New York: John Wiley, 1989.
- [8] Liang, G. C., et al., "Full-wave Analysis of Coplanar Waveguide and Slotline Using the Time-Domain Finite-Difference Method," *IEEE Trans.*, Vol. MTT-37, 1989, pp. 1949–1957.
- [9] Robinson, G. H., and J. L. Allen, "Slotline Application to Miniature Ferrite Devices," *IEEE Trans.*, Vol. MTT-17, 1969, pp. 1097–1101.
- [10] Galejs, J., "Excitation of Slots in a Conducting Screen Above a Lossy Dielectric Half Space," *IRE Trans.*, Vol. AP-10, 1962, pp. 436–443.
- [11] Garg, R., and K. C. Gupta, "Expressions for Wavelength and Impedance of Slotline," *IEEE Trans.*, Vol. MTT-24, 1976, p. 532.
- [12] Rozzi, et al., "Hybrid Modes, Substrate Leakage, and Losses of Slotline at Millimeter-wave Frequencies," *IEEE Trans.*, Vol. MTT-38, 1990, pp. 1069–1078.
- [13] Citerne, J., et al., "Fundamental and Higher Order Modes in Microslot Lines," *Proc. 5th European Microwave Conf.*, Hamburg, 1975, pp. 273–277.
- [14] Kitazawa, T., et al., "Analysis of the Dispersion Characteristics of Slot Line With Thick Metal Coating," *IEEE Trans.*, Vol. MTT-28, 1980, pp. 387–392.
- [15] Kitazawa, T., et al., "Slotline with Thick Metal Coating," *IEEE Trans.*, Vol. MTT-21, 1973, pp. 580–582.
- [16] Montgomery, C. G., et al., *Principles of Microwave Circuits*, New York: McGraw-Hill Book Company, 1948, p. 154.
- [17] Mariani, E. A., et al., "Slotline Characteristics," *IEEE Trans.*, Vol. MTT-17, 1969, pp. 1091–1096.
- [18] Garg, R., "Effect of Tolerances on Microstripline and Slotline Performances," *IEEE Trans.*, Vol. MTT-26, 1978, pp. 16–19.
- [19] Das, N. K., and D. M. Pozar, "Full-Wave Spectral-Domain Computation of Material, Radiation, and Guided Wave Losses in Infinite Multilayered Printed Transmission Lines," *IEEE Trans.*, Vol. MTT-39, 1991, pp. 54–63.
- [20] Kurpis, G. P., "Coplanar and Slotlines—Are They Here to Stay?," *Proc. Int. Microelectric Symp.*, Washington, 1972, pp. 3B.6.1–3B.6.5.
- [21] Jansen, R., "Hybrid Mode Analysis of End Effects of Planar Microwave and Millimeter Wave Transmission Lines," *Proc. Inst. Elec. Eng.*, Vol. 128, pt. H, 1981, pp. 77–86.
- [22] Yang, H., and N. G. Alexopoulos, "A Dynamic Model for Microstrip-slotline Transition and Related Structures," *IEEE Trans.*, Vol. MTT-36, 1988, pp. 286–293.
- [23] Knorr, J. B., and J. Saenz, "End Effect in a Shorted Slot," *IEEE Trans.*, Vol. MTT-21, 1973, pp. 579–580.
- [24] Chramiec, J., "Reactances of Slotline Short and Open Circuits on Alumina Substrate," *IEEE Trans.*, Vol. MTT-37, 1989, pp. 1638–1641.
- [25] Itoh, T., "Spectral Domain Imittance Approach for Dispersion Characteristics of Generalized Printed Transmission Lines," *IEEE Tran.*, Vol. MTT-28, 1980, pp. 733–736.
- [26] Jansen, R. H., "Microstrip Lines with Partially Removed Ground Metallization, Theory and Applications," *Archiv. Elekr. Übertr.*, Vol. 32, 1978, pp. 485–492.
- [27] Ogawa, H., and M. Aikawa, "Analysis of Coupled Microstrip-Slotlines," *Trans. IECE Jap.*, Vol. 62B, 1979, pp. 269–270.
- [28] Hoffmann, R. K. and J. Siegl, "Microstrip-Slot Coupler Design—Part I: S-Parameters of Uncompensated and Compensated Couplers," *IEEE Trans.*, Vol. MTT-30, 1982, pp. 1205–1210.

- [29] El-Sharawy, E. B., and R. W. Jackson, "Analysis and Design of Microstrip-slot Line for Phase Shifting Applications," *IEEE Trans.*, Vol. MTT-38, 1990, pp. 276–283.
- [30] Aikawa, M., and H. Ogawa, "Double-Sided MIC's and Their Applications," *IEEE Trans.*, Vol. MTT-37, 1989, pp. 406–413.
- [31] Tanaka, T., et al., "Slot-Coupled Directional Couplers Between Double Sided Substrate Microstrip Lines and Their Applications," *IEEE Trans.*, Vol. MTT-36, 1986, pp. 1752–1757.
- [32] Shigesawa, H., et al., "Conductor-Backed Slot Line and Coplanar Waveguide: Dangers and Full-Wave Analyses," *Proc. Int. Microwave Symp.*, 1988, pp. 199–202.
- [33] Rozzi, T., et al., "Radiation Modes of Slotline with Application to Millimetric Circuits," *IEEE MTT-S Digest*, 1992, pp. 503–506.
- [34] Das, N. K., "Characteristics of Modified Slotline Configurations," *Digest Int. Microwave Symp.*, 1991, pp. 777–780.
- [35] Knorr, J. B., "Slotline Transitions," *IEEE Trans.*, Vol. MTT-22, 1974, pp. 548–554.
- [36] Chamber, D., et al., "Microwave Active Network Synthesis," *Semiannual Report, Stanford Resr. Inst.*, June 1970.
- [37] Das, N. K., "Generalized Multiport Reciprocity Analysis of Surface-to-surface Transitions Between Multiple Printed Transmission Lines," *IEEE Trans.*, Vol. MTT-41, 1993, pp. 1164–1177.
- [38] Antar, Y. M. M., et al., "Microstrip-Slotline Transition Analysis Using the Spectral Domain Technique," *IEEE Trans.*, Vol. MTT-40, 1992, pp. 515–523.
- [39] Podcameni, A., and M. L. Coimbra, "Slotline-Microstrip Transition on Iso/Anisotropic Substrate: A More Accurate Design," *Electron. Lett.*, Vol. 16, 1980, pp. 780–781.
- [40] Schuppert, B., "Microstrip/Slotline Transitions: Modeling and Experimental Investigations," *IEEE Trans.*, Vol. MTT-36, 1988, pp. 1272–1282.
- [41] Schwab, W., and W. Menzel, "On the Design of Planar Microwave Components Using Multilayer Structures," *IEEE Trans.*, Vol. MTT-40, 1992, pp. 67–72.
- [42] Uwano, T., et al., "Characterization of Microstrip-to-Slotline Transition Discontinuities by Transverse Resonance Analysis," *Alta Freq.*, Vol. 57, No. 5, 1988, pp. 183–191.
- [43] de Ronde, F. C., "A New Class of Microstrip Directional Couplers," *Digest of Tech. Papers, G-MTT Symp.* 1970, pp. 184–189.
- [44] Schiek, B., and J. Kohler, "An Improved Microstrip-to-Microslot Transition," *IEEE Trans.*, Vol. MTT-24, 1976, pp. 231–233.
- [45] Aikawa, M., and H. Ogawa, "A New MIC Magic-T Using Coupled Slot Lines," *IEEE Trans.*, Vol. MTT-28, 1980, pp. 523–528.
- [46] Chua, L. W., "New Broadband Matched Hybrids for Microwave Integrated Circuits," *Proc. European Microwave Conf. (Stockholm)*, 1971, pp. C4/5.1–C4/5.4.
- [47] Hede, C., "High Speed Logic, Part 3," Tech. Report IR 127, Electromagnetics Institute, Technical University of Denmark, 1977.
- [48] Riblet, G. P., "Compact Planar Microstrip-slotline Symmetrical Ring Eightport Comparator Circuits," *IEEE Trans.*, Vol. MTT-38, 1990, pp. 1421–1426.
- [49] Schiek, B., "Hybrid Branchline Couplers—A Useful New Class of Directional Couplers," *IEEE Trans.*, Vol. MTT-22, 1974, pp. 864–869.
- [50] Hoffmann, R. K., and J. Siegl, "Microstrip-slot Coupler Design—Part II: Practical Design Aspects," *IEEE Trans.*, Vol. MTT-30, 1982, pp. 1211–1215.
- [51] Schiek, B., and J. Kohler, "Improving the Isolation of 3-dB Couplers in Microstrip-Slotline Technique," *IEEE Trans.*, Vol. MTT-26, 1978, pp. 5–7.
- [52] Mariani, E. A., and J. P. Agrios, "Slotline Filters and Couplers," *IEEE Trans.*, Vol. MTT-18, 1970, pp. 1089–1095.
- [53] Ogasawara, N., and M. Kaji, "Coplanar-Guide and Slot-Guide Junction Circulators," *Electron. Lett.*, Vol. 7, 1971, pp. 220–221.
- [54] De Vecchis, M., et al., "A New Slotline Broadband Isolator," *Proc. European Microwave Conf. (Brussels)*, 1973, Paper B.9.6.

- [55] Courtois, L., and M. de Vecchis, "A New Class of Non-Reciprocal Components Using Slotline," *IEEE Trans.*, Vol. MTT-23, 1975, pp. 511-516.

Appendix 5.A: Susceptance Calculation for the Transverse Resonance Method

The formula for susceptance ηB_t for the case of electric walls at $y = \pm b/2$ is given as

$$\begin{aligned} \eta B_t = & \frac{a}{2b} \left[-v + u \tan\left(\frac{\pi h u}{ap} - \tan^{-1} \frac{v}{u}\right) \right] \\ & + \frac{1}{p} \left\{ \left(\frac{\epsilon_r + 1}{2} - p^2 \right) \ell_n \frac{2}{\pi \delta} \right. \\ & \left. + \frac{1}{2} \sum_{n=1,2,3,\dots} \left[v^2 \left(1 - \frac{1}{F_n} \right) + M_n \right] \frac{\sin^2(\pi n \delta)}{n(\pi n \delta)^2} \right\} \end{aligned} \quad (\text{A.1})$$

For magnetic walls at $y = \pm b/2$ the expression for B_t is

$$\begin{aligned} \eta B_t = & \frac{1}{p} \left\{ \left(\frac{\epsilon_r + 1}{2} - p^2 \right) \ell_n \frac{8}{\pi \delta} \right. \\ & \left. + \frac{1}{2} \sum_{n=1/2,3/2,5/2,\dots} \left[v^2 \left(1 - \frac{1}{F_n} \right) + M_n \right] \frac{\sin^2(\pi n \delta)}{n(\pi n \delta)^2} \right\} \end{aligned} \quad (\text{A.2})$$

where $\eta = \sqrt{\mu_0/\epsilon_0} = 376.7 \Omega$, $\delta = W/b$, $p = \lambda_0/\lambda_s$, and

$$u = \sqrt{\epsilon_r - p^2} \quad v = \sqrt{p^2 - 1} \quad (\text{A.3})$$

$$F_n = \sqrt{1 + \left(\frac{b}{2an} \frac{v}{p} \right)^2} \quad (\text{A.4})$$

$$F_{nl} = \sqrt{1 - \left(\frac{b}{2an} \frac{u}{p} \right)^2} \quad (\text{A.5})$$

For F_{nl} real, M_n is

$$M_n = \frac{\epsilon_r \tanh r_n - p^2 F_{nl}^2 \coth q_n}{[1 + (b/2an)^2] F_{nl}} - u_2 \quad (\text{A.6})$$

where

$$r_n = \frac{2\pi nh F_{nl}}{b} + \tanh^{-1} \left(\frac{F_{nl}}{\epsilon_r F_n} \right) \quad (\text{A.7})$$

$$q_n = \frac{2\pi nh|F_{nl}|}{b} + \coth^{-1}\left(\frac{F_n}{|F_{nl}|}\right) \quad (\text{A.8})$$

For F_{nl} imaginary, M_n is

$$M_n = \frac{\epsilon_r \tan r'_n - p^2 |F_{nl}|^2 \cot q'_n}{[1 + (b/2an)^2] |F_{nl}|} - u^2 \quad (\text{A.9})$$

where

$$r'_n = \frac{2\pi nh|F_{nl}|}{b} + \tan^{-1}\left(\frac{|F_{nl}|}{\epsilon_r F_n}\right) \quad (\text{A.10})$$

$$q'_n = \frac{2\pi nh|F_{nl}|}{b} + \cot^{-1}\left(\frac{F_n}{|F_{nl}|}\right) \quad (\text{A.11})$$

Appendix 5.B: Sensitivity Expressions for Slotline Impedance and Wavelength

The following expressions can be obtained by using the definition of sensitivity, (2.99), and the expressions for slotline impedance and wavelength, (5.31) to (5.39).

1. For $0.02 \leq W/h < 0.2$

$$\begin{aligned} S_W^{Z_0s} = & \frac{50}{Z_{0s}} \left\{ 2 \frac{W}{h} - 0.12 - \frac{(W/h - 0.02)(W/h - 0.1)}{W/h} + \frac{0.4343}{50} \right. \\ & \cdot (44.28 - 19.58 \log \epsilon_r) \Big\} \\ & - \frac{W/h}{Z_{0s}} (1.07 \log \epsilon_r + 1.44) \\ & \cdot (11.4 - 6.072 \log \epsilon_r - h/\lambda_0 \times 10^2)^2 \end{aligned} \quad (\text{B.1})$$

$$S_h^{Z_0s} = -S_W^{Z_0s} + \frac{h}{Z_{0s}} \frac{1}{\lambda_0} \frac{\partial Z_{0s}}{\partial (h/\lambda_0)} \quad (\text{B.2})$$

where

$$\begin{aligned} \frac{\partial Z_{0s}}{\partial (h/\lambda_0)} = & -200(11.4 - 6.07 \log \epsilon_r - h/\lambda_0 \times 10^2) \\ & \cdot [0.32 \log \epsilon_r - 0.11 + \frac{W}{h} (1.07 \log \epsilon_r + 1.44)] \end{aligned}$$

$$\begin{aligned}
S_{\epsilon}^{Z_{0s}} = & - \frac{0.4343 \epsilon_r}{Z_{0s}} [35.19 + 19.58 \log(W/h \times 10^2) \\
& + (0.32 + 1.07 W/h)(11.4 - 6.07 \log \epsilon_r - h/\lambda_0 \times 10^2)^2 \\
& - 12.14(11.4 - 6.07 \log \epsilon_r - h/\lambda_0 \times 10^2) \\
& \cdot [0.32 \log \epsilon_r - 0.11 + W/h(1.07 \log \epsilon_r + 1.44)]]
\end{aligned} \quad (B.3)$$

$$S_W^{\epsilon_{re}} = -2 S_W^{\lambda/\lambda_0} = - \frac{2W/h}{\epsilon_{re}} [0.2 - 0.29 \log(h/\lambda_0 \times 10^2)] \quad (B.4)$$

$$S_h^{\epsilon_{re}} = -S_W^{\epsilon_{re}} + \frac{0.8686}{\epsilon_{re}} (0.29 W/h + 0.047) \quad (B.5)$$

$$S_{\epsilon}^{\epsilon_{re}} = 0.389 / \epsilon_{re} \quad (B.6)$$

2. For $0.2 \leq W/h \leq 1.0$

$$\begin{aligned}
S_W^{Z_{0s}} = & \frac{W/h}{Z_{0s}} \left[1.25(114.59 - 51.88 \log \epsilon_r) + 24 - 40 W/h \right. \\
& - \{10.25 - 5 \log \epsilon_r + W/h(2.1 - 1.42 \log \epsilon_r) - h/\lambda_0 \times 10^2\} \\
& \cdot \{(2.07 \log \epsilon_r - 0.79)[10.25 - 5 \log \epsilon_r + W/h(2.1 - 1.42 \log \epsilon_r) \\
& - h/\lambda_0 \times 10^2] + 2(2.1 - 1.42 \log \epsilon_r)[0.15 + 0.23 \log \epsilon_r \\
& \left. + W/h(2.07 \log \epsilon_r - 0.79)]\} \right]
\end{aligned} \quad (B.7)$$

$$S_h^{Z_{0s}} = -S_W^{Z_{0s}} + \frac{h}{Z_{0s}} \frac{1}{\lambda_0} \frac{\partial Z_{0s}}{\partial(h/\lambda_0)} \quad (B.8)$$

where

$$\begin{aligned}
\frac{\partial Z_{0s}}{\partial(h/\lambda_0)} = & 200[10.25 - 5 \log \epsilon_r + W/h(2.1 - 1.42 \log \epsilon_r) - h/\lambda_0 \times 10^2] \\
& \cdot [0.15 + 0.23 \log \epsilon_r + W/h(2.07 \log \epsilon_r - 0.79)]
\end{aligned}$$

$$S_{\epsilon_r}^{Z_{0s}} = \frac{0.4343 \epsilon_r}{Z_{0s}} \{ 53.55 + 64.85 W/h + (0.23 + 2.07 W/h) \\ \cdot [10.25 - 5 \log \epsilon_r + W/h(2.1 - 1.42 \log \epsilon_r) - h/\lambda_0 \times 10^2]^2 \\ - 2(5 + 1.42 W/h)[0.15 + 0.23 \log \epsilon_r + W/h(2.07 \log \epsilon_r - 0.79)] \\ \cdot [10.25 - 5 \log \epsilon_r + W/h(2.1 - 1.42 \log \epsilon_r) - h/\lambda_0 \times 10^2] \} \quad (B.9)$$

$$S_W^{\epsilon_r} = -\frac{2W/h}{\epsilon_{re}} [0.111 - 0.0022 \epsilon_r - 0.094 \log(h/\lambda_0 \times 10^2)] \quad (B.10)$$

$$S_h^{\epsilon_r} = -S_W^{\epsilon_r} + \frac{0.8686}{\epsilon_{re}} (0.121 + 0.094 W/h - 0.0032 \epsilon_r) \quad (B.11)$$

$$S_h^{\epsilon_{re}} = \frac{2}{\epsilon_{re}} [0.21 + 0.0022 \epsilon_r W/h - 0.0032 \epsilon_r \log(h/\lambda_0 \times 10^2)] \quad (B.12)$$

The logarithms are to the base 10 in the above expressions.

CHAPTER 6

Finlines

6.1 INTRODUCTION

Finline is a quasi-planar transmission line structure. It was first proposed by Meier [1, 2] as a new transmission line for circuit applications at millimeter wavelengths. The main characteristics of finline are its large bandwidth, compatibility with planar circuit technology, and absence of radiation. Although waveguides have been available and used for a long time and have relatively low losses, they are not amenable to integrated circuit fabrication. Microstrip, slotline, and coplanar lines have been used extensively in integrated circuits. However, these lines suffer from practical problems of tolerance requirements with the very narrow strip widths required at millimeter wavelengths. Multimoding and radiation are also of concern.

Some of the most commonly used finline structures are shown in Figure 6.1. The basic finline can be considered as a shielded slotline, with the slotline mounted in the E-plane of a rectangular waveguide. Thus, in a given frequency band, the finline dimensions are identical to that of a commensurate waveguide. The structures shown may also be regarded as printed versions of a ridged waveguide. A better appreciation of the unilateral, bilateral, and antipodal finlines may be had from Figure 6.2. In these structures, the fins concentrate the field in the fin-gap region as depicted in Figure 6.3, leading to the capacitive loading of the dominant HE mode of propagation in the slab loaded waveguide. This has the effect of lowering the cutoff frequency of the fundamental mode to a considerable degree and that of the next higher mode to a very small degree, thus leading to a larger bandwidth of operation for the fundamental mode.

Besides the larger bandwidth that is available, any devices that are connected to the fins for integrated circuit fabrication will be subjected to larger power densities, resulting in better matching. However, the field concentration will also result in larger conductor and dielectric losses, due to the presence of the dielectric slab

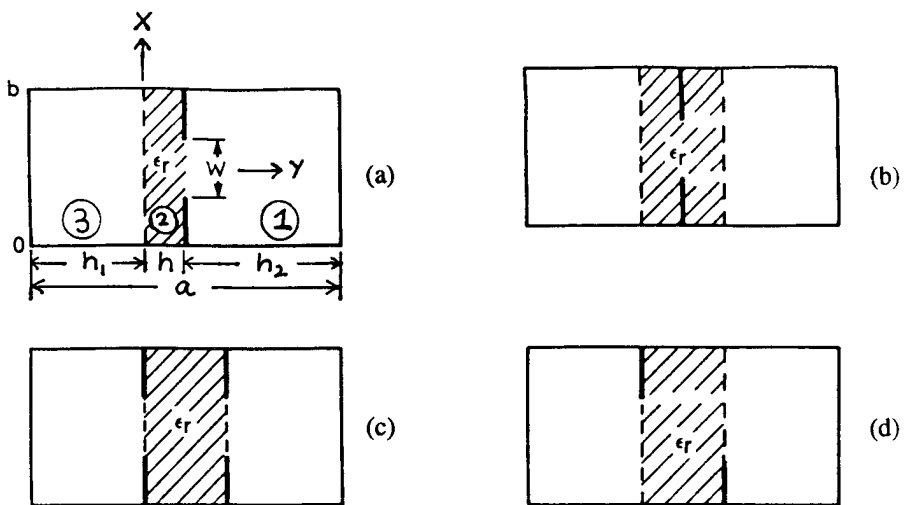


Figure 6.1 Cross section of several finlines: (a) unilateral finline; (b) insulated finline; (c) bilateral finline; and (d) antipodal finline.

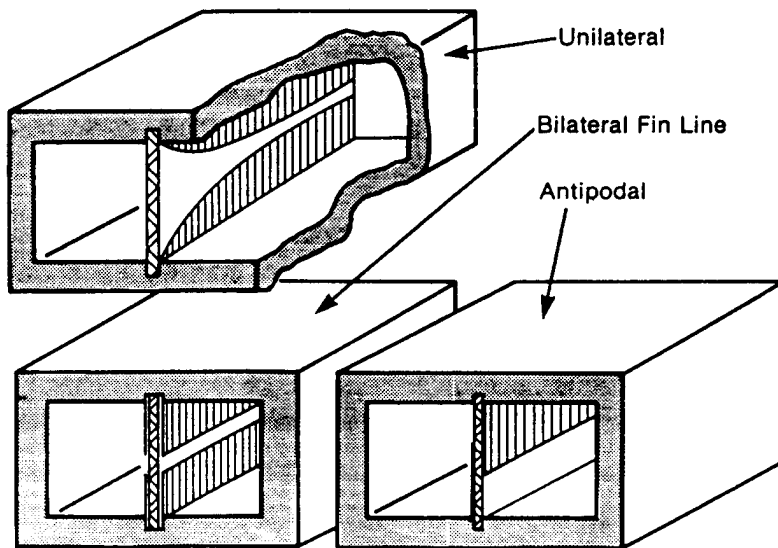


Figure 6.2 Schematic of three commonly used finlines.

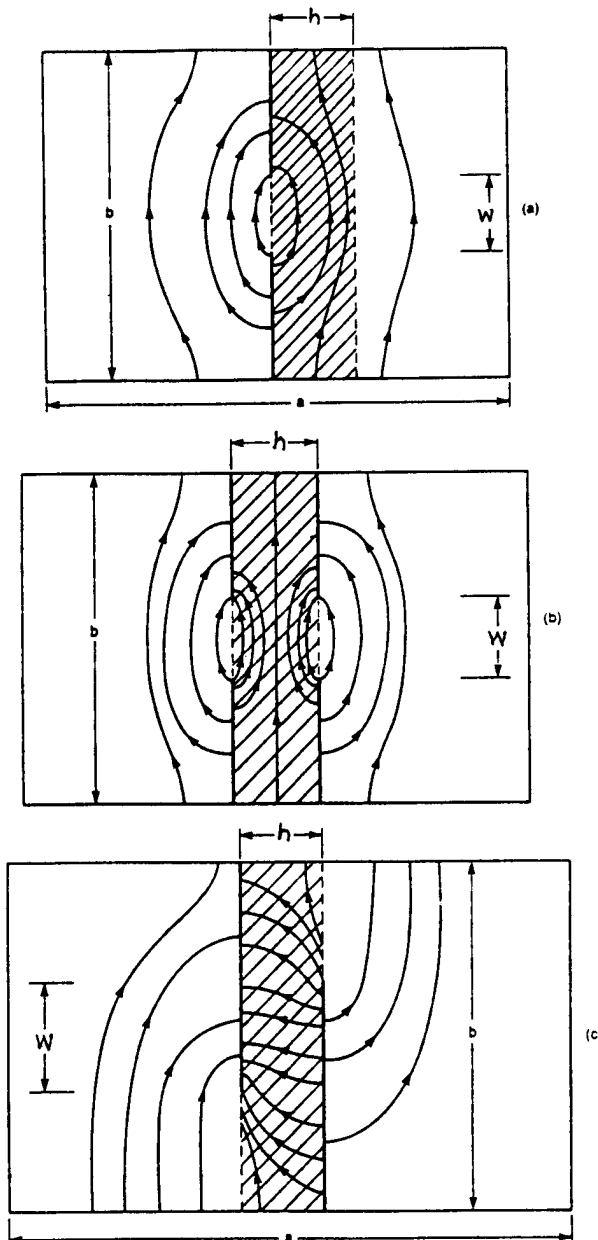


Figure 6.3 Distribution of transverse electric fields in (a) unilateral finline, (b) bilateral finline, and (c) antipodal finline.

and the higher current density near the fin edges. The attenuation in finline is typically on the order of 0.1 dB/wavelength, and therefore finline is unsuitable for long-distance power transmission.

Amongst the configurations shown in Figure 6.1, the unilateral finline is the simplest and best suited for the fabrication of finline components [3]. The metallization on both sides of the substrate in bilateral finline produces a lower transmission loss and provides greater flexibility in biasing of active devices. Bilateral finlines can be designed for a characteristic impedance as low as $100\ \Omega$. Antipodal finlines, on the other hand, offer impedance levels of the order of $10\ \Omega$ and are suitable for transitions between a microstrip line and a waveguide. The typical impedance transformation ratio is 20:1.

The growing applications of microwave integrated circuits (MICs) and the advantages offered by finlines in terms of concentration of fields on small diode dimensions, possibility of multiband device fabrication with high level of integration, suitability for small size, and low-cost circuits have resulted in the realization of virtually all important circuit components in finline configuration. These include RF receive/transmit front ends. In this chapter, the analysis and synthesis procedures for finlines are discussed. Transitions from finline to waveguide and microstrip are discussed at the end.

6.2 ANALYSIS OF FINLINES

Similar to the cases of planar transmission lines discussed earlier, the presence of sharp metal edges and inhomogeneous dielectric loading complicates the analysis of finline structures for the propagation characteristics. This is because such structures support HE and EH hybrid modes. These modes have dominant H_z and E_z fields, respectively, and at the cutoff reduce to pure TE and TM modes, respectively. Several techniques have been used for the analysis of finlines. These include, the transverse resonance method [4–9], the transmission line matrix method [10], space and spectral domain techniques [11–15], the Ritz-Galerkin method [16], and mode matching [17–19]. In addition, closed-form approximate expressions have been reported for some specific finline structures [20–28]. Details of the various techniques as applied to finlines are available in [7, 29, 30]. Of particular interest among the approximate techniques is the transverse resonance method developed by Cohn for the analysis of slotlines [31]. This method has been used for the analysis of finlines and is known to provide accurate results for narrow slots. It is discussed next. Since the analysis of finline is very much similar to that of slotline, only the important steps are described.

6.2.1 Transverse Resonance Method [7]

The application of the transverse resonance method, as described below, is a direct extension of the approach applied to the slotline (Section 5.2.2). In contrast to the

slotline geometry, the finline geometry can be analyzed as a rectangular waveguide problem without any modification of the basic structure.

To apply Cohn's approach [31] to the finline configurations, two transverse planes along the z -axis are placed to obtain a finline resonator. The planes are located at $z = 0$ and $z = c$ such that $c = \lambda_f/2$, where λ_f is the guide wavelength in finline. These planes do not disturb the field distribution. The finline is now analyzed as a slot or an iris (with dielectric support) placed in a rectangular waveguide. This is shown in Figure 6.4. Now the method of transverse resonance is applied to the resonator structure to determine the guide wavelength. As described in Section 5.2.2, the sum of susceptances at the iris plane is equated to zero. This sum includes the susceptance of the TE_{10} mode looking in the $+y$ - and $-y$ -directions (see Figure 6.1a) and the capacitive iris susceptance due to higher order modes on both sides of the iris. The full set of waveguide modes must be considered to satisfy the boundary conditions. The modes are TE_{1n} with $n \geq 0$ and TM_{1n} with $n \geq 1$. Thus, total susceptance ηB_t is given by

$$\eta B_t = \eta(B^+ + B^-) \quad (6.1)$$

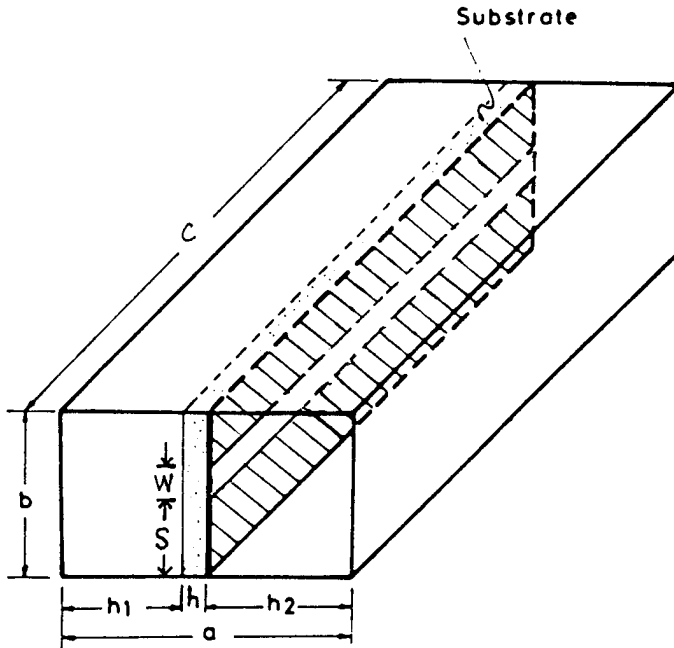


Figure 6.4 Schematic of an iris-loaded waveguide resonator used in the transverse resonance analysis of a unilateral finline.

where ηB^+ is the susceptance looking to the right and ηB^- is the susceptance looking to the left. The expression for the total susceptance for the unilateral finline is given in Appendix 6.A. For other finline configurations one can consult [7].

Roots of the equation $\eta B_i = 0$, with ηB_i given by (A.1) of Appendix 6.A, will give the finline wavelength λ_f . The wavelength λ_f appears in (A.1) through the parameter ξ . Therefore, for a given set of finline parameters a, b, c, W, h , and ϵ_r the value of ξ at which ηB_i becomes zero is computed numerically. The value of λ_0 is then determined by using $\lambda_0 = 2c\xi$ and λ_f from $\lambda_f = \lambda_0/\xi$. The characteristic impedance and the ratio v/v_g for the finline can be determined as for the slotline.

Due to the approximations used in the derivation of (A.1) the transverse resonance method can be used for narrow slots such that $W/b < 0.15$ and $W/h \leq 2$. The method described next does not suffer from this limitation.

6.2.2 Galerkin's Method in the Spectral Domain

An accurate analysis of the finline can be carried out based on Galerkin's method in the Fourier transform domain. The analysis of a finline using this approach is very similar to that carried out for the slotline in Section 5.2.3. The presence of the waveguide housing gives rise to some extra boundary conditions over and above those applicable to the slotline configuration. Some of the boundary conditions on the housing make the spectral variable α discrete in nature. It is denoted by α_n . Using the approach described in Section 5.2.3 on the geometry of the finline shown in Figure 6.1(a), a solution for transforms of scalar potentials in the three regions may be written as [12]

$$\psi_1^e(\alpha_n, y) = A^e(\alpha_n) \sinh[\gamma_1(h + h_2 - y)] \quad (6.2a)$$

$$\psi_2^e(\alpha_n, y) = B^e(\alpha_n) \sinh(\gamma_2 y) + C^e(\alpha_n) \cosh(\gamma_2 y) \quad (6.2b)$$

$$\psi_3^e(\alpha_n, y) = D^e(\alpha_n) \sinh[\gamma_3(h_1 + y)] \quad (6.2c)$$

and

$$\psi_1^h(\alpha_n, y) = A^h(\alpha_n) \cosh[\gamma_1(h + h_2 - y)] \quad (6.3a)$$

$$\psi_2^h(\alpha_n, y) = B^h(\alpha_n) \sinh(\gamma_2 y) + C^h(\alpha_n) \cosh(\gamma_2 y) \quad (6.3b)$$

$$\psi_3^h(\alpha_n, y) = D^h(\alpha_n) \cosh[\gamma_3(h_1 + y)] \quad (6.3c)$$

where

$$\begin{aligned} \gamma_i^2 &= \alpha_n^2 + \beta^2 - k_i^2 & i = 1, 2, 3 \\ k_1^2 &= k_3^2 = k_0^2 = \omega^2 \mu_0 \epsilon_0; \dots, k_2^2 = k_0^2 \epsilon_r \end{aligned} \quad (6.4)$$

and

$$\alpha_n = \begin{cases} n\pi/b & \text{for unsymmetrical metallization along } x \\ 2n\pi/b & \text{for electric wall at } x = b/2 \\ (2n+1)\pi/b & \text{for magnetic wall at } x = b/2 \end{cases}$$

Continuing the solution process in a manner identical to that used for a slotline, one obtains the matrix equation of (5.23) with α replaced by α_n , $n = 0, 1, 2, \dots$.

The choice of basis functions for the expansion of an unknown slot electric field plays an important role in determining the efficiency of the method. A frequently used choice consists of sinusoidal functions modified by an *edge condition* term. The basis functions are given as [13]

$$E_x = \sum_{m=1}^P a_m E_{xm} \quad (6.5)$$

$$E_{xm} = \begin{cases} \frac{\cos\{(m-1)\pi(2x/W+1)\}}{\sqrt{1-(2x/W)^2}} & |x| \leq \frac{W}{2} \\ 0 & \text{elsewhere} \end{cases} \quad (6.6)$$

$$E_z = \sum_{m=1}^Q b_m E_{zm} \quad (6.7)$$

$$E_{zm} = \begin{cases} \frac{\sin\{m\pi(2x/W+1)\}}{\sqrt{1-(2x/W)^2}} & |x| \leq \frac{W}{2} \\ 0 & \text{elsewhere} \end{cases} \quad (6.8)$$

The rest of the procedure is similar to that in the case of the slotline.

In addition to the propagation constants of the propagating modes, the characteristic impedance of the dominant mode is an important quantity for the circuit design. Out of three possible definitions of characteristic impedance for a non-TEM mode [7], the most frequently used definition is based on the slot voltage V and the time-averaged power flow P as in (5.11). In the spectral domain, these quantities are obtained as

$$V = \tilde{E}_x(\alpha_n = 0) \quad (6.9)$$

and

$$P = \frac{1}{2} \operatorname{Re} \left\{ \frac{1}{b} \sum_{n=-\infty}^{\infty} \int_{-h_2}^{h_1+d} \left[\tilde{E}_x(\alpha_n, y) \tilde{H}_y^*(\alpha_n, y) - \tilde{E}_y(\alpha_n, y) \tilde{H}_x^*(\alpha_n, y) \right] dy \right\} \quad (6.10)$$

The integration with respect to y can be carried out analytically in (6.10). Equation (6.10) is evaluated numerically in each of the three regions.

Variations of the normalized guide wavelength λ_f/λ_0 and the characteristic impedance Z_{of} for a unilateral finline with centered slot are plotted in Figure 6.5 as a function of normalized slot width W/a . It is observed that both the guide wavelength and characteristic impedance increase with the slot width W . The effect of dispersion on finline characteristics is shown in Figure 6.6. We observe that λ_f/λ_0 decreases as the frequency increases. However, Z_{of} is almost constant with frequency.

Higher order modes in the finline can also be studied using the basis functions of (6.6) and (6.8). For this, more than one zero of the determinant is sought. The real root with a lower value of β/k_0 corresponds to the higher order mode. To obtain the second root the frequency should be higher than the cutoff frequency of the first higher order mode. The $(\beta/k_0)^2$ values for the dominant and the next higher order modes for a Ka-band unilateral finline are plotted in Figure 6.7. The cutoff frequency for the higher order mode is nearly equal to the cutoff frequency for the higher order HE mode of the slab loaded waveguide. It means that the presence of fins centered in the broadwall of the waveguide do not disturb this mode. Since the cutoff frequency of the dominant mode is lowered considerably compared to the dominant HE mode cutoff frequency, the bandwidth of a finline is increased due to the presence of fins.

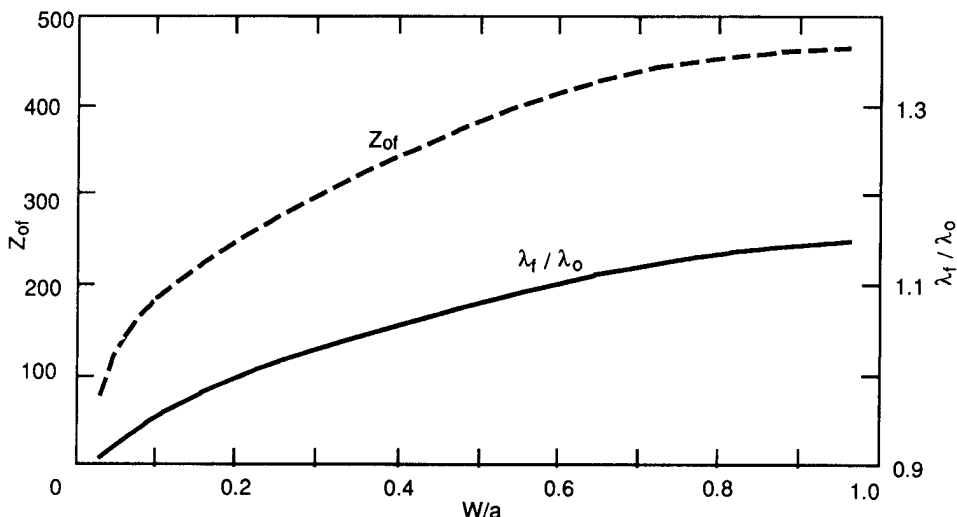


Figure 6.5 Normalized guide wavelength λ_f/λ_0 and characteristic impedance Z_{of} of a unilateral finline with centered fins: $\epsilon_r = 2.22$, $h = 0.127$ mm, $\tan\delta = 2 \times 10^{-4}$, frequency = 40 GHz, waveguide = WR(28) (from [15], © 1982 IEEE. Reprinted with permission.).

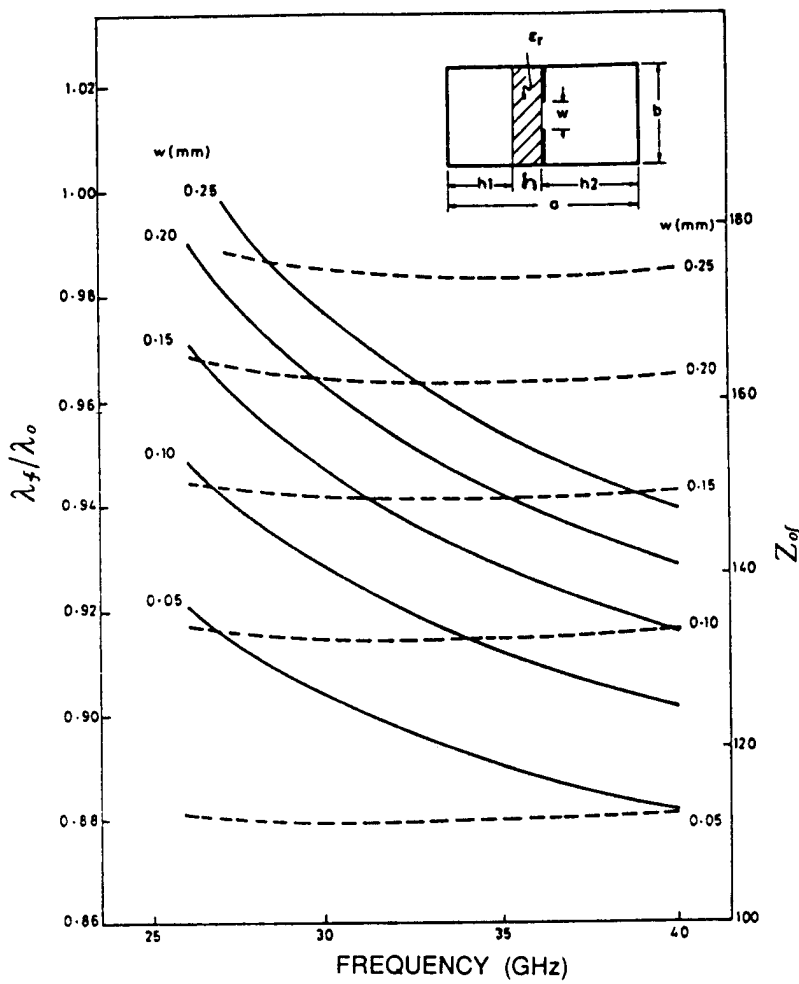


Figure 6.6 Dispersion in guide wavelength and characteristic impedance of a unilateral finline (from [7]): $\epsilon_r = 2.22$, $h = 0.127$ mm, $h_1 = 3.429$ mm, $h_2 = 3.556$ mm, — λ_f/λ_0 , - - - Z_0f , waveguide = WR(28).

6.3 DESIGN CONSIDERATIONS

6.3.1 Closed-Form Solutions [21, 24]

The foregoing section showed that the analysis of finline has to be carried out numerically and can involve a substantial amount of computer time. One can

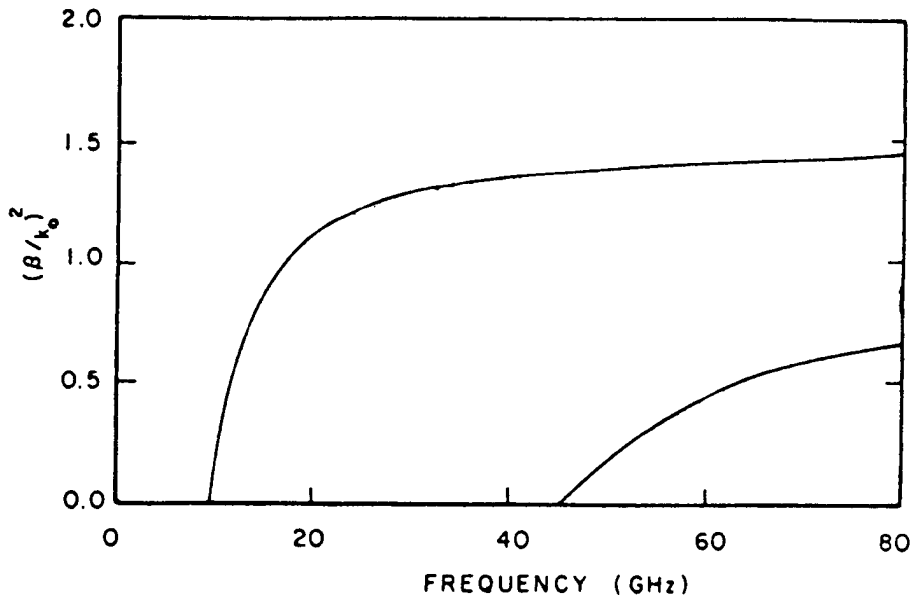


Figure 6.7 Normalized propagation constant $(\beta/k_0)^2$ for the dominant and the next higher order modes in a unilateral finline: $\epsilon_r = 3.0$, $h = 0.125$ mm, $W = 0.15$ mm, waveguide = WR(28) (from [13], © 1980 IEEE. Reprinted with permission.).

conclude from this that there is a need for a design procedure with tractable formulas.

Simple design equations for the characteristics of finlines have been obtained by modeling finline as a ridged waveguide uniformly filled with a dielectric of relative permittivity K_e . Based on this model the guide wavelength in finline may be defined as

$$\lambda_f = \frac{\lambda_0}{\sqrt{\epsilon_{re}(f)}} \quad (6.11)$$

where $\epsilon_{re}(f)$ is the frequency-dependent effective dielectric constant and is defined as [32]

$$\epsilon_{re}(f) = K_e - \left(\frac{\lambda_0}{\lambda_{ca}} \right)^2 \quad (6.12)$$

Here, K_e is also called the equivalent dielectric constant at frequency f corresponding to free space wavelength λ_0 and λ_{ca} is the cutoff wavelength of (finned waveguide)

finline with dielectric substrate replaced by air dielectric. For low $\epsilon_r (\leq 2.50)$ and thin substrates ($h/a \ll 1$), which is usually the case, K_e can be regarded as constant independent of frequency and can be equated to its value K_c at cutoff frequency [33]. The definition of K_c is derived from (6.12). At the cutoff $\lambda_0 = \lambda_{cf}$, and the effective dielectric constant is zero. Therefore,

$$K_c = \left(\frac{\lambda_{cf}}{\lambda_{ca}} \right)^2 \quad (6.13)$$

Here, λ_{cf} is the cutoff wavelength of the finline.

Next, we present the closed-form expression for the equivalent dielectric constant K_e due to Sharma and Hoefer [21]. These expressions are reported to be accurate in the frequency range $0.35 \leq b/\lambda_0 \leq 0.7$. The following abbreviations are used in this section

$$W_b = W/b \quad h_a = h/a \quad a_h = a/h$$

The expression for K_e is assumed to be of the form

$$K_e = K_c \cdot F(W/b, h/a, \lambda_0, \epsilon_r) \quad (6.14)$$

The factor F is obtained by curve fitting the results obtained from the rigorous methods. Expressions for λ_{cf} , λ_{ca} , and F are given below for unilateral and bilateral finlines with centered fins. For unilateral finlines $b/a = 1/2$. However, for bilateral finlines the dimensions of the waveguide considered are $2a \times b$ with $b/2a = 1/2$ and the dielectric thickness $2h$.

Cutoff Frequency for Finned Waveguide, λ_{ca}

For both unilateral and bilateral finlines

$$b/\lambda_{ca} = 0.245 (W_b)^{0.173} \quad \text{for } 1/16 \leq W_b \leq 1/4 \quad (6.15)$$

The accuracy of (6.15) is reported to be within $\pm 1\%$.

Cutoff Frequency for Finline, λ_{cf}

The general expression for λ_{cf} for both the unilateral and bilateral finlines is given by

$$b/\lambda_{cf} = A(W_b)^p(h_a)^q \quad (6.16)$$

The constants A , p , and q are available for $\epsilon_r = 2.22, 3.0$. These are valid for

$$1/16 \leq W_b \leq 1/4 \quad 1/32 \leq h_a \leq 1/4$$

and are as follows.

For the unilateral finline with $\epsilon_r = 2.22$

$$\begin{aligned} A &= 0.1748 \\ p &= \begin{cases} 0.16(h_a)^{-0.07} & \text{for } 1/32 \leq h_a \leq 1/20 \\ 0.16(h_a)^{-0.07} - 0.001 \ell_n(h_a - 1/32) & \text{for } 1/20 \leq h_a \leq 1/4 \end{cases} \\ q &= -0.0836 \end{aligned} \quad (6.17)$$

For the unilateral finline with $\epsilon_r = 3.0$

$$\begin{aligned} A &= 0.1495 \\ p &= \begin{cases} 0.1732(h_a)^{-0.073} & \text{for } 1/32 \leq h_a \leq 1/10 \\ 0.1453(h_a)^{-0.1463} & \text{for } 1/10 \leq h_a \leq 1/4 \end{cases} \\ q &= -0.1223 \end{aligned} \quad (6.18)$$

For the bilateral finline with $\epsilon_r = 2.22$

$$\begin{aligned} A &= 0.15 \\ p &= \begin{cases} 0.225(h_a)^{-0.042} & \text{for } 1/32 \leq h_a \leq 1/10 \\ 0.149(h_a)^{-0.23} & \text{for } 1/10 \leq h_a \leq 1/4 \end{cases} \\ q &= -0.14 \end{aligned} \quad (6.19)$$

For the bilateral finline with $\epsilon_r = 3.0$

$$\begin{aligned} A &= 0.1255 \\ p &= \begin{cases} 0.21772(h_a)^{-0.07155} & \text{for } 1/32 \leq h_a \leq 1/15 \\ 0.2907 - 0.3568h_a & \text{for } 1/15 \leq h_a \leq 1/4 \end{cases} \\ q &= -0.1865 \end{aligned} \quad (6.20)$$

The closed-form expressions for λ_{cf} are reported to be accurate within ± 1 percent.

Correction Factor, F

For the unilateral finline with $\epsilon_r = 2.22$

$$\begin{aligned} F &= \begin{cases} [1.0 + 0.43h_a](W_b)^{p_1} & \text{for } 1/32 \leq h_a \leq 1/8 \\ [1.02 + 0.264h_a](W_b)^{p_1} & \text{for } 1/8 \leq h_a \leq 1/4 \end{cases} \\ p_1 &= 0.096h_a - 0.007 \end{aligned} \quad (6.21)$$

For the unilateral finline with $\epsilon_r = 3.0$

$$\begin{aligned} F &= F' + 0.25308(b/\lambda_0) - 0.135 \\ F' &= \begin{cases} 1.368(h_a)^{0.086}(W_b)^{p_1} & \text{for } 1/32 \leq h_a \leq 1/8 \\ [1.122 + 0.176h_a](W_b)^{p_2} & \text{for } 1/8 \leq h_a \leq 1/4 \end{cases} \\ p_1 &= 0.375h_a - 0.0233 \\ p_2 &= 0.032 - 3.0(h_a - 3/16)^2 \end{aligned} \quad (6.22)$$

For the bilateral finline with $\epsilon_r = 2.22$

$$\begin{aligned} F &= \begin{cases} 0.78(h_a)^{-0.098}(W_b)^{0.109} & \text{for } 1/32 \leq h_a \leq 1/8 \\ [1.04 - 0.2h_a](W_b)^{p_1} & \text{for } 1/8 \leq h_a \leq 1/4 \end{cases} \\ p_1 &= 0.152 - 0.256h_a \end{aligned} \quad (6.23)$$

For the bilateral finline with $\epsilon_r = 3.0$

$$\begin{aligned} F &= F' + 0.08436(b/\lambda_0) - 0.045 \\ F' &= \begin{cases} 0.975(h_a)^{-0.026}(W_b)^{p_1} & \text{for } 1/32 \leq h_a \leq 1/8 \\ [1.0769 - 0.2424h_a](W_b)^{p_2} & \text{for } 1/8 \leq h_a \leq 1/4 \end{cases} \\ p_1 &= 0.089 + 0.288h_a \\ p_2 &= 0.16 - 0.28h_a \end{aligned} \quad (6.24)$$

Stationary Expressions [24]

Accurate closed-form expressions for the cutoff wavelength of a finline have been developed by Pramanick and Bhartia [24] by using a stationary formula in which unknown constants are obtained by curve fitting the numerical results. The expressions obtained are valid over the ranges

$$1 \leq \epsilon_r \leq 3.80 \quad 0 < b/a \leq 1 \quad 1/32 \leq W_b \leq 1 \quad 1/64 \leq h_a \leq 1/8 \quad (6.25)$$

Derivation of the Equations

Consider the finline structures shown in Figure 6.1. Each is modeled as a combination of a finned waveguide and a waveguide loaded with a dielectric slab in the **E**-plane. The cutoff wavelength λ_{cf} is then obtained as

$$\frac{b}{\lambda_{cf}} = \frac{2a}{b} \frac{b}{\lambda_{ca}} \frac{b}{\lambda_{cd}} \quad (6.26)$$

Here, λ_{cd} is the cutoff wavelength of a dielectric loaded waveguide and can be expressed as

$$b/\lambda_{cd} = (b/2a)[1 + F_1(h_a)(\epsilon_r - 1)]^{-1/2} \quad (6.27)$$

where $F_1(h_a)$ is a function of h/a . Now, the presence of the fins together with the dielectric slab makes the electric field concentrate in the vicinity of the fins. Therefore, the field distribution in the cross section of the finline no longer remains a function of h/a only but also becomes a function of W/b . Hence (6.27) should be modified to the form

$$b/\lambda_{cd} = (b/2a)[1 + F_1(h_a, W_b)(\epsilon_r - 1)]^{-1/2} \quad (6.28)$$

Expression (6.28) is stationary in nature. It means that a small change in h/a , W/b , ϵ_r , or frequency will have a second-order effect on b/λ_{cd} .

For finned waveguides, the general expression for the cutoff wavelength λ_{ca} can be written as [20]

$$b/\lambda_{ca} = (b/2a)[1 + NF_2(h_a, W_b)]^{-1/2} \quad (6.29)$$

where

$$N = (4/\pi)(b/a)(1 + 0.2\sqrt{b/a}) \quad (6.30)$$

Once the functions $F_1(\bullet)$ and $F_2(\bullet)$ are known, the cutoff wavelength λ_{cf} of the finline can be obtained using (6.28) and (6.29) in (6.26). One obtains

$$\frac{b}{\lambda_{cf}} = \frac{b}{2a}\{[1 + NF_2(h_a, W_b)][1 + F_1(h_a, W_b)(\epsilon_r - 1)]\}^{-1/2} \quad (6.31)$$

The functions $F_1(\bullet)$ and $F_2(\bullet)$ can be accurately determined by fitting (6.29) and (6.31) to the accurately computed values of λ_{ca} and λ_{cf} .

The function $F_1(h_a, W_b)$ is obtained as [24]

$$F_1(h_a, W_b) = h_a[A_1(h_a) \cdot \ell_n \{\text{cosec}(\pi W_b/2)\} + B_1(h_a)] \quad (6.32)$$

where

$$A_1(h_a) = 0.4020974(\ell_n a_h)^2 - 0.7684487 \cdot \ell_n a_h + 0.3932021$$

and

$$B_1(h_a) = 2.42 \cdot \sin(0.556 \cdot \ell_n a_h)$$

The function $F_2(h_a, W_b)$ may be written, in general, as [26]

$$F_2(h_a, W_b) = [1 + h_a \cdot p(h_a)] \cdot \ell_n \{\text{cosec}(\pi W_b/2)\} + h_a \cdot q(h_a) \quad (6.33)$$

For better accuracy, different expressions for $p(h/a)$ and $q(h/a)$ are used over different ranges of W/b . The following expressions are valid for $1/64 \leq h/a \leq 1/8$.

For $3/4 \leq W_b \leq 1$

$$p(h_a) = -3.185 \cdot (\ell_n a_h)^3 + 28.86(\ell_n a_h)^2 - 65.51 \ell_n a_h + 53.40$$

$$q(h_a) = 0$$

For $1/6 \leq W_b \leq 3/4$

$$p(h_a) = 0.3(\ell_n a_h)^3 - 3.155(\ell_n a_h)^2 + 13.46 \ell_n a_h - 13.34$$

$$q(h_a) = -0.33(\ell_n a_h)^3 + 2.95(\ell_n a_h)^2 - 7.8 \ell_n a_h + 7.1$$

For $1/32 \leq W_b \leq 1/6$

$$p(h_a) = -1.156(\ell_n a_h)^3 + 11.4(\ell_n a_h)^2 - 23.98 \ell_n a_h + 17.63$$

$$q(h_a) = 1.834(\ell_n a_h)^3 - 18.18(\ell_n a_h)^2 + 44.86 \ell_n a_h - 33.56$$

Expressions (6.29) and (6.33) yield a value of λ_{ca} that is accurate to within ± 1 percent for $\epsilon_r = 3.75$ [20, 24].

Equivalent Dielectric Constant at Cutoff, K_c

The expression for equivalent dielectric constant at cutoff can be obtained by using (6.26) in (6.29). One obtains

$$\begin{aligned} K_c &= (\lambda_{cd}/2a)^2 \\ &= 1 + F_1(h_a, W_b)(\epsilon_r - 1) \end{aligned} \quad (6.34)$$

More accurate expressions for K_c for unilateral, bilateral, and insulated finlines are available in [24, 26, 27].

Dielectric Filling Factor, q_f

The dielectric filling factor at cutoff q_f is defined as

$$q_f = (K_c - 1)/(\epsilon_r - 1) \quad (6.35)$$

From (6.34) and (6.35) we obtain

$$q_f = F_1(h_a, W_b) \quad (6.36)$$

Once the equivalent dielectric constant K_e and the cutoff wavelength λ_{ca} are known one can make a first-order approximation of the effective dielectric constant $\epsilon_{re}(f)$ by using K_e in place of K_c in (6.12). This approximation is valid for low values of ϵ_r (≤ 2.50) and thin substrates [33].

Although such an approximation for the phase velocity is accurate to within ± 2 percent for many practical sets of dimensions, it neglects the frequency dependence of K_e [34]. The equivalent dielectric constant K_e varies linearly with frequency for unilateral and bilateral finlines. The variation is faster for higher ϵ_r and larger h/a values. Sharma and Hoefer [21] have included the effect of dispersion in a purely empirical manner for $\epsilon_r = 3.0$. An accurate closed-form expression for $K_e(f)$, which is applicable to all types of finlines, is obtained by Pramanick and Bhartia from the LSE model of finline [35]. This model is described next.

6.3.2 LSE-Mode Dispersion Model [37]

The frequency independence of the equivalent dielectric constant K_e assumed by Saad and Schunemann [33] basically establishes an approximate rectangular waveguide equivalence for a finline. In this approximation the rigorous HE and EH hybrid modes of the finline have been approximated by their dominating TE and TM counterparts, respectively. As mentioned earlier such an approximation is valid only for low ϵ_r and thin substrates. The model makes no provision for the hybrid modes and K_e remains frequency independent. In the model developed by Pramanick and Bhartia [35], the finlines (Figure 6.1) are replaced by an LSE model of the rectangular waveguide, loaded with a dielectric slab at the center of the E-plane as shown in Figure 6.8. Since such a structure can support the hybrid modes,

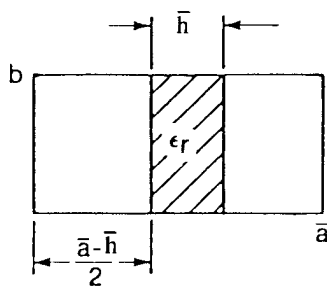


Figure 6.8 LSE-mode waveguide model of a finline (from [24], © 1985 IEEE. Reprinted with permission.).

it is expected to provide a better approximation to the finline than that obtained from a uniform rectangular waveguide approximation.

For the dominant HE mode the fields are concentrated around the edges of the fins and the dielectric slab supporting them. Near the fins, the magnetic field is predominantly normal to and the electric field is predominantly tangential to the air dielectric interface. This field distribution is characteristic of the LSE mode [36]. The finline structures of Figure 6.1 are intractable to direct analysis on this basis, but boundaries can be distorted to result in the model shown in Figure 6.8. The model consists of a rectangular waveguide of height b and width \bar{a} , centrally loaded with a dielectric slab of thickness h and relative dielectric constant ϵ_r . The analysis proceeds by forcing the model to have the same cutoff frequencies as the finline with and without the dielectric. This gives a transcendental equation, the solution of which provides the value of \bar{h}/\bar{a} . The value of \bar{h}/\bar{a} can also be obtained from the variational expression for K_c . The latter approach is simpler, and the following expression for \bar{h}/\bar{a} is obtained [29]:

$$\bar{y} \equiv \bar{h}/\bar{a} = \left(\frac{2q_f}{\pi^2} - S_1^3 \right)^{1/3} + S_1 + \frac{q_f}{3} \quad (6.37)$$

where

$$S_1 = [\sqrt{0.0666 + 0.0466q_f^2 + 0.015q_f^4 - 0.00137q_f^6} + (q_f/\pi^2)]^{1/3}$$

and q_f is given by (6.36).

Next, the calculated value of \bar{y} is used in the characteristic equation for the fundamental LSE mode in the dielectric loaded waveguide of Figure 6.8. The solution of the characteristic equation yields the propagation constant for the finline or the equivalent waveguide model. To obtain the closed-form expression for the propagation constant the characteristic equation is simplified to yield the following expression for the dispersive equivalent dielectric constant:

$$K_e(f) = K_c + \frac{K_e(1) - K_c}{b/\lambda_1 - b/\lambda_{cf}} \left(\frac{b}{\lambda_0} - \frac{b}{\lambda_{cf}} \right) \quad (6.38)$$

with

$$K_e(1) = 1 + \pi^2 \bar{y} (3 - 2\bar{y}) (\epsilon_r - 1)/12 \quad (6.39)$$

and

$$\lambda_1/\lambda_{ca} = \sqrt{K_e(1) - 1}$$

Once $K_e(f)$ is known from (6.38), the propagation constant β can be written as

$$\beta/k_0 = [K_e(f) - (\lambda_0/\lambda_{ca})]^{1/2} \equiv \sqrt{\epsilon_{re}(f)} \quad (6.40)$$

The dispersion model presented above is compared with the numerical results of Hofmann [11] and Shih [37]. The agreement is found to be excellent for unilateral and bilateral finlines. The above procedure has also been found to be applicable to insulated finlines.

Dispersion in Characteristic Impedance

Pramanick and Bhartia [24] have developed the following expression for the characteristic impedance Z_{0f} of a unilateral finline by curve fitting the results of the spectral domain technique, computed on the basis of the power-voltage definition

$$Z_{0f} = \frac{b}{a} \frac{240 \pi^2 (px + q)}{(0.385x + 1.762)^2 \sqrt{\epsilon_{re}(f)}} \quad (6.41)$$

where

$$x = \ell_n \{\text{cosec}(\pi W_b/2)\} \quad (6.42)$$

$$\begin{aligned} p &= 0.0098 + 0.17(b/\lambda_0) \\ q &= 0.873 + 0.138(b/\lambda_0) \end{aligned} \Bigg\} \text{for } W/b \leq 0.3$$

and for $W/b > 0.3$

$$p = -0.763(b/\lambda_0)^2 + 0.58(b/\lambda_0) + 0.0775(\ell_n a_h)^2 - 0.668(\ell_n a_h) + 1.262$$

$$q = 0.914 + 0.372(b/\lambda_0)$$

Equation (6.41) is accurate to within ± 2 percent for $h/a \leq 0.05$ and within ± 3 percent for $h/a > 0.05$.

6.3.3 Synthesis Equations

To fabricate the appropriate finline structure one needs to determine the fin-gap W , given the dimensions of the housing, substrate parameters h and ϵ_r , and the frequency for a specified value of the characteristic impedance Z_{0f} . This can be done by solving (6.41) for W/b . However, (6.41) is cumbersome and a simpler synthesis equation can be derived for unilateral finline by approximating $\epsilon_{re}(f)$ in (6.41).

First of all K_c in the definition of $\epsilon_{re}(f)$, (6.12), is replaced by K_c of (6.34). The expression for $\epsilon_{re}(f)$ is then further simplified to yield

$$\sqrt{\epsilon_{re}(f)} = \frac{\lambda_0}{\lambda_f} = \frac{Ax^2 + Bx + C}{Dx + E} \quad (6.43)$$

Combining (6.41) and (6.43) gives

$$Z_{0f} = \frac{b}{a} \frac{240\pi^2(px+q)}{(0.385x+1.7621)^2} \frac{Dx+E}{Ax^2+Bx+C} \quad (6.44)$$

Equation (6.44) can be expressed as a quartic equation of the form

$$x^4 + c_1x^3 + c_2x^2 + c_3x + c_4 = 0$$

where p and q have been defined before and

$$c_1 = 9.156 + B/A$$

$$c_2 = 20.95 + C/A + 9.156B/A - 6.748(pD)/(A\bar{Z})$$

$$c_3 = 9.156C/A + 20.95B/A - 6.748(pE + qD)/(A\bar{Z})$$

$$c_4 = 20.95C/A - 6.748qE/(A\bar{Z})$$

with

$$A = 4h_a A_1(h_a)(\epsilon_r - 1)D/E$$

$$B = E(D/8 + A/D)$$

$$C = E^2/8 - (\lambda_0/a)^2$$

$$D = (4/\pi)(b/a)(1 + 0.2\sqrt{b/a})E$$

$$E = 8[1 + h_a B_1(h_a)(\epsilon_r - 1)]^{1/2}$$

and

$$\bar{Z} = \frac{Z_{0f}}{240\pi^2} \frac{a}{b}$$

Equation (6.44) can be solved easily using a suitable numerical analysis algorithm to determine x and hence W/b , since

$$\frac{W}{b} = \frac{2}{\pi} \sin^{-1}[e^{-x}] \quad (6.45)$$

It is found that the synthesized value of Z_0 is within 3 percent and the guide wavelength is within 2 percent of the design values [24] for

$$b/a \leq 1 \quad h/a \leq 0.05 \quad 1 \leq \epsilon_r \leq 3.80$$

$$0.1 \leq b/\lambda_0 \leq 0.6 \quad 1/32 \leq W/b \leq 1$$

The synthesis technique may be used to obtain an initial design, after which the more accurate analysis equations may be used to improve the design, if required.

6.3.4 Conductor Loss in Finlines

Conductor loss in finlines is evaluated by using the definition (5.51). The power transmitted along the guide is given by (6.10). The expected singularity of J_z along the edges of the slot may give rise to an unbounded value of P_c , the power dissipated in the conductors. This happens if the basis functions for J_z are nonsingular in nature. Syahkal and Davies [15] have tackled this problem by using Legendre polynomials for the unbounded field E_x . Although required to approximate the unbounded nature of E_x , the individual Legendre polynomials are bounded and can be used to model the singularity of E_x efficiently. It was found that $P = Q = 4$ is sufficient to achieve the desired accuracy in conductor loss [15]. Colley and Rozzi have employed Swinger functions for modeling the slot electric field [16]. Figure 6.9 shows the conductor loss in decibels/wavelength for various fin gaps and copper metal. It is observed that a smaller fin-gap increasingly concentrates transverse fields in the slot region with increased fin currents and losses. But to support the increased fin currents, the currents in the waveguide housing must also increase. The housing material therefore has an appreciable influence on the overall conductor loss [16]. Dielectric loss is relatively small, and its evaluation is simple.

6.4 TRANSITIONS

Most practical finline circuits include one or several types of transitions, either between various types of finlines or between finlines and other types of transmission lines. Of particular importance is the transition between a finline and a commensurate waveguide because of the need to interface finline circuits with conventional components and systems. One way of realizing such transitions is with the use of tapered finlines. Finline tapers are often a part of standard waveguide-to-microstrip transition [35].

6.4.1 Finline-to-Waveguide Taper Transitions

Broadband transition between a finline and a rectangular waveguide generally employs a tapered finline in which the slot width of the finline is gradually increased

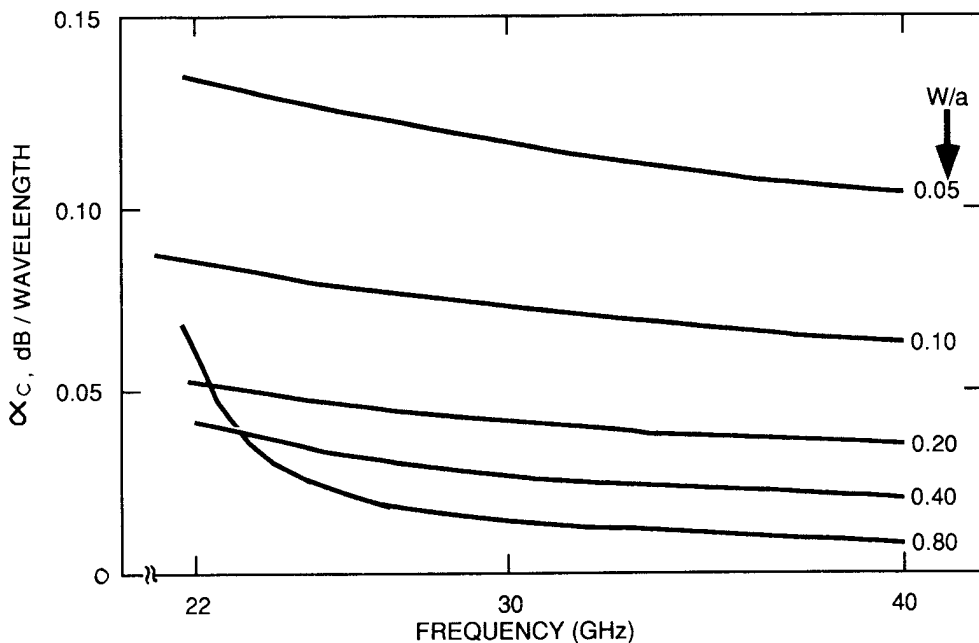


Figure 6.9 Copper loss for a unilateral finline in WR(28) waveguide housing (from [16], © 1988 IEEE. Reprinted with permission.).

to the full height of the waveguide. At the waveguide end of the taper transition the characteristic impedance is different from the waveguide impedance Z_0 due to dielectric loading by the substrate. This discontinuity effect is minimized by introducing one or two quarter-wave transformers in the form of stepped protrusions or notches cut in the substrate. A schematic of a typical transition is shown in Figure 6.10(a). Of the various approaches available in the literature for finline taper analysis and design [9, 38–43], a simple design approach is described below.

Designing a finline taper means choosing an impedance variation along the length so that the return loss is above a tolerable limit over a prescribed bandwidth, while keeping the physical length of the taper as small as possible. The requirements of small length and large return loss are contradictory, and a compromise is generally found. The small length ensures a low insertion loss. Further, the selected impedance variation should result in a smooth slot width variation necessary for ease of fabrication.

Analysis for Taper Design

The analysis of tapers in TEM lines is well documented [44]. Consider an impedance profile of the taper as shown in Figure 6.10(b). If $\rho(z)$ is the reflection coefficient

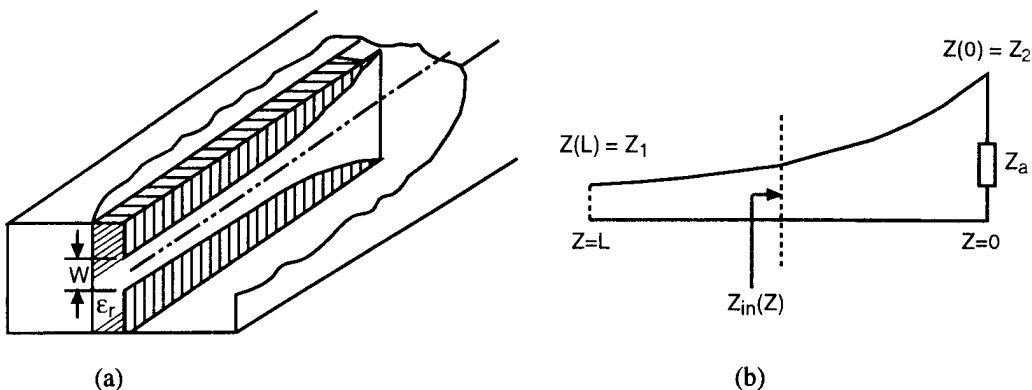


Figure 6.10 (a) Schematic of a waveguide-to-fineline transition and (b) representation of a tapered transmission line with a load.

at a distance z from the load end, then the input reflection coefficient for a taper in TEM line is obtained as

$$\Gamma = - \int_0^L \rho(z) e^{-2j\beta z} dz \quad (6.46)$$

where

$$\rho(z) = - \frac{1}{2} \frac{d}{dz} [\ell_n Z(z)] \quad (6.47)$$

where $Z(z)$ is the characteristic impedance or wave impedance of the line at a distance z , and β is the propagation constant. In the case of finlines, which are non-TEM in nature, β also becomes a function of distance z . Therefore, (6.46) gets modified to

$$\Gamma = - \int_0^L \rho(z) \exp[-2j \int_0^z \beta(\zeta) d\zeta] dz \quad (6.48)$$

Another approach for deriving the reflection coefficient of a taper in a non-TEM line is discussed next. This approach incorporates the effect of the load-reflection coefficient on the overall reflection coefficient of the taper.

Let us refer again to Figure 6.10(b). If Z_{in} is the input impedance at a distance z from the load end and $Z_{in} + dZ_{in}$ is the corresponding value at $z + dz$, then the following equation results from the transmission line transformation

$$Z_{in} + dZ_{in} = Z(z) \frac{Z_{in} + jZ(z) \tan\{d[\beta(z)z]\}}{Z(z) + jZ_{in} \tan\{d[\beta(z)z]\}} \quad (6.49)$$

It has been assumed in writing (6.49) that the impedance $Z(z)$ and the propagation constant $\beta(z)$ are constant over the incremental length dz . For a small value of $d[\beta(z)z]$, the value of $\tan \{d[\beta(z)z]\}$ is approximately equal to $\beta(z)dz$. Therefore, (6.49) reduces to the following Riccati equation, after neglecting $\beta Z_{in} dz$ compared to $Z(z)$,

$$\frac{dZ_{in}}{dz} = j\beta(z)Z(z) - j\frac{\beta(z)}{Z(z)}Z_{in}^2 \quad (6.50)$$

The reflection coefficient $\Gamma(z)$ and Z_{in} at a given point z on the line are related through the equation

$$Z_{in} = \frac{1 + \Gamma(z)}{1 - \Gamma(z)} Z(z) \quad (6.51)$$

Combining (6.50) and (6.51) gives

$$\frac{d\Gamma}{dz} = \frac{1}{2Z(z)} \left\{ (\Gamma^2(z) - 1) \frac{dZ(z)}{dz} - j4\Gamma(z)Z(z)\beta(z) \right\} \quad (6.52)$$

Integrating (6.52) gives the overall reflection coefficient of the taper plus load. Evaluating either (6.52) or (6.48) requires knowledge of the impedance function $Z(z)$ and $\beta(z)$. The impedance functions for some of the taper profiles are given as follows (refer to Figure 6.10(b)).

Exponential impedance profile:

$$Z(z) = Z_2 \cdot \exp \left[\frac{z}{L} \ell_n \left(\frac{Z_1}{Z_2} \right) \right]$$

Parabolic impedance profile:

$$Z(z) = \left[\pm \sqrt{Z_2} + \frac{z}{L} (\pm \sqrt{Z_1} \mp \sqrt{Z_2}) \right]^2$$

Cosine impedance profile:

$$Z(z) = Z_2 \cdot \cos \left[\frac{z}{L} \cos^{-1} \frac{Z_1}{Z_2} \right]$$

Cosine-squared impedance profile:

$$Z(z) = Z_2 \cdot \cos^2 \left[\frac{z}{L} \cos^{-1} \sqrt{\frac{Z_1}{Z_2}} \right]$$

In the actual taper design process first the length of the taper L and the impedance profile are selected. Then $Z(z)$ is calculated for various values of z on the taper. For a given $Z(z)$, which may be taken as the local characteristic impedance of the finline, the value of slot width W is obtained for the selected parameters a , b , h , and ϵ_r of the finline. For this purpose synthesis equations are used. Next, the value of $\beta(z)$ is obtained for the calculated value of $W(z)$, for which analysis equations are used.

Using the same procedure, reflection coefficient curves and design data curves can be generated. These are shown in Figure 6.11 for some of the impedance profiles [45]. These curves show that, although the exponential taper requires the narrowest fin-gap profile of the three tapers, it gives the best performance. Further, minima in the reflection coefficient occur at $L \equiv n\lambda_0/2$.

Verver and Hoefer [46] have presented a method for matching the finline with $W/b = 1$ to an air-filled rectangular waveguide using a quarter-wave transformer in the form of a notch or a protrusion. This is shown in Figure 6.12. The transformer improves the return loss of the taper by about 5 dB.

6.4.2 Finline-to-Microstrip Taper Transitions

This transition is useful in the mixed-media systems involving finline, waveguide, and microstrip. It also constitutes an integral part of waveguide-to-microstrip transition. Finline- or waveguide-to-microstrip transition is commonly realized via an intermediate section of antipodal finline [47–49]. Two different types of transitions have been proposed for converting the electric field lines of an antipodal finline to a microstrip line. These are shown in Figure 6.13 and 6.14. In Figure 6.13, the fins of the antipodal finline, on opposite sides of the substrate, are tapered to form a nearly circular arc over the transition length ℓ . Beyond this arc, one of the fins forms the ground plane of the microstrip and the other forms the top strip. The portion of the waveguide below the microstrip ground cannot propagate the signal because its cutoff frequency is well above the waveguide band. Therefore, it can be terminated in a short, slightly beyond the transition without affecting the performance of the transition. The radius R of the arc is critical to the performance. Its optimal value is 0.0375 in for a V-band transition designed at 53 GHz [47]. The metallization in the shaded area S serves to prevent transverse resonances in the operating band [48]. Measurements on a pair of transitions yielded an insertion loss of less than 0.8 dB and a VSWR of less than 1.35 over the 8.5-GHz to 12.5-GHz band.

The transition of Figure 6.14 was reported by van Heuven [49]. In this transition, the fins of antipodal finline are tapered symmetrically to form a broadside-coupled suspended stripline. Over this length the electric field of the antipodal finline changes to the odd mode of the coupled striplines. The (balanced) coupled line is then matched to the (unbalanced) microstrip line by means of a balun. In

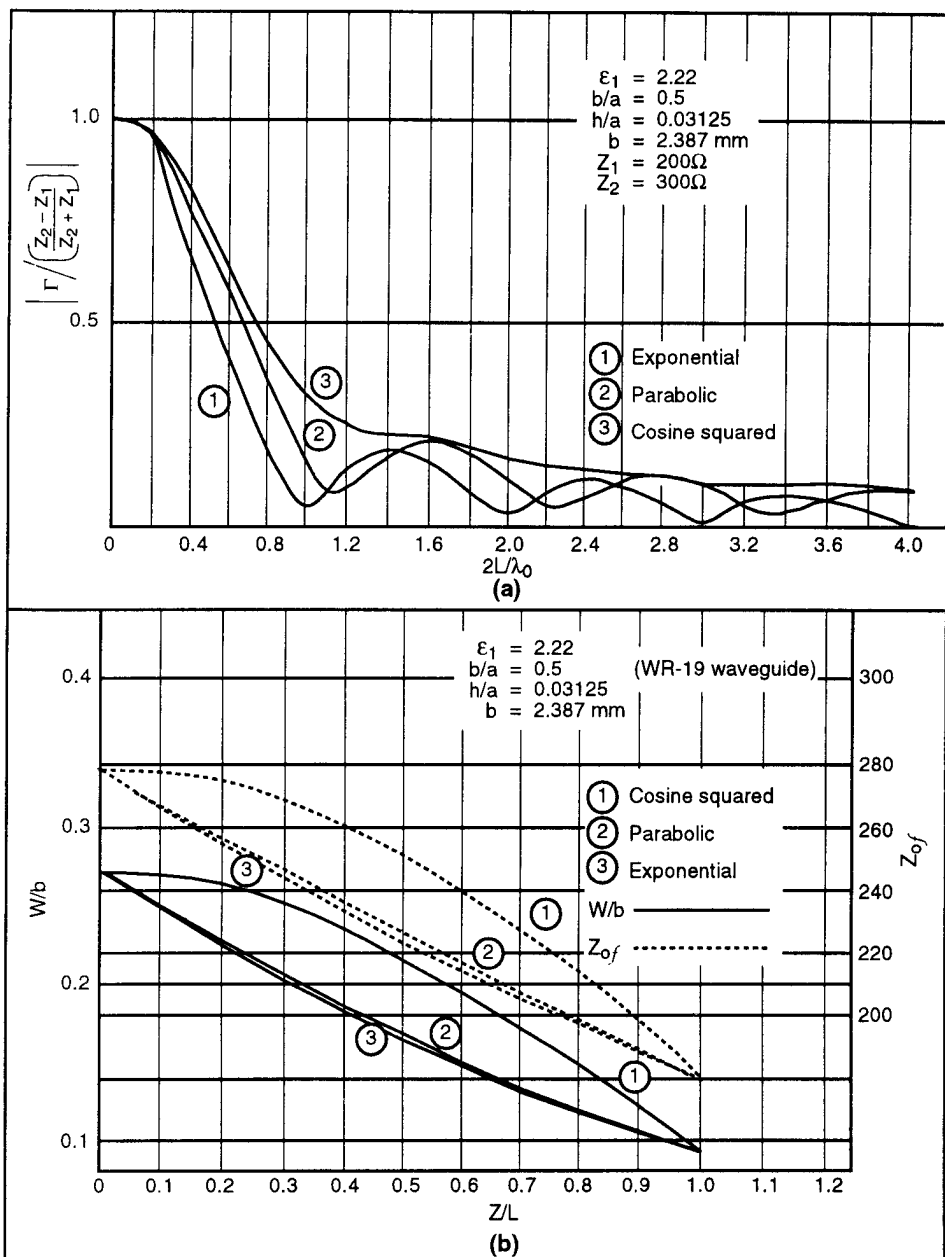


Figure 6.11 (a) Typical frequency response of a tapered finline (from [45]) and (b) fin-gap and characteristic impedance variation as a function of z for the finline tapers of (a) (from [45], © 1987 Penton Publishing. Reprinted with permission.).

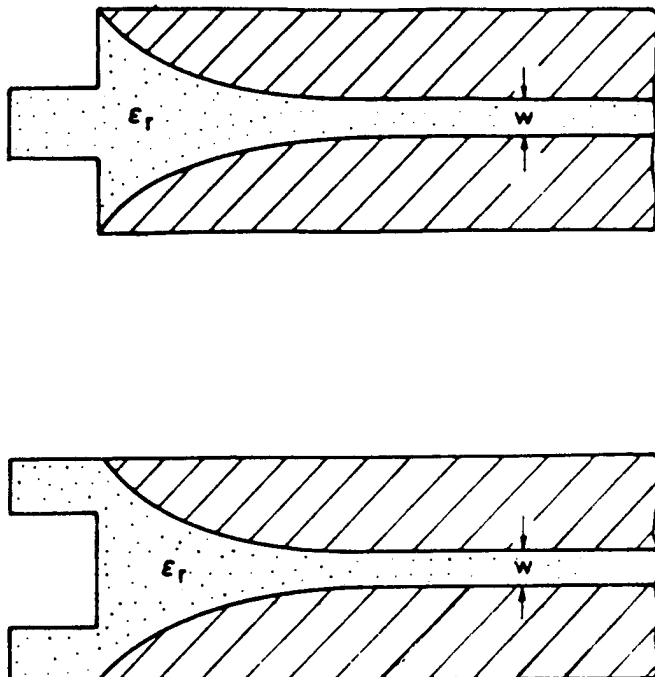


Figure 6.12 Use of single-section quarter-wave transformers to reduce the return loss in finline transitions (from [46], © 1984 IEEE. Reprinted with permission.).

the balun section, one of the strips is narrowed to the desired microstrip width, and the other strip is widened to the full height of the waveguide to serve as the ground plane of the microstrip. In addition, slots are cut in the ground plane to match the impedances of the two lines. The waveguide below the ground plane can be terminated in a short, similar to that in Figure 6.13. A number of transitions of this type were fabricated and tested. Maximum VSWR of 1.22 and an insertion loss of 1 dB was achieved over a 18-GHz to 26-GHz band [49]. The design of finline-to-microstrip transition can also be based on microstrip-to-waveguide transitions discussed in Section 1.4.2.

The characterization of discontinuities and various circuit applications of finline are well described in [7].

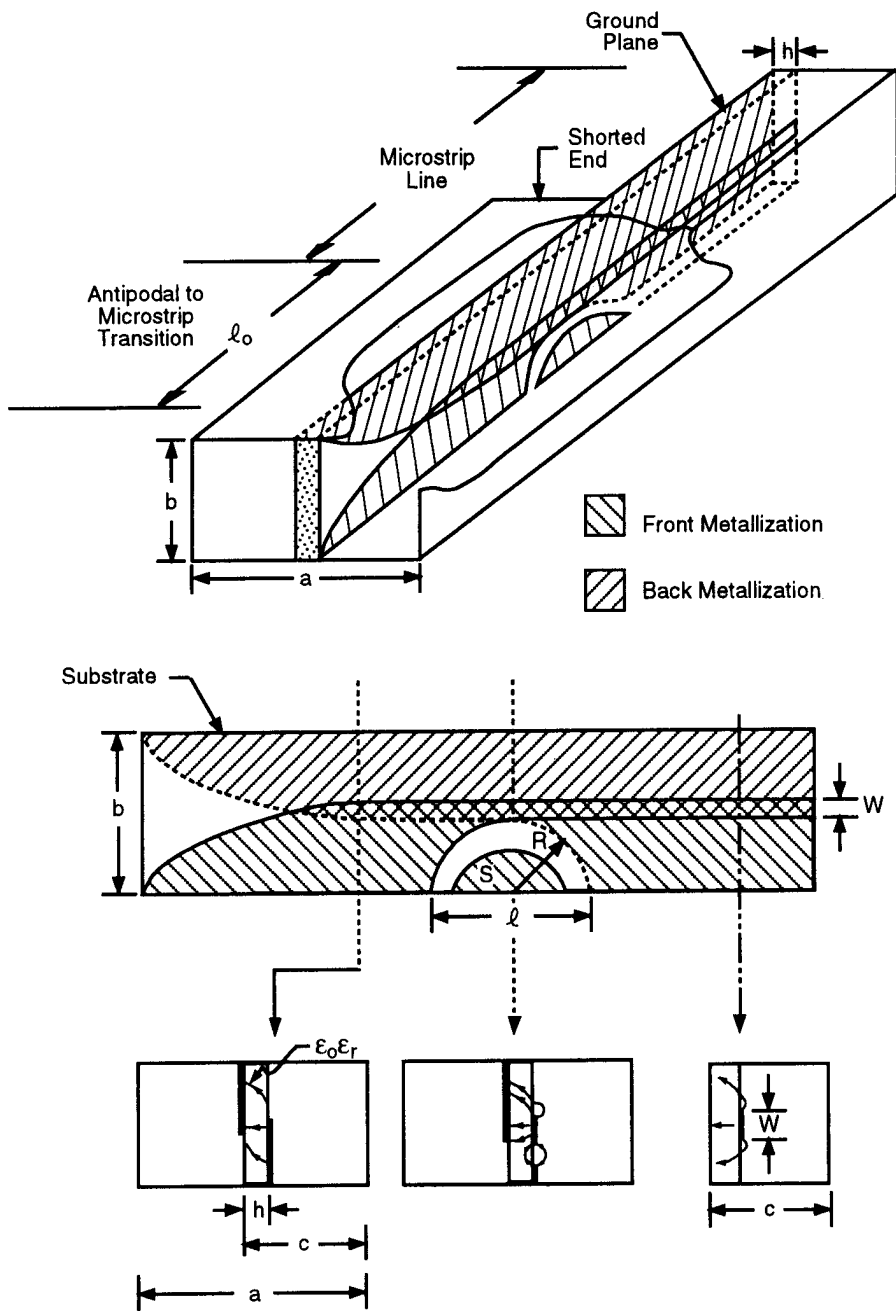


Figure 6.13 Finline-to-microstrip taper transition (from [47], © 1982 Penton Publishing. Reprinted with permission.).

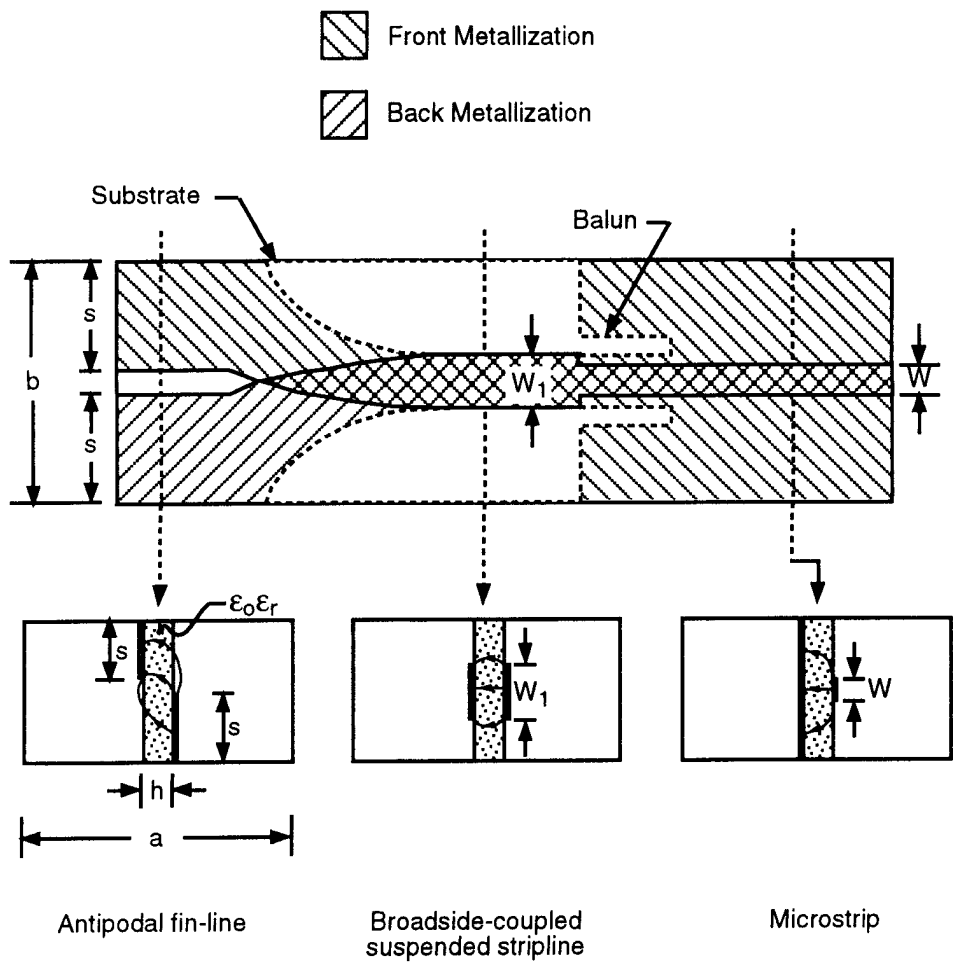


Figure 6.14 Finline-to-microstrip taper transition utilizing an intermediate section of coupled striplines (from [49], © 1976 IEEE. Reprinted with permission.).

References

- [1] Meier, P.J., "Two New Integrated-Circuit Media with Special Advantages at Millimeter Wave-lengths," *IEEE MTT-S Int. Microwave Symp. Digest*, 1972, pp. 221–223.
- [2] Meier, P. J., "Equivalent Relative Permittivity and Unloaded Q-Factor of Integrated Fin-Line," *Electron. Lett.*, Vol. 9, 1973, pp. 162–163.
- [3] Hofmann, H., et al., "New Integrated Millimeter-Wave Components Using Finlines," *IEEE MTT-S Int. Microwave Symp. Digest*, 1978, pp. 21–23.
- [4] Saad, A. M. K., and G. Begemann, "Electrical Performance of Finlines of Various Configurations," *IEE Proc. Microwaves, Optics, and Antennas, Part H*, Vol. 1, 1977, pp. 81–88.
- [5] Piotrowski, J. K., "Efficient Analysis of Finline with Finite Metallization Thickness," *IEEE MTT-S Int. Microwave Symp. Digest*, 1986, pp. 213–216.
- [6] Piotrowski, J. K., "Accurate and Simple Formulas for Dispersion in Finlines," *IEEE MTT-S Int. Microwave Symp. Digest*, 1984, pp. 333–336.
- [7] Bhatt, B., and S. K. Koul, *Analysis, Design and Applications of Fin Lines*, Norwood, MA: Artech House, 1987.
- [8] Simons, R. N., et al., "Analysis of Millimeter-Wave Integrated Finlines," *IEE Proc., Part H*, Vol. 130, pp. 166–169.
- [9] Schieblich, C., et al., "Synthesis of Optimum Finline Tapers Using Dispersion Formulas for Arbitrary Slot Widths and Locations," *IEEE Trans.*, Vol. MTT-32, 1984, pp. 1638–1645.
- [10] Shih, Y. C., and W. J. R. Hoefer, "Dominant and Second-Order Mode Cut-Off Frequencies in Finlines Calculated with a Two-Dimensional TLM Program," *IEEE Trans.*, Vol. MTT-28, 1980, pp. 1443–1448.
- [11] Hofmann, H., "Dispersion of Planar Waveguides for Millimeter-Wave Application," *Arch. Elek. Übertra.*, Vol. 31, No. 1, 1977, pp. 40–44.
- [12] Knorr, J. B., and P. M. Shayda, "Millimeter-Wave Finline Characteristics," *IEEE Trans.*, Vol. MTT-28, 1980, pp. 737–743.
- [13] Schmidt, L. P., and T. Ioth, "Spectral Domain Analysis of Dominant and Higher Order Modes in Finlines," *IEEE Trans.*, Vol. MTT-28, 1980, pp. 981–985.
- [14] Schmidt, L. P., et al., "Characteristics of Unilateral Finline Structures with Arbitrarily Located Slots," *IEEE Trans.*, Vol. MTT-29, 1981, pp. 352–355.
- [15] Syahkal, D. M., and J. B. Davies, "An Accurate, Unified Solution to Various Finline Structures, of Phase Constant, Characteristic Impedance, and Attenuation," *IEEE Trans.*, Vol. MTT-30, 1982, pp. 1854–1861.
- [16] Olley, C., and T. Rozzi, "Currents and Conduction Losses in Unilateral Finline," *IEEE Trans.*, Vol. MTT-36, 1988, pp. 86–95.
- [17] Beyer, A., "Analysis of the Characteristics of an Earthed Finline," *IEEE Trans.*, Vol. MTT-29, 1981, pp. 676–680.
- [18] Vahldieck, R., "Accurate Hybrid-Mode Analysis of Various Finline Configurations Including Multi-layered Dielectrics, Finite Metallization Thickness and Substrate-Supporting Grooves," *IEEE Trans.*, Vol. MTT-32, 1984, pp. 1454–1460.
- [19] Vahldieck, R., and J. Bornemann, "A Modified Mode-Matching Technique and its Application to a Class of Quasi-Planar Transmission Lines," *IEEE Trans.*, Vol. MTT-33, 1985, pp. 916–926.
- [20] Burton, M. N., and W. J. R. Hoefer, "Closed-Form Expressions for the Parameters of Finned and Ridged Waveguides," *IEEE Trans.*, Vol. MTT-30, 1982, pp. 2190–2194.
- [21] Sharma, A. K., and W. J. R. Hoefer, "Empirical Expressions for Finline Design," *IEEE Trans.*, Vol. MTT-31, 1983, pp. 350–356.
- [22] Saad, A. M. K. and K. Schunemann, "Closed Form Approximations for Finline Eigenmodes," *IEEE Proc., Part H*, Vol. 129, 1982, pp. 253–261.
- [23] Pramanick, P., et al., "Computer-Aided Design Models for Unilateral Finlines with Finite Metallization Thickness and Arbitrarily Located Slots," *IEEE MTT-S Int. Microwave Symp. Digest*, 1987.

- [24] Pramanick, P., and P. Bhartia, "Accurate Analysis Equations and Synthesis Technique for Unilateral Fin Lines," *IEEE Trans.*, Vol. MTT-33, 1985, pp. 24–30.
- [25] Pramanick, P., and P. Bhartia, "Computer-Aided Design Models for Millimeter-Wave Finlines and Suspended Substrate Microstrip Lines," *IEEE Trans.*, Vol. MTT-33, 1985, pp. 1429–1435.
- [26] Pramanick, P., and P. Bhartia, "Simple Formulae for Dispersion in Bilateral Fin Lines," *Arch. Elek. Übertra.*, Vol. 39, No. 6, 1985, pp. 383–386.
- [27] Pramanick, P., and P. Bhartia, "Accurate Analysis and Synthesis Equations for Insulated Fin Lines," *Arch. Elek. Übertra.*, Vol. 39, No. 1, 1985, pp. 31–36.
- [28] Pramanick, P., and P. Bhartia, "Frequency Dependence of Equivalent Dielectric Constant in Finlines," *Int. J. Infrared Millimeter Waves*, Vol. 7, No. 2, 1986, pp. 251–268.
- [29] Bhartia, P., and P. Pramanick, "Fin-Line Characteristics and Circuits," *Topics in Millimeter Wave Technology*, Vol. 1 (ed. K. J. Button), Boston, MA: Academic Press, 1988.
- [30] Pramanick, P., and P. Bhartia (Eds.), *E-Plane Integrated Circuits*, Norwood, MA: Artech House, 1987.
- [31] Cohn, S. B., "Slot-Line on a Dielectric Substrate," *IEEE Trans.*, Vol. MTT-17, 1969, pp. 768–778.
- [32] Meier, P. J., "Integrated Fin-Line Millimeter Components," *IEEE Trans.*, Vol. MTT-22, 1974, pp. 1209–1216.
- [33] Saad, A. M. K., and K. Schunemann, "A Simple Method for Analyzing Fin Line Structures," *IEEE Trans.*, Vol. MTT-26, 1978, pp. 1002–1007.
- [34] Saad, A. M. K., and K. Schunemann, "Efficient Eigenmode Analysis for Planar Transmission Lines," *IEEE Trans.*, Vol. MTT-30, 1982, pp. 2125–2132.
- [35] Pramanick, P., and P. Bhartia, "Analysis and Synthesis of Tapered Fin Lines," *IEEE MTT-S Int. Microwave Symp. Digest*, 1984, pp. 336–338.
- [36] Collin, R. E., *Field Theory of Guided Waves*, New York: McGraw-Hill, 1960.
- [37] Shih, Y. C., "Analysis of Finlines Using Transmission Line Matrix and Transverse Resonance Methods," M.A.Sc. Thesis, Dept. of Electrical Engineering, University of Ottawa, 1980, Canada.
- [38] Ahmed, M. J., "Impedance Transformation Equations for Exponential, Cosine-Squared and Parabolic Tapered Transmission Lines," *IEEE Trans.*, Vol. MTT-29, 1981, pp. 67–68.
- [39] Beyer, A., and I. Wolff, "Fin Line Taper Design Made Easy," *IEEE MTT-S Int. Microwave Symp. Digest*, 1985, pp. 493–496.
- [40] Saad, A. M. K., and K. Schunemann, "Design of Fin Line Tapers, Transitions, and Couplers," *11th European Microwave Conf. Proc.*, 1981, pp. 305–308.
- [41] Hinken, J. H., "Simplified Analysis and Synthesis of Fin Line Tapers," *Arch. Elek. Übertra.*, Vol. 37, 1983, pp. 375–380.
- [42] Syahkal, D. M., and J. B. Davies, "Accurate Analysis of Tapered Planar Transmission Lines for Microwave Integrated Circuits," *IEEE Trans.*, Vol. MTT-29, 1981, pp. 123–128.
- [43] Pramanick, P., and P. Bhartia, "A generalized Theory of Tapered Transmission Line Matching Transformers and Asymmetric Couplers supporting Non-TEM Modes," *IEEE Trans.*, Vol. MTT-37, 1989, pp. 1184–1191.
- [44] Collin, R. E., *Foundations for Microwave Engineering*, New York: McGraw-Hill, 1966.
- [45] Pramanick, P., and P. Bhartia, "Design Tapered Finlines Using a Calculator," *Microwaves and RF*, Vol. 26, 1987, pp. 111–114.
- [46] Verver, C. J., and W. J. R. Hoefer, "Quarter-Wave Matching of Waveguide to Fin Line Transitions," *IEEE Trans.*, Vol. MTT-32, 1984, pp. 1645–1648.
- [47] Dydyk, M., and B. D. Moore, "Shielded Microstrip Aids V-Band Receiver Designs," *Microwaves*, Vol. 21, March 1982, pp. 77–82.
- [48] Begemann, G., "An X-Band Balanced Fin Line Mixer," *IEEE Trans.*, Vol. MTT-26, 1978, pp. 1007–1011.
- [49] van Heuven, J. H. C., "An Integrated Waveguide-Microstrip Transition," *IEEE Trans.*, Vol. MTT-24, 1976, pp. 144–147.

Appendix 6.A: Susceptance Expression for the Unilateral Finline [7]

The formula for the total susceptance β_t for a unilateral finline is very similar in form but more accurate than that for a slotline (Appendix 5.A). This formula is (refer to Figure 6.4)

$$\eta B_t = \frac{cu}{2b} \tan \left[\frac{\pi u h}{\xi c} - \tan^{-1} \left(\frac{v}{u} P_{01} \right) \right] - \frac{cv}{2b} P_{02} + \frac{1 + \epsilon_r - 2\xi^2}{\xi} T + \frac{1}{\xi} \sum_{n>0} (H_{n1} + H_{n2}) W_n \quad (\text{A.1})$$

$$\xi = \lambda_0 / \lambda_f \quad \lambda_f = 2c \quad (\text{A.2a})$$

$$u = \sqrt{\epsilon_r - \xi^2} \quad (\text{A.2b})$$

$$v = \sqrt{\xi^2 - 1} \quad (\text{A.2c})$$

$$\gamma_0 = \frac{j\pi}{c\xi} \sqrt{1 - \xi^2} = \frac{\pi v}{c\xi} \quad (\text{A.2d})$$

$$G_n = \sqrt{1 + \left(\frac{bv}{nc\xi} \right)^2} = \frac{b\gamma_n}{\pi n} \quad (\text{A.2e})$$

$$G_{n1} = \sqrt{1 - \left(\frac{bu}{nc\xi} \right)^2} = \frac{b\gamma_{n1}}{\pi n} \quad (\text{A.2f})$$

$$\delta = w/b \quad \delta' = (2s + w)/b \quad (\text{A.2g})$$

$$P_{01} = \coth(\gamma_0 h_1) \quad P_{n1} = \coth(\gamma_n h_1) \quad (\text{A.2h})$$

$$P_{02} = \coth(\gamma_0 h_2) \quad P_{n2} = \coth(\gamma_n h_2) \quad (\text{A.2i})$$

$$W_n = \frac{\sin^2 \left(\frac{n\pi\delta}{2} \right) \cdot \cos^2 \left(\frac{n\pi\delta'}{2} \right)}{n \cdot \left(\frac{n\pi\delta}{2} \right)^2} \quad (\text{A.2j})$$

$$H_{n2} = \left\{ \begin{array}{l} \left(1 - \xi^2 G_n^2 \right) P_{n2} + v^2 \\ \left[1 + \left(\frac{b}{nc} \right)^2 \right] G_n \end{array} \right\} \quad (\text{A.3})$$

For G_{nl} real,

$$H_{nl} = \left\{ \frac{\left(\epsilon_r \tanh p_{nl} - \xi^2 G_{nl}^2 \coth q_{nl} \right)}{\left[1 + \left(\frac{b}{nc} \right)^2 \right] G_{nl}} - u^2 \right\} \quad (A.4)$$

$$p_{nl} = \frac{\pi n G_{nl} h}{b} + \tanh^{-1} \left[\frac{G_{nl}}{G_n \epsilon_r} P_{nl} \right] \quad (A.5a)$$

$$q_{nl} = \frac{\pi n G_{nl} h}{b} + \coth^{-1} \left[\frac{G_n}{G_{nl}} P_{nl} \right] \quad (A.5b)$$

If

$$\left[\frac{G_{nl}}{G_n \epsilon_r} P_{nl} \right] > 1$$

then replace $\tanh p_{nl}$ by $\coth p_{nl}$ in (A.4), where

$$p_{nl} = \frac{\pi n G_{nl} h}{b} + \coth^{-1} \left[\frac{G_{nl}}{G_n \epsilon_r} P_{nl} \right] \quad (A.6)$$

If

$$\left[\frac{G_n}{G_{nl}} P_{nl} \right] < 1$$

then replace $\coth q_{nl}$ by $\tanh q_{nl}$ in (A.4), where

$$q_{nl} = \frac{\pi n G_{nl} h}{b} + \tanh^{-1} \left[\frac{G_n}{G_{nl}} P_{nl} \right] \quad (A.7)$$

For G_{nl} imaginary,

$$H_{nl} = \left\{ \frac{\epsilon_r \tan p'_{nl} - \xi^2 |G_{nl}|^2 \cot q'_{nl}}{\left[1 + \left(\frac{b}{nc} \right)^2 \right] |G_{nl}|} - u^2 \right\} \quad (A.8)$$

$$p'_{nl} = \frac{\pi n |G_{nl}| h}{b} + \tan^{-1} \left[\frac{|G_{nl}|}{G_n \epsilon_r} P_{nl} \right] \quad (A.9a)$$

$$q'_{nl} = \frac{\pi n |G_{nl}| h}{b} + \cot^{-1} \left[\frac{|G_{nl}|}{|G_{nl}|} P_{nl} \right] \quad (\text{A.9b})$$

$$\begin{aligned} T = & \frac{1}{(\pi\delta)^2} \left\{ \frac{(\pi\bar{\delta})^2}{2} \ell_n(\pi\bar{\delta}) - \frac{(\pi\delta)^2}{2} \cdot \ell_n(\pi\delta) \right. \\ & - \frac{\pi(\delta + \bar{\delta})^2}{4} \cdot \ell_n[\pi(\delta + \bar{\delta})] - \frac{[\pi(\bar{\delta} - \delta)]^2}{4} \ell_n[\pi(\bar{\delta} - \delta)] \\ & \left. + \frac{3}{2} \cdot (\pi\delta)^2 + \frac{(\pi\delta)^4}{144} + \frac{(\pi\delta)^2(\pi\bar{\delta})^2}{48} \right\} \end{aligned}$$

$$\bar{\delta} = \begin{cases} \frac{2s + w}{b} & 0 < s \leq \frac{(b-w)}{2} \\ \frac{2(b-s-w/2)}{b} & \frac{(b-w)}{2} \leq s < (b-w) \end{cases} \quad (\text{A.10})$$

CHAPTER 7

Coplanar Lines: Coplanar Waveguide and Coplanar Strips

7.1 INTRODUCTION

The term *coplanar lines* is used for those transmission lines where all the conductors are in the same plane; namely, on the top surface of the dielectric substrate. These transmission lines include slotline, coplanar waveguide (CPW), and coplanar strips (CPS). The slotline has been discussed in Chapter 5. Coplanar waveguide and coplanar strips are discussed in this chapter. Some of the advantages of these two lines arise from the fact that the mounting of lumped (active or passive) components in shunt or series configuration is much easier, drilling of holes through the substrate is not needed to reach the ground plane, and transition to slotline is less cumbersome, thereby allowing greater flexibility in the use of mixed transmission media. The performance of coplanar lines is comparable to and sometimes even better than microstrip line in terms of guide wavelength, dispersion, and losses. Active elements such as MESFETs can easily be connected to coplanar lines because they are also coplanar in nature. Consequently, coplanar lines are used commonly in monolithic microwave integrated circuits (MMICs). Coplanar lines have some disadvantages also, such as parasitic modes, lower power-handling capability, and field nonconfinement.

The coplanar waveguide was proposed by Wen [1] in 1969. As shown in Figure 7.1(a) it consists of two slots each of width W printed on a dielectric substrate. The spacing between the slots is denoted by S . The electric and magnetic field configurations for quasi-static approximation are shown in Figure 7.1(b). At higher frequencies, the mode of propagation in the CPW becomes non-TEM because a

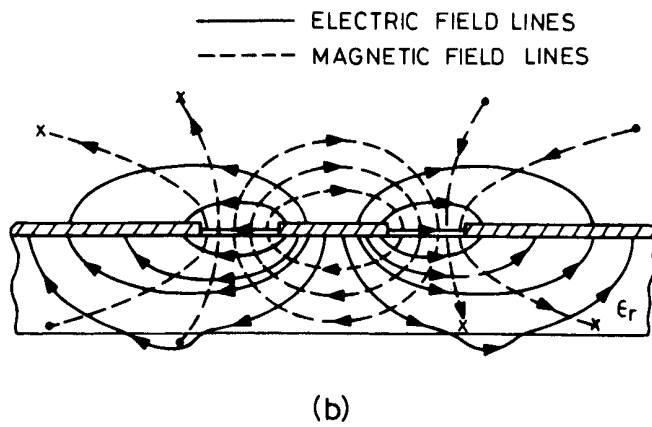
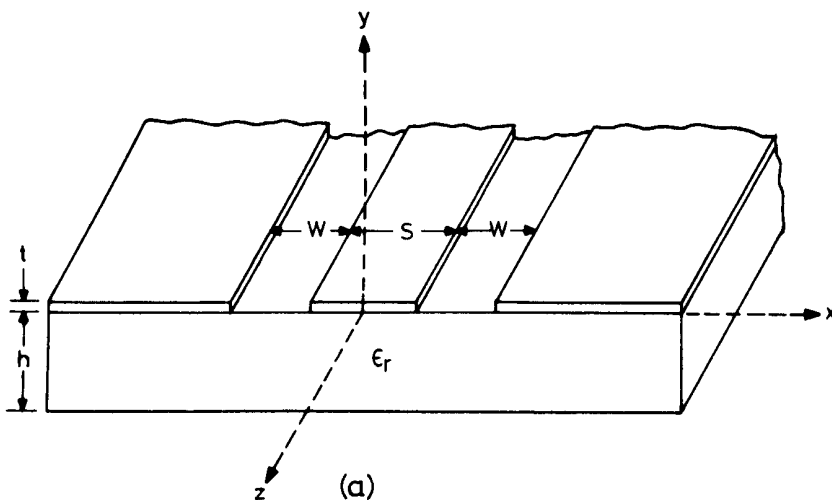


Figure 7.1 (a) Coplanar waveguide (CPW) geometry and (b) electric and magnetic field distributions in CPW.

longitudinal component of the magnetic field exists. In such a case the CPW has an elliptically polarized magnetic field in the slots at the air-dielectric interface and becomes suitable for nonreciprocal ferrite devices.

A configuration of coplanar strips, which is complementary to the CPW, is shown in Figure 7.2(a). It consists of two strips, generally of equal width W on a dielectric substrate. The spacing between the strips is denoted by S . The electric and magnetic field configurations are shown in Figure 7.2(b). In the lower range

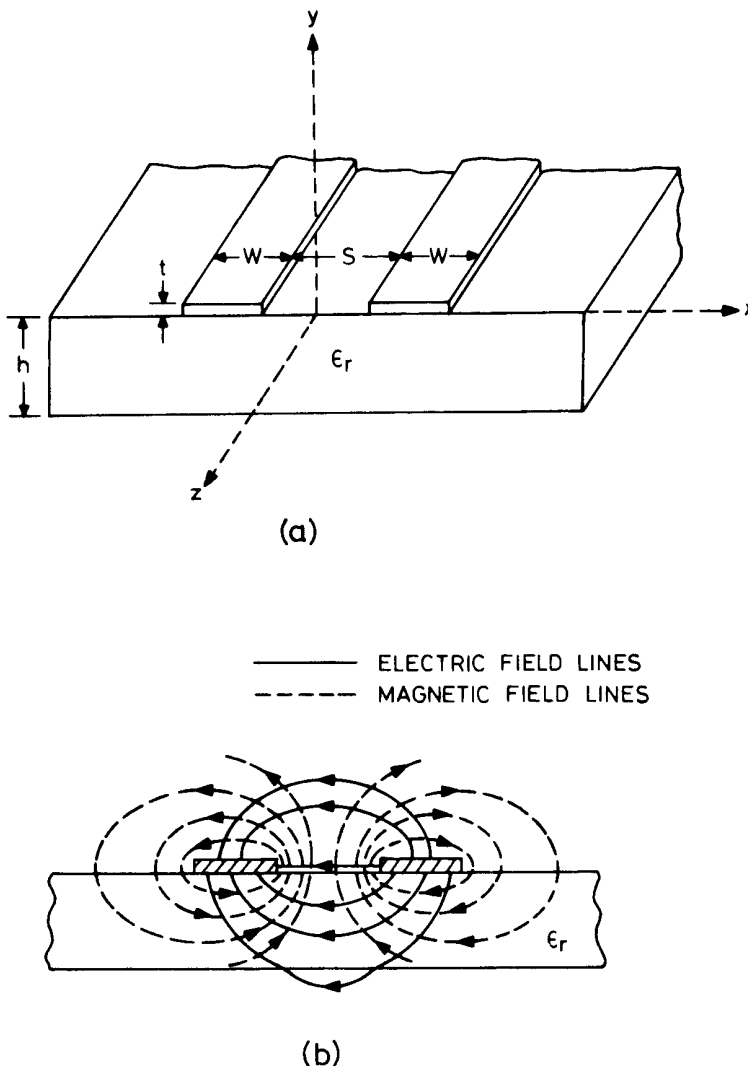


Figure 7.2 (a) Coplanar strips (CPS) geometry and (b) electric and magnetic field distributions in CPS.

of microwave frequencies, the CPS is also useful for carrying signals for high-speed computer circuits.

The conventional coplanar waveguide, introduced by Wen [1], cannot be used as such because of the requirement of infinitely thick substrate. For practical applications substrate thickness has to be finite as in Figure 7.3(a). Also, the ground

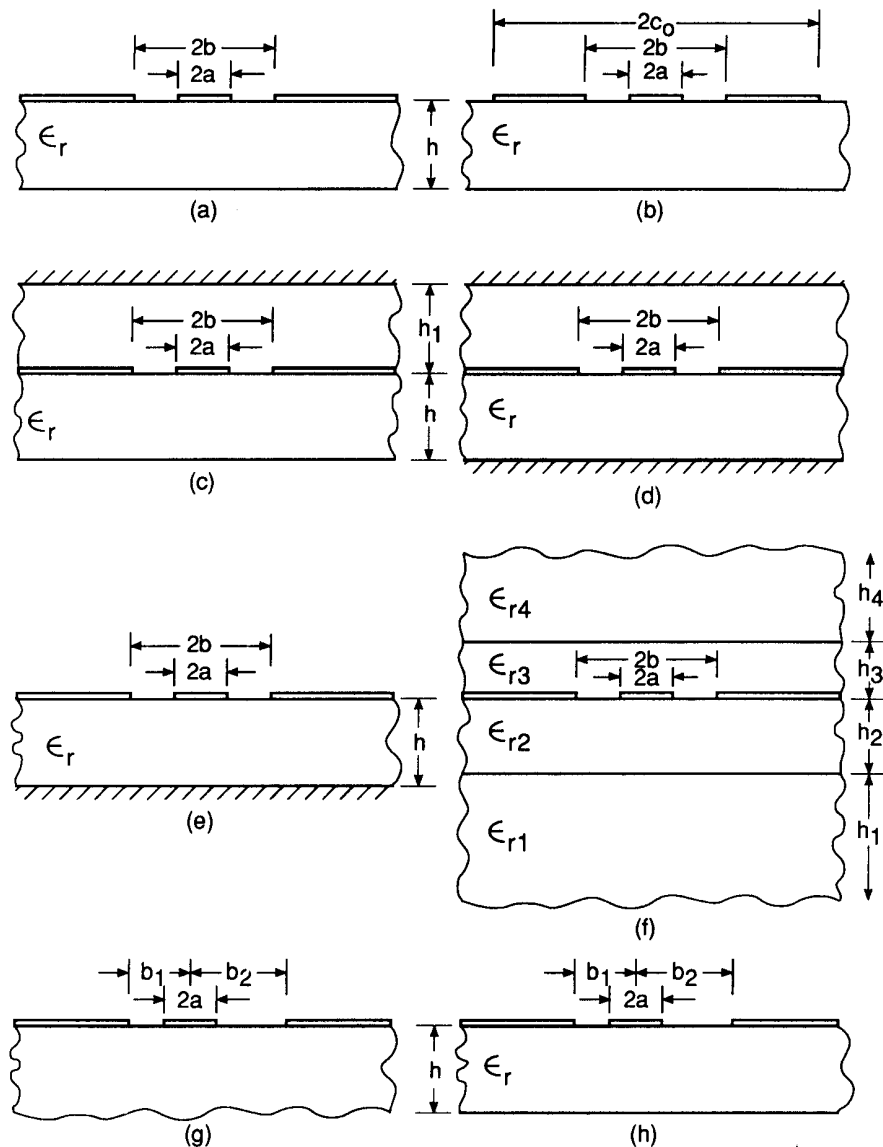


Figure 7.3 Various types of coplanar waveguides: (a) CPW with finite dielectric thickness; (b) CPW with finite width ground planes; (c) CPW with a cover shield; (d) conductor-backed CPW with a cover shield; (e) conductor-backed CPW; (f) multilayered CPW; (g) asymmetric CPW; and (h) asymmetric CPW with finite dielectric thickness.

planes of actual CPW have finite widths as in Figure 7.3(b). The width of the ground planes should be kept as small as possible since it has a direct bearing on the maximum line density and the circuit size achievable in coplanar circuits. The fields of a CPW are less confined than those of microstrip lines, thereby making them more sensitive to covers or shields placed above the guide (see Figure 7.3(c)). It is very tempting to introduce a conductor backing (see Figures 7.3(d, e)), to improve both the mechanical strength and the power-handling capability. Moreover, it allows easy implementation of mixed CPW-microstrip circuits. In MMIC applications, the semiconductor substrates are usually thin and fragile. They are mounted on low-permittivity materials such as quartz. Some applications may require a dielectric overlay or a multilayered configuration as shown in Figure 7.3(f). Sometimes, it is desirable to adjust the characteristic impedance of a CPW by changing the width of one of the slots, keeping the rest of the parameters unchanged. This configuration is called the asymmetric CPW (see Figures 7.3(g, h)). The effect of all these modifications (in conventional CPW) on propagation will be studied next, in order to exploit the flexibility provided by the additional parameters such as the cover height, lateral ground plane width, asymmetry, and multilayer configuration.

Methods of analysis for CPW and CPS are discussed in the following section. Design considerations for these lines are presented in Sections 7.3 through 7.5. Coplanar lines are compared with microstrip and slotline in Section 7.6. Various kinds of CPW transitions are described in Section 7.7, and CPW discontinuities are treated in Section 7.8. Circuits using CPW are included in Section 7.9.

7.2 ANALYSIS

Coplanar lines have been studied using the quasi-static approximation and the fullwave analyses [1–17]. Wen [1] has conducted a quasi-static analysis of these transmission lines using conformal mapping, with the assumption that the dielectric substrate is thick enough to be considered infinite. Conformal transformation has also been applied to take into account the effects of the finite thickness of the dielectric substrate, finite size of the ground planes, upper shield, ground plane below the substrate as in microstrip line, structural asymmetry, and multilayer configuration. A fullwave analysis of coplanar lines, which provides information regarding frequency dependence of phase velocity and characteristic impedance, has been carried out by a number of investigators. The techniques employed include Galerkin's method in the spectral domain [2–12], variational methods [13–15], integral equation [16], relaxation method [17], method of lines [18], mode-match technique [19], and finite-difference time-domain technique [20, 21].

7.2.1 Quasi-Static CPW Analysis Based on the Conformal Mapping Method

The basic approach used in the conformal transformation method, as applied to coplanar lines, is to assume that all the dielectric interfaces in the structure,

including slots, can be replaced by magnetic walls [22]. This assumption is strictly valid for those structures for which the electric field lies along the dielectric interfaces. Under this assumption, half-planes above and below the metallization plane of the structure can be analyzed separately for line capacitance. The total line capacitance is then the algebraic sum of the two capacitances. Further, if the dielectric substrate has finite thickness as in Figure 7.3, the contribution of the lower half-plane to the line capacitance can be determined as the sum of (1) the free space capacitance, obtained by replacing dielectric by air medium, and (2) the capacitance of the dielectric layer alone assumed to have the permittivity ($\epsilon_r - 1$) [22]. This approach yields exact results for infinitely thick substrate and for substrate thickness $h \rightarrow 0$ [23]. It has been found to give an accuracy of better than one percent for most of the practical ranges of physical dimensions [24].

The conformal mapping of coplanar lines gives rise to analytical expressions for the effective dielectric constant and characteristic impedance in terms of the ratio of complete elliptic integral of the first kind and its complement. These expressions can easily be computed using scientific calculators and the effect of various parameters understood clearly. The accuracy of analytical expressions are comparable with fabrication tolerances and measurement accuracy achievable.

For the various types of coplanar lines discussed in this section one attempts to determine suitable mapping functions so that the given configuration of coplanar lines is transformed into capacitors connected in parallel.

Since we are dealing with the quasi-static approximation of the mode of propagation, the values of phase velocity v_{ph} and the characteristic impedance Z_0 can be written as

$$\epsilon_{re} = \frac{C}{C^a} \quad (7.1)$$

$$v_{ph} = \frac{c}{\sqrt{\epsilon_{re}}} \quad (7.2)$$

and

$$Z_0 = \frac{1}{Cv_{ph}} = \frac{1}{c\sqrt{\epsilon_{re}} C^a} \quad (7.3)$$

where c is the velocity of electromagnetic waves in free space, C is the total capacitance per unit length of the coplanar line, and C^a is the capacitance of the corresponding line with all the dielectrics replaced by air.

Specific coplanar line configurations and the corresponding transformations are discussed next. The strip and the ground plane metallization thickness is considered negligible in deriving the various expressions. The capacitance for the

half-plane with air as dielectric is denoted by C_1 and that due to the dielectric layer is denoted by C_2 .

CPW with Infinitely Thick Substrate [1]

Making use of the symmetry of the CPW structure, consider only one-half of it for conformal transformation, as shown in Figure 7.4(a). The Schwarz–Christoffel transformation, which maps the dielectric portion of the z -plane of Figure 7.4(a) into the interior of a rectangle in the w -plane of Figure 7.4(b) with the conductor surfaces on the top and the bottom, is given by

$$w = \int_{z_0}^z \frac{dz}{\sqrt{(z-a)(z-b)}} \quad (7.4)$$

The size of the rectangle in the w -plane is obtained by carrying out the above integration. It is given by

$$\frac{\overline{12}}{\overline{23}} = \frac{K(k_1)}{K'(k_1)} \quad (7.5)$$

where \overline{ij} is the distance between points i and j in the w -plane and $K(\cdot)$ and $K'(\cdot)$ are the complete elliptic integrals of the first kind and its complement, respectively. They are simply related to each other through the equation

$$K'(k_1) = K(k'_1) \quad \text{with } k'_1 = \sqrt{1 - k_1^2} \quad (7.6)$$

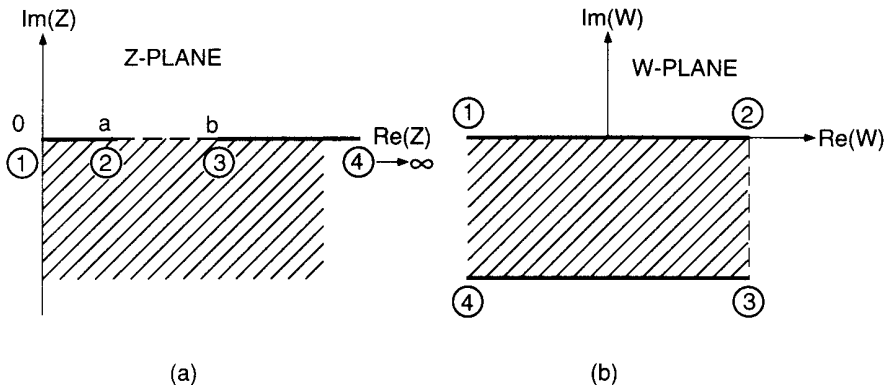


Figure 7.4 Conformal transformation planes for CPW analysis: (a) z -plane and (b) w -plane.

The argument of the elliptic integrals is obtained as

$$k_1 = a/b = S/(S + 2W) \quad (7.7)$$

The capacitance per unit length of the line contributed by the dielectric half-plane, C_2 , is then given by

$$C_2 = 2\epsilon_0\epsilon_r \frac{K(k_1)}{K'(k_1)} \quad (7.8a)$$

The capacitance C_1 due to the electric field in the air half-plane follows directly from (7.8a) and is given by

$$C_1 = 2\epsilon_0 \frac{K(k_1)}{K'(k_1)} \quad (7.8b)$$

The total line capacitance C becomes

$$C = C_1 + C_2 = 2\epsilon_0(\epsilon_r + 1) \frac{K(k_1)}{K'(k_1)} \quad (7.8c)$$

The effective dielectric constant of a CPW, obtained using (7.1), is then

$$\epsilon_{re} = \frac{\epsilon_r + 1}{2} \quad C^a = 2C_1 \quad (7.9)$$

Similarly, the phase velocity and the characteristic impedance of a conventional CPW obtained from (7.2) and (7.3) are

$$v_{cp} = c \sqrt{\frac{2}{\epsilon_r + 1}} \quad (7.10)$$

and

$$Z_{0cp} = \frac{30\pi}{\sqrt{\epsilon_{re}}} \frac{K'(k_1)}{K(k_1)} \quad (\text{ohm}) \quad (7.11)$$

respectively. An accurate but simple expression of the ratio K/K' is available in the literature [25] and is included here for the reader's convenience.

$$\frac{K(k)}{K'(k)} = \frac{\pi}{\ell_n [2(1 + \sqrt{k})/(1 - \sqrt{k})]} \quad \text{for } 0 \leq k \leq 0.707 \quad (7.12a)$$

$$\frac{K(k)}{K'(k)} = \frac{1}{\pi} \ell_n [2(1 + \sqrt{k})/(1 - \sqrt{k})] \quad \text{for } 0.707 \leq k \leq 1 \quad (7.12b)$$

Expressions (7.12) are accurate to within 3 parts per million. The ratio K/K' varies from 0 to ∞ as k varies from 0 to 1.

The value of the characteristic impedance computed using (7.11) and (7.12) is plotted in Figure 7.5(a) for GaAs substrate, $\epsilon_r = 13$ [26] (see the curve for $h/b = \infty$). The line impedance is found to decrease almost logarithmically as the aspect ratio a/b increases.

For practical applications the substrate thickness of a CPW has to be finite. This configuration is discussed next.

CPW with Finite Dielectric Thickness h [22]

For the analysis of this structure (Figure 7.3a) we invoke the assumption that the capacitance due to the lower half-plane is the sum of the free-space capacitance and the capacitance of the dielectric layer with permittivity $(\epsilon_r - 1)$. The free-space capacitance for the lower half-plane is exactly the same as that for the upper half-plane. It was calculated earlier and is denoted by C_1 . The capacitance of the dielectric layer is calculated next.

A pair of conformal transformations is used to transform the CPW into a parallel plate structure. The first transformation converts this CPW into a conventional CPW, that is, CPW with infinitely thick substrate. This transformation is

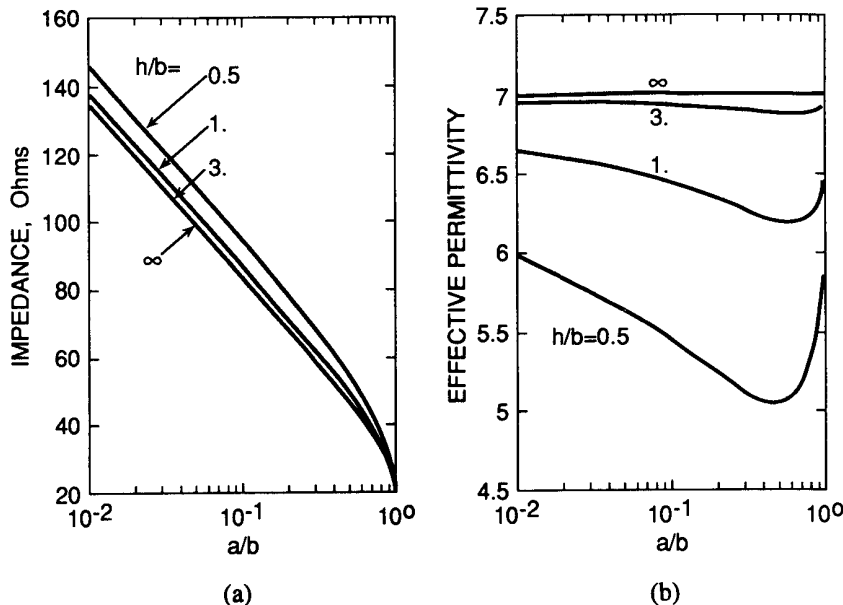


Figure 7.5 (a) Variation of characteristic impedance for CPW as a function of aspect ratio a/b with h/b as a parameter and (b) variation of effective dielectric constant for CPW as a function of aspect ratio a/b with h/b as a parameter (GaAs substrate with $\epsilon_r = 13$) [26].

$$t = \sinh\left(\frac{\pi z}{2h}\right) \quad (7.13)$$

The resulting configuration in the t -plane is shown in Figure 7.6(b), where

$$t_1 = \sinh\left(\frac{\pi a}{2h}\right) \quad (7.14a)$$

and

$$t_2 = \sinh\left(\frac{\pi b}{2h}\right) \quad (7.14b)$$

The configuration of Figure 7.6(b) is identical to that of the conventional CPW in Figure (7.4a) that was discussed earlier. Therefore, capacitance C_2 is given by

$$C_2 = 2\epsilon_0(\epsilon_r - 1) \frac{K(k_2)}{K'(k_2)} \quad (7.15)$$

The factor $(\epsilon_r - 1)$ appears in (7.15) because of the assumptions made in the analysis. The argument k_2 of the elliptic integral follows directly from (7.7) and (7.14),

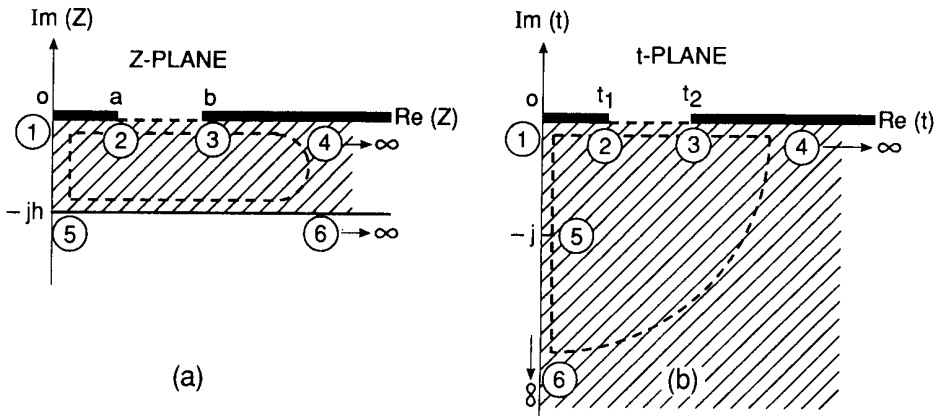


Figure 7.6 Transformation of CPW with substrate thickness h into a CPW with infinitely thick substrate using the mapping function $t = \sinh(\pi z / 2h)$: (a) z -plane and (b) t -plane (from [22], © 1980 IEE (U.K.). Reprinted with permission.).

$$k_2 = \frac{t_1}{t_2} = \frac{\sinh(\pi a/2h)}{\sinh(\pi b/2h)} \quad (7.16)$$

The capacitance C_1 contributed by the upper half-plane is that given by (7.8b). The total capacitance C is therefore given by

$$C = 2C_1 + C_2$$

and

$$C^a = 2C_1$$

Substituting for C and C^a in (7.1) we obtain the following expression for ϵ_{re}

$$\epsilon_{re} = 1 + \frac{\epsilon_r - 1}{2} \frac{K(k_2)}{K'(k_2)} \frac{K'(k_1)}{K(k_1)} \quad (7.17)$$

Quite frequently the effective dielectric constant is expressed in the form

$$\epsilon_{re} = 1 + q(\epsilon_r - 1) \quad (7.18)$$

where q is called the filling factor and can be obtained from a comparison of (7.17) and (7.18) as

$$q = \frac{1}{2} \frac{K(k_2)}{K'(k_2)} \frac{K'(k_1)}{K(k_1)} \quad (7.19a)$$

It may be observed from (7.19a) that the filling factor does not depend on the relative dielectric constant of the substrate layer. Through k_i , it depends on the dielectric thickness, strip width, and slot width. It may be defined in terms of the capacitances as [24]

$$q = C_s^a / C^a \quad (7.19b)$$

where C^a is the capacitance of the CPW structure with air as dielectric and C_s^a is the capacitance of the substrate layer replaced by air as dielectric. We shall use this definition of q in calculating the effective dielectric constant of a multilayered CPW.

The characteristic impedance can be expressed as

$$Z_{0cp} = \frac{30\pi}{\sqrt{\epsilon_{re}}} \frac{K'(k_1)}{K(k_1)} \quad (7.20)$$

It may be noted from a comparison of (7.11) and (7.20) that the effect of finite dielectric thickness is to decrease the effective dielectric constant of the CPW. Since the effective dielectric constant decreases with h (see Figure 7.5(b)), the characteristic impedance increases (see Figure 7.5(a)). As a rule of thumb, the substrate thickness h should be greater than $2b$ for Z_{0cp} to be almost independent of h . For a given set of substrate parameters h and ϵ_r , a given value of characteristic impedance can be realized using different combinations of a and b . The final choice is determined by the factors such as associated conductor loss of the line.

Practical coplanar waveguides have finite width ground planes. This geometry is analyzed next.

CPW with Finite Dielectric Thickness and Finite Width Ground Planes [23]

The lateral extent of the ground planes of a CPW (Figure 7.3b) is denoted by c_0 . In this case, the capacitance C_1 for the upper half-plane is determined by transforming the first quadrant of the CPW (see Figure 7.7(a)) into the upper half of the t -plane (see Figure 7.7(b)) by using the mapping function

$$t = z^2$$

This geometry is now transformed into a parallel plate capacitor in the w -plane as in Figure 7.7(c) through the transformation

$$w = \int_{t_0}^t \frac{dt}{\sqrt{t(t - t_1)(t - t_2)(t - t_3)}} \quad (7.21)$$

with

$$t_1 = a^2, \quad t_2 = b^2, \quad t_3 = c_0^2$$

The capacitance per unit length C_1 is then obtained as

$$C_1 = 2\epsilon_0 \frac{\overline{12}}{\overline{23}} = 2\epsilon_0 \frac{K(k_3)}{K'(k_3)} \quad (7.22)$$

where

$$k_3 = \frac{a}{b} \sqrt{\frac{1 - b^2/c_0^2}{1 - a^2/c_0^2}} \quad (7.23)$$

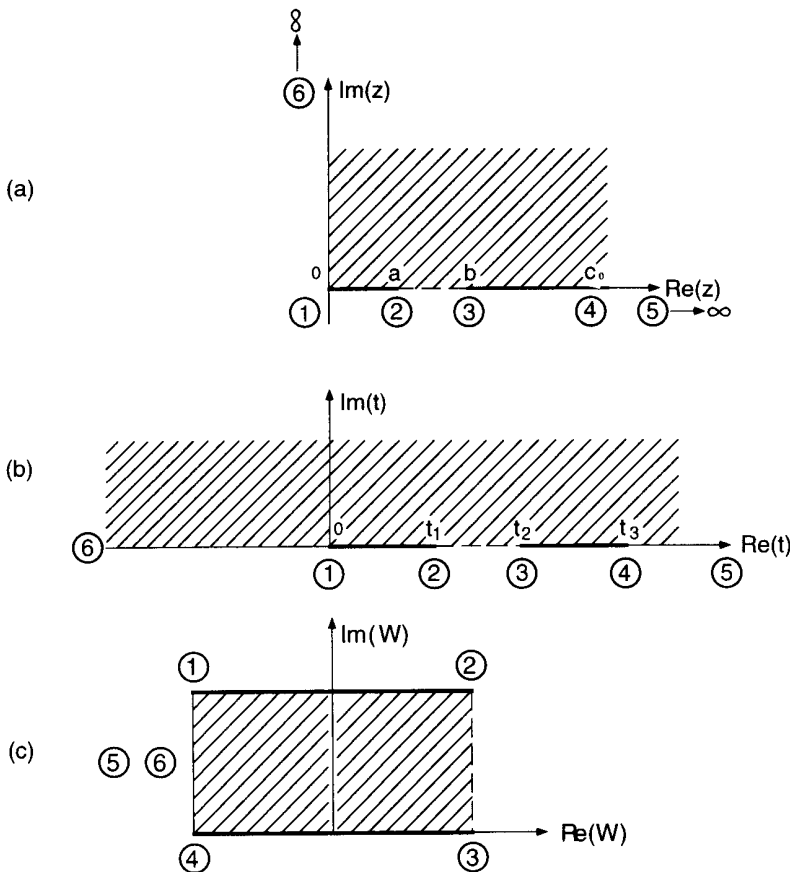


Figure 7.7 Conformal transformation of the first-quadrant of CPW with finite width ground planes into a parallel plate geometry: (a) z -plane; (b) t -plane; and (c) w -plane (from [23], © 1987 IEEE. Reprinted with permission.).

The capacitance C_2 is computed by transforming the dielectric region in Figure 7.8(a) into the upper half of the t -plane (see Figure 7.8(b)) by using the mapping function

$$t = \cosh^2\left(\frac{\pi z}{2h}\right) \quad (7.24)$$

The geometry of Figure 7.8(b) is converted into a parallel plate capacitor in the w -plane of Figure 7.7(c) via the transformation

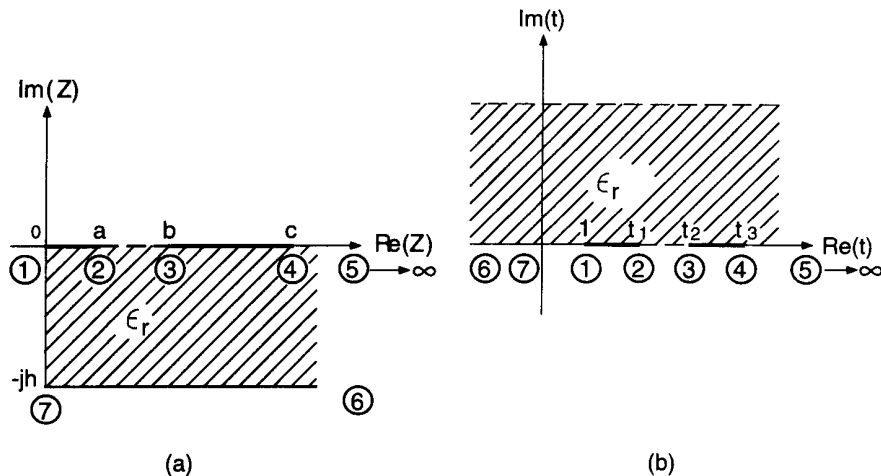


Figure 7.8 Conformal transformation of the fourth quadrant of CPW with finite width ground planes into a parallel plate geometry: (a) z -plane and (b) t -plane (from [23], © 1987 IEEE. Reprinted with permission.).

$$w = \int_{t_0}^t \frac{dt}{\sqrt{(t-1)(t-t_1)(t-t_2)(t-t_3)}} \quad (7.25)$$

with capacitance C_2 then given by

$$C_2 = 2\epsilon_0(\epsilon_r - 1) \frac{\overline{12}}{\overline{23}} = 2\epsilon_0(\epsilon_r - 1) \frac{K(k_4)}{K'(k_4)} \quad (7.26)$$

where

$$k_4 = \frac{\sinh(\pi a/2h)}{\sinh(\pi b/2h)} \sqrt{\frac{1 - \sinh^2(\pi b/2h)/\sinh^2(\pi c/2h)}{1 - \sinh^2(\pi a/2h)/\sinh^2(\pi c/2h)}} \quad (7.27)$$

Thus,

$$\epsilon_{re} = 1 + \frac{C_2}{2C_1} = 1 + \frac{\epsilon_r - 1}{2} \frac{K(k_4)}{K'(k_4)} \frac{K'(k_3)}{K(k_3)} \quad (7.28)$$

and

$$Z_{0cp} = \frac{30\pi}{\sqrt{\epsilon_r}} \frac{K'(k_3)}{K(k_3)} \quad (7.29)$$

Veyres and Fouad Hanna [22] have used different sets of conformal transformations, but the expressions for C_1 and C_2 obtained by them are identical with those obtained above. Evaluating (7.28) and (7.29) shows that the line impedance increases (see Figure 7.9(a)) and effective permittivity decreases (see Figure 7.9(b)) due to truncation of lateral ground planes. This configuration can also support a quasi-TEM slotline mode whose characteristic impedance could be comparable to the desired mode. To suppress this mode lateral ground planes are kept at the same potential by means of properly spaced conductive air bridges [23].

CPW with Finite Dielectric Thickness and a Cover Shield [23]

For this configuration (Figure 7.3c) the capacitance C^a can be divided into two portions: that due to the air region in the half-plane below the CPW metalization and that due to the air region between the cover shield and the CPW metalization, or C'_1 and C''_1 . The expression for C'_1 is the same as that of C_1 of (7.8b).

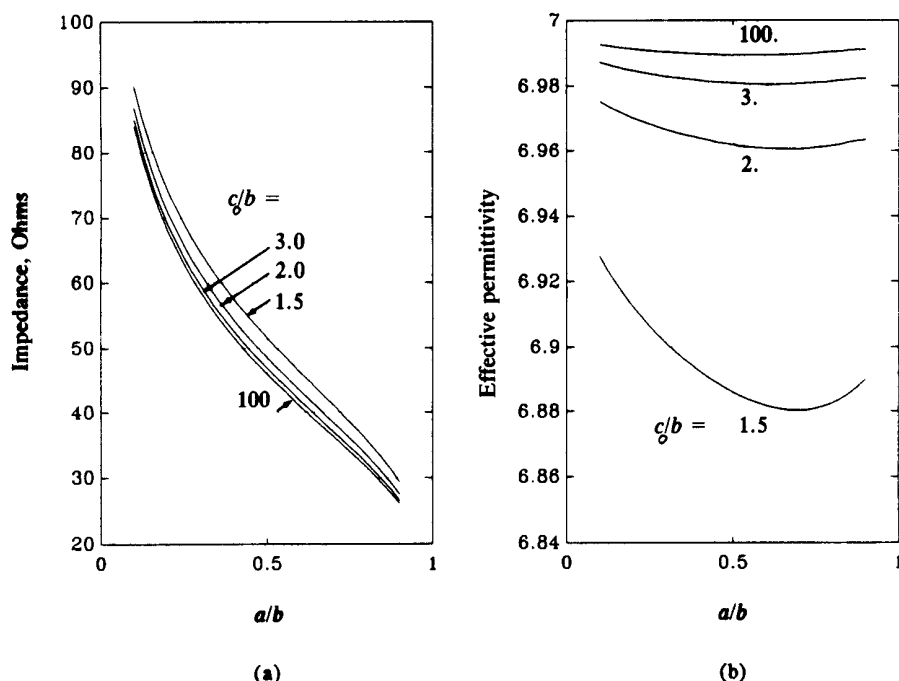


Figure 7.9 (a) Variation of the characteristic impedance for a CPW with finite width ground planes on GaAs substrate ($\epsilon_r = 13$, $h = 300 \mu\text{m}$, and $2b = 200 \mu\text{m}$) and (b) variation of the effective dielectric constant for a CPW with finite width ground planes on GaAs substrate ($\epsilon_r = 13$, $h = 300 \mu\text{m}$, and $2b = 200 \mu\text{m}$) (from [26]).

To obtain an expression for C''_1 , let us consider the first quadrant of Figure 7.3(c) as shown in Figure 7.10(a). The dashed region in this figure is first mapped into the upper-half t -plane as in Figure 7.10(b) by means of the mapping function

$$t = \cosh^2\left(\frac{\pi z}{2h_1}\right) \quad (7.30)$$

and then into the parallel plate capacitor in the w -plane through the conformal transformation

$$w = \int_{t_0}^t \frac{dt}{\sqrt{t(t-1)(t-t_2)(t-t_3)}} \quad t_2 = \cosh^2 \frac{\pi a}{2h_1}, \quad t_3 = \cosh^2 \frac{\pi b}{2h_1} \quad (7.31)$$

The capacitance C''_1 is then given by

$$C''_1 = 2\epsilon_0 \frac{K(k_5)}{K'(k_5)} \quad (7.32)$$

where

$$k_5 = \frac{\tanh(\pi a/2h_1)}{\tanh(\pi b/2h_1)} \quad (7.33)$$

The value of C_2 was obtained earlier and is given by (7.15). The total capacitance per unit length of the line is then

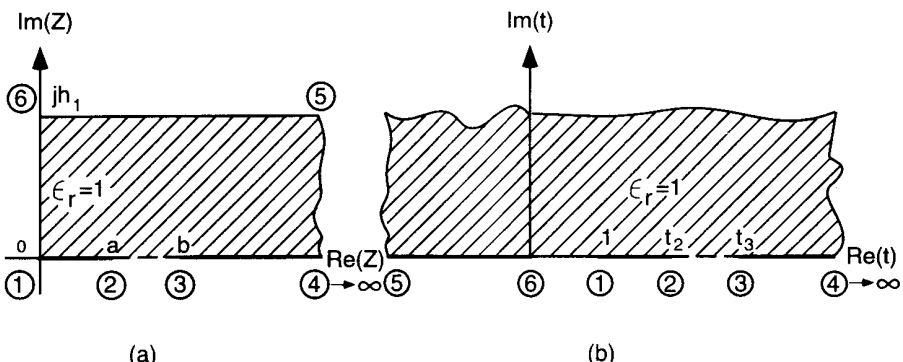


Figure 7.10 Mapping of the first quadrant of a CPW with a cover shield into the upper-half t -plane using the function $t = \cosh^2(\pi z/2h_1)$: (a) z -plane and (b) t -plane (from [23], © 1987 IEEE. Reprinted with permission.).

$$\begin{aligned} C &= C'_1 + C''_1 + C_2 \\ &= 2\epsilon_0 \frac{K(k_1)}{K'(k_1)} + 2\epsilon_0 \frac{K(k_5)}{K'(k_5)} + 2\epsilon_0(\epsilon_r - 1) \frac{K(k_2)}{K'(k_2)} \end{aligned} \quad (7.34)$$

Thus

$$\epsilon_{re} = 1 + \frac{C_2}{C'_1 + C''_1} = 1 + q(\epsilon_r - 1) \quad (7.35)$$

where q is called the filling factor and is obtained as

$$q = \frac{K(k_2)/K'(k_2)}{K(k_1)/K'(k_1) + K(k_5)/K'(k_5)} \quad (7.36)$$

and

$$Z_{0cp} = \frac{60\pi}{\sqrt{\epsilon_{re}}} \frac{1}{K(k_1)/K'(k_1) + K(k_5)/K'(k_5)} \quad (7.37)$$

The effect of cover height h_1 on Z_{0cp} appears through the factor $K(k_5)/K'(k_5)$. For a large value of cover height h_1 , (7.37) reduces to (7.20). Due to the additional term in (7.37) compared to (7.20), the line impedance decreases for a shielded CPW. As a conservative estimate the cover height should be at least four times the substrate thickness for the effect of the cover to be negligible.

Conductor-Backed CPW with a Cover Shield [23]

In this configuration (Figure 7.3d) the lower surface of the substrate is metallized. Therefore, the lower half and upper half portions of the CPW are similar except for different dielectric constants and thicknesses. Consequently, the capacitance C_2 contributed by the dielectric layer can be obtained from the same transformation that is used for the upper half portion. The resulting capacitance is

$$C_2 = 2\epsilon_0\epsilon_r \frac{K(k_6)}{K'(k_6)} \quad (7.38)$$

with

$$k_6 = \frac{\tanh(\pi a/2h)}{\tanh(\pi b/2h)} \quad (7.39)$$

The expression for C_1 in this case is the same as that for C_1'' for the earlier case, (7.32). Thus,

$$\epsilon_{re} = \frac{C_1 + C_2}{C_1 + C_2(\text{for } \epsilon_r = 1)} = 1 + q(\epsilon_r - 1)$$

with

$$q = \frac{K(k_6)/K'(k_6)}{K(k_5)/K'(k_5) + K(k_6)/K'(k_6)} \quad (7.40)$$

and

$$Z_{0cp} = \frac{60\pi}{\sqrt{\epsilon_{re}}} \frac{1}{K(k_5)/K'(k_5) + K(k_6)/K'(k_6)} \quad (7.41)$$

It may be observed from (7.40) that $q = 0.5$ when $k_5 = k_6$, which can be realized by $h_1 = h$; that is, conductor backing and the cover shield are equidistant from CPW metallization. This results in $\epsilon_{re} = (\epsilon_r + 1)/2$.

Conductor-Backed CPW [27]

This configuration (shown in Figure 7.3e) is the limiting case of Figure 7.3(d) when the cover shield recedes to infinity, that is, $h_1 \rightarrow \infty$. Therefore, expressions for q and Z_{0cp} can be obtained from (7.40) and (7.41), respectively. When $h_1 \rightarrow \infty$, it follows that $k_5 \rightarrow a/b = k_1$ and we obtain

$$q = \frac{K(k_6)/K'(k_6)}{K(k_1)/K'(k_1) + K(k_6)/K'(k_6)} \quad (7.42)$$

and

$$Z_{0cp} = \frac{60\pi}{\sqrt{\epsilon_{re}}} \frac{1}{K(k_1)/K'(k_1) + K(k_6)/K'(k_6)} \quad (7.43)$$

Conductor backing of the substrate improves the mechanical strength of the transmission line so that thin substrates can be used. However, conductor backing reduces the line impedance considerably (compare Figures 7.11 and 7.5(a)). Conductor-backed CPW looks like a mixed coplanar-microstrip structure. Therefore, this configuration supports the parasitic microstrip mode also. The microstrip behavior becomes dominant when the substrate is thin and the slots are wide such

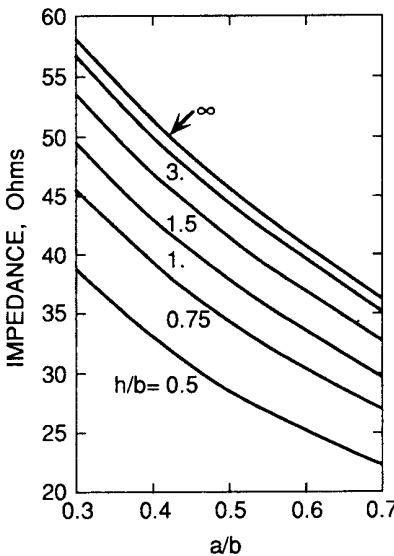


Figure 7.11 Characteristic impedance for conductor-backed CPW ($\epsilon_r = 13$) [26].

that $W/h > 2$. If the aim is to obtain coplanar behavior, the substrate should be thick and the slots should be narrow so that $W/h \ll 1$. For a moderate aspect ratio, for example, $S/2h = 1/3$ and $W/h = 2/3$, the conductor-backed CPW becomes less dispersive than the corresponding microstrip line with the same aspect ratio, $W/h = 2/3$ [8]. In addition to the parasitic microstrip mode, this structure also supports leaky modes, which will be discussed later.

Multilayered CPW Configuration [24]

For a multilayered structure (Figure 7.3f) the effective dielectric constant can be expressed as

$$\epsilon_{re} = q_1\epsilon_{r1} + q_2\epsilon_{r2} + q_3\epsilon_{r3} + \dots + q_n\epsilon_{rn} \quad (7.44)$$

where q_1, q_2, \dots, q_n describe the filling factors for the various dielectric regions. To illustrate how to obtain the filling factors for a multilayered CPW we shall first consider the double-layered CPW configurations discussed earlier.

For the double-layered geometries we obtained expressions for ϵ_{re} in the form

$$\epsilon_{re} = 1 + q(\epsilon_r - 1) \quad (7.45)$$

where

$$q = C_{s1}^a / C^a \quad (7.46)$$

Here C^a is the capacitance of the CPW structure with air as dielectric and $C_s^a = C_2$ (for $\epsilon_r = 1$) is the capacitance of the substrate layer replaced by air as dielectric. Expressions for C^a and C_s^a were in the form $K(k_i)/K'(k_i)$. These expressions for the capacitances can be used to obtain the general expression for a multilayered CPW configuration.

The general expression for the capacitance of the i th layer with dielectric replaced by air is

$$C_{si}^a = 2\epsilon_0 \frac{K(k_i)}{K'(k_i)} \quad (7.47)$$

where

$$k_i = \begin{cases} a/b & \text{for the half-plane} \end{cases} \quad (7.48a)$$

$$k_i = \begin{cases} \frac{\sinh(\pi a/2h)}{\sinh(\pi b/2h)} & \text{for a dielectric layer of thickness } h \end{cases} \quad (7.48b)$$

$$k_i = \begin{cases} \frac{\tanh(\pi a/2h)}{\tanh(\pi b/2h)} & \text{for a dielectric layer backed by a conductor} \end{cases} \quad (7.48c)$$

Let us now determine the filling factors for the four-layered configuration in Figure 7.3(f). In this case,

$$C^a = 4\epsilon_0 \frac{K(k)}{K'(k)}, \quad k = \frac{a}{b} \quad (7.49)$$

The filling factor for the second layer, defined per (7.46), is

$$q_2 = C_{s2}^a / C^a \quad (7.50)$$

with

$$C_{s2}^a = 2\epsilon_0 \frac{K(k_2)}{K'(k_2)}, \quad k_2 = \frac{\sinh(\pi a/2h_2)}{\sinh(\pi b/2h_2)} \quad (7.51)$$

Similarly,

$$q_3 = C_{s3}^a / C^a \quad (7.52)$$

with

$$C_{s3}^a = 2\epsilon_0 \frac{K(k_3)}{K'(k_3)}, \quad k_3 = \frac{\sinh(\pi a/2h_3)}{\sinh(\pi b/2h_3)} \quad (7.53)$$

For the topmost layer, the filling factor is defined as

$$q_4 = \frac{C^a/2 - C_{s3}^a}{C^a} = \frac{1}{2} - \frac{C_{s3}^a}{C^a} \quad (7.54)$$

Similarly, for the lowest layer

$$q_1 = \frac{C^a/2 - C_{s2}^a}{C^a} = \frac{1}{2} - \frac{C_{s2}^a}{C^a} \quad (7.55)$$

It can be verified that

$$q_1 + q_2 + q_3 + q_4 = 1 \quad (7.56)$$

The effective dielectric constant of the CPW in Figure 7.3(f) follows from the use of q_1 , q_2 , q_3 , and q_4 in (7.44). The characteristic impedance can be determined from ϵ_{re} and C^a . The parallel plate capacitor in the w -plane, corresponding to Figure 7.3(f), is shown in Figure 7.12.

The above analysis can be extended to any number of dielectric layers in a CPW.

Asymmetric CPW Without Dielectric Substrate [28]

Unlike a symmetric coplanar waveguide, the widths of the slots on either side of the strip are not equal in an asymmetric coplanar waveguide (ACPW), shown in

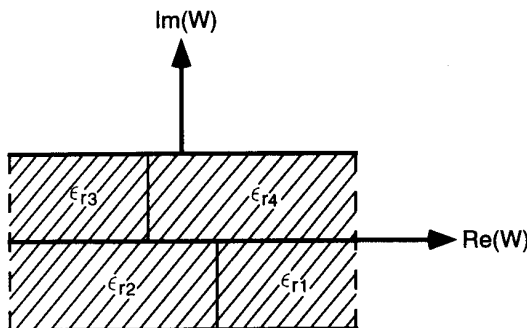


Figure 7.12 Approximate conformal mapped structure corresponding to the CPW of Figure 7.3(f).

Figure 7.3g. Unequal slot widths may occur due to fabrication tolerances. Sometimes unequal slot widths are desirable to introduce flexibility in design. Quasi-static analysis of an ACPW can be carried out as for the symmetric case except that we should now consider the complete lower half or upper half of the structure and not a quadrant as there is no plane of symmetry. We can perform the following sequence of conformal mappings to transform the ACPW of Figure 7.13(a) into a parallel plate of Figure 7.13(d):

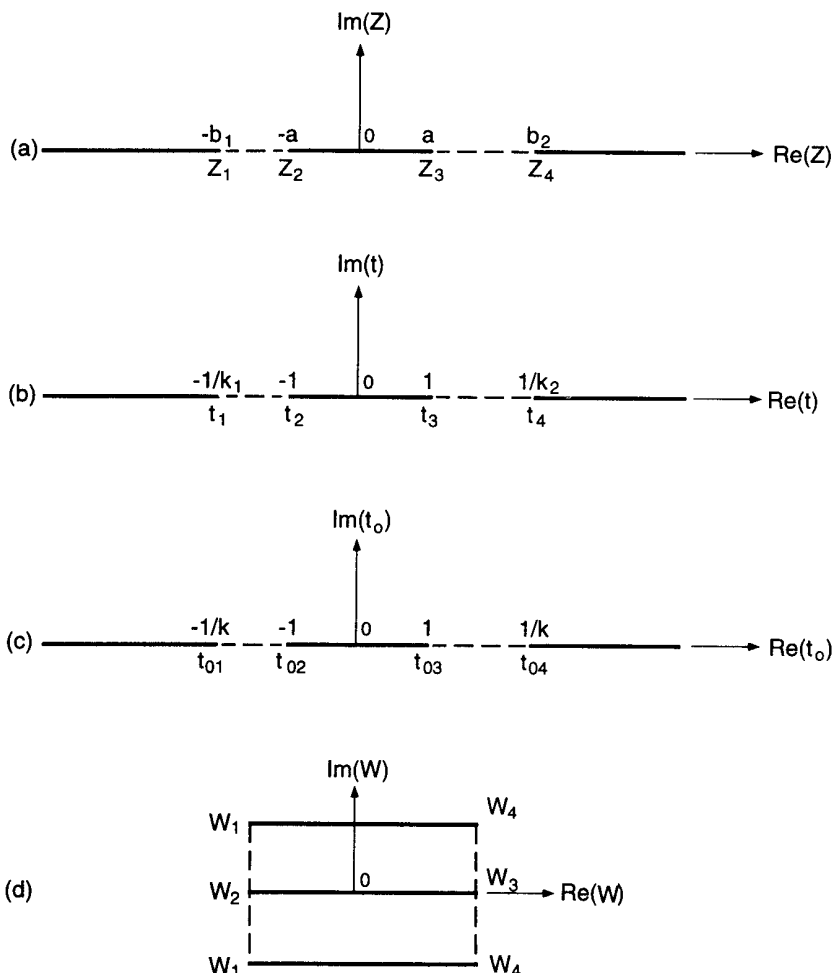


Figure 7.13 Conformal transformation of an asymmetric coplanar waveguide into a parallel plate geometry: (a) z -plane; (b) t -plane; (c) t_0 -plane; and (d) w -plane (from [28]).

$$t = \frac{z}{a} \text{ with } k_2 = \frac{a}{b_2}, \quad k_1 = \frac{a}{b_1} \quad [\text{Figure 7.13(b)}]$$

$$t_0^2 = \frac{t_3 + t_4}{2} \frac{t - t_3}{t - t_4} = \frac{1 + k_2}{2} \frac{t - 1}{k_2 t - 1} \text{ with } k^2 = \frac{2(k_1 + k_2)}{(1 + k_1)(1 + k_2)} \quad [\text{Figure 7.13(c)}]$$

$$w = \int \frac{dt_0}{\sqrt{(1 - t_0^2)(1 - k^2 t_0^2)}} \quad [\text{Figure 7.13(d)}]$$

The dimensions in the w -plane are

$$\frac{w_3 w_4}{ow_3} = \frac{w_5 w_4}{w_2 o} = 2 \frac{K'(k_7)}{K(k_7)}$$

where $w_3 w_4$, ow_3 , $w_2 o$ are distances in the w -plane as shown in Figure 7.13(d),

$$k_7^2 = k^2 = \frac{2(k_1 + k_2)}{(1 + k_1)(1 + k_2)}$$

or

$$k_7 = \sqrt{\frac{2a(b_1 + b_2)}{(a + b_1)(a + b_2)}} \quad (7.57a)$$

and

$$k'_7 = \sqrt{\frac{1 - k_1}{1 + k_1} \frac{1 - k_2}{1 + k_2}} = \sqrt{\frac{(b_1 - a)(b_2 - a)}{(b_1 + a)(b_2 + a)}} \quad (7.57b)$$

The capacitance of the parallel plate capacitor in Figure 7.13(d) then becomes

$$C^a = 2\epsilon_0 \frac{K(k_7)}{K'(k_7)} \quad (7.58)$$

Therefore,

$$Z_{0cp} = 60\pi \frac{K'(k_7)}{K(k_7)} \quad (7.59)$$

Identical expressions for k_7 and k'_7 are obtained in [25].

Asymmetric CPW with Finite Dielectric Thickness h [28]

Expressions for the capacitances for this geometry (Figure 7.3h) were derived in [29]. These expressions are based on a number of assumptions that are difficult to justify. We present an approach, due to Svacina [28], that is much simpler.

The mapping functions used are a combination of the mappings described for the symmetric CPW case with finite dielectric thickness and the asymmetric CPW case without dielectric substrate. Thus the sequence of mapping functions is

$$z_0 = \sinh\left(\frac{\pi}{2} \frac{z}{h}\right)$$

$$t = z_0/a$$

$$t_0^2 = \frac{1 + k_2}{2} \frac{t - 1}{k_2 t - 1}$$

and

$$w = \int \frac{dt_0}{\sqrt{(1 - t_0^2)(1 - k^2 t_0^2)}}$$

where k was defined in connection with Figure 7.13(c).

The transformed structure in the w -plane is identical with the lower half of Figure 7.13(d) but filled with the dielectric of permittivity ($\epsilon_r - 1$). The ratio of the height and the width of the parallel plate are, however,

$$\frac{w_3 w_4}{o w_3} = 2 \frac{K'(k_8)}{K(k_8)}$$

where

$$k_8^2 = \frac{2(k_{1\epsilon} + k_{2\epsilon})}{(1 + k_{1\epsilon})(1 + k_{2\epsilon})}$$

$$k_{1\epsilon} = \frac{\sinh(\pi a/2h)}{\sinh(\pi b_1/2h)}$$

and

$$k_{2\epsilon} = \frac{\sinh(\pi a/2h)}{\sinh(\pi b_2/2h)}$$

Thus

$$C_2 = \epsilon_0(\epsilon_r - 1) \frac{K(k_8)}{K'(k_8)} \quad (7.60)$$

The expression for C^a is still of the form (7.58). Therefore,

$$\epsilon_{re} = 1 + \frac{C_2}{C^a} = 1 + \frac{\epsilon_r - 1}{2} \frac{K(k_8)}{K'(k_8)} \frac{K'(k_7)}{K(k_7)} \quad (7.61)$$

and

$$Z_{0cp} = \frac{30\pi}{\sqrt{\epsilon_{re}}} \frac{K'(k_7)}{K(k_7)} \quad (7.62)$$

The above approach has been generalized to the multilayered ACPW in [30].

It has been observed from the computations of (7.61) and (7.62) that for a given shape ratio $2a/(2a + b_1 + b_2)$, the line asymmetry gives rise to a decrease in characteristic impedance and an increase in effective dielectric constant. However, these variations are not significant for asymmetry factors up to 25 percent [29] (asymmetry factor AF is defined as $AF = 1 - b_1/b_2$ for $b_1 \leq b_2$ and $AF = 1 - b_2/b_1$ for $b_1 \geq b_2$).

Equation (7.60) for C_2 does not reduce to the corresponding expression for the symmetric case merely by substituting $b_1 = b_2 = b$. This derivation is given next [28]. For the symmetric case, $k_{1\epsilon} = k_{2\epsilon} = k_\epsilon$. Then

$$k_8 = 2 \frac{\sqrt{k_\epsilon}}{1 + k_\epsilon}, \quad k_\epsilon = \frac{\sinh(\pi a/2h)}{\sinh(\pi b/2h)} \equiv k_2$$

Now, we use the following properties of $K(\cdot)$ and $K'(\cdot)$ [31]

$$K(k_8) = K\left(2 \frac{\sqrt{k_\epsilon}}{1 + k_\epsilon}\right) = (1 + k_\epsilon) K(k_\epsilon)$$

$$K'(k_8) = K(k'_8) = K\left(\frac{1 - k_\epsilon}{1 + k_\epsilon}\right) = \frac{1 + k_\epsilon}{2} K'(k_\epsilon)$$

Thus

$$\frac{K(k_8)}{K'(k_8)} = 2 \frac{K(k_\epsilon)}{K'(k_\epsilon)} = 2 \frac{K(k_2)}{K'(k_2)} \quad (7.63)$$

and (7.60) reduces to (7.15).

7.2.2 Quasi-Static Analysis of Coplanar Strips (CPS)

Coplanar strips (CPS), like coplanar waveguide, offer flexibility in the design of planar microwave and millimeter-wave circuits in that devices can be mounted in series as well as shunt. It is easier to realize high impedances with CPS than CPW. Further, CPS is a balanced transmission line like slotline and is useful in balanced circuits such as mixers and modulators and as interconnects in high-speed digital circuits. Coplanar strips are widely used in integrated optic traveling wave modulators [32, 33] and optical control microwave attenuators and modulators [34]. Like CPW, practical CPS lines use a finite substrate thickness. The geometry of this line and its field distributions are shown in Figure 7.2. Due to fabrication tolerances we may end up with a CPS in which the two strips do not have the same width. This line is called an asymmetric CPS. Sometimes, it is desirable to use an asymmetric CPS to adjust the characteristic impedance by changing the width of one of the strips while keeping the width of the other strip and the slot width fixed. The asymmetric CPS geometry is shown in Figure 7.14(a, b, c).

CPS can also be analyzed using the conformal mapping method. Since coplanar strips and coplanar waveguide geometries are complementary to each other in the metallization plane, the transformation used for CPW can also be applied to the CPS. However, the electric and magnetic walls of the parallel plate geometry derived earlier will get interchanged. Results for the various CPS geometries are given in this section.

Symmetric CPS with Infinitely Thick Substrate [35]

The geometry of this CPS line is similar to that shown in Figure 7.2(a) with $h \rightarrow \infty$. Capacitances C_1 and C_2 contributed by the electric field in the air and dielectric regions, respectively, are given by

$$C_1 = \epsilon_0 \frac{K'(k_1)}{K(k_1)} \quad k_1 = \frac{S}{S + 2W} = \frac{a}{b} \quad (7.64)$$

$$C_2 = \epsilon_0 \epsilon_r \frac{K'(k_1)}{K(k_1)} \quad (7.65)$$

$$\epsilon_{re} = \frac{C_1 + C_2}{2C_1} = \frac{\epsilon_r + 1}{2} \quad (7.66)$$

and

$$Z_{0cs} = \frac{120\pi}{\sqrt{\epsilon_{re}}} \frac{K(k_1)}{K'(k_1)} \quad (7.67)$$

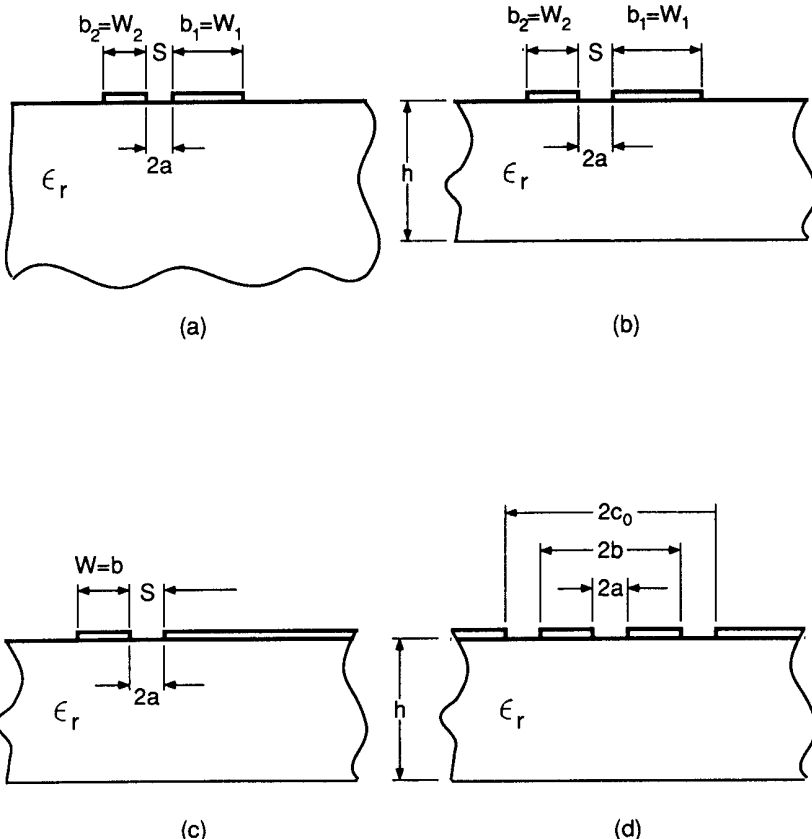


Figure 7.14 Various types of coplanar strips: (a) asymmetric CPS; (b) asymmetric CPS with finite dielectric thickness; (c) asymmetric CPS with an infinitely wide strip; and (d) CPS with lateral ground planes.

The characteristic impedance, computed from (7.67), is plotted in Figure 7.15 (curve $h/b \rightarrow \infty$).

Asymmetric CPS with Infinitely Thick Substrate [36]

In this case (shown in Figure 7.14a), the expressions obtained are

$$C_2 = 2\epsilon_0\epsilon_r \frac{K'(k_2)}{K(k_2)} \quad (7.68)$$

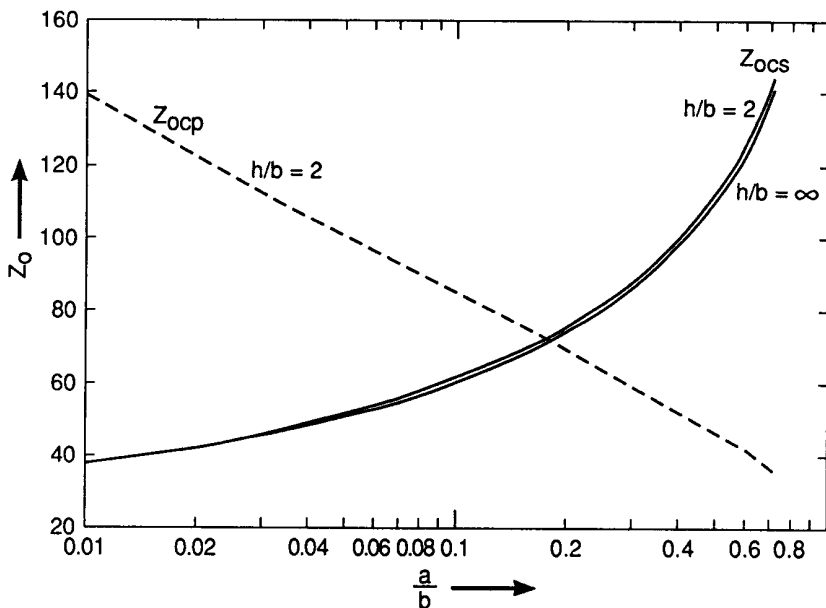


Figure 7.15 Variation of characteristic impedance for CPS and CPW as a function of aspect ratio a/b with h/b as a parameter ($\epsilon_r = 13$).

with

$$k'_2 = \sqrt{\frac{W_1}{W_1 + S} \frac{W_2}{W_2 + S}} \quad (7.69)$$

$$\epsilon_{re} = \frac{\epsilon_r + 1}{2} \quad (7.70)$$

and

$$Z_{0cs} = \frac{60\pi}{\sqrt{\epsilon_{re}}} \frac{K(k_2)}{K'(k_2)} \quad (7.71)$$

The above equations are similar to those given in [37, 38].

Asymmetric CPS with Finite Dielectric Thickness [39]

For this geometry (Figure 7.14b) we get,

$$\epsilon_{re} = 1 + \frac{\epsilon_r - 1}{2} \frac{K(k_4)}{K'(k_4)} \frac{K'(k_3)}{K(k_3)} \quad (7.72)$$

with $k_3 = k'_2$ of (7.69),

$$k_4 = \sqrt{\frac{\sinh(\pi W_1/2h)}{\sinh(\pi(W_1 + S)/2h)} \frac{\sinh(\pi W_2/2h)}{\sinh(\pi(W_2 + S)/2h)}} \quad (7.73)$$

and

$$Z_{0cs} = \frac{60\pi}{\sqrt{\epsilon_{re}}} \frac{K'(k_3)}{K(k_3)} \quad (7.74)$$

These expressions are similar to those available in [38].

Symmetric CPS with Finite Dielectric Thickness

Conformal transformation analysis of symmetric CPS with finite dielectric thickness (Figure 7.2a) has been conducted. But the values of ϵ_{re} and Z_{0cs} do not agree with the results of numerical analysis reported in [12]. It has been found that (7.17) for ϵ_{re} of CPW gives good agreement for $h/b > 1$. Ghione and Naldi [40] also have suggested the use of (7.17) because of the complementary natures of CPS and CPW. The expression for the characteristic impedance of a CPS is [40]

$$Z_{0cs} = \frac{120\pi}{\sqrt{\epsilon_{re}}} \frac{K(k_1)}{K'(k_1)} \quad (7.75)$$

Values of Z_{0cs} based on (7.75) and (7.17) have been calculated and are plotted in Figure 7.15 for two values of h/b . We also plotted the characteristic impedance of a CPW for $h/b = 2$. Comparison shows that $Z_{0cs} + Z_{0cp} \approx \text{constant}$ with the aspect ratio; that is, CPS and CPW are complementary in behavior.

Asymmetric CPS with an Infinitely Wide Strip [38]

A CPS with an infinitely wide strip (Figure 7.14c) is commonly used in electro-optic modulators [41, 42]. An expression for the effective dielectric constant is available in [38]. It is found that the expressions obtained for the earlier case, (7.72) to (7.74), reduce to the corresponding expressions for this configuration in the limit when one of the strip widths is increased to infinity. Let $W_2 \rightarrow \infty$ and $W_1 = W$. Then

$$q = \frac{K(k_7)}{K'(k_7)} \frac{K'(k_6)}{K(k_6)} \quad (7.76)$$

with

$$k_6 = k'_2|_{W_2 \rightarrow \infty, W_1 = W} = \sqrt{\frac{W}{W + S}} \quad (7.77)$$

$$k_7 = k_4|_{W_2 \rightarrow \infty, W_1 = W} = \sqrt{\frac{\sinh(\pi W/2h)}{\sinh(\pi(W + S)/2h)}} \sqrt{e^{-\pi S/2h}} \quad (7.78)$$

and

$$Z_{0cs} = \frac{60\pi}{\sqrt{\epsilon_{re}}} \frac{K'(k_6)}{K(k_6)} \quad (7.79)$$

CPS with Lateral Ground Planes on Finitely Thick Substrate [43]

The presence of ground planes in this configuration (Figure 7.14d) reduces line-to-line coupling and eliminates the parasitic TE_0 dielectric slab waveguide mode of a conventional CPS. The configuration of this CPS line is complementary to the CPW with finite width ground planes (see Figure 7.3(b)). It may be assumed that the propagation constant is the same for complementary lines in the quasi-static limit [44]. Therefore, the effective dielectric constant of this CPS line is given by (7.28). The characteristic impedance is, however, given by the expression

$$Z_{0cs} = \frac{120\pi}{\sqrt{\epsilon_{re}}} \frac{K(k_3)}{K'(k_3)} \quad (7.80)$$

where k_3 is defined by (7.23). It is found that this line is less dispersive compared to a conventional CPS. Further, lower values of characteristic impedance can be obtained by adjusting the width of the outer slots [40].

We have made two assumptions in this quasi-static analysis: (1) modeling of the slots and dielectric interfaces by magnetic walls, and (2) the filling factor is not a function of the type of dielectric interface but depends only on the physical dimensions of the dielectric layers. The first assumption leads to exact results in the limiting cases when the substrate thickness approaches zero or infinity or when the substrate is replaced by air. For other cases this assumption has been verified in [24]. However, comprehensive comparisons with results from a rigorous fullwave analysis should be carried out to determine the accuracy of the above assumptions. Hybrid-mode analysis is described next, and the propagation characteristics of coplanar lines based on the conformal mapping method and the hybrid-mode approach are compared. Higher order modes are also described.

7.2.3 Fullwave Analysis

Coplanar Waveguide (CPW)

A rigorous fullwave analysis of CPW has been carried out using Galerkin's method in the spectral domain [2–12]. It differs from the fullwave analysis of a single slotline (Section 5.2) only in selection of the basis functions, which now correspond to the physical configuration (Figure 7.1(a)) and the field distribution of a CPW. The slot electric field in the present case may be written as

$$E_x(x) = \sum_n a_n E_{xn}(x) \quad (7.81a)$$

and

$$E_z(x) = \sum_m b_m E_{zm}(x) \quad (7.81b)$$

The basis functions $E_{xn}(x)$ and $E_{zm}(x)$ for a CPW may be obtained from a translation of the corresponding basis functions, (5.25) and (5.27), for the slotline. One obtains [15]

$$E_{xn}(x) = \begin{cases} \frac{T_{n-1}(x'/\zeta)}{\sqrt{1 - (x'/\zeta)^2}} & n = 1, 2, 3 \dots \text{ for } a \leq |x| \leq b \\ 0 & \text{elsewhere} \end{cases} \quad (7.82a)$$

$$E_{zm}(x) = \begin{cases} U_m(x'/\zeta) & m = 1, 2, 3 \dots \text{ for } a \leq |x| \leq b \\ 0 & \text{elsewhere} \end{cases} \quad (7.82b)$$

where $\zeta = (b - a)/2$ and $x_0 = (a + b)/2$. $x' = x + x_0$ for the left slot and $x' = x - x_0$ for the right slot. The sine Fourier transform of $E_{xn}(x)$ and the cosine Fourier transform of $E_{zm}(x)$ are obtained as [3]

$$\hat{E}_{xn}(\alpha) = \pi \zeta J_{n-1}(\zeta \alpha) \begin{cases} (-1)^{(n-1)/2} \sin(x_0 \alpha) & \text{for } n \text{ odd} \\ (-1)^{(n/2)-1} \cos(x_0 \alpha) & \text{for } n \text{ even} \end{cases} \quad (7.83a)$$

$$\hat{E}_{zm}(\alpha) = m \pi \frac{J_n(\zeta \alpha)}{\alpha} \begin{cases} (-1)^{(m-1)/2} \cos(x_0 \alpha) & \text{for } m \text{ odd} \\ (-1)^{m/2} \sin(x_0 \alpha) & \text{for } m \text{ even} \end{cases} \quad (7.83b)$$

Another set of basis functions has been proposed by Fukuoka et al. [6]. This set is

$$E_{xn}(x) = \begin{cases} \frac{\cos\{n\pi x'/2\zeta\}}{\sqrt{\zeta^2 - x'^2}} & n = 0, 2, 4 \dots \text{ for } a \leq |x| \leq b \\ \frac{\sin\{n\pi x'/2\zeta\}}{\sqrt{\zeta^2 - x'^2}} & n = 1, 3, 5 \dots \text{ for } a \leq |x| \leq b \\ 0 & \text{elsewhere} \end{cases} \quad (7.84)$$

$$E_{zm}(x) = \begin{cases} \frac{\cos\{m\pi x'/2\zeta\}}{\sqrt{\zeta^2 - x'^2}} & m = 1, 3, 5 \dots \text{ for } a \leq |x| \leq b \\ \frac{\sin\{m\pi x'/2\zeta\}}{\sqrt{\zeta^2 - x'^2}} & m = 2, 4, 6 \dots \text{ for } a \leq |x| \leq b \\ 0 & \text{elsewhere} \end{cases} \quad (7.85)$$

The Fourier transforms of these basis functions are [6]

$$\tilde{E}_{xn}(\alpha) = \begin{cases} j\sqrt{\pi/2}\sin(\alpha x_0)[J_0(r_n) + J_0(s_n)] & n = 0, 2, 4 \dots \\ -j\sqrt{\pi/2}\cos(\alpha x_0)[J_0(r_n) - J_0(s_n)] & n = 1, 3, 5 \dots \end{cases} \quad (7.86a)$$

$$\tilde{E}_{zm}(\alpha) = \begin{cases} \sqrt{\pi/2}\cos(\alpha x_0)[J_0(r_m) + J_0(s_m)] & m = 1, 3, 5 \dots \\ \sqrt{\pi/2}\sin(\alpha x_0)[J_0(r_m) - J_0(s_m)] & m = 2, 4, 6 \dots \end{cases} \quad (7.86b)$$

where $J_0(\bullet)$ denotes the zeroth-order Bessel function of the first kind and

$$r_n = \left| \frac{2\zeta\alpha + n\pi}{2} \right| \quad \text{and} \quad s_n = \left| \frac{2\zeta\alpha - n\pi}{2} \right|$$

It may be noted that these sets of basis functions account for the edge effects of the slot field.

The characteristic impedance may be calculated using the voltage-current definition

$$Z_{0cp} = \frac{V}{I} = \frac{\int_{\sqrt{2}/2}^{\sqrt{2+w}} E_x(x) dx}{2 \int_0^{\sqrt{2}/2} J_z(x) dx} \quad (7.87)$$

One could also use a power-voltage definition, which yields

$$Z_{0cp} = \frac{V^2}{2P_{avg}} \quad (7.88)$$

As in the case of the slotline, P_{avg} is calculated in the spectral domain from the equation

$$P_{\text{avg}} = \frac{1}{4\pi} \int_{-\infty}^{\infty} \int_{-\infty}^{\infty} \{ \tilde{E}_x(\alpha, y) \tilde{H}_y^*(\alpha, y) - \tilde{E}_y(\alpha, y) \tilde{H}_x^*(\alpha, y) \} d\alpha dy \quad (7.89)$$

where α is the variable in the Fourier transform domain and the superscript \sim denotes the transform of the field.

The details of the method are similar to those used for analyzing microstrip lines (Section 2.2.2) and slotlines (Section 5.2) and will not be discussed here. A comparison of fullwave results with the quasi-static values is shown in Figure 7.16 for the guide wavelength of a CPW with finite dielectric thickness [14]. The basis functions used are the Chebyshev polynomials of (7.82). A good agreement is observed. Fullwave analysis for other configurations of CPW have been reported in [8, 45, 46]. Higher order modes in a CPW have also been investigated by using the above method of analysis [3, 14]. In [14] the substrate used is sapphire, which is anisotropic in nature with $\epsilon_1 = 9.4$ and $\epsilon_2 = 11.6$. The results are presented in Figure 7.17 for $h = 1$ mm, $a = 0.25$ mm, and $b = 1.25$ mm. The normalized propagation constant for the dominant even and odd modes, first higher order mode, and TM_0 mode for a grounded sapphire substrate are plotted as functions of frequency. It is seen from the figure that the undesired odd mode can propagate down to dc. However, this mode can be suppressed by connecting both the ground plane conductors together by wires or air bridges. Dispersion characteristics of the first higher order mode of the CPW and the TM_0 mode for a grounded slab are found to be similar. The characteristic impedance calculated using the voltage-current definition of (7.87) compares favorably at low frequencies with those calculated using the quasi-static approximation [4].

Coplanar Strips (CPS)

Fullwave analysis using Galerkin's method in the spectral domain has also been conducted for coplanar strips. In this case, the problem is formulated in terms of surface currents J_x and J_z on the strips. These currents are expressed in terms of sets of basis functions as

$$J_x(x) = \sum_n a_n J_{xn}(x) \quad (7.90a)$$

and

$$J_z(x) = \sum_m b_m J_{zm}(x) \quad (7.90b)$$

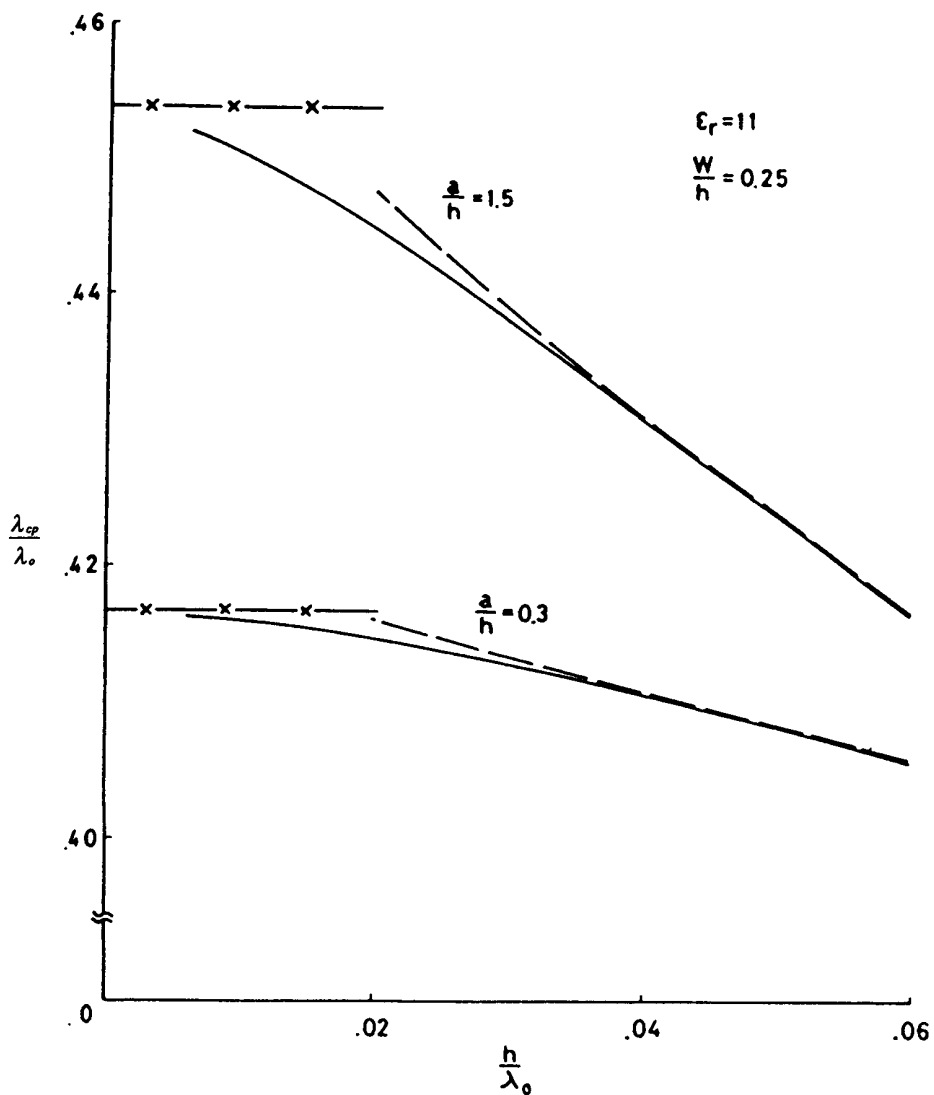


Figure 7.16 Comparison of fullwave and quasi-static results for CPW (from [14], © 1981 IEEE. Reprinted with permission.) (—X—X— quasi-static value, — fullwave value, - - - - from [2]).

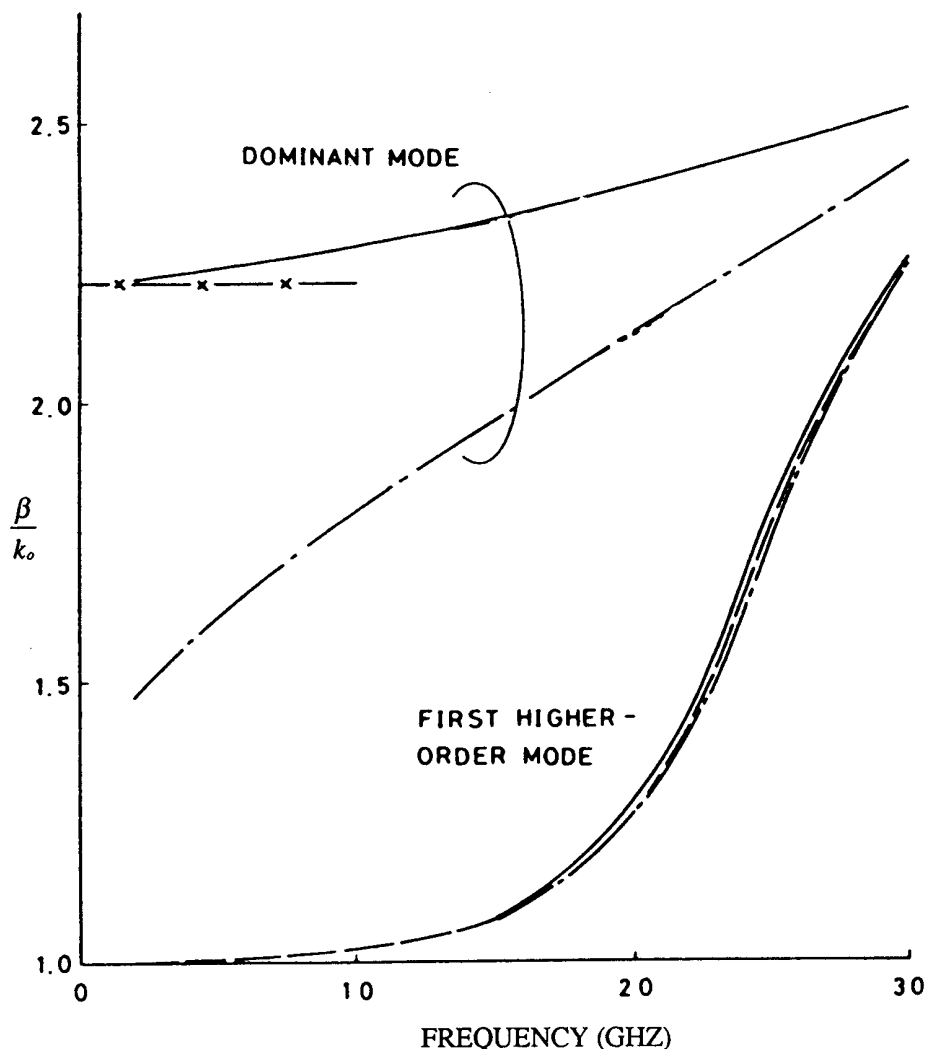


Figure 7.17 Dispersion curves for the dominant and first higher order modes in CPW (from [14], © 1981 IEEE. Reprinted with permission.) (—X—X— quasi-static value, — even modes, - - - odd modes, - - - TM₀ mode of a conductor-coated substrate).

A first-order solution, which is accurate enough for narrow strips, is obtained assuming that the transverse surface current J_x is negligible. However, for wide strips and for better accuracy both the components of current density should be considered. The basis functions $J_{zm}(x)$ are of the same form as $E_{xn}(x)$ for CPW. Similarly, $J_{sn}(x)$ are identical with $E_{zn}(x)$. These are given [7] as

$$J_{zm}(x) = \begin{cases} \pm \frac{\cos\{m\pi x'/2\zeta\}}{\sqrt{\zeta^2 - x'^2}} & m = 0, 2, 4 \dots \text{ for } a \leq |x| \leq b \\ \frac{\sin\{m\pi x'/2\zeta\}}{\sqrt{\zeta^2 - x'^2}} & m = 1, 3, 5 \dots \text{ for } a \leq |x| \leq b \\ 0 & \text{elsewhere} \end{cases} \quad (7.91a)$$

$$J_{zn}(x) = \begin{cases} \frac{\cos\{n\pi x'/2\zeta\}}{\sqrt{\zeta^2 - x'^2}} & n = 1, 3, 5 \dots \text{ for } a \leq |x| \leq b \\ \frac{\pm \sin\{(n+2)\pi x'/2\zeta\}}{\sqrt{\zeta^2 - x'^2}} & n = 2, 4, 6 \dots \text{ for } a \leq |x| \leq b \\ 0 & \text{elsewhere} \end{cases} \quad (7.91b)$$

The \pm sign for the two different strips, for even values of n and m , accounts for proper symmetry of the current distribution. In (7.91), $x' = x + x_0$ for the left strip and $x' = x - x_0$ for the right strip. The normalized propagation constant for symmetric CPS is plotted as a function of frequency in Figure 7.18 [47]. The substrate chosen has $\epsilon_r = 10.5$. It is observed that β/k_0 for the CPS mode increases very slowly with

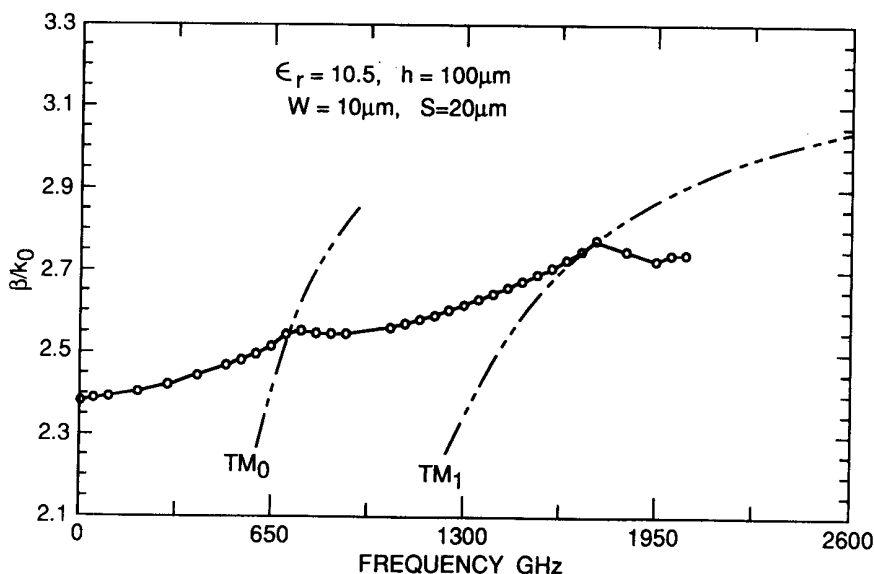


Figure 7.18 Dispersion curves for the dominant CPS mode and surface wave modes (from [47], © 1990 IEEE. Reprinted with permission.).

frequency. Therefore, over the bandwidth of components, $\epsilon_{re} = (\beta/k_0)^2$ can be considered to be almost constant. Dispersion curves for the surface wave modes TM_0 and TM_1 are also shown in this figure. Break points in the dispersion curve for the CPS mode occurs whenever β/k_0 for the mode becomes lower than that for the surface wave mode. These breaks are indications of strong coupling between the modes. Excitation of surface waves gives rise to an additional loss, as discussed later in Section 7.4.3.

The basis functions for these slots/strips can be used for the various CPW/CPS geometries discussed in Section 7.2.1. For the asymmetric geometries x_0 should be modified to the corresponding midpoints of the slots/strips.

Study of the numerical data for ϵ_{re} and Z_0 as a function of frequency and aspect ratio a/b for various types of coplanar lines brings out a number of interesting facts about dispersion. These are summarized in Section 7.3.2.

7.3 DESIGN CONSIDERATIONS

Analytical techniques for calculating the effective dielectric constant and characteristic impedance of coplanar lines were described in the last section. The effect of substrate thickness, finite width of the ground planes, conductor backing, cover height, and asymmetry were taken into account. Although the quasi-static values are good enough for some of the structures in the near millimeter region, fullwave analysis should be carried out for frequencies above 40 GHz. Similarly, the losses can be determined using the fullwave approach. But the computations are very time consuming and costly. An alternative to this approach is to use design equations that include the effect of dispersion in quasi-static values. The effect of metallization thickness on the characteristics of coplanar lines becomes important when the substrate ϵ_r is large and the aspect ratio a/b is small. Some of the coplanar line configurations become leaky due to the presence of parasitic modes. Coupling of power from the transmission line mode to the surface wave modes of the substrate may give rise to an increase in losses and unwanted coupling. The effect of dimensional tolerances becomes important when the fabrication limit for very narrow strips and slots is approached. All these aspects that influence the design of coplanar lines are discussed next. Finally, coplanar lines are compared with microstrip lines.

7.3.1 Design Equations

Closed-form expressions for the characteristic impedance and effective dielectric constant for various types of coplanar lines were obtained in the last section. They are simple enough to be calculated using scientific calculators. However, a design engineer requires the value of aspect ratio a/b for a desired value of Z_0 and substrate parameters ϵ_r and h . This type of expression is called the synthesis equation and is not available at present. For synthesis, search algorithms along with the analysis

equations may be used. For the initial guess in the search algorithm one can use the value of a/b (for a given Z_0) applicable for the infinitely thick substrate. The synthesis expression for this geometry can be obtained very easily by inverting (7.11) as follows.

For $0 \leq k_1 \leq 0.707$, that is, $K'(k_1)/K(k_1) \geq 1$ or $Z_{0cp}\sqrt{(\epsilon_r + 1)/2} \geq 30\pi$

$$\frac{a}{b}(= k_1) = \left[1 - \left(\frac{e^x - 2}{e^x + 2} \right)^4 \right]^{1/2} \quad (7.92a)$$

For $0.707 \leq k_1 \leq 1$, that is, $K'(k_1)/K(k_1) \leq 1$ or $Z_{0cp}\sqrt{(\epsilon_r + 1)/2} \leq 30\pi$

$$\frac{a}{b}(= k_1) = \left(\frac{e^{\pi^2/x} - 2}{e^{\pi^2/x} + 2} \right)^2 \quad (7.92b)$$

where

$$x = \frac{Z_{0cp}}{30} \sqrt{\frac{\epsilon_r + 1}{2}}$$

The synthesized value of a/b for the CPS can be obtained from (7.92) and the following relationship between Z_{0cp} and Z_{0cs} for an infinitely thick substrate (see (7.11) and (7.67))

$$\frac{Z_{0cp} Z_{0cs}}{(60\pi)^2} \frac{\epsilon_r + 1}{2} = 1 \quad (7.93)$$

To understand the use of (7.93) let us design a coplanar strip line for a given value of Z_0 . The corresponding Z_{0cp} for the CPW obtained from (7.93) is

$$Z_{0cp} = \frac{2}{\epsilon_r + 1} \frac{(60\pi)^2}{Z_0}$$

Now determine the value of a/b from (7.92) corresponding to the value of Z_{0cp} calculated above. The calculated value of a/b will yield the desired Z_{0cs} . Alternatively, one can invert (7.67) and obtain expressions similar to (7.92).

7.3.2 Dispersion

The synthesis procedure described above is based on quasi-static values for ϵ_{re} and Z_0 . The resulting design is strictly applicable at the lower end of microwave band

but can be used up to the lower end of the millimeter-wave band, that is, when $h/\lambda_0 \ll 1$. However, at millimeter-wave frequencies or for frequency-selective components, even at lower frequencies the effect of dispersion on Z_0 and especially on ϵ_{re} should be included in the design. For this purpose, a simple expression, similar to (2.131) for the microstrip line, is available. This expression, obtained by curve fitting the results of numerical simulation, is [48]

$$\sqrt{\epsilon_{re}(f)} = \sqrt{\epsilon_{re}(0)} + \frac{\sqrt{\epsilon_r} - \sqrt{\epsilon_{re}(0)}}{1 + G(f/f_{TE})^{-1.8}} \quad (7.94)$$

where

$$\begin{aligned} G &= e^{u\ell_n(2a/(b-a))+v} \\ u &= 0.54 - 0.64p + 0.015p^2 \\ v &= 0.43 - 0.86p + 0.54p^2 \\ p &= \ell_n(2a/h) \end{aligned}$$

In (7.94), $\epsilon_{re}(0)$ is the quasi-static value of ϵ_{re} and f_{TE} is the cutoff frequency for the TE_0 surface wave mode for the substrate. Its value can be obtained from (5.10) and is given by

$$f_{TE} = \frac{c}{4h\sqrt{\epsilon_r - 1}} \quad (7.95)$$

The accuracy of (7.94) is claimed to be 5 percent for the following range of parameters

$$\begin{array}{ll} 0.1 < W/h < 5 & 0.1 < S/W < 5 \\ 1.5 < \epsilon_r < 50 & 0 < f/f_{TE} < 10 \end{array}$$

It has been observed that $\epsilon_{re}(0)$ in (7.94) should be replaced by $(\epsilon_r + 1)/2$ so as to obtain a better match with experimental data for frequencies above 200 GHz [49].

As with microstrip lines, dispersion in coplanar lines modeled by (7.94) amounts to an increase in ϵ_{re} from the low-frequency value of $\epsilon_{re}(0)$ to the asymptote of ϵ_r . Coplanar lines on thinner substrates are less dispersive due to the larger value of f_{TE} . Moreover, conductor-backed CPW and those with finite width ground planes are found to be less dispersive than others. An analytical expression for the effect of dispersion on Z_0 is not available. But, it is understood that the amount of dispersion in Z_0 is of the same order as for the microstrip line [45]. To a first-order approximation one can include the effect of dispersion on Z_0 through the dispersion in ϵ_{re} , that is,

$$Z_0(f) = \frac{Z_0^a}{\sqrt{\epsilon_{re}(f)}}, \quad Z_0^a = \frac{1}{cC^a} \quad (7.96)$$

where Z_0^a is the characteristic impedance with air as dielectric.

7.3.3 Effect of Metallization Thickness

The values of Z_0 and ϵ_{re} obtained earlier are valid for infinitesimally thin metallic strip conductor and ground planes. But in practice, the metallization has a finite thickness t that affects the characteristics. The effect of t on the characteristic impedance and the effective dielectric constant of a CPW has been analyzed in [15, 50–52] based on the quasi-static approximation [50] as well as frequency-dependent solution [15, 51, 52]. It has been observed that an increase in metallization thickness is accompanied by a corresponding decrease in ϵ_{re} and Z_0 . The decrease in ϵ_{re} is larger for the case of a substrate with higher dielectric constant and lower aspect ratio. On the contrary, the decrease in Z_0 with increase in t is smaller for the higher dielectric constant substrate [15]. For example, for $\epsilon_r = 20$ and $t/W = 0.1$, the decrease in ϵ_{re} is about 11 percent and the decrease in Z_0 is about 7 percent. For $\epsilon_r = 2.6$ and for the same value of t/W , the decrease in ϵ_{re} is about 5 percent and the decrease in Z_0 is about 10 percent. The decrease in ϵ_{re} and Z_0 with increase in t can be explained from the observation that a higher metallization thickness gives rise to additional concentration of the electric field between the metalized portions of the slots, thus increasing the value of C^a . The increase in C^a is expected to be higher for narrow slots.

The effect of metallization thickness on the characteristics of coplanar lines can be taken into account empirically by defining effective values of strip width and slot width. This is similar to the concept of increasing microstrip width W due to thickness t , discussed in Section 2.4.5. For a CPW (Figure 7.20), we can write

$$S_e = S + \Delta \quad (7.97a)$$

and therefore

$$W_e = W - \Delta \quad (7.97b)$$

where

$$\Delta = (1.25t/\pi)[1 + \ell n(4\pi S/t)] \quad (7.98)$$

The characteristic impedance is found as

$$Z_{0cp} = \frac{30\pi}{\sqrt{\epsilon_{re}^t}} \frac{K'(k_e)}{K(k_e)} \quad (7.99)$$

where k_e is the effective aspect ratio given by

$$k_e = S_e / (S_e + 2W_e) \cong k + (1 - k^2)\Delta/2W$$

and ϵ'_{re} is the effective dielectric constant for a thick CPW. An expression for ϵ'_{re} is derived by adding a term due to metal thickness to the expression for capacitance of CPW and modifying the subsequent result empirically such that the results agree with numerically evaluated values given in [50] (for $\epsilon_r = 20$ and $t/W \leq 0.1$). The final expression for ϵ'_{re} may be written as

$$\epsilon'_{re} = \epsilon_{re} - \frac{0.7(\epsilon_{re} - 1)t/W}{[K(k)/K'(k)] + 0.7t/W} \quad (7.100)$$

Variations of Z_{0cp} and the effective dielectric constant for a CPW with aspect ratio for various values of t/W are shown in Figure 7.19. As expected Z_{0cp} and ϵ'_{re} decrease with increasing t/W . The effect of t/W on these characteristics is higher for smaller values of the aspect ratio. These results are in good agreement with those reported by Kitazawa [50]. The model presented in (7.97) and (7.98) is less accurate for narrow slots.

For coplanar strips, the effect of strip thickness on Z_{0cs} and ϵ'_{re} is similar to that in CPW, and closed-form expressions are obtained as

$$Z_{0cs} = \frac{120\pi}{\sqrt{\epsilon'_{re}}} \frac{K(k_e)}{K'(k_e)} \quad (7.101)$$

where (for $W_e = W + \Delta$ and $S_e = S - \Delta$)

$$k_e = S_e / (S_e + 2W_e) \cong k - (1 - k^2)\Delta/2W$$

and

$$\Delta = (1.25t/\pi)[1 + \ell_n(4\pi W/t)]$$

The effective dielectric constant for a CPS may be written as

$$\epsilon'_{re} = \epsilon_{re} - \frac{1.4(\epsilon_{re} - 1)t/S}{[K'(k)/K(k)] + 1.4t/S} \quad \epsilon_r \geq 9, t/W < 0.1 \quad (7.102)$$

7.4 LOSSES

7.4.1 Dielectric Loss

Coplanar lines have three types of losses: dielectric, ohmic, and radiation/surface wave. The expressions for the attenuation constant due to dielectric loss in CPW

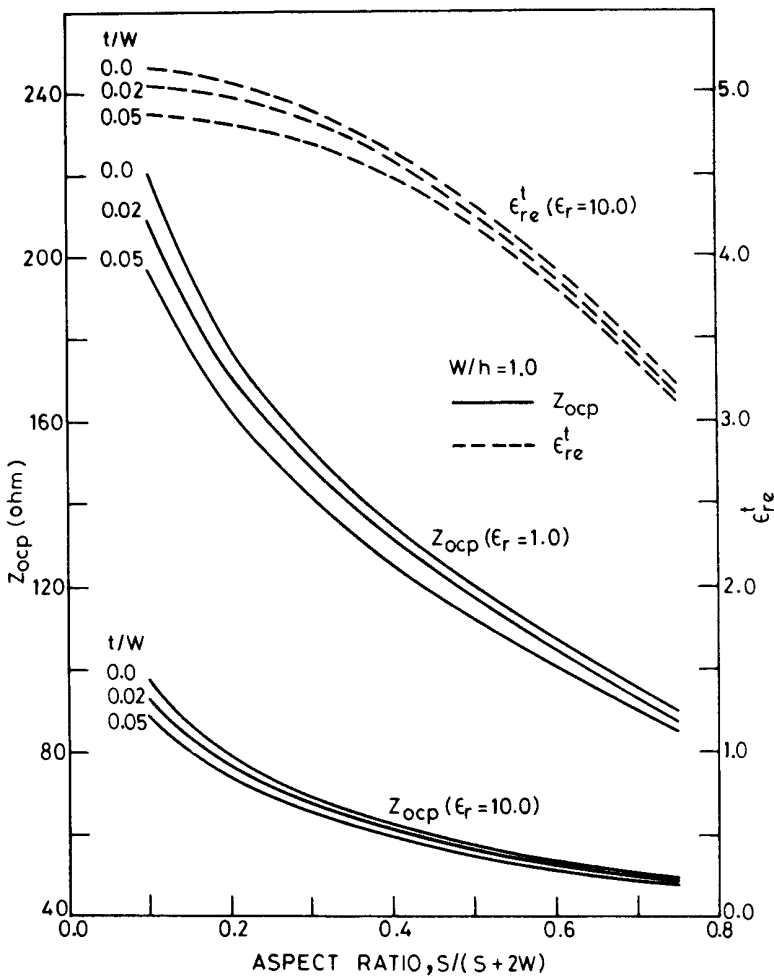


Figure 7.19 Effect of strip thickness on CPW characteristics.

is the same as that for a microstrip. This was discussed in Chapter 2, (2.81), and is reproduced here

$$\alpha_d = 2.73 \frac{\epsilon_r}{\sqrt{\epsilon_{re}}} \frac{\epsilon_{re} - 1}{\epsilon_r - 1} \frac{\tan \delta}{\lambda_0} \text{ dB/unit length} \quad (7.103)$$

In (7.103), ϵ_{re} represents the effective dielectric constant of the coplanar line.

7.4.2 Conductor Loss

When the quasi-static approximation is valid, one can use Wheeler's incremental inductance formula to evaluate ohmic loss. This formula was discussed in Chapter 2. Various recessions considered in CPW configuration (see Figure 7.20), are as follows:

$$\delta S = -2\delta n \quad (\text{due to recession of edges of strip conductor})$$

$$\delta W = -2\delta n \quad (\text{due to recession of edges of strip conductor and edges of ground conductors})$$

$$\delta t = -2\delta n \quad (\text{due to recession of top and bottom of conductors})$$

where δn is one-half the skin depth δ ($= \sqrt{2/\omega\mu\sigma}$).

Symmetric CPW and CPS

After taking into account recessions in all the conductor walls, the expression for the attenuation constant due to ohmic losses for a symmetric CPW may be written as

$$\alpha_c^{cw} = 0.023 \frac{R_s}{Z_{0cp}} \left[\frac{\partial Z_{0cp}^a}{\partial W} - \frac{\partial Z_{0cp}^a}{\partial S} - \frac{\partial Z_{0cp}^a}{\partial t} \right] \quad \text{dB/unit length} \quad (7.104)$$

where Z_{0cp}^a is the characteristic impedance of a CPW with air as dielectric and R_s is the surface resistivity of the conductors. After substituting various partial derivatives in (7.104), the final expression for conductor loss may be written as

$$\alpha_c^{cw} = 4.88 \times 10^{-4} R_s \epsilon_{re} Z_{0cp} \frac{P'}{\pi W} \left(1 + \frac{S}{W} \right) \cdot \left\{ \frac{1 + 1.25t/\pi S + (1.25/\pi) \ell_n(4\pi S/t)}{[2 + S/W - (1.25t/\pi W)(1 + \ell_n(4\pi S/t))]^2} \right\} \quad \text{dB/unit length} \quad (7.105)$$

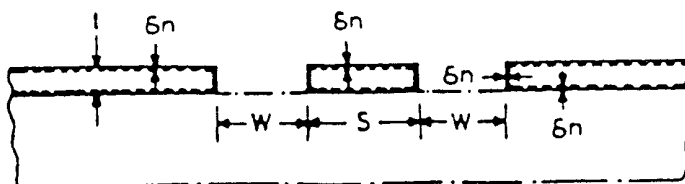


Figure 7.20 Recession of conductors of CPW for loss calculation using incremental inductance rule.

where

$$P' = \left[\frac{K(k_1)}{K'(k_1)} \right]^2 P \quad (7.106)$$

and

$$P = \begin{cases} \frac{k_1}{(1 - \sqrt{1 - k_1^2})(1 - k_1^2)^{3/4}} & \text{for } 0 \leq k_1 \leq 0.707 \\ \frac{1}{(1 - k_1)\sqrt{k_1}} \left(\frac{K'(k_1)}{K(k_1)} \right)^2 & \text{for } 0.707 \leq k_1 \leq 1.0 \end{cases} \quad (7.107)$$

In the above approach the value of the attenuation constant is very much dependent on the accuracy of the model used for finding equivalent strip width and slot width to account for the metallization thickness. The model presented in (7.97) to (7.98) is such that it is likely to be less accurate for narrow slots, that is, large values of aspect ratio, because the change Δ in strip widths depends on t and S only and not on slot width W .

Numerical evaluation of the derivatives in (7.104) has been proposed by Yamashita et al. [53]. In this approach, the change in the inductance per unit length of the line due to recession of all the metal surfaces by half a skin depth δ is evaluated in terms of the change of the line capacitance C^a with air as dielectric. If C_δ^a is the new capacitance of the line obtained by recessing all the metal surfaces by $\delta/2$, then [53]

$$\sum_m \frac{\partial L}{\partial n_m} \frac{\delta}{2} = \frac{1}{v_p^2} \left(\frac{1}{C^a} - \frac{1}{C_\delta^a} \right)$$

where v_p is the phase velocity. Substituting the above expression in (2.76) one obtains for the conductor attenuation

$$\alpha_c = \frac{\pi}{\lambda_0} \sqrt{\epsilon_{re}} \left(\frac{C^a - C_\delta^a}{C_\delta^a} \right) \text{ neper/unit length} \quad (7.108)$$

One advantage of the above approach is that one does not need to obtain analytical expressions for the derivatives of Z_0 with respect to various parameters of the line. Instead, the expression or the technique used to evaluate C^a can be used to determine C_δ^a and also to obtain the numerical derivative of C^a implied in (7.108). Moreover, the factor $C^a - C_\delta^a$ cancels the inaccuracies in C_δ^a and C^a that are inherent in the formulation and numerical computation.

Owyang and Wu [54] and Tuncer et al. [55] have used a direct approach to determine the effect of metal thickness on conductor loss. They have evaluated the power dissipated in the line through conformal mapping of the current density in the finite metal thickness structure. Their expression for conductor loss of a CPW has been corrected by Ghione [36] and is given as

$$\alpha_c^{\text{cw}} = \frac{8.68 R_s \sqrt{\epsilon_{\text{re}}}}{480 \pi K(k_1) K'(k_1) (1 - k_1^2)} \left\{ \frac{1}{a} \left[\pi + \ell_n \left(\frac{8\pi a(1 - k_1)}{t(1 + k_1)} \right) \right] + \frac{1}{b} \left[\pi + \ell_n \left(\frac{8\pi b}{t} \frac{1 - k_1}{1 + k_1} \right) \right] \right\} \text{ dB/unit length} \quad (7.109)$$

It is assumed in deriving the above expression that the strip thickness $t > 3\delta$ and $t \ll a$ and $(b - a)$. Equation (7.109) is valid for symmetric CPW configurations with finite and infinite dielectric thickness and for multilayered structures. These effects are manifested in (7.109) through ϵ_{re} . Due to the complementary nature of a CPW and CPS, (7.109) is applicable for the conductor loss of symmetric CPS also with the appropriate meanings for a , b , and ϵ_{re} .

Series expansions for $K(k)$, needed for the evaluation of (7.109), are available. These are given as follows [31].

For $0 \leq k \leq 0.707$

$$K(k) = \frac{\pi}{2} \left\{ 1 + 2 \frac{k^2}{8} + 9 \left(\frac{k^2}{8} \right)^2 + 50 \left(\frac{k^2}{8} \right)^3 + 306.25 \left(\frac{k^2}{8} \right)^4 + \dots \right\} \quad (7.110a)$$

and, for $0.707 \leq k \leq 1$

$$K(k) = p + (p - 1)(k'^2/4) + 9(p - 7/6)(k'^4/64) + 25(p - 37/30)(k'^6/256) + \dots \quad (7.110b)$$

where

$$p = \ell_n(4/k') \quad (7.111)$$

The maximum error in the series of (7.110a) and (7.110b) occurs at the crossover point $k = 0.707$ and is about 0.3 percent. For $k \rightarrow 0$ or $k \rightarrow 1$ the error also approaches zero.

Ghione [36] has compared the values of normalized attenuation obtained from (7.105), (7.109) with the quasi-static numerical values obtained by Gopinath [56] for metal thickness $t = 5 \mu\text{m}$, $2b = 1.2 \text{ mm}$, and substrate $\epsilon_r = 13.0$. This comparison is shown in Figure 7.21. It may be observed from this figure that (7.109) gives values of attenuation comparable to the numerical results. However, (7.105)

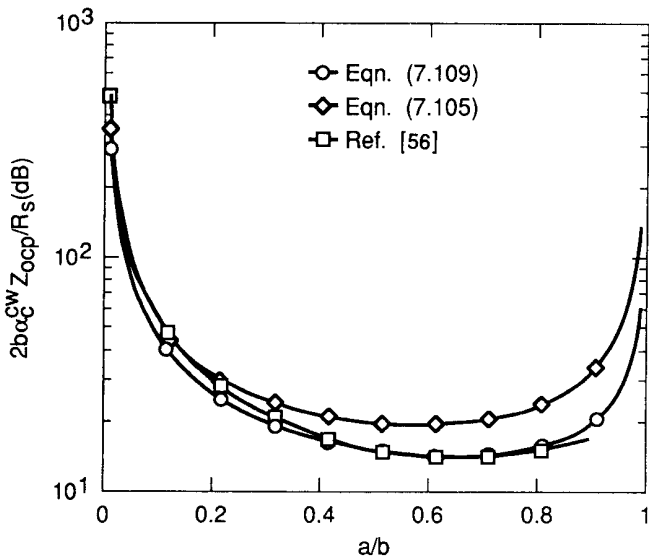


Figure 7.21 Comparison of quasi-static values of normalized conductor attenuation constant for symmetric CPW as a function of a/b (from [36], © 1993 IEEE. Reprinted with permission.).

yields higher values for the aspect ratio $a/b > 0.2$. This is due to the fact that the model presented in (7.97) to (7.98) is less accurate for narrow slots.

Tuncer et al. [55] have developed a quasi-static model for the conductor loss of a CPW. The CPW is conformal mapped into a parallel plate configuration, where conductor loss is evaluated using a conductor surface impedance that is scaled by the conformal mapping. The effects of skin depth and current crowding are taken into account in the model. A comparison between experimental measurements and the calculated values show an excellent agreement without the need of a scaling factor.

Asymmetric CPW and CPS

An expression for the conductor loss of an asymmetric CPW has also been derived [36]. The derivation is based on the approach described by Owyang and Wu [54] and gives

$$\alpha_c^{acw} = \frac{8.68 R_s \sqrt{\epsilon_{re}}}{480 \pi K(k) K(k')} \cdot \{ \Phi(b_1 - a, k) + \Phi(b_2 - a, k) + \Phi(2a, k') - \Phi(b_1 + b_2, k') \} \text{ dB/unit length} \quad (7.112)$$

where

$$\Phi(p, k) = \frac{1}{p} \left\{ \ell_n \left(\frac{4\pi p k}{t} \right) + \pi \right\} \quad (7.113)$$

and k and k' were defined earlier by (7.57a) and (7.57b), respectively.

Like the symmetric case, (7.112) is also valid for strip thickness much greater than the skin depth, and much less than the strip width and both the slot widths. It may also be pointed out that due to the complementary nature of an asymmetric CPW and asymmetric CPS, (7.112) holds for the conductor loss of ACPS also with the appropriate meanings for a , b_1 , b_2 , and ϵ_{re} .

Conductor loss for an ACPS with an infinitely wide strip can be obtained from the limiting case of an ACPW when $b_1 \rightarrow \infty$ and $b_2 = b$ [36]. One obtains

$$\alpha_c^{acs} = \frac{8.68R_s\sqrt{\epsilon_{re}}}{480\pi K(k)K(k')} \{ \Phi(b-a, k) + \Phi(2a, k') \} \text{ dB/unit length} \quad (7.114)$$

where $\Phi(\bullet)$ is defined by (7.113) and

$$k = \sqrt{2a/(b+a)} \quad k' = \sqrt{(b-a)/(b+a)} \quad (7.115)$$

The expressions (7.104) to (7.114) for the conductor loss are based on the incremental inductance rule. Their accuracy should be checked against the more accurate fullwave computations. This study has been carried out by a number of investigators [4, 57, 58]. Impedance boundary conditions are imposed on the metallizations with finite conductivity in [57]. The perturbation method along with spectral-domain approach are used in [4, 58] to determine the conductor loss. Equation (5.51) is used along with the appropriate values for the fields of coplanar lines. Figure 7.22 shows the value of $\alpha_c + \alpha_d$ as a function of Z_0 for a symmetric CPW on finite thickness GaAs substrate. The dielectric loss is negligible compared to the conductor loss. The numerical results of [4, 58] are compared in this figure with the analytical values based on (7.109). The agreement is seen to be fairly good even at a frequency of 60 GHz. So, the conductor loss calculations based on the incremental inductance rule can be used in the millimeter-wave frequency range as long as the assumptions stated there are satisfied; that is, conductor thickness should be much greater than the skin depth, and much less than the strip width and slot widths. It is observed from Figure 7.22 that conductor loss is minimum near $Z_0 = 50 \Omega$ and is higher for low-impedance and high-impedance lines. This behavior can be explained from the conductor losses in strips and slots. High-impedance CPW is characterized by narrow strips and, therefore, higher current density. Similarly, low-impedance coplanar waveguides have narrow slots and, therefore, higher current density at the edges of the slots as in slotline (see Figure 5.12).

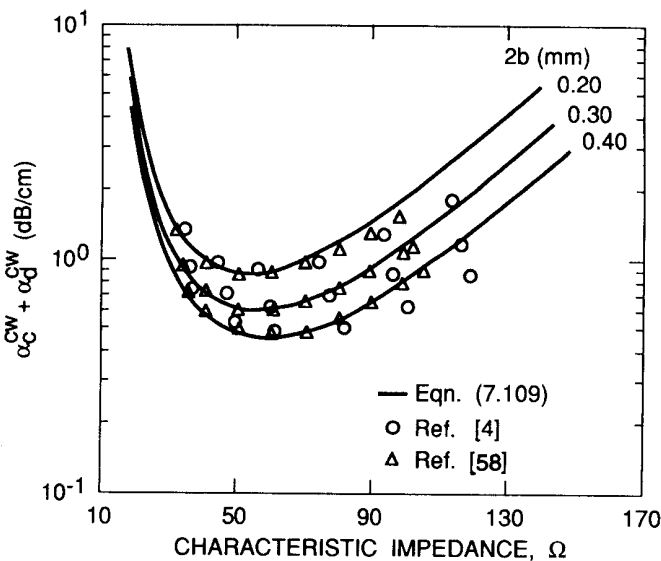


Figure 7.22 Comparison of quasi-static and fullwave values of $\alpha_c + \alpha_d$ as a function of characteristic impedance for symmetric CPW ($h = 100 \mu\text{m}$, $\epsilon_r = 12.8$, $\tan\delta = 0.0006$, $t = 3 \mu\text{m}$, $f = 60 \text{ GHz}$, $R_s = 8.24 \times 10^{-3} \sqrt{f_{\text{GHz}}}$) (from [36], © 1993 IEEE. Reprinted with permission.).

for losses in slotline). Although the same line impedance can be achieved using different values of b , loss considerations dictate choosing a larger value of b .

7.4.3 Radiation and Surface Wave Losses

In addition to the dielectric and ohmic losses, coupling of power to surface waves and radiation from unwanted (parasitic) modes contribute to the total loss of the coplanar lines. The parasitic mode in a coplanar waveguide is the odd mode with antiphase voltages in the two slots. This mode can be excited at the discontinuities, and radiation may occur. Radiation from this mode can be minimized by maintaining symmetry of the circuits and thus avoiding its excitation or by using air bridges at regular intervals to short it out [4]. In a conductor-backed coplanar waveguide the parallel plate waveguide mode is another parasitic mode. Surface waves or the substrate modes can give rise to radiation [7]. Some of these losses are important at microwave frequencies, while others become significant in the mm-wave frequency region only.

To understand the physical process involved in radiation through the parasitic modes, let us consider a conductor-backed CPW that has been analyzed exhaustively using different techniques [45, 57, 59–63]. It is found that the leakage in this transmission line occurs when the dominant transmission line mode of the CPW

travels faster than the parasitic parallel plate mode, which is TEM in nature [59]. In a conductor-backed CPW, this condition is always satisfied independent of frequency and the dimensions of the structure. Therefore, this CPW is said to be unconditionally leaky [57]. This phenomenon is identical to that in a conductor-backed slotline, as discussed in Section 5.5.2. Again, as in a slotline, leakage in a CPW can be controlled by introducing an additional layer of dielectric either as a superstrate, that is, on top of the CPW metallization or between the metallization plane and the substrate. The dielectric constant and the dielectric thickness of this layer are chosen in such a manner that the dominant CPW mode becomes slower than the parasitic LSM_0 mode. Liu and Itoh [62] have analyzed this structure using the fullwave approach. The normalized phase and the attenuation constant for the structure are shown in Figure 7.23 as a function of the thickness of the additional layer. As shown in this figure, β/k_0 for the CPW mode is smaller than that of the parasitic mode, and the structure is leaky for small thickness h_2 . The value of β/k_0 increases as layer thickness h_2 is increased and reaches the value for the LSM_0 mode at $h_2 = 0.027$ mm. This thickness is called the critical thickness. As h_2 is increased beyond this value, the CPW mode becomes slower than the parasitic mode. There are corresponding changes in the leakage constant denoted by α/k_0 . At the start, $h_2 = 0$ and the structure is leaky with $\alpha/k_0 = 0.003$. As h_2 increases, α/k_0 decreases quickly and goes down abruptly to zero at the critical thickness. Similar behavior for α/k_0 and β/k_0 is observed when the additional layer is used as a superstrate [59].

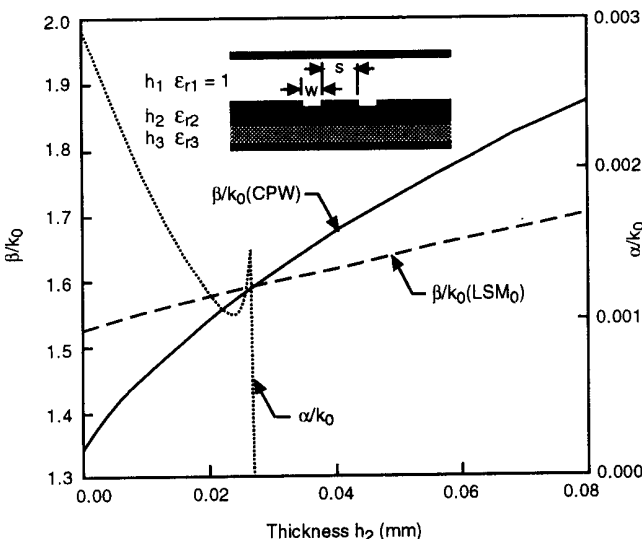


Figure 7.23 Normalized phase and attenuation for different thickness h_2 . ($\epsilon_{r2} = 10.5$, $\epsilon_{r3} = 2.33$, $W = 0.254$ mm, $S = 0.254$ mm, $h_3 = 0.635$ mm, $h_1 = 15$ mm, and $f = 10$ GHz) (from [62], © 1993 IEEE. Reprinted with permission.).

For a CPW with infinitely thick substrate there are two modes of propagation: (1) CPW guided mode with $\beta/k_0 = \sqrt{(\epsilon_r + 1)/2}$ and (2) the TEM wave of the substrate with $\beta_s/k_0 = \sqrt{\epsilon_r}$. In this case $\beta < \beta_s$, therefore the guided mode becomes unconditionally leaky and radiates into the substrate with $v_{ph} = c/\sqrt{\epsilon_r}$. For constructive interference, the phase velocities of the guided wave and the radiated wave should be the same along the direction of propagation. This is called phase synchronism or phase match condition [63] and leads to the following condition on the direction θ of maximum radiation:

$$\cos\theta = \frac{\beta}{\beta_s} = \sqrt{\frac{\epsilon_r + 1}{2\epsilon_r}}$$

Energy transfer from the guided wave into the substrate causes attenuation of the guided wave.

Effect of Finite Thickness Substrate

Coplanar lines with finite thickness substrate can also be leaky. Although the mechanism of radiation is similar to the infinite thickness case, the substrate modes are different. It is the surface wave modes of the substrate/slab that are responsible for leakage. Surface waves of the structure are the guided modes of a conductor-backed dielectric slab of thickness h . These modes are the same as the odd TE modes and even TM modes of a dielectric slab with thickness $2h$ and no metallization. Dispersion curves for TM modes are plotted in Figures 7.17 and 7.18 along with other modes of CPW and CPS, respectively. These modes are encountered in a microstrip line also. Excitation of substrate modes depends on the polarizations and symmetries of the transmission line mode and the substrate mode. For example, it has been proved analytically that a CPS with narrow strips can lose energy to TM-type substrate modes only because the transverse current on the strips is very weak to excite the TE-type modes [7]. When wider strips are used in the analysis, both TE- and TM-type modes can be excited. Coupling to the substrate modes is expected to be stronger when the substrate thickness is comparable to the wavelength in dielectric λ_d .

The amount of loss due to leakage from coplanar lines on infinitely thick substrates has been calculated using reciprocity [64, 65] as well as the fullwave approach [7, 63, 66, 67]. The reciprocity approach leads to simple expressions for the attenuation constant. Phatak et al. [7] have modified the expressions for a CPS to fit the numerical results of the fullwave approach. These expressions are given as

$$\alpha_{rad}^{cps} = (3 - \sqrt{8}) \frac{\pi^2}{4} \sqrt{\frac{\epsilon_{re}(f)}{\epsilon_r}} \frac{\sin^4\theta}{K(k_1)K'(k_1)} \frac{W^2}{\lambda_d^3} \quad \text{neper/unit length, } \lambda_d = \frac{\lambda_0}{\sqrt{\epsilon_r}} \quad (7.116)$$

where θ , the angle at which maximum radiation occurs, is measured from the direction of propagation, and is defined as

$$\cos\theta = \beta/\beta_s \quad (7.117)$$

where β is the propagation constant for the CPS mode and β_s is the propagation constant for the surface mode.

The radiation loss for a coplanar waveguide has also been expressed in a simple form [65, 68]. This expression has been modified by Frankel et al. [49] to fit the experimental data for the attenuation constant of a picosecond pulse. The modified expression is given by [49]

$$\alpha_{\text{rad}}^{\text{CPW}} = \left(\frac{\pi}{2}\right)^5 2 \frac{(1 - \epsilon_{\text{re}}(f)/\epsilon_r)^2}{\sqrt{\epsilon_{\text{re}}(f)/\epsilon_r}} \frac{(S + 2W)^2}{K(k)K'(k)} \frac{1}{\lambda_d^3} \text{ neper/unit length} \quad (7.118)$$

Expressions for the surface mode attenuation constant for a CPW and a CPS on finitely thick substrate are given as [7, 65]

$$\alpha_{\text{sw}}^{\text{TE}} = \frac{\pi^4}{2\sqrt{2}} \frac{\sqrt{1 + 1/\epsilon_r}}{K(k)K'(k)h_e} \left(\frac{W}{\lambda_d}\right)^2 \sin^3\theta \sin\theta_d \cos^2\Phi_{\text{TE}} \text{ neper/unit length} \quad (7.119)$$

$$\alpha_{\text{sw}}^{\text{TM}} = \frac{\pi^4}{2\sqrt{2}} \frac{\sqrt{1 + 1/\epsilon_r}}{K(k)K'(k)h_e} \left(\frac{W}{\lambda_d}\right)^2 \sin\theta \cos^2\theta \sin\theta_d \cos^2\theta_d \sin^2\Phi_{\text{TM}} \text{ neper/unit length} \quad (7.120)$$

where θ_d is the angle of incidence of the ray on the dielectric interface (see Figure 7.24), and is given by [64]

$$\cos\theta_d = \frac{k_y}{k_0\sqrt{\epsilon_r}} \quad (7.121)$$

Φ_{TE} and Φ_{TM} are the phase shifts for TE and TM plane waves, respectively, due to total internal reflection at the dielectric-air interface, and the effective dielectric thickness h_e is defined as [64]

$$h_e = h + 2\Delta \quad (7.122)$$

Δ is the apparent ray penetration in the air region on total internal reflection as shown in Figure 7.24. Leakage from CPW with finite-sized ground planes, with and without backside metallization, has been studied [63, 66]. Sharp peaks in attenuation are found to occur at the onset of leakage.

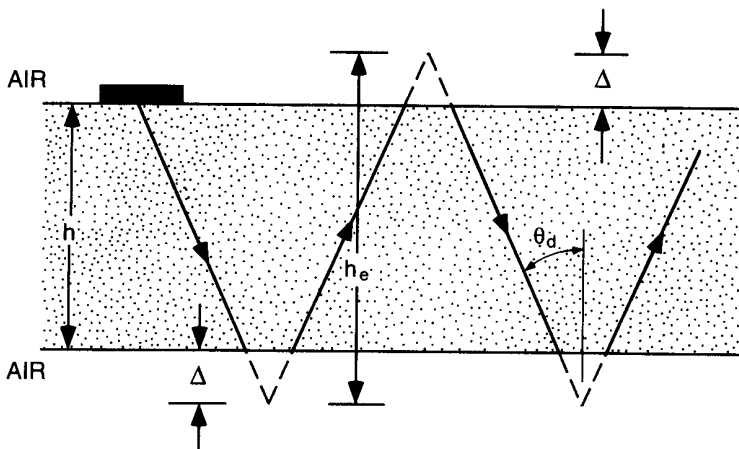


Figure 7.24 Definition of effective thickness, $h_e = h + d\Delta$ (from [64], © 1993 IEEE. Reprinted with permission.).

Leakage of power not only gives rise to increased attenuation but can also result in cross talk with neighboring portions of the circuit. Power leakage can be avoided if a thin substrate is used so that the cutoff frequency of the surface modes is pushed above the operating frequency. For this, the substrate thickness h should be chosen such that $h\sqrt{\epsilon_r} < 0.12\lambda_0$ [63].

7.5 EFFECT OF TOLERANCES

The sensitivity analysis described earlier for microstrip line and slotline can also be applied to coplanar lines to evaluate the effect of tolerances. The maximum change in the values of characteristic impedance and effective dielectric constant may be written as

$$\frac{|(\Delta Z_0)|_{\max}}{Z_0} = \left| \frac{\Delta W}{W} S_W^{Z_0} \right| + \left| \frac{\Delta S}{S} S_S^{Z_0} \right| + \left| \frac{\Delta h}{h} S_h^{Z_0} \right| + \left| \frac{\Delta \epsilon_r}{\epsilon_r} S_{\epsilon_r}^{Z_0} \right| + \left| \frac{\Delta t}{t} S_t^{Z_0} \right| \quad (7.123)$$

$$\frac{|(\Delta \epsilon_{re})|_{\max}}{\epsilon_{re}} = \left| \frac{\Delta W}{W} S_W^{\epsilon_{re}} \right| + \left| \frac{\Delta S}{S} S_S^{\epsilon_{re}} \right| + \left| \frac{\Delta h}{h} S_h^{\epsilon_{re}} \right| + \left| \frac{\Delta \epsilon_r}{\epsilon_r} S_{\epsilon_r}^{\epsilon_{re}} \right| + \left| \frac{\Delta t}{t} S_t^{\epsilon_{re}} \right| \quad (7.124)$$

The sensitivity of Z_0 with respect to a parameter γ may be evaluated from the sensitivities of Z_0^a and ϵ_{re} using the relation

$$S_\gamma^{Z_0} = S_\gamma^{Z_0^a} - S_\gamma^{\epsilon_{re}}/2 \quad (7.125)$$

where Z_0^a ($= Z_0\sqrt{\epsilon_{re}}$) is the characteristic impedance of a coplanar line with air as dielectric.

Expressions for sensitivities of the characteristics of CPW with respect to various parameters (W , S , h , ϵ_r , and t) can be calculated using the closed-form expressions for Z_{0cp}^a and ϵ_{re} derived earlier and the definition of sensitivity given by (2.99). The effect of strip thickness ($t/W \leq 0.005$) on CPW characteristics is very small and therefore has not been included here. Sensitivity expressions for the symmetric coplanar lines with finite dielectric thickness h are given next. Sensitivities for other geometries may be derived in a similar manner.

$$S_W^{Z_{0cp}^a} = -S_S^{Z_{0cp}^a} = \frac{60P}{Z_{0cp}^a} \frac{W}{S} k_1^2 \quad (7.126)$$

where $k_1 = S/(S + 2W)$ and P is as defined in (7.107).

Sensitivities of Z_{0cp}^a with respect to h and ϵ_r are zero because characteristics of CPW with air as dielectric do not depend on h and ϵ_r . Sensitivities of ϵ_{re} with respect to various parameters for $0 \leq k_1 \leq 0.707$ and $0 \leq k_2 \leq 0.707$ are as follows:

$$S_{\epsilon_r}^{\epsilon_{re}} = \frac{\epsilon_r}{\epsilon_r - 1} \frac{\epsilon_{re} - 1}{\epsilon_{re}} \quad (7.127)$$

$$S_S^{\epsilon_{re}} = \frac{\epsilon_r - 1}{2\epsilon_{re}} \frac{K(k_2)}{K'(k_2)} \left\{ \frac{S}{2h} \frac{\epsilon_{re} - 1}{\epsilon_r - 1} \frac{1}{1 - k'_2} \frac{k_2}{\sqrt[3]{k'_2}} \frac{\sinh(\pi W/2h)}{\sinh^2(\pi(S + 2W)/4h)} - \frac{2}{\pi} \frac{1}{1 - k'_1} \left(\frac{k_1}{k'_1} \right)^3 \frac{W}{S} \right\} \quad (7.128)$$

$$S_W^{\epsilon_{re}} = \frac{W}{2h} \frac{\epsilon_r - 1}{\epsilon_{re}} \frac{K(k_2)}{K'(k_2)} \left\{ \frac{2}{\pi} \frac{h}{S + 2W} \frac{1 + k'_1}{\sqrt[3]{k'_1}} - \frac{\epsilon_{re} - 1}{\epsilon_r - 1} \frac{1}{1 - k'_2} \frac{k_2^2}{\sqrt[3]{k'_2}} \frac{\cosh(\pi(S + 2W)/4h)}{\sinh(\pi(S + 2W)/4h)} \right\} \quad (7.129)$$

$$S_h^{\epsilon_{re}} = -S_W^{\epsilon_{re}} - S_S^{\epsilon_{re}} \quad (7.130)$$

The sensitivities of characteristic impedance and effective dielectric constant of a coplanar waveguide with respect to various parameters are plotted in Figures 7.25 and 7.26. It may be noted from Figure 7.25 that sensitivities of Z_{0cp} with respect to W and h increase when h/b is decreased. A similar observation can be made for sensitivities of ϵ_{re} with respect to h , S , and W . Thus the effect of fabrication tolerances is small when thick substrates are used. When $h/b = 0.5$, ϵ_{re} is very much sensitive to variations in h . For $h/b \geq 3$, the sensitivities of ϵ_{re} , and therefore of Z_{0cp} , with respect to ϵ_r are independent of the h/b ratio and also the aspect ratio. The values of these two sensitivities are 0.927 and -0.463 , respectively, for $\epsilon_r = 13$.

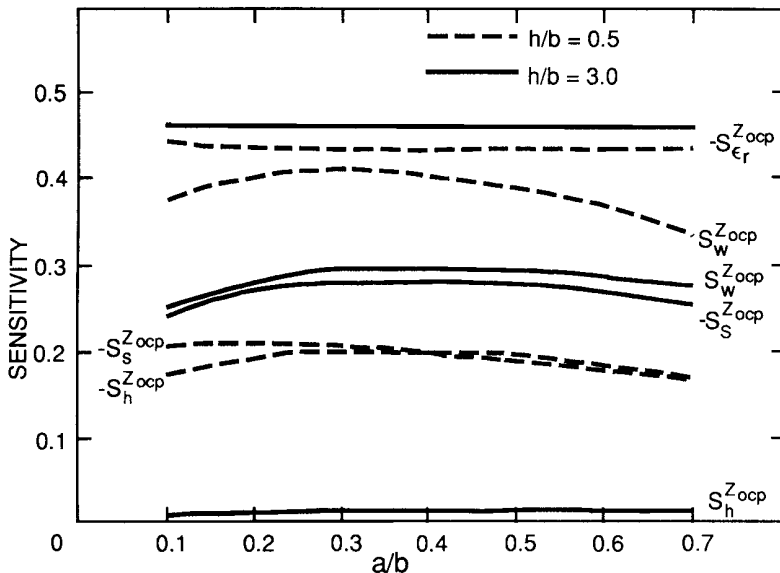


Figure 7.25 Sensitivities of characteristic impedance of CPW with respect to various parameters ($\epsilon_r = 13.0$).

The sensitivity values thus obtained are used in (7.124) to determine the maximum change in ϵ_{re} . Variation of $(\Delta\epsilon_{re})_{max}/\epsilon_{re}$ as a function of characteristic impedance is shown in Figure 7.27. The value of $(\Delta\epsilon_{re})_{max}/\epsilon_{re}$ is almost constant with impedance. The fractional change is higher for a lower value of h/b .

For coplanar strips, the sensitivities of impedance with air as dielectric (Z_{0cs}^a) with respect to parameters S and W are

$$S_W^{Z_{0cs}^a} = -S_S^{Z_{0cs}^a} = - \frac{120k_1(1-k_1)P'}{Z_{0cs}^a} \quad (7.131)$$

where P' is as defined in (7.106).

As for the CPW, the sensitivities with respect to h and ϵ_r are zero in this case also. The expression for $S_{\epsilon_r}^{Z_{0cs}^a}$ is the same as that for a CPW; see (7.127). The rest of the sensitivity expressions for a CPS for $0 \leq k_1 \leq 0.707$ and $0 \leq k_2 \leq 0.707$ are

$$S_W^{Z_{0cs}^a} = \frac{W}{4h} \frac{\epsilon_r - 1}{\epsilon_{re}} \frac{K(k_1)}{K'(k_1)} \left\{ \frac{1 + k'_2}{3\sqrt{k'_2}} \coth \left(\frac{\pi(S + 2W)}{4h} \right) - \frac{\epsilon_{re} - 1}{\epsilon_r - 1} \frac{8h}{\pi(S + 2W)} \frac{1 + k'_1}{3\sqrt{k'_1}} \right\} \quad (7.132)$$

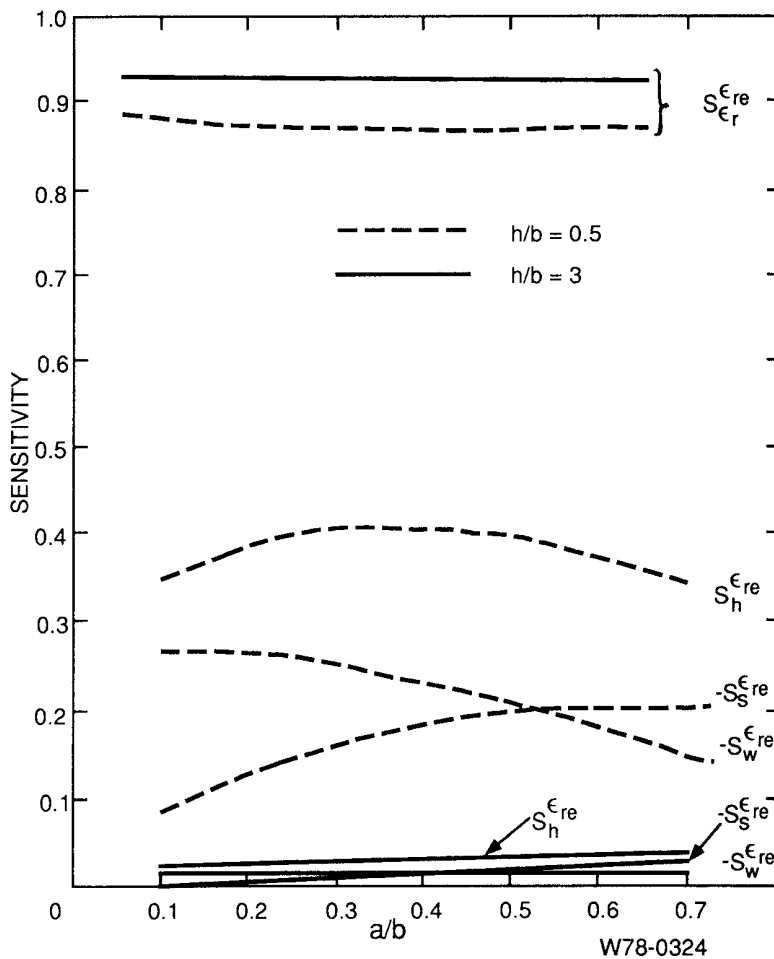


Figure 7.26 Sensitivities of effective dielectric constant of CPW with respect to various parameters ($\epsilon_r = 13.0$).

$$S_S^{\epsilon_r} = \frac{S}{8h} \frac{\epsilon_r - 1}{\epsilon_{re}} \frac{K(k_1)}{K'(k_1)} \left\{ \frac{\epsilon_{re} - 1}{\epsilon_r - 1} \frac{8h}{\pi(S + 2W)} \frac{k_1(1 - k_1)}{\sqrt[3]{k'_1}(1 - k'_1)} \right. \\ \left. - \frac{k_2}{1 - k'_2} \frac{1}{\sqrt[3]{k'_2}} \frac{\sinh(\pi W/2h)}{\sinh^2(\pi(S + 2W)/4h)} \right\} \quad (7.133)$$

and

$$S_h^{\epsilon_r} = -S_W^{\epsilon_r} - S_S^{\epsilon_r} \quad (7.134)$$

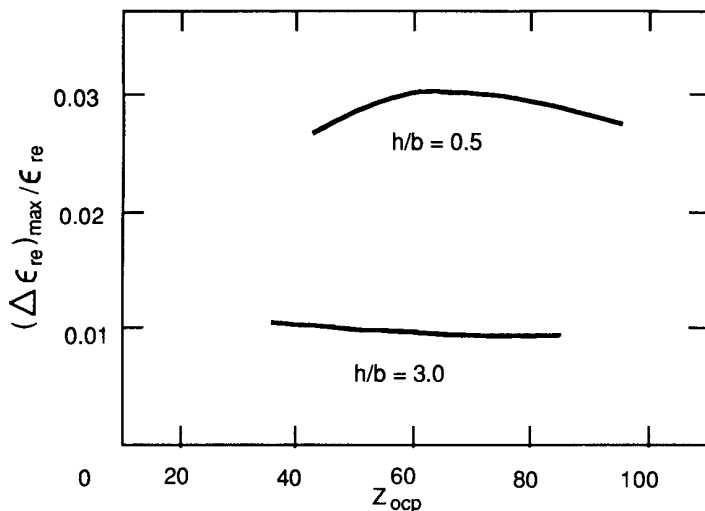


Figure 7.27 Effect of tolerances on the change in effective dielectric constant of CPW ($\epsilon_r = 13.0 \pm 0.1$, $h = 100 \pm 5 \mu\text{m}$, $\Delta W = \Delta S = \pm 1 \mu\text{m}$).

7.6 COMPARISON WITH MICROSTRIP LINE AND SLOTLINE

Four types of planar transmission lines suitable for microwave integrated circuits have been discussed so far: (1) microstrip line, (2) slotline, (3) coplanar waveguide, and (4) coplanar strips. In this section we compare the characteristics of these lines. Various features considered include the range of impedance achievable, losses, and effect of tolerances. The microstrip line has been compared with a coplanar waveguide in [4, 26].

Range of Impedance

The range of characteristic impedance that can be practically realized with any particular transmission line is limited by two factors. Technological processes such as photoetching limit the minimum strip width and the spacing between two adjacent strips. For comparison, this minimum dimension has been taken as $5 \mu\text{m}$ (although smaller dimensions are possible with careful processing). The other limitation comes from the possibility of excitation of higher order modes. To avoid the excitation of higher order modes, the substrate thickness and the lateral dimensions should be kept below a quarter wavelength. The impedance limits calculated in this manner are shown in Table 7.1 for three types of lines. In this table the letter "m" in parentheses indicates that the limit is caused by higher

Table 7.1
Comparison of Z_0 Limits ($\epsilon_r = 13$, $h = 100 \mu\text{m}$, and frequency = 30 GHz)

Transmission Line	Lower Limit for Z_0 (ohm)	Upper Limit for Z_0 (ohm)
Microstrip	11 (m)	110 (d)
Slotline	35(d)	250 (m)
Coplanar waveguide	20(m, d)	250(m,d)
Coplanar strips	20(m, d)	250(m,d)

order modes and the letter “d” indicates that the limit is due to small dimensions. This comparison indicates that microstrip lines are capable of providing low impedance whereas slotlines and coplanar waveguides may be used for very high impedances.

Losses

Losses or attenuation constant is another important characteristic for the comparison of these lines. Conductor loss in planar lines has been computed and compared by Heinrich in [69, 70]. The value of conductor loss for the microstrip, slotline, and CPW is compared in Figures 7.28 and 7.29 as a function of characteristic impedance. A comparison of the conductor loss in a microstrip line and a CPW (see Figure 7.28) shows that for lower impedance lines the microstrip has lower loss whereas for high impedances a CPW can be designed to have lower loss. For medium impedance lines, the conductor loss in a microstrip and a CPW are substantially similar. The conductor loss for a slotline and a CPW is plotted in Figure 7.29. This comparison shows that high-impedance lines are less lossy if realized in slotline configuration and that a CPW configuration with wider strips should be chosen for low impedance levels. Fabrication constraints are also less stringent if wider slots and strips are used.

Effect of Tolerances

As discussed earlier, impedance variations caused by tolerances are expressed in terms of the maximum value of VSWR presented to an ideal line connected at the input. The effects of tolerances on the impedance and effective dielectric constant for the three types of lines are compared in Table 7.2. For this comparison, the fabrication accuracy of strip width and gap width has been assumed to be $1 \mu\text{m}$. The assumed tolerances in h and ϵ_r are $5 \mu\text{m}$ and 0.1 , respectively. The table shows that slotline impedance is less sensitive to variations in parameters as compared to other lines.

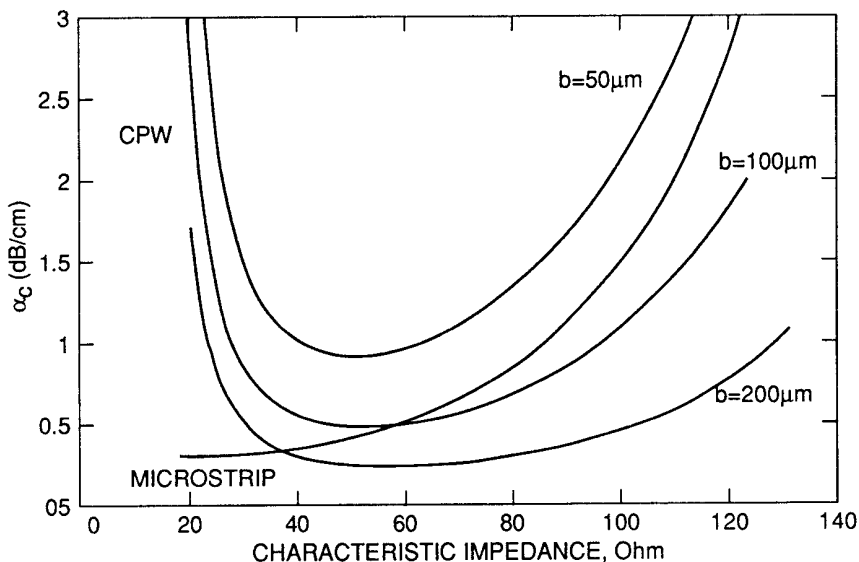


Figure 7.28 Comparison of conductor loss for microstrip and CPW on 100 μm GaAs substrate ($\epsilon_r = 13$) at $f = 20$ GHz as a function of line impedance. A 3 μm -thick copper metallization is assumed [26].

Other Parameters

Several other parameters of the four types of lines are compared qualitatively in Table 7.3. It can generally be seen that CPW and CPS combine some advantageous features of microstrip lines and slotlines. Perhaps the best features of the coplanar lines is the ease of mounting components in series and shunt configurations, whereas microstrip lines are convenient only for series mounting and slotlines can accommodate only shunt-mounted components. A coplanar waveguide has the advantage of easier fabrication, no via holes, and good grounding for active devices. It suffers from the disadvantages of larger size, parasitic odd mode, and poor heat transfer for active devices [4].

7.7 TRANSITIONS

Integration of coplanar lines with other transmission lines requires a suitable transition. Further, transitions between coplanar lines and slotline transform an unbalanced (CPW) mode into a balanced (slotline) mode and is especially useful in balanced circuits such as balanced mixers and modulators. Transitions from CPW to coax, microstrip line, slotline, and CPS, as well as from CPS to slotline, are discussed in this section.

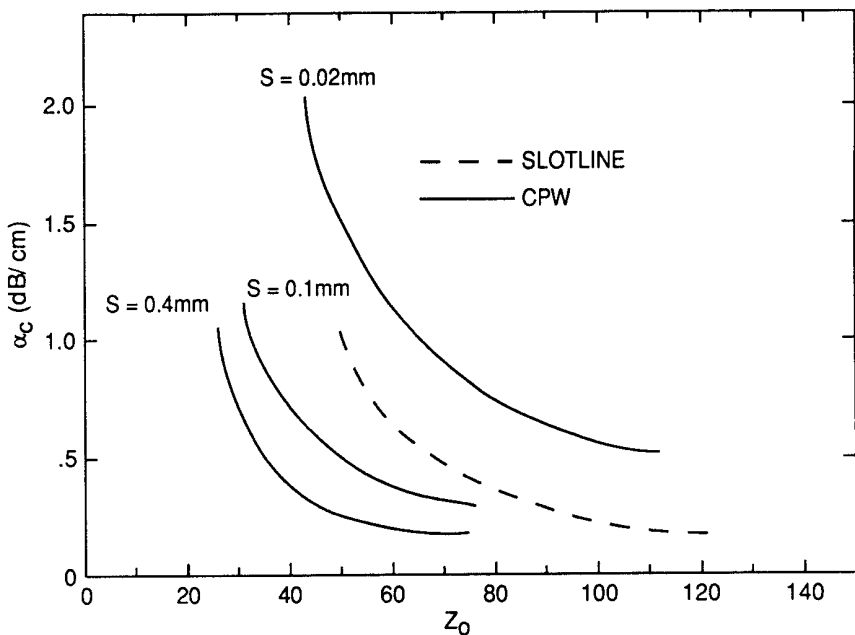


Figure 7.29 Comparison of conductor loss for slotline and CPW on 100- μm GaAs substrate ($\epsilon_r = 12.8$) at $f = 20$ GHz as a function of line impedance. A 3- μm -thick conductor with $\rho = 1.7 \mu\Omega\text{cm}$ is assumed (from [58], © 1991 IEEE. Reprinted with permission.).

Table 7.2
Comparison of the Effect of Tolerances on Various Lines ($\epsilon_r = 13 \pm 0.1$, $h = 100 \pm 5 \mu\text{m}$, $\Delta W = \Delta S = 1 \mu\text{m}$, and $Z_0 = 50 \Omega$)

Transmission Line	Max. VSWR	Max. $ \Delta\epsilon_{re}/\epsilon_{re} $
Microstrip ($W/h = 0.731$)	1.033	0.013
Slotline ($W/h = 0.1$, $h/\lambda_0 = 0.01$)	1.015	0.0036
Coplanar waveguide ($h/b = 8$, $a/b = 0.4$)	1.07	0.044

7.7.1 Coax-to-CPW Transitions [71]

This transition is one of the simplest and most frequently used CPW transitions. It is used for testing CPW circuits. Depending upon the sealing requirement, one of

Table 7.3
Qualitative Comparison of Various MIC Lines

Characteristic	Microstrip	Slotline	Coplanar Waveguide	Coplanar Strips
Effective dielectric constant ($\epsilon_r = 13$ and $h = 100 \mu\text{m}$)	≈ 8.6	≈ 5.07	≈ 7	≈ 7
Power handling capability	High	Medium	Medium	Medium
Radiation loss	Low	Medium	Medium	Medium
Unloaded Q	Medium	Low	Medium	Low (lower impedances) High (higher impedances)
Dispersion	Small	Large	Small	Small
Mounting of components:				
in shunt config.	Difficult	Easy	Easy	Easy
in series config.	Easy	Difficult	Easy	Easy
Technological difficulties	Ceramic holes Edge plating	— —	— —	— —
Elliptically polarized magnetic field config.	Not available	Available	Available	Available
Enclosure dimensions	Small	Large	Large	Large

the two transitions shown in Figure 7.30 is used. The transition (a) is useful for the nonhermetic case, while transition (b) is made with a hermetic seal connector. In both the transitions, the pin of the coax connector rests on the strip part of the CPW and the ground planes of the CPW and coax connector make electrical contact with each other. The strip width of the CPW is changed slightly at the beginning to optimize the reflection coefficient of the transition. Houdart and Aury obtained a VSWR less than 1.35 for frequencies below 18 GHz for two transitions connected back-to-back [71].

7.7.2 Microstrip-to-CPW Transitions [71]

Two types of microstrip-to-CPW transitions have been reported [7]. The transition in Figure 7.31(a) is nonplanar in nature and consists of a CPW and microstrip lines fabricated on different substrates. The CPW is terminated at one end by joining the ground planes at a short distance away from the strip. The ground planes of the CPW and the microstrip line are made common by placing the microstrip line on top of the CPW ground plane. Strips of the two transmission lines are joined to each other through a metal ribbon. The open-end capacitance of the microstrip line, ribbon inductance, and the open-end capacitance of the CPW constitute a

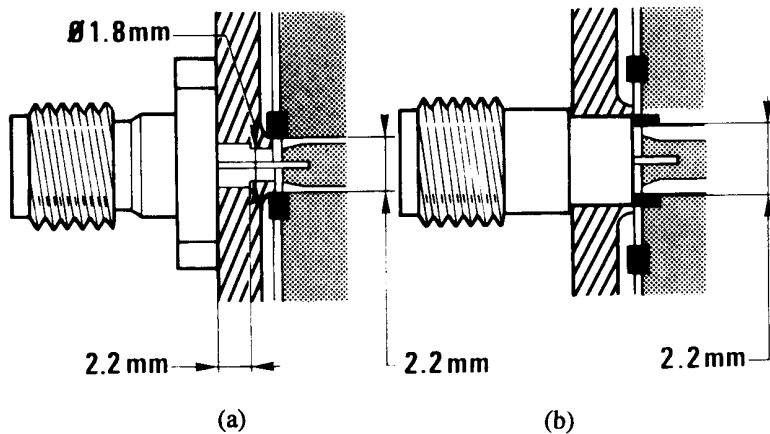


Figure 7.30 Coax-to-CPW transitions: (a) for nonhermetic sealing and (b) hermetic sealing (from [71], © 1979 IEEE. Reprinted with permission.).

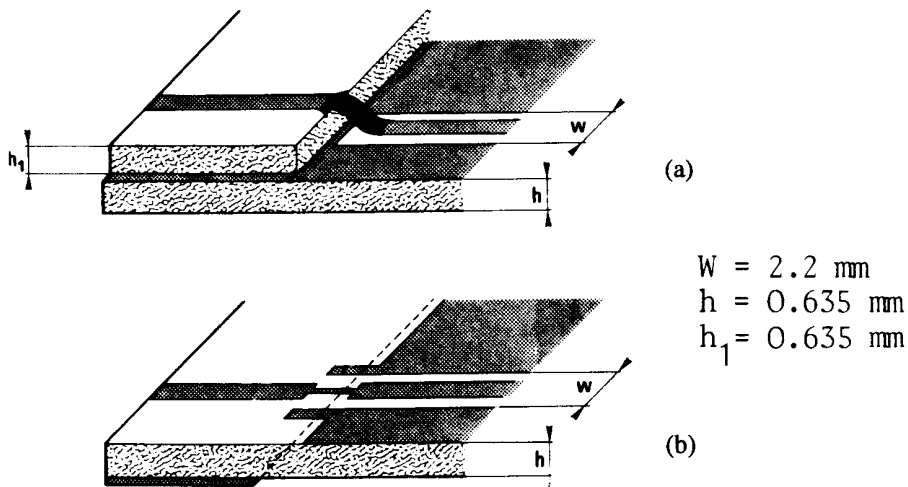


Figure 7.31 Microstrip-to-CPW transitions: (a) nonplanar transition and (b) planar transition (from [71], © 1979 IEEE. Reprinted with permission.).

low-pass filter whose cutoff frequency can be varied by varying the substrate thickness of the microstrip line. An assembly of coax-to-microstrip transition, microstrip-to-CPW transition, and CPW-to-coax transition on 0.635-mm-thick alumina substrate was tested to give a maximum VSWR of less than 1.4 over the 2-GHz to 18-GHz frequency band [71].

The planar transitions between a microstrip line and a CPW in Figure 7.31(b) uses symmetrical three-coupled microstrip lines as an intermediate transition. The coupled microstrip line can be designed as a bandpass filter whose center frequency can be controlled by the length ℓ of the coupled lines. Two transitions were designed and optimized in the 5-GHz to 11-GHz band and 11-GHz to 18-GHz band by properly selecting the value of ℓ . The maximum VSWR for a back-to-back transition assembly was found to be 1.3 for the first transition and 1.4 for the second transition.

7.7.3 Slotline-to-CPW Transitions

This transition has been studied most comprehensively. Various types of transitions that have been proposed are shown in Figure 7.32. The transition in Figure 7.32(a) is based on the CPW-slotline T-junction of Figure 7.43(b) [72, 73]. This junction works like a power divider. If one of the output ports of the power divider is terminated in an open circuit, we obtain the CPW-to-slotline transition of Figure 7.32(a). In this transition there is complete transfer of current from the CPW to the slotline. While current on the strip of the CPW flows into one of the conductors of the slotline, the backward current on the ground planes of the CPW flows from the other conductor of the slotline through a bonding wire. The open circuit on one of the slots of the CPW and the use of a bonding wire (not shown in Figure 7.32) help transform the CPW mode to the slotline mode. A variation of this transition uses a slotline open circuit in the form of a circular slot (see Figure 7.32(b)) [74, 75]. In Figure 7.32(c) the open circuits of Figure 7.32(a, b) have been replaced by a quarter-wave shorted stub [76], which provides a tuning capability. To improve the bandwidth, the slot in Figure 7.32(d) is terminated in a 90° radial slotline stub. The transitions in Figure 7.32(e) to (i) borrow the concept of a quarter-wave cross-junction of the microstrip slotline transition of Figure 5.29 [68, 73, 76, 77]. To increase the bandwidth, uniform impedance stubs have been replaced by nonuniform impedance radial stubs. A comparative study of these transitions shows that the transition in Figure 7.32(d) is the best in terms of bandwidth and insertion loss [76]. The 1-dB insertion loss bandwidth for this transition is found to be more than 5.2:1. Further, this transition can be designed such that the CPW and slotlines are colinear, that is, the right-hand slot of the CPW can run straight instead of bending at right angles as shown in the figure. This introduces flexibility in the layout.

The simplified equivalent circuit of the transitions in Figure 7.32(e–i) is shown in Figure 7.33. It consists of an open-circuited quarter-wave CPW section in series and a shorted quarter-wave slotline section in shunt across the CPW-slotline junction. For a 50- Ω CPW line the optimum value of Z_{01} is obtained as [73]

$$Z_{01} = \frac{Z_{02}\tan^2(\pi f_x/2f_0)}{1 + (Z_{02}/Z_{\text{slot}})^2\tan^2(\pi f_x/2f_0)} \quad (7.135)$$

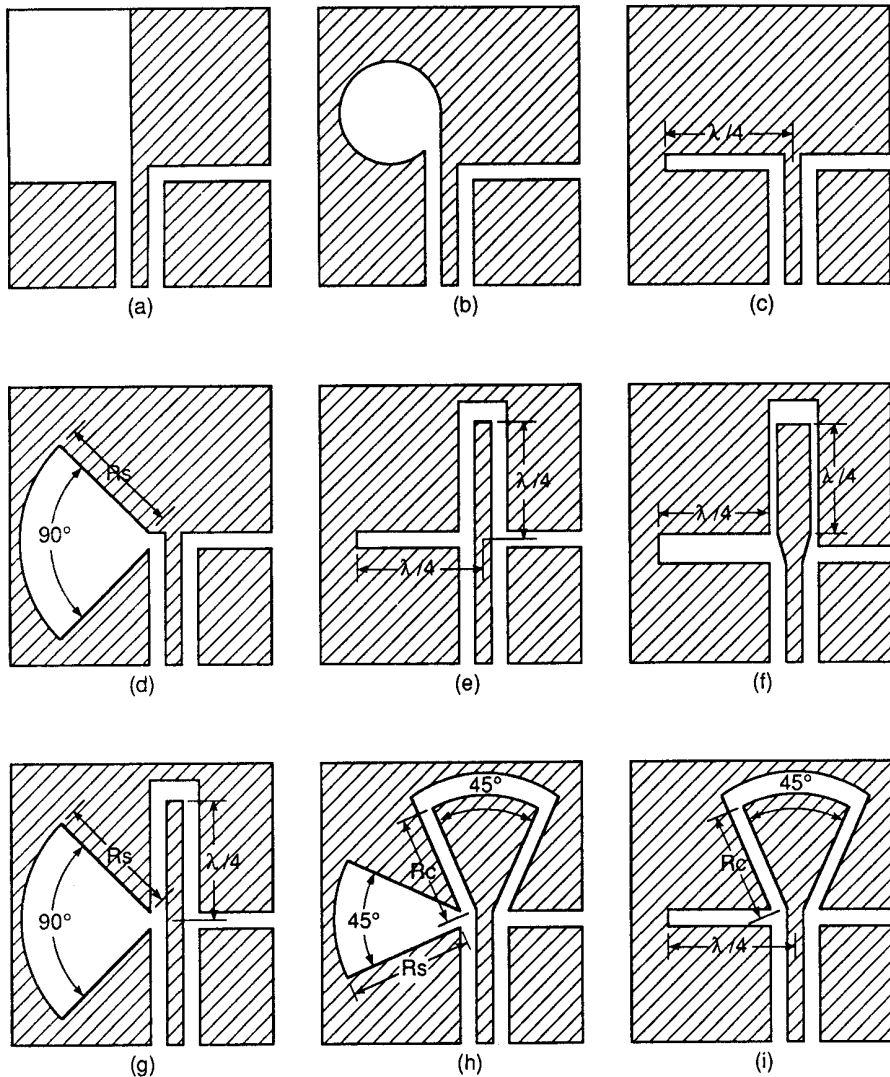


Figure 7.32 (a) through (i): Slotline-to-CPW transitions with different types of terminations.

where f_x represents either the lower (f_{x1}) or the upper (f_{x2}) band edge of the transition with center frequency $f_0 = (f_{x1} + f_{x2})/2$. A fullwave analysis of the transition in Figure 7.32(e) has been reported in [78].

The transition shown in Figure 7.34(a) employs a six-port junction between the CPW and the slotline [73, 79]. The equivalent circuit of this transition can be

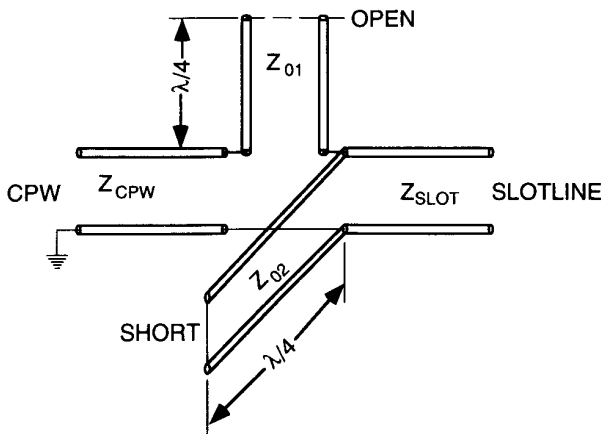


Figure 7.33 Simplified equivalent circuit for the slotline-to-CPW transitions of Figure 7.32.

expressed in the form of an impedance bridge of Figure 7.34(b). A simple analysis of the impedance bridge gives the following expression for the input impedance at the CPW port of the transition:

$$\overline{Z}_{in} = \frac{1}{\overline{Z}_2 + \overline{Z}_3 + 1} \left[\frac{(\overline{Z}_2 + \overline{Z}_3)(\overline{Z}_2 + 1)(\overline{Z}_3 + 1)}{\overline{Z}_2 + \overline{Z}_3 + 2} \right] \quad (7.136)$$

where Z_2 , Z_3 , Z_5 , and Z_6 are input impedances of respective stubs at the junction and all the impedances in (7.136) have been normalized to the characteristic impedance Z_4 of the slotline; and it is assumed that $Z_2 = Z_5$ and $Z_3 = Z_6$. For a perfect match, $\overline{Z}_{in} = 1$. Equation (7.136) then reduces to the condition

$$\overline{Z}_2 \overline{Z}_3 = 1 \quad (7.137)$$

or equivalently

$$\Gamma_2 = -\Gamma_3 \quad (7.138)$$

Equation (7.138) implies that if all the stubs are of the same electrical length, then a perfect match is maintained at all the frequencies. In reality, the bandwidth is limited by unequal dispersion between the slotline and the CPW, junction reactances, and mode conversion. Stub lengths are kept short ($\approx \lambda_g/8$) to minimize dispersion and attenuation effects. Test results of this transition on a 0.33-mm-thick silicon substrate with $\epsilon_r = 11.9$ are available in [73]. The return loss was found to be greater than 15 dB from 20 GHz to 35 GHz.

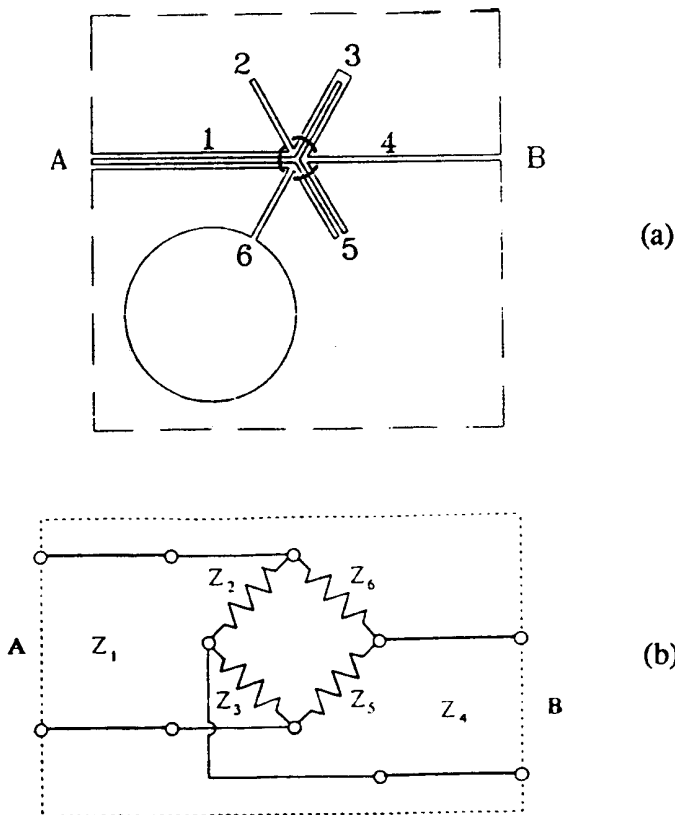


Figure 7.34 Slotline-to-CPW transition using a double junction: (a) schematic and (b) equivalent circuit (from [73], © 1993 IEEE. Reprinted with permission.).

All the slotline-CPW transitions discussed above can be modified to introduce biasing of active devices across the slotline as discussed in [65].

7.7.4 CPW-to-CPS Transition [76]

A transition between a CPW and a CPS is shown in Figure 7.35. It includes a CPW-to-slotline transition of Figure 7.32(d) as an intermediate transition. The transition from slotline to CPS is achieved by reducing the width of the conductors of the slotline. The measured frequency response of the CPW-CPS back-to-back transitions shows that the insertion loss is less than 1 dB over the 1.6-GHz to 7.0-GHz band and the return loss is higher than 13 dB from 1.6 GHz to 8.0 GHz [76].

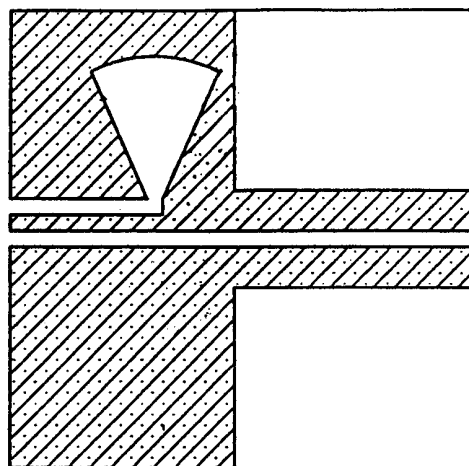


Figure 7.35 CPW-to-CPS transition (from [76], © 1993 IEEE. Reprinted with permission.).

7.7.5 CPS-to-Slotline Transitions

Uniplanar CPS-to-slotline transitions can be implemented as in Figure 7.35. A biplanar transition between CPS and slotline has been reported by Simons [80]. This is shown in Figure 7.36. In this transition the CPS is first transformed into coupled microstrip lines by using the conductor of the slotline as the ground plane for coupled microstrip lines. The spacing between the coupled lines is then slowly flared so that they get uncoupled and cross the slot underneath at right angle, in a way exactly similar to the microstrip-slotline transition of Figure 5.29. The transition was fabricated on 0.295-mm-thick 2500- Ω cm to 3300- Ω cm resistivity silicon wafer with $\epsilon_r = 11.7$. The measured return loss and insertion loss per transition are found to be better than 10 dB and 1.5 dB, respectively, over the 8.0-GHz to 11.2-

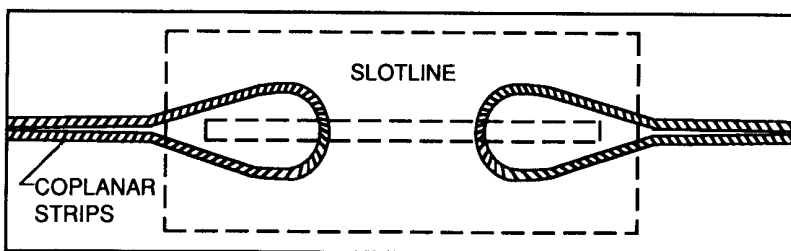


Figure 7.36 CPS-to-slotline transition (from [80], © 1994 IEEE. Reprinted with permission.).

GHz band [80]. The insertion loss includes the insertion loss of the 3.56-mm slotline and the 10.3-mm CPS line.

7.8 DISCONTINUITIES IN COPLANAR WAVEGUIDE

Some of the most common discontinuities that occur in CPW are shown in Figure 7.37. The theoretical modeling of these discontinuities has been carried out extensively [81–115]. A complete library for CAD-oriented simulation of CPW structures is available in [113–115]. Both quasi-static as well as fullwave approaches have been used. However, design information suitable for CAD tools is still lacking for most of these discontinuities. The main reason for this appears to be that there are a large number of parameters in CPW discontinuities and it is, therefore, difficult to develop expressions covering the useful range of parameters. Simple guidelines for open- and short-circuit discontinuities have been published in [90].

Open and Short Circuits [90]

The open circuit in a coplanar waveguide is commonly realized as shown in Figure 7.38(a). The short end is shown in Figure 7.38(b). The behavior of open and short circuits in a CPW is very similar to that in a microstrip line; that is, the open circuit is capacitive in nature and the short circuit is inductive. A number of papers have appeared on the analysis of these discontinuities [81, 89–92]. Beilenhoff et al. [90] have provided a very simple approximation for the equivalent length extension $\Delta\ell$ associated with the fringing fields of these discontinuities. For the open end, the value of $\Delta\ell$ is not influenced significantly by the metallization thickness and the gap width g when $g > 2b$. Also, the effect of frequency and aspect ratio a/b is relatively weak. Therefore, one can write

$$\Delta\ell_{\text{open}} = \frac{C_{\text{open}}}{C} \approx \frac{b}{2} \quad (7.139)$$

where C_{open} is the open-end capacitance and C is the capacitance per unit length of CPW. The above approximation is valid for $\epsilon_r = 12.9$, $0.2 \leq a/b \leq 0.8$, and $h = 200 \mu\text{m}$. For other line geometries, a deviation of up to 20 percent may occur. Equation (7.139) can be used for other substrates also because the substrate permittivity affects C_{open} and the line capacitance C in the same way. Similarly, for a short circuit

$$\Delta\ell_{\text{short}} = \frac{L_{\text{short}}}{L} \approx \frac{b}{4} \quad (7.140)$$

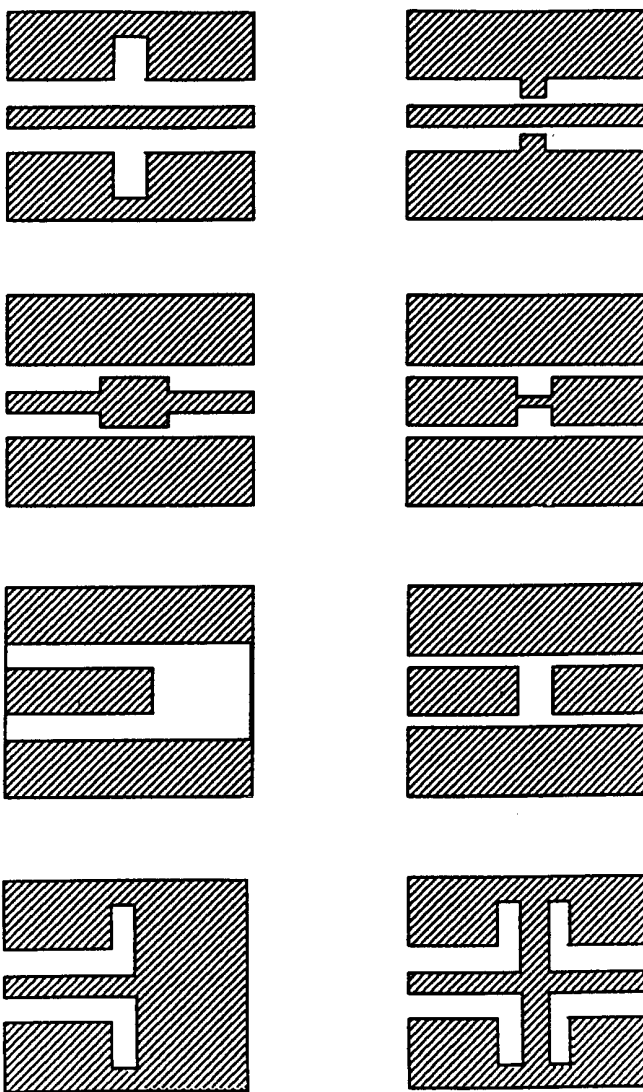


Figure 7.37 Some common CPW discontinuities (from [111], © 1993 IEEE. Reprinted with permission.).

Equation (7.140) is valid when the metallization thickness t does not become too large ($t < W/3$).

Some of the discontinuities and their equivalent circuits are described in the next section.

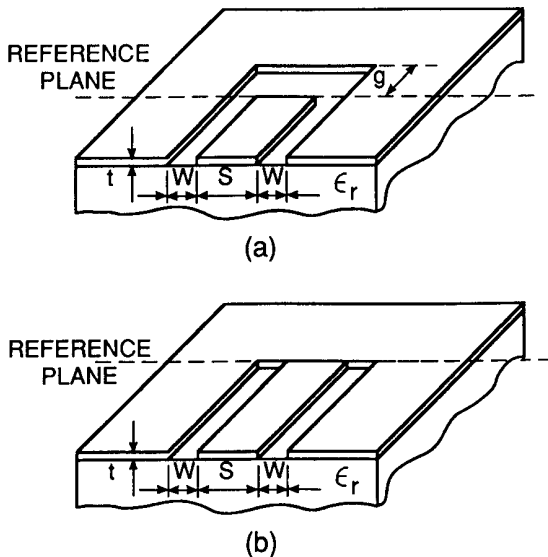


Figure 7.38 (a) Open-circuit discontinuity in CPW and (b) short-circuit discontinuity in CPW.

7.9 COPLANAR LINE CIRCUITS

Several circuits using CPW have been reported, but CPS circuits have not gained much popularity. Circuit applications of CPW can be grouped as follows:

- Circuits with series and shunt reactances in CPW;
- Circuits using slotline-CPW junctions.

7.9.1 Circuits with Series and Shunt Reactances in CPW

The first group of CPW circuits uses the flexibility of the coplanar waveguide configuration to accommodate both the series- and the shunt-connected components. Various circuit elements that may be realized in a CPW configuration [116] are shown in Figure 7.39, 7.40, and 7.41. While calculating line lengths it should be remembered that the propagation velocities are not equal for the different impedance sections.

Figure 7.39 represents the realization of series-connected inductances and capacitances. Circuit representations in Figure 7.39(b) use another coplanar waveguide configuration inside the central strip of the main CPW. The basic idea is borrowed from similar coaxial line circuits [117]. The series inductance is obtained by a CPW section (smaller than $\lambda_{cp}/4$) shorted at the far end, whereas the series

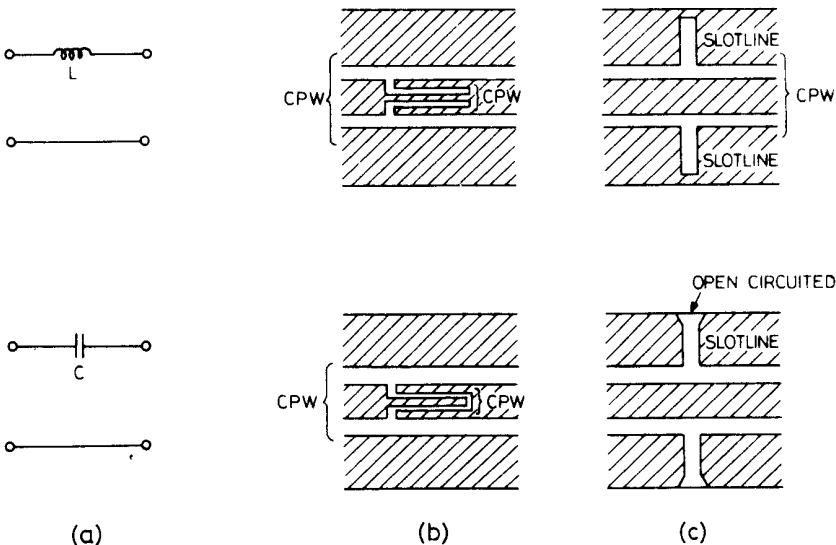


Figure 7.39 Series circuit elements in a CPW configuration: (a) circuit element; (b) realization using CPWs; and (c) realization using CPW and slotline.

capacitance is realized by a CPW section (again smaller than $\lambda_{cp}/4$) open at the far end.

Use of slotline sections, as shown in Figure 7.39(c), is another way of obtaining series-connected elements. Short-circuited slotlines are used for inductances and open-circuited slotlines for capacitances.

Figure 7.40 represents a realization of shunt-connected reactances obtained by adding coplanar waveguide stubs to the main CPW. Open-circuited stubs are used for capacitance and short-circuited stubs for inductance. The conducting straps are bonded at the junction of the main line and the stubs to ensure that the two ground planes of the CPW stubs are at the same potential. A shunt-mounted series-resonant circuit can be realized by using stubs comprising two CPWs of different impedances. An open-circuit high-impedance section provides the capacitance, whereas the low-impedance section provides inductance. The shunt-mounted series-resonant circuit is useful for designing stop-band filters.

It is also possible to realize pi or tee shaped reactance networks by using CPW stubs. Figure 7.41(a) shows a shorted CPW stub without any strap to equalize the potentials of the two ground planes of the stub. Thus the stub can support two types of modes: normal CPW mode and the odd mode of coupled slotlines. The latter mode presents an inductance L that appears in series with the main line. When the straps are added, the odd mode of coupled slotlines cannot exist (that

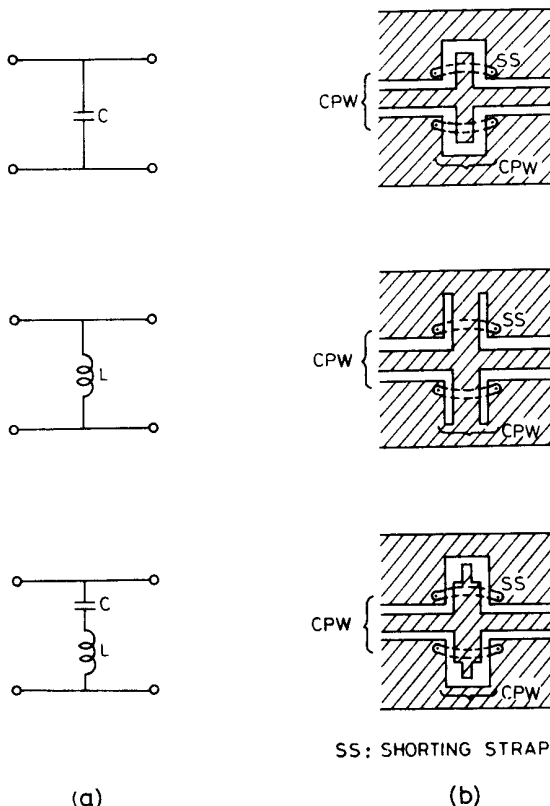


Figure 7.40 Shunt circuit elements in a CPW configuration: (a) circuit element and (b) realization using CPWs.

is, the inductance L gets shorted) and the equivalent circuit reduces to that shown in Figure 7.40(b). An external capacitance C can be connected in parallel to the series inductance L by bonding chip capacitors across the stubs as shown in Figure 7.41(b). This provides a useful circuit element for filter circuits. A pi-network having shunt capacitances can be realized by using an open circuited stub without the shorting strap. One can use chip capacitors to provide a capacitance in parallel to L in this case also.

Schematic diagrams of the Schottky diode detector and the CPW equivalent are shown in Figure 7.42. The circuit uses series and shunt reactances realized by using CPW sections as discussed above. This detector circuit has a VSWR less than 2.0 and a tangential sensitivity less than -52 dBm in the 2-GHz to 4.5-GHz band [116].

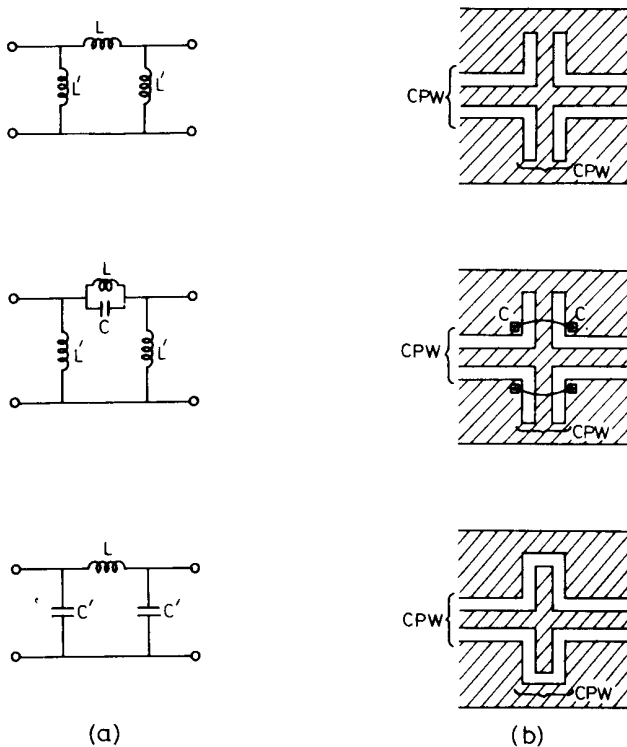


Figure 7.41 Series and shunt circuit elements in a CPW configuration: (a) circuit element and (b) realization using CPWs.

7.9.2 Circuits Using Slotline-CPW Junctions

CPW-slotline T-junctions are being used in MMICs [71]. There are four types of T-junctions that can be realized between CPW and slotline, and these are illustrated in Figure 7.43, and Table 7.4 classifies the parallel and series T-junctions in accordance with the input and output transmission lines. For the parallel T-junction the input line should be an unbalanced (CPW) line, while the series T-junction requires a balanced (slot) input line. Equivalent circuits of parallel and series T-junctions are shown in Figure 7.44. Applications of these junctions in realizing a magic-T and a balanced mixer are described next.

Magic-T [76]

The magic-T can be realized in a CPW-slotline configuration. It makes use of the properties of a slotline (parallel) T-junction and a CPW-slotline (series) T-junction

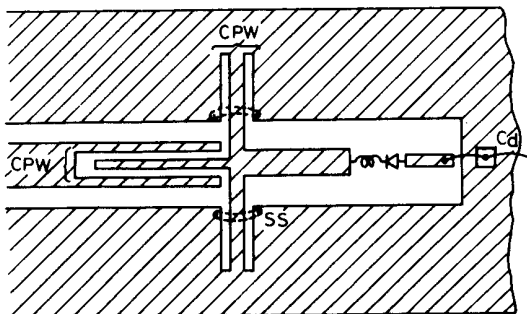
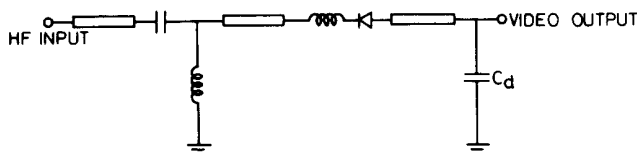


Figure 7.42 Coplanar waveguide detector (from [116], © 1976 Microwave Exhibitions & Publishers (U.K.). Reprinted with permission.).

along with the concept of a rat-race hybrid ring. A configuration of the magic-T is illustrated in Figure 7.45. It consists of a slot ring of radius r such that the circumference of the ring is equal to one guide wavelength of slotline. This circumference is divided equally into four quarter-wave sections. Each of these sections constitutes the output arms of the T-junction associated with them as shown in the figure. Ports 1, 2, and H are the CPW feed ports, and port E is the slotline feed port. The slotline T-junction has the property that outputs have 180° phase difference between them (see Figure 7.43(d)). As a consequence of this the separation between port E and port 2 can be reduced to $\lambda_s/4$ from the value of $3\lambda_s/4$ in a conventional hybrid ring. Other design aspects of magic-T remain the same, namely, $Z_{\text{slot}} = \sqrt{2} Z_{\text{cpw}}$. Measurements carried out on a magic-T built on a 1.27-mm-thick substrate with $\epsilon_r = 10.8$ provided the following characteristics in the S-band [76]:

Power dividing balance of the E-arm	$<\pm 0.4$ dB
Isolation between E- and H-arms	>36 dB
Power dividing balance of the H-arm	$\leq \pm 0.3$ dB
Isolation between ports 1 and 2	>12 dB
Phase balance of H-arm	$-0.75^\circ \pm 0.75^\circ$
Phase balance of E-arm	$-181^\circ \pm 1^\circ$

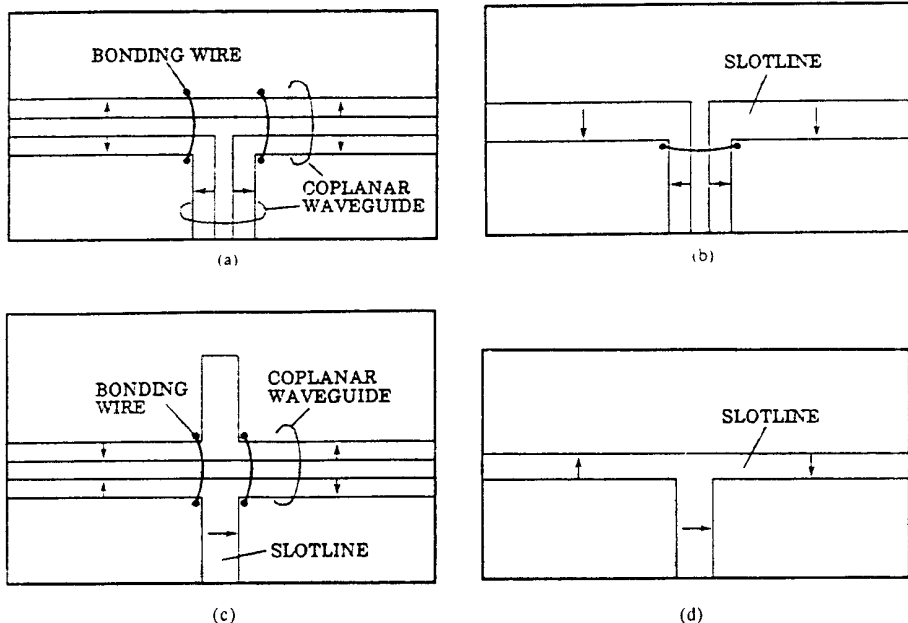


Figure 7.43 Various types of CPW, slotline T-junctions: (a) CPW-CPW T-junction; (b) CPW-slotline T-junction; (c) slotline-CPW T-junction; and (d) slotline-slotline T-junction (from [72], © 1987 IEEE. Reprinted with permission.).

Table 7.4 [72]
Classification of CPW-Slotline T-Junctions

<i>Input Transmission Line</i>	<i>Output Transmission Line</i>	
	<i>CPW</i>	<i>Slotline</i>
CPW	Parallel Figure 7.43(a)	Parallel Figure 7.43(b)
Slotline	Series Figure 7.43(c)	Series Figure 7.43(d)

Circuits Using Both Balanced and Unbalanced Signals

A CPW can propagate a signal in two modes: (1) an unbalanced signal in the even mode of coupled slotlines and (2) a balanced signal in the odd mode of coupled slotlines. The impedances for these modes (balanced and unbalanced) are different.

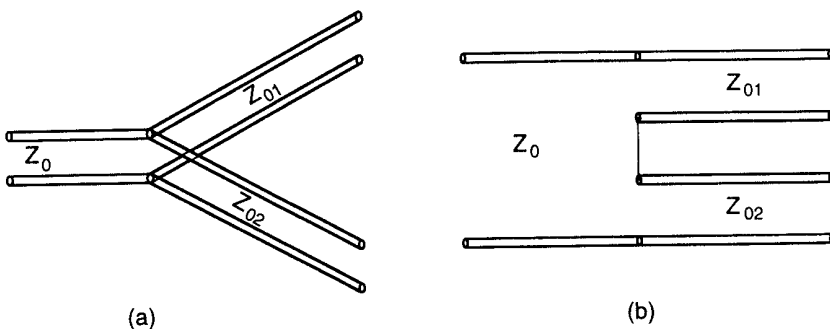


Figure 7.44 Equivalent circuit for T-junctions of Figure 7.43: (a) equivalent circuit for T-junctions with CPW as input transmission line and (b) equivalent circuit for T-junctions with slotline as input transmission line.

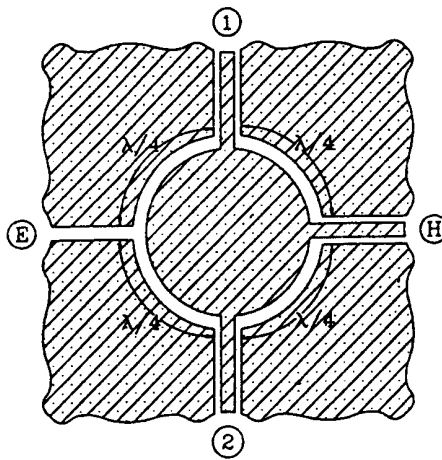


Figure 7.45 Coplanar magic-T (from [76], © 1993 IEEE. Reprinted with permission.).

The slotline-to-CPW junction shown in Figure 7.46(a) excites a balanced signal in CPW. On the other hand, when a CPW is fed from a coaxial line as in Figure 7.46(b) or through a microstrip as in Figure 7.46(c), an unbalanced signal is launched on the CPW. Therefore, a microstrip-CPW-slotline (or a coax-CPW-slotline) combination may be used in circuits where both the balanced and the unbalanced signals are employed. Such circuits are balanced mixers, double balanced mixers, balanced modulators, balanced frequency multipliers. A number of these circuits in coplanar configuration have been reported [72, 77, 118–122]. The balanced mixer is discussed next.

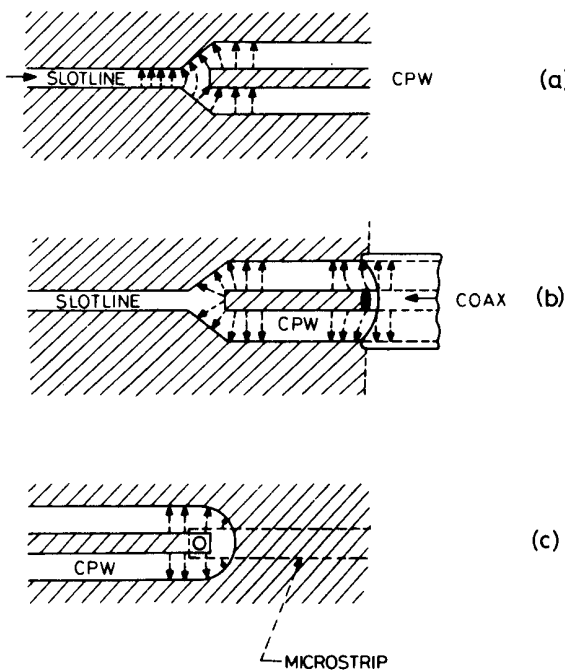


Figure 7.46 (a) Excitation of a balanced mode in CPW by a slotline, (b) an unbalanced mode in CPW excited by a coaxial line, and (c) an unbalanced mode in CPW excited by a microstrip.

Balanced Mixer

An arrangement for a balanced mixer using CPW is shown in Figure 7.47 [118]. This circuit uses a balanced local oscillator input and an unbalanced signal input. Local oscillator voltage is applied via the slotline, and the signal is fed through the coaxial line. This circuit was designed for the 1-GHz to 4-GHz frequency range and uses chrome-gold metallization on one side of a 2-mm-thick sheet of magnesium titanate dielectric ($\epsilon_r = 16$). The sheet is suspended in the center of a metal box. Connection to the slotline is made by a small copper coaxial cable at right angles to the axis, while a coaxial connection to the CPW is made directly along the axis. The unbalanced signal from the CPW cannot propagate past the CPW-slot junction. Also, the balanced signal from the slotline can propagate only up to the coaxial connection point where it faces a short circuit. Four beam-lead Schottky diodes are connected across the CPW as shown. The filter capacitors are the silicon dioxide type, which also serve as bonding pads for the tiny beam-lead diodes. The IF connecting wires are brought through holes in the substrate to the filter inductors located below. This circuit has demonstrated a frequency range capability of 6:1

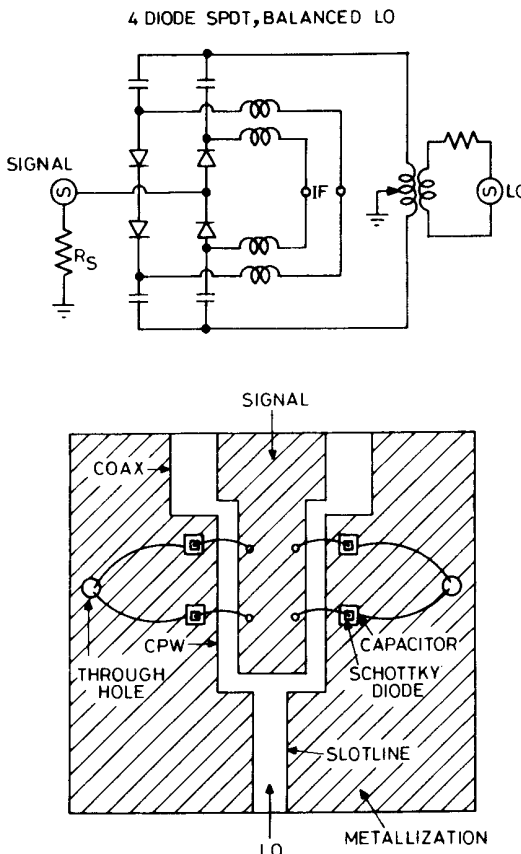


Figure 7.47 A circuit arrangement for a double balanced mixer using CPW (from [118], © 1969 IEEE. Reprinted with permission.).

with 6.5-dB to 7.0-dB conversion loss (with 10-mW incident power). Another mixer circuit using a slotline-CPW junction has been described by Dickens and Maki in [122].

References

- [1] Wen, C. P., "Coplanar Waveguide: A Surface Strip Transmission Line Suitable for Non-Reciprocal Gyromagnetic Device Application," *IEEE Trans.*, Vol. MTT-17, 1969, pp. 1087–1090.
- [2] Knorr, J. B., and K. D. Kuchler, "Analysis of Coupled Slots and Coplanar Strips on Dielectric Substrate," *IEEE Trans.*, Vol. MTT-23, 1975, pp. 541–548.
- [3] Fujiki, Y., et al., "Higher-Order Modes in Coplanar-Type Transmission Lines," *Electron. Comm. in Japan*, Vol. 58-B, Number 2, 1975, pp. 74–80.

- [4] Jackson, R. W., "Considerations in the Use of Coplanar Waveguide for Millimeter-Wave Integrated Circuits," *IEEE Trans.*, Vol. MTT-34, 1986, pp. 1450–1456.
- [5] Itoh, T., and R. Mittra, "Spectral-Domain Approach for Calculating Dispersion Characteristics of Microstrip Lines," *IEEE Trans.*, Vol. MTT-21, 1973, pp. 496–498.
- [6] Fukuoka, Y., et al., "Analysis of Slow-Wave Coplanar Waveguide for Monolithic Integrated Circuits," *IEEE Trans.*, Vol. MTT-31, 1983, pp. 567–573.
- [7] Phatak, D. S., et al., "Dispersion Characteristics of Optically Excited Coplanar Striplines: Comprehensive Full-Wave Analysis," *IEEE Trans.*, Vol. MTT-38, 1990, pp. 1719–1730.
- [8] Shih, Y. C., and T. Itoh, "Analysis of Conductor-Backed Coplanar Waveguide," *Electron. Lett.*, Vol. 18, 1982, pp. 538–540.
- [9] Itoh, T. (Ed.), *Numerical Techniques for Microwave and Millimeter-Wave Passive Structures*, New York: Wiley, 1989.
- [10] Das, N. K., and D. M. Pozar, "Generalized Spectral-Domain Green's Function for Multilayered Dielectric Substrates with Application to Multilayer Transmission Lines," *IEEE Trans.*, Vol. MTT-35, 1987, pp. 326–335.
- [11] Mirshekar-Syahkal, D., and J. B. Davies, "Accurate Solution of Microstrip and Coplanar Structures for Dispersion and for Dielectric and Conductor Losses," *IEEE Trans.*, Vol. MTT-27, 1979, pp. 694–699.
- [12] Pintzos, S. G., "Full-Wave Spectral Domain Analysis of Coplanar Strips," *IEEE Trans.*, Vol. MTT-39, 1991, pp. 239–246.
- [13] Pregla, R., and S. G. Pintzos, "Determination of the Propagation Constants in Coupled Microslots by a Variational Method," *Proc. V Colloq. Microwave Comm.*, Budapest, June, 1974, pp. Mt-491–500.
- [14] Kitazawa, T., and Y. Hayashi, "Coupled Slots on an Anisotropic Sapphire Substrate," *IEEE Trans.*, Vol. MTT-29, 1981, pp. 1035–1040.
- [15] Kitazawa, T., and Y. Hayashi, "Quasistatic Characteristics of a Coplanar Waveguide with Thick Metal Coating," *Proc. IEE, Part H*, Vol. 133, 1986, pp. 18–20.
- [16] Yamashita, E., and K. Atsuki, "Analysis of Microstrip-Like Transmission Lines by Nonuniform Discretization of Integral Equations," *IEEE Trans.*, Vol. MTT-24, 1976, pp. 195–200.
- [17] Hatsuda, T., "Computation of Coplanar-Type Strip Line Characteristics by Relaxation Method and Its Applications to Microwave Circuits," *IEEE Trans.*, Vol. MTT-23, 1975, pp. 795–802.
- [18] Diestel, H., and S. B. Worm, "Analysis of Hybrid Field Problems by the Method of Lines with Nonequidistant Discretization," *IEEE Trans.*, Vol. MTT-32, 1984, pp. 633–638.
- [19] Sorrentino, R., et al., "Characteristics of Metal-Insulator-Semiconductor Coplanar Waveguides for Monolithic Microwave Circuits," *IEEE Trans.*, Vol. MTT-32, 1984, pp. 410–416.
- [20] Liang, G. C., et al., "Analysis of Coplanar Waveguides and Slotlines using Time-Domain Finite-Difference Method," *IEEE Trans.*, Vol. MTT-37, 1989, pp. 1949–1957.
- [21] Shlager, K. L., et al., "Relative Accuracy of Several Finite-Difference Time-Domain Methods in Two and Three Dimensions," *IEEE Trans.*, Vol. AP-41, 1993, pp. 1732–1737.
- [22] Veyres, C., and V. F. Hanna, "Extension of the Application of Conformal Mapping Techniques to Coplanar Lines with Finite Dimensions," *Int. J. Electron.*, Vol. 48, 1980, pp. 47–56.
- [23] Ghione, G., and C. U. Naldi, "Coplanar Waveguides for MMIC Applications: Effect of Upper Shielding, Conductor Backing, Finite Extent Ground Planes, and Line-to-Line Coupling," *IEEE Trans.*, Vol. MTT-35, 1987, pp. 260–267.
- [24] Bedair, S. S., and I. Wolff, "Fast, Accurate and Simple Approximate Analytic Formulas for Calculating the Parameters of Supported Coplanar Waveguides," *IEEE Trans.*, Vol. MTT-40, 1992, pp. 41–48.
- [25] Hilberg, W., "From Approximations to Exact Relations for Characteristic Impedances," *IEEE Trans.*, Vol. MTT-17, 1969, pp. 259–265.
- [26] Goyal, R., (Ed.), *Monolithic Microwave Integrated Circuits: Technology and Design*, Norwood, MA: Artech House, 1989, Section 4.7.
- [27] Ghione, G., and C. Naldi, "Parameters of Coplanar Waveguides with Lower Ground Plane," *Electron. Lett.*, Vol. 19, 1983, pp. 734–735.

- [28] Svacina, J., Private Communication.
- [29] Hanna, V. F., and D. Thebault, "Theoretical and Experimental Investigations of Asymmetric Coplanar Waveguides," *IEEE Trans.*, Vol. MTT-32, 1984, pp. 1649–1651.
- [30] Svacina, J., "A Simple Quasi-static Determination of Basic Parameters of Multilayer Microstrip and Coplanar Waveguide," *IEEE Microwave Guided Wave Lett.*, Vol. 2, 1992, pp. 385–387.
- [31] Jahnke, E., F. Emde, and F. Losch, *Tables of Higher Functions*, New York: McGraw-Hill, 1960.
- [32] Haga, H., et al., "Travelling Wave Modulator Switch with an Etched Grave," *IEEE J. Quantum Electron.*, Vol. QE-22, 1986, pp. 902–906.
- [33] Izutsu, M., et al., "Broad-Band Travelling-Wave Modulator Using a LiNbO₃ Optical Waveguide," *IEEE J. Quantum Electron.*, Vol. QE-13, 1977, pp. 287–290.
- [34] Platle, W., and B. Saurer, "Optically CW-Induced Losses in Semiconductor Waveguides," *IEEE Trans.*, Vol. MTT-37, 1989, pp. 139–149.
- [35] Crampagne, R., and G. Khoo, "Synthesis of Certain Transmission Lines Employed in Microwave Integrated Circuits," *IEEE Trans.*, Vol. MTT-25, 1977, pp. 440–442.
- [36] Ghione, G., "A CAD-Oriented Analytical Model for the Losses of General Asymmetric Coplanar Lines in Hybrid and Monolithic MICs," *IEEE Trans.*, Vol. MTT-41, 1993, pp. 1499–1510.
- [37] Bedair, S. S., "Characteristics of Some Asymmetrical Coupled Transmission Lines," *IEEE Trans.*, Vol. MTT-32, 1984, pp. 108–110.
- [38] Hoffmann, R. K., *Handbook of Microwave Integrated Circuits*, Norwood, MA: Artech House, 1987.
- [39] Gevorgian, S. S., and I. G. Mironenko, "Asymmetric Coplanar-Strip Transmission Lines for MMIC and Integrated Optic Applications," *Electron. Lett.*, Vol. 26, 1990, pp. 1916–1918.
- [40] Ghione, G., and C. Naldi, "Analytical Formulas for Coplanar Lines in Hybrid and Monolithic MICs," *Electron. Lett.*, Vol. 20, 1984, pp. 179–181.
- [41] Chung, H., et al., "Modeling and Optimization of Traveling Wave LiNbO₃ Interferometric Modulators," *IEEE J. Quantum Electron.*, Vol. QE-27, 1991, pp. 608–617.
- [42] Donnelly, J. P., and A. Gopinath, "A Comparison of Power Requirements of Traveling-Wave LiNbO₃ Optical Couplers and Interferometric Modulators," *IEEE J. Quantum Electron.*, Vol. QE-23, 1987, pp. 30–41.
- [43] McLean, J. S., and T. Itoh, "Analysis of a New Configuration of Coplanar Stripline," *IEEE Trans.*, Vol. MTT-40, 1992, pp. 772–774.
- [44] Hanna, V. F., "Finite Boundary Corrections to Coplanar Stripline Analysis," *Electron. Lett.*, Vol. 16, 1980, pp. 604–606.
- [45] Chou, L., et al., "A WH/GSMT Based Full-Wave Analysis of the Power Leakage from Conductor-Backed Coplanar Waveguide," *IEEE MTT-S Digest*, 1992, pp. 219–222.
- [46] Janiczak, B. J., "Analysis of Coplanar Waveguide with Finite Ground Planes," *AEU*, Vol. 38, 1984, pp. 341–342.
- [47] Phatak, D. S., and A. P. Defonzo, "Dispersion Characteristics of Optically Excited Coplanar Striplines: Pulse Propagation," *IEEE Trans.*, Vol. MTT-38, 1990, pp. 654–661.
- [48] Hasnain, G., et al., "Dispersion of Picosecond Pulses in Coplanar Transmission Lines," *IEEE Trans.*, Vol. MTT-34, 1986, pp. 738–741.
- [49] Frankel, M. Y., et al., "Terahertz Attenuation and Dispersion Characteristics of Coplanar Transmission Lines," *IEEE Trans.*, Vol. MTT-39, 1991, pp. 910–916.
- [50] Kitazawa, T., et al., "A Coplanar Waveguide with Thick Metal-Coating," *IEEE Trans.*, Vol. MTT-24, 1976, pp. 604–608.
- [51] Wu, K., et al., "The Influence of Finite Conductor Thickness and Conductivity on Fundamental and Higher-Order Modes in Miniature Hybrid MICs (MHMICs) and MMICs," *IEEE Trans.*, Vol. MTT-41, 1993, pp. 421–430.
- [52] Ke, J. Y., and C. H. Chen, "The Coplanar Waveguides with Finite Metal Thickness and Conductivity," *IEEE MTT-S Digest*, 1994, pp. 1681–1684.
- [53] Yamashita, E., et al., "Characterization Method and Simple Design Formulas of MCS Lines Proposed for MMICs," *IEEE Trans.*, Vol. MTT-35, 1987, pp. 1355–1362.

- [54] Owyang, O. H., and T. T. Wu, "The Approximate Parameters of Slot Lines and Their Complement," *IRE Trans.*, Vol. AP-6, 1958, pp. 49–55.
- [55] Tuncer, E., et al., "Quasi-Static Conductor Loss Calculations in Transmission Lines Using a New Conformal Mapping Technique," *IEEE Trans.*, Vol. MTT-42, 1994, pp. 1807–1815.
- [56] Gopinath, A., "Losses in Coplanar Waveguides," *IEEE Trans.*, Vol. MTT-30, 1982, pp. 1101–1104.
- [57] Das, N. K., and D. M. Pozar, "Full-Wave Spectral Domain Computation of Material, Radiation, and Guided Wave Losses in Infinite Multilayered Printed Transmission Lines," *IEEE Trans.*, Vol. MTT-39, 1991, pp. 54–63.
- [58] Kitazawa, T., and T. Itoh, "Propagation Characteristics of Coplanar-Type Transmission Lines with Lossy Media," *IEEE Trans.*, Vol. MTT-39, 1991, pp. 1694–1700.
- [59] Shigesawa, H., et al., "Conductor-Backed Slot Line and Coplanar Waveguide: Dangers and Full-Wave Analysis," *IEEE MTT-S Digest*, 1988, pp. 199–202.
- [60] Shigesawa, H., et al., "Dominant Mode Power Leakage from Printed-Circuit Waveguides," *Radio Sci.*, Vol. 26, 1991, pp. 559–564.
- [61] McKinzie, W. E., and N. G. Alexopoulos, "Leakage Loss for the Dominant Mode of Conductor-Backed Coplanar Waveguide," *IEEE Microwave Guided Wave Lett.*, Vol. 2, 1992, pp. 65–67.
- [62] Liu, Y., and T. Itoh, "Leakage Phenomena in Multilayered Conductor-Backed Coplanar Waveguides," *IEEE Microwave Guided Wave Lett.*, Vol. 3, 1993, pp. 426–427.
- [63] Riazat, M., et al., "Propagation Modes and Dispersion Characteristics of Coplanar Waveguides," *IEEE Trans.*, Vol. MTT-38, 1990, pp. 245–251.
- [64] Kasilingam, D. P., and D. B. Rutledge, "Surface Wave Losses of Coplanar Transmission Lines," *IEEE MTT-S Digest*, 1983, pp. 113–116.
- [65] Rutledge, D. B., et al., *Planar Integrated Circuit Antennas*, Vol. 10, *Millimeter Components and Techniques*, Infrared and Millimeter Waves, Part II, (ed. K. J. Button), New York: Academic Press, 1983, Chapter 1.
- [66] Tsuji, M., et al. "New Interesting Leakage Behavior on Coplanar Waveguides of Finite and Infinite Widths," *IEEE Trans.*, Vol. MTT-39, 1991, pp. 2130–2137.
- [67] Ke, J.-Y., et al., "Dispersion and Leakage Characteristics of Coplanar Waveguides," *IEEE Trans.*, Vol. MTT-40, 1992, pp. 1970–1973.
- [68] Grischkowsky, D., et al., "Electromagnetic Shock Waves from Transmission Lines," *Phys Rev. Lett.*, Vol. 59, 1987, pp. 1663–1666.
- [69] Heinrich, W., "Full-Wave Analysis of Conductor Losses on MMIC Transmission Lines," *IEEE Trans.*, Vol. MTT-38, 1990, pp. 1468–1472.
- [70] Heinrich, W., "Conductor Loss on Transmission Lines in Monolithic Microwave and Millimeter-Wave Integrated Circuits," *Int. J. Microwave MM-Wave CAE*, Vol. 2, No. 3, 1992, pp. 155–167.
- [71] Houdart, M., and C. Aury, "Various Excitations of Coplanar Waveguide," *IEEE MTT-S Digest*, 1979, pp. 116–118.
- [72] Ogawa, H., and A. Minagawa, "Uniplanar MIC Balanced Multiplier—A Proposed New Structure for MICs," *IEEE Trans.*, Vol. MTT-35, 1987, pp. 1363–1368.
- [73] Grammer, W., and K. S. Yngvesson, "Coplanar Waveguide Transitions to Slotline: Design and Microprobe Characterization," *IEEE Trans.*, Vol. MTT-41, 1993, pp. 1653–1658.
- [74] Ho, T. Q., and S. M. Hart, "A Broad-Band Coplanar Waveguide to Slotline Transition," *IEEE Microwave Guided Wave Lett.*, Vol. 2, 1992, pp. 415–416.
- [75] Ho, C. H., et al., "Broadband Uniplanar Hybrid-Ring Couplers," *Electron. Lett.*, Vol. 29, 1993, pp. 44–45.
- [76] Ho, C. H., et al., "Broadband Uniplanar Hybrid-Ring and Branch-Line Couplers," *IEEE Trans.*, Vol. MTT-41, 1993, pp. 2116–2125.
- [77] Cahana, D., "A New Coplanar Waveguide/Slotline Double-Balanced Mixer," *IEEE MTT-S Digest*, 1989, pp. 967–968.
- [78] Vourch, E., et al., "A Full-Wave Analysis of Coplanar Waveguide-Slotline Transition," *IEEE MTT-S Digest*, 1994, pp. 1309–1312.

- [79] Trifunovic, V., and B. Jokanovic, "New Uniplanar Balun," *Electron. Lett.*, Vol. 27, 1991, pp. 813–815.
- [80] Simons, R. N., "Novel Coplanar stripline to slotline Transition on High Resistivity Silicon," *Electron. Lett.*, Vol. 30, 1994, pp. 654–655.
- [81] Jansen, R. H., "Hybrid Mode Analysis of End Effects of Microwave and Millimeterwave Transmission Lines," *Proc. IEE, Part H*, Vol. 128, No. 2, 1981, pp. 77–86.
- [82] Dib, N., et al., "A Comparative Study Between Shielded and Open Coplanar Waveguide Discontinuities," *Int. J. Microwave MM-Wave Computer Aided Eng.*, Vol. 2, No. 4, 1992, pp. 331–341.
- [83] Dib, N., et al., "A Theoretical and Experimental Study of CPW Shunt Stubs," *IEEE Trans.*, Vol. MTT-41, 1993, pp. 38–44.
- [84] Dib, N., et al., "Theoretical and Experimental Characterization of Coplanar Waveguide Discontinuities for Filter Applications," *IEEE Trans.*, Vol. MTT-39, 1991, pp. 873–882.
- [85] Naghed, M., and I. Wolff, "Equivalent Capacitances of Coplanar Waveguide Discontinuities and Interdigitated Capacitors Using a 3-Dimensional Finite Difference Method," *IEEE Trans.*, Vol. MTT-38, 1990, pp. 1808–1815.
- [86] Kuo, W. W., and T. Itoh, "Characterization of Shielded Coplanar Type Transmission Line Junction Discontinuities Incorporating the Finite Metalization Thickness Effect," *IEEE Trans.*, Vol. MTT-40, 1992, pp. 72–80.
- [87] Jackson, R. W., "Mode Conversion at Discontinuities in Finite-Width Conductor-Backed Coplanar Waveguide," *IEEE Trans.*, Vol. MTT-37, 1989, pp. 1582–1589.
- [88] Drissi, M., et al., "Analysis of Coplanar Waveguide Radiating End Effects Using the Integral Equation Technique," *IEEE Trans.*, Vol. MTT-39, 1991, pp. 112–116.
- [89] Simons, R. N., and G. E. Ponchak, "Modeling of Some Coplanar Waveguide Discontinuities," *IEEE Trans.*, Vol. MTT-36, 1988, pp. 1796–1803.
- [90] Beilenhoff, K., et al., "Open and Short Circuits in Coplanar MMIC's," *IEEE Trans.*, Vol. MTT-41, 1993, pp. 1534–1537.
- [91] Bartolucci, G., and J. Piotrowski, "Full-Wave Analysis of Shielded Coplanar Waveguide Short-End," *Electron. Lett.*, Vol. 26, 1990, pp. 1615–1616.
- [92] Naghed, M., and I. Wolff, "A Three-Dimensional Finite-Difference Calculation of Equivalent Capacitances of Coplanar Waveguide Discontinuities," *IEEE MTT-S Digest*, 1990, pp. 1143–1146.
- [93] Jin, H., and R. Vahldieck, "Calculation of Frequency Dependent S-Parameters of CPW Air Bridges Considering Finite Metalization Thickness and Conductivity," *IEEE MTT-S Digest*, 1992, pp. 207–210.
- [94] Sinclair, C., and S. Nightingale, "An Equivalent Model for the Coplanar Waveguide Step Discontinuity," *IEEE MTT-S Digest*, 1992, pp. 1461–1464.
- [95] Naghed, M., et al., "A New Method for the Calculation of the Equivalent Inductances of Coplanar Waveguide Discontinuities," *IEEE MTT-S Digest*, 1991, pp. 747–750.
- [96] Rittweger, M., et al., "Full-Wave Analysis of Coplanar Discontinuities Considering Three-Dimensional Bond Wires," *IEEE MTT-S Digest*, 1991, pp. 465–468.
- [97] Beilenhoff, K., et al., "Analysis of T-Junctions for Coplanar MMICs," *IEEE MTT-S Digest*, 1994, pp. 1301–1304.
- [98] Dib, N., et al., "Analysis of Shielded CPW Discontinuities with Air Bridges," *IEEE MTT-S Digest*, 1991, pp. 469–472.
- [99] Rittweger, M., et al., "Full-Wave Analysis of a Modified Coplanar Air Bridge T-Junction," *Proc. 21st European Microwave Conf.*, 1991, pp. 993–998.
- [100] Dib, N., and L. P. Katehi, "Modeling of Shielded CPW Discontinuities Using the Space Domain Integral Equation Method (SDIE)," *J. Electromagnetic Waves Appl.*, Vol. 5, Nos 4/5, 1991, pp. 503–523.
- [101] Dib, N., and L. P. Katehi, "The Effect of Mitering on CPW Discontinuities," *Proc. 21st European Microwave Conf.*, 1991, pp. 223–228.
- [102] Harokopus, W., and L. P. Katehi, "Radiation Loss From Open Coplanar Waveguide Discontinuities," *IEEE MTT-S Digest*, 1991, pp. 743–746.

- [103] Rahman, K. M., and C. Nguyen, "On the Analysis of Single- and Multiple-Step Discontinuities for a Shielded Three-Layer Coplanar Waveguide," *IEEE Trans.*, Vol. MTT-41, 1993, pp. 1484–1488.
- [104] Chiu, C. W., and R. B. Wu, "A Moment Method Analysis for Coplanar Waveguide Discontinuity Inductances," *IEEE Trans.*, Vol. MTT-41, 1993, pp. 1511–1514.
- [105] Radisic, V., et al., "Experimentally Verifiable Modeling of Coplanar Waveguide Discontinuities," *IEEE Trans.*, Vol. MTT-41, 1993, pp. 1524–1533.
- [106] Jin, H., and R. Vahldieck, "Full-Wave Analysis of Coplanar Waveguide Discontinuities Using the Frequency Domain TLM Method," *IEEE Trans.*, Vol. MTT-41, 1993, pp. 1538–1542.
- [107] Dib, N. I., et al., "Characterization of Asymmetric Coplanar Waveguide Discontinuities," *IEEE Trans.*, Vol. MTT-41, 1993, pp. 1549–1558.
- [108] Chung, S. J., and T. R. Chrang, "Full-Wave Analysis of Discontinuities in Conductor-Backed Coplanar Waveguides Using the Method of Lines," *IEEE Trans.*, Vol. MTT-41, 1993, pp. 1601–1605.
- [109] Tran, A. M., and T. Itoh, "Full-Wave Modeling of Coplanar Waveguide Discontinuities with Finite Conductor Thickness," *IEEE Trans.*, Vol. MTT-41, 1993, pp. 1611–1615.
- [110] Alessandri, F., et al., "A 3-D Mode Matching Technique for the Efficient Analysis of Coplanar MMIC Discontinuities with Finite Metalization Thickness," *IEEE Trans.*, Vol. MTT-41, 1993, pp. 1625–1629.
- [111] Yu, M., et al., "Theoretical and Experimental Characterization of Coplanar Waveguide Discontinuities," *IEEE Trans.*, Vol. MTT-41, 1993, pp. 1638–1641.
- [112] Wu, K., et al., "Rigorous Analysis of 3-D Planar Circuit Discontinuities Using the Space-Spectral Domain Approach (SSDA)," *IEEE Trans.*, MTT-40, 1992, pp. 1475–1483.
- [113] Kulke, R., and T. Sporkmann, "Coplanar Waveguide Elements for a European CAD Environment," *Proc. 23rd European Microwave Conf.*, 1993, pp. 209–211.
- [114] Pogatzki, P., and O. Kramer, "A Coplanar Element Library for the Accurate CAD of (M)MICs," *Microwave Eng. Europe*, December/January 1994.
- [115] Pogatzki, P., et al., "A Comprehensive Evaluation of Quasi-Static 3D-FD Calculation for More Than 14 CPW Structures—Lines, Discontinuities and Lumped Elements," *IEEE MTT-S Digest*, 1994, pp. 1289–1292.
- [116] Houdart, M., "Coplanar Lines: Applications to Broadband Microwave Integrated Circuits," *Proc. Sixth European Microwave Conference (Rome)*, 1976, pp. 49–53.
- [117] Saad, T. S., et al. (Eds.), *Microwave Engineers Handbook*, Vol. I, Dedham, MA: Artech House, Inc., 1971, p. 114.
- [118] Hunton, J. K., "A Microwave Integrated Circuit Balanced Mixer with Broad-Bandwidth," *Proc. (IEEE-MTT) Microelectronics Symp.*, 1969, pp. A3.1–A3.2.
- [119] Hunton, J. K., and J. S. Takeuchi, "Recent Developments in Microwave Slotline Mixers and Frequency Multipliers," *Digest of Tech. Papers, G-MTT Symp.*, 1970, pp. 196–199.
- [120] Merkee, J., "A d.c. to 20 GHz Thin Film Signal Sampler for Microwave Instrumentation," *H. P. J.*, Vol. 24, 1973, pp. 10–13.
- [121] Hoss, B., and F. Reisch, "Behind the Design of a Portable Analyser," *Microwaves*, Vol. 14, January 1975, pp. 36–40.
- [122] Dickens, L. E., and D. W. Maki, "An Integrated-Circuit Balanced Mixer Image and Sum Enhanced," *IEEE Trans.*, Vol. MTT-23, 1975, pp. 276–281.

CHAPTER 8

Coupled Microstrip Lines

8.1 INTRODUCTION

A “coupled line” configuration consists of two transmission lines placed parallel to each other and in close proximity as shown in Figure 8.1. In such a configuration there is a continuous coupling between the electromagnetic fields of the two lines. Coupled lines are utilized extensively as basic elements for directional couplers, filters, and a variety of other useful circuits.

Because of the coupling of electromagnetic fields, a pair of coupled lines can support two different modes of propagation. These modes have different characteristic impedances. The velocity of propagation of these two modes is equal when the lines are imbedded in a homogeneous dielectric medium (as, for example, in a triplate stripline structure). This is a desirable property for the design of circuits such as directional couplers and filters. However, for transmission lines such as coupled microstrip lines, the dielectric medium is not homogeneous. A part of the field extends into the air above the substrate. This fraction is different for the two modes of coupled lines. Consequently, the effective dielectric constants (and the phase velocities) are not equal for the two modes. This nonsynchronous feature deteriorates the performance of circuits using these types of coupled lines.

When the two conductors of a coupled line pair are identical we have a symmetrical configuration. This symmetry is very useful for simplifying the analysis and design of such coupled lines. If the two lines do not have the same impedance, the configuration is called asymmetric.

For the lines operating in the TEM mode or when the analysis can be based on quasi-static approximation, the properties of coupled lines can be determined from the self- and mutual inductances and capacitances for the lines. In the case of lines operating in the non-TEM mode (for example, coupled slotlines), a fullwave analysis is needed for the two modes of propagation.

In this chapter, coupled microstrip lines are discussed. The configuration for these lines is shown in Figure 8.1. Some of the important techniques for analyzing coupled lines are outlined. Coupled mode formulation and the even- and odd-mode method are described. Both quasi-static and fullwave analyses are used to evaluate the characteristics of symmetric and asymmetric coupled microstrip lines. The effects of nonzero strip thickness, dispersion, enclosure, fabrication tolerances, dielectric overlay, and dielectric anisotropy on the characteristics are presented. Methods of measuring the characteristics of coupled microstrip lines are included. The last section of this chapter contains a discussion of discontinuities in coupled microstrip lines.

8.2 GENERAL ANALYSIS OF COUPLED LINES

8.2.1 Methods of Analysis

Several analytical techniques are available for determining the propagation characteristics of the coupled lines shown in Figure 8.1(a). The four different methods that are generally employed are the even- and odd-mode method [1], the coupled mode formulation [2, 3], the graph transformation technique [4], and the congruent transformation technique [5, 6].

The even- and odd-mode method is the most convenient way of describing the behavior of symmetrical coupled lines. In this method wave propagation along a coupled pair of lines is expressed in terms of two modes corresponding to an even or an odd symmetry about a plane that can, therefore, be replaced by a magnetic or electric wall for the purpose of analysis.

In the coupled mode approach, the wave propagation is expressed in terms of the modes of propagation on individual uncoupled lines modified by the coupling because of mutual capacitances and inductances. This approach, therefore, provides an insight into the mechanism of coupling. The method is quite general and is applicable to asymmetric coupled lines also. This approach finds applications in all types of coupled systems used in various disciplines.

The other two approaches employ the representation of coupled line systems in terms of equivalent networks. The “graph transformation technique” involves the use of a graph equivalent to the general coupled transmission line network for analysis [4]. The use of Richards’s transformation [7] allows the coupled line structures to be treated in exactly the same manner as lumped networks.

The equivalent circuit for the coupled lines can also be established using the congruent transformation technique [8]. This is believed to be a powerful method for establishing coupled line properties when there is a large number of lines coupled together. Using this technique, n -conductor coupled transmission lines can be reduced to a set of n decoupled transmission lines connected to two congruent transformers.

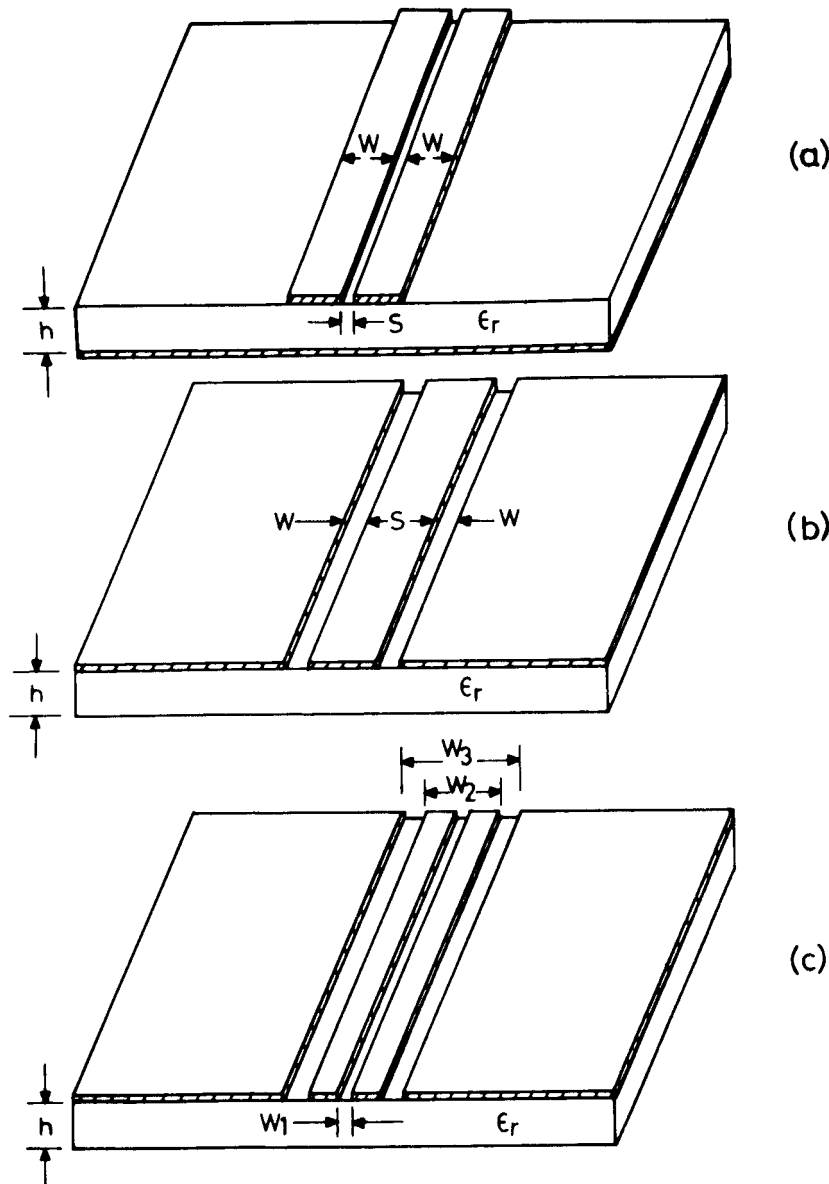


Figure 8.1 Configuration of coupled lines: (a) coupled microstrips, (b) coupled slotlines, and (c) coupled coplanar waveguides.

Graph transformation and congruent transformation methods are very useful when one deals with a number of lines (more than two) coupled together. Of the remaining two approaches, the coupled mode technique is more powerful as it can be applied to asymmetric coupled structures also. This approach is discussed in Section 8.2.2 and the even- and odd-mode method is discussed in Section 8.2.3.

8.2.2 Coupled Mode Approach [9-11]

In this approach coupled lines are characterized by the characteristic impedances (or admittances) and phase velocities for the two modes. These two modes are obtained by considering the effect of the self- and the mutual inductances and capacitances on the modes in the individual uncoupled lines.

For coupled mode analysis, the voltage on one line is written in terms of the currents on both lines and the self- and mutual impedances. Similarly the current is written in terms of voltages and admittances. Eliminating currents or voltages yields the coupled equations. The solution of these coupled equations determines the propagation constants for the two modes.

The coupled mode analysis for coupled lines with unequal impedances, shown in Figure 8.2, is described next.

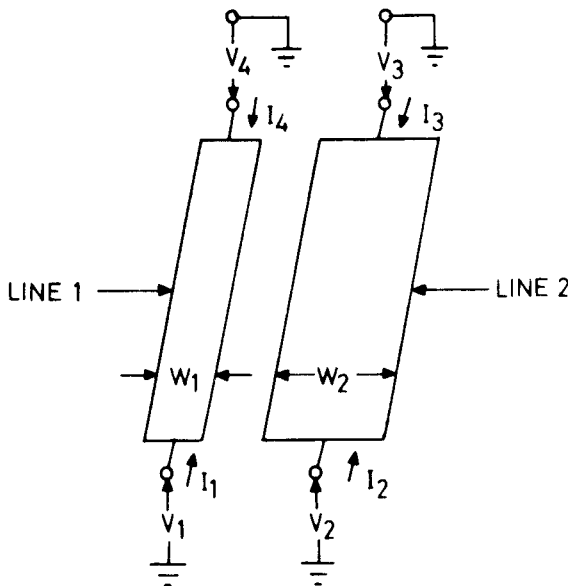


Figure 8.2 A pair of coupled lines with unequal impedances.

Analysis

The behavior of two lossless coupled transmission lines is described in general by the following set of differential equations:

$$-\frac{dv_1}{dz} = Z_1 i_1 + Z_m i_2 \quad (8.1)$$

$$-\frac{dv_2}{dz} = Z_m i_1 + Z_2 i_2 \quad (8.2)$$

$$-\frac{di_1}{dz} = Y_1 v_1 + Y_m v_2 \quad (8.3)$$

$$-\frac{di_2}{dz} = Y_m v_1 + Y_2 v_2 \quad (8.4)$$

where Z_j , Y_j ($j = 1, 2$) are self-impedances and self-admittances per unit length of lines 1 and 2 and Z_m and Y_m are mutual impedance and mutual admittance per unit length, respectively. Voltages and currents, which are functions of z , are represented by v_k and i_k ($k = 1, 2$), respectively. A time variation $e^{j\omega t}$ is assumed.

Eliminating i_1 and i_2 from (8.1) to (8.4) gives the following set of coupled equations for the voltages v_1 and v_2 :

$$\frac{d^2v_1}{dz^2} - a_1 v_1 - b_1 v_2 = 0 \quad (8.5)$$

$$\frac{d^2v_2}{dz^2} - a_2 v_2 - b_2 v_1 = 0 \quad (8.6)$$

where

$$\begin{aligned} a_1 &= Y_1 Z_1 + Y_m Z_m \\ b_1 &= Z_1 Y_m + Y_2 Z_m \\ a_2 &= Y_2 Z_2 + Y_m Z_m \\ b_2 &= Z_2 Y_m + Y_1 Z_m \end{aligned} \quad (8.7)$$

The coefficients a_1 , a_2 , b_1 , and b_2 are constants.

Assuming a variation of the type $v(z) = v_0 e^{-\gamma z}$ for the voltages v_1 and v_2 , the coupled equations (8.5) and (8.6) reduce to the eigenvalue equation

$$[\gamma^4 - \gamma^2(a_1 + a_2) + a_1 a_2 - b_1 b_2] v_0 = 0 \quad (8.8)$$

The solution of (8.8) leads to the following four roots for γ :

$$\gamma_{1,2} = \pm \gamma_c \quad \text{and} \quad \gamma_{3,4} = \pm \gamma_\pi \quad (8.9)$$

where

$$\gamma_{c,\pi}^2 = \frac{a_1 + a_2}{2} \pm \frac{1}{2} [(a_1 - a_2)^2 + 4 b_1 b_2]^{1/2} \quad (8.10)$$

The subscripts “c” and “ π ” refer to the c and π modes for asymmetric coupled lines. The propagation constants for these modes, γ_c and γ_π , correspond to in-phase and anti-phase waves, which reduce to even- and odd-mode waves respectively, for symmetrical lines. The roots with plus and minus signs in (8.9) represent waves travelling in the $+z$ - and $-z$ -directions, respectively.

The ratio of voltages v_2 and v_1 on the two lines for the c and π modes is obtained from (8.5), (8.6), and (8.10) and is given as

$$\frac{v_2}{v_1} = \frac{\gamma^2 - a_1}{b_1} = \frac{b_2}{\gamma^2 - a_2} \quad (8.11)$$

If the corresponding ratios for the c and π modes are represented by R_c and R_π , then

$$R_c \left(= \frac{v_2}{v_1} \quad \text{for } \gamma = \pm \gamma_c \right) = \frac{1}{2b_1} [(a_2 - a_1) + \{(a_2 - a_1)^2 + 4 b_1 b_2\}^{1/2}] \quad (8.12)$$

and

$$R_\pi \left(= \frac{v_2}{v_1} \quad \text{for } \gamma = \pm \gamma_\pi \right) = \frac{1}{2b_1} [(a_2 - a_1) - \{(a_2 - a_1)^2 + 4 b_1 b_2\}^{1/2}] \quad (8.13)$$

It may be observed from (8.12) and (8.13) that R_c is positive real and R_π is negative real, thus representing in-phase and anti-phase waves.

In terms of the four waves, with propagation constants $\pm \gamma_c$ and $\pm \gamma_\pi$, the general solution for the voltages on the two lines may be written as

$$v_1 = A_1 e^{-\gamma_c z} + A_2 e^{\gamma_c z} + A_3 e^{-\gamma_\pi z} + A_4 e^{\gamma_\pi z} \quad (8.14)$$

$$v_2 = R_c (A_1 e^{-\gamma_c z} + A_2 e^{\gamma_c z}) + R_\pi (A_3 e^{-\gamma_\pi z} + A_4 e^{\gamma_\pi z}) \quad (8.15)$$

The currents i_1 and i_2 are obtained by substituting the corresponding voltages v_1 and v_2 from (8.14) and (8.15) in (8.1) and (8.2) and may be written as

$$i_1 = Y_{c1}(A_1 e^{-\gamma_c z} - A_2 e^{\gamma_c z}) + Y_{\pi 1}(A_3 e^{-\gamma_\pi z} - A_4 e^{\gamma_\pi z}) \quad (8.16)$$

$$i_2 = Y_{c2}R_c(A_1 e^{-\gamma_c z} - A_2 e^{\gamma_c z}) + Y_{\pi 2}R_\pi(A_3 e^{-\gamma_\pi z} - A_4 e^{\gamma_\pi z}) \quad (8.17)$$

where Y_{c1} , Y_{c2} , $Y_{\pi 1}$, and $Y_{\pi 2}$ are the characteristic admittances of lines 1 and 2 for the two modes. These are given by

$$Y_{c1} = \gamma_c \frac{Z_2 - Z_m R_c}{Z_1 Z_2 - Z_m^2} = \frac{1}{Z_{c1}} \quad (8.18)$$

$$Y_{c2} = \frac{\gamma_c}{R_c} \frac{Z_1 R_c - Z_m}{Z_1 Z_2 - Z_m^2} = \frac{1}{Z_{c2}} \quad (8.19)$$

Similar relations hold for the π mode. Substituting the values of R_c and R_π in (8.18) and (8.19) gives

$$\frac{Y_{c1}}{Y_{c2}} = -R_c R_\pi = \frac{Y_{\pi 1}}{Y_{\pi 2}} \quad (8.20)$$

The above analysis has been carried out in terms of the two independent modes of propagation termed “c” and “ π ” modes with propagation constants γ_c and γ_π . The voltages v_1 and v_2 on the two lines are related through $v_2/v_1 = R_c$ and R_π . The corresponding ratios for the currents are given by $i_2/i_1 = -1/R_\pi$ and $-1/R_c$, respectively. For symmetric lines, “c” and “ π ” modes reduce to even and odd modes, respectively.

Symmetric Lines

For the case of symmetric lines, $a_2 = a_1$ and $b_2 = b_1$. Therefore, (8.12) and (8.13) give for v_2/v_1

$$\begin{aligned} v_2/v_1 &= R_c = +1 \quad \text{for c mode (even mode)} \\ v_2/v_1 &= R_\pi = -1 \quad \text{for } \pi \text{ mode (odd mode)} \end{aligned} \quad (8.21)$$

Also, (8.16) and (8.17) yield

$$\begin{aligned} i_2/i_1 &= +1 \quad \text{for c mode (even mode)} \\ i_2/i_1 &= -1 \quad \text{for } \pi \text{ mode (odd mode)} \end{aligned} \quad (8.22)$$

Evaluation of Characteristics for c and π Modes

As discussed above, asymmetric coupled lines can be represented in terms of two modes called c and π modes. The phase constants and the characteristic impedances of these modes are related to the line constants in the following manner [10]:

$$\gamma_{c,\pi} = j\beta_{c,\pi} = j \frac{\omega}{\sqrt{2}} \left[L_1 C_1 + L_2 C_2 - 2L_m C_m \pm \sqrt{(L_2 C_2 - L_1 C_1)^2 + 4(L_m C_1 - L_2 C_m)(L_m C_2 - L_1 C_m)} \right]^{1/2} \quad (8.23)$$

$$Z_{c1} = \frac{\omega}{\beta_c} \left(L_1 - \frac{L_m}{R_\pi} \right) = \frac{\beta_c}{\omega} \left(\frac{1}{C_1 - R_c C_m} \right) \quad (8.24)$$

$$Z_{\pi 1} = \frac{\omega}{\beta_\pi} \left(L_1 - \frac{L_m}{R_c} \right) = \frac{\beta_\pi}{\omega} \left(\frac{1}{C_1 - R_\pi C_m} \right) \quad (8.25)$$

and

$$R_{c,\pi} = \frac{L_2 C_2 - L_1 C_1 \pm \sqrt{(L_2 C_2 - L_1 C_1)^2 + 4(L_m C_2 - L_1 C_m)(L_m C_1 - L_2 C_m)}}{2(L_m C_2 - L_1 C_m)} \quad (8.26)$$

Self-capacitances C_1 and C_2 , self-inductances L_1 and L_2 as well as mutual capacitance C_m and mutual inductance L_m can be determined from quasi-static analysis.

8.2.3 Even- and Odd-Mode Approach

Thus far the analysis of coupled lines has been very general. Now we will restrict our attention to the case of symmetric coupled lines, that is, identical lines of equal characteristic impedances.

It was pointed out earlier that the c and π modes reduce to the even and odd modes, respectively, for symmetric coupled lines. The propagation constants for these modes are given by

$$\gamma_{e,0} = \gamma_{c,\pi} = [(Y_0 \pm Y_m)(Z_0 \pm Z_m)]^{1/2} \quad (8.27)$$

where

$$Y_0 = Y_1 \text{ or } Y_2 \quad Z_0 = Z_1 \text{ or } Z_2$$

In terms of line constants, the characteristics of even and odd modes can be obtained from (8.23) to (8.25) by substituting $L_1 = L_2 = L_o$ and $C_1 = C_2 = C_o$. The expressions are given as

$$\beta_{e,o} = \omega [L_o C_o - L_m C_m \pm (L_m C_o - L_o C_m)]^{1/2} \quad (8.28)$$

$$Z_{0e} = \frac{\omega}{\beta_e} (L_o + L_m) = \frac{\beta_e}{\omega} \left(\frac{1}{C_o - C_m} \right) \quad Y_{0e} = \frac{1}{Z_{0e}} \quad (8.29)$$

$$Z_{0o} = \frac{\omega}{\beta_o} (L_o - L_m) = \frac{\beta_o}{\omega} \left(\frac{1}{C_o + C_m} \right) \quad Y_{0o} = \frac{1}{Z_{0o}} \quad (8.30)$$

where $\beta_{e,o}$ are the phase constants of lossless coupled lines given by $\gamma_{e,o} = j\beta_{e,o}$. The lines are characterized by inductance per unit length L_o and capacitance per unit length C_o . The mutual inductance is L_m and the mutual capacitance is C_m .

Alternatively, the propagation constants may be written in terms of the phase constants of the lines and the coefficients of inductive and capacitive couplings k_L and k_C . If we define [12]

$$k_L = L_m / L_o \quad (8.31)$$

$$k_C = C_m / C_o \quad (8.32)$$

and

$$\beta_o = \omega \sqrt{L_o C_o} \quad (8.33)$$

We can write (8.28) as

$$\beta_{e,o} = \beta_{eff} \sqrt{1 \pm \delta} \quad (8.34)$$

where effective propagation constant β_{eff} is given by

$$\beta_{eff} = \beta_o (1 - k_L k_C)^{1/2} \quad (8.35)$$

and

$$\delta = \frac{k_L - k_C}{1 - k_L k_C} \quad (8.36)$$

In (8.34), positive and negative signs correspond to the even and odd modes, respectively.

For coupled lines propagating TEM modes, coupled mode parameters are normally expressed in terms of even- and odd-mode capacitances C_e^a , C_o^a for the air dielectric ($\epsilon_r = 1$) structure and those with dielectric substrate $C_e(\epsilon_r)$, $C_o(\epsilon_r)$. These are related to self- and mutual inductances and capacitances through the equations

$$L_o = \frac{\mu_0 \epsilon_0}{2} \left\{ \frac{1}{C_o^a} + \frac{1}{C_e^a} \right\} \quad (8.37)$$

$$L_m = \frac{\mu_0 \epsilon_0}{2} \left\{ \frac{1}{C_e^a} - \frac{1}{C_o^a} \right\} \quad (8.38)$$

$$C_o = \frac{1}{2} [C_o(\epsilon_r) + C_e(\epsilon_r)] \quad (8.39)$$

and

$$C_m = \frac{1}{2} [C_o(\epsilon_r) - C_e(\epsilon_r)] \quad (8.40)$$

The coupling coefficients k_L and k_C are defined by

$$k_L = \frac{L_m}{L_o} = \frac{C_o^a - C_e^a}{C_o^a + C_e^a} \quad (8.41)$$

and

$$k_C = \frac{C_m}{C_o} = \frac{C_o(\epsilon_r) - C_e(\epsilon_r)}{C_o(\epsilon_r) + C_e(\epsilon_r)} \quad (8.42)$$

The effective propagation constant, β_{eff} , can be expressed as

$$\beta_{\text{eff}} = \frac{\omega}{c} \sqrt{\epsilon_{re}} \sqrt{\frac{1 - k_L k_C}{1 - k_L^2}} \quad (8.43)$$

where

$$\epsilon_{re} = \frac{C_o(\epsilon_r) + C_e(\epsilon_r)}{C_o^a + C_e^a} \quad (8.44)$$

and impedances can be written as

$$Z_{0e} = \frac{\omega}{\beta_e} \frac{\mu_0 \epsilon_0}{C_e^a} \quad (8.45)$$

$$Z_{00} = \frac{\omega}{\beta_0} \frac{\mu_0 \epsilon_0}{C_o^a} \quad (8.46)$$

with

$$\beta_{e,o} = \omega \sqrt{\mu_0 \epsilon_0} \sqrt{\frac{C_{e,o}(\epsilon_r)}{C_{e,o}^a}} \quad (8.47)$$

The methods for evaluating the even- and odd-mode capacitances will be described in Section 8.3 and closed-form expressions will be presented in Section 8.5.

8.3 CHARACTERISTICS OF COUPLED MICROSTRIP LINES

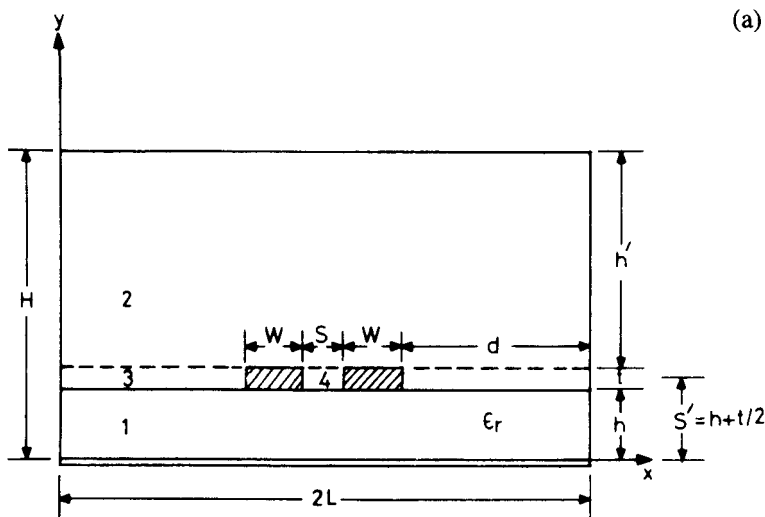
The methods of analysis discussed in the previous section are quite general. They may be applied to coupled lines in a homogeneous medium such as coupled striplines or coupled lines in an inhomogeneous medium such as coupled microstrip lines. Whereas coupled striplines are nondispersive in nature, coupled microstrip lines exhibit dispersive characteristics at higher frequencies. Quite often, coupled microstrip lines are used at frequencies where quasi-static analysis holds good and dispersion effects are negligible. Nevertheless, fullwave analysis helps in determining the frequency range of validity of quasi-static analysis. Both the quasi-static analysis as well as fullwave analysis for coupled microstrip lines with equal impedances are described in this section. The geometry of coupled microstrip lines is shown in Figure 8.3(a), and the field distributions for even and odd modes are given in Figure 8.3(b).

8.3.1 Quasi-Static Analysis

Almost all the methods described in Chapter 1 for the quasi-static analysis of a microstrip have also been employed to calculate even- and odd-mode capacitances of coupled microstrip lines. The conformal transformation method does not yield a simple closed-form solution in this case [13]. Green's function technique has been described by Bryant and Weiss [14–15]. The variational method in the space domain has been used by Krage and Haddad [12] and Bergandt and Pregla [16] to determine the upper bound on capacitances for the coupled line configuration enclosed in a box. The variational method in FTD has been described in [17].

Variational Method in Space Domain [12, 16]

In this method scalar potential functions, which are solutions of Laplace's equation, are expanded in a Fourier series. The Fourier coefficients are determined from



— ELECTRIC FIELD LINES
- - - MAGNETIC FIELD LINES

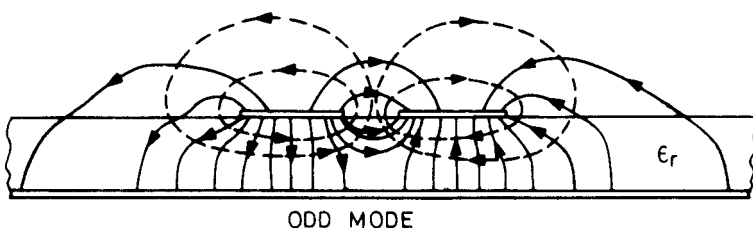
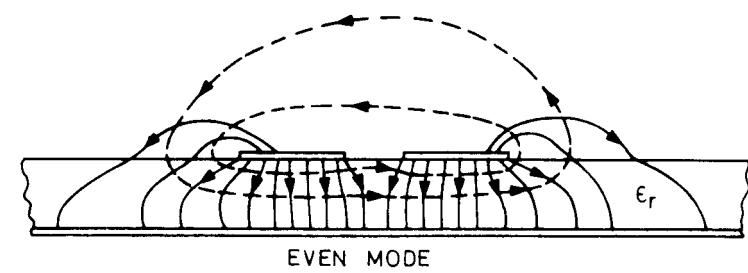


Figure 8.3 (a) Symmetric coupled microstrip lines in an enclosure and (b) even- and odd-mode field configurations in coupled microstrip lines.

the continuity conditions of potential functions and the stationary property of the stored electric energy with respect to Fourier coefficients. Once the potential functions for even and odd modes are known, these can be used to determine the capacitances for these modes.

For the purpose of analysis, the coupled microstrip configuration can be divided into four separate regions as shown in Figure 8.3(a).

Potentials are assumed to be $\phi = V_1$ and $\phi = V_2$ on the left and right strips, respectively. The outer conducting walls are at $\phi = 0$ potential. The field configuration in each of the four regions is obtained from a solution of Laplace's equation

$$\nabla^2 \phi_i = 0 \quad i = 1, 2, 3, 4 \quad (8.48)$$

The potentials ϕ_i that satisfy Laplace's and the boundary conditions on the enclosure equation may be written in terms of Fourier expansions as

$$\phi_1 = \sum_{m=1}^{\infty} A_m \sinh\left(\frac{m\pi y}{H}\right) \sin\left(\frac{m\pi x}{2L}\right) \quad (8.49)$$

$$\phi_2 = \sum_{m=1}^{\infty} B_m \sinh\frac{m\pi(H-y)}{H} \sin\left(\frac{m\pi x}{2L}\right) \quad (8.50)$$

$$\begin{aligned} \phi_3 = & \sum_{m=1}^{\infty} \left\{ \left[C_m \sinh \frac{m\pi(Y-S')}{d} + D_m \cosh \frac{m\pi(Y-S')}{d} \right] \right. \\ & \cdot \left. \sin \frac{m\pi x}{d} + V_1 \frac{x}{d} \right\} \end{aligned} \quad (8.51)$$

$$\begin{aligned} \phi_4 = & \sum_{m=1}^{\infty} \left\{ \left[E_m \sinh \frac{m\pi(Y-S')}{S} + F_m \cosh \frac{m\pi(Y-S')}{S} \right] \right. \\ & \cdot \left. \sin \frac{m\pi(x-d-W)}{S} + V_1 + (V_2 - V_1)(x-d-W)/S \right\} \end{aligned} \quad (8.52)$$

where $S' = h + t/2$ and $d = (2L - 2W - S)/2$. For the even mode $V_1 = V_2$, and $V_1 = -V_2$ for the odd mode.

The Fourier coefficients A_m, B_m, \dots, F_m are determined from the continuity of potentials at the boundaries and the stationary property of the stored electric energy with respect to Fourier coefficients. The stored energy in region i is given by

$$W_i = \frac{\epsilon_i}{2} \iint [(E_{xi})^2 + (E_{yi})^2] dx dy \quad (8.53)$$

where

$$E_{xi} = -\frac{\partial \phi_i}{\partial x} \quad E_{yi} = -\frac{\partial \phi_i}{\partial y}$$

The total capacitance of the structure may then be obtained from

$$C = \frac{2}{V^2} (W_1 + W_2 + W_3 + W_4) \quad (8.54)$$

where $V (= |V_1| = |V_2|)$ is the potential of a strip. The value of C is twice the even- or odd-mode capacitance of a single strip to ground.

Evaluation of Fourier Coefficients

The stored energy W_i can be evaluated in terms of the coefficients A_m , B_m , C_m , D_m , E_m , and F_m . The continuity of potential at $y = h$ and $y = h + t$ helps in eliminating A_m and B_m . Therefore, W_i can be written in terms of C_m , D_m , E_m , and F_m .

The stationary property of the energy W_i with respect to Fourier coefficients C_m , D_m , E_m , and F_m gives

$$\frac{\partial W_i}{\partial C_m} = 0 \quad \frac{\partial W_i}{\partial D_m} = 0 \quad \frac{\partial W_i}{\partial E_m} = 0 \quad \frac{\partial W_i}{\partial F_m} = 0 \quad (8.55)$$

for $m = 1, 2, 3, \dots, \infty$ and $i = 1, 2, 3, 4$.

Equation (8.55) generates four sets of equations. Each set contains an infinite number of simultaneous, linear, inhomogeneous equations. These equations can be solved with a computer to determine the Fourier coefficients.

For an exact computation the series in (8.49) to (8.52) should be infinite. However, in practice only a finite number of terms M are used. Detailed convergence considerations indicate that [16] convergence using a finite number of terms is faster for larger values of ϵ_r , large W/H and small S/H . Moreover, convergence is faster for even-mode capacitance compared to odd-mode capacitance. It has also been observed that $M = 23$ gives a reasonable compromise between accuracy and computation time [16].

Variational Method in the Spectral Domain [17]

This method is similar to the variational method in the spectral domain described for a single microstrip in Chapter 1.

In this method the capacitance is calculated from a variational expression in terms of charge distribution. Evaluation is carried out in the Fourier transform domain, and the capacitance may be written as

$$\frac{\epsilon_0}{C} = \frac{1}{\pi} \int_0^{\infty} G(\alpha) \tilde{\rho}^2(\alpha) d\alpha \quad (8.56)$$

For coupled lines (8.56) becomes

$$\frac{\epsilon_0}{C_e} = \frac{1}{\pi} \int_0^{\infty} G(\alpha) \tilde{\rho}_e^2(\alpha) d\alpha \quad (8.57)$$

and

$$\frac{\epsilon_0}{C_o} = \frac{1}{\pi} \int_0^{\infty} G(\alpha) \tilde{\rho}_o^2(\alpha) d\alpha \quad (8.58)$$

where

$$G(\alpha) = \frac{1}{\alpha [\epsilon_r \coth(\alpha h) + \coth(\alpha h')]} \quad (8.59)$$

$\tilde{\rho}_e$ and $\tilde{\rho}_o$ are the Fourier transforms of charge density functions for the even and odd mode, respectively. One may use the following expressions for charge density distribution:

$$\begin{aligned}\tilde{\rho}_e(\alpha) &= J_0(\alpha W/2) \cos\{\alpha(W+S)/2\} \\ \tilde{\rho}_o(\alpha) &= J_0(\alpha W/2) \sin\{\alpha(W+S)/2\}\end{aligned}$$

Discussion of Results

Figure 8.4 shows the variation of even- and odd-mode impedances with strip width W/h and gap spacing S/h for $\epsilon_r = 9.6$ [18]. It has been assumed that the strip thickness t is zero and the enclosure recedes to infinity. The effect of gap spacing and strip width on effective dielectric constants ϵ_{re}^e and ϵ_{re}^o is shown in Figure 8.5. It may be observed from these figures that impedances decrease and effective dielectric constants increase with an increase in strip width. For a given value of S/h and W/h , the even-mode impedance and effective dielectric constant are higher than odd-mode values. Even- and odd-mode characteristics show opposite variations with an increase in S/h such that, for S/h tending to infinity, the even- and the odd-mode characteristics approach each other and are equal to single microstrip values.

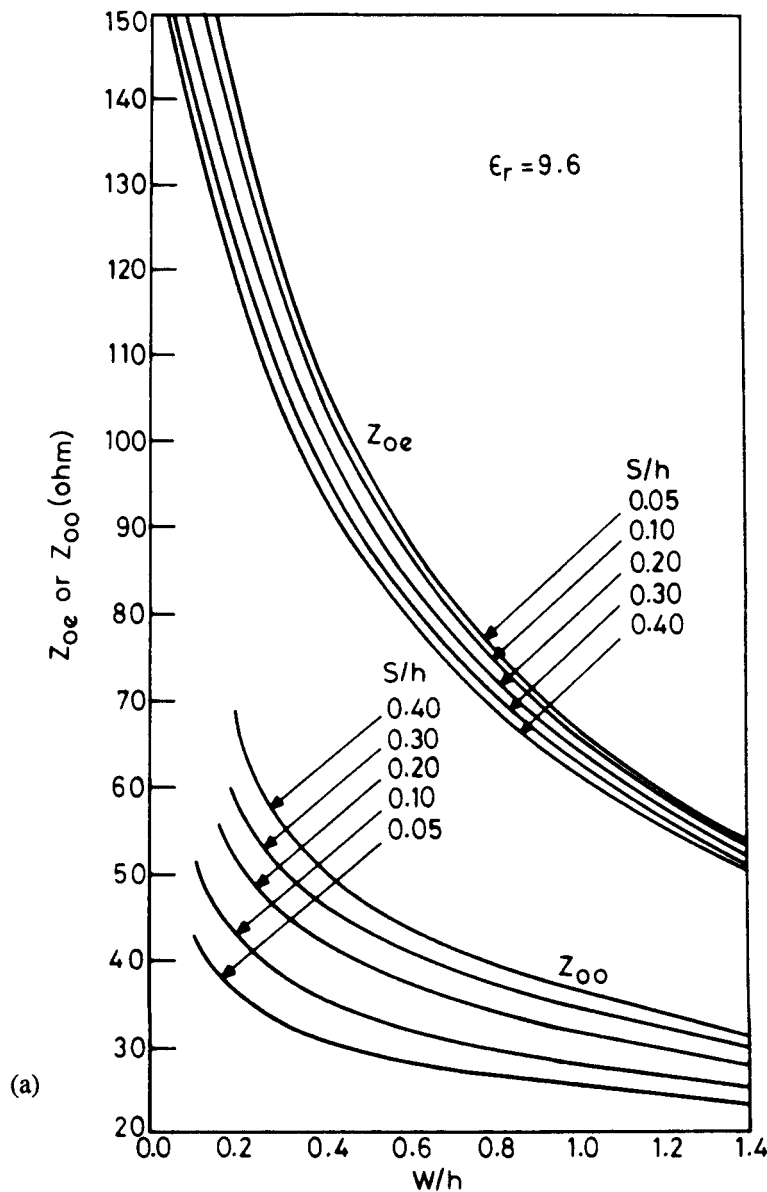


Figure 8.4 Even- and odd-mode characteristic impedances for coupled microstrip lines: (a) $\epsilon_r = 9.6$, $S/h = 0.05$ to 0.4, $W/h = 0.1$ to 1.4; (b) $\epsilon_r = 9.6$, $S/h = 0.6$ to 5.0, $W/h = 0.04$ to 1.4; and (c) $\epsilon_r = 9.6$, $S/h = 0.05$ to 2.0, $W/h = 1.0$ to 5.0 (from [18], © 1972 Van Nostrand Reinhold. Reprinted with permission.).

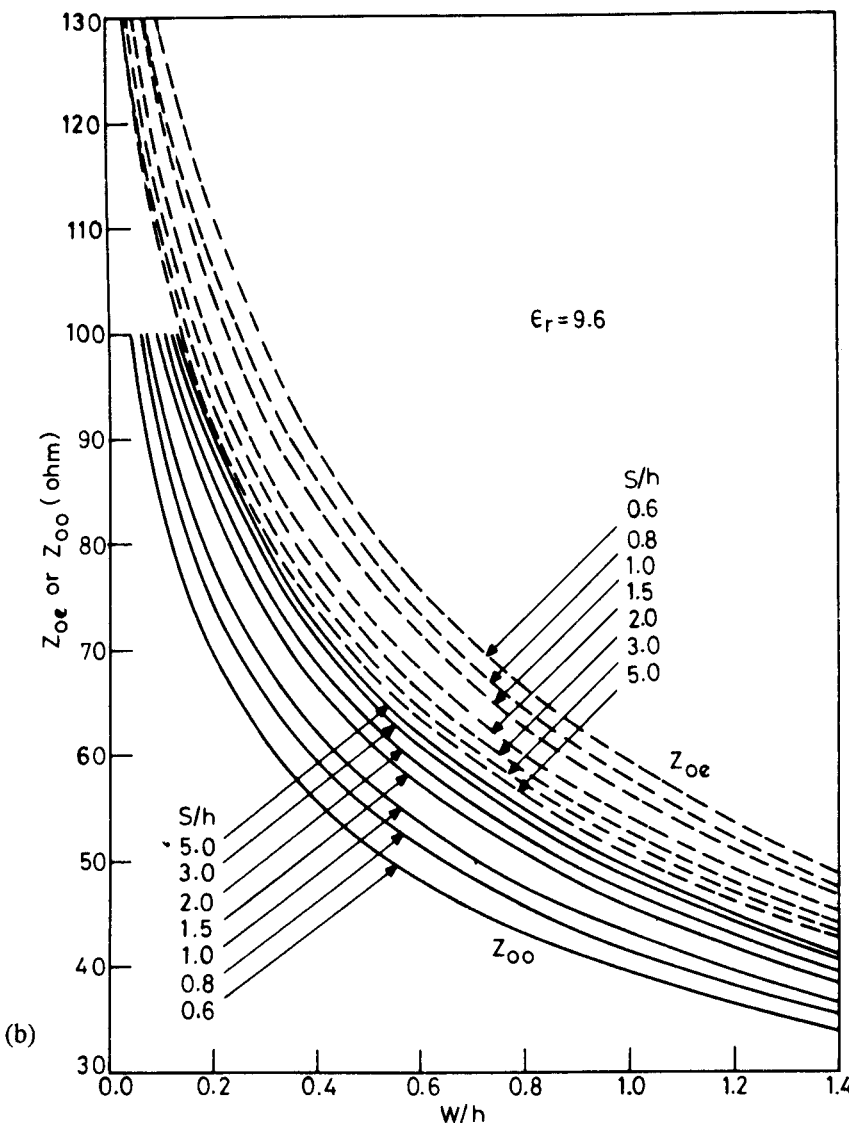


Figure 8.4 (continued).

For the special case of $H = 2h$ and $L = \infty$ the characteristics of coupled microstrip lines can be obtained in a simple closed-form expression by using the method of conformal transformation. In this case coupled microstrip lines behave like coupled striplines with the effective dielectric constant given by $(\epsilon_r + 1)/2$. The even- and odd-mode impedances are obtained [19] as

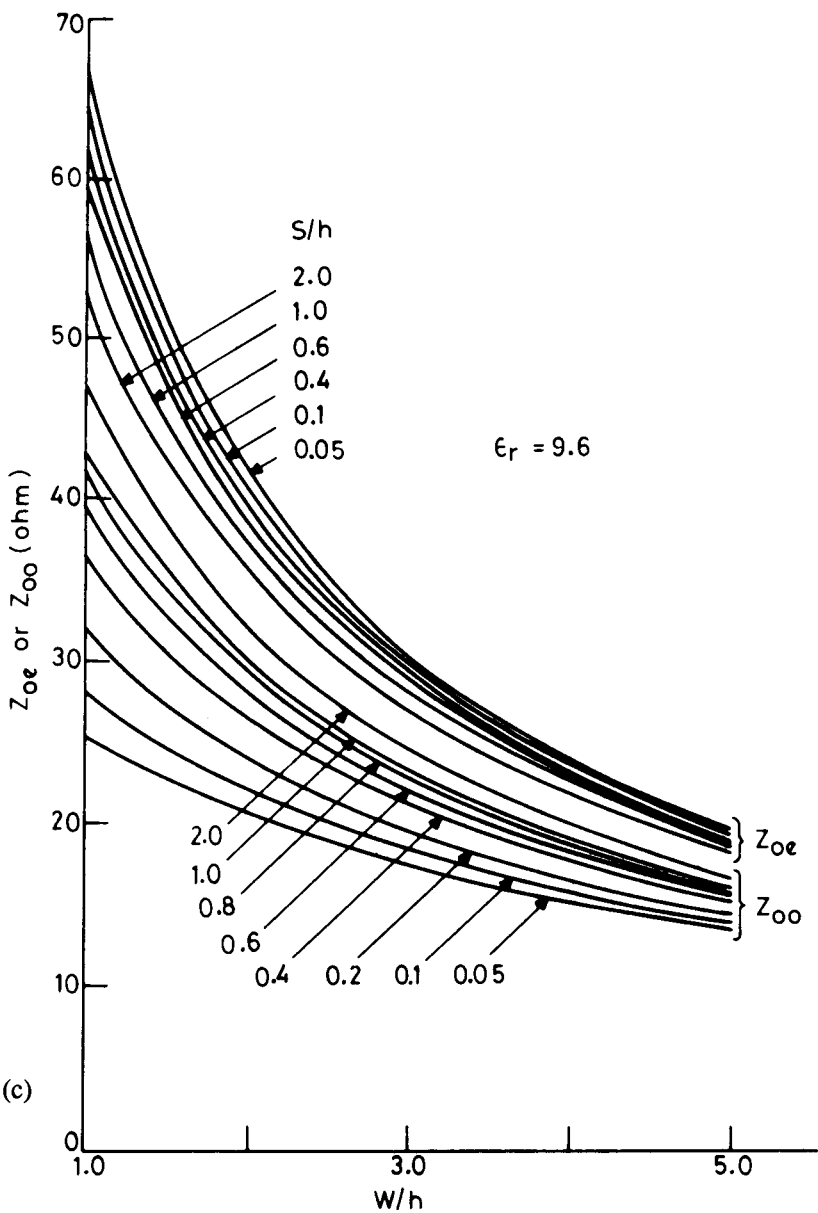


Figure 8.4 (continued).

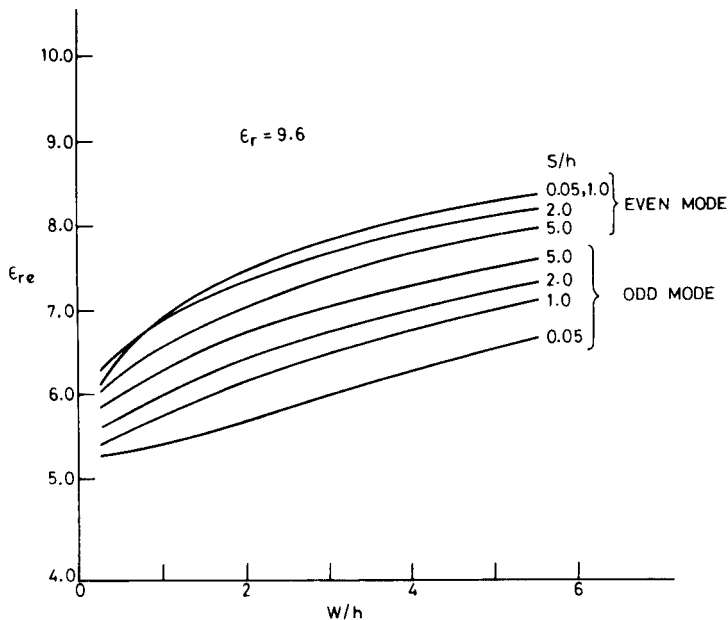


Figure 8.5 Even- and odd-mode effective dielectric constants for coupled microstrip lines ($\epsilon_r = 9.6$, $S/h = 0.05$ to 5.0 , $W/h = 0.2$ to 5.5) (from [18], © 1972 Van Nostrand Reinhold. Reprinted with permission.).

$$Z_{0o} = \frac{30\pi}{\sqrt{(\epsilon_r + 1)/2}} \frac{K(k'_o)}{K(k_o)} \quad (8.60)$$

$$Z_{0e} = \frac{30\pi}{\sqrt{(\epsilon_r + 1)/2}} \frac{K(k'_e)}{K(k_e)} \quad (8.61)$$

where $K(k_e)$ and $K(k'_e)$ are the elliptic function and its complement with

$$k_e = \tanh\left(\frac{\pi}{4} \frac{W}{h}\right) \tanh\left[\frac{\pi}{4} \left(\frac{W+S}{h}\right)\right] \quad k'^2_e = 1 - k_e^2 \quad (8.62a)$$

$$k_o = \tanh\left(\frac{\pi}{4} \frac{W}{h}\right) \coth\left[\frac{\pi}{4} \left(\frac{W+S}{h}\right)\right] \quad k'^2_o = 1 - k_o^2 \quad (8.62b)$$

8.3.2 Fullwave Analysis

It was pointed out in Chapter 2 that quasi-static analysis for microstrip holds for wavelengths greater than the transverse dimensions of the line. At higher

frequencies, the line shows a dispersive nature and a fullwave analysis is needed. The analytical technique used for fullwave analysis of single microstrip, slotline, and coplanar lines can also be applied to the coupled line configuration. Krage and Haddad [20] have used the same field-matching technique for both single microstrip and coupled microstrip configurations. The spectral domain technique has been used in references [21–36] for the fullwave analysis of coupled microstrip lines. Its application by various authors to the same configuration differs only in the choice of basis functions for expressing current density (for microstrip lines) and electric field (for slotline). The rate of convergence of the resultant series depends upon the choice of basis functions.

In this section Galerkin's method in the spectral domain is employed to analyze both symmetric and asymmetric coupled microstrip lines.

Symmetric Coupled Microstrip Lines

The current basis functions for the symmetric coupled microstrips may be obtained from a translation of the corresponding basis functions for the single microstrip line (see (2.27)). These functions may be either of sinusoidal type [23, 27] or of Chebyshev type [28, 29] with proper edge singularity. Sinusoidal type basis functions and their Fourier transforms were described earlier in connection with the fullwave analysis of coplanar strips in Section 7.2.3. The Chebyshev polynomials are found to be efficient especially for tightly coupled lines [30]. The current distribution on the strips in terms of these basis functions is described (see Figure 8.9 for the co-ordinate system) [28] as

$$J_z(x) = \sum_{m=1}^{\infty} a_m J_{zm}(x) \quad (8.63)$$

$$J_x(x) = \sum_{n=0}^{\infty} b_n J_{xn}(x) \quad (8.64)$$

where

$$J_{zm}(x) = \begin{cases} \frac{T_{m-1}(2x'/W)}{\sqrt{1 - (2x'/W)^2}} & m = 1, 2, 3 \dots \text{ for } |S/2| \leq x \leq |S/2 + W| \\ 0 & \text{elsewhere} \end{cases} \quad (8.65a)$$

$$J_{xn}(x) = \begin{cases} U_n(2x'/W) \sqrt{1 - (2x'/W)^2} & n = 0, 1, 2 \dots \text{ for } |S/2| \leq x \leq |S/2 + W| \\ 0 & \text{elsewhere} \end{cases} \quad (8.65b)$$

where $T_n(x)$ and $U_n(x)$ are Chebyshev polynomials of the first and second kind, respectively.

Here, $x' = x + x_0$ for the left strip and $x' = x - x_0$ for the right strip with $x_0 = (W + S)/2$. Fourier transforms of the Chebyshev polynomials, (8.65), can be obtained by using the identities [29]

$$\int_{-1}^1 \frac{\cos(\alpha x) T_n(x)}{\sqrt{1 - x^2}} dx = \pi J_n(\alpha) \operatorname{Re}\{j^n\} \quad (8.66a)$$

$$\int_{-1}^1 \frac{\sin(\alpha x) T_n(x)}{\sqrt{1 - x^2}} dx = \pi J_n(\alpha) \operatorname{Im}\{j^n\} \quad (8.66b)$$

$$\int_{-1}^1 \sqrt{1 - x^2} \cos(\alpha x) U_n(x) dx = \frac{\pi(n+1)}{\alpha} J_{n+1}(\alpha) \operatorname{Re}\{j^n\} \quad (8.66c)$$

$$\int_{-1}^1 \sqrt{1 - x^2} \sin(\alpha x) U_n(x) dx = \frac{\pi(n+1)}{\alpha} J_{n+1}(\alpha) \operatorname{Im}\{j^n\} \quad (8.66d)$$

where $j = \sqrt{-1}$. Other details of this method are similar to those discussed for a single microstrip in Chapter 2.

The characteristic impedances for the even and odd modes defined on power-current basis agree well with experimental results and may be obtained from the relation

$$Z_0 = 2 \frac{\iint P_z dx dy}{|I_z|^2 + |I_x|^2} \quad I_z = \sum_m a_m \int_{S/2}^{(W+S)/2} J_{zm} dx \quad I_x = \sum_n b_n \int_{S/2}^{(W+S)/2} J_{xn} dx \quad (8.67)$$

where P_z is the z -component of the Poynting vector and the integral is evaluated over the cross section of a coupled microstrip configuration.

The numerical results obtained in [29] are shown in Figures 8.6 and 8.7. Figure 8.6 shows the propagation constants for the even and odd modes as a function of separation between the strips. It is observed that for small values of S/W , $\beta_e > \beta_{iso} > \beta_o$; where β_e , β_{iso} , and β_o are the phase constants corresponding to even-mode, isolated microstrip and odd-mode, respectively. When $S \rightarrow 0$ the strips contact on inside edges, and phase constant for the even mode approaches the phase constant of an isolated strip with twice the width. For large separation between the strips ($S/W > 4$) the phase constants of the even and odd modes converge to the phase constant of an isolated strip. This feature of coupling can be used as a guideline in the layout of strips to avoid coupling between the neighboring strips. Dispersion behavior of β/k_o for the coupled modes is plotted in Figure 8.7. As in

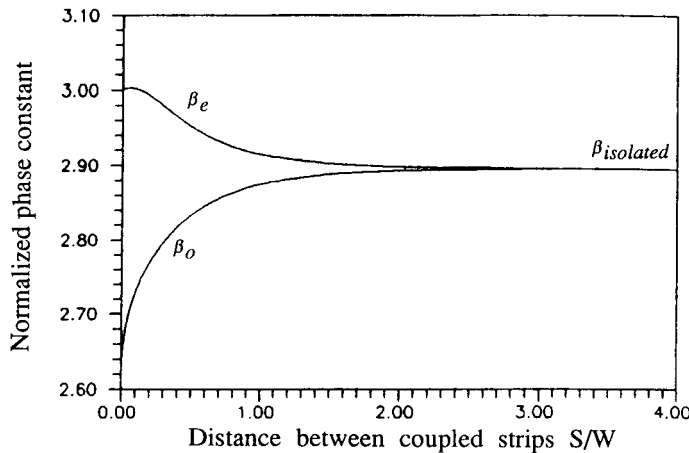


Figure 8.6 Dependence of phase constants of coupled microstrip lines on the spacing ($\epsilon_r = 9.8$, $h/\lambda_0 = 0.0212$, $W/h = 4.72$) (from [29], © 1992 IEEE. Reprinted with permission.).

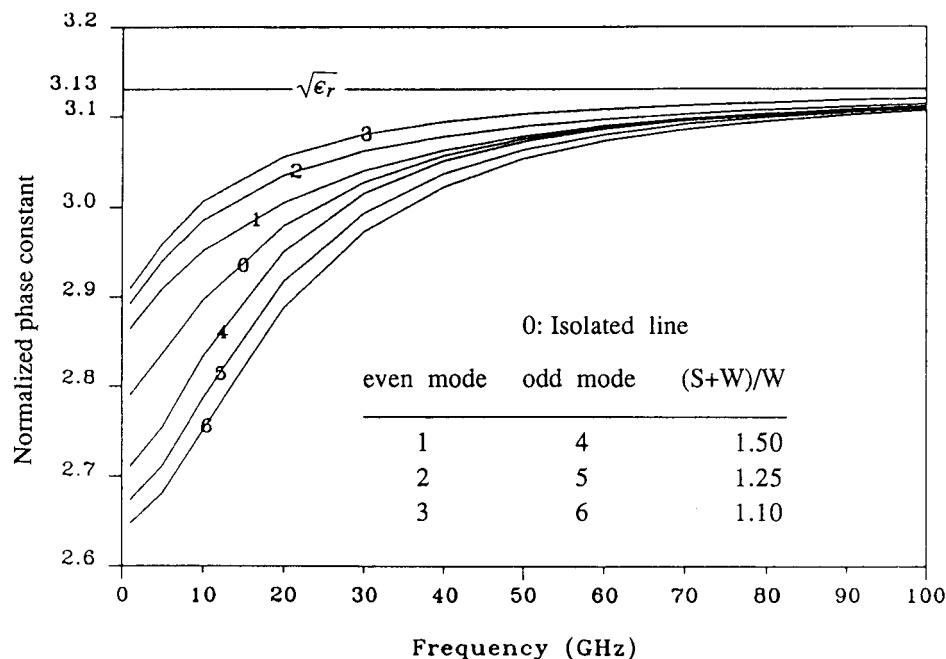


Figure 8.7 Effect of dispersion on even- and odd-mode phase constants of coupled microstrip lines ($\epsilon_r = 9.8$, $h/W = 0.2115$, $W = 0.635$ mm) (from [29], © 1992 IEEE. Reprinted with permission.).

the case of isolated microstrip, the value of β/k_0 increases with frequency for the modes of a coupled microstrip line, ultimately reaching $\sqrt{\epsilon_r}$ for very high frequencies. The dispersion behavior of the characteristic impedance is shown in Figure 8.8.

Asymmetric Coupled Microstrip Lines

Galerkin's method in the spectral domain has also been applied to evaluate the characteristics of asymmetric coupled microstrip lines (see Figure 8.9). The total

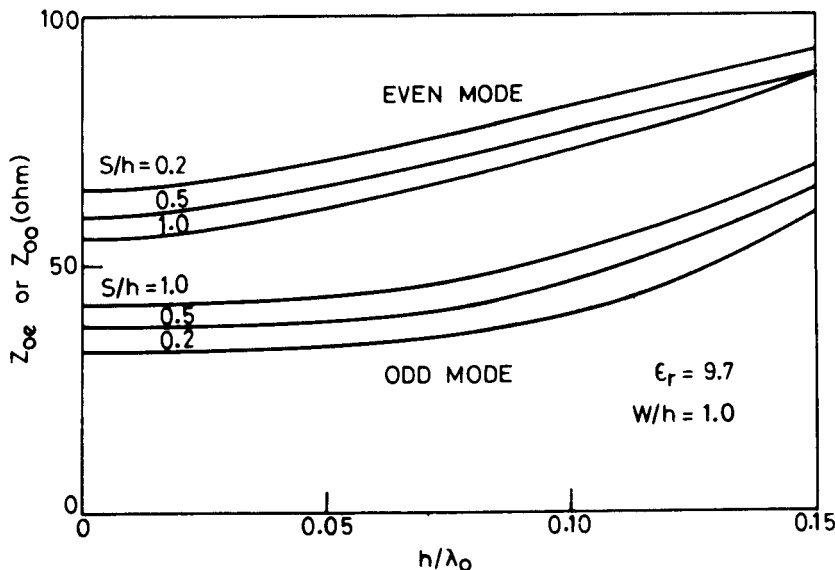


Figure 8.8 Effect of dispersion on even- and odd-mode impedances of coupled microstrip lines (from [23], © 1972 S. Hirzel Verlag. Reprinted with permission.).

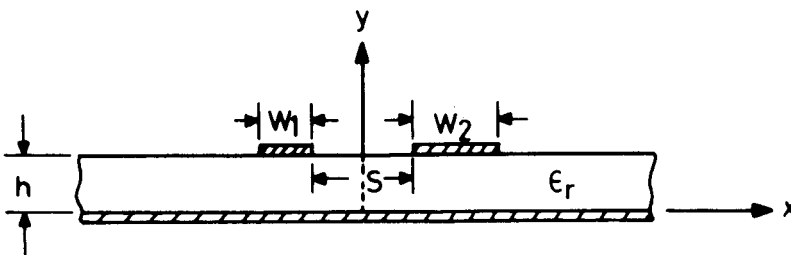


Figure 8.9 Coupled microstrip lines with unequal impedances (asymmetric lines).

strip current is the sum of the current on each strip. Also, the current on the strips are not equal to each other because of the absence of symmetry. Therefore, we can write [35]

$$J_z(x) = \begin{cases} \sum_{m=1}^{M_1} a_{m1} J_{zm1}(x) & \text{for the left strip} \\ \sum_{m=1}^{M_2} a_{m2} J_{zm2}(x) & \text{for the right strip} \end{cases} \quad (8.68a)$$

$$J_x(x) = \begin{cases} \sum_{n=0}^{N_1} b_{n1} J_{xn1}(x) & \text{for the left strip} \\ \sum_{n=0}^{N_2} b_{n2} J_{xn2}(x) & \text{for the right strip} \end{cases} \quad (8.68b)$$

Here, subscripts 1 and 2 define the strips. The basis functions can be obtained by generalizing the basis functions of (8.65) for different strip widths. For the coordinate system shown in Figure 8.9, the basis functions can be expressed as [35]

$$J_{zmi}(x) = \begin{cases} \frac{T_{m-1}(2x'_i/W_i)}{\sqrt{1 - (2x'_i/W_i)^2}} & i = 1, 2 \text{ and } m = 1, 2, 3 \dots \text{ over the strips} \\ 0 & \text{outside the strips} \end{cases} \quad (8.69a)$$

$$J_{xnj}(x) = \begin{cases} U_n(2x'_j/W_j) \sqrt{1 - (2x'_j/W_j)^2} & j = 1, 2 \text{ and } n = 0, 1, 2 \dots \text{ over the strips} \\ 0 & \text{outside the strips} \end{cases} \quad (8.69b)$$

where $x'_1 = x + x_{o1}$ for the left strip and $x'_2 = x - x_{o2}$ for the right strip, with $x_{oi} = (W_i + S)/2$.

The characteristic impedance for the two strips may be defined on a voltage-current basis. This is given below

$$Z_o^{(1)} = \frac{V^{(1)}}{I^{(1)}} = \frac{\int_o^h E_y(-(W_1 + S)/2, y) dy}{\sum_m a_{m1} \int_{-(W_1 + S/2)}^{-S/2} J_{zm1}(x') dx'} \quad (8.70)$$

$$Z_0^{(2)} = \frac{V^{(2)}}{I^{(2)}} = \frac{\int_0^h E_y((W_2 + S)/2, y) dy}{\sum_m a_{m2} \int_{S/2}^{(W_2+S/2)} J_{zm2}(x') dx'} \quad (8.71)$$

The analysis of asymmetric coupled lines is described in terms of c and π modes defined in Section 8.2.

Figure 8.10 shows the characteristic impedances for the case of asymmetric coupled microstrip lines [25]. Note that the two lines have different impedances for the c and π modes. The narrow line has a higher impedance than the wider

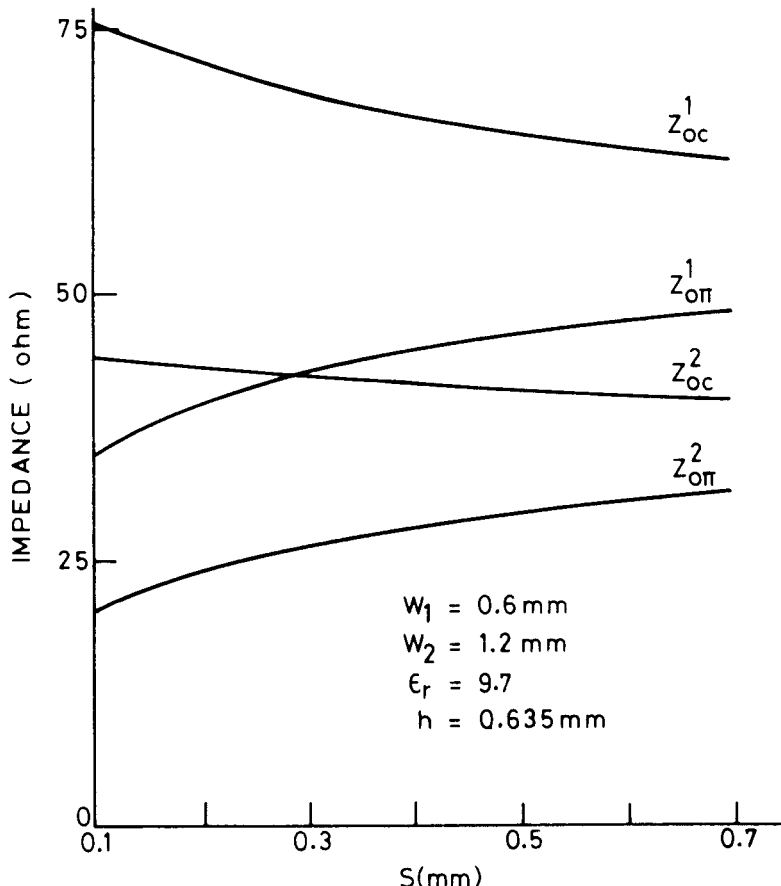


Figure 8.10 Variation of characteristic impedances of asymmetric coupled microstrip lines with gap spacing S (from [25], © 1977 Microwave Exhibitions & Publishers. Reprinted with permission.).

line. Moreover, for larger spacing the c- and π -mode impedances for the two lines approach their respective single line impedances. The effect of dispersion on the effective dielectric constant for the two modes is shown in Figure 8.11. It may be observed from this figure that the effective dielectric constants of the c and π modes increase with the increase in strip width of line 2. Also, the measured values show good agreement with calculated results.

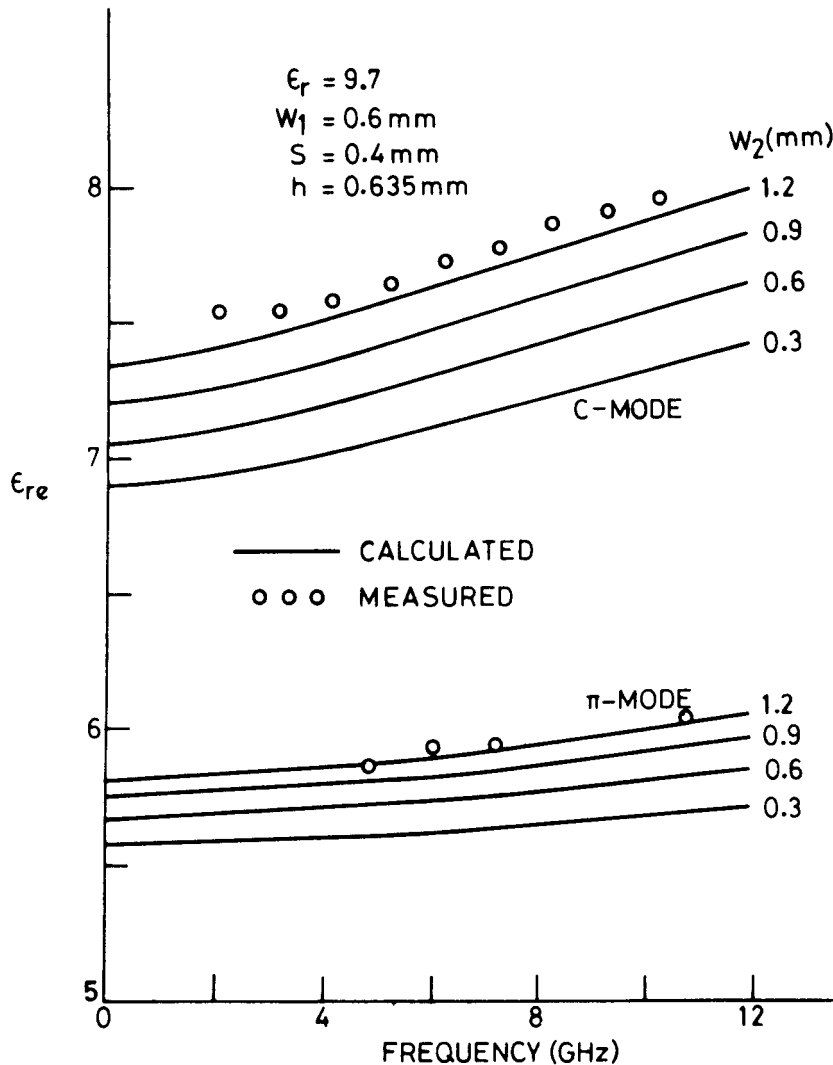


Figure 8.11 Effect of dispersion on the effective dielectric constants of asymmetric coupled microstrip lines (from [25], © 1977 Microwave Exhibitions & Publishers. Reprinted with permission.).

The characteristic impedance of asymmetric coupled microstrip lines may also be defined in terms of power and current. This definition in its most general form is [28]

$$Z_{\ell m} = \frac{\text{Power associated with line } \ell \text{ for mode } m (= P_{\ell m})}{(\text{Normalized current on line } \ell \text{ for mode } m)^2 = I_{\ell m}^2} \quad (8.72)$$

In (8.72), $P_{\ell m}$ is calculated by integrating the z -component of the Poynting vector over the cross section of the coupled microstrip line configuration when the current distribution on line ℓ corresponds to the solution for currents when $\beta = \beta_m$ and all the other line currents are zero.

Fullwave analysis of coupled microstrip lines has been extended to configurations with more than two strips, symmetric as well as asymmetric [27, 32–35]. The basis functions for the analysis can be based on symmetry considerations for the symmetric cases [27] and in a general form for the asymmetric cases [28]. The number of basis functions required increases with the increase in the number of strips, asymmetry, and the tightness of coupling.

Fullwave analysis is useful for calculating very accurately the effect of dispersion on the even- and odd-mode phase velocities and characteristic impedances. However, sufficient accuracy compatible with fabrication tolerances and measurement errors can also be achieved in the limited range of parameters by using suitable dispersion models. These models have the advantage of saving computational time. Dispersion models for coupled microstrip lines are described in the following subsection.

8.3.3 Dispersion Models

It has been observed [37] that the LSE-mode model for the dispersion in a single microstrip line can be used for coupled microstrip lines also. For its application to coupled microstrip lines, Z_{0m} in (1.72) and (1.73) should represent even- and odd-mode impedances of the total parallel-coupled configuration rather than that of a single line of the coupled pair. Relations (1.71) and (1.73) modified for a coupled microstrip line are rewritten below

$$\epsilon_{re}^{e,o}(f) = \epsilon_r - \frac{\epsilon_r - \epsilon_{re}^{e,o}(0)}{1 + G(f/f_p)^2} \quad (8.73)$$

where

$$f_p = \frac{Z_{0m}}{2\mu_0 h} \quad (8.74)$$

$$G \approx 0.6 + 0.009 Z_{0m} \quad (8.75)$$

For the even mode, the total mode impedance is half that of a single line of the coupled pair since the two strips are at the same potential and the total current is twice that of a single strip. Therefore, the effect of dispersion on ϵ_{re} for the even mode can be computed by substituting $Z_{0e}/2$ for Z_{0m} in (8.74) and (8.75). In the case of the odd mode, the two strips are at opposite potentials, and the voltage between the strips is twice that of a single strip to ground. Thus Z_{0m} should be replaced by $2 Z_{0o}$ for the odd mode. Consequently, (8.74) and (8.75) for constants f_p and G may be written for the two modes as follows:

$$f_p = \begin{cases} \frac{Z_{0e}}{4\mu_0 h} & \text{even mode} \\ \frac{Z_{0o}}{\mu_0 h} & \text{odd mode} \end{cases} \quad (8.76)$$

$$G = \begin{cases} 0.6 + 0.0045 Z_{0e} & \text{even mode} \\ 0.6 + 0.018 Z_{0o} & \text{odd mode} \end{cases} \quad (8.77)$$

The odd mode is less dispersive compared to the even mode. For example, the increase in the effective dielectric constant is about 12 percent for the odd mode and about 19 percent for the even mode at a frequency of 30 GHz for 50Ω coupled microstrip lines on 0.64-mm alumina substrate. Dispersion at other frequencies can be obtained from Figure 8.12.

Getsinger's dispersion model [37] gives relatively accurate results for alumina substrate for which it has been adjusted. However, it has been found to give inaccurate values for extreme values of gap width [38]. Kirschning and Jansen have reported closed-form expressions that model the dispersion in coupled microstrip lines with better accuracy and larger range of parameters [39]. These expressions have been obtained by curve-fitting the numerical results of the spectral-domain hybrid-mode approach. The range of validity is specified to be [39]

$$0.1 \leq u \leq 10 \quad 0.1 \leq g \leq 10 \quad 1 \leq \epsilon_r \leq 18 \quad f_n \leq 25 \quad (8.78)$$

for an error of not more than 1.4 percent. In (8.78), u ($= W/h$) denotes the normalized strip width and g ($= S/h$) is the normalized gap width. The normalized frequency f_n is defined in (8.80).

To account for a more complicated form of frequency dependence Kirschning and Jansen have modified (8.73). The modified expression is given as

$$\epsilon_{re}^{e,o}(f_n) = \epsilon_r - \frac{\epsilon_r - \epsilon_{re}^{e,o}(0)}{1 + F_{e,o}(f_n)} \quad (8.79)$$

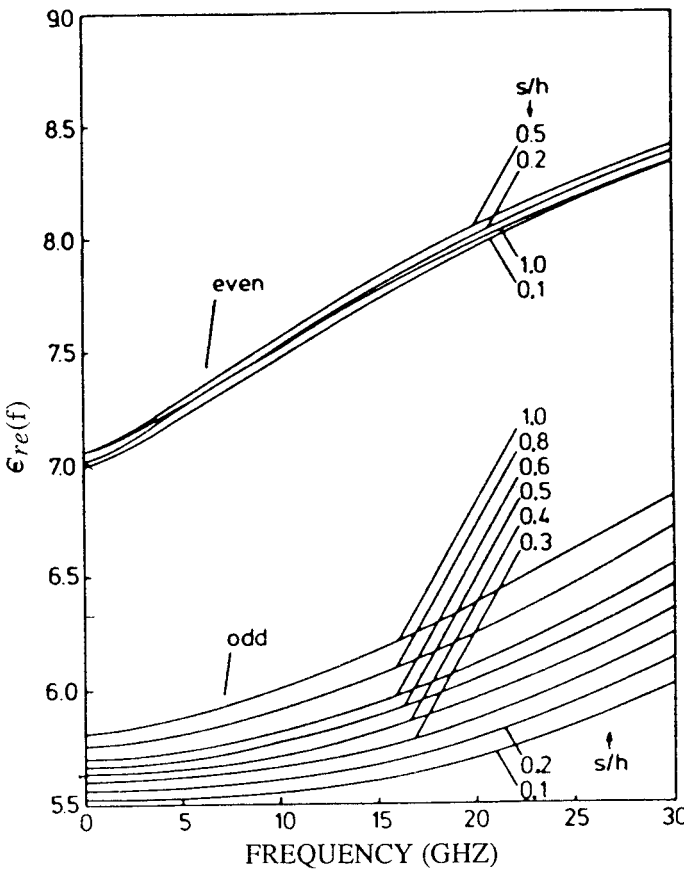


Figure 8.12 Effect of dispersion in ϵ_{re} for symmetric coupled microstrip lines ($\epsilon_r = 9.7$, $h = 0.64$ mm, $W/h = 1$) (from [39], © 1984 IEEE. Reprinted with permission.).

Here, $\epsilon_{re}^{e,o}(0)$ denotes the static value of the effective dielectric constant for the even and odd modes. Accurate expressions for these are given in Section 8.5. The variable f_n denotes the normalized frequency and is defined as

$$f_n = f \text{ (GHz)} \cdot h \text{ (mm)} \quad (8.80)$$

Equation (8.80) implies that frequency f is in gigahertz and the substrate thickness h is in millimeters.

The factor $F_{e,o}(f_n)$ accounts for the dispersion of effective dielectric constant in (8.79). The expression for $F_e(f_n)$ is given as

$$F_e(f_n) = P_1 P_2 [(P_3 P_4 + 0.1844 P_7) f_n]^{1.5763} \quad (8.81)$$

with

$$\begin{aligned}
 P_1 &= 0.27488 + \left(0.6315 + \frac{0.525}{(1 + 0.0157 f_n)^{20}} \right) u - 0.065683 e^{-8.7513 u} \\
 P_2 &= 0.33622(1 - e^{-0.03442 \epsilon_r}) \\
 P_3 &= 0.0363 e^{-4.6 u} [1 - \exp(-(f_n/38.7)^{4.97})] \\
 P_4 &= 1 + 2.751[1 - \exp(-(\epsilon_r/15.916)^8)] \\
 P_5 &= 0.746 + 0.334 \exp(-3.3(\epsilon_r/15)^3) \\
 P_6 &= P_3 \exp(-(f_n/18)^{0.368}) \\
 P_7 &= 1 + 4.069 P_6 \cdot g^{0.479} \exp(-1.347 g^{0.595} - 0.17 g^{2.5})
 \end{aligned}$$

For the odd-mode effective dielectric constant, the effect of dispersion is described by

$$F_o(f_n) = P_1 P_2 [(P_3 P_4 + 0.1844) P_{15} f_n]^{1.5763} \quad (8.82)$$

with

$$\begin{aligned}
 P_8 &= 0.7168 \left(1 + \frac{1.076}{1 + 0.0576(\epsilon_r - 1)} \right) \\
 P_9 &= P_8 - 0.7913 [1 - \exp(-(f_n/20)^{1.424})] \tan^{-1}(2.481(\epsilon_r/8)^{0.946}) \\
 P_{10} &= 0.242(\epsilon_r - 1)^{0.55} \\
 P_{11} &= 0.6366(e^{-0.3401 f_n} - 1) \tan^{-1}[1.263(u/3)^{1.629}] \\
 P_{12} &= P_9 + \frac{1 - P_9}{1 + 1.183 u^{1.376}} \\
 P_{13} &= \frac{1.695 P_{10}}{0.414 + 1.605 P_{10}} \\
 P_{14} &= 0.8928 + 0.1072[1 - \exp(-0.42(f_n/20)^{3.215})] \\
 P_{15} &= \left| 1 - \frac{0.8928(1 + P_{11}) P_{12} \exp(-P_{13} g^{1.092})}{P_{14}} \right|
 \end{aligned}$$

The upper frequency limit for (8.81) and (8.82) is $f_n = 25$, that is, 25 GHz for a substrate thickness of 1 mm and higher for thinner substrates.

Dispersion in the characteristic impedance has also been modeled with a maximum error of less than 2.5 percent over the range of parameters specified in (8.78) other than $f_n \leq 20$ [39]. It is observed that the impedances increase with

frequency, and the rate of increase for the odd mode is very small for frequencies up to 30 GHz for microstrip lines on alumina substrate.

8.4 MEASUREMENTS ON COUPLED MICROSTRIP LINES

Symmetrical coupled microstrip lines are characterized by even- and odd-mode impedances and even- and odd-mode propagation constants. Knowledge of these characteristics is essential for designing directional couplers and edge-coupled resonators. Under ordinary conditions, both of the modes are excited and it is difficult to determine the odd- and even-mode parameters from the measured data. One way to measure these characteristics is to selectively excite one mode and measure its characteristics. The selective excitation of modes and measurements becomes easier with the use of a microwave network analyzer. Measurement techniques for impedances and phase constants are described in the following sections.

8.4.1 Impedance Measurements

The setup for measuring even- and odd-mode impedances is illustrated in Figure 8.13 [40]. As shown, the signal from the source is divided equally into the two transmission lines. The path length of one of these lines is adjustable so that the relative phase of the waves propagating in them can be controlled for selectively exciting the even or odd mode. The amplitude ratio of the waves is unity. The relative phase and amplitude can be measured using a harmonic frequency converter and a phase-gain indicator (two subunits of the network analyzer system).

The coupled microstrip section is now introduced between the transmission test unit and harmonic frequency converter. The mode of excitation can be selected by controlling the phase. The phase indicator should read 0° for even-mode excitation and 180° for odd-mode excitation.

The characteristic impedance can be determined from the VSWR measurement. To measure VSWR, a slotted line should be inserted to one arm between the transmission test unit and the coupled lines. A compensating air line length

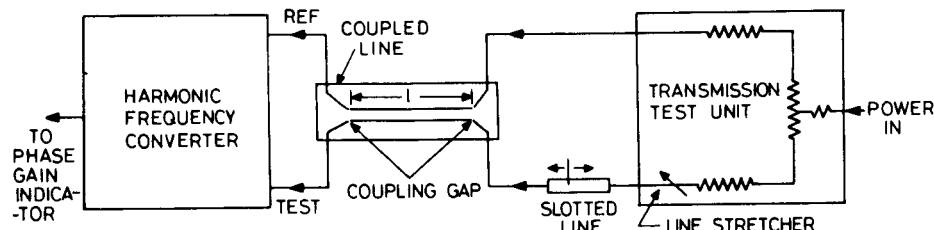


Figure 8.13 Test setup for measuring even- and odd-mode impedances of coupled lines.

should be inserted in the other arm. The measurements should preferably be carried out at a frequency where the coupling length is approximately $\lambda_m/4$, because at this wavelength the effect of the even- or odd-mode impedance on VSWR is at a maximum. At the same time, the effect of any discontinuity capacitance is minimum.

Even- and odd-mode impedances can be obtained from the relations

$$Z_{0e} = Z_0 \sqrt{\text{VSWR}_e} \quad Z_{0o} = Z_0 / \sqrt{\text{VSWR}_o} \quad (8.83)$$

since Z_{0e} is greater than Z_0 and Z_{0o} is less than Z_0 . VSWR_e and VSWR_o are the VSWR values for even- and odd-mode excitations, respectively.

8.4.2 Phase Constant Measurements

The phase constants for the two modes can be determined by measuring the resonance frequencies corresponding to these modes. Loading effects on the resonator due to the transmission test unit and the harmonic frequency converter can be minimized by introducing coupling gaps between them and the coupled lines, as shown in Figure 8.14. The coupled pair will act as a lightly loaded single resonator and will exhibit two resonant frequencies. The odd-mode resonance frequency will be higher than the even-mode resonance frequency. While calculating guide wavelength from resonance frequency, the effect of gap capacitance should be taken into account. The guide wavelength for a half-wave coupled section is given by

$$\lambda = 2(\ell + 2\Delta\ell_g) \quad (8.84)$$

where ℓ is the length of resonant line and $\Delta\ell_g$ is the equivalent line length associated with the gap capacitance C_g , which is given approximately by

$$\Delta\ell_g = f\lambda_m C_g Z_0 \quad (8.85)$$

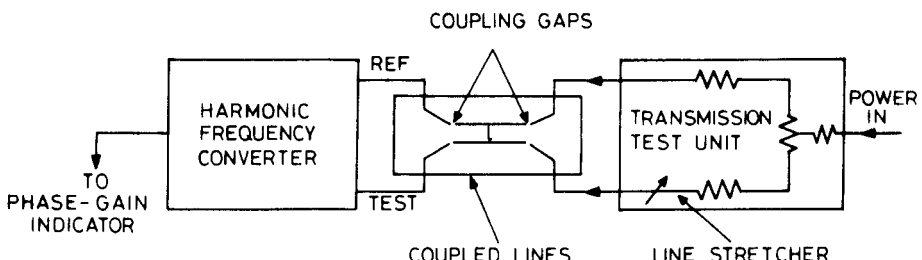


Figure 8.14 Setup for measuring phase velocities in coupled lines.

and f is the resonance frequency for the half-wave resonator.

Even- and odd-mode resonances may also be obtained by proper terminations at the two ends of a coupled line section [41]. If a coupled line section is $(2n + 1)\lambda/4$ long and the two ends are connected in parallel, an even-mode resonator is obtained when one end is open and the other is grounded. This situation is shown in Figure 8.15(a).

Voltage distribution on the two lines (for the case $n = 0$) is shown in Figure 8.15(b). Since the two lines are connected in parallel at both ends, the voltages on these two lines are in phase everywhere. This structure behaves as an even-mode resonator for any excitation, and the network analyzer setup is not needed for exciting the even mode. A similar arrangement for an odd-mode resonator is shown in Figure 8.15(c). At one end of the coupled section, the two lines are connected in parallel and shorted to ground. This end becomes a voltage node. At the other end the two lines are loaded by two susceptances of opposite sign, and thus the antiphase nature of the voltage waveform on two lines is ensured.

Even- and odd-mode parameters can now be evaluated by measuring resonance frequency, Q -factor, and input VSWR for two types of resonators [41].

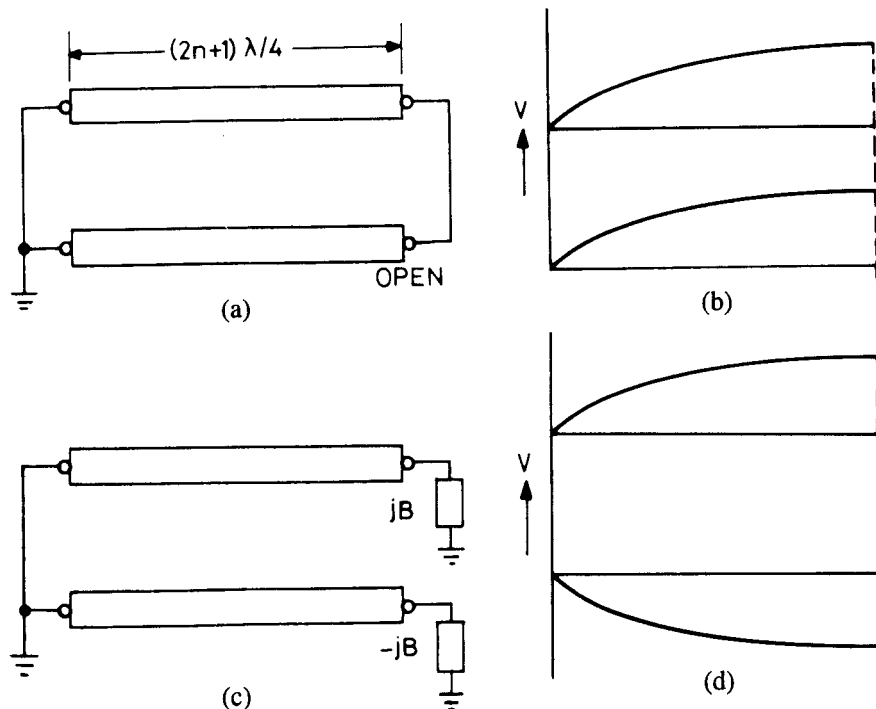


Figure 8.15 Voltage distribution for even- and odd-mode excitations: (a) configuration for enforcing the even mode, (b) voltage distribution for the even mode, (c) configuration for enforcing the odd mode, and (d) voltage distribution for the odd mode.

Excitation of these structures is carried out by a gap-coupled microstrip feedline placed close to the coupled line configuration.

8.5 DESIGN CONSIDERATIONS FOR COUPLED MICROSTRIP LINES

Coupled microstrip structures are characterized by the characteristic impedances (or admittances) and phase velocities for the two modes. The analysis of coupled microstrip lines for these characteristics can be carried out by using one of the methods outlined in Section 8.2 and 8.3. Although the analysis can be carried out to determine the characteristics for a given set of coupled line parameters, it does not provide simple design equations for the direct synthesis of coupled line circuits. For purposes of synthesis, one prepares either a table or a graph for a number of sets of coupled line parameters and uses these tables, for example, to obtain the desired information. This procedure is time consuming and may also involve some sacrifice in accuracy. However, to avoid these disadvantages, one can write synthesis design equations instead. These equations may be derived from the results of analysis. In order to save computation time the analysis results may also be written in the form of closed-form equations.

Closed-form approximate expressions can be used to initiate the analysis or synthesis procedure. These can also be used as final results whenever the demand on specifications of the circuit is not very tight. Closed-form approximate expressions for the capacitances of symmetric coupled microstrip lines are derived in the following section.

8.5.1 Design Equations

Design equations for coupled lines should relate mode impedances and effective dielectric constants to the coupled line geometry; that is, strip width, spacing S between the strips, dielectric thickness h , and dielectric constant ϵ_r . One may write design equations for these characteristics directly in terms of the parameters of coupled lines. Alternatively, static capacitances for the coupled line geometry may be used as an intermediate step. It is seen that the latter approach yields simpler design equations. Therefore, mode characteristics will be described in terms of static capacitances. Even- and odd-mode capacitances for the symmetric coupled lines are obtained first.

Even-Mode Capacitance [42]

As shown in Figure 8.16(a) the even-mode capacitance C_e can be divided into three capacitances; that is,

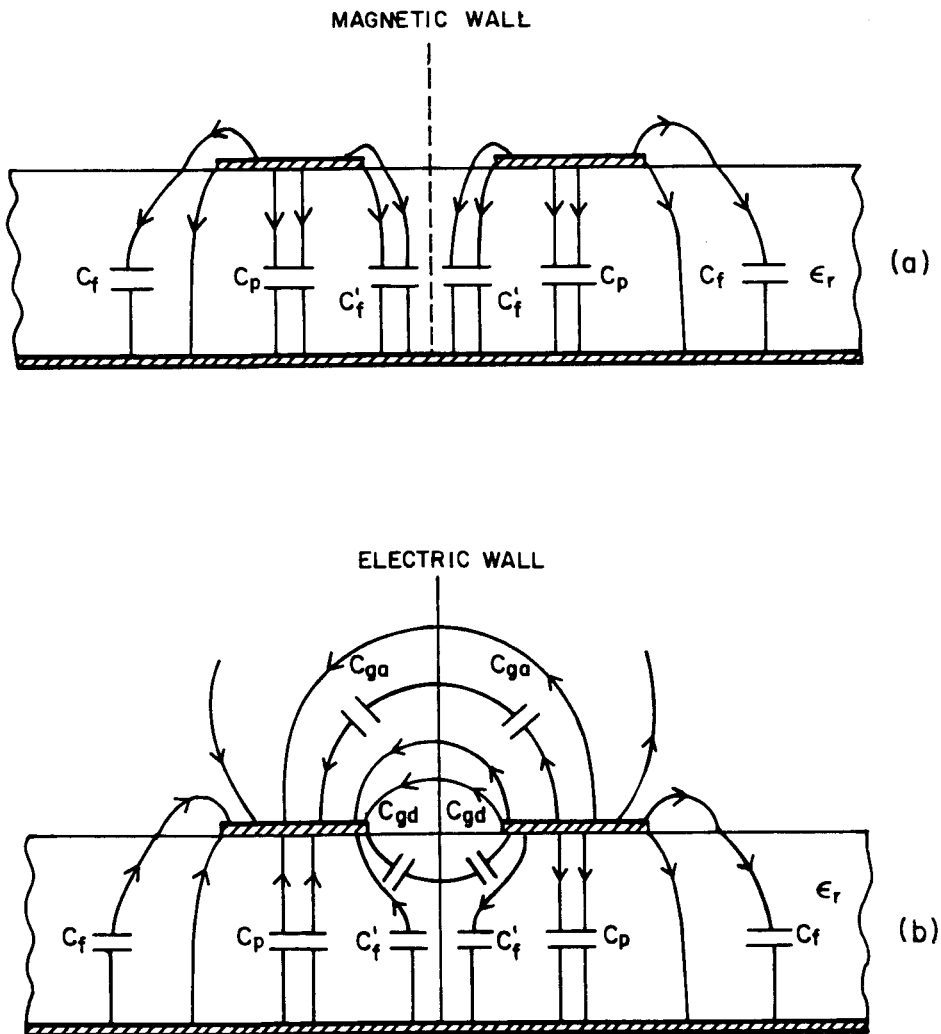


Figure 8.16 Analysis of coupled microstrip lines in terms of capacitances: (a) even-mode capacitance and (b) odd-mode capacitance.

$$C_e = C_p + C_f + C'_f \quad (8.86)$$

C_p denotes the parallel plate capacitance between the strip and the ground plane. C_f is the parallel plate capacitance at the outer edge of the strip. It is the fringe capacitance of a single microstrip line and can be evaluated from the capacitance of the microstrip line and the value of C_p . The term C'_f accounts for the modification of fringe

capacitance C_f of a single line due to the presence of another line. Expressions for C_p , C_f , and C'_f are given below

$$C_p = \epsilon_0 \epsilon_r W/h \quad (8.87)$$

$$2C_f = \sqrt{\epsilon_{re}/(cZ_{0m})} - \epsilon_0 \epsilon_r W/h \quad (8.88a)$$

and

$$C'_f = \frac{C_f}{1 + A(h/S)\tanh(10S/h)} \left(\frac{\epsilon_r}{\epsilon_{re}} \right)^{1/4} \quad (8.88b)$$

where

$$A = \exp[-0.1\exp(2.33 - 1.5 W/h)]$$

The capacitances obtained by using the above design equations were compared with those obtained from [39]. The values are found to be accurate to within 3 percent over the following range of parameters

$$0.1 \leq W/h \leq 10 \quad 0.1 \leq S/h \leq 5 \quad 1 \leq \epsilon_r \leq 18$$

Odd-Mode Capacitance [43]

The odd-mode capacitance C_o can be decomposed into five constituents C_f , C_p , C'_f , C_{gd} and C_{ga} as shown in Figure 8.16(b); that is,

$$C_o = C_p + C_f + C'_f + C_{gd} + C_{ga} \quad (8.89)$$

Expressions for C_p , C_f , and C'_f are the same as those given earlier in the case of even mode. The capacitance C_{gd} may be calculated from the corresponding coupled stripline geometry with the spacing between the ground planes given by $2h$. The value of C_{gd} is obtained from the relation

$$C_{gd} = 0.5(C_{os} - C_{es}) \quad (8.90)$$

where C_{os} and C_{es} are the odd- and even-mode capacitances of the corresponding coupled striplines.

The capacitance C_{ga} describes the gap capacitance in air. Its value can be obtained from the capacitance of the corresponding coplanar strips with air as

dielectric and the fringe capacitances. Bedair has suggested the following expression for C_{ga} [43]:

$$C_{ga} = C_{cps} - (C_f - C_{fs}) - (C'_f - C'_{fs}) \quad (8.91a)$$

with

$$C_{fs} + C'_{fs} = 0.5 C_{os} - C_p - C_{gd} \quad (8.91b)$$

where C_{cps} is the capacitance of CPS in the half space. From (7.64) one obtains

$$C_{cps} = \epsilon_0 \frac{K(k')}{K(k)} \quad k = \frac{S}{S + 2W} \quad (8.92)$$

A direct substitution of (8.90) and (8.91) in (8.89) yields the following simple expression for C_o :

$$C_o = 0.5 C_{os} + C_{cps} \quad (8.93)$$

Equation (8.93) has a very simple interpretation. According to this the lower-half portion of the coupled microstrip line is modeled as a coupled stripline and the upper-half portion as a CPS. The capacitance C_{os} is calculated from

$$C_{os} = 4\epsilon_0\epsilon_r \frac{K(k_o)}{K(k'_o)} \quad (8.94)$$

The modulus k_o has been defined in (8.62b).

The capacitances obtained by using the above design equations are accurate to within 3 percent, compared with the values obtained from [39], over the range of parameters

$$0.1 \leq W/h \leq 10 \quad 0.1 \leq S/h \leq 4 \quad 2 \leq \epsilon_r \leq 18$$

More accurate values of capacitances can be obtained from the closed-form expressions for static impedances and effective dielectric constants given next.

Effective Static Dielectric Constants

Effective dielectric constants ϵ_{re}^e and ϵ_{re}^o for even and odd modes, respectively, can be obtained from C_e and C_o by using the relations

$$\epsilon_{re}^e = C_e / C_a \quad (8.95a)$$

and

$$\epsilon_{re}^o = C_o / C_a \quad (8.95b)$$

Accurate closed-form expressions for the effective dielectric constants are available [39]. These are reproduced here as

$$\epsilon_{re}^e(0) = \frac{\epsilon_r + 1}{2} + \frac{\epsilon_r - 1}{2} \left(1 + \frac{10}{v} \right)^{-a_r b_r} \quad (8.96)$$

with

$$\begin{aligned} v &= \frac{u(20 + g^2)}{10 + g^2} + g e^{-g} \\ a_r &= 1 + \frac{1}{49} \ell_n \left[\frac{v^4 + (v/52)^2}{v^4 + 0.432} \right] + \frac{1}{18.7} \ell_n \left[1 + \left(\frac{v}{18.1} \right)^3 \right] \\ b_r &= 0.564 \left(\frac{\epsilon_r - 0.9}{\epsilon_r + 3} \right)^{0.053} \end{aligned}$$

The error in ϵ_{re}^e is within 0.7 percent over the range of parameters

$$0.1 \leq u (= W/h) \leq 10 \quad 0.1 \leq g (= S/h) \leq 10 \quad 1 \leq \epsilon_r \leq 18 \quad (8.97)$$

$$\epsilon_{re}^o(0) = \epsilon_{re}(0) + \{0.5(\epsilon_r + 1) - \epsilon_{re}(0) + a_o\} e^{-c_o(g^{d_o})} \quad (8.98)$$

with

$$a_o = 0.7287(\epsilon_{re}(0) - 0.5(\epsilon_r + 1))(1 - e^{-0.179u})$$

$$b_o = \frac{0.747\epsilon_r}{0.15 + \epsilon_r}$$

$$c_o = b_o - (b_o - 0.207)e^{-0.414u}$$

$$d_o = 0.593 + 0.694 e^{-0.562u}$$

where $\epsilon_{re}(0)$ is the static effective dielectric constant of a single microstrip of width W as discussed in Chapters 1 and 2. The error in $\epsilon_{re}^e(0)$ is stated to be on the order of 0.5 percent.

Characteristic Impedances

Characteristic impedances Z_{0e} and Z_{0o} can be obtained from the expressions for capacitances and (8.45) to (8.47). One obtains

$$Z_{0e} = \left(c\sqrt{C_e^a C_e} \right)^{-1} \quad (8.99a)$$

$$Z_{0o} = \left(c\sqrt{C_o^a C_o} \right)^{-1} \quad (8.99b)$$

where C_e^a and C_o^a are even- and odd-mode capacitances for the coupled microstrip line configuration with air as dielectric.

Accurate closed-form expressions for the static characteristic impedance for the even and odd modes have been obtained by Kirschning and Jansen [39]. These are accurate to within 0.6 percent over the range of parameters specified in (8.97) and are given as

$$Z_{0e} = Z_0 \frac{\sqrt{\epsilon_{re}(0) / \epsilon_{re}^e(0)}}{1 - Q_4 \sqrt{\epsilon_{re}(0)} \cdot Z_0 / 377} \quad (8.100)$$

with

$$Q_1 = 0.8695 u^{0.194}$$

$$Q_2 = 1 + 0.7519 g + 0.189 g^{2.31}$$

$$Q_3 = 0.1975 + \left[16.6 + \left(\frac{8.4}{g} \right)^6 \right]^{-0.387} + \frac{1}{241} \ell_n \left[\frac{g^{10}}{1 + (g/3.4)^{10}} \right]$$

$$Q_4 = \frac{2Q_1}{Q_2} \cdot \frac{1}{u^{Q_3} e^{-g} + (2 - e^{-g}) u^{-Q_3}}$$

$$Z_{0o} = Z_0 \frac{\sqrt{\epsilon_{re}(0) / \epsilon_{re}^o(0)}}{1 - Q_{10} \sqrt{\epsilon_{re}(0)} \cdot Z_0 / 377} \quad (8.101)$$

with

$$\begin{aligned}
 Q_5 &= 1.794 + 1.14\ell_n \left[1 + \frac{0.638}{g + 0.517g^{2.43}} \right] \\
 Q_6 &= 0.2305 + \frac{1}{281.3} \ell_n \left[\frac{g^{10}}{1 + (g/5.8)^{10}} \right] + \frac{1}{5.1} \ell_n (1 + 0.598g^{1.154}) \\
 Q_7 &= \frac{10 + 190g^2}{1 + 82.3g^3} \\
 Q_8 &= e^{-[6.5 + 0.95\ell_n(g) + (g/0.15)^5]} \\
 Q_9 &= \ell_n(Q_7)(Q_8 + 1/16.5) \\
 Q_{10} &= Q_4 - \frac{Q_5}{Q_2} \exp \left[\frac{Q_6 \ell_n(u)}{u^{Q_9}} \right]
 \end{aligned}$$

In (8.100) and (8.101) $\epsilon_{re}(0)$ is the static effective dielectric constant, Z_0 is the static characteristic impedance for a microstrip line of width W , and $\epsilon_{re}^{e,o}(0)$ represents the static effective dielectric constant for a coupled microstrip line.

Closed-form expressions for characteristic impedances and effective dielectric constants, as given above, may also be used to obtain accurate values of capacitances for the even and odd modes. The relationship between these quantities is obtained from (8.95) and (8.99) and is given as

$$C_{e,o} = \frac{1}{c} \frac{\sqrt{\epsilon_{re}^{e,o}(0)}}{Z_{0(e,o)}} \quad (8.102a)$$

$$C_{e,o}^a = \frac{1}{c} \frac{1}{Z_{0(e,o)} \sqrt{\epsilon_{re}^{e,o}(0)}} \quad (8.102b)$$

Design equations for the analysis and synthesis of coupled microstrip lines have been reported by Akhtarzad et al. [44] also. But their results indicate an error on the order of 10 percent. Nomograms for the design of coupled lines have been reported in [45, 46]. A scaling procedure is also available [47, 48] for determining even- and odd-mode impedances, which requires for its usage the accurate design values for any other dielectric. Empirical formulas for the capacitance of multiple-coupled microstrip lines have been reported by Dalby [49].

Asymmetric Coupled Microstrip Lines

Asymmetric coupled microstrip lines have been studied extensively [9, 10, 25, 28, 36, 50–56] because they provide design flexibility in addition to their impedance

transformation property. Analysis of asymmetric coupled lines was described in Section 8.2.2. Mode characteristics were obtained in terms of primary parameters of the lines: self-capacitances C_1 and C_2 , self-inductances L_1 and L_2 , as well as mutual capacitance C_m and mutual inductance L_m . Expressions for self- and mutual capacitances have been derived in [52]. The inductances L_1 , L_2 , and L_m can be obtained from the self- and mutual capacitances, C_1^a , C_2^a and C_m^a , of the corresponding geometry with air as dielectric. The relationship between the capacitance matrix $[C^a]$ and the inductance matrix $[L]$ of the coupled lines is

$$[L] = \mu_0 \epsilon_0 [C^a]^{-1} \quad (8.103)$$

where

$$[L] = \begin{bmatrix} L_1 & L_m \\ L_m & L_2 \end{bmatrix} \quad \text{and} \quad [C^a] = \begin{bmatrix} C_1^a & C_m^a \\ C_m^a & C_2^a \end{bmatrix} \quad (8.104)$$

From (8.103) and (8.104) one obtains

$$L_1 = \mu_0 \epsilon_0 \frac{C_2^a}{\Delta C} \quad L_2 = \mu_0 \epsilon_0 \frac{C_1^a}{\Delta C} \quad L_m = \mu_0 \epsilon_0 \frac{C_m^a}{\Delta C} \quad (8.105)$$

where

$$\Delta C = C_1^a C_2^a - (C_m^a)^2$$

Capacitances for the asymmetric coupled shielded microstrip lines have been obtained in [53]. Characteristic impedance values for the shielded and open configurations are found to be in agreement with available published data.

The capacitance expressions discussed above are valid for coupled microstrip lines with zero strip thickness. In actual practice, the metal strips have finite thickness, and the coupled lines are enclosed in a metallic box for purposes of handling, for example. In addition, the effect of fabrication tolerances and the finite amount of losses should also be considered while designing a coupled line circuit. These effects are considered next.

Effect of Strip Thickness

When the strip conductors are of finite thickness t , C_e can be evaluated using (8.87) for C_p and modifying C_f (8.88a) to include the effect of strip thickness. In this case C_f becomes [42]

$$C_f(t) = 0.5 \left\{ \frac{\sqrt{\epsilon_{re}(t)}}{cZ_{0m}(t)} - \epsilon_0 \epsilon_r \frac{W}{h} \right\} \quad (8.106)$$

where $\epsilon_{re}(t)$ and $Z_{0m}(t)$ are the characteristics of microstrip with finite thickness t and are given by (2.124) to (2.127). The increase in the value of C_o due to finite thickness t is given by $C_f(t)$, (8.106), and another term representing gap capacitance evaluated from

$$C_{gt} = 2\epsilon_0 t/S \quad (8.107)$$

Due to the increase in even- and odd-mode capacitances with finite strip thickness, the even- and odd-mode impedances are expected to decrease. The amount of the decrease in impedance can be evaluated. It is seen that the percentage of increase in C_o^a or C_e^a with thickness is more than that in C_o or C_e . Therefore, effective dielectric constants $\epsilon_{re}^e(t)$ and $\epsilon_{re}^o(t)$ should decrease with thickness. The percentage decrease in $\epsilon_{re}^o(t)$ is found to be more than that in $\epsilon_{re}^e(t)$ because of an additional gap capacitance C_{gt} with air as dielectric. These observations are verified by exact numerical results available in [16, 57]. The percentage increase in C_o is found to be twice that of C_e . The effect of strip thickness on the modal characteristics could be considerable for coupled lines with $t/S = 0.1$ and $t/W = 0.1$ [58].

Effect of Enclosure

When coupled microstrip lines are enclosed in a metallic box the electric field lines in air terminate prematurely at the walls of the box. This will give rise to an increase in the mode capacitances resulting in a decrease in the mode impedances and effective dielectric constants. The percentage decrease in odd-mode values (with the size of the enclosure) should be less than that for the even mode because a few lines for the odd mode terminate on the walls of the enclosure. Figure 8.17 (a, b), obtained from exact numerical evaluation, shows this trend [15]. Coupled microstrip lines with a top cover have been modeled by Bedair [53, 59].

8.5.2 Losses [60]

The coupled microstrip lines also has two types of losses: ohmic and dielectric. The even- and odd-mode attenuation constants due to ohmic losses in coupled microstrip lines can be determined using Wheeler's incremental inductance formula. Its application to the coupled line configuration (Figure 8.18) gives for the odd-mode attenuation constant (due to strips only)

$$\alpha_{co} = \frac{8.688 R_s}{240 \pi Z_{0o}} \frac{\delta(\sqrt{\epsilon_{re}^o} Z_{0o})}{\delta n} \quad (\text{dB/unit length}) \quad (8.108)$$

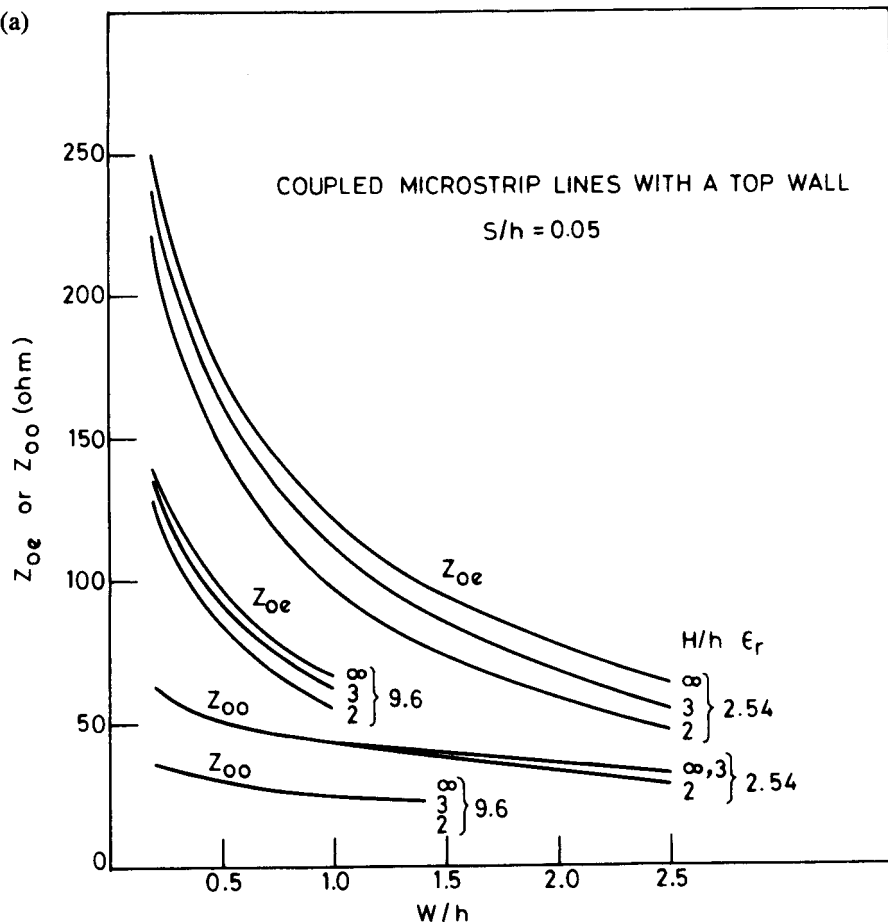


Figure 8.17 (a) Variation of characteristic impedances of coupled microstrip lines with shield: height ratio H/h and (b) variation of phase velocities in coupled microstrip lines with shield: height ratio H/h .

where

$$\frac{\delta(\sqrt{\epsilon_{re}} Z_{0o})}{\delta n} = \frac{2}{h} \left\{ \left(1 - \frac{S}{2h} \right) \frac{\partial(\sqrt{\epsilon_{re}} Z_{0o})}{\partial(S/h)} - \left(1 + \frac{t}{2h} \right) \frac{\partial(\sqrt{\epsilon_{re}} Z_{0o})}{\partial(t/h)} \right. \\ \left. - \left(1 + \frac{W}{2h} \right) \frac{\partial(\sqrt{\epsilon_{re}} Z_{0o})}{\partial(W/h)} \right\} \quad (8.109)$$

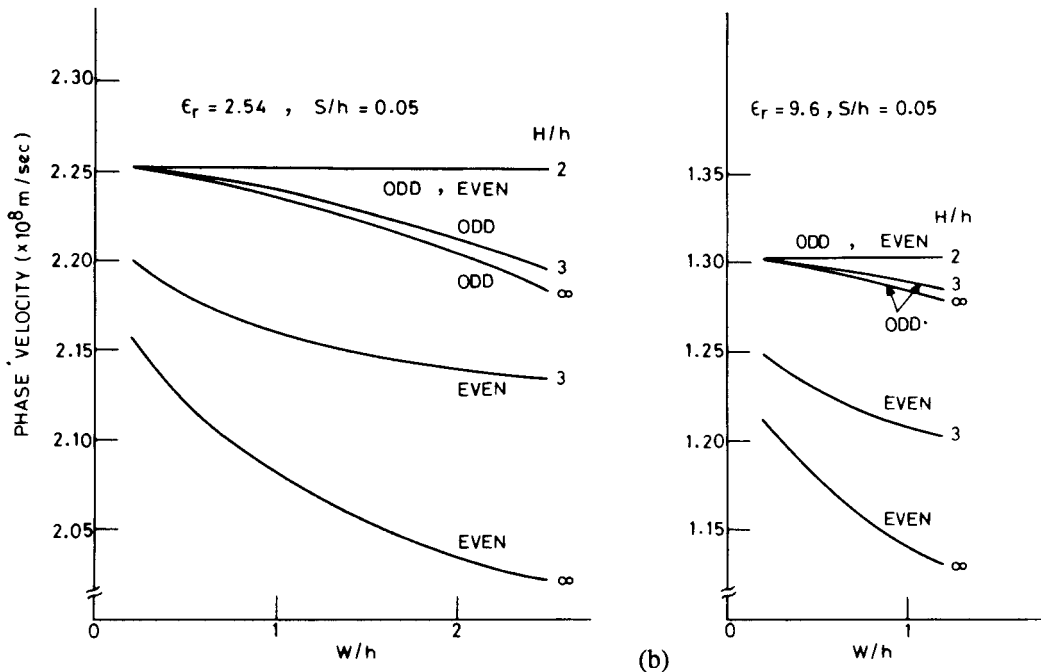


Figure 8.17 (continued).

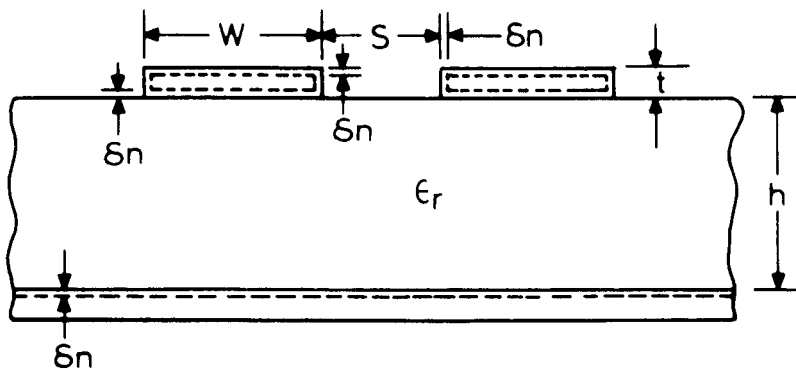


Figure 8.18 Coupled microstrip lines configuration for the calculation of ohmic losses.

Similarly, the even-mode attenuation constant is given by

$$\alpha_{ee} = \frac{8.686 R_s}{240 \pi Z_{0e}} \frac{\delta(\sqrt{\epsilon_{re}} Z_{0e})}{\delta n} \quad (\text{dB/unit length}) \quad (8.110)$$

where

$$\frac{\delta(\sqrt{\epsilon_{re}^e} Z_{0e})}{\delta n} = \frac{2}{h} \left\{ \left(1 - \frac{S}{2h} \right) \frac{\partial(\sqrt{\epsilon_{re}^e} Z_{0e})}{\partial(S/h)} - \left(1 + \frac{t}{2h} \right) \frac{\partial(\sqrt{\epsilon_{re}^e} Z_{0e})}{\partial(t/h)} \right. \\ \left. - \left(1 + \frac{W}{2h} \right) \frac{\partial(\sqrt{\epsilon_{re}^e} Z_{0e})}{\partial(W/h)} \right\} \quad (8.111)$$

In the above relations R_s is the sheet resistivity of metallization. It is observed that the odd-mode attenuation constant is always higher than the even-mode value. Also, it is more sensitive to changes in the spacing S between the lines than is α_{ce} . This is borne out by the plot of even- and odd-mode losses in Figure 8.19.

The attenuation due to dielectric loss α_d is given by [60]

$$\alpha_{do} = 27.3 \frac{\epsilon_r}{\sqrt{\epsilon_{re}^o}} \frac{\epsilon_{re}^o - 1}{\epsilon_r - 1} \frac{\tan \delta}{\lambda_0} \quad (\text{dB/unit length}) \quad (8.112)$$

$$\alpha_{de} = 27.3 \frac{\epsilon_r}{\sqrt{\epsilon_{re}^e}} \frac{\epsilon_{re}^e - 1}{\epsilon_r - 1} \frac{\tan \delta}{\lambda_0} \quad (\text{dB/unit length}) \quad (8.113)$$

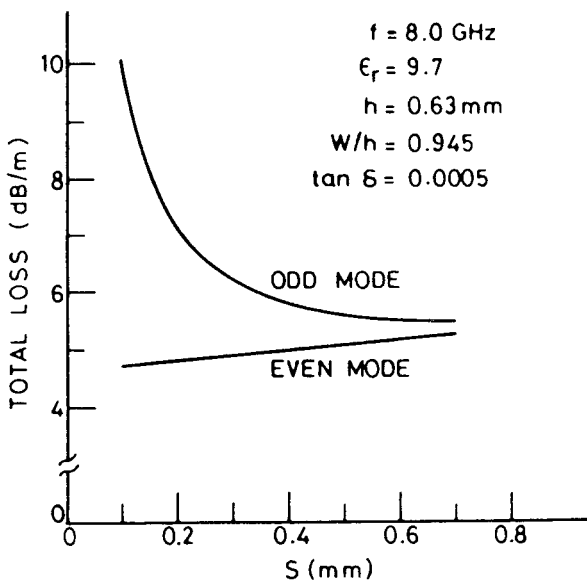


Figure 8.19 Even- and odd-mode losses in coupled microstriplines (from [42], © 1979 IEEE. Reprinted with permission.).

where $\tan\delta$ is the loss tangent of the dielectric substrate.

The total attenuation constants α_o and α_e for odd and even modes are given by

$$\alpha_o = \alpha_{co} + \alpha_{do} \quad (8.114)$$

and

$$\alpha_e = \alpha_{ce} + \alpha_{de} \quad (8.115)$$

The resultant even- and odd-mode impedances of lossy coupled lines are complex and may be obtained from the relations

$$Z_{0o}(\text{Lossy}) = Z_{0o} \left\{ 1 - j \frac{\alpha_{co}}{\beta_o} + j \frac{\alpha_{do}}{\beta_o} \right\} \quad (8.116)$$

$$Z_{0e}(\text{Lossy}) = Z_{0e} \left\{ 1 - j \frac{\alpha_{ce}}{\beta_e} + j \frac{\alpha_{de}}{\beta_e} \right\} \quad (8.117)$$

The relations for impedances are useful for studying the effect of line losses on circuit performance, for example, directivity of a directional coupler.

Like in a microstrip line, slotline, and coplanar lines, leaky modes have also been found to exist in coupled microstrip lines. Excitation of these modes gives rise to an additional loss. Effects of metal thickness and finite substrate width on leaky waves in coupled microstrip lines is discussed in [61].

8.5.3 Effect of Fabrication Tolerances [62]

The sensitivity analysis described earlier for other lines can also be applied to coupled transmission lines to account for the effect of tolerances. Since coupled lines are characterized by even- and odd-mode impedances and phase velocities, the effect of tolerances on coupled lines can be represented in terms of the effect on these characteristics.

The maximum change in the value of impedances may be written as

$$\left| \frac{\Delta Z_{0x}}{Z_0} \right|_{\max} = \left| \frac{\Delta W}{W} S_W^{Z_{0x}} \right| + \left| \frac{\Delta S}{S} S_S^{Z_{0x}} \right| + \left| \frac{\Delta h}{h} S_h^{Z_{0x}} \right| + \left| \frac{\Delta \epsilon_r}{\epsilon_r} S_{\epsilon_r}^{Z_{0x}} \right| \quad (8.118)$$

where x designates the mode, even or odd. Similarly the maximum change in the effective dielectric constants is given by

$$\left| \frac{\Delta \epsilon_{re}^x}{\epsilon_{re}} \right|_{max} = \left| \frac{\Delta W}{W} S_W^{x_{re}} \right| + \left| \frac{\Delta S}{S} S_S^{x_{re}} \right| + \left| \frac{\Delta h}{h} S_h^{x_{re}} \right| + \left| \frac{\Delta \epsilon_r}{\epsilon_r} S_{\epsilon_r}^{x_{re}} \right| \quad (8.119)$$

The above relations can be utilized to determine the change in coupled line characteristics like VSWR performance and change in coupling constant. Alternatively, for a given set of values of ΔZ_{0x} and $\Delta \epsilon_{re}^x$ the trade-off between tolerances can be determined; that is, tolerance on one parameter may be increased or decreased at the cost of tolerances in other parameters.

The effects of tolerances on VSWR performance and coupling constant are described below.

VSWR Performance of Coupled Microstrip Lines

The VSWR performance of coupled microstrip lines may be obtained from

$$VSWR = \left[1 - \frac{|\Delta Z_0|_{max}}{Z_0} \right]^{-1} \quad (8.120)$$

where the change in coupler impedance Z_0 ($= \sqrt{Z_{0e} Z_{0o}}$) represented by $|\Delta Z_0|_{max}$ is obtained from

$$\frac{|\Delta Z_0|_{max}}{Z_0} = \left| \frac{\Delta Z_{0o}}{Z_{0o}} S_{Z_{0o}}^{Z_0} \right| + \left| \frac{\Delta Z_{0e}}{Z_{0e}} S_{Z_{0e}}^{Z_0} \right| \quad (8.121)$$

Since $Z_0 = \sqrt{Z_{0e} Z_{0o}}$,

$$S_{Z_{0e}}^{Z_0} = S_{Z_{0o}}^{Z_0} = 0.5 \quad (8.122)$$

and (8.121) becomes

$$\frac{|\Delta Z_0|_{max}}{Z_0} = 0.5 \left[\left| \frac{\Delta Z_{0o}}{Z_{0o}} \right| + \left| \frac{\Delta Z_{0e}}{Z_{0e}} \right| \right] \quad (8.123)$$

where

$$\left| \frac{\Delta Z_{0e}}{Z_{0e}} \right| = \left| \frac{\Delta W}{W} S_W^{Z_{0e}} \right| + \left| \frac{\Delta S}{S} S_S^{Z_{0e}} \right| + \left| \frac{\Delta \epsilon_r}{\epsilon_r} S_{\epsilon_r}^{Z_{0e}} \right| + \left| \frac{\Delta h}{h} S_h^{Z_{0e}} \right| \quad (8.124)$$

and a similar relation holds for ΔZ_{0o} .

Change in the Coupling Constant C

The coupling constant C is defined by

$$C = \frac{Z_{0e} - Z_{0o}}{Z_{0e} + Z_{0o}} \quad (8.125)$$

Since the coupling constant is a function of W , h , S , and ϵ_r , one can write

$$\frac{|\Delta C|_{\max}}{C} = \left| \frac{\Delta W}{W} S_W^C \right| + \left| \frac{\Delta h}{h} S_h^C \right| + \left| \frac{\Delta \epsilon_r}{\epsilon_r} S_\epsilon^C \right| + \left| \frac{\Delta S}{S} S_S^C \right| \quad (8.126)$$

Using equations (8.123) and (8.126) the effect of tolerances on the coupled microstrip characteristics can be estimated. It is shown in Figure 8.20 for the VSWR performance and the change in the coupling constant for $\epsilon_r = 9.7$ [42]. It may be observed from this figure that the effect of tolerances increases with the increase in the coupling constant. Further analysis shows that the dielectric thickness h and the gap width S are the most critical parameters affecting the coupling constant [62]. Also, VSWR is mainly controlled by variations in h and ϵ_r .

8.5.4 Coupled Microstrip Lines with Dielectric Overlays

The analysis of coupled microstrip lines reported in Section 8.3 shows that the effective dielectric constants for even and odd modes of coupled microstrip lines

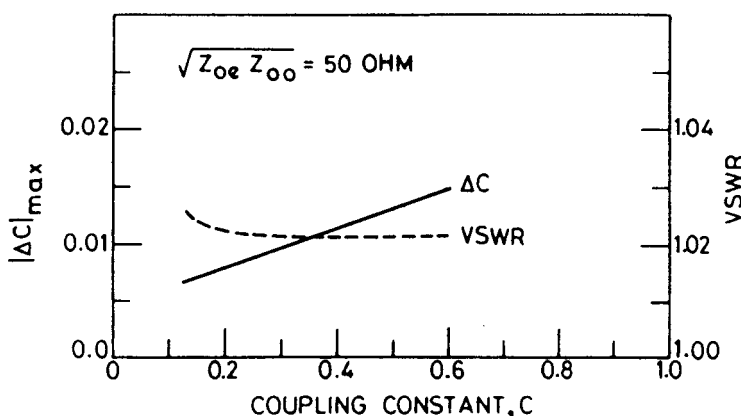


Figure 8.20 Effect of tolerances on coupling constant and VSWR performance of coupled microstrip lines ($\epsilon_r = 9.7 \pm 0.25$, $h = 0.63 \pm 0.025$ mm, $\Delta W = \pm 0.0025$ mm, $\Delta S = \pm 0.0025$ mm) (from [42], © 1979 IEEE. Reprinted with permission.).

are not equal. The even-mode effective dielectric constant is higher than its odd-mode counterpart value. This is because of the relatively higher density of the electric field lines in air for the odd mode. On alumina substrate, this difference is normally less than 12 percent. Although different even- and odd-mode phase velocities produce only a small perturbation on the coupler impedance $Z_0 = \sqrt{Z_{0o} Z_{0e}}$ and the midband voltage coupling coefficient C (Equation 8.125) in most practical cases, the change in directivity of the coupler is significant. From infinite directivity for an ideal coupler, the directivity of a microstrip 10-dB coupler on alumina substrate with $v_{\text{odd}}/v_{\text{even}} = 1.125$ decreases to about 12.5 dB. The deterioration in directivity is higher for loose coupling [63].

If a dielectric slab having dielectric constant equal to that of the substrate is placed over the coupled lines (see Figure 8.21), the odd-mode effective dielectric constant will increase more than that of the even mode. The increase in $\epsilon_{\text{re}}^{\text{o}}$ will be higher for thick overlay slabs. With the right amount of overlay thickness the effective dielectric constants for the two modes can be made equal. The use of a dielectric overlay not only improves the velocity ratio, but it also tightens the midband coupling compared to coupled microstrip lines without dielectric overlays. One would also expect a decrease in coupler impedance Z_0 because of the increased effective dielectric constants for the two modes.

The change in the amount of coupling and impedance due to the overlay can be determined analytically if the equalized value of phase velocity is known. For coupled lines without overlay we know that the coupler impedance Z_0 is given by

$$Z_0 = \sqrt{Z_{0o} Z_{0e}} \quad (8.127)$$

with

$$Z_{0o} = Z_{0o}^{\text{a}} / \sqrt{\epsilon_{\text{re}}^{\text{o}}} \quad (8.128)$$

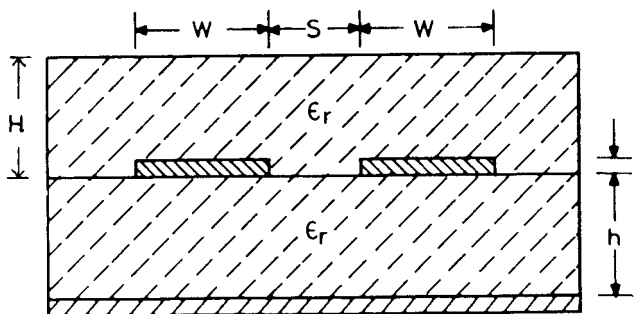


Figure 8.21 Coupled microstrip lines with a dielectric overlay to equalize even- and odd-mode phase velocities.

and

$$Z_{0e} = Z_{0e}^a / \sqrt{\epsilon_{re}^c} \quad (8.129)$$

Now, with the dielectric overlay in place, let the effective dielectric constant for both modes be ϵ_{re}^c (where c stands for coupled lines). Then, the new values of impedances are given by

$$Z'_{0o} = Z_{0o}^a / \sqrt{\epsilon_{re}^c} = Z_{0o} \sqrt{\epsilon_{re}^o / \epsilon_{re}^c} \quad (8.130)$$

$$Z'_{0e} = Z_{0e}^a / \sqrt{\epsilon_{re}^c} = Z_{0e} \sqrt{\epsilon_{re}^e / \epsilon_{re}^c} \quad (8.131)$$

Therefore,

$$Z'_0 = \sqrt{Z'_{0o} Z'_{0e}} = Z_0 (\sqrt{\epsilon_{re}^o \epsilon_{re}^e} / (\epsilon_{re}^c)^{1/2}) \quad (8.132)$$

The change in coupling can be estimated as follows. The voltage coupling coefficient with overlay is

$$C' = \frac{Z'_{0e} - Z'_{0o}}{Z'_{0e} + Z'_{0o}} \quad (8.133)$$

or

$$C' = \frac{Z_{0e} - Z_{0o} g}{Z_{0e} + Z_{0o} g} \quad (8.134)$$

where $g = \sqrt{\epsilon_{re}^o / \epsilon_{re}^e}$. Substituting the value of Z_{0e}/Z_{0o} from (8.125) gives

$$C' = \frac{(1 + C) - (1 - C) g}{(1 + C) + (1 - C) g} \quad (8.135)$$

It shows that the new coupling C' depends on the ratio of ϵ_{re}^e and ϵ_{re}^o and the coupling of the uncompensated coupler. It does not depend on the final value of ϵ_{re}^c nor on Z'_0 .

Coupled microstrip lines with a dielectric overlay have been analyzed comprehensively [64–69]. Characteristic impedance and wavelength ratio λ_0/λ_g have been determined as a function of the overlay thickness H , gap S , and frequency. Results

for $S/h = 0.4$, $W/h = 1$, and $\epsilon_r = 10$ as a function of H/h are plotted in Figure 8.22. It is observed that a crossing of even- and odd-mode wavelength ratios occurs at a relatively small overlay thickness. Klein and Chang have reported an improvement in isolation from 25 dB to 60 dB in a 10-dB coupler with an overlay [69].

8.5.5 Effect of Dielectric Anisotropy

It has been assumed in the analysis presented in Section 8.3 and in the design equations given in this section that the dielectric substrate is isotropic. However, substrates such as sapphire and Epsilam-10¹ are anisotropic. This anisotropy can

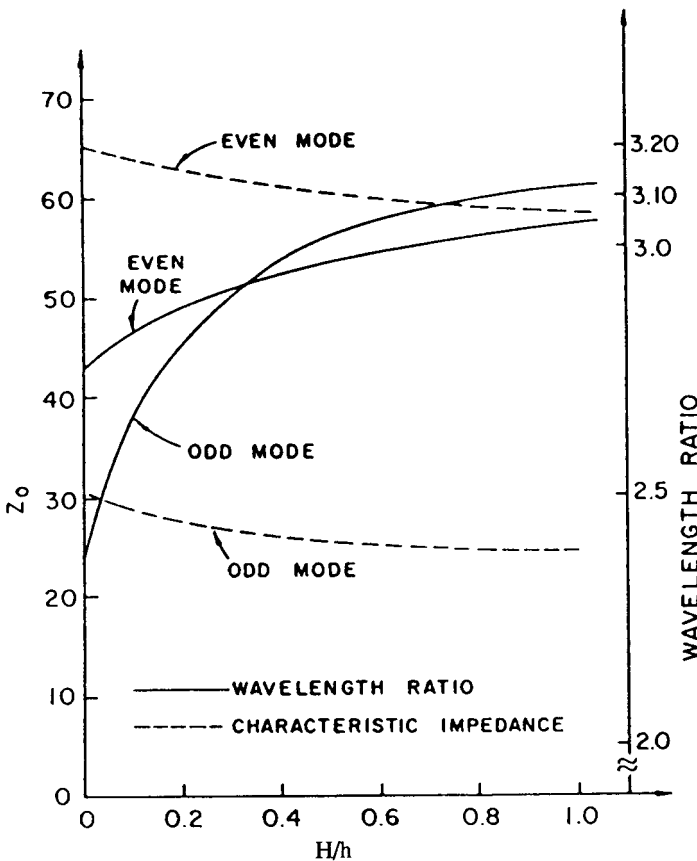


Figure 8.22 Characteristic impedance Z_0 and wavelength ratio λ_0/λ_g for the coupled microstrip lines with an overlay ($\epsilon_r = 10$, $W/h = 1$, $S/h = 0.4$, $2\pi h/\lambda_0 = 0.1$) (from [68]).

¹Trademark of Rogers, Inc.

be used to advantage in the design of coupled microstrip lines as shown by Szentkuti [70]. The transformation from anisotropic to the isotropic case can be carried out in the same manner as has been done for the single microstrip (discussed in Section 2.4.4). The relative difference between the odd- and even-mode phase velocities is plotted in Figure 8.23 for four types of substrates. It may be observed from here that the difference in phase velocities decreases with the increase in ratio $\epsilon_r^x/\epsilon_r^y$, where ϵ_r^x and ϵ_r^y are the x and y components, respectively, of the anisotropic dielectric constant.

8.6 COUPLED MULTICONDUCTOR MICROSTRIP LINES

Two strip coupled microstrip lines are used in many circuits. The performance of these circuits can be improved by using multistrip/multiconductor microstrip lines. These lines also find applications in VLSI interconnections and antennas [27, 31–34, 71–76]. Analysis of these lines is briefly summarized next.

Very large scale integrated (VLSI) chips require millions of closely spaced interconnection lines that integrate the components on a chip. Multilayer interconnections in two or more planes play the most significant role in determining the size, power consumption, and clock frequency. In particular, capacitances, inductances, cross talk, and propagation delays associated with the interconnections in high-density environments on a chip or wafer have become the major factors in the evolution of very high-speed integrated circuit technology. Capacitances and

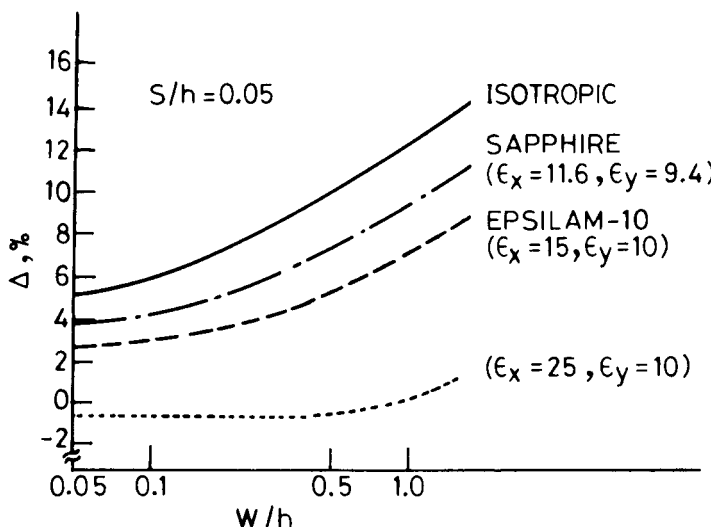


Figure 8.23 Relative difference between odd- and even-mode phase velocities for anisotropic substrates (from [70], © 1976 IEE (U.K.). Reprinted with permission.)

inductances associated with interconnections on the same plane are discussed next. For other characteristics such as propagation delays, cross talk, and failure analysis the reader may refer to [75].

The schematic diagram of a few interconnection lines on the same plane is shown in Figure 8.24. For the switching speeds commonly encountered in VLSI circuits the system of lines shown in Figure 8.24 can be characterized by a capacitance matrix $[C]$ and an inductance matrix $[L]$. The inductance matrix can be obtained from the capacitance matrix as in (8.103). The diagonal elements of the capacitance matrix C_{ii} are called self-capacitances and represent the capacitance between the strip conductors and the ground. The off-diagonal elements are called coupling (interconnection) capacitances or mutual capacitances.

The capacitance for a single microstrip line was determined in Chapter 1 using various techniques. Some of these techniques were extended to coupled microstrip lines in Section 8.2. The same techniques can also be used to determine the capacitance matrix of multiconductor microstrip lines. The most commonly used methods are the integral equation method of Section 1.2.3, the variational method in FTD of Section 1.2.4, the congruent transformation technique [8], and the network analog method [77].

The various capacitances for three coupled microstrip lines are shown in Figure 8.25. For the symmetric layout the even- and odd-mode approach can be used to reduce the computational effort. The even mode corresponds to the situation when all the strips are at the same potential, say $+V_0$. In the odd-mode case, one of the strips is at the potential $-V_0$, and the rest are at $+V_0$. The capacitances (per unit length) shown in Figure 8.25 are related to the even- and odd-mode capacitances (per unit length) defined above by the set of equations [75]

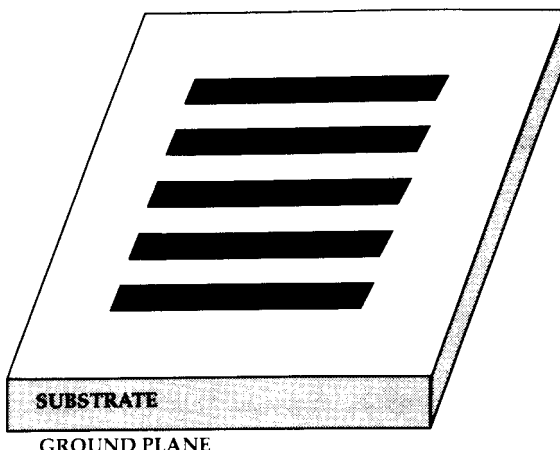


Figure 8.24 Schematic of a few interconnections printed as microstrip lines.

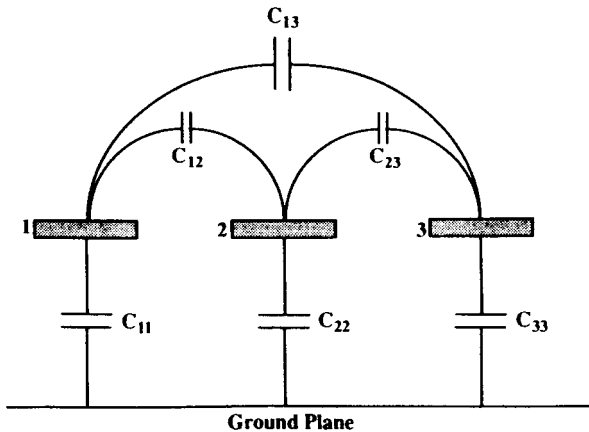


Figure 8.25 Various capacitances between three coupled microstrip lines (from [75], © 1994 John Wiley. Reprinted with permission.).

$$C_1^e = C_{11} \quad C_2^e = C_{22} \quad C_3^e = C_{33} \quad (8.136)$$

$$C_1^o = C_{11} + 2C_{12} + 2C_{13} \quad (8.137a)$$

$$C_2^o = C_{22} + 2C_{12} + 2C_{23} \quad (8.137b)$$

$$C_3^o = C_{33} + 2C_{13} + 2C_{23} \quad (8.137c)$$

The dependence of the self- and mutual capacitances on the strip width W is shown in Figure 8.26 for single-level three-strip interconnections on GaAs substrate [75]. T is the strip thickness in this figure. It is observed from Figure 8.26(a) that the self-capacitances increase almost linearly with strip width W . The capacitance C_{22} for the middle strip is lower than C_{11} or C_{33} because of the shielding effect of outer strips. The mutual capacitances C_{12} and C_{23} between the nearest neighbors is higher than between the next-to-nearest neighbor C_{13} (see Figure 8.26(b)). The inductance values can be obtained from the capacitance values and (8.103). Mutual inductances are plotted in Figure 8.27 as a function of strip width W .

Design equations for the even- and odd-mode capacitances and inductances (per unit length) for the multiconductor microstrip lines are available in [49]. The open-end capacitance may be added to these capacitance values to obtain the overall capacitance for a given line length L .

For digital circuits the quasi-static analysis is valid only when switching speeds are on the order of one nanosecond. When the rise time of the switching pulse reduces to tens of picoseconds, a fullwave analysis of the multiconductor microstrip lines becomes necessary [27].

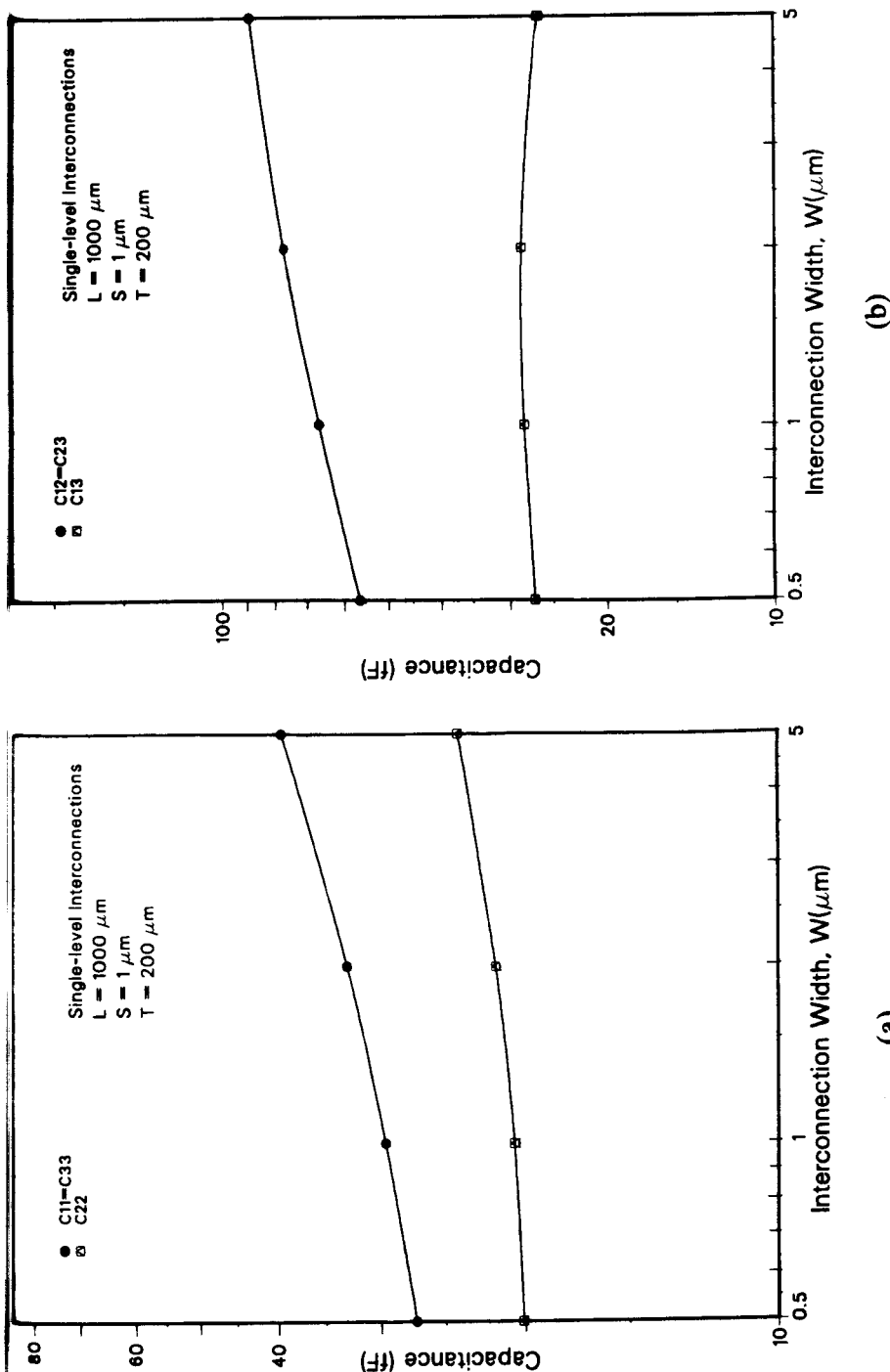


Figure 8.26 (a) Variation of the self-capacitances with the strip width W for three strip interconnections on GaAs and (b) variation of the mutual-capacitances with the strip width W for three strip interconnections on GaAs (from [75], © 1994 John Wiley. Reprinted with permission.).

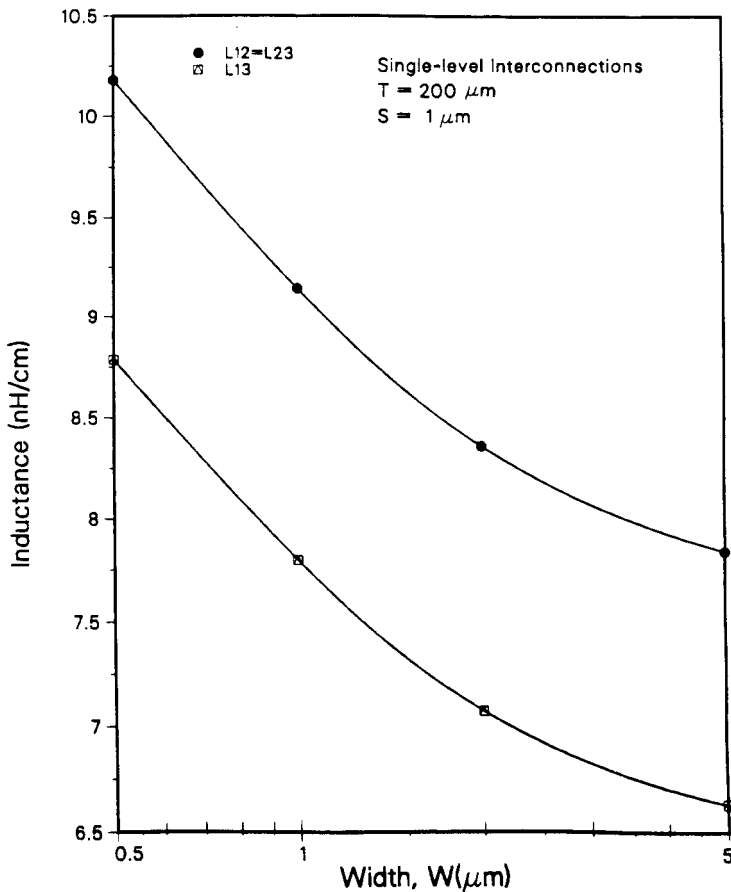


Figure 8.27 Variation of the mutual-inductances with the strip width W for three strip interconnections on GaAs (from [75], © 1994 John Wiley. Reprinted with permission.).

8.7 DISCONTINUITIES IN COUPLED MICROSTRIP LINES

Sections of coupled microstrip lines are used extensively for the design of directional couplers, filters, and other components. Although characteristics of uniformly coupled microstrip lines have been studied extensively, characterization of discontinuities and junctions in coupled lines is not readily available. An open end is perhaps the only coupled microstrip line discontinuity described in detail [78]. A closed-form expression is also available for open-end discontinuity. In this section we describe an approach that can be used to analyze discontinuities in coupled microstrip lines with a considerable savings in computation time. It is called the *network model* of coupled microstrip lines. This model makes use of the planar waveguide model of microstrip line discussed in Chapter 1.

8.7.1 Network Model [79]

A network model for coupled microstrip lines has been developed. The model consists of two parallel plate waveguide sections that are coupled to each other through a lumped-element network. The coupled line section and its planar-lumped model are shown in Figure 8.28. The parallel plate sections, also called planar segments, model the electric fields underneath the strips and the fringing fields at the outer edges ϵ_1 . The lumped-element network represents the electromagnetic coupling between the strips. The coupling due to the electric field across the gap is modeled by a capacitive network, and the magnetic field coupling is represented by an inductive network. Some details of the parallel plate section and the lumped network are given next.

The parallel plate waveguide model for the microstrip line has been described in Chapter 1. In the present context, the parallel plate waveguide accounts for the fringing fields only at the outer edges. So their effective widths $W_e(f)$ are chosen to account for outward extension at outer edges only. Keeping this in mind we write

$$\begin{aligned} W_e(f) &= W + \frac{W_{em}(f) - W}{2} \\ &= \frac{W_{em}(f) + W}{2} \end{aligned} \quad (8.138)$$

where W is the physical width of the strip and W_{em} is the width of an equivalent parallel plate waveguide for a single microstrip line. The value of W_{em} can be obtained from (1.84b) and is repeated here:

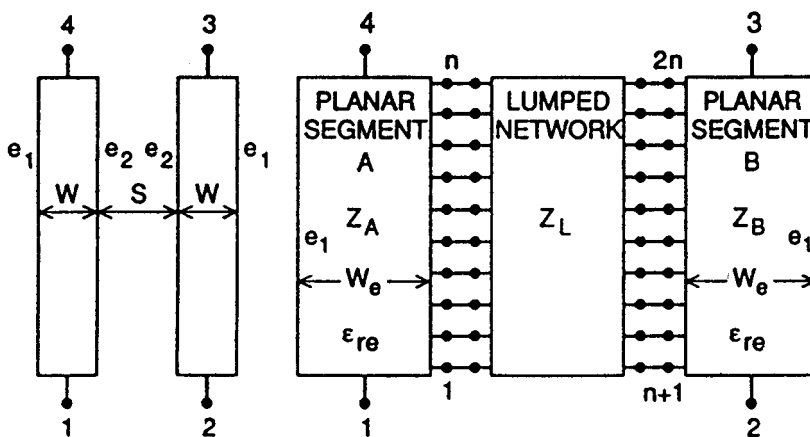


Figure 8.28 A section of coupled microstrip lines and its planar-lumped model (from [79], © 1992 IEEE. Reprinted with permission.).

$$W_{\text{em}}(f) = \frac{120\pi h}{Z_{0m}(f)\sqrt{\epsilon_{re}(f)}}$$

Lengths of these sections are equal to the physical length of the coupled line section. The parallel plate waveguide sections in Figure 8.28 are connected through a multiport network. To implement this connection a number of ports are introduced on the inner edge of each of the parallel plate sections. Multiport impedance matrices for the waveguide sections are derived from the two-dimensional Green's function for the rectangular geometry [80].

Capacitive Network

The capacitive network represents the electric field coupling between the parallel plate waveguide sections. Electric field coupling is very similar to the gap coupling between microstrip lines described in Section 3.4.2. A π -network model of the resultant capacitive network was discussed there. The capacitive network for a coupled line section of length $\Delta\ell$ is shown in Figure 8.29(a). Here capacitance C_f accounts for the fringe electric field between the inner edge of the strip and the ground plane. The value of C_f is obtained by subtracting the parallel plate capacitance from the even-mode capacitance of the coupled microstrip lines. One obtains

$$C_f = \left(C_e - \frac{\epsilon_0 \epsilon_{re} W_e}{h} \right) \Delta\ell \quad (8.139)$$

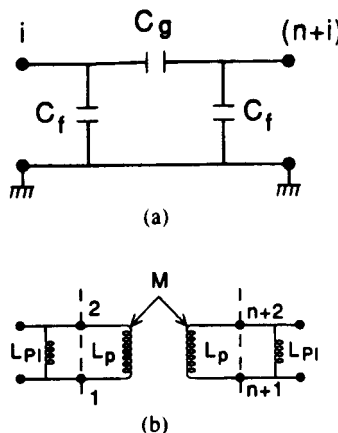


Figure 8.29 Coupling networks between coupled lines: (a) capacitive network representation of coupling between coupled lines section of length $\Delta\ell$ and (b) inductive network representation of coupling between coupled lines section of length $\Delta\ell$ (from [79], © 1992 IEEE. Reprinted with permission.).

The capacitance C_g represents the electric field across the gap. It is defined as

$$C_g = \frac{C_o - C_e}{2} \Delta\ell \quad (8.140)$$

where C_o and C_e are the odd- and even-mode capacitances per unit length of the coupled line (Section 8.5.1). The π -network shown in Figure 8.29(a) has the admittance matrix

$$[\mathbf{Y}_C] = j\omega \begin{bmatrix} C_f + C_g & -C_g \\ -C_g & C_f + C_g \end{bmatrix} \equiv j\omega [\mathbf{C}_G] \quad (8.141)$$

When the lumped network of Figure 8.28 has n ports on each side, the complete \mathbf{Y}_C -matrix will be $2n \times 2n$ with four $n \times n$ submatrices. Each of these submatrices is diagonal in nature.

Inductive Network

The magnetic field between the strips is modeled by the self- and mutual inductances. Let us consider Figure 8.28 in which two adjacent ports of the planar waveguide network A (say 1 and 2) face the corresponding ports ($n+1$) and ($n+2$) of the planar waveguide network B. The inductive coupling network between these ports may be drawn as shown in Figure 8.29(b). Values of L_p and M are obtained from an analysis of the coupled line section with air as dielectric, as described by (8.104). The inductance per unit length of the parallel plate section is denoted by L_{pl} and is given by

$$L_{pl} = \frac{\mu_0 h}{W_e} \quad (8.142)$$

The admittance matrix associated with the inductive coupling network is tridiagonal in nature. It is given by

$$[\mathbf{Y}_L] = \frac{-j}{\omega(L_p^2 - M^2)} [\mathbf{L}_G] \quad (8.143)$$

The details of matrix $[\mathbf{L}_G]$ can be found in [79]. The admittance matrix of the gap network is then obtained as

$$[\mathbf{Y}_G] = [\mathbf{Y}_C] + [\mathbf{Y}_L] = j\omega [\mathbf{C}_G] - \frac{j}{\omega(L_p^2 - M^2)} [\mathbf{L}_G] \quad (8.144)$$

Multiport admittance matrices of the planar waveguide sections are now combined with the admittance matrix of the gap network to obtain the characteristics of the coupled line section. The network model described above has been found to correctly predict the coupling coefficient S_{21} and the higher order mode cutoff frequencies. It has been used to analyze a coupled microstrip section with chamfered right-angled bends discontinuity to single microstrip lines (see Figure 8.30). Calculated S_{21} parameter for this circuit is found to agree with measured values. The network model can be applied to various types of discontinuities in coupled microstrip lines.

8.7.2 Open-End Discontinuity

Similar to the open end in a microstrip line, the open end in coupled microstrip lines is capacitive in nature and can be characterized in the form of an additional line length $\Delta\ell_{o,e}$ for each mode. Closed-form expressions for $\Delta\ell_{o,e}$ have been reported [39, 81]. These are given as

$$\begin{aligned}\Delta\ell_e &= \Delta\ell_{oc}(u, \epsilon_r) + [\Delta\ell_{oc}(2u, \epsilon_r) - \Delta\ell_{oc}(u, \epsilon_r) + 0.0198h \cdot g^{R_1}] \\ &\quad \cdot \exp(-0.328g^{2.24})\end{aligned}\quad (8.145a)$$

$$\Delta\ell_o = \Delta\ell_{oc}(u, \epsilon_r)(1 - e^{-R_4}) + hR_3 \cdot e^{-R_4} \quad (8.145b)$$

with

$$\begin{aligned}R_1 &= 1.187\{1 - \exp(-0.069u^{2.1})\} \\ R_2 &= 0.343 \cdot u^{0.6187} + \frac{0.45\epsilon_r}{1 + \epsilon_r} u^{|1.357 + 1.65/(1+0.7\epsilon_r)|} \\ R_3 &= 0.2974(1 - e^{-R_2}) \\ R_4 &= (0.271 + 0.0281\epsilon_r) \cdot g^{|1.167\epsilon_r/(0.66+\epsilon_r)|} + \frac{1.025\epsilon_r}{0.687 + \epsilon_r} \cdot g^{|0.958\epsilon_r/(0.706+\epsilon_r)|}\end{aligned}$$

$$u = W/h \quad \text{and} \quad g = S/h$$

The quantities $\Delta\ell_{oc}(u, \epsilon_r)$ and $\Delta\ell_{oc}(2u, \epsilon_r)$ represent open-end extension values for a single line with widths W and $2W$, respectively. The range of applicability of (8.145) is again defined by (8.97), and the associated accuracy is about 5 percent. It is found that line length extension $\Delta\ell_e$ decreases asymptotically to $\Delta\ell_{oc}(u, \epsilon_r)$ as the spacing S/h is increased.

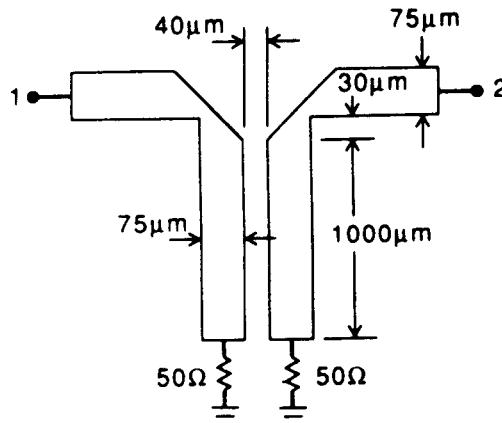


Figure 8.30 A coupled microstrip section with chamfered bends analyzed in (from [79], © 1992 IEEE. Reprinted with permission.).

References

- [1] Ozaki, H., and J. Ishii, "Synthesis of a Class of Stripline Filters," *IRE Trans.*, Vol. CT-5, 1958, pp. 104–109.
- [2] Louisell, W. H., *Coupled Mode and Parametric Electronics*, New York: John Wiley, 1960.
- [3] Isaacs, J. C., and N. A. Strakhov, "Crosstalk in Uniformly Coupled Lossy Transmission Lines," *Bell System Tech. J.*, Vol. 52, 1973, pp. 101–115.
- [4] Sato, R., and E. G. Cristal, "Simplified Analysis of Coupled Transmission-Line Network," *IEEE Trans.*, Vol. MTT-18, 1970, pp. 122–131.
- [5] Hazony, D., *Elements of Network Synthesis*, New York: Reinhold, 1963, Ch. 13.
- [6] Chang, F. Y., "Transient Analysis of Lossless Coupled Transmission Lines in a Non-Homogeneous Dielectric Medium," *IEEE Trans.*, Vol. MTT-18, 1970, pp. 616–626.
- [7] Richards, P. I., "Resistor Transmission Line Circuits," *Proc. IRE*, Vol. 36, 1948, pp. 217–220.
- [8] Chao, C. L., "On the Analysis of Inhomogeneous Asymmetrical Coupled Transmission Lines," *18th Mid-West Symp. Circuits and Systems*, Montreal, 1975, pp. 568–572.
- [9] Tripathi, V. K., "Asymmetric Coupled Transmission Lines in an Inhomogeneous Medium," *IEEE Trans.*, Vol. MTT-23, 1975, pp. 734–739.
- [10] Tripathi, V. K., "Properties and Applications of Asymmetric Coupled Line Structures in an Inhomogeneous Medium," *Proc. 5th European Microwave Conf.*, Hamburg, 1975, pp. 278–282.
- [11] Costamagna, E., and U. Maltese, "Linee Accoppiate Asimmetriche in Dielettrico non Omogeneo," *Alta Freq.*, Vol. 40, 1971, pp. 737–741. (in Italian)
- [12] Krage, M. K., and G. I. Haddad, "Characteristics of Coupled Microstrip Transmission Lines—I: Coupled-Mode Formulation of Inhomogeneous Lines, II: Evaluation of Coupled-Line Parameters," *IEEE Trans.*, Vol. MTT-18, 1970, pp. 217–228.
- [13] Pregla, R., "Calculation of the Distributed Capacitances and Phase Velocities in Coupled Microstrip Lines by Conformal Mapping Techniques," *AEU*, Vol. 26, 1972, pp. 470–474.
- [14] Bryant, T. G., and J. A. Weiss, "Parameters of Microstrip Transmission Lines and of Coupled Pairs of Microstrip Lines," *IEEE Trans.*, Vol. MTT-16, 1968, pp. 1021–1027.
- [15] Young, L., and H. Sobol (Eds.), *Advances in Microwaves*, Vol. 8, New York: Academic Press, 1974, pp. 295–320.

- [16] Bergndt, H. G., and R. Pregla, "Calculation of Even- and Odd-Mode Capacitance Parameters for Coupled Microstrips," *Archiv. Elektr. Übertr.*, Vol. 26, 1972, pp. 153–158.
- [17] Kowalski, G., and R. Pregla, "Calculation of the Distributed Capacitances of Coupled Microstrips Using a Variational Integral," *Archiv. Elektr. Übertr.*, Vol. 27, 1973, pp. 51–52.
- [18] Gunston, M. A. R., *Microwave Transmission Line Impedance Data*, London: Van Nostrand Reinhold, 1972, Ch. 6.
- [19] Gladwell, G. M. L., and S. Coen, "A Chebyshev Approximation Method for Microstrip Problems," *IEEE Trans.*, Vol. MTT-23, 1975, pp. 865–870.
- [20] Krage, M. K., and G. I. Haddad, "Frequency Dependent Characteristics of Microstrip Transmission Lines," *IEEE Trans.*, Vol. MTT-20, 1972, pp. 678–688.
- [21] Knorr, J. B., et al., "Hybrid Mode Analysis of Planar Lines," *Proc. 8th Asilomar Conf.*, 1974.
- [22] Knorr, J. B., and K. D. Kuchler, "Analysis of Coupled Slots and Coplanar Strips and Dielectric Substrate," *IEEE Trans.*, Vol. MTT-23, 1975, pp. 541–548.
- [23] Kowalski, G., and R. Pregla, "Dispersion Characteristics of Single and Coupled Microstrips," *Archiv. Elektr. Übertr.*, Vol. 26, 1972, pp. 276–280.
- [24] Davies, J. B., and D. G. Corr, "Computer Analysis of the Fundamental and Higher Order Modes in Single and Coupled Microstrip," *Electron. Lett.*, Vol. 6, 1970, pp. 806–808; see errata, Vol. 7, 1971, p. 284.
- [25] Jansen, R. H., "Fast Accurate Hybrid Mode Computation of Nonsymmetrical Coupled Microstrip Characteristics," *Proc. 7th European Microwave Conf.*, Copenhagen, 1977, pp. 135–139.
- [26] Jansen, R. H., "High-Speed Computation of Single and Coupled Microstrip Parameters Including Dispersion, High-Order Modes, Loss and Finite Strip Thickness," *IEEE Trans.*, Vol. MTT-26, 1978, pp. 75–82.
- [27] Farr, E. G., et al., "A Frequency-Dependent Coupled-Mode Analysis of Multiconductor Microstrip Lines with Application to VLSI Interconnect Problems," *IEEE Trans.*, Vol. MTT-34, 1986, pp. 307–310.
- [28] Tripathi, V. K., and H. Lee, "Spectral-Domain Computation of Characteristic Impedances and Multiport Parameters of Multiple Coupled Microstrip Lines," *IEEE Trans.*, Vol. MTT-37, 1989, pp. 215–221.
- [29] Bagby, J. S., et al., "Entire-Domain Basis MOM Analysis of Coupled Microstrip Transmission Lines," *IEEE Trans.*, Vol. MTT-40, 1992, pp. 49–57.
- [30] Tzhang, C. K. C., and J. T. Kuo, "Modal Current Distributions on Closely Coupled Microstrip Lines: A Comparative Study of the SDA Basis Functions," *Electron. Lett.*, Vol. 26, 1990, pp. 464–465.
- [31] Mu, T. C., et al., "Characteristics of Multiconductor, Asymmetric Slow Wave Microstrip Transmission Lines," *IEEE Trans.*, Vol. MTT-34, 1986, pp. 767–772.
- [32] Marx, K. D., "Propagation Modes, Equivalent Circuits and Characteristic Terminations for Multiconductor Transmission Lines with Inhomogeneous Dielectrics," *IEEE Trans.*, Vol. MTT-21, 1973, pp. 450–457.
- [33] Tripathi, V. K., "On the Analysis of Symmetrical Three-Line Microstrip Circuits," *IEEE Trans.*, Vol. MTT-25, 1977, pp. 726–729.
- [34] Janiczak, B. J., "Phase Constant Characteristic of Generalized Asymmetric Three-Coupled Microstrip Lines," *Proc. IEE, Part H*, Vol. 132, 1985, pp. 23–26.
- [35] Qian, Y., and E. Yamashita, "Characterization of Picosecond Pulse Crosstalk Between Coupled Microstrip Lines with Arbitrary Conductor Width," *IEEE Trans.*, Vol. MTT-41, 1993, pp. 1011–1016.
- [36] Kitazawa, T., and R. Mittra, "Analysis of Asymmetric Coupled striplines," *IEEE Trans.*, Vol. MTT-33, 1985, pp. 643–646.
- [37] Getsinger, W. J., "Dispersion of Parallel-Coupled Microstrip," *IEEE Trans.*, Vol. MTT-21, 1973, pp. 144–145.
- [38] Hammerstad, E., and O. Jensen, "Accurate Models for Microstrip Computer-Aided Design," *IEEE MTT-S Digest*, 1980, pp. 407–409.
- [39] Kirschning, M., and R. H. Jansen, "Accurate Wide-Range Design Equations for Parallel Coupled

- Microstrip Lines," *IEEE Trans.*, Vol. MTT-32, 1984, pp. 83–90; see also corrections, *IEEE Trans.*, Vol. MTT-33, 1985, p. 288.
- [40] Napoli, L. S., and J. J. Hughes, "Characteristics of Coupled Microstrip Lines," *RCA Review*, Vol. 31, 1970, pp. 479–498.
- [41] Rizzoli, V., "Resonance Measurement of Even and Odd Mode Propagation Constants in Coupled Microstrips," *Int. Microwave Symp. Digest*, 1975, pp. 106–108.
- [42] Garg, R., and I. J. Bahl, "Characteristics of Coupled Microstrip Lines," *IEEE Trans.*, Vol. MTT-27, 1979, pp. 700–705; see also corrections, *IEEE Trans.*, Vol. MTT-28, 1980, p. 272.
- [43] Bedair, S. S., "On the Odd-Mode Capacitance of the Coupled Microstriplines," *IEEE Trans.*, Vol. MTT-28, 1980, pp. 1225–1227.
- [44] Akhtarzad, S., et al., "The Design of Coupled Microstrip Lines," *IEEE Trans.*, Vol. MTT-23, 1975, pp. 486–492.
- [45] Shamanna, K. N., et al., "Parallel-Coupled Microstrip Line is Easy to Determine with Nomograms," *Electron. Design*, Vol. 11, May 24, 1976, pp. 78–81.
- [46] Avdeyev, E. V., and V. I. Potapova, "Nomograms for Coupled Open Microstrip Lines," *Telecomm. Radio Eng.*, Part 2, Vol. 28, 1973, pp. 89–93.
- [47] Shamasundara, S. D., and N. Singh, "Design of Coupled Microstrip Lines," *IEEE Trans.*, Vol. MTT-25, 1977, pp. 232–233.
- [48] Shamasundara, S. D., et al., "Apply Standard Curves to Strange Substrates," *Microwaves*, Vol. 16, September 1977, pp. 116–117.
- [49] Dalby, A. B., "Interdigital Microstrip Circuit Parameters Using Empirical Formulas and Simplified Model," *IEEE Trans.*, Vol. MTT-27, 1979, pp. 744–752.
- [50] Tripathi, V. K., and C. L. Chang, "Quasi-TEM Parameters of Non-Symmetrical Coupled Microstrip Lines," *Int. J. Electron.*, Vol. 45, No. 2, 1978, pp. 215–223.
- [51] Kal, S., et al., "Normal-Mode Parameters of Microstrip Coupled Lines of Unequal Width," *IEEE Trans.*, Vol. MTT-32, 1984, pp. 198–200.
- [52] Bedair, S. S., "Characteristics of Some Asymmetrical Coupled Transmission Lines," *IEEE Trans.*, Vol. MTT-32, 1984, pp. 108–110.
- [53] Bedair, S. S., "Characteristics of Asymmetrical Coupled Shielded Microstrip Lines," *Proc. IEE, Part H*, Vol. 132, 1985, pp. 342–343.
- [54] Allen, J. L., "Non-Symmetrical Coupled Lines in an Inhomogeneous Dielectric Medium," *Int. J. Electron.*, Vol. 38, 1975, pp. 337–347.
- [55] Llinner, I. J. P., "A Method for the Computation of the Characteristic Impittance Matrix of Multiconductor Striplines with Arbitrary Widths," *IEEE Trans.*, Vol. MTT-22, 1974, pp. 930–937.
- [56] El-Deeb, N. A., et al., "Design Parameters of Inhomogeneous Asymmetrical Coupled Transmission Lines," *IEEE Trans.*, Vol. MTT-31, 1983, pp. 592–596.
- [57] Kollipara, R. T., and V. K. Tripathi, "Dispersion Characteristics of Moderately Thick Microstrip Lines by the Spectral Domain Method," *IEEE Microwave Guided Wave Lett.*, Vol. 2, 1992, pp. 100–101.
- [58] Jansen, R. H., "A Comprehensive CAD Approach to the Design of MMIC's up to MM-Wave Frequencies," *IEEE Trans.*, Vol. MTT-36, 1988, pp. 208–219.
- [59] Bedair, S. S., and M. I. Sobhy, "Accurate Formulas for the Computer-Aided Design of Shielded Microstrip Circuits," *Proc. IEE, Part H*, Vol. 127, 1980, pp. 305–308.
- [60] Rama Rao, B., "Effect of Loss and Frequency Dispersion on the Performance of Microstrip Directional Couplers and Coupled Line Filters," *IEEE Trans.*, Vol. MTT-22, 1974, pp. 747–750.
- [61] Tien, C. C., et al., "Effects of Metal Thickness and Finite Substrate Width on Leaky Waves in Coupled Microstrip Lines," *IEEE MTT-S Digest*, 1992, pp. 499–502.
- [62] Shamasundara, S. D., and K. C. Gupta, "Sensitivity Analysis of Coupled Microstrip Directional Couplers," *IEEE Trans.*, Vol. MTT-26, 1978, pp. 788–794.
- [63] Buntschuh, C., "High Directivity Microstrip Couplers Using Dielectric Overlays," *IEEE G-MTT Symp. Digest*, 1975, pp. 125–127.
- [64] Wolters, K. C., et al., "Analysis and Experimental Evaluation of Distributed Overlay Structures in Microwave Integrated Circuits," *IEEE G-MTT Symp. Digest*, 1968, pp. 123–130.

- [65] Sheleg, B., and B. E. Spielman, "Broad-Band Directional Couplers using Microstrip with Dielectric Overlays," *IEEE Trans.*, Vol. MTT-22, 1974, pp. 1216–1220.
- [66] Paolino, D. D., "MIC Overlay Coupler Design using Spectral Domain Techniques," *IEEE Trans.*, Vol. MTT-26, 1978, pp. 646–649.
- [67] Atsuki, K., and E. Yamashita, "Three Methods for Equalizing the Even and Odd-Mode Phase Velocity of Coupled Strip Lines with an Inhomogeneous Medium," *Trans. IECE Japan*, Vol. 55-B, No. 7, 1972, pp. 424–426.
- [68] Su, L., et al., "Design of an Overlay Directional Coupler by a Full-Wave Analysis," *IEEE Trans.*, Vol. MTT-31, 1983, pp. 1017–1022.
- [69] Klein, J. L., and K. Chang, "Optimum Dielectric Overlay Thickness for Equal Even and Odd-Mode Phase Velocities in Coupled Microstrip Circuits," *Electron. Lett.*, Vol. 26, 1990, pp. 274–276.
- [70] Szentkuti, B. T., "Simple Analysis of Anisotropic Microstrip Lines by a Transform Method," *Electron. Lett.*, Vol. 12, 1976, pp. 672–673.
- [71] Fukuoka, Y., et al., "Analysis of Multilayer Interconnection Lines for a High-Speed Digital Integrated Circuit," *IEEE Trans.*, Vol. MTT-33, 1985, pp. 527–532.
- [72] Carin, L., and K. J. Webb, "Isolation Effects in Single- and Dual-Plane VLSI Interconnects," *IEEE Trans.*, Vol. MTT-38, 1990, pp. 396–404.
- [73] Gilb, J. P. K., and C. A., Balanis, "Asymmetric, Multi-Conductor Low-Coupling Structures for High-Speed, High-Density Digital Interconnects," *IEEE Trans.*, Vol. MTT-39, 1991, pp. 2100–2106.
- [74] Kiziloglu, K., et al., "Experimental Analysis of Transmission Line Parameters in High-Speed GaAs Digital Circuits Interconnects," *IEEE Trans.*, Vol. MTT-39, 1991, pp. 1361–1367.
- [75] Goel, A. K., *High-Speed VLSI Interconnections: Modeling, Analysis and Simulation*, New York: John Wiley, 1994.
- [76] Anandan, C. K., et al., "Broad-Band Gap Coupled Microstrip Antenna," *IEEE Trans.*, Vol. AP-38, 1990, pp. 1581–1586.
- [77] Goel, A. K., and Y. R. Huang, "Parasitic Capacitances and Inductances for Multilevel Interconnections on GaAs-Based Integrated Circuits," *Electromag. Waves Appl.*, Vol. 5, 1991, pp. 477–502.
- [78] Jansen, R. H., and N. H. L. Koster, "Accurate Results on the End Effect of Single and Coupled Microstrip Lines for Use in Microwave Circuit Design," *Arch. Elektr. Ubertra.*, Vol. 34, 1980, pp. 453–459.
- [79] Sabban, A., and K. C. Gupta, "A Planar-Lumped Model for Coupled Microstrip Lines and Discontinuities," *IEEE Trans.*, Vol. MTT-40, 1992, pp. 245–252.
- [80] Chadha, R., and K. C. Gupta, "Segmentation Method Using Impedance Matrices for Analysis of Planar Microwave Circuits," *IEEE Trans.*, Vol. MTT-29, 1981, pp. 71–74.
- [81] Kirschning, M., et al., "Coupled Microstrip Parallel Gap Model for Improved Filter and Coupler Design," *Electron. Lett.*, Vol. 19, 1983, pp. 377–379.

About the Authors

Kuldip C. Gupta received the B.E. and M.E. degrees in Electrical Communication from the Indian Institute of Science, Bangalore, India, in 1961 and 1962, respectively, and the Ph.D. degree from Birla Institute of Technology and Science, Pilani, India, in 1969.

Dr. Gupta was affiliated with the Indian Institute of Technology, Kanpur, from 1969 to 1983, first as an assistant professor and, from 1975 on, as a professor in Electrical Engineering. He joined the University of Colorado in 1983 as a visiting professor and has since become a full-time professor there. Currently, he also serves as the research coordinator for NSF IUCR Center for Advanced Manufacturing and Packaging of Microwave, Optical, and Digital Electronics (CAMPmode) at the University of Colorado. Dr. Gupta's current research interests are in the area of computer-aided design techniques for microwave and millimeter-wave integrated circuits and integrated antennas. He is the author or co-author of six books, has published over 150 research papers, and holds three patents in the microwave area.

Dr. Gupta is a Fellow of Institute of Electrical and Electronics Engineers (IEEE), a Fellow of the Institution of Electronics and Telecommunications Engineers (India), a charter member of URSI (Commission D, USA), and a member of the Electromagnetics Academy (MIT, USA). He is also co-chair of the IEEE MTT-S Technical Committee on CAD (MTT-1), a member of IEEE Technical Committee on Microwave Field Theory (MTT-15), and the founding editor of the *International Journal of Microwave and Millimeter-Wave Computer-Aided Engineering*, published by John Wiley since 1991. In addition, Dr. Gupta serves on the Technical Program Committees for MTT-S International Symposia and on the editorial boards of *IEEE Transactions on Microwave Theory and Techniques*, *Microwave and Optical Technology Letters* (John Wiley, U.K.), the *International Journal of Numerical Modelling*, and three journals of IETE (India). He is listed in *Who's Who in America*, *Who's Who in the World*, *Who's Who in Engineering*, and *Who's Who in American Education*.

Ramesh Garg was born in Hissar, India, on October 18, 1945. He received the M.Sc. Hons. degree in Physics from Panjab University, Chandigarh, India, in 1968 and the Ph.D. degree from the Indian Institute of Technology (IIT), Kanpur, in 1975. From 1975 to 1981, he was with the Advanced Centre for Electronic Systems, IIT Kanpur, as a Research Engineer, working on transmission lines for microwave integrated circuits and computer-aided design.

Since 1981, Dr. Garg has been with the IIT Kharagpur (India), first as Assistant Professor with the Radar and Communication Centre and now as Professor with the Department of Electronics and Electrical Communication Engineering. He was Visiting Assistant Professor at the University of Houston, University Park (U.S.A.), from 1985 to 1987 and Research Associate at the University of Ottawa (Canada) in 1994. His research activities have primarily been in the areas of microwave integrated circuits, leaky wave antennas, Gunn circuits, and microstrip antennas. He has published more than 50 papers in reference journals and conferences. He is a co-author of the book *Computer Aided Design of Microwave Circuits* (Artech House).

Dr. Garg was a recipient of the outstanding paper award at the 1976 IEEE (India Section) Annual Convention. He has also received the Best Paper Award from the Institution of Electronics and Telecommunication Engineers (IETE), India, and the 1987 IIT Kharagpur Silver Jubilee Research Award. He was Chairman of IEEE Kharagpur Section in 1991. He is a Senior Member of IEEE and a Fellow of IETE, India.

Inder J. Bahl was born in India on January 27, 1944. He received the B.S. degree from Punjab University, India, in 1965 and the M.S. degree in physics and the M.S. degree in electronics engineering from Birla Institute of Technology and Science, Pilani, India, in 1967 and 1969, respectively. In 1975, he received the Ph.D. degree in electrical engineering from the Indian Institute of Technology (IIT), Kanpur, India.

From 1969 to 1974, he was a senior research assistant at IIT Kanpur. From 1974 to 1978, he was with the Advanced Centre for Electronic Systems, where, as a research engineer, he was engaged in research on pin diode phase shifters, microwave integrated circuits, and printed antennas. From 1979 to 1981, he was a research associate at the University of Ottawa, Ottawa, Canada. Prior to joining ITT in 1981, he spent five months at the Defense Research Establishment, Ottawa, Canada, working on millimeter-wave systems as a research scientist. In his present capacity as an executive scientist at ITT GTC, he is responsible for providing directions in the development of device models and GaAs MMICs.

Dr. Bahl is the author/coauthor of over 120 research papers. He authored/coauthored four books: *Microstrip Lines and Slotlines* (Artech House), *Microstrip Antennas* (Artech House), *Millimeter Wave Engineering and Applications* (John Wiley), and *Microwave Solid State Circuit Design* (John Wiley), and coedited the books on *Microwave and Millimeter-Wave Heterostructure Transistors and Their Applications* (Artech House), and *Gallium Arsenide IC Applications Handbook* (Academic Press). He also

contributed two chapters to the *Handbook of Microwave and Optical Components* (John Wiley) and one chapter to the *Handbook of Electrical Engineering* (CRC Press). He holds eight patents in the areas of microstrip antennas and microwave circuits.

Dr. Bahl is an IEEE Fellow and a member of the Electromagnetic Academy.

Prakash Bhartia obtained his B.Tech. (Hons.) degree in electrical engineering from the Indian Institute of Technology, Bombay, India, in 1966, and his M.S. and Ph.D. degrees from the University of Manitoba in Winnipeg, Canada, in 1968 and 1971, respectively. He served as a research associate at the University of Manitoba from 1971 to 1973, when he joined the Faculty of Engineering at the University of Regina, Regina, Canada. In 1976, he was promoted to the rank of Associate Professor and served as Assistant Dean of Engineering. In September 1977, he joined the Defence Research Establishment, Ottawa, as a defense scientist and in 1982, was appointed section head of the Electromagnetics Section, responsible for programs in navigation, electromagnetic compatibility, and nuclear electromagnetic pulse effects. In February 1985, he was appointed Director Research and Development Air at National Defence Headquarters. From September 1985 to June 1986, Dr. Bhartia attended the National Defence College of Canada at Kingston and, on his return, was appointed Director of Research and Development Communication and Space, where he served for three years. In September 1989, he was appointed Director of the Underwater Acoustics Division at the Defence Research Establishment Atlantic at Dartmouth, Nova Scotia, and in July 1991, he returned to Ottawa as Director of the Radar Division at Defence Research Establishment Ottawa. In July 1992, he was appointed Chief of the Defence Research Establishment Atlantic.

Dr. Bhartia has had considerable consulting experience with many companies while serving at the university and is the author of over 100 papers in the areas of radar, microwave and millimeter wave circuits, components, and transmission lines. He is also the co-author of a number of books including *Microstrip Antennas* (Artech House), *Millimeter Wave Engineering and Applications* (J. Wiley and Sons), *E-Plane Integrated Circuits* (Artech House), and *Microwave Solid State Circuit Design* (J. Wiley and Sons). He has also contributed chapters to other texts and holds a number of patents.

Dr. Bhartia is a Fellow of the IEEE, a Fellow of the Institution of Electrical and Telecommunication Engineers, and a member of a number of technical societies. He has served and continues to serve on the editorial board or as a reviewer for many scientific journals. He has served as a Director of the Canadian Microelectronics Centre, on the Queen's University Engineering Advisory Council, and on the Tradex Management Inc. board and is currently on the board of the Canadian Centre for Marine Communications and the Nova Scotia Premier's Council in Applied Science and Technology. Dr. Bhartia is also Chairman of the Scientific Committee of National Representatives for SACLANTCEN in Italy.

Index

- Absorbing boundary condition, 253
ACPW. *See* Asymmetric coplanar waveguide
Active circuit, 138–143
Airbridge, 124, 128–29, 132
Air dielectric, 95, 350, 357, 376, 394, 404, 417, 418, 427, 428, 466, 515
Alumina substrate, 89, 92, 94, 111–14, 135–36, 144–45, 205, 291, 295, 310, 505
Ambient temperature, 88
Amplifier, 125
Amplitude shift key modulator, 324
Anisotropic substrate, 150, 152, 311, 407, 508
Anisotropy, dielectric, 98–102, 507–8
Antenna design, 239
Antipodal finline, 342–44, 364
Aperture coupling, 47–48
APHC. *See* Average power handling capability
ASK modulator. *See* Amplitude shift key modulator
Assembly, microwave, 143–45
Asymmetric coplanar strip loss, 420–22
Asymmetric coplanar waveguide, 378
 conductor loss in, 420–22
 with finite dielectric thickness, 398–99
 without dielectric substrate, 395–97
Asymmetric coupled microstrip
 line, 464, 479–83, 496–97
Asymmetric impedance, 457
Attenuation constant, 44, 54–56
Average power handling capability, 88, 92–94
Balanced circuit, and coplanar strips, 400
Balanced microstrip-slotline circuit, 321–24
Balanced mixer, 450–51
Balanced signal, 448–51
Balun, 125, 321–23, 325, 364
Bandwidth
 finline, 341, 348
 improvement of, 310–13
Basic capacitance matrix, 19, 21–23
Bends
 capacitance of, 175, 194–96, 231
 compensation of, 205–8
 linear resonator method for, 257–59
 multiple ports in, 239
 planar waveguide model for, 227–34
 radiation from, 242–43
 scattering parameters method for, 264
Beryllium oxide substrate, 89, 92, 94, 136
Bessel function, 52
Bilateral finline, 342–44, 351–53
Bipolar junction transistor, 141
BJT. *See* Bipolar junction transistor
Boundary conditions
 in fullwave analysis, 63–64
 in Galerkin's method, 346
 in variational method, 17–18
Boundary element method. *See* Segmentation and boundary element method
Branchline coupler, 327–34
Broadband waveguide-to-microstrip transition, 37
Broad frequency range, 27–29
Capacitance
 bend, 175, 194–96, 231
 coplanar strip, 400
 coplanar waveguide, 380, 382–99

- Capacitance (continued)
 - coupled microstrip line, 470, 488, 510–11
 - coupling/mutual, 509
 - cross junction, 200–4
 - and dielectric anisotropy, 98
 - even- and odd-mode, 490–93, 498
 - gap discontinuity, 183–89
 - multiconductor microstrip line, 509
 - multilayered microstrip, 118, 123
 - open-end discontinuity, 180–83
 - in quasi-static analysis, 6
 - steps in width, 189–94
 - T-junction, 196–200, 228*See also* Discontinuity capacitance evaluation
- Capacitance matrix, 19–23
- Capacitive network, 514–15
- Capacitors
 - interdigital, 124
 - lumped-element, 132–34
 - MIM, 124
- Cascading, 38
- Cavity resonance measurement method, 45–47
- Chamfered bend, 516–17
- Chamfered discontinuity technique, 204–6
- Chebyshev polynomials, 281, 407, 476–77
- Circuit fabrication, 1
- Circuits
 - coplanar line, 443–51
 - hybrid coupler, 327–34
 - open and short, 441–43
 - with series/shunt reactances, 443–46
 - types of, 334
 - using slotline-CPW junction, 446–51
 - using slotline resonator, 334
 - using T-junction, 313–24
 - using wideband phase shift, 324–27
- Circular disc open end, 295
- Closed-form equations, 102–3, 105–6
 - for bends, 194–95, 206–7
 - for coplanar lines, 411–15
 - for coupled microstrip lines, 490–98
 - for cross junctions, 201–4
 - for discontinuity analysis, 180, 182, 192, 516
 - for finline design, 349–57
 - for gap discontinuity, 185–89
 - for Green's function, 173
 - for losses, 107–9
 - for microstrip design, 102–3, 105–6
 - for microstrip-to-slotline transition, 308–9
 - for slotline design, 281–86
 - for T-junctions, 196–200
- Closed-form frequency solutions, 23–33
- Coaxial-to-microstrip transition, 34–37, 41
- Coaxial-to-slotline transition, 302–5
- Coax-to-coplanar wave transition, 433–34
- Cohn's method, 281–82, 308
 - See also* Transverse resonance method
- Combiner, 140
- Comparision technique for attenuation constant, 55
- Compensated microstrip discontinuities, 204
 - bend, 205–8
 - reactance, 234
 - step in width, 205
 - T-junction, 208–10
- Conductor-backed coplanar waveguide, 378–79, 391–93, 413, 422–23
- Conductor-backed slotline, 297–302
- Conductor loss
 - in coplanar line, 417–22
 - in coupled microstrip line, 498–501
 - in dielectric substrate, 108–9
 - in finline, 341, 344, 360
 - and heat flow density, 88–90
 - in microstrip, 83–85
 - in microstrip versus slotline, 431–433
 - in slotline, 288–291
- Conformal mapping, 379–99, 420
- Conformal transformation method, 6–12, 467
- Congruent transformation technique, 458, 509
- Control circuit, 125
- Convergence, 13
 - in matrix inversion method, 164
 - in slotline analysis, 280
- Coplanar lines, 375–79
 - design equations for, 411–12
 - dispersion of, 412–14
 - effect of tolerances on, 426–30
 - metallization thickness of, 414–15
 - with series/shunt reactances, 443–46
 - with slotline-CPW junctions, 446–51
- Coplanar strip, 1, 375–79
 - asymmetric, 401–4
 - conductor loss in, 417–22
 - configuration of, 375–79
 - fullwave analysis of, 407–11
 - with lateral ground planes, 404
 - quasi-static analysis of, 400–404
 - symmetric, 400–1, 403
 - versus other MIC lines, 434
- Coplanar strip-to-slotline transition, 440–41
- Coplanar waveguide, 1, 375–79
 - asymmetric, 395–97
 - circuits using slotline-CPW junction, 446–51

- conductor-backed, 391–93, 413, 422–23
- conductor loss in, 417–22
- configuration of, 375–79
- discontinuities in, 441–43
- with cover shield, 389–91
- with finite dielectric thickness, 378, 383–91, 398–99
- with finite width ground planes, 386–89
- fullwave analysis of, 405–7
- high-impedance, 421
- with infinitely thick substrate, 381–83
- low-impedance, 421
- multilayered, 378, 393–95
- series/shunt reactances in, 443–46
- versus other MIC lines, 434
- Coplanar wave-to-coplanar strip**
 - transition, 439–40
- Copper loss**, 361
- Corner coupling**, 47
- Correction factor**, finline, 352–53
- Cosine impedance**, 363
- Coupled microstrip line**
 - analysis methods for, 458–60
 - asymmetric, 479–83, 496–97
 - characteristics of, 457–58
 - coupled mode analysis of, 460–64
 - design equations for, 490–98
 - dielectric anisotropy effect on, 507–8
 - with dielectric overlays, 504–7
 - discontinuities in, 512–17
 - dispersion models for, 483–87
 - even- and odd-mode analysis of, 464–67
 - fabrication tolerances for, 502–4
 - fullwave analysis of, 475–83
 - impedance measurements for, 487–88
 - loss in, 498–502
 - multiconductor, 508–12
 - phase measurements for, 488–90
 - quasi-static analysis of, 467–75
 - symmetric, 476–79
- Coupled microstrip-slotline**, 295–97
- Coupled mode analysis**, 458, 460–64
- Coupled multiconductor microstrip line**, 508–12
- Coupled stripline**, 364–66
- Coupled TEM/TM modes dispersion model**, 24
- Couplers**, 125, 140
 - hybrid/de Ronde's, 327–34
- Coupling**
 - aperture, 47–48
 - corner, 47
 - crosstalk due to, 144
 - and discontinuities, 235
- errors in measurement, 47
- magic-T circuit**, 315–20
- spurious, 244–45
- to substrate modes, 424
- See also Circuits*
- Coupling capacitance**, 509
- Coupling constant**, 504
- Coupling integral**, 215
- Cover shield**, 378–79, 389–92
- CPS**. *See Coplanar strip*
- CPW**. *See Coplanar waveguide*
- Cross junction**
 - inductance evaluation of, 159–60, 179, 200–4
 - in linear resonator method, 260
 - planar waveguide model for, 227–234
- Cross-junction transition**, 305–13
- Curvature effect**, 50, 52
- Cutoff frequency**, 348, 351–52
 - finline, 353–54, 357
- Delay line**, 125
- Delta function**, 20
- de Ronde's branchline coupler**, 327–34
- de Ronde's magic-T**, 320, 322
- Design**, microstrip
 - and dielectric anisotropy, 98–102
 - equations for, 102–11
 - and fabrication tolerances, 95–98
 - and frequency range, 111–15
 - and microstrip losses, 83–87
 - and power handling capability, 87–95
- Dielectric-air interface**, 3–4
- Dielectric anisotropy**, 98–102, 507–8
- Dielectric constant**, 9–11
 - anisotropic substrate, 101–2
 - coplanar line, 415, 426, 429–30
 - coplanar waveguide, 380, 385–86, 395, 399
 - coupled microstrip line, 457, 493–95, 505–6
 - design equations for, 103–4
 - finline, 355–58
 - frequency-dependent, 23–24, 29, 32
 - in fullwave analysis, 71
 - high-temperature superconductor, 151
 - in linear resonator measurement, 52–54
 - measured by reflection coefficient, 49
 - and microstrip packaging, 145
 - multilayered microstrip, 118
 - in non-TEM behavior, 23
 - in ring resonator measurement, 50–52
 - sensitivity of, 99
 - slotline, 289, 296–97
 - in substrate measurement, 44–49
 - suspended/inverted microstrip, 116–17

- Dielectric constant (continued)
 - thin film microstrip, 118–20
- Dielectric filling factor, finline, 355–56
- Dielectric-loaded ridged waveguide model, 25–27
- Dielectric loss
 - in coplanar line, 415–16
 - in coupled microstrip line, 498, 501–2
 - density heat flow due to, 90–91
 - in finline, 341, 344, 360
 - in microstrip, 85–87, 108–9
 - in slotline, 287–288, 291
- Dielectric medium, inhomogeneous, 2
- Dielectric overlay, coupled microstrip, 504–7
- Dielectric resonator oscillator, 141–42
- Dielectric strength, of air, 95
- Dielectric substrate, 350
 - for coplanar waveguide, 378, 395–97
 - properties of, 89
 - for slotline, 269–70
- Dielectric thickness, 423
- Digital circuit, 510
- Diode, for microwave integrated circuit, 141
- Diode mismatching, 323
- Dirac's delta function, 168
- Discontinuities, fullwave analysis of, 245–46
 - Galerkin's method, 246–49
 - integral equation method, 249–50
 - time domain method, 250–55
- Discontinuities, microstrip, 159–61
 - bend, 194–96
 - compensated, 204–10
 - in coplanar waveguide, 441–43
 - in coupled microstrip line, 512–17
 - cross junction, 200–4
 - gap, 183–189
 - network model of, 513–16
 - notch, 204
 - open-end, 180–83, 516–17
 - open and short circuit, 441–43
 - steps in width, 189–94
 - T-junction, 196–200
- Discontinuities, in planar waveguide analysis
 - bend/cross junction, 227–34
 - steps in width, 213–17
 - T-junction, 217–27
- Discontinuities, slotline
 - open-end, 294–95
 - short-end, 292–94
- Discontinuity capacitance evaluation
 - Galerkin's method in FTD, 171–73
 - matrix inversion method, 161–67
 - use of line sources, 173–75
- variational method, 167–71
- Discontinuity measurement, 255–56
 - linear resonator method, 256–60
 - ring resonator method, 260–63
 - scattering parameters method, 263–66
- Discretization errors, 81
- Dispersion
 - coplanar line, 412–14
 - coplanar waveguide, 407, 409–11
 - coupled microstrip line, 482–87
 - even- and odd-mode, 478
 - finline guide wavelength, 349
 - in fullwave analysis, 79–80
 - and impedance, 358
 - LSE-mode, 356–58
 - and microstrip design, 107
 - in open-end discontinuity, 182
- Dispersion models. *See* Microstrip dispersion models
- Double substrate directional coupler, 296
- Edge condition, 347
- Effective filling fraction, 8
- Eigenvalue equation, 50, 52
- Eisenhart connector, 36, 39–41
- Eisenhart transition, 35, 38
- Electric field, and heat flow, 88–89
- Electric field coupling, 514
- Electric field matching, 37, 42
- Electric flux, 22–23
- Electronic warfare, 141
- Enclosed microstrip, 12–13, 71–83
- Enclosure, 105–7, 498
- End effects, 52–53
- Epsilon-lam-10 substrate, 98, 102
- Equivalent circuit, congruent transformation of, 458
- Equivalent magnetic current formulation, 238–43
- Even- and odd-mode analysis, 458, 464–67
- Even- and odd-mode phase, 471–75, 478–79, 484–88, 498, 505, 508–9
- Even-mode attenuation, 500–2
- Even-mode capacitance, 490–492, 498
- Even-mode dielectric constant, 505
- EW. *See* Electronic warfare
- Excitation
 - coplanar line, 422
 - coplanar waveguide, 422
 - coupled microstrip-slotline, 296
 - even- and odd-mode, 331–34, 487–88
 - higher order modes, 430
 - in-phase and out-of-phase, 317, 319, 321

- microstrip, 111, 113
 - in planar waveguide analysis, 214
 - in ring resonator method, 260, 262
 - short-end discontinuity, 294
 - slotline, 297
 - substrate mode, 424
 - in time domain analysis, 251, 253
 - T-junction, 227–31
- Exponential impedance, 363
- Fabrication tolerances. *See* Tolerances, fabrication
- Far field radiation, 239
- FDTD. *See* Finite-difference time domain
- Ferrite devices, 334, 376
- Field decay, slotline, 272–73
- Field distribution, slotline, 271–72
- Field-matching technique, 476
- Field perturbation, 47
- Filling factor, 385, 391, 393–95, 404
- Filters, 125
- Finite dielectric thickness, 383–86
 - asymmetric coplanar waveguide with, 398–99
 - coplanar waveguide with, 389–91, 402–3
- Finite difference method, 12–14, 76–79, 81–82, 98–101
- Finite-difference time domain, 250–55
- Finitely thick substrate, 404, 424–26
- Finite width ground plane, 386–89
- Finline
 - closed-form design of, 349–56
 - conductor loss in, 360
 - configuration of, 341–44
 - Galerkin's method for, 346–49
 - LSE-mode dispersion model, 356–58
 - synthesis equations, 358–60
 - transverse resonance method for, 344–46
- Finline transitions
 - to microstrip taper, 364–68
 - to waveguide taper, 360–64
- Flared open end, 295
- Flared slot/half-disc open end, 295
- Fourier series, 467–70
- Fourier transform, 17, 405–6
 - in fullwave analysis, 63–71
 - in time domain analysis, 251
- Fourier transform domain
 - variational method in, 15–18, 470–71

See also Galerkin's method in spectral domain
- Fredholm integral equations, 73
- Frequency dependency
 - of coupled microstrip, 484–85
 - of cross junction, 233
- of dielectric constant, 23–24, 29, 32
- of discontinuity, 175, 213, 218
- of finline, 350
- of impedance, 23–24, 29–30, 33
- of phase and group velocities, 115
- of T-junction, 223–26
- Frequency independency
 - of finline, 356
 - of rat-race circuit, 325
- Frequency range, 111–15
- Fringing field, 5, 45–46, 98
- Fringing flux lines, 105
- FTD. *See* Fourier transform domain
- Full-wave analysis, 245–46
 - of coplanar line, 379
 - of coplanar strip, 407–11
 - of coplanar waveguide, 405–7, 422
 - of coupled microstrip, 475–83
 - dispersion in, 79–80
 - of enclosed microstrip, 71–83
 - finite difference method of, 76–79
 - Galerkin's method of, 66–68, 246–49
 - higher order modes in, 80–83
 - of high-temperature superconductor, 151
 - integral equation method
 - of, 64–66, 71–76, 249–50
 - methods of, 61–63
 - of non-TEM mode lines, 457
 - of open microstrip, 63–71
 - radiation evaluated from, 243–44
 - time domain method of, 250–55
- Full-wave resonator, 257
- Fullwave spectral domain method, 298
- Galerkin's method in spectral domain
 - for coupled microstrip lines, 476–83
 - for discontinuity capacitance evaluation, 171–73
 - for enclosed microstrip, 74–76
 - for finline, 346–49
 - for fullwave analysis of CPS, 407–11
 - for fullwave analysis of CPW, 405–7
 - for fullwave discontinuity analysis, 246–49
 - for open microstrip, 27, 66–68
 - for slotline, 277–82, 284, 296
- Gallium arsenide IC, 117
- Gallium arsenide substrate, 89, 94, 108–9, 111–12, 118, 135–37, 139, 141, 205, 421
- Gap coupling, 514
- Gaps, 159–60, 165–66, 168–69, 176, 183–89
 - fullwave analysis of, 246–49
 - linear resonator analysis of, 256–57
- Gaussian pulse excitation, 253

- Gaussian quadrature formula, 21
 Getsinger's formula, 26–27, 484
 Glass, 45
 Glass fiber teflon substrates, 94
 Gold-plated inductor, 129
 Graded mesh, 77
 Graph transformation technique, 458
 Green's function, 14–15, 19–20, 68, 161–62,
 167–69, 173–75, 177, 179, 249–50,
 309, 467, 514
 Green's third identity, 19
 Ground planes, finite width, 386–89
 Guide wavelength, finline, 348–50
 Gunn diode, 141
 Half-wave resonator, 113, 257
 Harmonics, 323
 HBT. *See* Heterojunction bipolar transistor
 Heat flow density
 due to conductor loss, 88–90
 due to dielectric loss, 90–91
 HEMT. *See* High electron mobility transistor
 Heterojunction bipolar transistor, 141
 Hewlett Packard dielectric probe, 49
 High electron mobility transistor, 141
 Higher order modes
 for coplanar waveguide, 407, 409
 excitation of, 430
 in finline, 348, 350
 in fullwave analysis, 80–83, 113, 115
 in slotline design, 281–82
 High-impedance coplanar waveguide, 421
 High-temperature superconducting, 147–52
 HTS. *See* High-temperature superconducting
 Hybrid branchline coupler, 295
 Hybrid circuit, magic-T, 315–20
 Hybrid/de Ronde's branchline coupler, 327–34
 Hybrid microwave integrated
 circuit, 1, 61, 127, 138
 Hybrid modes, for finline, 356–57
 Hybrid propagation analysis methods, 5–6
 Hybrid slotline, 269, 313
 IF. *See* Intermediate frequency signal
 Immittance approach, 68
 Impact avalanche and transit time, 141
 IMPATT. *See* Impact avalanche and transit time
 Impedance, 380
 coplanar line, 414, 426, 428
 coplanar strip, 400–4, 428
 coplanar waveguide, 380, 382–83, 385–86, 389,
 392–93, 399, 406–7, 422
 coplanar wave transition, 438
 coupled microstrip line, 481, 483, 495–96, 505
 de Ronde's coupler, 331
 design equations for, 103–4
 even- and odd-mode, 331–32, 471–75, 477–79,
 487–88, 498
 finline, 344, 347–49, 358
 frequency-dependent, 23, 29–30, 33
 in fullwave analysis, 68, 70–71
 of high-temperature superconductor, 151
 measurement of, 43–44, 49–50
 microstrip, 10–11
 microstrip line versus slotline, 430–31
 and microstrip line width, 1
 and microstrip packaging, 145
 multilayered microstrip, 118, 122
 and non-TEM behavior, 23
 sensitivity of, 98
 slotline, 276–77, 281, 296–97, 308, 312, 338–40
 suspended and inverted microstrip, 116
 symmetrical and asymmetrical, 457
 taper transition, 361–64
 thin film microstrip, 119–20, 124
 of T-junction, 225–27
 valley microstrip, 127
 Impedance stub, 200, 436
 Impedance transformer, 125, 127
 Incremental inductance
 rule, 84–85, 288, 417, 421, 498
 Inductance, 193, 510, 512
 asymmetric coupled microstrip, 497
 bend, 231
 cross junction, 203
 microstrip notch, 204
 multilayered microstrip, 118, 123
 step discontinuity, 192
 T-junction, 198–99, 228
 See also Incremental inductance rule
 Inductive network, 515–16
 Inductor design, lumped-element, 127–32
 Infinitely thick substrate, 380–83, 400–2, 412, 424
 Infinitely wide strip, 403–4
 In-phase coupling, 317–19, 321
 Insertion loss, 311–12, 318, 436
 Insulated finline, 342
 Integral equation method, 14–16, 64–66,
 71–76, 509
 Galerkin's method of, 74–76
 space domain approach to, 73, 249–50
 Interdigital capacitor, 124, 128, 132, 134
 Intermediate frequency signal, 322–23
 Inverse iteration method, 78
 Inverted microstrip, 2–3, 115–17

- Inverted strip dielectric waveguide, 2–3
 Iris-loaded waveguide resonator, 345
 Itoh's result, 297
- Jacobian elliptic function, 7
- Knorr's analysis, 309
 Kobayashi's dispersion formula, 28–29
- Lange coupler, 140
 Lanthanum aluminate, 148–49
 Laplace's equation, 12–13, 17, 19, 99–100, 177, 467, 469
 Lateral ground planes, 404
 Launcher, 33
 Leaky slotline, 299
 Leaky wave, 298
 "Leap frog" algorithm, 253
 Legendre polynomial, 360
 Linear resonator measurement method, 52–54, 256–60
 Line capacitance, coplanar waveguide, 380
 Line charge distribution, 14
 Line sources, in discontinuity evaluation, 173–75
 Lithium nitrate, 148
 Load-reflection coefficient, 362
 Longitudinal components, 5, 61–62
 LO port, 323
 Loss, 432–33
 - conductor, 83–85, 417–22, 498–501
 - coupled microstrip line, 498–502
 - dielectric, 85–87, 360, 415–16
 - finline, 366
 - finline conductor, 341, 344, 360
 - finline copper, 361
 - finline dielectric, 341, 344
 - insertion, 318, 436
 - microstrip line versus slotline, 431
 - radiation, 241–42, 422–26
 - short-end, 293
 - slotline, 287–91, 298, 311–12
 - surface wave, 422–26*See also* Microstrip losses
- Lossless fields, 288
- Lossy transmission line, 145
 LSE mode, 81, 356–58
 LSM, 81, 83
- Lumped-element network, 513
 Lumped elements, 124, 126–27
 - and capacitor design, 132–134
 - and coplanar line, 375
 - and inductor design, 127–132
 - and thin film resistor design, 134–135
- Lumped inductor, 202
- Magic-T hybrid circuit, 315–20, 446–48
 Magnetic field, slotline, 273
 Magnetic substrate, 176
 Magnetic walls, 404
 Matrix equation, 14, 21
 Matrix inversion method, 161–67
 Maxwell's curl equations, 77
 Maxwell's equations, 3–5, 177, 251
 MCN. *See* Multiport coupling network
 MESFET. *See* Metal semiconductor field effect transistor
 Metal-insulator-metal, 124, 128, 132, 134
 Metallization thickness, 286–87
 - effect on conductor loss, 419
 - effect on coplanar line, 414–15
 - effect on coplanar waveguide, 441
 - effect on radiation loss, 423
- Metalized substrate resonator, 46–47
 Metal semiconductor field effect transistor, 136, 141, 324, 375
- MIC. *See* Microwave integrated circuit
 Microstrip applications, 122–26
 - active components, 138–43
 - lumped elements, 126–35
 - packages and assemblies, 143–45
 - passive components, 135–38
 - superconducting circuits, 145–52
- Microstrip dispersion models, 6, 23–24
 - broad frequency range, 27–29
 - coupled TEM/TM modes, 24
 - dielectric-loaded waveguide, 25–27
 - dispersion deviation data, 32–33
 - empirical relations in, 24–25
 - planar waveguide, 29–31
- Microstrip guide wavelength, 80
 Microstrip line
 - analysis methods, 5–6
 - compared to slotline, 430–32
 - with composite substrate, 18
 - enclosed, 12–13
 - field configuration, 2–5
 - multilayer, 12, 117–18
 - narrow, 8, 10
 - as planar transmission structure, 1–2
 - quasi-static analyses of, 5–23
 - suspended/inverted, 115–17
 - thin film, 118–22
 - valley, 122
 - wide, 8, 10*See also* Coupled microstrip line
- Microstrip losses
 - closed-form equations for, 107–9

- Microstrip losses (continued)**
- conductor, 88–85
 - dielectric, 85–87
 - in GaAs substrate, 54–56
 - and quality factor, 109–11
 - and substrate thickness, 109–10
 - thin film microstrip, 118, 124
 - versus slotline, 431
- See also Loss*
- Microstrip measurement**, 43–45
- and attenuation constant, 54–56
 - and characteristic impedance, 49–50
 - and effective dielectric constant, 50–54
 - and phase velocity, 50–54
 - and substrate dielectric constant, 45–49
- Microstrip-slotline circuit**, balanced, 321–24
- Microstrip-to-coplanar waveguide**
- transition, 434–36
- Microstrip-to-slotline cross-junction**
- transition, 305–13
- Microstrip transitions**, 33–34
- coaxial-to-microstrip, 34–37
 - waveguide-to-microstrip, 37–43
- Microstrip with overlay**, 2–3
- Microwave integrated circuit**, 1
- MIM**. *See Metal-insulator-metal*
- Mixer**, 125
- MMIC**. *See Monolithic microwave integrated circuit*
- Mode matching method**, 38, 298
- Modified conformal transformation method**, 6–12
- Modulator**
- amplitude shift key, 324
 - phase shift key, 322
- Monocrystalline material**, 45
- Monolithic microwave integrated circuit**, 1, 108, 118, 122, 127–29, 132, 135, 141, 143, 144, 147, 159, 375, 379
- MPIE**, 249
- Multichip ceramic package**, 146
- Multiconductor microstrip**, coupled, 508–12
- Multilayered coplanar**
- waveguide, 378–79, 393–95
- Multilayered dielectric microstrip**, 117–18
- Multilayer microstrip line**, 12, 19, 123
- Multiport coupling network**, 244–45
- Mutual capacitance**, 509
- Mutual inductance**, 512, 515
- Network analyzer**, 47–49
- Network model**, coupled microstrip, 513–16
- Nonintegrable singularity**, 290
- Normalized phase**, coplanar waveguide, 423
- Notch**, microstrip, 204
- Numerical efficiency**, 75
- Numerical evaluation**, of loss, 418
- Observation point**, 167
- Odd-mode attenuation**, 498–99, 501–2
- Odd-mode capacitance**, 491, 491–493, 498
- Odd-mode dielectric constant**, 505
- Odd-mode phase**. *See Even- and odd-mode phase*
- Ohmic loss**. *See Conductor loss*
- Ohm's law**, 177
- Open circuit**, coplanar waveguide, 441–43
- Open end**, slotline, 294–95
- Open-end discontinuity**, 516–17
- Open ends**, 159–160, 164, 168, 175, 180–83
- in finite-difference time domain, 254
 - fullwave analysis of, 246–249
 - and linear resonator method, 256–257
 - wide frequency modeling of, 255
- Open microstrip**
- configuration of, 2–3, 62
 - fullwave analysis of, 63–71
- Orthogonality property**, 215
- Oscillator**, 125, 450
- Oscilloscope trace**, 326, 329
- Out-of-phase coupling**, 317–19, 321
- Packaging**, microwave, 143–45
- Parabolic impedance**, 363
- Parallel plate**, 90, 396–98, 420, 422, 513–14
- Parallel plate resonator**, 46
- Parallel T-junction**, 320, 322, 446
- Parasitic coupling**, 234–35, 244–45
- Parasitic mode**, coplanar line, 422
- Parseval's formula**, 17, 75
- Passive circuits**, 125, 132, 135–38
- Peak power handling capability**, 94–95
- Perfectly matched layer**, 253–54
- Permittivity**
- anisotropy in, 98
 - in boundary element method, 21
- Perturbation method**, 421
- Phase constant**, even- and odd-mode, 487–88
- Phase shift key modulator**, 322
- Phase velocity**, 43–44, 50–54
- Photoetching**, 1, 430
- Photolithography**, 1
- Planar segment**, 513
- Planar transmission structure**, 1–2
- Planar waveguide analysis**, 29–31, 52
- of discontinuity characterization, 213–34
 - of discontinuity compensation, 234

- of radiation and parasitic coupling, 234–45
- of right-angled bend/cross junction, 227–34
- of step in width, 213–17
- of T-junction, 217–27
- Plastic substrate, 45, 92
- PML. *See* Perfectly matched layer
- Poisson's equation, 14, 19, 171
- Polycrystalline material, 45
- Polyimide structure, 118
- Polystyrene substrate, 89, 92–94, 111, 114
- Port, 23
- Potentials, in space domain, 249
- Power divider/combiner, 125
- Power handling capability, 87–95
- Poynting vector method, 236–38, 242, 477, 483
- PPHC. *See* Peak power handling capability
- Probe measurement method, 49
- Probe waveguide-to-microstrip transition, 43–44
- Propagation, 407
 - coplanar waveguide, 375–76
 - coupled microstrip line, 457
 - even- and odd-mode, 464–67
 - finline, 347, 350, 357
 - non-TEM hybrid, 3, 5
 - without quasi-static assumptions, 61–63
 - slotline, 269, 281–82, 287, 293, 296, 298, 300–1
 - transverse electro magnetic, 1
- PSK modulator. *See* Phase shift key modulator
- Pulse function, 20
- Pulse inverter, 326–27
- Quality factor, 109–11
- Quarter-wave resonator, 111–12
- Quartz substrate, 89, 94, 111–13, 136, 144, 379
- Quasi-static analysis
 - and conformal mapping, 379–99
 - of coplanar line, 379
 - of coplanar strip, 400–4
 - of coplanar waveguide, 380, 396, 408, 422
 - of coupled microstrip line, 467–75
 - of discontinuities, 160, 175
 - of TEM mode line, 457
- Quasi-static field distribution, 3
- Quasi-static microstrip analysis, 5–6
 - conformal transformation method, 6–12
 - finite difference method, 12–14
 - integral equation method, 14–15
 - segmentation/boundary element method, 18–23
 - variational method, 15–18
- Radiation
 - and discontinuities, 234–37
 - and equivalent current, 238–43
 - fullwave analysis of, 243–44
 - Poynting vector method for, 237–38
 - spurious, 244–45
- Radiation conductance, open-end, 182–83
- Radiation loss, 111, 422–26
- Rat-race hybrid circuit, 324–25, 327
- Real-estate requirements, 127
- Reciprocity method, loss analysis, 424–25
- Rectangular waveguide-to-microstrip transition, 42
- Reflection coefficient, 49, 236, 363
- Relaxation method, 12–13, 77
- Resonator cavity, 45–46
- Resonator measurement method, 50–54
- Resonators
 - and discontinuity measurement, 255–66
 - equivalent circuits for, 137
 - loaded Q factor of, 150
 - slotline, 334
- RF port, 323
- Riccati equation, 363
- Richards's transformation, 458
- Ridged waveguide, 37–38, 42–43
- Right-angled bend, 159–60
- Ring resonator measurement
 - method, 50–52, 260–63
- Ritz-Galerkin's method. *See* Galerkin's method
 - in spectral domain
- RT Duroid substrate, 135
- Sapphire substrate, 89, 92, 94, 98, 102, 148, 150, 263, 407
- SBEM. *See* Segmentation and boundary element method
- Scalar potential functions, 467, 469
- Scattering parameters measurement
 - method, 263–66
- Schottky diode, 136, 141, 445
- Schwarz-Christoffel transformation, 381
- Segmentation and boundary element method, 18–23
- Self-inductance, 511, 515
- Semi-infinite line, 173–74, 249
- Sensitivity analysis, 95–97
 - of coplanar lines, 426–30
 - of multilayered microstrip, 122
 - of slotline, 338
- Series connections, 327–28, 330, 375
- Series expansions, for conductor loss, 419
- Series inductance, and microstrip notch, 204
- Series reactances, in coplanar waveguide, 443–46
- Series Tjunction, 320, 322, 446
- Shielded microstrip, 68

- Short circuit, coplanar waveguide, 441–43
 Short end, slotline, 292–94
 Shunt capacitance, 191
 Shunt connections, 328, 330, 375
 Shunt reactances, coplanar waveguide, 443–46
 Silicon substrate, 86, 89, 94, 108–9, 139, 148
 Silver-plated inductor, 129
Singularities
 nonintegrable, 290
 and slotline design, 290–291
Sinusoidal basis functions, 476
Slotline discontinuities
 open-end, 294–95
 short-end, 292–94
Slotline resonator, 334
Slotlines
 approximate analysis of, 271–74
 circuit types for, 334
 closed-form equations for, 282–86
 compared to microstrip line, 430–32
 conductor-backed, 297–302
 configuration of, 269–70
 coupled microstrip, 295–97
 ferrite devices using, 334
 Galerkin's analysis method for, 277–83
 and hybrid/de Ronde's coupler, 327–34
 impedance/wavelength equations for, 338–40
 losses in, 287–91
 and metal thickness, 286–87
 as planar transmission structure, 1
 with superstrate, 300–2
 using T-junctions, 313–24
 and tolerances, 287
 transverse resonance analysis of, 274–77
 using wideband phase shift, 324–27
Slotline transitions
 coaxial-to-slotline, 302–5
 microstrip-to-slotline cross-junction, 305–13
 slotline-to-coplanar wave, 436–39, 446–51
Slot wavelength, 273–76
Solid-state circuit, 141
Sommerfeld integrals, 250
Source point, 167
Space domain
 integral equation method in, 64–66, 249–50
 variational method in, 467–70
 fullwave analysis and, 73
Spectral domain
 Galerkin's method in, 27, 66–68, 74–76, 171–73,
 246–49, 277–82, 284, 346–49
 variational method in, 15–18, 470–71
Spectral domain immittance approach, 68
Spiral inductor, 124, 128–29
Spurious coupling, 244–45
Stationary expressions, for finline, 353
Step junction, radiation from, 243
 Steps in width, 159–60, 165, 175, 179, 189–94
 compensation of, 205
 frequency-dependent circuit for, 218
 and linear resonator method, 257–59
 planar waveguide model for, 213–17
 reflection coefficients for, 235
 and ring resonator method, 263–64
 and scattering parameters method, 264
Strip dielectric waveguide, 2–3
Striplines
 configuration of, 2–3
 coupled, 364–66
Strip thickness, 104–5, 416, 497–98
Substrate
 dielectric strength of, 95
 finitely thick, 404, 424–26
 infinitely thick, 381–83, 400–2, 412, 424
 thickness of, 109–12, 115, 135–36, 144, 377,
 379–80, 427, 430
Substrate dielectric constant, 44–49
Substrate thermal conductivity, 88
Superconducting microstrip circuits, 145–52
Superstrate, in conductor-backed slotline, 300–2
Surface area, of strip conductor, 88
Surface wave loss, coplanar line, 422–26
Susceptance, 274, 277, 345–46
 equations for, 337–38
 expression for unilateral finline, 371–73
Suspended microstrip, 2–3, 115–17
Swinger functions, 360
Symmetrical discontinuity, 260–61
Symmetrical impedance, 457
Symmetric coplanar strip, 410, 417–20
Symmetric coplanar waveguide, 417–20
Symmetric coupled microstrip
 line, 463, 468, 476–79
Symmetric matrix, 77–78
Symmetric T-junction, 197, 199
Synthesis equations, finline, 358–60
Taper, 205, 208
Taper transition, 360–68
TDR. *See* Time domain reflectometry
TE mode. *See* Transverse electric mode
TEM mode. *See* Transverse electro
 magnetic mode
Temperature rise, 92–93
Temperature transition, 147
Testing function, 20

- TFM. *See* Thin film microstrip
 Thallium barium calcium copper oxide, 148
 Theta function, 7
 Thin film microstrip, 118–22, 124
 Thin film resistor, 124, 128, 134–35
 Through-hole conductor, 322–23
 Thru-reflect-line calibration
 Time average, 347
 Time domain method, 250–55
 Time domain reflectometry, 50, 205
 T-junction, 159–60, 175, 179, 196–200
 - circuits using, 313–24
 - compensation of, 208–10
 - equivalent circuits for, 449
 - in linear resonator method, 259–60
 - planar waveguide model for, 217–27
 - radiation from, 243
 - and scattering parameters method, 264
 - types of coplanar wave, 448
 - See also* Magic-T hybrid circuit
- TLM. *See* Transmission line matrix
 TM dispersion mode model, 24
 Tolerances, fabrication
 - coplanar line, 426–30
 - coplanar strip, 400
 - coplanar waveguide, 396
 - coupled microstrip line, 502–4
 - microstrip line, 95–98, 111
 - microstrip line versus slotline, 431
 - slotline, 287, 290
- Transcental equation, 357
 Transform method, and dielectric anisotropy, 101–2
 Transistors, 141
 Transitions
 - coax-to-coplanar wave, 433–34
 - coplanar line, 432–41
 - coplanar strip-to-slotline, 440–41
 - coplanar wave-to-coplanar strip, 439–40
 - microstrip-to-coplanar wave, 434–36
 - slotline-to-coplanar wave, 436–39
 - See also* Finline transitions; Slotline transitions
- Transition temperature, 147
 Transmission line loss, 88, 145
 Transmission line matrix, 251
 Transmission line resonance
 - measurement, 47–49
- Transverse electric mode, 214, 216, 220, 222, 253
 Transverse electro magnetic mode
 - coupled dispersion model, 24
 - for coupled line, 466
 - in planar waveguide analysis, 214, 220, 223–25
 - propagation, 1, 5
 - for slotline, 298
- Transverse equivalent network approach, 298
 Transverse field components, 62
 Transverse resonance method, 274–77, 281–82, 308, 337–38
 - for finline, 344–46
- Triplate line, 2–3
 TRL. *See* Thru-reflect-line calibration
 Tunnel diode, 141
 Two-conductor transmission line, 2
 Two-fluid theory, 148
 Two-wire line, 2, 4
 Unbalanced signal, 448, 450
 Unilateral finline, 342–45, 348–49, 351–53, 358
 - susceptance expression for, 371–73
- Unsymmetrical discontinuity, 263
 Valley microstrip line, 192, 127
 Variational method, 15–18, 77
 - in discontinuity analysis, 167–71
 - in Fourier transform domain, 15–18, 470–71
 - in space domain, 467–70
 - in spectral domain, 509
- Very large scale integrated chips, 508–9
 VLSI chips. *See* Very large scale integrated chips
 VSWR, 34–36, 50, 97, 100, 205, 287, 290, 295, 309–13, 364, 366, 431, 435, 445, 489
 - microstrip compared to slotline, 433
 - performance, of coupled microstrip, 503–4
- Waveguide model, 274
 Waveguide-to-microstrip transition, 37–43
 Weighted residual method, 20
 Wideband phase shift, 324–27
 Wilkinson coupler/combiner, 140
 YBCO. *See* Yttrium barium copper oxide
 Yttrium barium copper oxide, 147